Vol. 65 ■ No. 3 ■ March 2024

# JNM

## The Journal of Nuclear Medicine

**JNM Podcasts**
jnm.snmjournals.org/podcasts

The debut episode discussing FAP is online now!

**FEATURED ARTICLE**

Prostate-Specific Membrane Antigen–Targeted Radioguided Pelvic Lymph Node Dissection in Newly Diagnosed Prostate Cancer Patients with a Suspicion of Locoregional Lymph Node Metastases: The DETECT Trial. Melline G.M. Schilham et al. See page 423.

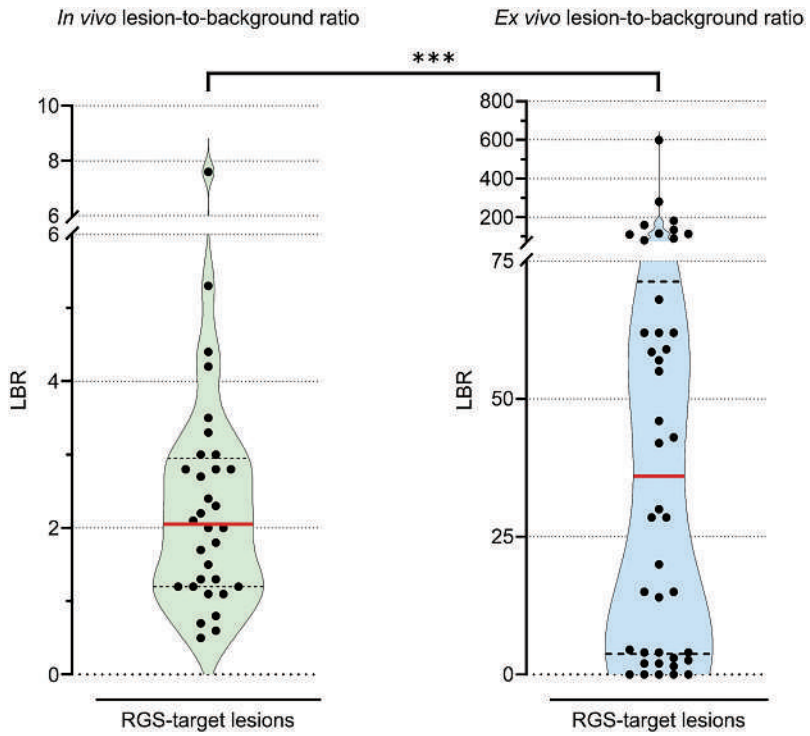


**Mapping fructolysis with [$^{18}$F]4-FDF:** Intracellular tracer trapping for PET elucidation of fructose metabolism. Alexia Kirby et al. See page 475.

SNMMI SOCIETY OF NUCLEAR MEDICINE & MOLECULAR IMAGING


# 2024 ACNM/SNMMI **HOT TOPICS** Webinar Series

SNMMI and ACNM are excited to announce the lineup for the 2024 Hot Topics Webinar Series. **These informative webinars will take place at 12:00 pm ET on the second Tuesday of each month and are complimentary for ACNM and SNMMI members.**

- **History of Nuclear Medicine Technology**
  On Demand | *Fred Fahey*
- **AI in Nuclear Medicine: State of the Union**
  On Demand | *Katherine Zukotynski*
- **Prostate Radioligand Therapy Prior to Chemotherapy**
  March 12 | *Oliver Sartor*
- **PET/MR for Pediatrics**
  April 9 | *Helen Nadel*
- **Evolving Landscape of Prostate Cancer Imaging**
  May 14 | *François Bénard*
- **The Evolution of PRRT for NET–Y90, Lu177, Ac225**
  June-SNMMI AM | *Lisa Bodei*
- **Advancing Precision Therapeutics in Dementia–How Does Imaging Fit In?**
  July 9 | *Sandra Black*
- **Contemporary Approach to PET Myocardial Perfusion Imaging**
  August 13 | *Panithaya Chareonthaitawee*
- **ER/PR/HER2-Targeted Imaging for Breast Cancer**
  September 10 | *Farrokh Dehdashti*
- **PET for Histiocytosis/ Erdheim Chester Disease**
  October 8 | *Sonia Mahajan*
- **What is New in Infection Imaging?**
  November 12 | *Ora Israel*
- **Prostate Cancer Imaging Agents–Is There a Difference?**
  December 10 | *Wolfgang Weber*

SNMMI SOCIETY OF NUCLEAR MEDICINE & MOLECULAR IMAGING

ACNM American College of Nuclear Medicine

Register today!

**www.acnmonline.org/webinars**

022024-20

JNM

Volume 65 • Number 3 • March 2024

## NEUROLOGY

### Clinical



## MOLECULAR IMAGING

### Basic



## AI/ADVANCED IMAGE ANALYSIS



## THE ILLUSTRATED POST



## LETTERS TO THE EDITOR



## IN MEMORIAM



## DEPARTMENTS

JNM The Journal of NUCLEAR MEDICINE

The Official Publication of **SNMMI**



**MISSION STATEMENT:** *The Journal of Nuclear Medicine* advances the knowledge and practice of molecular imaging and therapy and nuclear medicine to improve patient care through publication of original basic science and clinical research.

*JNM* (ISSN 0161-5505 [print]; ISSN 2159-662X [online]) is published monthly by SNMMI, 1850 Samuel Morse Drive, Reston, VA 20190-5316. Periodicals postage is paid at Herndon, VA, and additional mailing offices. Postmaster, send address changes to *The Journal of Nuclear Medicine,* 1850 Samuel Morse Drive, Reston, VA 20190-5316. The costs of publication of all nonsolicited articles in *JNM* were defrayed in part by the payment of page charges. Therefore, and solely to indicate this fact, these articles are hereby designated "advertisements" in accordance with 18 USC section 1734.

**DISCLOSURE OF COMMERCIAL INTEREST:** Johannes Czernin, MD, editor-in-chief of *The Journal of Nuclear Medicine,* has indicated that he is a founder of Sofie Biosciences and holds equity in the company and in intellectual property invented by him, patented by the University of California, and licensed to Sofie Biosciences. He is also a founder and board member of Trethera Therapeutics and holds equity in the company and in intellectual property invented by him, patented by the University of California, and licensed to Triangle. He also serves on the medical advisory board of Actinium Pharmaceuticals and on the scientific advisory boards of POINT Biopharma, RayzeBio, and Jubilant Pharma and is a consultant for Amgen. No other potential conflicts of interest were reported. Manuscripts submitted to *JNM* with potential conflicts are handled by a guest editor.

**EDITORIAL COMMUNICATIONS** should be sent to: Editor-in-Chief, Johannes Czernin, MD, *JNM* Office, SNMMI, 1850 Samuel Morse Drive, Reston, VA 20190-5316. Phone: (703) 326-1185; Fax: (703) 708-9018. To submit a manuscript, go to https://submit-jnm.snmjournals.org.

**BUSINESS COMMUNICATIONS** concerning permission requests should be sent to the publisher, SNMMI, 1850 Samuel Morse Drive, Reston, VA 20190-5316; (703) 708-9000; home page address: jnm.snmjournals.org. Subscription requests and address changes should be sent to Membership Department, SNMMI at the address above. Notify the Society of change of address and telephone number at least 30 days before date of issue by sending both the old and new addresses. Claims for copies lost in the mail are allowed within 90 days of the date of issue. Claims are not allowed for issues lost as a result of insufficient notice of change of address. For information on advertising, contact Team SNMMI (Kevin Dunn, Rich Devanna, and Charlie Meitner; (201) 767-4170; fax: (201) 767-8065; TeamSNMMI@cunnasso.com). Advertisements are subject to editorial approval and are restricted to products or services pertinent to nuclear medicine. Closing date is the first of the month preceding the date of issue.

**INDIVIDUAL SUBSCRIPTION RATES** for the 2024 calendar year are $665 within the United States and Canada; $714 elsewhere. Make checks payable to the SNMMI. CPC IPM Sales Agreement No. 1415158. Sales of individual back copies from 1999 through the current issue are available for $60 at http://www.snmmi.org/subscribe (subscriptions@snmmi.org; fax: (703) 667-5134). Individual articles are available for sale online at http://jnm.snmjournals.org.

**Discussions with leaders:** David Mankoff talked with mother and daughter Martine Piccart and Géraldine Gebhart about their careers as leaders in medical oncology and molecular imaging. . . . . *Page 337*

**Sequencing of SSR-targeted therapies:** Strosberg and colleagues examine evidence supporting use of somatostatin receptor–targeted treatments within the larger landscape of neuroendocrine tumor therapy and offer insights into patient selection, benefits/risks, and treatment sequencing. . . . . *Page 340*

**Precision oncology in breast cancer:** Jacene and colleagues provide an educational overview of current treatment paradigms and the expanding role of molecular imaging as a precision medicine biomarker for advanced breast cancer.. . . . *Page 349*

**Acute GvHD molecular imaging:** Bernardi and colleagues summarize current molecular imaging approaches for noninvasive detection of acute graft-versus-host disease, with a specific focus on PET, its integration into the clinical setting, and associated challenges. . . . . *Page 357*

**Rethinking RNT dosimetry:** Strosberg and colleagues offer perspective on the effectiveness of extrapolating external-beam–defined normal organ constraints to radionuclide therapy dosimetry and call for evidence-based strategies to improve personalized treatment. . . . . *Page 362*

**$^{68}$Ga-FAPI PET/CT accuracy in HNCUP:** Gu and colleagues investigate the potential of $^{68}$Ga-labeled fibroblast activation protein inhibitor PET/CT compared with that of $^{18}$F-FDG PET/CT for detection of primary tumors in patients with head and neck cancer of unknown primary. . . . . *Page 365*

**$^{68}$Ga-FAPI vs. $^{18}$F-FDG for oncologic PET:** Hirmas and colleagues report on a head-to-head comparison of $^{68}$Ga-labeled fibroblast activation protein inhibitor and $^{18}$F-labeled FDG PET across a range of tumor entities.. . . . . *Page 372*

**Imaging intraprostatic radiorecurrent disease:** Light and colleagues detail the results of a study of $^{68}$Ga-PSMA-11 PET/CT and multiparametric MRI in patients referred for radiorecurrence of prostate cancer. . . . . *Page 379*

**Site-specific $^{89}$Zr-pertuzumab:** Yeh and colleagues describe a first-in-humans PET study in human epidermal growth factor receptor 2–positive breast cancer, looking at the safety, biodistribution, and dosimetrics of this site-specifically labeled radioimmunoconjugate.. . . . . *Page 386*

**$^{68}$Ga-FAPI-LM3 PET in NPC:** Zhao and colleagues design and synthesize a heterobivalent fibroblast activation protein inhibitor molecule radiolabeled with $^{68}$Ga and evaluate its effectiveness in tumor xenografts and in patients with nasopharyngeal carcinoma. . . . . *Page 394*

**$^{225}$Ac-nimotuzumab in colon cancer models:** Tikum and colleagues assess the effectiveness of this anti–epidermal growth factor receptor antibody radioimmunoconjugate in both in vitro and in vivo colorectal cancer studies. . . . . *Page 402*

**Posttreatment SPECT/CT and PRRT:** Yadav and colleagues determine the impact of qualitative posttreatment imaging on management of patients with advanced neuroendocrine tumors undergoing $^{177}$Lu-DOTATATE peptide receptor radionuclide therapy. . . . . *Page 409*

**[$^{18}$F]FET-βAG-TOCA PET/CT in NET detection:** Dubash and colleagues report on a prospective, noninferiority comparison of [$^{18}$F]FET-βAG-TOCA PET/CT with [$^{68}$Ga]Ga-DOTA-peptide PET/CT in patients with neuroendocrine tumors, highlighting the advantages of an $^{18}$F-labeled tracer. . . . . *Page 416*

**PSMA-radioguided pelvic LN dissection:** Schilham and colleagues evaluate the safety and feasibility of $^{111}$In-PSMA–radioguided surgery in primary cancer patients with at least 1 suggestive lymph node on preoperative $^{18}$F-PSMA PET/CT. . . . . *Page 423*

**Perspective on DETECT trial:** Maurer and colleagues offer commentary on a report in this issue of *JNM* on a prospective clinical trial of PSMA-radioguided surgery in primary prostate cancer. . . . . *Page 430*

**$^{177}$Lu-rhPSMA-10.1 in prostate cancer:** Dierks and colleagues detail efficacy and safety findings from dosimetry studies on this $^{177}$Lu-labeled agent in a small group of patients with PSMA-positive metastatic prostate cancer. . . . . *Page 432*

**$^{177}$Lu-PSMA international survey:** Farolfi and colleagues report on responses to a survey documenting operational differences and similarities among $^{177}$Lu-PSMA treatment centers and comment on the need for standardization/harmonization among theranostic sites. . . . . *Page 438*

**DAT SPECT with multipinhole collimators:** Buchert and colleagues explore the potential to reduce scan duration in dopamine transporter SPECT when using a second-generation multiple-pinhole collimator designed for brain SPECT, with improved count sensitivity and spatial resolution. . . . . *Page 446*

**Longitudinal [$^{18}$F]PI-2620 PET in AD:** Oh and colleagues use this second-generation tau PET tracer to investigate changes over time in cortical tau accumulation and associated cognitive decline in early- and late-onset Alzheimer disease. . . . . *Page 453*

**$^{18}$F-SynVesT-2 brain kinetics:** Drake and colleagues evaluate the fast brain kinetics, test–retest reproducibility, and extent of specific binding of this recently developed synaptic vesicle glycoprotein 2A PET ligand. . . . . *Page 462*

**Triggered seizures for ictal SPECT**: Barlatey and colleagues use $^{99m}$Tc-HMPAO SPECT to image planned seizures triggered by direct stimulation of epileptic networks via stereotactic electroencephalography electrodes in patients with left temporal epilepsy. . . . . *Page 470*

**Mapping fructolysis with [$^{18}$F]4-FDF:** Kirby and colleagues generate a radiodeoxyfluorinated fructose analog, evaluate its metabolic flux in vitro, and assess preclinical PET imaging for mapping fructose metabolism in models of cancer and systemic inflammation. . . . . *Page 475*

**$^{161}$Tb- and $^{177}$Lu-Labeled GRPR antagonists:** Holzleitner and colleagues compare preclinical performances of the gastrin-releasing peptide receptor antagonists RM2 and AMTG, each labeled with $^{177}$Lu and $^{161}$Tb, to elucidate potential benefits of the Auger-electron–emitting radionuclide $^{161}$Tb. . . . . *Page 481*

**Task-based evaluation segmentation:** Liu and colleagues investigate whether evaluating PET segmentation algorithms based on task-agnostic figures of merit yields interpretations consistent with evaluation on clinically relevant quantitative tasks. . . . . *Page 485*

**CCK$_2$R-directed PET in MTC:** Viering and colleagues provide an illustrated case report on postoperative [$^{68}$Ga]Ga-DOTA-CCK-66 PET/CT in a patient with medullary thyroid cancer to assess eligibility for cholecystokinin-2 receptor–directed radioligand therapy. . . . . *Page 493*

# Molecular Imaging in Breast Cancer

## Martine Piccart and Géraldine Gebhart Talk with David Mankoff About 2 Generations of Research

Géraldine Gebhart[1], Martine Piccart[1], and David Mankoff[2]

*[1]Université Libre de Bruxelles, Hôpital Universitaire de Bruxelles, Institut Jules Bordet, Brussels, Belgium; and [2]Perelman School of Medicine, University of Pennsylvania, Philadelphia, Pennsylvania*

David Mankoff, MD, PhD, the Matthew J. Wilson Professor of Research Radiology at the University of Pennsylvania Perelman School of Medicine (Philadelphia) and an associate editor for *The Journal of Nuclear Medicine* (*JNM*), talked with breast cancer oncology and molecular imaging (MI) leaders Martine Piccart, MD, PhD, and Géraldine Gebhart, MD, PhD. Dr. Piccart, an honorary professor of oncology at the Université Libre de Bruxelles (ULB; Belgium) and scientific director at Institut Jules Bordet (Brussels), and Dr. Gebhart, Oncologic Clinical Director of the Nuclear Medicine Department of the Hôpital Universitaire de Bruxelles, are mother and daughter.

Dr. Piccart is an international leader in medical oncology with a focus on breast cancer research. In 1999, she cofounded the Breast International Group (BIG), the largest network of groups conducting clinical breast cancer research in the world. She is a member of the Belgian Royal Academy of Medicine and served as president of the European Cancer Organization, the European Organization for the Research and Treatment of Cancer, and the European Society for Medical Oncology (ESMO). Dr. Piccart also served on the American Society of Clinical Oncology (ASCO) board, as well as on the board of the American Association for Cancer Research. She has published over 600 peer-reviewed articles and received multiple awards.

Dr. Gebhart is a rising star in oncologic MI and focuses on breast cancer research. She studied medicine at ULB. In 2009, with a solid background in internal medicine, she began her work in nuclear medicine under the supervision of Patrick Flamen, MD, PhD, at the Institut Bordet. She focused on MI as an emerging field in oncology. Her PhD project was on the contribution of MI to early evaluation of response to anti–human epidermal growth factor receptor 2 (anti-HER2) agents in breast cancer. She played lead roles in seminal studies testing PET as a predictive and response biomarker for HER2-targeted breast cancer, including the NEOALTTO and ZEPHIR trials, and was a key contributor to the recently published PHERGAIN study. Gebhart has been recognized with *JNM* Editor's Choice Award for 2013, the Alavi–Mandell Award for a *JNM* article published in 2013, and the 2023 Marie Curie Award from the European Association of Nuclear Medicine (EANM).

***Dr. Mankoff:*** *Martine and Géraldine, it is a pleasure to speak to you as leaders in breast cancer oncology and MI, as well as medical oncology and nuclear medicine collaborators in breast cancer research at Jules Bordet and in leading international trials. As an oncologist and as an imager who both work in breast cancer, what do you see as the greatest areas of need in which MI can impact breast cancer treatment and outcomes?*

**Martine Piccart, MD, PhD (left), and Géraldine Gebhart, MD, PhD (right)**

**Dr. Piccart:** The last decade has witnessed the successful development of several new anticancer drugs for the 3 main breast cancer subtypes: cyclin-dependent kinase 4 and 6 inhibitors and selective estrogen receptor downregulators (SERDs) for luminal disease (2/3 of patients); anti-HER2 monoclonal antibodies, tyrosine kinase receptor inhibitors, and antibody–drug conjugates (ADCs) for HER2-positive disease (~15% of patients); and immune checkpoint inhibitors and ADCs for triple-negative breast cancer (TNBC; ~12% of patients). These agents are quite expensive, and there is a huge unmet need for clinically useful biomarkers allowing a better selection of patients likely to benefit from

Published online Feb. 8, 2024.

DOI: 10.2967/jnumed.124.267461

these drugs. As a result, many patients are over- or undertreated. In advanced breast cancer, disease heterogeneity is increasingly recognized as a limiting factor for the efficacy of targeted drugs. This is, in our view, an area where MI could play a critical role.

**Dr. Gebhart:** The ZEPHIR imaging study in advanced HER2 breast cancer nicely showed how HER2 PET can predict the antitumor efficacy of the ADC trastuzumab emtansine: only patients showing a strong and generalized uptake of $^{89}$Z-trastuzumab across their metastatic sites enjoyed a prolonged time to treatment failure.

***Dr. Mankoff:*** *What do you see as the biggest hurdles for moving breast cancer MI from early-stage studies into clinical practice?*

**Dr. Piccart:** As noted, MI should be viewed as a powerful biomarker with the potential to reduce overtreatment as well as undertreatment. This great potential is largely ignored by the community of medical oncologists. Indirect proof of this is the very limited space given to MI in famous cancer congresses such as those of ASCO or ESMO.

**Dr. Gebhart:** On the other hand, the MI community should invest more time and energy in the full validation of MI as a biomarker, meaning going beyond analytic/clinical validity and demonstrating clinical utility. This can be best achieved through a much-reinforced crosstalk and collaboration between these 2 worlds. This type of research, however, is not inexpensive and will not always be viewed as attractive by the pharmaceutical industry, given that it could restrict their drug market. Hopefully, governments and charities will understand the value of MI, because it is likely that the cost of sophisticated imaging will be offset by the ability to prescribe the right expensive anticancer drugs for the right patient at the right time.

***Dr. Mankoff:*** *Breast cancer was one of the earliest areas in which individualized targeted systemic therapy was used. Targeted therapy remains a key part of breast cancer treatment, with an increasing array of drugs matched to specific targets and with new diagnostic agents that can image these targets. Despite advances in imaging breast cancer targets, such as the estrogen receptor (ER) and HER2, there seems to be relatively slow acceptance of these tools in the breast cancer community. What are the barriers for imagers and oncologists to more widespread acceptance and use of imaging biomarkers to help guide targeted therapy in breast cancer?*

**Dr. Gebhart:** Again, prospective trials designed to robustly demonstrate the clinical utility of an imaging modality are quite expensive and not necessarily welcomed by pharma. In addition, these trials must be conducted with rigor: standardization of the imaging test must be performed in all participating centers. They should ideally be supported by data on cost effectiveness to be able to refute the frequently heard argument that PET scans are "too expensive."

**Dr. Piccart:** From the viewpoint of an experienced clinical trialist, the high level of multidisciplinary expertise required might discourage many research groups. What is needed is a few enthusiastic teams able to perform these trials with the needed quality and statistical power.

***Dr. Mankoff:*** *You both provide excellent examples of team players at the intersection of breast cancer and imaging. On a related topic, radiopharmaceutical therapy has had a large impact on some endocrine-related cancers, such as thyroid, neuroendocrine, and prostate cancers. However, radiopharmaceutical therapy has had only a limited role in breast cancer thus far. Is this due to the number of other effective systemic therapies for breast cancer, or are there other considerations limiting the use of radiopharmaceutical therapy for breast cancer? What do you see as the areas in which radiopharmaceutical therapy might be helpful?*

**Dr. Piccart:** It is true that radiopharmaceutical therapy for breast cancer is in its infancy. We can see 4 potential explanations: the "wave" of new effective drugs developed for this disease in the last 10 years; the recognition that breast cancer is not a single disease but a collection of "subtypes," which complicates the design and conduct of trials exploring innovative therapies; the marked heterogeneity in target expression, which has been particularly well documented in HER2-positive breast cancer; and the extra burden that may be imposed by health authorities on trials with radiopharmaceuticals for safety reasons, sometimes associated with limited access to PET devices.

**Dr. Gebhart:** We are hopeful that this situation will improve in the near future, particularly for 2 clinical scenarios: advanced TNBC, a very aggressive subtype with poor clinical outcomes despite the introduction of immunotherapy, and brain metastases.

> ˜We really need the kind of evidence that oncologists look for in drug trials: well-powered and randomized trials to demonstrate that patients treated with the help of MI guidance do better than patients who do not receive MI . . . .This is an area in which the model of European–U.S. collaborative trials that has changed treatment practice could support changes in diagnostic practice.˝

Our colleagues from the Vrije Universiteit Brussel are exploring HER2-targeted nanobodies for refractory brain metastases, and we are currently investigating targets such as prostate-specific membrane antigen or, in the near future, fibroblast-activation protein inhibitor in advanced TNBC.

***Dr. Mankoff:*** *Géraldine, you have led groundbreaking trials of novel MI approaches for breast cancer in European studies that have often been well ahead of those in the United States. What's the secret to your ability to implement and perform these trials?*

**Dr. Gebhart:** First, I have greatly benefited from a fantastic research team in the nuclear medicine department at my institute, including Dr. Flamen, an enthusiastic head of unit who trusted me from the beginning. I started my research in collaboration with Zéna Wimana, PhD, MBA, without whose great expertise in the radiopharmacy field I don't think I could have managed an ambitious imaging trial such as ZEPHIR. And I work with 2 brilliant bioengineers, Julie Gaye and Thomas Guiot. Second, with the help of my mother I was introduced to a network of cancer centers in Belgium and The Netherlands with prime interests in novel MI approaches as powerful tools for development of "precision oncology." In particular, I found great partners in Groningen: for example, Elisabeth de Vries, MD, PhD, and Carolien Schröder, MD, PhD, both medical oncologists with long-standing interest in MI. I also enjoyed working closely with the team of C. Willemien Menke-van der Houven van Oordt, MD, in Amsterdam. Finally, I had the chance to finalize the primary endpoint of the ZEPHIR

study with Magdalena Mileva. Results were presented in the recent EANM congress and recognized with the Marie Curie Award.

***Dr. Mankoff:*** *You've had the good fortune to work with other outstanding leaders in the field and have the skill and diplomacy to encourage team science. We in the United States can learn from your success. Martine, you are among the world's leaders in breast cancer oncology and medical oncology in general. What advice can you give us on how best to use PET MI to help oncologists care for their breast cancer patients?*

**Dr. Piccart:** There are 2 families of new drugs that my colleagues are excited about: the ER-targeting agents (SERDs, proteolysis-targeting chimeras, etc.) and the ADCs, which show an exponential growth with more than 100 compounds in development and groundbreaking results already shown for a few of them. It should not be too difficult to convince oncologists that MI will increase our ability to identify the good (or poor) candidates for these agents as well as clarify how best to sequence them with the goal of extending disease control and overall survival. These are very promising new classes of drugs, especially for metastatic breast cancer, where MI assessment of target expression and early response to therapy could be attractive to oncologists.

***Dr. Mankoff:*** *Partnerships between imagers and oncologists have been important in advancing MI research and translation of new methods to the oncology clinic. In addition to being leaders in your fields working together, you have unique insights on that partnership as mother and daughter. How has this partnership influenced your research and practice and impacted your careers?*

**Dr. Piccart:** When my daughter decided to specialize in nuclear medicine, I realized how little I knew about the specialty and decided to learn about its multiple facets. It literally opened my eyes.

**Dr. Gebhart:** Living close to a breast medical oncologist is a huge advantage, because I heard my mother complaining about the extremely slow development of predictive biomarkers in her field beyond ER and HER2. This unique context has been instrumental in our desire to bring the 2 communities—the medical oncologists and nuclear medicine specialists—closer to each other.

**Both:** … and through beneficial complicity!

***Dr. Mankoff:*** *Very interesting! This is a wonderful and unique scenario that has benefited breast cancer research and patients. One last question, primarily directed to you, Martine: In my experience in leading studies testing MI biomarkers as adjuncts to tissue biomarkers to help direct individualized breast cancer therapy, there seems to be some hesitancy among oncologists to accept imaging as a way to select a therapy. In the United States, we now have an approved agent to image ER expression, [$^{18}$F]-fluoroestradiol ([$^{18}$F]-FES), with 2 level 1 evidence studies from Korea and Europe showing the equivalence of PET imaging findings and biopsy results. Documentation of ER expression by biopsy is a widely accepted gold standard for selecting ER-targeted therapy; however, many oncologists remain reluctant to use [$^{18}$F]-FES PET results to direct therapy. What will it take to change their minds?*

**Dr. Piccart:** That's an interesting question. We have to be much more ambitious when we collaborate between the 2 specialties (oncology and imaging). We really have to come up with powerful studies that will show that using MI will result in better outcomes for our patients. The benefit of having imaging biomarkers that can avoid therapy when the intended target is absent, stop a treatment early on that's never going to work, or identify a treatment that is going to be quite effective is appealing. But we need to have strong evidence to support these uses of MI—not just the small trials with 30–60 patients that are commonly published. We really need the kind of evidence that oncologists look for in drug trials: well-powered and randomized trials to demonstrate that patients treated with the help of MI guidance do better than patients who do not receive MI. This is a big challenge, because it means conducting prospectively powered multicenter studies in which the use of a diagnostic imaging test is randomized and where imaging and image interpretation are standardized and therapeutic choices are harmonized across centers. You will likely need several hundred patients for this type of study. It will not be easy, but, with collaboration and funding, it can be done. This is an area in which the model of European–U.S. collaborative trials that has changed treatment practice could support changes in diagnostic practice.

***Dr. Mankoff:*** *I agree 100%. Let's figure out how to do this! Géraldine and Martine, thank you for the fascinating discussion and chance to talk to 2 leaders in the field with a passion for imaging and breast cancer research. I hope we can follow up on Martine's suggestion to generate international trials to provide level 1 evidence of the ability of MI to improve breast cancer patient outcomes.*

# Sequencing of Somatostatin-Receptor–Based Therapies in Neuroendocrine Tumor Patients

Jonathan R. Strosberg[1], Taymeyah Al-Toubah[1], Ghassan El-Haddad[2], Diane Reidy Lagunes[3], and Lisa Bodei[4]

[1]*Department of GI Oncology, Moffitt Cancer Center and Research Institute, Tampa, Florida;* [2]*Department of Radiology, Moffitt Cancer Center and Research Institute, Tampa, Florida;* [3]*Department of Medicine, Memorial Sloan Kettering Cancer Center, New York, New York; and* [4]*Department of Radiology, Memorial Sloan Kettering Cancer Center, New York, New York*

Most well-differentiated neuroendocrine tumors (NETs) express high levels of somatostatin receptors, particularly subtypes 2 and 5. Somatostatin analogs (SSAs) bind to somatostatin receptors and are used for palliation of hormonal syndromes and control of tumor growth. The long-acting SSAs octreotide long-acting release and lanreotide are commonly used in the first-line metastatic setting because of their tolerable side effect profile. Radiolabeled SSAs are used both for imaging and for treatment of NETs. $^{177}$Lu-DOTATATE is a β-emitting radiolabeled SSA that has been proven to significantly improve progression-free survival among patients with progressive midgut NETs and is approved for treatment of metastatic gastroenteropancreatic NETs. A key question in management of patients with gastroenteropancreatic and lung NETs is the sequencing of $^{177}$Lu-DOTATATE in relation to other systemic treatments (such as everolimus) or liver-directed therapies. This question is particularly complicated given the heterogeneity of NETs and the near absence of randomized trials comparing active treatment options. This state-of-the-art review examines the evidence supporting use of somatostatin-receptor–targeted treatments within the larger landscape of NET therapy and offers insights regarding optimal patient selection, assessment of benefit versus risk, and treatment sequencing.

**Key Words:** radionuclide therapy; PRRT; lanreotide; neuroendocrine tumors; octreotide; somatostatin analogs

**J Nucl Med 2024; 65:340–348**
DOI: 10.2967/jnumed.123.265706

Somatostatin receptor (SSTR) expression is a key feature of well-differentiated neuroendocrine tumors (NETs). Since the 1980s, somatostatin analogs (SSAs) have been used to palliate hormonal syndromes associated with NETs and inhibit tumor growth (*1*). More recently, radiolabeled SSAs have been developed for diagnostic and therapeutic purposes. $^{111}$In(In)-pentetreotide scintigraphy (OctreoScan; Curium) was the first widely used SSTR-based scan for staging NETs and characterizing the degree of SSTR expression (*2*,*3*). In the past decade, it has been supplanted by SSTR PET imaging, including $^{68}$Ga(Ga)-DOTATATE and $^{64}$Cu(Cu)-DOTATATE PET scans, which have substantially higher sensitivity and image resolution (*4*,*5*).

β-emitting radiolabeled SSAs, such as $^{177}$Lu(Lu)-DOTATATE or DOTATOC, deliver therapeutic doses of β-radiation (high-energy electrons) to SSTR-expressing tumors and can result in tumor shrinkage in addition to substantial improvement in progression-free survival (PFS). Newer forms of peptide receptor radionuclide therapy (PRRT) include α-emitting radiolabeled SSAs such as $^{212}$Pb(Pb)-DOTAMTATE and $^{225}$Ac(Ac)-DOTATATE (*6*,*7*). By emitting much larger particles (2 protons and neutrons) with higher linear energy transfer over an ultrashort particle range, α-emitters can induce double-strand DNA damage and a higher level of cytotoxicity with an improved therapeutic index.

In this state-of-the-art review, we evaluate the role of SSTR-based treatments in patients with advanced NETs of the gastrointestinal tract, pancreas, and lungs. We discuss evidence regarding the efficacy of conventional and radiolabeled SSAs, risks and toxicities, patient selection, and the sequencing of these therapies within the larger therapeutic landscape. Additional topics include early use of PRRT, retreatment with PRRT after progression, and combination approaches.

## OVERVIEW OF GASTROENTEROPANCREATIC AND LUNG NETS

NETs can be categorized on the basis of multiple features, including primary site, stage, differentiation, grade, and SSTR expression. Well-differentiated NETs morphologically resemble endocrine cells of origin. Poorly differentiated neuroendocrine carcinomas are highly aggressive malignancies that tend to express SSTRs weakly and are outside the scope of this review. Most well-differentiated NETs are low-grade (Ki-67 index, 0%–2%) or intermediate-grade (Ki-67, 3%–20%) but can occasionally be high-grade (Ki-67 > 20%). For lung NETs, the terms *typical carcinoid* versus *atypical carcinoid* persist and correspond roughly to low and intermediate grades, respectively (*8*).

Metastatic NETs of different primary sites are quite distinct. Midgut (typically ileal or ileocecal) primaries are the most common and tend to be slow-growing. They are characterized by a high propensity to metastasize to mesenteric lymph nodes (often with desmoplastic features), liver, and, less commonly, peritoneum, ovaries, and bone (*9*). Metastatic midgut NETs often secrete serotonin, among other vasoactive substances, resulting in diarrhea, flushing, and damage to right heart valves, a condition known as carcinoid syndrome. Metastatic pancreatic NETs also tend to metastasize to the liver and are generally more aggressive than midgut NETs (*10*). Approximately 10%–20% are associated with hormonal syndromes such as Zollinger–Ellison syndrome (gastrinoma) or Verner–Morrison syndrome (vasoactive intestinal peptide tumors). Metastatic rectal NETs are rare, often aggressive, and hormonally nonfunctioning (unassociated with a syndrome). Metastatic lung NETs are variable

Received Aug. 18, 2023; revision accepted Dec. 20, 2023.
For correspondence or reprints, contact Jonathan R. Strosberg (jonathan.strosberg@moffitt.org).
Published online Jan. 18, 2024.

in behavior: most are nonfunctioning, although some can produce serotonin or adrenocorticotropic hormone.

SSTR expression also varies by primary site. Midgut NETs almost universally express SSTRs, particularly SSTR subtypes 2 and 5, which are targeted by SSAs. Expression is a bit more heterogeneous in pancreatic NETs, particularly higher-grade tumors, and quite heterogeneous in lung NETs, especially atypical ones that can often be SSTR-negative (*11*).

## SOMATOSTATIN ANALOG THERAPY

The SSAs octreotide and lanreotide are often prescribed as a first-line systemic treatment for metastatic NETs. They are considered ideal first-line therapies because of their favorable side effect profile and efficacy, particularly in patients with hormone-related symptoms such as carcinoid syndrome. In a landmark phase II study of short-acting octreotide in patients with carcinoid syndrome, diarrhea and flushing were palliated in 88% of patients, and 5-hydroxyindoleacitic acid was reduced by more than 50% in 72% of patients (*12*). Subsequent small studies demonstrated equivalent palliation in rarer hormonal syndromes associated with gastrinomas, vasoactive intestinal peptide tumors, and glucagonomas. An exception was insulinomas, in which the effect of SSAs was inconsistent, sometimes leading to improvement and other times exacerbating hypoglycemia because of suppression of the counterregulatory hormone glucagon (*13*).

After the approval of octreotide for syndrome control, several single-arm studies suggested that SSA therapy may inhibit tumor growth despite the absence of objective radiographic responses. These preliminary observations led to 2 randomized phase III studies designed to test the so-called antiproliferative effect of SSAs. The first of these studies was the PROMID trial, in which 85 patients with metastatic midgut NETs were randomized to 30 mg of long-acting-release octreotide every 4 wk versus placebo, with a primary endpoint of time to progression (*14*). The study was strongly positive, with an improvement of median time to progression from 6 mo on placebo to 14.5 mo with octreotide (hazard ratio [HR], 0.34; $P < 0.001$).

Subsequently, the CLARINET trial randomized 204 patients with nonfunctioning enteropancreatic NETs to receive 120 mg of lanreotide versus placebo with a primary endpoint of PFS (*15*). Eligibility requirements included a tumor Ki-67 of less than 10% and SSTR expression on imaging. This trial also met its primary endpoint, with significant improvement in PFS (18 mo on placebo, not reached with lanreotide at the time of primary analysis; HR, 0.47; $P < 0.001$). The HR for progression in the midgut NET population of the CLARINET trial was nearly identical to the HR on the PROMID trial, suggesting that the 2 drugs are likely quite similar in efficacy.

There was no trend for overall survival (OS) benefit in either the PROMID or the CLARINET study (*16*,*17*). However, it is essential to note that patients crossed over from the placebo arm to SSA on progression, and neither study was sufficiently powered to evaluate for OS.

Side effects of both drugs tend to be minor. Abdominal cramping and nausea tend to occur more often early in treatment. Steatorrhea is a common side effect that can be palliated with pancreatic enzymes. Gallstone formation is also common but rarely of clinical significance.

As a result of the proven inhibitory effect of SSAs and their benign toxicity profile, either octreotide or lanreotide is typically recommended as first-line treatment for metastatic NETs, both for inhibition of tumor growth and for palliation of hormonal syndromes in patients with functioning tumors. There is little evidence that SSAs inhibit tumor growth in patients with SSTR-negative tumors, although they can still be used to palliate hormonal syndromes. There is also limited evidence to support their use in patients with relatively aggressive tumors (e.g., Ki-67 > 10%) (*18*). However, it is not unreasonable to try SSAs alone in patients who lack significant symptoms related to tumor burden. It is also important to note that high-level evidence for tumor control exists only for gastroenteropancreatic NETs since neither the PROMID nor the CLARINET trial enrolled patients with lung NETs. In addition, a randomized trial of lanreotide versus placebo in lung NETs (SPINET trial) closed prematurely for poor accrual (*19*). Nevertheless, it is reasonable to consider SSA therapy in lung NETs, especially if all tumors express SSTR. In tumors with significant symptoms related to tumor burden, or in patients with higher-grade or more aggressive biology, other therapies described below should also be considered in the first-line setting.

**NOTEWORTHY**

- SSAs (octreotide and lanreotide) are often the first-line treatment for patients with metastatic well-differentiated, somatostatin-receptor–positive NETs.
- PRRT with $^{177}$Lu-DOTATATE is used in patients with progressive, somatostatin-receptor–positive metastatic disease; however, optimal sequencing of treatments vis-à-vis other systemic and liver-directed therapies, in the absence of dedicated randomized trials, depends on many factors such as primary site, grade, symptom burden, and distribution of metastatic disease.
- Not all patients with metastatic NETs are appropriate candidates for PRRT: particular attention is needed in patients with high-grade or lung NETs (in which SSTR expression is often heterogeneous) and patients with high-burden peritoneal disease (which may increase risk of bowel obstruction)
- Emerging studies (e.g., the COMPETE and COMPOSE trials) will help determine how to best sequence PRRT compared with other standards of care.
- The future of PRRT may include combinations of systemic therapy with PRRT, α-emitting particles, and SSTR antagonists.

## PRRT

Since the 1990s, labeling SSAs with radioactive isotopes has been devised to deliver targeted radiation to SSTR-expressing NETs. Radiolabeled SSAs belong to a broader category of treatment known as PRRT. The first generation of PRRT used high doses of $^{111}$In-pentetreotide (*3*). The Auger electrons emitted by this isotope were weakly cytotoxic and rarely led to radiographic responses. The high-energy β-emitting isotopes $^{90}$Y and $^{177}$Lu were next to be tested, using DOTA as the linker and either octreotide (DOTATOC) or octreotate (DOTATATE) as the peptide in most studies (*20–22*). Octreotate has an exceptionally high affinity to SSTR subtype 2, strongly expressed in NETs. Early studies using $^{90}$Y-peptides reported high rates of severe, grade 3 or 4, nephrotoxicity related to the high tissue penetration and energy of the β-particles (maximum range, 11 mm; maximum energy, 2.27 MeV), despite renal

protection with positively charged prophylactic amino acid infusions consisting of arginine and lysine (*20*,*22*). $^{177}$Lu was less nephrotoxic because of its shorter particle range and lower β-energy (maximum range, 2 mm; maximum energy, 0.5 MeV).

Both $^{90}$Y- and $^{177}$Lu-based radiolabeled SSAs resulted in radiographic responses and relatively long median durations of PFS. Several large institutional databases reported on outcomes in hundreds of treated patients (*23*–*25*). One prospectively defined cohort study from Erasmus Hospital in The Netherlands described outcomes in 443 patients with NETs originating in the pancreas, gastrointestinal tract, lung, and unknown primary. Treatment consisted of a fixed administered activity of $^{177}$Lu-DOTATATE, 7.4 GBq (200 mCi), administered every 8 wk for 4 treatments with prophylactic arginine/lysine. An objective response rate of 39% was reported for the entire cohort, with a median PFS of 29 mo and a median OS of 63 mo. It is important, however, to note that these outcomes were analyzed only among patients who had received at least 3 cycles of therapy (*23*).

A prospective phase I/II study conducted at the Institute of European Oncology in Milan enrolled 51 NET patients with escalating administered activities of $^{177}$Lu-DOTATATE (*26*). Among 46 patients assessable for response, an objective response rate of 33% was reported with a median time to progression of 36 mo.

The NETTER-1 trial was the first prospective randomized phase III study of a radiolabeled SSA (*27*). In this trial, 231 patients with metastatic low- and intermediate-grade, SSTR-positive midgut NETs progressing on standard-dose octreotide were randomized to receive 4 cycles of $^{177}$Lu-DOTATATE plus standard-dose octreotide or high-dose octreotide (60 mg). The primary endpoint was PFS. The study met its primary endpoint with a clinically and statistically significant improvement in PFS on the $^{177}$Lu-DOTATATE arm (HR, 0.21; $P < 0.0001$). An objective response rate of 18% was observed on the $^{177}$Lu-DOTATATE arm versus 3% in the control group. On final analysis, the median investigator-assessed PFS was 25 mo with $^{177}$Lu-DOTATATE versus 8.5 mo with high-dose octreotide (*28*). A nonsignificant 12-mo improvement in OS was reported (48 mo vs. 36.3 mo), likely attenuated by crossover to PRRT in over a third of patients from the control arm (*29*).

Although the NETTER-1 trial enrolled patients with midgut NETs only, $^{177}$Lu-DOTATATE was approved for all gastroenteropancreatic NETs by the Food and Drug Administration and the European Medicines Agency on the basis of both the NETTER-1 trial and the Rotterdam database study. Since the trial was conducted only in patients progressing on SSAs, the current recommendations are to use $^{177}$Lu-DOTATATE after progression and not in the first-line setting.

## SIDE EFFECTS OF PRRT

Cytopenias are a common side effect of PRRT. Although lymphopenia is the most frequent toxicity, it is rarely of clinical significance, and opportunistic infections are seldom observed, as B lymphocytes are the main subpopulation involved (*30*). On the NETTER-1 trial, grade 3 or 4 anemia, neutropenia, and thrombocytopenia occurred in 0%, 1%, and 2% of $^{177}$Lu-DOTATATE–treated patients. In the Rotterdam study, grade 3/4 anemia, thrombocytopenia, and leukopenia occurred in 5%, 4%, and 5% of patients, respectively (*23*).

Myelodysplastic syndrome and acute leukemia are among the most serious potential complications of PRRT. The combined incidence of myelodysplastic syndrome and acute myeloid leukemia is approximately 2%–3%, and the prognosis is poor among patients who experience treatment-related myelodysplasia (*23*,*24*). In addition, some evidence indicates that concurrent or sequential administration of cytotoxic chemotherapy may increase the risk of myelodysplastic syndrome or acute leukemia (*31*–*33*). Current research focuses on early detection or screening for chronic myelotoxicity evaluating the role of clonal hematopoiesis analysis.

Renal toxicity is a known consequence of $^{90}$Y-based PRRT but appears negligible among patients receiving $^{177}$Lu-DOTATATE with coadministration of amino acids, if they have an acceptable renal function (e.g., estimated glomerular filtration rate $> 30$ mL/min) (*23*,*24*,*29*,*34*). The NETTER-1 study allowed for a controlled assessment of renal function over time. Study patients randomized to $^{177}$Lu-DOTATATE demonstrated no evidence of a long-term decline in renal function compared with high-dose octreotide (*29*).

The risk of bowel obstruction appears to be increased in patients with peritoneal or mesenteric carcinomatosis receiving PRRT (*35*). In some instances, radiation peritonitis can lead to a frozen abdomen with an irreversible intestinal blockage. There is some evidence that prophylactic corticosteroids may diminish radiation-induced tumor inflammation and complications arising from such inflammatory changes. However, some experts caution against administering steroids before treatment because steroids can reduce SSTR expression.

## PRRT AND QUALITY OF LIFE

Large cohort studies have demonstrated that treatment with $^{177}$Lu-DOTATATE can improve health-related quality of life and global health status in patients with gastroenteropancreatic and lung NETs (*36*). A small retrospective study of patients with midgut NETs and carcinoid syndrome treated with $^{177}$Lu-DOTATATE demonstrated statistically significant reductions in flushing and diarrhea compared with baseline (*37*). On the NETTER-1 trial, analysis of health-related quality of life using European Organization for Research and Treatment of Cancer questionnaires demonstrated a statistically significant delay in the decline of quality of life in key metrics including global health, physical functioning, pain, and diarrhea on the $^{177}$Lu-DOTATATE arm compared with control. Differences in flushing were not statistically significant between the 2 arms of the study (*38*). However, another analysis of symptom diaries on NETTER-1 indicated that $^{177}$Lu-DOTATATE was associated with a decline in the number of days per month with flushing, diarrhea, and abdominal pain, compared with high-dose octreotide (*39*).

## PRRT IN LUNG NETS

Lung NETs appear to express SSTR relatively heterogeneously; consequently, the number of patients eligible for PRRT is low compared with small-bowel or pancreatic NETs (*11*,*40*–*42*). However, when patients are appropriately selected, outcomes can be comparable to the results of treatment in gastroenteropancreatic NETs (*43*). $^{177}$Lu-DOTATATE is not approved by regulatory authorities for advanced lung NETs but is recommended by guidelines (*44*).

## PRRT IN HIGH-GRADE NETS

Research on PRRT in high-grade NETs is relatively limited. The NETTER-1 study was restricted to patients with grade 1 and 2 tumors (Ki-67 $< 20\%$). However, some retrospective studies have indicated benefits among patients with a Ki-67 of up to 30%–40% (*45*). Beyond that, median PFS durations tend to be short.

Therefore, when treating patients with high-grade NETs, ensuring that all tumors express SSTR strongly is crucial. Although not mandatory, obtaining dual $^{18}$F-FDG and DOTATATE PET scans can help ensure that all hypermetabolic tumors also express SSTRs and is in fact considered standard practice in many institutions to determine whether a more aggressive component of disease exists that should be treated with an alternate therapy.

## PREDICTIVE MARKERS

PRRT is the archetype of a theranostic treatment, with radiolabeled SSAs used for diagnosis and therapy. Not surprisingly, data indicate that the degree of SSTR expression correlates with objective radiologic response. The Krenning scale is used to quantify the degree of radiotracer uptake on $^{111}$In(In)-pentetreotide scintigraphy: grade 1 indicates tumoral uptake below the normal liver, grade 2 indicates uptake equivalent to the liver, grade 3 indicates uptake above the liver, and grade 4 indicates avidity above splenic uptake (*46*). A minimum Krenning grade 2 uptake on measurable lesions is considered a threshold for PRRT, and higher degrees of uptake correlate with response. DOTATATE PET scans are more sensitive, and SUVs greater than normal liver are considered a minimum requirement for treatment. Some studies suggest that SUVs double that of the normal liver are predictive of response (*47*). A blood RNA-based biomarker in development, the PRRT predictive quotient, integrates a gene expression score with Ki-67 to predict, at baseline, the clinical benefit (disease stabilization or response vs. progression) with $^{177}$Lu-DOTATATE treatment (*48*). The PRRT predictive quotient was studied in prospective clinical trials in Europe and the United States and demonstrated 96% accuracy in predicting PRRT response (*49*).

## SEQUENCING SSTR-BASED THERAPIES

A key question in managing patients with metastatic NETs is how to best sequence therapies. This issue is complicated because NETs are extremely heterogeneous cancers for which a uniform algorithmic approach is particularly unsuitable. Moreover, until recently, there have been virtually no prospective randomized studies comparing active therapies. Existing trials evaluate primarily PFS and are highly underpowered to assess differences in OS. Thus, recommendations on treatment sequencing are derived from low-level evidence. Table 1 provides a summary of key randomized clinical trials.

**TABLE 1**
Randomized NET Clinical Trials

| Trial | NET type | Patients treated (*n*) | PFS (mo) | OS (mo) | Objective response rate |
|---|---|---|---|---|---|
| PROMID | Midgut NETs | 85 (42 octreotide; 43 placebo) | 14.3 (octreotide) vs. 6 (placebo) (HR, 0.34; $P < 0.0005$) | Not reported; (HR, 0.81, $P = 0.77$) | 2% in both arms |
| CLARINET | Grade 1 and 2 GEP NETs + unknown primary | 204 (101 lanreotide; 103 placebo) | Not reached (lanreotide) vs. 18 (placebo) (HR, 0.47; $P < 0.001$) | Not reported | Not reported |
| ECOG 2211 | Grade 1 and 2 pancreatic NETs | 133 (65 TEM; 68 CAPTEM) | 14.4 (TEM) vs. 22.7 (CAPTEM) (HR, 0.58; $P = 0.022$) | 53.8 (TEM) vs. 58.7 (CAPTEM) (HR, 0.82; $P = 0.42$) | 33.7% TEM; 39.7% CAPTEM |
| Sunitinib | Pancreatic NETs | 171 (86 sunitinib; 85 placebo) | 12.6 (sunitinib) vs. 5.8 (placebo) (HR, 0.32; $P < 0.0005$) | 38.6 (sunitinib) vs. 29.1 (placebo) (HR, 0.73; $P = 0.094$) | 9.3% sunitinib; 0% placebo |
| OCLURANDOM | Pancreatic NETs | 84 (41 PRRT; 43 sunitinib) | 20.7 (PRRT) vs. 11 (sunitinib) | Not reported | Not reported |
| NETTER-1 | Grade 1 and 2 midgut NETs | 223 (111 PRRT; 112 high-dose octreotide) | 28.4 (PRRT) vs. 8.5 (high-dose octreotide) | 48 (PRRT) vs. 36.3 (high-dose octreotide) (HR, 0.84; $P = 0.30$) | 18% PRRT; 3% high-dose octreotide |
| RADIANT-2* | Carcinoid syndrome NETs | 429 (200 everolimus; 203 placebo + octreotide) | 16.4 (everolimus) vs. 11.3 (control) (HR, 0.77; $P = 0.026$) | Not reported | 2.5% everolimus; 1.9% control |
| RADIANT-3 | Grade 1 and 2 pancreatic NETs | 410 (207 everolimus; 203 placebo) | 11 (everolimus) vs. 4.6 (placebo) (HR, 0.35; $P < 0.001$) | Not reported | 5% everolimus; 2% placebo |
| RADIANT-4 | Grade 1 and 2 gastrointestinal and lung NETs (nonfunctional) | 302 (205 everolimus; 97 placebo + best supportive care) | 11.0 (everolimus) vs. 3.9 (control) (HR, 0.48; $P < 0.0005$) | Not reported | 2% everolimus; 1% control |

*RADIANT-2 PFS statistical significance was set to 0.0246 and was 0.026.
GEP = gastroenteropancreatic; TEM = temozolomide; CAPTEM = capecitabine and temozolomide.

As noted, we recommend that patients with newly diagnosed metastatic grade 1 or 2 SSTR-positive gastroenteropancreatic NETs be treated with an SSA in the first line. The basis for this is that both octreotide and lanreotide have a proven inhibitory effect on tumor progression and carry a low risk of significant toxicity. A minority of patients may be eligible for cytoreductive surgery. Patients with low symptom and tumor burden and who lack a hormonal syndrome may be eligible for watchful waiting rather than active treatment. In such cases, SSAs can be started after progression. As indicated above, there have been no completed randomized trials of SSAs for patients with metastatic lung NETs; however, evidence suggests that SSAs can be used to treat SSTR-positive tumors, particularly in patients with relatively unaggressive disease.

Evidence for SSA monotherapy in patients with relatively aggressive tumors (e.g., Ki-67 > 10%) is limited. However, octreotide or lanreotide can be considered if the tumor or symptom burden is relatively low. The NETTER-2 study evaluates first-line $^{177}$Lu-DOTATATE versus high-dose octreotide in tumors with a Ki-67 of 10%–55% (NCT03972488).

Beyond first-line treatment, options depend on the primary site. Small-bowel (midgut) NETs are relatively resistant to most systemic therapies (*50*). Most tyrosine kinase inhibitors and cytotoxic drugs have demonstrated lower response rates in midgut NETs than in pancreatic NETs (*51*). A randomized phase III study of everolimus plus octreotide versus placebo plus octreotide in patients with a history of carcinoid syndrome (RADIANT 2) did not meet its primary endpoint of improvement in PFS (*52*). Given the fact that most cases of carcinoid syndrome originate in midgut NETs, everolimus appears to be relatively ineffective in this population.

On the other hand, liver-directed therapies, such as hepatic transarterial embolization, appear to be quite effective in midgut NETs, although evidence derives primarily from small retrospective studies (*53–56*). Since the liver is the dominant site of metastatic disease, liver-directed therapies represent the main second-line alternative to PRRT in patients with metastatic midgut NETs. There is currently no high-level evidence favoring a particular method of transarterial embolization, with data suggesting similar responses to bland embolization, chemoembolization, or radioembolization. There are also no randomized studies comparing any mode of embolization with PRRT. Thus, decisions on sequencing embolic therapy versus $^{177}$Lu-DOTATATE are individualized, depending on the degree of hepatic versus extrahepatic tumor burden, disease progression sites, SSTR expression, and patient preference (Fig. 1).

Patients with pancreatic NETs have the largest number of approved or guideline-recommended therapies. Beyond first-line SSAs, systemic options include everolimus, sunitinib, temozolomide, or streptozocin-based chemotherapy regimens, and $^{177}$Lu-DOTATATE. Approval of everolimus was based on the RADIANT 3 study, in which patients with progressive metastatic pancreatic NETs were randomized to everolimus versus placebo (*57*). Despite response rates of less than 10%, the study showed statistically significant improvement in PFS (median, 11.0 vs. 4.6 mo; HR, 0.35; $P < 0.001$). Toxicities include oral aphthous ulcers, pneumonitis, hyperglycemia, fatigue, and immunosuppression. Approval of sunitinib was based on a phase III trial in which patients with progressive metastatic pancreatic NETs were randomized to sunitinib versus placebo (*58*). The outcomes were remarkably similar to RADIANT 3, with statistically significant improvement in PFS (median, 11.4 vs. 5.5 mo; HR, 0.42; $P < 0.001$) and an objective response rate of 9% with sunitinib. Side effects of sunitinib include fatigue, hypertension, diarrhea, palmar–plantar erythrodysesthesia, and increased risk of cardiovascular events.

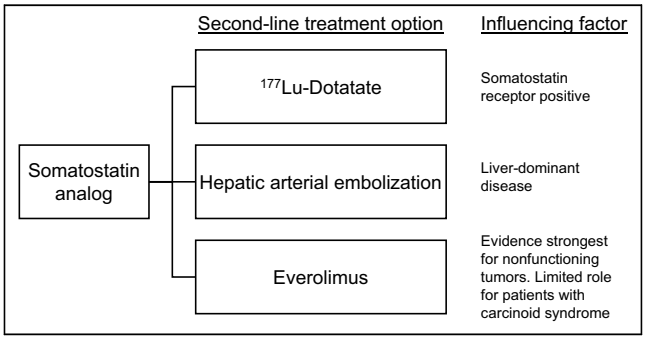


**FIGURE 1.** Second-line options for patients with metastatic, SSTR-positive, progressive midgut NET after SSA.

The capecitabine/temozolomide chemotherapy regimen is associated with much higher objective radiographic response rates of approximately 50% (*59*). In the randomized phase II ECOG2211 trial, capecitabine/temozolomide was compared with single-agent temozolomide in patients with progressive pancreatic NETs (*60*). Median PFS was 22.7 mo with capecitabine/temozolomide (vs. 14.4 mo with temozolomide; $P = 0.02$), and the confirmed radiographic response rate was 40%. This regimen is relatively well tolerated, with the main toxicities consisting of cytopenias.

The sequencing of therapies beyond first-line SSAs is particularly complicated for patients with SSTR-positive pancreatic NETs. The OCLURANDOM trial was among the first prospective trials to randomize patients to 2 active treatments: $^{177}$Lu-DOTATATE versus sunitinib (*61*). Although this randomized phase II study of 84 patients was too underpowered to allow for statistical comparison of the 2 arms, the differences in outcomes favoring $^{177}$Lu-DOTATATE were stark: a median PFS of 20.7 mo (90% CI, 17.2–23.7) with $^{177}$Lu-DOTATATE versus 11 mo (8.8–12.4) with sunitinib. This study strongly suggests (although it does not prove) that second-line $^{177}$Lu-DOTATATE is a superior option to sunitinib for progressive pancreatic NETs. The larger phase III COMPETE study, which compares $^{177}$Lu-DOTATOC with everolimus in progressive nonfunctioning gastroenteropancreatic NETs, has completed accrual, but results are still pending.

It is important to note that liver embolization is also an option for patients with liver-dominant pancreatic NETs. Most guidelines do not currently recommend a particular sequence of therapies for patients with metastatic pancreatic NETs (*62*). However, for patients with extrahepatic disease and strong SSTR expression, $^{177}$Lu-DOTATATE represents an option that likely has the least adverse impact on patient quality of life. Median PFS almost certainly exceeds outcomes with everolimus or sunitinib. The advantage of PRRT compared with capecitabine/temozolomide chemotherapy is less certain. For patients with high tumor and symptom burden who require rapid cytoreduction, chemotherapy with capecitabine/temozolomide (or other cytotoxic regimens) may be preferred because of the rapid responses and the ability to initiate treatment quickly (Fig. 2). The capecitabine/temozolomide regimen is also appropriate for patients with well-differentiated grade 3 pancreatic NETs (*63–66*).

For metastatic lung NETs, everolimus is the only therapy approved by regulatory authorities on the basis of the phase III RADIANT 4 trial in which patients with nonfunctioning gastrointestinal and lung NETs were randomized to everolimus versus

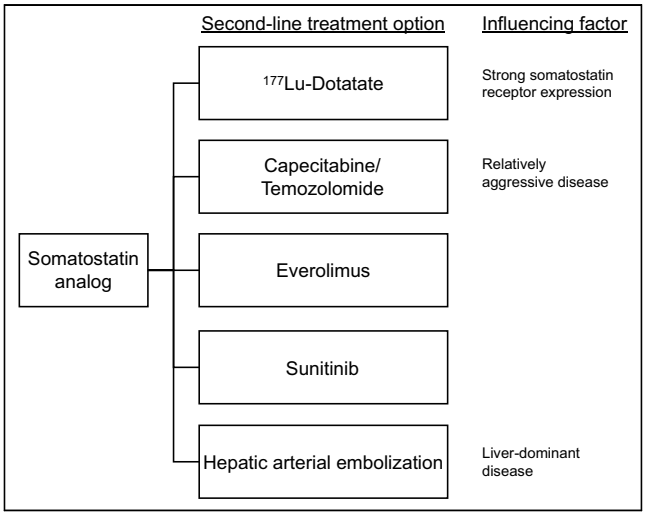


**FIGURE 2.** Second-line options for patients with metastatic, SSTR-positive, progressive pancreatic NET after SSA.

placebo (*67*). The study, which included a plurality of lung NETs, demonstrated an improvement in median PFS from 3.9 mo on placebo to 11.0 mo with everolimus (HR, 0.48; $P < 0.001$). Nonrandomized studies suggest that median PFS is likely higher with $^{177}$Lu-DOTATATE in patients with SSTR-positive lung NETs (*43*). However, $^{177}$Lu-DOTATATE is not approved by regulatory authorities for lung NETs. Some guidelines recommend $^{177}$Lu-DOTATATE only after progression or intolerance of everolimus based on a higher level of evidence supporting the latter drug. A randomized phase II study comparing $^{177}$Lu-DOTATATE with everolimus in metastatic lung NETs is open (NCT04665739).

For patients with other uncommon primary sites (e.g., rectum, stomach, or duodenum), the main alternative to PRRT is everolimus, also based on the RADIANT 4 study. The COMPETE study will help determine the optimal sequence of systemic therapies in patients with these tumor types (NCT03049189). As with other primary sites, liver embolization represents an option for patients with unresectable, liver-dominant disease (Fig. 3).

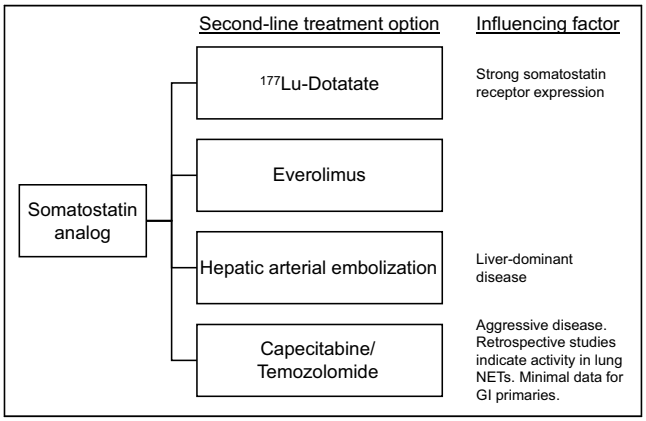


**FIGURE 3.** Second-line options for patients with metastatic, SSTR-positive, progressive nonmidgut gastrointestinal or lung NET after SSA. GI = gastrointestinal.

## SSAS BEYOND PROGRESSION

In patients with hormonally functional tumors, the SSA octreotide or lanreotide is typically continued indefinitely beyond progression through multiple lines of treatment to control hormonal syndromes. Even patients with suboptimal control of symptoms such as flushing or diarrhea may derive some benefit from these drugs compared with discontinuation.

A more controversial question is whether to continue SSAs beyond progression in patients with nonfunctional tumors. This question is particularly salient among patients receiving PRRT. On the NETTER-1 trial, which enrolled patients with functional and nonfunctional tumors, all patients in the $^{177}$Lu-DOTATATE arm continued standard-dose octreotide despite having progressed on this drug before enrollment. Retrospective studies have yielded data supporting this practice: one study showed markedly prolonged PFS and OS in patients who continued SSA during or after PRRT compared with those who stopped (*68*). However, confounding variables probably substantially impact nonrandomized studies such as these. For example, patients who progress rapidly on SSAs are more likely to discontinue the drug than patients with mild progression. A small, randomized trial comparing maintenance octreotide versus observation after PRRT showed no PFS benefit from maintenance SSA (*69*). Therefore, we can say that there is currently no compelling evidence to support maintenance SSA after progression in patients with nonfunctioning tumors.

## CONTINUING SSA IN FUNCTIONING TUMORS WHILE ON PRRT

Patients with carcinoid syndrome or other hormonal symptoms typically continue octreotide or lanreotide while receiving PRRT. In many studies, including NETTER-1, long-acting SSAs were stopped more than 6 wk before each PRRT cycle, and short-acting octreotide was stopped more than 24 h before treatment. The rationale for this practice was the concern that cold SSAs would compete with radiolabeled SSAs for SSTR binding. However, numerous recent studies have called this practice into question by demonstrating that the impact of SSAs on SSTR imaging is minimal and that SSAs can preferentially decrease the SSTR expression of normal organs compared with NETs. Food and Drug Administration guidance recommends suspending long-acting SSA for 4 wk or more before PRRT treatment. Therefore, one potential option is to administer a long-acting SSA after each treatment and then 4 wk later, precisely at the midpoint between the 8-wk cycle of $^{177}$Lu-DOTATATE. However, it is debatable whether there is a need for any precise synchronization of SSAs and PRRT.

## FIRST-LINE PRRT

Because of risks associated with PRRT, including myelodysplastic syndrome or acute leukemia, using $^{177}$Lu-DOTATATE as first-line therapy is generally not recommended. Exceptions may include patients with a high tumor burden in whom early aggressive treatment is necessary. The NETTER 2 trial is investigating $^{177}$Lu-DOTATATE versus high-dose octreotide in patients with gastroenteropancreatic NETs and high-intermediate–grade or high-grade disease (Ki-67, 10%–55%) (NCT03972488). The COMPOSE study is also evaluating the early use of PRRT with $^{177}$Lu-DOTATOC in patients with relatively high-grade tumors (NCT04919226). The primary endpoint of both trials is PFS. However, it will be challenging to ascertain whether the earlier use of PRRT impacts the ultimate endpoint of OS.

There are also small retrospective series describing the neoadjuvant use of PRRT, particularly in patients with borderline-resectable pancreatic NETs or patients with oligometastases in whom some tumor shrinkage is necessary to enable surgery with negative margins (*70*). However, no evidence supports postoperative adjuvant PRRT to eradicate micrometastases. Indeed, the relatively long particle range of β-emitters such as $^{177}$Lu-DOTATATE may be poorly suited for targeting submillimeter tumors.

### AGGRESSIVE TRANSFORMATION OF NETS

The transformation of metastatic NETs from relatively slow-growing to highly aggressive is a phenomenon that has been documented, particularly for pancreatic NETs. It is possible (but not certain) that cytotoxic drugs such as chemotherapy or PRRT increase the risk of this occurrence by inducing somatic intratumoral mutations or by selectively killing the more differentiated population. Indeed, one case series documented the transformation of well-differentiated NETs to poorly differentiated neuroendocrine carcinomas in 7 of 152 patients (5%) who had received PRRT (*71*). All 7 had pancreatic NETs (among 39 patients with pancreatic NETs) and had also received prior temozolomide chemotherapy. It is unclear whether this phenomenon should influence treatment sequencing for patients with pancreatic NETs.

Once transformation develops, prognosis is poor, and treatments used in low-intermediate–grade tumors are of doubtful efficacy, even if SSTR expression is retained. For very aggressive disease, platinum-based regimens such as carboplatin/etoposide or 5-fluorouracil/oxaliplatin are often recommended (*72*).

### RETREATMENT, COMBINATION THERAPY, AND NOVEL PRRT AGENTS

Retreatment with PRRT beyond the standard 4 doses is recommended for patients who experience benefit from initial treatment, ideally those who have at least 12 mo of disease control after therapy (*73–76*). The lifetime maximum of standard-dose PRRT is typically 6–8 cycles. This practice is currently based on retrospective data; there is currently a trial exploring this in a randomized fashion (retreatment with $^{177}$Lu-DOTATATE vs. everolimus; NCT05773274).

There have been several studies exploring the combination of PRRT with various cytotoxic and targeted therapies. The combination of capecitabine/temozolomide and PRRT with either $^{177}$Lu-DOTATATE or $^{90}$Y-DOTATOC has been explored in several small studies, either sequentially or in a sandwich fashion, and although response rates tend to be higher than for monotherapy, there have not been significant improvements in PFS or OS compared with PRRT alone (*31*,*33*,*77*). Other avenues are exploring combinations of PRRT with radiosensitizing drugs (*78–80*).

In addition to combination therapies, novel PRRT agents—α-emitters and SSTR antagonists—are being explored in several trials (*6*,*7*,*81*). α-emitters allow for a more targeted therapy because of their shorter penetration range and higher linear energy, and SSTR antagonists can occupy more binding sites with a lower dissociation rate than SSTR analogs, leading to higher tumor uptake and lower risk of damage to surrounding healthy tissue. There are several ongoing clinical trials, phase II and phase III, exploring α-PRRT with $^{212}$Pb-DOTAMTATE and $^{225}$Ac-DOTATATE in the PRRT-naïve and -refractory settings. A clinical trial with the SSTR antagonist $^{177}$Lu-satoreotide tetraxetan recently reported a response rate of 21% and median PFS of 28 mo, warranting further evaluation of the drug in future studies (*82*).

### CONCLUSION

The SSAs octreotide and lanreotide represent a standard first-line therapy for patients with metastatic, unresectable well-differentiated gastroenteropancreatic NETs, both for control of tumor growth and for inhibition of hormonal syndrome. They are also probably effective in patients with SSTR-positive lung NETs, although high-level evidence is lacking. The radiolabeled SSA $^{177}$Lu-DOTATATE is an appropriate therapy for patients with SSTR-positive disease progression in the second-line setting or beyond. Evidence from a phase III trial exists only for midgut NETs (NETTER-1). More recently, a randomized phase II study (OCLURANDOM) demonstrated substantially improved PFS with $^{177}$Lu-DOTATATE versus sunitinib, although the small sample size precluded definitive conclusions. When PRRT is initiated, SSAs should be continued in most patients with carcinoid syndrome or other hormonal syndromes. Evidence for continuation of SSAs beyond progression in nonfunctioning NETs is weak.

As of now, no phase III trials have been completed comparing PRRT with other standard, approved systemic or liver-directed therapies. Decisions on treatment sequencing should be individualized on the basis of disease and patient factors. Multidisciplinary tumor boards at centers of expertise, incorporating perspectives from relevant medical specialties (e.g., medical oncology, interventional radiology, surgery, and nuclear medicine), can help to optimize treatment strategies.

The future of PRRT in NETs will likely include α-emitting isotopes that have the potential to improve the therapeutic index of radiolabeled SSAs. Prospective clinical trials will help determine whether these agents will replace the β-emitter $^{177}$Lu-DOTATATE or whether they will be used primarily for patients who are refractory to standard PRRT.

### DISCLOSURE

Jonathan Strosberg is a consultant or on the speaker bureau for Novartis and Ipsen and receives institutional research funding from RayzeBio and Alphamedix. Ghassan El-Haddad is a consultant for Bayer, Boston Scientific Corp., Novartis, Terumo, and NorthStar. Diane Reidy Lagunes is a consultant for Novartis and receives institutional research funding from Novartis, Ipsen, and Merck. Lisa Bodei is a consultant (uncompensated) for Novartis, Ipsen, ITM, Point Biopharma, RayzeBio, Precirix, and Great Point Partners and receives institutional research funding from Novartis. No other potential conflict of interest relevant to this article was reported.

## REFERENCES


1. Öberg K, Lamberts SW. Somatostatin analogues in acromegaly and gastroenteropancreatic neuroendocrine tumours: past, present and future. *Endocr Relat Cancer.* 2016;23:R551–R566.
2. Krenning EP, Kwekkeboom DJ, Oei HY, et al. Somatostatin-receptor scintigraphy in gastroenteropancreatic tumors. An overview of European results. *Ann N Y Acad Sci.* 1994;733:416–424.
3. Valkema R, De Jong M, Bakker WH, et al. Phase I study of peptide receptor radionuclide therapy with [In-DTPA]octreotide: the Rotterdam experience. *Semin Nucl Med.* 2002;32:110–122.
4. Kjaer A, Binderup T, Johnbeck C, et al. $^{64}$Cu-DOTATATE somatostatin receptor imaging in neuroendocrine tumors: experience from 500 patients at Copenhagen ENETS Center of Excellence [abstract]. *J Nucl Med.* 2019;60(suppl 1):504.
5. Deppen SA, Liu E, Blume JD, et al. Safety and efficacy of $^{68}$Ga-DOTATATE PET/CT for diagnosis, staging, and treatment management of neuroendocrine tumors. *J Nucl Med.* 2016;57:708–714.
6. Ballal S, Yadav MP, Tripathi M, Sahoo RK, Bal C. Survival outcomes in metastatic gastroenteropancreatic neuroendocrine tumor patients receiving concomitant

$^{225}$Ac-DOTATATE–targeted α-therapy and capecitabine: a real-world-scenario management-based long-term outcome study. *J Nucl Med.* 2023;64:211–218.
7. Delpassand ES, Tworowska I, Esfandiari R, et al. Targeted α-emitter therapy with $^{212}$Pb-DOTAMTATE for the treatment of metastatic SSTR-expressing neuroendocrine tumors: first-in-humans dose-escalation clinical trial. *J Nucl Med.* 2022;63: 1326–1333.
8. Fillinger J. Pathology of lung neuroendocrine tumors [in Hungarian]. *Magy Onkol.* 2018;62:83–89.
9. Strosberg JR, Weber JM, Feldman M, Coppola D, Meredith K, Kvols LK. Prognostic validity of the American Joint Committee on Cancer staging classification for midgut neuroendocrine tumors. *J Clin Oncol.* 2013;31:420–425.
10. Strosberg JR, Cheema A, Weber J, Han G, Coppola D, Kvols LK. Prognostic validity of a novel American Joint Committee on Cancer staging classification for pancreatic neuroendocrine tumors. *J Clin Oncol.* 2011;29:3044–3049.
11. Al-Toubah T, Montilla-Soler J, El-Haddad G, Haider M, Strosberg J. Somatostatin receptor expression in lung neuroendocrine tumors: an analysis of DOTATATE PET scans. *J Nucl Med.* 2023;64:1895–1898.
12. Kvols LK, Moertel CG, O'Connell MJ, Schutt AJ, Rubin J, Hahn RG. Treatment of the malignant carcinoid syndrome. Evaluation of a long-acting somatostatin analogue. *N Engl J Med.* 1986;315:663–666.
13. Eriksson B, Oberg K. Summing up 15 years of somatostatin analog therapy in neuroendocrine tumors: future outlook. *Ann Oncol.* 1999;10(suppl 2):S31–S38.
14. Rinke A, Muller HH, Schade-Brittinger C, et al. Placebo-controlled, double-blind, prospective, randomized study on the effect of octreotide LAR in the control of tumor growth in patients with metastatic neuroendocrine midgut tumors: a report from the PROMID Study Group. *J Clin Oncol.* 2009;27:4656–4663.
15. Caplin ME, Pavel M, Cwikla JB, et al. Lanreotide in metastatic enteropancreatic neuroendocrine tumors. *N Engl J Med.* 2014;371:224–233.
16. Caplin ME, Pavel M, Phan AT, et al. Lanreotide autogel/depot in advanced enteropancreatic neuroendocrine tumours: final results of the CLARINET open-label extension study. *Endocrine.* 2021;71:502–513.
17. Rinke A, Wittenberg M, Schade-Brittinger C, et al. Placebo-controlled, double-blind, prospective, randomized study on the effect of octreotide LAR in the control of tumor growth in patients with metastatic neuroendocrine midgut tumors (PROMID): results of long-term survival. *Neuroendocrinology.* 2017;104:26–32.
18. Merola E, Alonso Gordoa T, Zhang P, et al. Somatostatin analogs for pancreatic neuroendocrine tumors: any benefit When Ki-67 is ≥10%? *Oncologist.* 2021;26: 294–301.
19. Baudin E, Horsch D, Singh S, et al. Lanreotide autogel/depot (LAN) in patients with advanced bronchopulmonary (BP) neuroendocrine tumors (NETs): results from the phase III SPINET study [abstract]. *Ann Oncol.* 2021;32(suppl 5):S906.
20. Otte A, Herrmann R, Heppeler A, et al. Yttrium-90 DOTATOC: first clinical results. *Eur J Nucl Med.* 1999;26:1439–1447.
21. Kwekkeboom DJ, Teunissen JJ, Bakker WH, et al. Radiolabeled somatostatin analog [$^{177}$Lu-DOTA$^{0}$,Tyr$^{3}$]octreotate in patients with endocrine gastroenteropancreatic tumors. *J Clin Oncol.* 2005;23:2754–2762.
22. Imhof A, Brunner P, Marincek N, et al. Response, survival, and long-term toxicity after therapy with the radiolabeled somatostatin analogue [$^{90}$Y-DOTA]-TOC in metastasized neuroendocrine cancers. *J Clin Oncol.* 2011;29:2416–2423.
23. Brabander T, van der Zwan WA, Teunissen JJM, et al. Long-term efficacy, survival, and safety of [$^{177}$Lu-DOTA$^{0}$,Tyr$^{3}$]octreotate in patients with gastroenteropancreatic and bronchial neuroendocrine tumors. *Clin Cancer Res.* 2017;23:4617–4624.
24. Bodei L, Kidd M, Paganelli G, et al. Long-term tolerability of PRRT in 807 patients with neuroendocrine tumours: the value and limitations of clinical factors. *Eur J Nucl Med Mol Imaging.* 2015;42:5–19.
25. Baum RP, Kulkarni HR, Singh A, et al. Results and adverse events of personalized peptide receptor radionuclide therapy with $^{90}$yttrium and $^{177}$lutetium in 1048 patients with neuroendocrine neoplasms. *Oncotarget.* 2018;9:16932–16950.
26. Bodei L, Cremonesi M, Grana CM, et al. Peptide receptor radionuclide therapy with $^{177}$Lu-DOTATATE: the IEO phase I-II study. *Eur J Nucl Med Mol Imaging.* 2011;38:2125–2135.
27. Strosberg J, El-Haddad G, Wolin E, et al. Phase 3 trial of $^{177}$Lu-Dotatate for midgut neuroendocrine tumors. *N Engl J Med.* 2017;376:125–135.
28. Kunz P, Benson A, Bodei L, et al. The phase 3 NETTER-1 study of $^{177}$Lu-DOTATATE in patients with midgut neuroendocrine tumors: updated progression-free survival analyses. Presented at: 2021 NANETS' Multidisciplinary NET Medical Symposium; November 4–6, 2021; Chicago, IL.
29. Strosberg JR, Caplin ME, Kunz PL, et al. $^{177}$Lu-Dotatate plus long-acting octreotide versus high-dose long-acting octreotide in patients with midgut neuroendocrine tumours (NETTER-1): final overall survival and long-term safety results from an open-label, randomised, controlled, phase 3 trial. *Lancet Oncol.* 2021;22:1752–1763.
30. Sierra ML, Agazzi A, Bodei L, et al. Lymphocytic toxicity in patients after peptide-receptor radionuclide therapy (PRRT) with $^{177}$Lu-DOTATATE and $^{90}$Y-DOTATOC. *Cancer Biother Radiopharm.* 2009;24:659–665.
31. Kesavan M, Grover P, Lam WS, Claringbold PG, Turner JH. Long-term hematologic toxicity of $^{177}$Lu-octreotate-capecitabine-temozolomide therapy of GEPNET. *Endocr Relat Cancer.* 2021;28:521–527.
32. Fröss-Baron K, Garske-Roman U, Welin S, et al. $^{177}$Lu-DOTATATE therapy of advanced pancreatic neuroendocrine tumors heavily pretreated with chemotherapy: analysis of outcome, safety, and their determinants. *Neuroendocrinology.* 2021; 111:330–343.
33. Al-Toubah T, Pelle E, Strosberg J. Risk of myelodysplastic syndrome/acute leukemia with sequential capecitabine/temozolomide and $^{177}$Lu-Dotatate. Endocrine Abstracts website. https://www.endocrine-abstracts.org/ea/0089/ea0089c7. Published 2022. Accessed January 3, 2024.
34. Bergsma H, Konijnenberg MW, van der Zwan WA, et al. Nephrotoxicity after PRRT with $^{177}$Lu-DOTA-octreotate. *Eur J Nucl Med Mol Imaging.* 2016;43:1802–1811.
35. Strosberg JR, Al-Toubah T, Pelle E, et al. Risk of bowel obstruction in patients with mesenteric or peritoneal disease receiving peptide receptor radionuclide therapy. *J Nucl Med.* 2021;62:69–72.
36. Khan S, Krenning EP, van Essen M, Kam BL, Teunissen JJ, Kwekkeboom DJ. Quality of life in 265 patients with gastroenteropancreatic or bronchial neuroendocrine tumors treated with [$^{177}$Lu-DOTA$^{0}$,Tyr$^{3}$]octreotate. *J Nucl Med.* 2011;52: 1361–1368.
37. Zandee WT, Brabander T, Blažević A, et al. Symptomatic and radiological response to $^{177}$Lu-DOTATATE for the treatment of functioning pancreatic neuroendocrine tumors. *J Clin Endocrinol Metab.* 2019;104:1336–1344.
38. Strosberg J, Wolin E, Chasen B, et al. Health-related quality of life in patients with progressive midgut neuroendocrine tumors treated with $^{177}$Lu-dotatate in the phase III NETTER-1 trial. *J Clin Oncol.* 2018;36:2578–2584.
39. Strosberg JR, Srirajaskanthan R, El-Haddad G, et al. Symptom diaries of patients with midgut neuroendocrine tumors treated with $^{177}$Lu-DOTATATE. *J Nucl Med.* 2021;62:1712–1718.
40. Prosperi D, Carideo L, Russo VM, et al. A systematic review on combined [$^{18}$F]FDG and $^{68}$Ga-SSA PET/CT in pulmonary carcinoid. *J Clin Med.* 2023;12: 3719.
41. Zidan L, Iravani A, Kong G, Akhurst T, Michael M, Hicks RJ. Theranostic implications of molecular imaging phenotype of well-differentiated pulmonary carcinoid based on $^{68}$Ga-DOTATATE PET/CT and $^{18}$F-FDG PET/CT. *Eur J Nucl Med Mol Imaging.* 2021;48:204–216.
42. Albano D, Dondi F, Bauckneht M, et al. The diagnostic and prognostic role of combined [$^{18}$F]FDG and [$^{68}$Ga]-DOTA-peptides PET/CT in primary pulmonary carcinoids: a multicentric experience. *Eur Radiol.* 2023;33:4167–4177.
43. Mariniello A, Bodei L, Tinelli C, et al. Long-term results of PRRT in advanced bronchopulmonary carcinoid. *Eur J Nucl Med Mol Imaging.* 2016;43:441–452.
44. Hope TA, Abbott A, Colucci K, et al. NANETS/SNMMI procedure standard for somatostatin receptor-based peptide receptor radionuclide therapy with $^{177}$Lu-DOTATATE. *J Nucl Med.* 2019;60:937–943.
45. Thang SP, Lung MS, Kong G, et al. Peptide receptor radionuclide therapy (PRRT) in European Neuroendocrine Tumour Society (ENETS) grade 3 (G3) neuroendocrine neoplasia (NEN): a single-institution retrospective analysis. *Eur J Nucl Med Mol Imaging.* 2018;45:262–277.
46. Forbes S, Baghdadi Y, Parkar F, Abraham T, Love C. Evaluating Ga-68 DOTATATE images: SUVmax vs Krenning score [abstract]. *J Nucl Med.* 2019;60(suppl 1):1535.
47. Kratochwil C, Stefanova M, Mavriopoulou E, et al. SUV of [$^{68}$Ga]DOTATOC-PET/CT predicts response probability of PRRT in neuroendocrine tumors. *Mol Imaging Biol.* 2015;17:313–318.
48. Bodei L, Kidd MS, Singh A, et al. PRRT genomic signature in blood for prediction of $^{177}$Lu-octreotate efficacy. *Eur J Nucl Med Mol Imaging.* 2018;45:1155–1169.
49. Bodei L, Raj N, Do RK, et al. Interim analysis of a prospective validation of 2 blood-based genomic assessments (PPQ and NETest) to determine the clinical efficacy of $^{177}$Lu-DOTATATE in neuroendocrine tumors. *J Nucl Med.* 2023;64:567–573.
50. Al-Toubah T, Morse B, Strosberg J. Efficacy of capecitabine and temozolomide in small bowel (midgut) neuroendocrine tumors. *Curr Oncol.* 2022;29:510–515.
51. Das S, Dasari A. Novel therapeutics for patients with well-differentiated gastroenteropancreatic neuroendocrine tumors. *Ther Adv Med Oncol.* 2021;13: 17588359211018047.
52. Pavel ME, Hainsworth JD, Baudin E, et al. Everolimus plus octreotide long-acting repeatable for the treatment of advanced neuroendocrine tumours associated with carcinoid syndrome (RADIANT-2): a randomised, placebo-controlled, phase 3 study. *Lancet.* 2011;378:2005–2012.

53. Touloupas C, Faron M, Hadoux J, et al. Long term efficacy and assessment of tumor response of transarterial chemoembolization in neuroendocrine liver metastases: a 15-year monocentric experience. *Cancers (Basel).* 2021;13:5366.
54. Strosberg JR, Cheema A, Kvols LK. A review of systemic and liver-directed therapies for metastatic neuroendocrine tumors of the gastroenteropancreatic tract. *Cancer Control.* 2011;18:127–137.
55. Barat M, Cottereau A-S, Kedra A, et al. The role of interventional radiology for the treatment of hepatic metastases from neuroendocrine tumor: an updated review. *J Clin Med.* 2020;9:2302.
56. Strosberg JR, El-Haddad G, Al-Toubah T, et al. Radioembolization versus bland or chemoembolization for liver-dominant neuroendocrine tumors: is it an either/or question? *J Nucl Med.* 2021;62:1669–1671.
57. Yao JC, Shah MH, Ito T, et al. Everolimus for advanced pancreatic neuroendocrine tumors. *N Engl J Med.* 2011;364:514–523.
58. Raymond E, Dahan L, Raoul JL, et al. Sunitinib malate for the treatment of pancreatic neuroendocrine tumors. *N Engl J Med.* 2011;364:501–513.
59. Al-Toubah T, Pelle E, Valone T, Haider M, Strosberg JR. Efficacy and toxicity analysis of capecitabine and temozolomide in neuroendocrine neoplasms. *J Natl Compr Canc Netw.* 2021;20:29–36.
60. Kunz PL, Graham NT, Catalano PJ, et al. A randomized study of temozolomide or temozolomide and capecitabine in patients with advanced pancreatic neuroendocrine tumors (ECOG-ACRIN E2211). *J Clin Oncol.* 2022:101200JCO2201013.
61. Baudin E, Walter TA, Beron A, et al. First multicentric randomized phase II trial investigating the antitumor efficacy of peptide receptor radionuclide therapy with $^{177}$lutetium-octreotate (OCLU) in unresectable progressive neuroendocrine pancreatic tumor: results of the OCLURANDOM trial [abstract]. *Ann Oncol.* 2022;33(suppl 7):S954.
62. Shah MH, Goldner WS, Benson AB, et al. Neuroendocrine and adrenal tumors, version 2.2021, NCCN clinical practice guidelines in oncology. *J Natl Compr Canc Netw.* 2021;19:839–868.
63. Chan DL, Bergsland EK, Chan JA, et al. Temozolomide in grade 3 gastroenteropancreatic neuroendocrine neoplasms: a multicenter retrospective review. *Oncologist.* 2021;26:950–955.
64. Arrivi G, Verrico M, Roberto M, et al. Capecitabine and temozolomide (CAPTEM) in advanced neuroendocrine neoplasms (NENs): a systematic review and pooled analysis. *Cancer Manag Res.* 2022;14:3507–3523.
65. Eads JR, Catalano PJ, Fisher GA, et al. Randomized phase II study of platinum and etoposide (EP) versus temozolomide and capecitabine (CAPTEM) in patients (pts) with advanced G3 non-small cell gastroenteropancreatic neuroendocrine neoplasms (GEPNENs): ECOG-ACRIN EA2142 [abstract]. *J Clin Oncol.* 2022;40(suppl):4020.
66. Jeong H, Shin J, Jeong JH, et al. Capecitabine plus temozolomide in patients with grade 3 unresectable or metastatic gastroenteropancreatic neuroendocrine neoplasms with Ki-67 index <55%: single-arm phase II study. *ESMO Open.* 2021;6:100119.
67. Yao JC, Fazio N, Singh S, et al. Everolimus for the treatment of advanced, non-functional neuroendocrine tumours of the lung or gastrointestinal tract (RADIANT-4): a randomised, placebo-controlled, phase 3 study. *Lancet.* 2016;387:968–977.
68. Yordanova A, Wicharz MM, Mayer K, et al. The role of adding somatostatin analogues to peptide receptor radionuclide therapy as a combination and maintenance therapy. *Clin Cancer Res.* 2018;24:4672–4679.
69. Syguła A, Ledwon A, Hasse-Lazar K, et al. In patients with well-differentiated neuroendocrine tumours, there is no apparent benefit of somatostatin analogues after disease control by peptide receptor radionuclide therapy. *Eur J Nucl Med Mol Imaging.* 2022;49:3841–3851.
70. Li Y, Fan Z, Zhang F, et al. Neoadjuvant therapy in pancreatic neuroendocrine neoplasms: a systematic review and meta-analysis. *Front Oncol.* 2022;12:981575.
71. Cordero-Hernandez I, Ross AC, Dasari A, et al. Transformation of G1-G2 neuroendocrine tumors (NETs) to neuroendocrine carcinomas (NECs) following peptide receptor radionuclide therapy (PRRT): a case series. Endocrine Abstracts website. https://www.endocrine-abstracts.org/ea/0089/ea0089c19. Published 2022. Accessed January 3, 2024.
72. Al-Toubah T, Morse B, Pelle E, Strosberg J. Efficacy of FOLFOX in patients with aggressive pancreatic neuroendocrine tumors after prior capecitabine/temozolomide. *Oncologist.* 2021;26:115–119.
73. Vaughan E, Machta J, Walker M, Toumpanakis C, Caplin M, Navalkissoor S. Retreatment with peptide receptor radionuclide therapy in patients with progressing neuroendocrine tumours: efficacy and prognostic factors for response. *Br J Radiol.* 2018;91:20180041.
74. Rudisile S, Gosewisch A, Wenter V, et al. Salvage PRRT with $^{177}$Lu-DOTA-octreotate in extensively pretreated patients with metastatic neuroendocrine tumor (NET): dosimetry, toxicity, efficacy, and survival. *BMC Cancer.* 2019;19:788.
75. Strosberg J, Leeuwenkamp O, Siddiqui MK. Peptide receptor radiotherapy re-treatment in patients with progressive neuroendocrine tumors: a systematic review and meta-analysis. *Cancer Treat Rev.* 2021;93:102141.
76. van der Zwan WA, Brabander T, Kam BLR, et al. Salvage peptide receptor radionuclide therapy with [$^{177}$Lu-DOTA,Tyr$^3$]octreotate in patients with bronchial and gastroenteropancreatic neuroendocrine tumours. *Eur J Nucl Med Mol Imaging.* 2019;46:704–717.
77. Parghane RV, Mitra A, Bannore TU, Rakshit S, Banerjee S, Basu S. Initial clinical evaluation of indigenous $^{90}$Y-DOTATATE in sequential duo-PRRT approach ($^{177}$Lu-DOTATATE and $^{90}$Y-DOTATATE) in neuroendocrine tumors with large bulky disease: observation on tolerability, $^{90}$Y-DOTATATE post-PRRT imaging characteristics (bremsstrahlung and PETCT) and early adverse effects. *World J Nucl Med.* 2020;20:73–81.
78. Parghane RV, Ostwal V, Ramaswamy A, et al. Long-term outcome of "sandwich" chemo-PRRT: a novel treatment strategy for metastatic neuroendocrine tumors with both FDG- and SSTR-avid aggressive disease. *Eur J Nucl Med Mol Imaging.* 2021;48:913–923.
79. Pach D, Sowa-Staszczak A, Kunikowska J, et al. Repeated cycles of peptide receptor radionuclide therapy (PRRT): results and side-effects of the radioisotope $^{90}$Y-DOTA TATE, $^{177}$Lu-DOTA TATE or $^{90}$Y/$^{177}$Lu-DOTA TATE therapy in patients with disseminated NET. *Radiother Oncol.* 2012;102:45–50.
80. Purohit NK, Shah RG, Adant S, Hoepfner M, Shah GM, Beauregard JM. Potentiation of $^{177}$Lu-octreotate peptide receptor radionuclide therapy of human neuroendocrine tumor cells by PARP inhibitor. *Oncotarget.* 2018;9:24693–24706.
81. Strosberg J, Herrmann K, Bodei L. The future of targeted α-therapy is bright, but rigorous studies are necessary to advance the field. *J Nucl Med.* 2023;64:219–220.
82. Wild D, Grønbæk H, Navalkissoor S, et al. A phase I/II study of the safety and efficacy of [$^{177}$Lu]Lu-satoreotide tetraxetan in advanced somatostatin receptor-positive neuroendocrine tumours. *Eur J Nucl Med Mol Imaging.* 2023;51:183–195.

# The Current and Future Roles of Precision Oncology in Advanced Breast Cancer

Heather Jacene[1], Eric Dietsche[2], and Jennifer Specht[3]

[1]*Imaging/Radiology, Dana-Farber/Brigham Cancer Center, Boston, Massachusetts;* [2]*Department of Radiology, Rhode Island Hospital, Warren Alpert Medical School of Brown University, Providence, Rhode Island; and* [3]*Fred Hutch Cancer Center, Divisions of Hematology and Oncology and of Clinical Research, Department of Medicine, University of Washington, Seattle, Washington*

**Learning Objectives:** On successful completion of this activity, participants should be able to (1) define prognostic and predictive imaging biomarkers and name at least 1 prognostic and predictive imaging biomarker for advanced breast cancer; (2) list the current roles of $^{18}$F-FDG PET/CT imaging in advanced breast cancer; and (3) list 3 non–$^{18}$F-FDG radiotracers that may serve as imaging biomarkers in advanced breast cancer.

**Financial Disclosure:** Dr. Jacene is a consultant for Blue Earth Diagnostics and Spectrum Dynamics Ltd.; receives research support from Blue Earth Diagnostics, Inc. (to the institute); received speaker honoraria from ITM and Monrol; and receives royalties from Cambridge University Press. Dr. Specht receives research support from Lyell Immunopharma, Merck, Cascadian Therapeutics, Pfizer, Seattle Genetics, Genentech, Xencor, Abbvie, Inc., Celcuity, Inc., Novartis, Myriad Pharmaceuticals, AstraZeneca, and Carisma Therapeutics; is a consultant for GE Healthcare, Sensei Biotherapeutics, Lyell Immunopharma, A2 Biotherapeutics, and Volastra; is on the advisory board for Daiichi Sankyo, GlaxoSmithKline, GE Healthcare, Sensei Biotherapeutics, and Lyell Immunopharma; and is an investigative meeting participant for A2 Biotherapeutics. The authors of this article have indicated no other relevant relationships that could be perceived as a real or apparent conflict of interest.

**CME Credit:** SNMMI is accredited by the Accreditation Council for Continuing Medical Education (ACCME) to sponsor continuing education for physicians. SNMMI designates each *JNM* continuing education article for a maximum of 2.0 AMA PRA Category 1 Credits. Physicians should claim only credit commensurate with the extent of their participation in the activity. For CE credit, SAM, and other credit types, participants can access this activity through the SNMMI website (http://www.snmmilearningcenter.org) through March 2027.

Breast cancer is a common but heterogeneous disease characterized by several biologic features, including tumor grade, hormone receptor status, human epidermal growth factor receptor 2 status, and gene expression assays. These biologic and genomic features drive treatment decisions. In the advanced disease setting, inter- and intrapatient tumor heterogeneity is increasingly recognized as a challenge for optimizing treatment. Recent evidence and the recent approval of novel radiopharmaceuticals have increased recognition and acceptance of the potential of molecular imaging as a biomarker to impact and guide management decisions for advanced breast cancer.

**Key Words:** breast cancer; molecular imaging; precision; FDG; FES; PET

**J Nucl Med 2024; 65:349–356**
DOI: 10.2967/jnumed.122.264882

Breast cancer represents a broad spectrum of diseases with treatment outcomes varying on the basis of disease stage and inherent tumor biology. Precision medicine aims at treatment customization based on a patient's specific disease, the disease's molecular makeup, and the environmental factors in the patient's life (*1*). In the late 1970s, tamoxifen, a selective estrogen receptor (ER) modulator that blocks the effects of estrogen, was approved by the U.S. Food and Drug Administration (FDA), becoming one of the first agents in the precision medicine arsenal (*2*). Numerous other targeted therapies have since been approved. Target identification relies on examining tissue from the biopsy of the primary tumor or a metastatic site.

Molecular imaging is the "visualization, characterization, and measurement of biological processes at the molecular and cellular levels in humans and other living systems (*3*)." Molecular imaging with radiotracers, by providing functional information, is thereby distinguished from anatomic imaging, which is currently used more often for systemic staging, detecting recurrent disease, and assessing response to therapy in patients with advanced breast cancer.

Recent evidence and the approval of novel radiopharmaceuticals have driven recognition and acceptance of the potential of molecular imaging as a biomarker to guide management decisions for advanced breast cancer. After providing a brief background on breast cancer pathophysiology, this narrative review summarizes the current treatment paradigms and the expanding role of molecular imaging as a precision medicine biomarker for advanced breast cancer.

## ANATOMIC AND PROGNOSTIC INDICATORS OF BREAST CANCER

Most breast cancers are carcinomas. The 2 most common histologic subtypes are infiltrating ductal (~76%) and infiltrating lobular (~8%) (*4*). Infiltrating ductal carcinomas typically present as firm masses on physical examination. They invade surrounding tissue in a nonregular pattern, and the malignant cells cause a fibrous reaction in the normal tissue. In contrast, infiltrating lobular carcinoma may be nonmasslike, invading normal tissue in a linear, single-cell–like infiltrative pattern (*5*). Both histologic subtypes may be detected on screening mammography and receive similar treatment based on clinical stage and molecular subtype. Compared with infiltrating ductal carcinomas, classic infiltrating lobular carcinomas are often of lower grade and larger, with a higher

Received Sep. 27, 2023; revision accepted Jan. 5, 2024.
For correspondence or reprints, contact Heather Jacene (hjacene@bwh.harvard.edu).
Published online Feb. 1, 2024.

incidence of bilateral involvement at diagnosis, and are more challenging to detect by mammography (*6–8*).

Hormone receptor expression (ER and progesterone receptor [PR]), human epidermal growth factor receptor 2 (HER2) overexpression or gene amplification, histologic grade, the Ki-67 proliferation marker, and genomic profiling classify breast cancer into distinct clinical subtypes with differing prognoses and treatment paradigms. Gene expression profiling identifies intrinsic subtypes (luminal A, luminal B, basal, and HER2-enriched), which can be approximated by immunohistochemical findings obtained in clinical practice (Table 1) (*2,9*).

## BREAST CANCER STAGING

Breast cancer staging follows the American Joint Committee on Cancer staging system, which includes biologic features such as tumor grade; HER2, ER, and PR status; and genomic characteristics (*10*). Anatomic stage considers primary tumor size, nodal status, and the presence or absence of distant metastases (Tables 2 and 3). Clinical T, N, M, and biomarker information from genomic assays (Oncotype DX [Exact Sciences], MammaPrint [Agendia]) determines pathologic prognostic stage.

Advanced breast cancer includes locally advanced breast cancer (LABC), inflammatory breast cancer (IBC), and metastatic breast cancer (MBC). Historically, LABC was defined clinically as those breast cancers deemed inoperable at presentation. LABC includes patients with anatomic stage 3 disease and some with stage 2B (*10,11*). IBC is clinically distinct, with the diagnosis being based on findings including breast pain, edema, erythema, a rapidly enlarging breast, and a *peau d'orange* appearance. IBC has a higher likelihood of regional and distant metastases (*12*). Though IBC technically meets the criteria for LABC, the natural history, treatment paradigms, and outcomes differ from non-IBC (*12*). MBC, or stage 4 disease, involves organs and lymph nodes outside the locoregional nodal stations. Treatment is generally considered palliative; however, survival for some patients with de novo metastatic HER2-positive or oligometastatic (<5 distant sites) breast cancer may be prolonged (*13*).

## MOLECULAR IMAGING AS A BIOMARKER: KEY TERMINOLOGY

Precision medicine uses biomarkers, defined as a "characteristic that is measured as an indicator of normal biological processes, pathogenic processes, or biological responses to an exposure or intervention, including therapeutic interventions" (*14*). The FDA–National Institutes of Health Biomarker Working Group established the *BEST (Biomarkers, EndpointS, and other Tools) Resource* to provide a comprehensive glossary of all biomarker types (*14*). For advanced breast cancer, several biomarkers, including blood, tissue, and imaging measures, play a role in clinical care, and several key terms are important.

**TABLE 1**
Major Molecular Subtypes of Breast Cancer (*9*)

| Molecular subtype | Proportion of breast cancer | 4-y estimated survival |
|---|---|---|
| HR-positive/HER2-negative | 66.6% | 92.5% |
| HR-positive/HER2-positive | 9.7% | 90.3% |
| HR-negative/HER2-positive | 4.3% | 82.7% |
| Triple-negative | 10.8% | 77.0% |

HR = hormone receptor.

A prognostic biomarker correlates with a future event or disease outcome with or without treatment; a key example is hormone receptor status. Patients with ER- or PR-positive tumors survive longer than those with hormone receptor–negative tumors (*15*). A predictive biomarker determines potential benefit derived from a specific treatment based on the biomarker's presence or absence. Predictive biomarkers in advanced breast cancer include HER2 overexpression and ER positivity to predict response to HER2-targeted or endocrine therapy, respectively (*16,17*).

Biomarkers may be both prognostic and predictive (i.e., ER). An integral biomarker directs decision-making in clinical practice or clinical trial settings. An integrated biomarker is included and under investigation in a clinical trial setting but is not used to make decisions (*3*).

## LABC

*Treatment.* Neoadjuvant systemic therapy is recommended in the setting of LABC to decrease primary tumor size or to make an unresectable primary tumor operable, reduce distant recurrence risk, and inform adjuvant therapy choice based on neoadjuvant treatment response. Achieving a pathologic complete response (pCR, i.e., absence of invasive breast cancer in the breast and axillary nodes) with neoadjuvant therapy reduces recurrence risk, particularly in HER2-positive and triple-negative breast cancer (TNBC) (*18*).

Breast cancer subtype dictates neoadjuvant therapy selection. HER2-targeted agents (trastuzumab, pertuzumab) are used for HER2-positive breast cancer. Chemotherapy remains the backbone of neoadjuvant and adjuvant treatment for TNBC. Recent studies demonstrated the benefit of adding the immune checkpoint inhibitor pembrolizumab to neoadjuvant chemotherapy for patients with stage 2 or 3 TNBC (*19,20*). For patients with germline BRCA1, 2 mutations, and high-risk HER2-negative breast cancer, adjuvant olaparib is recommended on the basis of improvements in disease-free and overall survival (*21*).

For ER-positive, HER2-negative breast cancer, neoadjuvant chemotherapy is associated with a substantially lower pCR rate (*18,20*). There is emerging interest in a role for immune checkpoint inhibitors for patients with high-risk luminal breast cancers (*19*). After local therapy, adjuvant endocrine therapy is recommended for hormone receptor–positive breast cancer, with duration varied depending on the clinical risk at presentation and agent used. For premenopausal patients with LABC, ovarian function suppression and aromatase inhibitors are recommended (*22*). Cyclin-dependent kinase 4 and 6 (CDK4/6) inhibitors are considered in the adjuvant setting in specific clinical situations, such as high-risk hormone receptor–positive, HER2-negative breast cancer (*23*).

For all breast cancer subtypes, breast surgery follows neoadjuvant systemic therapy. Multiple factors influence choice of breast conservation versus mastectomy and axillary lymph node dissection versus sentinel lymph node biopsy or targeted axillary dissection. Radiation therapy reduces the risk of local or regional disease recurrence in LABC, even after mastectomy, because of nodal disease involvement at presentation.

Neoadjuvant therapy for LABC is an optimal setting for investigating molecular imaging biomarkers because the pCR endpoint obtained at surgery is a surrogate of survival outcomes (*24*). The

**TABLE 2**
Description of T, N, and M Stages for Breast Cancer (*10*)

| T stage | N stage | M stage |
|---|---|---|
| Tx: primary not assessable | Nx: not assessable | M0: no distant metastases |
| T0: no evidence of primary | N0: no regional LN | cM0(i+): tumor cells on circulating blood markers, marrow, or nonregional nodal tissue < 0.2 mm |
| Tis: ductal carcinoma in situ | N1: ipsilateral level I or II axillary LN | M1: distant metastases |
| T1: ≤20 mm | N2: clinically fixed/matted ipsilateral level I or II axillary LN or clinically detected ipsilateral internal mammary LN | |
| T2: >20 but ≤50 mm | N3: ipsilateral level III axillary LN, clinically detected ipsilateral internal mammary LN with level I or II axillary LN, or ipsilateral supraclavicular LN | |
| T3: >50 mm | | |
| T4: any size with direct chest wall or skin extension | | |
| T4d: IBC | | |

LN = lymph node.

increasing drug armamentarium available in the neoadjuvant setting also provides opportunities to evaluate biologic tumor changes related to the drug's mechanism of action.

*Imaging.* Accurate staging of LABC is essential to guide the initial treatment plan, and the primary modalities for initial staging are CT, bone scanning, and $^{18}$F-FDG PET/CT. National Comprehensive Cancer Network guidelines endorse $^{18}$F-FDG PET/CT for initial staging of at least stage 3 and in select cases of stage 2A or 2B disease in which CT or bone scanning is equivocal or there is a high suspicion of metastatic disease (*11*). Occult metastases occur in 6%–14% of patients undergoing initial staging $^{18}$F-FDG PET/CT, with increasing frequency as stage increases. Up to 30% of patients with stage 3 disease may be upstaged, with similar rates across triple-negative, HER2-positive, and HER2-negative disease (*25–27*).

Although $^{18}$F-FDG PET/CT is increasingly recognized as a single imaging modality for staging LABC (*28*), its clinical use for this purpose remains variable and even debated, driven mainly by a lack of homogeneous prospective data on how upstaging to stage 4 disease affects clinical outcomes for those otherwise thought to have curable disease. A prospective, randomized trial in patients with stage 2B or 3 invasive ductal carcinomas confirmed more upstaging ($n$ = 43/184, 23.3%) with $^{18}$F-FDG PET/CT than with conventional imaging ($n$ = 21/185, 11.3%), leading to less curative-intent treatment in the $^{18}$F-FDG PET/CT group. Longer-term data are still needed to determine whether the changed treatment approach affected survival outcomes and whether these results will further standardize $^{18}$F-FDG PET/CT use for initial staging of 2B/3 disease. These data do provide evidence that tips the scales to further investigate $^{18}$F-FDG PET/CT as an imaging biomarker to explore novel treatment strategies in clinical indications with unmet needs, such as oligometastatic disease, and also demonstrate that randomized imaging trials testing relevant clinical endpoints in specific populations are feasible and of interest (*29*).

**TABLE 3**
TNM Stages for Early, Locally Advanced, and Metastatic Breast Cancer (*10*)

| Category | Stage | TNM description |
|---|---|---|
| Early | 1A | T1N0M0 |
| | 1B | T0/T1, N1mi, M0 |
| | 2A | T0/or T1, N1, M0 |
| | | T2, N0, M0 |
| | 2B | T2, N1, M0 |
| Locally advanced | 2B | T3, N0, M0 |
| | 3A | T0/T1/T2, N2, M0 |
| | | T3, N1/N2, M0 |
| | 3B | T4, N0, N1/N2, M0 |
| | 3C | Any T, N3, M0 |
| Metastatic | 4 | Any T, Any N, M1 |

Beyond initial staging, a significant advantage of molecular imaging across many tumor types is visualization of changes indicating response or lack of response before anatomic imaging. Such early changes provide the opportunity for response-adapted therapy. Early during preoperative therapy,$^{18}$F-FDG PET/CT measures the pharmacodynamic response of breast cancer to predict the likelihood of a pCR at surgery (*30,31*), mostly studied in HER2-positive disease. In TBCRC026, 83 women with newly diagnosed stage 2 or 3 HER2-positive breast cancer underwent $^{18}$F-FDG PET/CT before and 15 d after starting pertuzumab and trastuzumab (*31*). Most strikingly, patients with less than a 40% decrease in $SUV_{max}$ at day 15 were unlikely to achieve a pCR at surgery, with a high negative predictive value of 91% (*31*). A cycle 1, day 15, $SUV_{max}$ of 3 or less in the primary tumor may also be associated with recurrence-free and overall survival at a 53.7-mo median follow-up (*32*).

The DIRECT trial (NCT05710328) aims to validate the results of TBCRC026 across several standard neoadjuvant regimens for HER2-positive LABC to subsequently use interim $^{18}$F-FDG PET/CT as an integral biomarker to test optimization strategies for patients with HER2-positive disease. PHERGain (NCT03161353) demonstrated

the feasibility of this response-adapted approach (*30*). In treatment arm B, early $^{18}$F-FDG PET/CT adds chemotherapy to trastuzumab and pertuzumab if more than a 40% decline in $SUV_{max}$ is not observed. The results of these important trials are eagerly awaited.

Studies of early $^{18}$F-FDG PET/CT for predicting pCR in TNBC cancer have yielded mixed results and been limited by small sample sizes and various treatment regimens (*33–36*). Larger well-designed studies are needed, but this represents a clinical need for which treatment optimization would be highly beneficial.

Another advantage of PET imaging is the ability to perform dynamic imaging and derive tumor kinetics. In 75 patients with LABC who underwent $^{18}$F-FDG PET at baseline and midway through neoadjuvant chemotherapy and after adjusting for ER status and axillary stage, models including kinetic parameters ($K_1$ and inhibition constant [flux]) for predicting pCR were more robust than SUV (area under the receiver-operating-characteristic curve, 0.97 vs. 0.84; $P = 0.005$). Further changes in $K_1$, but not SUV, independently prognosticated for disease-free and overall survival (*37*). Practically, deriving kinetic PET parameters is more complex than deriving static parameters but is feasible. Kazerouni et al. evaluated changes in dynamic $^{18}$F-FDG PET and dynamic contrast-enhanced MRI prospectively in 35 patients with LABC (*38*). They found that mid-treatment changes in both $^{18}$F-FDG PET and dynamic contrast-enhanced MRI measures were predictive of pathologic response by residual cancer burden and recurrence-free survival after neoadjuvant chemotherapy. The 2 modalities offer complementary measures of metabolism and perfusion, and greater reductions in metabolism–perfusion mismatch were associated with improved recurrence-free survival. These noninvasive imaging-based markers could help guide treatment decisions and facilitate more personalized therapies for optimal patient outcomes.

$^{18}$F-3′-deoxy-3′-fluorothymidine ($^{18}$F-FLT) images tumor proliferation, correlates with Ki-67 (*39*), and has generated interest as a biomarker for predicting LABC response to preoperative chemotherapy. Crippa et al. found that changes in tumor $^{18}$F-FLT $SUV_{max}$ could separate responders with residual cancer burden 0 + 1 from those with residual cancer burden 2 + 3 and proposed a predictive score (*40*). The prospective phase 2 ACRIN 6688 study showed that changes in $^{18}$F-FLT uptake could predict pCR after 1 cycle or at the completion of neoadjuvant therapy, but with a higher area under the curve (0.83 vs. 0.68) at the later time point (*39*). Additional smaller studies also demonstrated potential for serial $^{18}$F-FLT as a predictive imaging biomarker (*39,41–43*).

Despite its promise, several factors limit $^{18}$F-FLT's clinical applicability. $^{18}$F-FLT is not widely available, nor is it FDA-approved. High uptake in the bone marrow and liver limit evaluation of these organs and use for initial staging. $^{18}$F-FLT may predict pCR better after neoadjuvant therapy, whereas $^{18}$F-FDG PET/CT may be predictive within 2 wk of starting neoadjuvant therapy, sparing exposure to ineffective therapy. Consequently, at present, $^{18}$F-FLT PET is unlikely to supplant $^{18}$F-FDG as an imaging biomarker for predicting pCR.

Furthermore, as more targeted drugs become available in the neoadjuvant setting for LABC, it will be essential to match the therapeutic drug mechanism of action with the radiotracer mechanism of uptake and even downstream processes to identify and optimize the use of molecular imaging biomarkers.

## MBC

*Treatment.* MBC is generally not considered curable, although patients with HER2-positive breast cancer may experience long disease-free periods because of highly efficacious therapies (*44*). If metastatic disease presents at diagnosis, surgical resection and radiation therapy are not typically options but may become appropriate if tumor burden affects the quality of life (*45*). Treatment recommendations are based on tumor biology, previous treatments, disease burden, patient's performance status, preferences, and comorbidities (*46*). The acquisition of metastatic tumor tissue and evaluation of genetic makeup for actionable mutations (PIK3CA, ESR1), tumor mutational burden, and microsatellite stability are recommended to inform systemic therapy. Medical genetics counseling and germline testing are also recommended for all patients with MBC because of the efficacy of poly(adenosine diphosphate-ribose) polymerase (PARP) inhibitors in patients harboring germline BRCA1, BRCA2, and PALB2 mutations. However, the treatment goal is often more individualized and centers around symptomatic management after providing systemic therapy (*47*).

For hormone receptor–positive tumors, first-line systemic therapy usually consists of endocrine therapy with a CDK4/6 inhibitor. Endocrine therapies include selective ER modulators (i.e., tamoxifen), aromatase inhibitors, and selective ER degraders (i.e., fulvestrant and elacestrant) (*47*). Prolongation of overall survival has been demonstrated with targeted treatments such as CDK4/6 inhibitors (ribociclib, abemaciclib), and prolongation of progression-free survival (PFS) has been demonstrated with CDK4/6 inhibitors, mammalian-target-of-rapamycin inhibitors (i.e., everolimus), and alpelisib (phosphatidylinositol-3′-kinase inhibitor) (*47*). Resistance to first-line therapy is common. For patients with tumors harboring *ESR1* mutations, elacestrant demonstrated improved PFS versus standard-of-care endocrine therapy and received FDA approval in 2023 (*48*). Once endocrine resistance has been established, systemic therapy options for patients with ER-positive, HER2-negative breast cancer include sequential chemotherapy and antibody–drug conjugates (*49,50*).

For HER2-positive MBC, first-line standard treatment is trastuzumab and pertuzumab (anti-HER2 monoclonal antibodies) and taxane chemotherapy (*47*). The second-line standard is presently a HER2-targeted antibody–drug conjugate (trastuzumab emtansine). However, many other highly effective HER2-targeted agents are available in the advanced disease setting. Most recently, in the DESTINY-Breast03 trial, trastuzumab deruxtecan demonstrated a significant improvement in overall survival versus trastuzumab emtansine (*51*).

For TNBC, chemotherapy is the treatment mainstay. For patients with PDL1-positive tumors (assessed by a combined positive score $\geq$ 10%), pembrolizumab plus chemotherapy improved PFS in the KEYNOTE 355 trial (*52*). Recently developed highly potent antibody–drug conjugates offer additional therapy options for patients with metastatic TNBC. Sacituzumab govitecan is a monoclonal antibody against Trop2 conjugated via a cleavable linker to SN-38, the active metabolite of irinotecan. The ASCENT trial reported improved PFS and overall survival for sacituzumab govitecan versus the physician's choice of chemotherapy for advanced TNBC and led to FDA approval in 2021 (*53*). For patients with germline BRCA-associated TNBC, incorporation of platinum is associated with higher objective response rates (*54*) and PARP inhibitors are recommended on the basis of the results of the OlympiAD and EMBRCA trials (*55,56*).

For patients with osseous metastases, regardless of breast cancer subtype, bone-modifying drugs such as bisphosphonates or denosumab are recommended to reduce the risk of skeleton-related

complications (hypercalcemia of malignancy, pathologic fractures, or need for radiation) (*47*).

*Imaging.* The current radiopharmaceuticals approved for assessing MBC are $^{18}$F-FDG, $^{18}$F-NaF, and $^{18}$F-fluoroestradiol ($^{18}$F-FES). $^{18}$F-FDG PET/CT better detects recurrent disease and lytic bone metastases than conventional imaging (i.e., CT, MRI, and bone scanning) (*57,58*). $^{18}$F-FDG PET/CT is also a valuable biomarker for response and outcome, particularly for patients with bone-dominant or bone-only MBC, who are often excluded from drug trials because of lack of measurable disease by RECIST 1.1. In 28 women with bone-dominant or bone-only MBC, Peterson et al. demonstrated that changes on $^{18}$F-FDG PET/CT after 4 mo of standard-of-care treatment predicted time to skeletal-related event and time to progression but not overall survival using modified PERCIST (*59*). Serial $^{18}$F-NaF PET/CT did not predict time to skeletal-related event and time to progression but did predict overall survival. Makhlin et al. recently reported longer, albeit nonsignificant, PFS, overall survival, and time to skeletal-related event in 23 women with ER-positive bone-dominant or bone-only MBC (*60*). The lack of significance could be related to the small sample size. The FEATURE/EA1183 clinical trial (NCT04316117) is under way to validate these findings. If validated, $^{18}$F-FDG PET/CT may serve as an imaging biomarker in routine practice and clinical trials for this group of patients.

Given that endocrine therapy is the backbone of treatment for ER-positive disease, the 2020 FDA approval of $^{18}$F-FES has opened a potential door to advance precision medicine for patients with ER-positive MBC. $^{18}$F-FES selectively binds ER, and in contrast to tissue and blood biomarkers, $^{18}$F-FES PET/CT surveys the whole body to assess tumor burden heterogeneity, functional expression of the target, and ligand binding. This is relevant because over the disease course, hormone receptor status may change 30%–41% of the time, and loss of initial ER positivity increases risk of death compared with stable ER status (*61*).

$^{18}$F-FES PET/CT can help clarify ER tumor status and distinguish the origin of the metastasis in the setting of multiple primary breast malignancies (*62*). $^{18}$F-FES PET/CT detects infiltrating lobular cancer metastases with higher sensitivity than $^{18}$F-FDG (Fig. 1), particularly osseous metastases, though larger trials are required (*63*). In 16 women with ER-positive MBC undergoing $^{18}$F-FDG PET and $^{18}$F-FES PET before rintodestrant therapy $^{18}$F-FES PET was prognostic, with a trend for longer PFS with higher $^{18}$F-FDG and $^{18}$F-FES uptake (*64*). Baseline tumor $^{18}$F-FES uptake has also been suggested to predict responsiveness to endocrine therapy in those with ER-positive disease (*65*). EAI142 (NCT02398773) investigated the negative predictive value of $^{18}$F-FES PET/CT for clinical benefit at 6 mo of endocrine treatment, and the results are awaited to help design future clinical trials. For predicting endocrine therapy response, $^{18}$F-FES PET/CT primarily characterizes tumor for functional target, and correlation with concurrent $^{18}$F-FDG PET/CT is likely important to quantify tumor heterogeneity, that is, burden of ER-positive and ER-negative metastases (*16*).

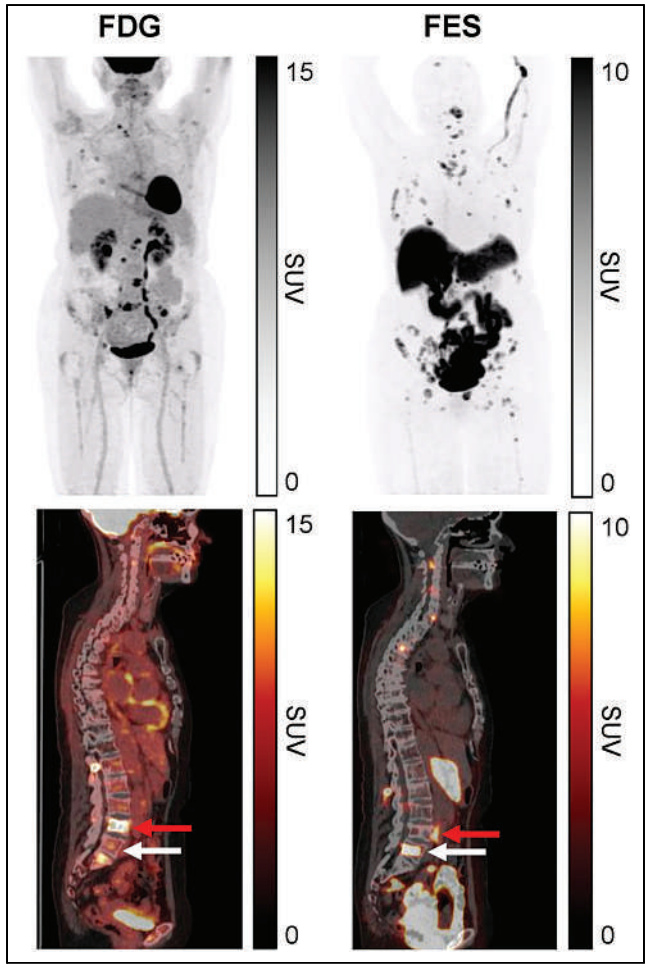


**FIGURE 1.** 66-y-old woman with de novo metastatic, ER-positive lobular breast cancer. $^{18}$F-FES PET/CT shows more lesions than $^{18}$F-FDG PET/CT. ER tumor heterogeneity is also demonstrated with both $^{18}$F-FDG–negative, $^{18}$F-FES–positive lesions (white arrows) and $^{18}$F-FDG–positive, $^{18}$F-FES–negative lesions (red arrows).

## FUTURE DIRECTIONS OF MOLECULAR IMAGING AND THERAPY IN LABC

Other radiotracers have been or are being explored for molecular imaging of LABC. A full review of all of these is beyond this article's scope. In this section, several promising radiotracers that image pathways already targeted for treatment in LABC are reviewed.

As previously discussed, PARP inhibitors are efficacious in patients with metastatic HER2-negative breast cancer with germline BRCA1 and BRCA2 mutations (*28*). Several PARP-targeting agents have been radiolabeled (*66,67*). In early-phase clinical trials, $^{18}$F-fluorthanatrace uptake in tumors was variable but correlated with PARP-1 expression. In 4 patients with stage 3 or 4 breast cancer, 3 with increased $^{18}$F-fluorthanatrace uptake at baseline had a decline in uptake after PARP inhibitor therapy, with a partial response or stable disease. The fourth patient had no $^{18}$F-fluorthanatrace uptake at baseline and had subsequent disease progression. These, and other (*68*), early data on radiolabeled PARP inhibitors suggest a potential future role as a pharmacodynamic or predictive imaging biomarker for those being considered for PARP inhibitor therapy.

The HER2-targeted therapies trastuzumab and pertuzumab have both been radiolabeled for noninvasively imaging HER2 expression. In a study of 24 women with HER2-negative primary breast cancer, 6 had $^{89}$Zr-pertuzumab uptake in metastases: 3 HER2-positive on biopsy, 2 negative, and 1 inconclusive (*69*). In a single-institution study of 50 patients (34 with HER2-positive

disease) and using an $SUV_{max}$ cutoff of 3.2, $^{89}$Zr-trastuzumab PET/CT correctly characterized HER2 status with a sensitivity of 76%, specificity of 62%, positive predictive value of 83%, and negative predictive value of 50%. Twenty percent of patients with multiple lesions had variable $^{89}$Zr-trastuzumab uptake (*70*). Like ER, the global in vivo assessment of tumor heterogeneity overcomes the limitation of assessing HER2 status from a single biopsy site or when biopsy is not feasible (*69–71*). HER2-targeted PET could help identify those who may have otherwise been thought not likely to benefit from HER2-targeted therapy, particularly with emergence of the HER2-low category, which benefits from some of the newer HER2-targeted drugs, likely trastuzumab deruxtecan (*49*). Both trastuzumab and pertuzumab have also been radiolabeled with therapeutic radioisotopes for theranostic application, but work in this domain is early (*72*).

Endocrine therapy for advanced breast cancer currently targets the ER. Over time, resistance to endocrine therapy develops. PR imaging with $^{18}$F-fluorofuranylnorprogesterone has been evaluated, and in vitro studies demonstrated that changes in PR expression could provide insight into the development of resistance to endocrine therapy (*73*).

Fibroblast activation protein has emerged as a new diagnostic and therapeutic target across a variety of cancer types (*74*), with multiple radiolabeled fibroblast activation protein inhibitors (FAPIs) under investigation. Stromal cancer-associated fibroblasts and tumor-associated macrophages express fibroblast activation protein in all breast cancer subtypes (*75*). Early studies of FAPI PET/CT in breast cancer were generally small, used different FAPI radiotracers, and included heterogeneous subtypes of breast cancer but consistently demonstrated increased FAPI uptake and tumor-to-background ratios in primary breast cancer, lymph node metastases, and bone metastases compared with $^{18}$F-FDG (*66,76*). FAPI PET/CT appears advantageous for detecting smaller lesions and those breast cancers with low-level $^{18}$F-FDG uptake (*77*).

Backhaus et al. evaluated the use of $^{68}$Ga-FAPI-46 PET/MRI for predicting pCR after neoadjuvant therapy in 13 women with mixed subtypes of invasive breast cancer (*78*). After neoadjuvant therapy, those with pCR had a lower FAPI-to-background ratio than those with no pCR. A limited number of patients with MBC have been treated with $^{177}$Lu- or $^{90}$Y-labeled FAPI. Adverse events were manageable, with several instances of stable disease or partial response reported (*79*). Fibroblast activation protein–targeting breast cancer for imaging and therapy seems feasible. Still, the data are too early to draw conclusions about the future use of precision medicine in specific subtypes of breast cancer.

## CONCLUSION

Given the heterogeneity of advanced breast cancer, precision medicine and targeting of different biomarkers have proven highly beneficial in treatment, with many other potential therapeutic targets currently under investigation. Several approved radiotracers are also now available or under investigation. Molecular imaging is uniquely positioned to aid in treatment planning by detecting disease, determining disease extent, and characterizing biomarker status in vivo and across the entire disease burden. As medical oncology and molecular imaging continue to evolve, it will remain essential to match processes based on biologic mechanisms for treatment and imaging to take advantage of the full potential of precision medicine. Finally, some of these imaging biomarkers may not need clinical implementation. They could also be helpful as pharmacodynamic markers to determine optimal dosing for drug development or to study mechanisms of action or resistance.

## ACKNOWLEDGMENTS

We thank Dr. Lanell Peterson for assistance with Figure 1.

## REFERENCES

1. Odle TG. Precision medicine in breast cancer. *Radiol Technol.* 2017;88:401M–421M.
2. Sachdev JC, Sandoval AC, Jahanzeb M. Update on precision medicine in breast cancer. *Cancer Treat Res.* 2019;178:45–80.
3. Mankoff DA. A definition of molecular imaging. *J Nucl Med.* 2007;48(6):18N, 21N.
4. Li CI, Uribe DJ, Daling JR. Clinical characteristics of different histologic types of breast cancer. *Br J Cancer.* 2005;93:1046–1052.
5. Wasif N, Maggard M, Ko CY, Giuliano A. Invasive lobular vs. ductal breast cancer: a stage-matched comparison of outcomes. *Ann Surg Oncol.* 2010;17:1862–1869.
6. Orvieto E, Maiorano E, Bottiglieri L, et al. Clinicopathologic characteristics of invasive lobular carcinoma of the breast: results of an analysis of 530 cases from a single institution. *Cancer.* 2008;113:1511–1520.
7. Pestalozzi BC, Zahrieh D, Mallon E, et al. Distinct clinical and prognostic features of infiltrating lobular carcinoma of the breast: combined results of 15 International Breast Cancer Study Group clinical trials. *J Clin Oncol.* 2008;26:3006–3014.
8. Porter AJ, Evans EB, Foxcroft LM, Simpson PT, Lakhani SR. Mammographic and ultrasound features of invasive lobular carcinoma of the breast. *J Med Imaging Radiat Oncol.* 2014;58:1–10.
9. Howlader N, Cronin KA, Kurian AW, Andridge R. Differences in breast cancer survival by molecular subtypes in the United States. *Cancer Epidemiol Biomarkers Prev.* 2018;27:619–626.
10. Teichgraeber DC, Guirguis MS, Whitman GJ. Breast cancer staging: updates in the *AJCC Cancer Staging Manual*, 8th ed., and current challenges for radiologists, from the *AJR* special series on cancer staging. *AJR.* 2021;217:278–290.
11. Amin AB Edge SB, Greene FL, et al., eds. *AJCC Cancer Staging Manual.* 8th ed. Springer; 2018:589–636.
12. Jagsi R, Mason G, Overmoyer BA, et al. Inflammatory breast cancer defined: proposed common diagnostic criteria to guide treatment and research. *Breast Cancer Res Treat.* 2022;192:235–243.
13. Baselga J, Cortes J, Kim SB, et al. Pertuzumab plus trastuzumab plus docetaxel for metastatic breast cancer. *N Engl J Med.* 2012;366:109–119.
14. *BEST (biomarkers, endpoints, and other tools) resource.* National Center for Biotechnology Information website. https://www.ncbi.nlm.nih.gov/books/NBK326791/. Published 2016. Accessed January 11, 2024.
15. Stuart-Harris R, Shadbolt B, Palmqvist C, Chaudri Ross HA. The prognostic significance of single hormone receptor positive metastatic breast cancer: an analysis of three randomised phase III trials of aromatase inhibitors. *Breast.* 2009;18:351–355.
16. Linden HM, Stekhova SA, Link JM, et al. Quantitative fluoroestradiol positron emission tomography imaging predicts response to endocrine treatment in breast cancer. *J Clin Oncol.* 2006;24:2793–2799.
17. Wolff AC, Hammond MEH, Allison KH, et al. Human epidermal growth factor receptor 2 testing in breast cancer: American Society of Clinical Oncology/College of American Pathologists clinical practice guideline focused update. *J Clin Oncol.* 2018;36:2105–2122.
18. Cortazar P, Zhang L, Untch M, et al. Pathological complete response and long-term clinical benefit in breast cancer: the CTNeoBC pooled analysis. *Lancet.* 2014;384:164–172.
19. Nanda R, Liu MC, Yau C, et al. Effect of pembrolizumab plus neoadjuvant chemotherapy on pathologic complete response in women with early-stage breast cancer: an analysis of the ongoing phase 2 adaptively randomized I-SPY2 trial. *JAMA Oncol.* 2020;6:676–684.
20. Spring LM, Fell G, Arfe A, et al. Pathologic complete response after neoadjuvant chemotherapy and impact on breast cancer recurrence and survival: a comprehensive meta-analysis. *Clin Cancer Res.* 2020;26:2838–2848.
21. Geyer CE Jr, Garber JE, Gelber RD, et al. Overall survival in the OlympiA phase III trial of adjuvant olaparib in patients with germline pathogenic variants in BRCA1/2 and high-risk, early breast cancer. *Ann Oncol.* 2022;33:1250–1268.
22. Pagani O, Walley BA, Fleming GF, et al. Adjuvant exemestane with ovarian suppression in premenopausal breast cancer: long-term follow-up of the combined TEXT and SOFT trials. *J Clin Oncol.* 2023;41:1376–1382.
23. Harbeck N, Rastogi P, Martin M, et al. Adjuvant abemaciclib combined with endocrine therapy for high-risk early breast cancer: updated efficacy and Ki-67 analysis from the monarchE study. *Ann Oncol.* 2021;32:1571–1581.

24. Pusztai L, Foldi J, Dhawan A, DiGiovanna MP, Mamounas EP. Changing frameworks in treatment sequencing of triple-negative and HER2-positive, early-stage breast cancers. *Lancet Oncol.* 2019;20:e390–e396.
25. Riedl CC, Slobod E, Jochelson M, et al. Retrospective analysis of $^{18}$F-FDG PET/CT for staging asymptomatic breast cancer patients younger than 40 years. *J Nucl Med.* 2014;55:1578–1583.
26. Krammer J, Schnitzer A, Kaiser CG, et al. $^{18}$F-FDG PET/CT for initial staging in breast cancer patients: is there a relevant impact on treatment planning compared to conventional staging modalities? *Eur Radiol.* 2015;25:2460–2469.
27. Koolen BB, Vrancken Peeters MJ, Aukema TS, et al. $^{18}$F-FDG PET/CT as a staging procedure in primary stage II and III breast cancer: comparison with conventional imaging techniques. *Breast Cancer Res Treat.* 2012;131:117–126.
28. Gradishar WJ, Moran MS, Abraham J, et al. NCCN Guidelines® insights: breast cancer, version 4.2023. *J Natl Compr Canc Netw.* 2023;21:594–608.
29. Pusztai L. Systemic staging of locally advanced breast cancer: how hard to look? *J Clin Oncol.* 2023;41:3891–3894.
30. Pérez-Garcia JM, Gebhart G, Ruiz Borrego M, et al. Chemotherapy de-escalation using an $^{18}$F-FDG-PET-based pathological response-adapted strategy in patients with HER2-positive early breast cancer (PHERGain): a multicentre, randomised, open-label, non-comparative, phase 2 trial. *Lancet Oncol.* 2021;22:858–871.
31. Connolly RM, Leal JP, Solnes L, et al. Updated results of TBCRC026: phase II trial correlating standardized uptake value with pathological complete response to pertuzumab and trastuzumab in breast cancer. *J Clin Oncol.* 2021;39:2247–2256.
32. Hennessy MA, Leal JP, Huang CY, et al. Correlation of SUV on early interim PET with recurrence-free survival and overall survival in primary operable HER2-positive breast cancer (the TBCRC026 trial). *J Nucl Med.* 2023;64:1690–1696.
33. Zucchini G, Quercia S, Zamagni C, et al. Potential utility of early metabolic response by $^{18}$F-2-fluoro-2-deoxy-D-glucose-positron emission tomography/computed tomography in a selected group of breast cancer patients receiving preoperative chemotherapy. *Eur J Cancer.* 2013;49:1539–1545.
34. Koolen BB, Pengel KE, Wesseling J, et al. FDG PET/CT during neoadjuvant chemotherapy may predict response in ER-positive/HER2-negative and triple negative, but not in HER2-positive breast cancer. *Breast.* 2013;22:691–697.
35. Humbert O, Riedinger JM, Charon-Barra C, et al. Identification of biomarkers including $^{18}$FDG-PET/CT for early prediction of response to neoadjuvant chemotherapy in triple-negative breast cancer. *Clin Cancer Res.* 2015;21:5460–5468.
36. Groheux D, Biard L, Giacchetti S, et al. $^{18}$F-FDG PET/CT for the early evaluation of response to neoadjuvant treatment in triple-negative breast cancer: influence of the chemotherapy regimen. *J Nucl Med.* 2016;57:536–543.
37. Dunnwald LK, Doot RK, Specht JM, et al. PET tumor metabolism in locally advanced breast cancer patients undergoing neoadjuvant chemotherapy: value of static versus kinetic measures of fluorodeoxyglucose uptake. *Clin Cancer Res.* 2011;17:2400–2409.
38. Kazerouni AS, Peterson LM, Jenkins I, et al. Multimodal prediction of neoadjuvant treatment outcome by serial FDG PET and MRI in women with locally advanced breast cancer. *Breast Cancer Res.* 2023;25:138.
39. Kostakoglu L, Duan F, Idowu MO, et al. A phase II study of 3′-deoxy-3′-$^{18}$F-fluorothymidine PET in the assessment of early response of breast cancer to neoadjuvant chemotherapy: results from ACRIN 6688. *J Nucl Med.* 2015;56:1681–1689.
40. Crippa F, Agresti R, Sandri M, et al. $^{18}$F-FLT PET/CT as an imaging tool for early prediction of pathological response in patients with locally advanced breast cancer treated with neoadjuvant chemotherapy: a pilot study. *Eur J Nucl Med Mol Imaging.* 2015;42:818–830.
41. Fantini L, Belli ML, Azzali I, et al. Exploratory analysis of $^{18}$F-3′-deoxy-3′-fluorothymidine ($^{18}$F-FLT) PET/CT-based radiomics for the early evaluation of response to neoadjuvant chemotherapy in patients with locally advanced breast cancer. *Front Oncol.* 2021;11:601053.
42. Lubberink M, Direcks W, Emmering J, et al. Validity of simplified 3′-deoxy-3′-[$^{18}$F]fluorothymidine uptake measures for monitoring response to chemotherapy in locally advanced breast cancer. *Mol Imaging Biol.* 2012;14:777–782.
43. Romine PE, Peterson LM, Kurland BF, et al. $^{18}$F-fluorodeoxyglucose (FDG) PET or $^{18}$F-fluorothymidine (FLT) PET to assess early response to aromatase inhibitors (AI) in women with ER+ operable breast cancer in a window-of-opportunity study. *Breast Cancer Res.* 2021;23:88.
44. Swain SM, Miles D, Kim SB, et al. Pertuzumab, trastuzumab, and docetaxel for HER2-positive metastatic breast cancer (CLEOPATRA): end-of-study results from a double-blind, randomised, placebo-controlled, phase 3 study. *Lancet Oncol.* 2020;21:519–530.
45. Khan SA, Zhao F, Goldstein LJ, et al. Early local therapy for the primary site in de novo stage IV breast cancer: results of a randomized clinical trial (EA2108). *J Clin Oncol.* 2022;40:978–987.
46. Cardoso F, Senkus-Konefka E, Fallowfield L, Costa A, Castiglione M, Group EGW. Locally recurrent or metastatic breast cancer: ESMO clinical practice guidelines for diagnosis, treatment and follow-up. *Ann Oncol.* 2010;21(suppl 5):v15–v19.
47. Harbeck N, Gnant M. Breast cancer. *Lancet.* 2017;389:1134–1150.
48. Bidard FC, Kaklamani VG, Neven P, et al. Elacestrant (oral selective estrogen receptor degrader) versus standard endocrine therapy for estrogen receptor-positive, human epidermal growth factor receptor 2-negative advanced breast cancer: results from the randomized phase III EMERALD trial. *J Clin Oncol.* 2022;40:3246–3256.
49. Modi S, Jacot W, Yamashita T, et al. Trastuzumab deruxtecan in previously treated HER2-low advanced breast cancer. *N Engl J Med.* 2022;387:9–20.
50. Rugo HS, Bardia A, Marme F, et al. Sacituzumab govitecan in hormone receptor-positive/human epidermal growth factor receptor 2-negative metastatic breast cancer. *J Clin Oncol.* 2022;40:3365–3376.
51. Hurvitz SA, Hegg R, Chung WP, et al. Trastuzumab deruxtecan versus trastuzumab emtansine in patients with HER2-positive metastatic breast cancer: updated results from DESTINY-Breast03, a randomised, open-label, phase 3 trial. *Lancet.* 2023;401:105–117.
52. Cortes J, Cescon DW, Rugo HS, et al. Pembrolizumab plus chemotherapy versus placebo plus chemotherapy for previously untreated locally recurrent inoperable or metastatic triple-negative breast cancer (KEYNOTE-355): a randomised, placebo-controlled, double-blind, phase 3 clinical trial. *Lancet.* 2020;396:1817–1828.
53. Bardia A, Hurvitz SA, Tolaney SM, et al. Sacituzumab govitecan in metastatic triple-negative breast cancer. *N Engl J Med.* 2021;384:1529–1541.
54. Tutt A, Tovey H, Cheang MCU, et al. Carboplatin in BRCA1/2-mutated and triple-negative breast cancer BRCAness subgroups: the TNT trial. *Nat Med.* 2018;24:628–637.
55. Litton JK, Hurvitz SA, Mina LA, et al. Talazoparib versus chemotherapy in patients with germline BRCA1/2-mutated HER2-negative advanced breast cancer: final overall survival results from the EMBRACA trial. *Ann Oncol.* 2020;31:1526–1535.
56. Robson ME, Tung N, Conte P, et al. OlympiAD final overall survival and tolerability results: olaparib versus chemotherapy treatment of physician's choice in patients with a germline BRCA mutation and HER2-negative metastatic breast cancer. *Ann Oncol.* 2019;30:558–566.
57. Groheux D. FDG-PET/CT for primary staging and detection of recurrence of breast cancer. *Semin Nucl Med.* 2022;52:508–519.
58. Paydary K, Seraj SM, Zadeh MZ, et al. The evolving role of FDG-PET/CT in the diagnosis, staging, and treatment of breast cancer. *Mol Imaging Biol.* 2019;21:1–10.
59. Peterson LM, O'Sullivan J, Wu QV, et al. Prospective study of serial $^{18}$F-FDG PET and $^{18}$F-fluoride PET to predict time to skeletal-related events, time to progression, and survival in patients with bone-dominant metastatic breast cancer. *J Nucl Med.* 2018;59:1823–1830.
60. Makhlin I, Korhonen KE, Martin ML, et al. $^{18}$F-FDG PET/CT for the evaluation of therapy response in hormone receptor-positive bone-dominant metastatic breast cancer. *Radiol Imaging Cancer.* 2022;4:e220032.
61. Lindström LS, Karlsson E, Wilking UM, et al. Clinically used breast cancer markers such as estrogen receptor, progesterone receptor, and human epidermal growth factor receptor 2 are unstable throughout tumor progression. *J Clin Oncol.* 2012;30:2601–2608.
62. Boers J, Loudini N, Brunsch CL, et al. Value of $^{18}$F-FES PET in solving clinical dilemmas in breast cancer patients: a retrospective study. *J Nucl Med.* 2021;62:1214–1220.
63. Ulaner GA, Jhaveri K, Chandarlapaty S, et al. Head-to-head evaluation of $^{18}$F-FES and $^{18}$F-FDG PET/CT in metastatic invasive lobular breast cancer. *J Nucl Med.* 2021;62:326–331.
64. Iqbal R, Yaqub M, Bektas HO, et al. [$^{18}$F]FDG and [$^{18}$F]FES PET/CT imaging as a biomarker for therapy effect in patients with metastatic ER+ breast cancer undergoing treatment with rintodestrant. *Clin Cancer Res.* 2023;29:2075–2084.
65. Dehdashti F, Mortimer JE, Trinkaus K, et al. PET-based estradiol challenge as a predictive biomarker of response to endocrine therapy in women with estrogen-receptor-positive breast cancer. *Breast Cancer Res Treat.* 2009;113:509–517.
66. O'Brien SR, Ward R, Wu GG, et al. Other novel PET radiotracers for breast cancer. *PET Clin.* 2023;18:557–566.
67. Puentes LN, Makvandi M, Mach RH. Molecular imaging: PARP-1 and beyond. *J Nucl Med.* 2021;62:765–770.
68. Makvandi M, Pantel A, Schwartz L, et al. A PET imaging agent for evaluating PARP-1 expression in ovarian cancer. *J Clin Invest.* 2018;128:2116–2126.
69. Ulaner GA, Carrasquillo JA, Riedl CC, et al. Identification of HER2-positive metastases in patients with HER2-negative primary breast cancer by using HER2-targeted $^{89}$Zr-pertuzumab PET/CT. *Radiology.* 2020;296:370–378.
70. Dehdashti F, Wu N, Bose R, et al. Evaluation of [$^{89}$Zr]trastuzumab-PET/CT in differentiating HER2-positive from HER2-negative breast cancer. *Breast Cancer Res Treat.* 2018;169:523–530.
71. Ulaner GA, Hyman DM, Lyashchenko SK, Lewis JS, Carrasquillo JA. $^{89}$Zr-trastuzumab PET/CT for detection of human epidermal growth factor receptor 2-positive metastases in patients with human epidermal growth factor receptor 2-negative primary breast cancer. *Clin Nucl Med.* 2017;42:912–917.

72. Miladinova D. Molecular imaging of HER2 receptor: targeting HER2 for imaging and therapy in nuclear medicine. *Front Mol Biosci.* 2023;10: 1144817.
73. Kumar M, Salem K, Jeffery JJ, Yan Y, Mahajan AM, Fowler AM. Longitudinal molecular imaging of progesterone receptor reveals early differential response to endocrine therapy in breast cancer with an activating ESR1 mutation. *J Nucl Med.* 2021;62:500–506.
74. Kratochwil C, Flechsig P, Lindner T, et al. $^{68}$Ga-FAPI PET/CT: tracer uptake in 28 different kinds of cancer. *J Nucl Med.* 2019;60:801–805.
75. Tchou J, Zhang PJ, Bi Y, et al. Fibroblast activation protein expression by stromal cells and tumor-associated macrophages in human breast cancer. *Hum Pathol.* 2013;44:2549–2557.
76. Evangelista L, Filippi L, Schillaci O. What radiolabeled FAPI pet can add in breast cancer? A systematic review from literature. *Ann Nucl Med.* 2023;37:442–450.
77. Alçın G, Arslan E, Aksoy T, et al. $^{68}$Ga-FAPI-04 PET/CT in selected breast cancer patients with low FDG affinity: a head-to-head comparative study. *Clin Nucl Med.* 2023;48:e420–e430.
78. Backhaus P, Burg C, Asmus I, et al. Initial results of $^{68}$Ga-FAPI-46 PET/MRI to assess response to neoadjuvant chemotherapy in breast cancer. *J Nucl Med*. 2023;64:717–723.
79. Yadav MP, Ballal S, Martin M, et al. Therapeutic potential of [$^{177}$Lu]Lu-DOTAGA-FAPi dimers in metastatic breast cancer patients with limited treatment options: efficacy and safety assessment. *Eur J Nucl Med Mol Imaging.* November 7, 2023 [Epub ahead of print].

# Molecular Imaging of Acute Graft-Versus-Host Disease

Chiara Bernardi[1,2], Valentina Garibotto[2–4], Behnaz Mobashwera[5], Robert S. Negrin[6], Israt S. Alam*[7], and Federico Simonetta*[1,2]

[1]*Division of Hematology, Department of Oncology, Geneva University Hospitals, Geneva, Switzerland;* [2]*Translational Research Center for Oncohematology, Department of Medicine, University of Geneva, Geneva, Switzerland;* [3]*Division of Nuclear Medicine and Molecular Imaging, Geneva University Hospitals, Geneva, Switzerland;* [4]*CIBM Center for Biomedical Imaging, Geneva, Switzerland;* [5]*Department of Hematology, Southampton General Hospital, University Hospital Southampton, Southampton, United Kingdom;* [6]*Division of Blood and Marrow Transplantation and Cellular Therapy, Stanford University, Stanford, California; and* [7]*Molecular Imaging Program at Stanford, Department of Radiology, Stanford University School of Medicine, Stanford, California*

Noninvasive molecular imaging of acute graft-versus-host disease (GvHD) after allogeneic hematopoietic stem cell transplantation has great potential to detect GvHD at the early stages, aid in grading of the disease, monitor treatment response, and guide therapeutic decisions. Although the specificity of currently available tracers appears insufficient for clinical GvHD diagnosis, recently, several preclinical studies have identified promising new imaging agents targeting one or more biologic processes involved in GvHD pathogenesis, ranging from T-cell activation to tissue damage. In this review, we summarize the different approaches reported to date for noninvasive detection of GvHD using molecular imaging with a specific focus on the use of PET. We discuss possible applications of molecular imaging for the detection of GvHD in the clinical setting, as well as some of the predictable challenges that are faced during clinical translation of these approaches.

**Key Words:** hematology; molecular imaging; PET/CT; graft-versus-host disease; clinical; preclinical

**J Nucl Med 2024; 65:357–361**
DOI: 10.2967/jnumed.123.266552

Allogeneic hematopoietic stem cell transplantation (HSCT) is a potentially curative therapy for a broad range of hematologic diseases. Unfortunately, allogeneic HSCT is still associated with significant morbidity and mortality related to transplant complications, namely acute graft-versus-host disease (GvHD). During acute GvHD, donor-derived T cells interact with host tissues, leading to their activation, proliferation, and migration to target organs, notably skin, liver, and intestine (*1*). Current approaches for the diagnosis of acute GvHD are based on clinical and pathologic elements that are restricted to later, symptomatic, stages of the disease. Given the importance of timely therapeutic interventions for acute GvHD treatment, the use of noninvasive imaging modalities to predict and detect GvHD early, prior to symptom onset, could greatly benefit patient outcomes. Conventional radiology using ultrasound, contrast-enhanced CT, or MRI is of limited utility for acute GvHD diagnosis as any morphologic changes are often nonspecific (*2*).

Molecular imaging allows noninvasive measurements of biologic processes at the cellular and subcellular levels, and its application to the study of the immune system is a rapidly expanding field. PET imaging is a highly sensitive and quantitative clinical molecular imaging modality, perfectly poised to provide noninvasive, whole-body mechanistic insights into disease pathogenesis. The use of targeted PET probes specifically allowing detection of cellular or molecular processes involved in GvHD pathogenesis thus represents a promising approach for early detection of acute GvHD at presymptomatic stages.

According to the classic model, acute GvHD pathogenesis can be divided into 3 phases (Fig. 1): host tissue damage resulting from the conditioning chemotherapy; activation of donor and recipient antigen-presenting cells and subsequent donor T-cell activation and expansion; and an effector phase in which activated donor T cells cause tissue damage by targeting host cells, inducing apoptosis. Using current tools, acute GvHD is diagnosed predominantly during the third phase on the basis of a combination of clinical symptoms and histologic findings. Major efforts have been undertaken to identify biomarkers to predict and diagnose GvHD at earlier stages. Molecular imaging approaches have the potential to allow diagnosis as early as the second phase, before overt signs of GvHD (Fig. 1). Imaging agents targeting metabolic pathways have the potential to report on all 3 phases of GvHD, whereas the use of small molecules or monoclonal antibodies (mAbs) to image T cells could help elucidate phase 2 dynamics. Finally, imaging agents evaluating tissue damage may allow detection and monitoring of immunopathologic processes resulting from phase 3 of GvHD pathogenesis. In this review, we summarize the clinical and preclinical molecular imaging technologies available for acute GvHD diagnosis and monitoring and discuss future prospects for clinical translation.

## IMAGING METABOLISM

### $^{18}$Fluorine-fluorodeoxyglucose ([$^{18}$F]FDG)

[$^{18}$F]FDG, the most widely used PET tracer in clinical practice, takes advantage of the higher glucose consumption by metabolically active tissues. Given the wide range of metabolically active cells and tissues, [$^{18}$F]FDG is thought to annotate all 3 phases of GvHD

Received Oct. 26, 2023; revision accepted Jan. 11, 2024.
For correspondence or reprints, contact Federico Simonetta (federico.simonetta@unige.ch) or Israt S. Alam (israt@stanford.edu).
*Contributed equally to this work.
Published online Feb. 15, 2024.

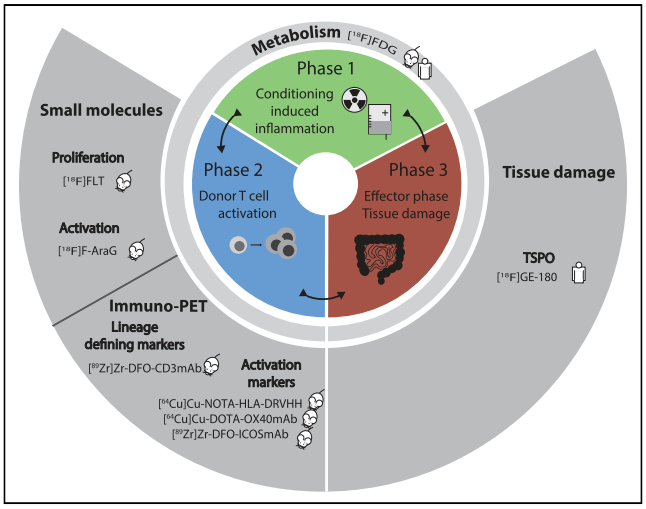


**FIGURE 1.** Summary of preclinical (mouse icon) or clinical (human icon) studies to image different phases of acute GvHD pathogenesis. VHH = variable fragments of heavy chain antibody.

pathogenesis (Fig. 1). Early reports suggested that [$^{18}$F]FDG PET can visualize tissue inflammation associated with acute gastrointestinal GvHD (GI-GvHD). In a retrospective analysis conducted on 101 patients with suspected acute GI-GvHD, 74 of whom were clinically or histologically proven to have acute GI-GvHD, [$^{18}$F]FDG PET had a sensitivity of 93% and specificity of 73% (*3*). Moreover, $SUV_{max}$ discriminated between patients with a fast or slow/no response to immunosuppressive therapies. False-positive cases were related mostly to intestinal infections. In a more recent prospective study, 51 allogeneic HSCT recipients with clinically suspected acute GI-GvHD underwent PET/CT followed by endoscopy and histologic analysis (Fig. 2, left panel) (*4*). Twenty-three patients had histologically proven upper or lower acute GI-GvHD. [$^{18}$F]FDG PET was not able to distinguish between acute GvHD and non-GvHD inflammatory changes in the colon, yielding a sensitivity of 69%, a specificity of 57%, a negative predictive value of 73%, and a positive predictive value of 59%. To increase sensitivity and specificity, a pilot study on 21 patients with acute GI-GvHD used [$^{18}$F]FDG PET/MRI (*5*). The acute GI-GvHD detection rate increased from 57% of [$^{18}$F]FDG PET alone or 61% of MRI alone to 100% for [$^{18}$F]FDG PET/MRI.

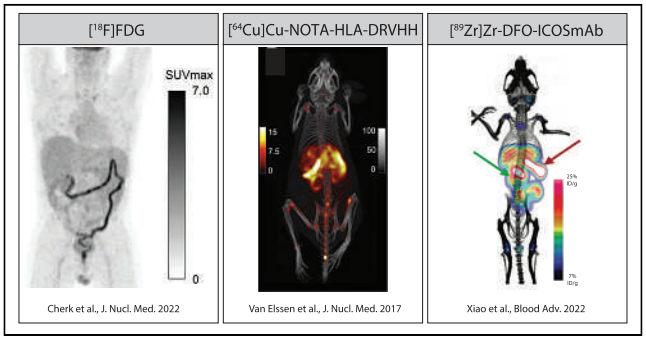


**FIGURE 2.** Examples of preclinical and clinical PET-imaging approaches to imaging acute GvHD. In Cherk et al. (*4*), patients received [$^{18}$F]FDG (3 MBq/kg) and were imaged 60–80 min later. In Van Elssen et al. (*11*), mice were given 1.85 MBq (~5 μg) of [$^{64}$Cu]Cu-DOTA-OX40mAb and were imaged 2 h after injection. In Xiao et al. (*16*), mice received 1.85 MBq (~7 μg) of [$^{89}$Zr]Zr-DFO-ICOSmAb and were imaged 48 h later. VHH = variable fragments of heavy chain antibody. (Reprinted from (*4,11,16*).)

Collectively, these prospective and retrospective studies show promise that [$^{18}$F]FDG PET/CT will have a role in GvHD diagnosis, but additional investigations are needed to evaluate the impact of the limited specificity of [$^{18}$F]FDG in this indication.

## IMAGING T-CELL RESPONSES

Given the importance of T cells in GvHD pathogenesis, molecular imaging targeting T cells would be ideal for GvHD detection and monitoring, allowing imaging of the second, and to some extent the third, phase of GvHD (Fig. 1). Strategies to track T cells in vivo using molecular imaging have been reviewed extensively (*6,7*). The simplest approach, ex vivo radiolabeling of T cells before infusion, is limited by the short time frame in which analysis can be performed, which is due both to radioisotope decay and to tracer dilution caused by cell proliferation. Using such a strategy for GvHD would be challenging given the variable time frame in which GvHD develops after transplantation. T-cell–specific tracers will be likely required.

### Small Molecules

*$^{18}$F-3′-Deoxy-3′-Fluorothymidine ([$^{18}$F]FLT).* Given the high proliferation rate of T cells during GvHD, the use of [$^{18}$F]FLT PET imaging has been attempted in murine models of allogeneic HSCT (*8*). FLT is a thymidine analog that is incorporated into the DNA at the time of replication and therefore reflects cellular proliferation. In murine models of GvHD, [$^{18}$F]FLT allowed differentiation of control mice from mice that developed GvHD after receiving alloreactive T cells, by detecting higher tracer uptake in the lymph nodes and spleen of the latter. However, tracer uptake in GvHD-target organs, mainly the gastrointestinal tract, did not differ between GvHD and control mice because of high variability. This potentially represents a major limitation for the use of [$^{18}$F]FLT for GvHD diagnosis given that signal outside target organs can originate from proliferation of hematopoietic cells other than T cells during engraftment. An early phase I study is ongoing and will show whether [$^{18}$F]FLT uptake can predict GvHD development in patients who underwent HSCT (NCT03546556).

*2′-Deoxy-2′-[$^{18}$F]Fluoro-9-β-D-Arabinofuranosyl Guanine ([$^{18}$F]F-AraG).* AraG is the water-soluble prodrug of nelarabine, a drug known for its specific cytotoxicity toward T cells and clinically used in T-cell malignancies. AraG enters cells using nucleoside transporters and is phosphorylated by either cytosolic deoxycytidine kinase or mitochondrial deoxyguanosine kinase. At high doses, phosphorylated AraG induces T-cell death by inhibiting DNA synthesis at the low picomolar mass levels required for imaging, AraG specifically accumulates in T cells without inducing detectable cell death. Ronald et al. evaluated [$^{18}$F]F-AraG in a mouse model of GvHD (*9*) and showed that this small molecule is able to visualize T-cell expansion in secondary lymphoid organs during GvHD. Unfortunately, the tracer's high background hepatic signal precluded analysis of both the gastrointestinal tract and liver itself, 2 major GvHD-target organs. Given the spatial resolution and the favorable kinetics observed with [$^{18}$F]F-AraG in humans, clinical evaluation of this approach for GvHD diagnosis was explored in a limited number of subjects (NCT03367962), although the trial was closed because of challenges in patient recruitment and selection.

### Immuno-PET

Immuno-PET exploits the high specificity of mAbs to selectively bind cells expressing the target antigen; radiolabeling these moieties with PET isotopes allows for in vivo visualization of

those targeted cells. This technique is rapidly gaining traction as an approach to monitoring T cells without the need for their ex vivo manipulation. Most T-cell–targeting immuno-PET tracers developed so far can be classified on the basis of the antigen they target and fall into 2 major categories: tracers targeting T-cell lineage-defining molecules, (e.g., CD3, CD4, and CD8) and those targeting T-cell activation makers (e.g., HLA-DR [human leukocyte antigen–DR isotype], CD69, OX40 [CD134], 41BB [CD137], and inducible T-cell costimulator [ICOS]).

*Immuno-PET Targeting T-Cell Lineage Markers.* Targeting T-cell lineage-defining markers such as CD3, CD4, or CD8 is an obvious approach to immuno-PET imaging of T-cell–mediated processes, including GvHD. Given the importance of T-cell expansion in GvHD pathogenesis, namely during phase 2, the specific quantification of T-cell numbers at the target-tissue level and, moreover, the dynamic quantification of T-cell burden over time have great potential for GvHD diagnosis. The most clinically advanced T-cell–specific tracers to date are those targeting CD8, which have yet to be evaluated in the context of GvHD. To date, only CD3 immuno-PET has been reported in murine models of GvHD.

Pektor et al. used PET/MRI with a $^{89}$Zr (half-life, 78.4 h)-labeled antihuman CD3 mAb in a murine model of xenogeneic GvHD (*10*). The tracer exhibited higher uptake in GvHD-target organs, namely the liver, as well as in secondary lymphoid organs at different time points after peripheral blood mononuclear cell administration into lymphodepleted mice. Interestingly, the authors administered regulatory T cells as GvHD prophylaxis; this approach significantly reduced T-cell infiltration in regulatory T-cell–treated mice, visualized with CD3 immuno-PET. Although promising, this proof-of-concept report did not address one of the major risks of targeting CD3 in immunopathogenic contexts such as GvHD: that of potentially interfering with T-cell biology and exacerbating the disease. Targeting CD3 could also induce chronic T-cell stimulation and eventually lead to T-cell exhaustion, thus potentially limiting the graft-versus-tumor effect.

*Immuno-PET Targeting T-Cell Activation Markers.* Targeting T-cell–restricted markers upregulated specifically during T-cell activation has the potential advantage of providing not only quantitative and qualitative information but also functional information about the activation status of T cells and their dynamics. Several approaches for different activation markers have been assessed preclinically.

HLA-DR is a human class II major histocompatibility complex molecule expressed on a variety of immune cells, including T cells during activation. A $^{64}$Cu (half-life, 12.7 h)-radiolabeled variable fragment of heavy chain antibodies was developed to target human HLA-DR and used to image T-cell activation in a murine model of xenogeneic GvHD (*11*). [$^{64}$Cu]Cu-NOTA-HLA-DRVHH uptake was higher within the liver of mice displaying signs of severe GvHD (Fig. 2, middle panel) than in control mice, but the authors were unable to correlate early PET findings with subsequent GvHD before the occurrence of overt disease. Given the broad and unspecific expression of HLA-DR, the tracer uptake could be a consequence of tissue infiltration by activated T cells or by other non-T HLA-DR–positive cells, such as monocytes and macrophages.

OX40 is a member of the tumor necrosis factor receptor superfamily, and its cell-surface expression is highly restricted to activated T cells, on which it acts as a costimulatory molecule. We have previously developed a murine OX40-specific mAb ([$^{64}$Cu]Cu-DOTA-OX40mAb) that enables noninvasive imaging of murine OX40-positive activated T cells (*12*). This tracer was assessed in vivo using a major histocompatibility complex–mismatch HSCT murine model of GvHD (*13*), given the increased expression and the role of OX40 during acute GvHD (*14,15*). OX40 immuno-PET successfully detected T-cell activation, expansion, and target-tissue infiltration. Importantly, because of its high sensitivity, OX40 immuno-PET could detect signs of GvHD even before the manifestation of clinical symptoms and could distinguish these signs from the toxicities of the conditioning regimen. However, a major limitation of this approach was the agonistic nature of the mAb used: at the mass doses used for PET imaging, the [$^{64}$Cu]Cu-DOTA-OX40mAb tracer led to further T-cell activation and subsequent exacerbation of GvHD when administered early after HSCT. These results stress the need to develop biologically inert immuno-PET tracers for imaging purposes and to carefully select imaging targets and epitopes to avoid interfering with T-cell activation and disease pathogenesis.

A search for alternative target molecules for immuno-PET tracers to circumvent the toxicity encountered with OX40 immuno-PET identified the inducible T-cell costimulator (ICOS), an extracellular T-cell activation marker and costimulatory molecule, which is selectively upregulated on activated T cells during GvHD (*16*). Using a previously reported [$^{89}$Zr]Zr-DFO-ICOSmAb tracer (*17,18*), we demonstrated that ICOS immuno-PET efficiently allowed monitoring of alloreactive T-cell activation, expansion, and tissue infiltration in a major histocompatibility complex–mismatch murine model of acute GvHD (*16*) (Fig. 2, right panel). Importantly, ICOS immuno-PET was not associated with any detectable toxicity and did not interfere with the graft-versus-tumor effect. The combination of highly specific and sensitive detection of T-cell activation, in the absence of detectable toxicity, renders ICOS immuno-PET a compelling method that warrants further evaluation in patients for the early detection of GvHD.

## IMAGING TISSUE DAMAGE

Once considered a passive target of T-cell cytotoxic function during acute GvHD, the target tissue epithelium is increasingly being recognized as an active player of GvHD pathogenesis. For this reason, target tissue damage can be exploited as a molecular imaging target to visualize phase 3 of the disease pathogenesis (Fig. 1). The analysis of phenotypic and functional changes of enterocytes during acute GvHD led to the identification of tryptophan-rich sensory protein (TSPO), a stress-related protein, as a marker expressed by enterocytes during acute GI-GvHD (*19*). TSPO is an outer mitochondrial membrane protein previously reported to be overexpressed by enterocytes after stimulation with inflammatory mediators such as tumor necrosis factor, leading to its overexpression in inflammatory bowel disease. After demonstrating enterocytic TSPO expression in tissue biopsies from patients with acute GI-GvHD, Scott et al. (*19*) performed a prospective pilot study of PET/CT using [$^{18}$F]-flutriciclamide ([$^{18}$F]GE-180), an already-reported third-generation high-affinity TSPO radiotracer, in 8 allogeneic HSCT adult recipients with a clinical suspicion of acute GI-GvHD. They demonstrated tracer uptake specifically at the intestinal level and correlation between uptake and histology in 6 of 8 participants (75%) including 4 true-positive and 2 true-negative. The correlation with histology was greater in small bowel and colon. Even though TSPO detection is not completely specific to enterocytes and although preliminary, this proof-of-concept study provided the first evidence for molecular imaging of target epithelium during GvHD as a strategy to

detect tissue damage and potentially to monitor response to treatment during the healing process. Another drawback of [$^{18}$F]GE-180 and other TSPO tracers is their sensitivity to the TSPO single-nucleotide polymorphism (rs6971-SNP), which affects the binding of these tracers. TSPO PET studies typically require patients to be genotyped to ascertain whether they are low-, medium-, or high-affinity binders and thus their eligibility for the scan.

## OPPORTUNITIES AND CHALLENGES FOR CLINICAL TRANSLATION

### Tracer Development and Optimization

The studies performed so far using the widely available PET tracer [$^{18}$F]FDG have highlighted both the potential and the limitations of using molecular imaging for GvHD diagnosis, stressing the importance of developing new imaging agents designed with acute GvHD pathogenesis in mind. The ideal tracer will target molecules or biologic pathways specifically involved in acute GvHD, allowing for accurate distinction between GvHD-target tissues both from healthy tissues and from tissues affected by other pathologic processes, namely infections. Despite the well-established utility of murine models of GvHD for reproducing human GvHD pathogenesis, animal models are ultimately limited in their ability to fully assess the specificity of a tracer given the absence of confounding factors, such as infection risk, encountered in the clinic. It will therefore be essential to test the most promising tracer candidates in well-conducted clinical trials.

In addition to the target molecule/pathway recognized by the new tracers, the choice of PET radionuclide is also of crucial importance. Use of radionuclides with a longer half-life, such as $^{89}$Zr, might provide the advantage of obtaining sequential longitudinal images over several days, thus allowing imaging for both diagnosis and monitoring. The resulting prolonged radiation exposure and associated excretion in biologic materials may require specific radiosafety measures that may not be compatible with an outpatient setting. As such, shorter-lived radionuclides, such as $^{64}$Cu, also warrant consideration, as do advanced scanner technologies such as total-body PET, which are capable of generating high-resolution images with significantly reduced administered radioactive doses (*20*). Finally, combining molecular imaging by PET with anatomic modalities other than CT, such MRI, might further increase the diagnostic potential of new tracers, in particular immuno-PET tracers, similarly to what has been shown for [$^{18}$F]FDG (*5*).

### Defining the Optimal Use of Molecular Imaging for GvHD Diagnosis and Monitoring

Once one or more promising radiotracers are identified, it remains to be defined how best to implement molecular imaging of GvHD into clinical practice. One option would be to use it as a screening strategy in all allogeneic HSCT recipients at selected time points after transplantation. Given the high complexity and significant costs of PET, it is, however, unlikely that this approach will prove to be cost-effective when used as a general screening tool. One option could be to restrict its use to patient populations at particular risk of developing GvHD on the basis of certain clinical criteria (e.g., the donor type used). Alternatively, the use of PET for detection of GI-GvHD could be triggered by other clinical signs frequently preceding or accompanying it, such as skin GvHD. Given the great results accomplished with blood biomarkers of GvHD, such as regenerating islet-derived 3α and suppression of tumorigenicity 2, we can imagine a scenario in which molecular imaging use will be triggered by positive results from the cheaper and more easily accessible blood biomarkers.

Virtually all patients receive GvHD prophylaxis after allogeneic HSCT in clinical practice. Early detection of GvHD using molecular therapy will likely not eliminate the need for such pharmacologic prophylaxis but could crucially help clinicians define its optimal duration and tapering schedule. Moreover, molecular imaging might indicate the transition from GvHD prophylaxis to therapy based on imaging findings and without the need to wait for clinical signs, and therefore tissue damage, before intervention, thereby enabling a personalized approach to GvHD treatment. Molecular imaging might be used to guide histologic sampling for GI-GvHD diagnosis in cases of clinical suspicion, thus increasing the sensitivity of tissue biopsies. In addition to acute GvHD diagnosis, molecular imaging has great potential as a tool to assess the severity of GvHD and guide therapy accordingly. We have recently seen promising results from clinical trials adjusting the intensity of anti-GvHD therapy on the basis of the severity of GvHD assessed on clinical and biologic criteria (*21,22*). Similarly, molecular imaging could be used to evaluate the extent and severity of GvHD in a more comprehensive way than is possible with endoscopy and biopsies, thus allowing identification of patients at low and high risk of GvHD and helping to adapt treatment protocols accordingly. Moreover, early reassessment using molecular imaging after treatment introduction might predict the response to therapy earlier than with currently available methods, thus allowing earlier adaptation of therapy.

## CONCLUSION

Diagnosis of acute GvHD currently relies on a combination of clinical symptoms and tissue biopsies. However, especially for liver and GI-GvHD, endoscopic biopsies are associated with significant morbidity and even mortality. Molecular imaging of GvHD has the potential to diagnose and monitor the disease while circumventing the use of invasive biopsies and to make a diagnosis earlier during GVHD, when intervention may be more successful. We have summarized how different molecular imaging strategies can be applied to the study of different phases of GvHD pathogenesis (Fig. 1), including [$^{18}$F]FDG as a nonspecific but sensitive and versatile marker across all phases and several investigational target molecules for various molecular processes. Preclinical studies suggest that molecular imaging has the potential to detect the GvHD process before tissue damage and symptoms actually occur. Clinical trials are needed to define the optimal timing of molecular imaging for early GvHD diagnosis and additionally assess its potential for risk stratification and for monitoring response to therapy.

## DISCLOSURE

Israt Alam was supported by NIH/NCI (R01 CA286998-01). Federico Simonetta was supported by the Geneva Cancer League (LGC 20 11) and the Dubois-Ferriere-Dinu-Lipatti Foundation. No other potential conflict of interest relevant to this article was reported.

## REFERENCES

1. Zeiser R, Blazar BR. Acute graft-versus-host disease: biologic process, prevention, and therapy. *N Engl J Med.* 2017;377:2167–2179.
2. Lubner MG, Menias CO, Agrons M, et al. Imaging of abdominal and pelvic manifestations of graft-versus-host disease after hematopoietic stem cell transplant. *AJR.* 2017;209:33–45.

3. Roll W, Evers G, Strotmann R, et al. Fluorodeoxyglucose F 18 for the assessment of acute intestinal graft-versus-host disease and prediction of response to immunosuppressive therapy. *Transplant Cell Ther.* 2021;27:603–610.
4. Cherk MH, Khor R, Barber TW, et al. Noninvasive assessment of acute graft-versus-host disease of the gastrointestinal tract after allogeneic hemopoietic stem cell transplantation using $^{18}$F-FDG PET. *J Nucl Med.* 2022;63:1899–1905.
5. Roll W, Schindler P, Masthoff M, et al. $^{18}$F-FDG-PET-MRI for the assessment of acute intestinal graft-versus-host-disease (GvHD). *BMC Cancer.* 2021;21:1015.
6. Li C, Han C, Duan S, Li P, Alam IS, Xiao Z. Visualizing T-cell responses: the T-cell PET imaging toolbox. *J Nucl Med.* 2022;63:183–188.
7. Alam IS, Shaffer TM, Gambhir SS. Nuclear imaging of endogenous markers of lymphocyte response. In: Harsini S, Alavi A, Rezaei N, eds. *Nuclear Medicine and Immunology.* Springer International Publishing; 2022:15–59.
8. Lee YZ, Akinnagbe-Zusterzeel E, Fowler KA, Coghill JM. $^{18}$F-3′-deoxy-3′-fluorothymidine positron emission tomography imaging for the prediction of acute graft-versus-host disease in mouse hematopoietic stem cell transplant models. *Biol Blood Marrow Transplant.* 2018;24:2184–2189.
9. Ronald JA, Kim B-S, Gowrishankar G, et al. A PET imaging strategy to visualize activated T cells in acute graft-versus-host disease elicited by allogenic hematopoietic cell transplant. *Cancer Res.* 2017;77:2893–2902.
10. Pektor S, Schlöder J, Klasen B, et al. Using immuno-PET imaging to monitor kinetics of T cell-mediated inflammation and treatment efficiency in a humanized mouse model for GvHD. *Eur J Nucl Med Mol Imaging.* 2020;47:1314–1325.
11. Van Elssen CHMJ, Rashidian M, Vrbanac V, et al. Noninvasive imaging of human immune responses in a human xenograft model of graft-versus-host disease. *J Nucl Med.* 2017;58:1003–1008.
12. Alam IS, Mayer AT, Sagiv-Barfi I, et al. Imaging activated T cells predicts response to cancer vaccines. *J Clin Invest.* 2018;128:2569–2580.
13. Alam IS, Simonetta F, Scheller L, et al. Visualization of activated T cells by OX40-immunoPET as a strategy for diagnosis of acute graft-versus-host disease. *Cancer Res.* 2020;80:4780–4790.
14. Tkachev V, Furlan SN, Watkins B, et al. Combined OX40L and mTOR blockade controls effector T cell activation while preserving Treg reconstitution after transplant. *Sci Transl Med.* 2017;9:eaan3085.
15. Tripathi T, Yin W, Xue Y, et al. Central roles of OX40L-OX40 interaction in the induction and progression of human T cell-driven acute graft-versus-host disease. *Immunohorizons.* 2019;3:110–120.
16. Xiao Z, Alam IS, Simonetta F, et al. ICOS immunoPET enables visualization of activated T cells and early diagnosis of murine acute gastrointestinal GvHD. *Blood Adv.* 2022;6:4782–4792.
17. Xiao Z, Mayer AT, Nobashi TW, Gambhir SS. ICOS is an indicator of T-cell–mediated response to cancer immunotherapy. *Cancer Res.* 2020;80:3023–3032.
18. Simonetta F, Alam IS, Lohmeyer JK, et al. Molecular imaging of chimeric antigen receptor T cells by ICOS-immunoPET. *Clin Cancer Res.* 2021;27:1058–1068.
19. Scott AP, Thomas P, Pattison DA, et al. [$^{18}$F]GE-180 PET/CT assessment of enterocytic translocator protein (TSPO) over-expression: a pilot study in gastrointestinal GVHD. *Bone Marrow Transplant.* 2022;57:517–519.
20. Cherry SR, Jones T, Karp JS, Qi J, Moses WW, Badawi RD. Total-body PET: maximizing sensitivity to create new opportunities for clinical research and patient care. *J Nucl Med.* 2018;59:3–12.
21. Pidala J, Hamadani M, Dawson P, et al. Randomized multicenter trial of sirolimus vs prednisone as initial therapy for standard-risk acute GVHD: the BMT CTN 1501 trial. *Blood.* 2020;135:97–107.
22. Etra A, Gergoudis S, Morales G, et al. Assessment of systemic and gastrointestinal tissue damage biomarkers for GVHD risk stratification. *Blood Adv.* 2022;6(12): 3707–3715 [erratum]. Blood Adv. 2022;6:4437–4438.

# Rethinking Dosimetry: The Perils of Extrapolated External-Beam Radiotherapy Constraints to Radionuclide Therapy

Jonathan Strosberg[1], Michael S. Hofman[2,3], Taymeyah Al-Toubah[1], and Thomas A. Hope[4]

*[1]Department of Gastrointestinal Oncology, H. Lee Moffitt Cancer Center and Research Institute, Tampa, Florida; [2]Prostate Cancer Theranostics and Imaging Centre of Excellence, Molecular Imaging and Therapeutic Nuclear Medicine, Cancer Imaging, Peter MacCallum Centre, Melbourne, Victoria, Australia; [3]Sir Peter MacCallum Department of Oncology, University of Melbourne, Melbourne, Victoria, Australia; and [4]Department of Radiology and Biomedical Imaging, University of California San Francisco, San Francisco, California*

Ongoing discussion within the nuclear medicine community suggests that all radionuclide therapies (RNTs) should include posttreatment quantitative dosimetry as part of standard clinical care. The hypothesis is that fixed administered activities limit the potential efficacy of RNT and increase the risk of side effects; therefore, patient-specific dosimetry should be leveraged to improve patient outcomes. Furthermore, the development of new radionuclides is often constrained by dosimetry-defined limits to normal organs extrapolated from external-beam radiation therapy (EBRT).

At the same time, with few exceptions, nonradioactive oncologic therapies are administered as fixed or calculated doses based on patient weight or body surface area. Although personalized dosing schemes based on tumor burden, pharmacokinetics, and pharmacodynamics can potentially improve the therapeutic index of cancer treatments, very few such regimens have been adopted in clinical practice (*1*–*3*). Large, randomized clinical trials are required to validate personalized treatment regimens compared with conventional ones, and few such trials have been conducted.

RNTs differ from nonradioactive systemic cancer treatments, as absorbed doses to tumors and normal organs can be quantified directly. Many experts argue that the similarities between RNT and EBRT mandate dosimetry: no radiation oncologist would conceive of treating a patient without a precise dose calculation to target tumor and surrounding tissues. Once a threshold of radioactivity administered to a field is exceeded, toxicity can be irreversible. By analogy, no systemic RNT should be administered without analyzing the absorbed dose to at-risk organs and tumors (*4*,*5*).

However, in many other ways, this comparison fails. EBRT is administered in a prescriptive fashion to a specific region. Effective dose ranges (typically measured in grays) for particular cancers have been well established, and the radiation sensitivities of surrounding tissues are known. Precise radiation doses to tumors and adjacent organs can be calibrated using increasingly sophisticated techniques to maximize response and minimize toxicity (*6*). None of these features of EBRT can be translated to systemically administered RNT. Instead, RNT dosimetry estimates absorbed dose to tumors and organs using imaging after the administration of the therapy. Additionally, absorbed doses and their biologic effects vary substantially on the basis of radionuclide properties, including pathlength and linear energy transfer (*7*).

In EBRT, dosimetry is calculated for tissues within a radiation field. With RNT, the usual organs of concern are typically the kidneys (for renally excreted radiopharmaceuticals) and the bone marrow, the organ most sensitive to the effects of systemic radiation. Renal doses are more straightforward to estimate than marrow doses, and therefore, the kidneys are commonly treated as the target organ. Traditionally, a threshold absorbed dose of 23 Gy to the kidneys has been considered a maximum tolerable dose, guided by the International Commission on Radiological Protection recommendations or QUANTEC (Quantitative Analyses of Normal Tissue Effects in the Clinic) (*7*–*9*). However, there are obvious pitfalls when trying to correlate the biologic effects of EBRT on the entire kidney with the effects of radionuclides excreted through renal tubules. Even among β-emitting radionuclides, the differences in nephrotoxicity between $^{90}$Y (12-mm pathlength) and $^{177}$Lu (2-mm pathlength) are substantial when administered at a similar estimated absorbed dose to the kidney (*10*).

Let us assume that we could accurately measure normal-organ–absorbed doses. With respect to kidney-based dosing, it is increasingly apparent that the kidney is not a dose-limiting organ. Although single-arm studies have suggested that $^{177}$Lu-DOTATATE causes a modest annual decrease in glomerular filtration rate, the randomized phase III NETTER 1 trial showed no difference in creatinine clearance over time between the $^{177}$Lu-DOTATATE and control arms (*11*). Studies that calibrate administered activity on the basis of absorbed renal doses nearly uniformly lead to an increase in total administered activity (*12*). However, if the kidney is not a dose-limiting organ, administration up to an artificial renal dose threshold should not be considered a personalized form of treatment but rather a simple dose escalation.

The bone marrow is a dose-limiting organ for many patients, and an absorbed dose of 2 Gy to the red marrow is considered a maximum threshold, extrapolated from $^{131}$I therapy (*13*). However, marrow dosimetric calculations are imprecise. Uptake on

Received Nov. 28, 2023; revision accepted Dec. 8, 2023.
For correspondence or reprints, contact Jonathan R. Strosberg (jonathan.strosberg@moffitt.org).
Published online Jan. 11, 2024.

DOI: 10.2967/jnumed.123.267167

posttherapy imaging may be reduced because of partial-volume effects or may be overestimated because of background noise. Even with the addition of plasma sampling, calculated marrow doses may vary depending on the technique, and different radionuclides can produce substantial variations in marrow toxicity (*14*). Moreover, patient-specific factors (age, genomic predisposition, prior treatments, etc.) influence sensitivity to radiation (as is the case with chemotherapy) (*15–17*). Some studies have shown no correlation between bone marrow dose and cytopenias; others have shown weak correlations (*10*,*18*,*19*). However, a more straightforward method of assessing bone marrow toxicity and adjusting administered activity is the complete blood count. There is no evidence that dosimetric calculations are superior to a simple complete blood count for personalizing treatment. Additionally, there is no evidence that dosimetry can predict the most catastrophic long-term complications of treatment: myelodysplastic syndrome or acute leukemia (*20*,*21*).

Dosimetry can also be used to calculate absorbed tumor doses. Although dose–response relationships are expected, our understanding of tumor dosimetry in RNT lags far behind our knowledge of optimal dosing in EBRT. Traditional approaches using several manually identified index tumor lesions, typically with the highest activity, fail to correlate with survival outcomes or lead to actionable changes in management (*22*). This is not surprising given tumor heterogeneity and the varying doses delivered to sites within an individual. Newer approaches using whole-body tumor dosimetry may be superior. For example, among 11 patients who received less than a 10-Gy median whole-body tumor dose after $^{177}$Lu-PSMA-617 treatment, only one achieved a prostate-specific antigen response (*23*). However, it is not yet clear how tumor dosimetry data can be leveraged to improve patient outcomes. For example, should a low absorbed tumor dose prompt additional cycles of treatment or early discontinuation for futility?

Dosimetry has evolved enormously in the last decade. There has been a transition from planar imaging to quantitative SPECT/CT imaging. This has enabled a shift from dosimetry modeling based on a standard human with assumed organ masses and shapes to direct measurements using voxel-based techniques (*24*). New PET-like ring-designed SPECT/CT devices using solid-state detectors enable more accurate dose estimates with better resolution and speed. Contouring of normal organs has moved from a manual process at multiple time points to semiautomated techniques using defined thresholds or fully automated techniques using deep learning algorithms assisted by the CT (*25*). The number of time points required for accurate dosimetry is decreasing, with even single time points feasible, using either patient-specific parameters from cycle 1 or population-based databases (*26*).

Dosimetry sits at a crossroads. It is time to move away from extrapolating external-beam–defined normal-organ constraints to RNT. Direct observation of adverse effects is simpler and superior. We must still monitor for longer-term adverse effects, especially within organs of interest. Advances in quantitative SPECT/CT and software open new opportunities to redefine the use of dosimetry to improve patient outcomes. Undoubtedly, there are superior personalized administration schedules that modulate the amount and frequency of the administered activity. However, only well-designed randomized clinical trials with long-term follow-up can accurately evaluate whether novel dosimetry-based prescriptions are superior to fixed schedules. As with any other oncologic therapy, the burden of proof is on us to demonstrate that these strategies yield superior efficacy or safety outcomes. We hope that improved evidence-based strategies will be developed to improve patient care.

## DISCLOSURE

Michael Hofman acknowledges philanthropic/government grant support from the Prostate Cancer Foundation (PCF), including CANICA Oslo Norway, the Peter MacCallum Foundation, the Medical Research Future Fund (MRFF), an NHMRC Investigator Grant, Movember, and the Prostate Cancer Foundation of Australia (PCFA); other funding (in the last 10 y) from the U.S. Department of Defense; research grant support (to the Peter MacCallum Cancer Centre) from Novartis (including AAA and Endocyte), ANSTO, Bayer, Isotopia, and MIM; and consulting fees for lectures or advisory boards from Astellas and AstraZeneca (in the last 2 y) and from Janssen, Merck/MSD, and Mundipharma (in the last 5 y). Thomas Hope has received grant funding to the institution from Clovis Oncology, GE Healthcare, Lantheus, Janssen, the Prostate Cancer Foundation, Telix, and the National Cancer Institute (R01CA235741 and R01CA212148); personal fees from Bayer, BlueEarth Diagnostics, and Lantheus; and fees from and has an equity interest in RayzeBio and Curium. Jonathan Strosberg has received grant funding to the institution from Rayzebio, Radiomedix, Novartis, and ITM. No other potential conflict of interest relevant to this article was reported.

## REFERENCES

1. Masson E, Zamboni WC. Pharmacokinetic optimisation of cancer chemotherapy. Effect on outcomes. *Clin Pharmacokinet.* 1997;32:324–343.
2. Larson RA, Druker BJ, Guilhot F, et al. Imatinib pharmacokinetics and its correlation with response and safety in chronic-phase chronic myeloid leukemia: a subanalysis of the IRIS study. *Blood.* 2008;111:4022–4028.
3. Lau DK, Fong C, Arouri F, et al. Impact of pharmacogenomic DPYD variant guided dosing on toxicity in patients receiving fluoropyrimidines for gastrointestinal cancers in a high-volume tertiary centre. *BMC Cancer.* 2023;23:380.
4. Stabin MG. Update: the case for patient-specific dosimetry in radionuclide therapy. *Cancer Biother Radiopharm.* 2008;23:273–284.
5. Wahl RL, Sunderland J. Radiopharmaceutical dosimetry for cancer therapy: from theory to practice. *J Nucl Med.* 2021;62(suppl 3):1S–2S.
6. Jaffray DA. Image-guided radiotherapy: from current concept to future perspectives. *Nat Rev Clin Oncol.* 2012;9:688–699.
7. Wahl RL, Sgouros G, Iravani A, et al. Normal-tissue tolerance to radiopharmaceutical therapies, the knowns and the unknowns. *J Nucl Med.* 2021;62(suppl 3):23S–35S.
8. Wessels BW, Konijnenberg MW, Dale RG, et al. MIRD pamphlet no. 20: the effect of model assumptions on kidney dosimetry and response—implications for radionuclide therapy. *J Nucl Med.* 2008;49:1884–1899.
9. Emami B, Lyman J, Brown A, et al. Tolerance of normal tissue to therapeutic irradiation. *Int J Radiat Oncol Biol Phys.* 1991;21:109–122.
10. Bodei L, Kidd M, Paganelli G, et al. Long-term tolerability of PRRT in 807 patients with neuroendocrine tumours: the value and limitations of clinical factors. *Eur J Nucl Med Mol Imaging.* 2015;42:5–19.
11. Strosberg JR, Caplin ME, Kunz PL, et al. $^{177}$Lu-Dotatate plus long-acting octreotide versus high-dose long-acting octreotide in patients with midgut neuroendocrine tumours (NETTER-1): final overall survival and long-term safety results from an open-label, randomised, controlled, phase 3 trial. *Lancet Oncol.* 2021;22:1752–1763.
12. Del Prete M, Buteau FA, Arsenault F, et al. Personalized $^{177}$Lu-octreotate peptide receptor radionuclide therapy of neuroendocrine tumours: initial results from the P-PRRT trial. *Eur J Nucl Med Mol Imaging.* 2019;46:728–742.
13. Benua RS, Cicale NR, Sonenberg M, Rawson RW. The relation of radioiodine dosimetry to results and complications in the treatment of metastatic thyroid cancer. *AJR.* 1962;87:171–182.
14. Reidy-Lagunes D, Pandit-Taskar N, O'Donoghue JA, et al. Phase I trial of well-differentiated neuroendocrine tumors (NETs) with radiolabeled somatostatin antagonist $^{177}$Lu-satoreotide tetraxetan. *Clin Cancer Res.* 2019;25:6939–6947.
15. Huang RX, Zhou PK. DNA damage response signaling pathways and targets for radiotherapy sensitization in cancer. *Signal Transduct Target Ther.* 2020;5:60.

16. Asadollahi R, Britschgi C, Joset P, et al. Severe reaction to radiotherapy provoked by hypomorphic germline mutations in ATM (ataxia-telangiectasia mutated gene). *Mol Genet Genomic Med.* 2020;8:e1409.
17. Mylavarapu S, Das A, Roy M. Role of BRCA mutations in the modulation of response to platinum therapy. *Front Oncol.* 2018;8:16.
18. Bergsma H, Konijnenberg MW, Kam BL, et al. Subacute haematotoxicity after PRRT with $^{177}$Lu-DOTA-octreotate: prognostic factors, incidence and course. *Eur J Nucl Med Mol Imaging.* 2016;43:453–463.
19. Garske-Román U, Sandström M, Fröss Baron K, et al. Prospective observational study of $^{177}$Lu-DOTA-octreotate therapy in 200 patients with advanced metastasized neuroendocrine tumours (NETs): feasibility and impact of a dosimetry-guided study protocol on outcome and toxicity. *Eur J Nucl Med Mol Imaging.* 2018;45:970–988.
20. Bergsma H, van Lom K, Raaijmakers MHGP, et al. Persistent hematologic dysfunction after peptide receptor radionuclide therapy with $^{177}$Lu-DOTATATE: incidence, course, and predicting factors in patients with gastroenteropancreatic neuroendocrine tumors. *J Nucl Med.* 2018;59:452–458.
21. Goncalves I, Burbury K, Michael M, et al. Characteristics and outcomes of therapy-related myeloid neoplasms after peptide receptor radionuclide/chemoradionuclide therapy (PRRT/PRCRT) for metastatic neuroendocrine neoplasia: a single-institution series. *Eur J Nucl Med Mol Imaging.* 2019;46:1902–1910.
22. Alipour R, Jackson P, Bressel M, et al. The relationship between tumour dosimetry, response, and overall survival in patients with unresectable neuroendocrine neoplasms (NEN) treated with $^{177}$Lu DOTATATE (LuTate). *Eur J Nucl Med Mol Imaging.* 2023;50:2997–3010.
23. Violet J, Jackson P, Ferdinandus J, et al. Dosimetry of $^{177}$Lu-PSMA-617 in metastatic castration-resistant prostate cancer: correlations between pretherapeutic imaging and whole-body tumor dosimetry with treatment outcomes. *J Nucl Med.* 2019;60:517–523.
24. Jackson PA, Beauregard JM, Hofman MS, Kron T, Hogg A, Hicks RJ. An automated voxelized dosimetry tool for radionuclide therapy based on serial quantitative SPECT/CT imaging. *Med Phys.* 2013;40:112503.
25. Jackson P, Hardcastle N, Dawe N, Kron T, Hofman MS, Hicks RJ. Deep learning renal segmentation for fully automated radiation dose estimation in unsealed source therapy. *Front Oncol.* 2018;8:215.
26. Jackson PA, Hofman MS, Hicks RJ, Scalzo M, Violet J. Radiation dosimetry in $^{177}$Lu-PSMA-617 therapy using a single posttreatment SPECT/CT scan: a novel methodology to generate time- and tissue-specific dose factors. *J Nucl Med.* 2020;61:1030–1036.

# Imaging of Tumor Stroma Using $^{68}$Ga-FAPI PET/CT to Improve Diagnostic Accuracy of Primary Tumors in Head and Neck Cancer of Unknown Primary: A Comparative Imaging Trial

Bingxin Gu[1–4], Ziyi Yang[1–4], Xinyue Du[1–4], Xiaoping Xu[1–4], Xiaomin Ou[5], Zuguang Xia[6], Qing Guan[7], Silong Hu[1–4], Zhongyi Yang[1–4], and Shaoli Song[1–4]

*[1]Department of Nuclear Medicine, Fudan University Shanghai Cancer Center, Shanghai, China; [2]Department of Oncology, Shanghai Medical College, Fudan University, Shanghai, China; [3]Center for Biomedical Imaging, Fudan University, Shanghai, China; [4]Shanghai Engineering Research Center of Molecular Imaging Probes, Shanghai, China; [5]Department of Radiation Oncology, Fudan University Shanghai Cancer Center, Shanghai, China; [6]Department of Medical Oncology, Fudan University Shanghai Cancer Center, Shanghai, China; and [7]Department of Head and Neck Surgery, Fudan University Shanghai Cancer Center, Shanghai, China*

The low detection rate of primary tumors by current diagnostic techniques remains a major concern for patients with head and neck cancer of unknown primary (HNCUP). Therefore, in this study, we aimed to investigate the potential role of $^{68}$Ga-labeled fibroblast activation protein inhibitor ($^{68}$Ga-FAPI) PET/CT compared with $^{18}$F-FDG PET/CT for the detection of primary tumors of HNCUP. **Methods:** In this prospective comparative imaging trial conducted at Fudan University Shanghai Cancer Center, 91 patients with negative or equivocal findings of a primary tumor by comprehensive clinical examination and conventional imaging were enrolled from June 2020 to September 2022. The presence of a primary tumor was recorded by 3 experienced nuclear medicine physicians. Primary lesions were validated by histopathologic analysis and a composite reference standard. **Results:** Of the 91 patients (18 women, 73 men; median age, 60 y; age range, 24–76 y), primary tumors were detected in 46 (51%) patients after a thorough diagnostic work-up. $^{68}$Ga-FAPI PET/CT detected more primary lesions than $^{18}$F-FDG PET/CT (46 vs. 17, $P < 0.001$) and showed better sensitivity, positive predictive value, and accuracy in locating primary tumors (51% vs. 25%, 98% vs. 43%, and 51% vs. 19%, respectively). Furthermore, $^{68}$Ga-FAPI PET/CT led to treatment changes in 22 of 91 (24%) patients compared with $^{18}$F-FDG PET/CT. The Kaplan–Meier curve illustrated that patients with unidentified primary tumors had a significantly worse prognosis than patients with identified primary tumors (hazard ratio, 5.77; 95% CI, 1.86–17.94; $P = 0.0097$). **Conclusion:** $^{68}$Ga-FAPI PET/CT outperforms $^{18}$F-FDG PET/CT in detecting primary lesions and could serve as a sensitive, reliable, and reproducible imaging modality for HNCUP patients.

**Key Words:** fibroblast activation protein; FDG; PET/CT; head and neck cancer; cancer of unknown primary

**J Nucl Med 2024; 65:365–371**
DOI: 10.2967/jnumed.123.266556

Head and neck cancer of unknown primary (HNCUP) is a group of highly heterogeneous malignancies and usually manifests as an enlarged cervical lymph node at initial diagnosis (*1*). The low incidence of HNCUP, accounting for 1%–5% of all head and neck cancers (*2*), and the uneven medical level lead to a lack of normative experience among different medical centers in locating primary tumors. The increase in multidisciplinary teams may improve the quality of assessment and management for HNCUP patients based on previously proposed guidelines, for example, the National Comprehensive Cancer Network (*3*) and American Society of Clinical Oncology (*4*) guidelines. Nevertheless, the low detection rate of primary tumors by current diagnostic techniques (e.g., CT, MRI, nasopharyngoscopy, and laryngoscopy) remains a major concern for patients with HNCUP (*5*).

Molecular imaging using $^{18}$F-FDG PET/CT improves the detection of primary tumors compared with CT and MRI by reflecting the level of glucose metabolism in tumor cells (*6*). Schaarschmidt et al. (*7*) demonstrated that $^{18}$F-FDG PET/CT or PET/MRI outperformed MRI alone for T staging in terms of accuracy (59% or 75% vs. 50%). However, elevated nonspecific uptake of $^{18}$F-FDG by normal tissues or inflammatory cells in the head and neck region may lead to false-positive findings and may conceal small primary tumors, especially in the oropharynx, resulting in a false-negative diagnosis (*8–10*). In addition to noninvasive and minimally invasive methods, diagnostic tonsillectomy is recommended for patients with metastatic squamous cell carcinoma on the neck and human papillomavirus positivity but no obvious signs of primary tumors on clinical examination, imaging, or panendoscopy (*4*). Alzahrani et al. (*11*) reported a detection rate of 49.2% for locating primary tumors via transoral robotic mucosectomy in 65 patients with negative findings on comprehensive clinical examination and standard imaging. Nevertheless, postoperative complications, for example, pneumonia, feeding difficulty, and hemorrhage, may prolong hospitalization and delay antineoplastic therapy (*12*). Therefore, noninvasive diagnostic techniques to improve the detection of primary tumors before definitive therapy for HNCUP patients are urgently need.

Recently, PET imaging targeting fibroblast activation protein (FAP) has shown great potential in depicting non–$^{18}$F-FDG-avid malignant tumors (*13*,*14*). FAP is overexpressed on cancer-associated

Received Aug. 17, 2023; revision accepted Dec. 19, 2023.
For correspondence or reprints, contact Shaoli Song (shaoli-song@163.com) or Zhongyi Yang (yangzhongyi21@163.com).
Published online Jan. 25, 2024.

fibroblasts, which account for most tumor stromata in more than 90% of epithelial carcinomas (*15*). By imaging the tumor stroma rather than tumor cells, $^{68}$Ga-labeled FAP inhibitor (FAPI) PET/CT reveals elevated radioactivity on primary and metastatic lesions and low background uptake in normal tissues among various tumors, including gastrointestinal tumors (*16*), hepatobiliary tumors (*17*), and head and neck cancers (*18*). Serfling et al. (*18*) demonstrated that noninvasive imaging of FAP expression by $^{68}$Ga-FAPI PET/CT resulted in better visual detection of the malignant primary tumors in the Waldeyer tonsillar ring, thereby avoiding diagnostic tonsillectomy.

Inspired by the promising results of $^{68}$Ga-FAPI PET/CT imaging in patients with various head and neck cancers (e.g., nasopharyngeal carcinoma, oropharyngeal cancer, and salivary ductal carcinoma), we hypothesized that $^{68}$Ga-FAPI PET/CT would outperform $^{18}$F-FDG PET/CT in localizing primary tumors in HNCUP patients. Thus, in this study, we aimed to investigate the potential usefulness of $^{68}$Ga-FAPI PET/CT compared with $^{18}$F-FDG PET/CT for the detection of primary tumors in patients with HNCUP. The primary objective of this study was to compare the sensitivity, positive predictive value, and accuracy of $^{68}$Ga-FAPI and $^{18}$F-FDG PET/CT in localizing primary tumors. Secondary objectives were to compare $^{68}$Ga-FAPI and $^{18}$F-FDG uptake by primary and metastatic lesions and progression-free survival.

## MATERIALS AND METHODS

### Patients

This was a prospective comparative imaging trial performed at Fudan University Shanghai Cancer Center from June 2020 to September 2022. Patients were eligible if they met the following inclusion criteria: older than 18 y, pathology-confirmed metastatic cervical carcinoma, negative or equivocal finding of a primary tumor by comprehensive clinical examination and conventional imaging modalities (e.g., contrast-enhanced CT and MRI), and paired $^{18}$F-FDG and $^{68}$Ga-FAPI PET/CT scans within 1 wk. Patients with non–head and neck primary carcinomas, lymphoepitheliomalike carcinoma, 2 or more malignances, and unavailable clinical data were excluded.

The Standards for Reporting of Diagnostic Accuracy checklist is included in Supplemental Data 1 (supplemental materials are available at http://jnm.snmjournals.org), and the flow diagram is shown in Supplemental Figure 1 and Supplemental Data 2. The study was approved by the Fudan University Shanghai Cancer Center Institutional Review Board (2004216-25), and written informed consent was obtained from each patient. The data of 18 patients have been reported previously (*10*).

### PET/CT Acquisition and Image Interpretation

$^{18}$F-FDG and $^{68}$Ga-FAPI PET/CT were performed within 1 wk. The 2 radionuclide PET/CT scans were obtained from a Biograph mCT Flow scanner (Siemens Medical Solutions). The detailed protocols for image acquisition and reconstruction are presented in Supplemental Data 2 (*19*).

Three experienced nuclear medicine physicians analyzed and interpreted the $^{18}$F-FDG and $^{68}$Ga-FAPI PET/CT images independently, and they reached a consensus in cases of inconsistency. Lesions with increased radioactivity compared with the surrounding normal tissue and not associated with physiologic uptake were considered suspected malignant lesions. $SUV_{max}$ and $SUV_{mean}$ normalized to body weight were manually computed by drawing a 3-dimensional volume of interest for the tumor lesion and normal liver, respectively. Meanwhile, the tumor-to-liver ratio (TLR) was calculated according to the following formula: $TLR = tSUV_{max}/lSUV_{mean}$, where $tSUV_{max}$ is the $SUV_{max}$ of the tumor lesion and $lSUV_{mean}$ is the $SUV_{mean}$ of the liver.

### Clinical Assessment and Follow-up

All suspected primary sites detected by $^{18}$F-FDG or $^{68}$Ga-FAPI PET/CT were verified by biopsy or histopathologic examination. Suspected metastatic lesions were confirmed by biopsy or 6-mo follow-up. Suspected metastatic lesions with typical malignant features on PET/CT images or a significant reduction or progression in size after anticancer treatment during follow-up were considered malignant. After a thorough diagnostic work-up, including medical history, imaging, and endoscopy or tonsillectomy, all patients with or without an identified primary tumor received treatment based on the decision of the multidisciplinary head and neck cancer team. Treatment response was assessed by imaging examination according to RECIST version 1.1 (*20*). The endpoint was set as progression-free survival, defined as the time randomization to disease progression or death.

### Statistical Analysis

Differences in general information between patients with identified and those with unidentified primary tumors were evaluated using the Mann–Whitney test (for continuous characteristics) and the $\chi^2$ test or Fisher exact test (for discrete characteristics). The differences in $SUV_{max}$ and TLR between $^{18}$F-FDG and $^{68}$Ga-FAPI PET/CT were assessed using the paired *t* test and Wilcoxon signed-rank test, respectively. Diagnostic performance was evaluated by receiver-operating-characteristic curve analysis. The survival analyses were performed using the Kaplan–Meier method. SPSS version 26 (IBM) was used for statistical analyses. A 2-tailed *P* value of less than 0.05 was considered statistically significant.

## RESULTS

### Patient Characteristics

From June 2020 to September 2022, 91 patients (18 women, 73 men; median age, 60 y; age range, 24–76 y) were enrolled in this prospective study. Of the 91 patients, a primary tumor was detected in 46 (51%) patients after a thorough diagnostic work-up. The baseline characteristics for the patients with identified and unidentified primary tumors are presented in Table 1 and Supplemental Data 3. Among these clinical characteristics, the presence of Epstein–Barr virus DNA and the Epstein–Barr virus–encoded small RNA status showed significant differences between these 2 cohorts, whereas there was no significant difference in the human papillomavirus or p16 status. With regard to the therapeutic regimen, chemotherapy and radiotherapy were the main choices for patients with identified primary tumors, whereas chemotherapy was the main choice for patients with unidentified primary tumors.

### Assessment of Metastatic Lesions on $^{18}$F-FDG and $^{68}$Ga-FAPI PET/CT

In total, 121 lymph node metastases and 15 bone metastases were involved in the analysis (Fig. 1; Supplemental Table 1). In terms of lymph node metastases, $^{18}$F-FDG PET/CT detected all metastatic lesions with significantly higher semiquantitative $SUV_{max}$ than $^{68}$Ga-FAPI PET/CT ($12.48 \pm 6.10$ and $9.80 \pm 5.02$, respectively; $P < 0.001$). Nevertheless, TLR presented more favorable uptake of $^{68}$Ga-FAPI than $^{18}$F-FDG ($18.65 \pm 10.50$ and $5.64 \pm 2.81$, respectively; $P < 0.001$). With regard to bone metastases, $^{68}$Ga-FAPI PET/CT outperformed $^{18}$F-FDG PET/CT in terms of $SUV_{max}$ ($13.65 \pm 5.12$ and $10.85 \pm 6.17$, respectively; $P = 0.173$) and TLR ($21.99 \pm 9.70$ and $4.94 \pm 2.90$, respectively; $P < 0.001$).

### Evaluation of Primary Tumors on $^{18}$F-FDG and $^{68}$Ga-FAPI PET/CT

Among the 46 patients with identified primary tumors, 39 patients received confirmation by pathology, whereas the other 7

**TABLE 1**
Baseline Characteristics

| Characteristic | Total, $n = 91$ | Primary tumor identified, $n = 46$ | Primary tumor unidentified, $n = 45$ | $P$ |
|---|---|---|---|---|
| Sex | | | | 0.793 |
| Female | 18 (20) | 10 (22) | 8 (18) | |
| Male | 73 (80) | 36 (78) | 37 (82) | |
| Age (y) | 60 (24–76) | 55 (33–76) | 61 (24–73) | 0.238 |
| Body mass index (kg/m$^2$) | 23 (10–31) | 23 (10–29) | 24 (18–31) | 0.149 |
| Pathologic type of cervical lymph node | | | | 0.198 |
| Squamous cell carcinoma | 81 (89) | 42 (91) | 39 (86) | |
| Adenocarcinoma | 7 (8) | 4 (9) | 3 (7) | |
| Poorly differentiated carcinoma | 3 (3) | 0 (0) | 3 (7) | |
| EBV DNA status | | | | 0.024* |
| Positive | 16 (17) | 13 (28) | 3 (7) | |
| Negative | 47 (52) | 20 (44) | 27 (60) | |
| Unknown | 28 (31) | 13 (28) | 15 (33) | |
| Human papillomavirus status | | | | 0.787 |
| Positive | 10 (11) | 6 (13) | 4 (9) | |
| Negative | 11 (12) | 5 (11) | 6 (13) | |
| Unknown | 70 (77) | 35 (76) | 35 (78) | |
| EBV-encoded RNA status | | | | 0.028* |
| Positive | 18 (20) | 13 (28) | 5 (11) | |
| Negative | 39 (43) | 14 (31) | 25 (56) | |
| Unknown | 34 (37) | 19 (41) | 15 (33) | |
| p16 status | | | | 0.405 |
| Positive | 20 (22) | 12 (26) | 8 (18) | |
| Negative | 27 (30) | 11 (24) | 16 (35) | |
| Unknown | 44 (48) | 23 (50) | 21 (47) | |
| Surgery | | | | 0.677 |
| Yes | 45 (49) | 24 (52) | 21 (47) | |
| No | 46 (51) | 22 (48) | 24 (53) | |
| Chemotherapy | | | | 0.026* |
| Yes | 70 (77) | 40 (87) | 30 (67) | |
| No | 21 (23) | 6 (13) | 15 (33) | |
| Radiotherapy | | | | <0.001* |
| Yes | 54 (59) | 37 (80) | 17 (38) | |
| No | 37 (41) | 9 (20) | 28 (62) | |
| Targeted therapy | | | | 0.231 |
| Yes | 12 (13) | 4 (9) | 8 (18) | |
| No | 79 (87) | 42 (91) | 37 (82) | |
| Immunotherapy | | | | 0.714 |
| Yes | 8 (9) | 5 (11) | 3 (7) | |
| No | 83 (91) | 41 (89) | 42 (93) | |
| Progression-free survival | | | | 0.014* |
| Progression | 12 (13) | 2 (4) | 10 (22) | |
| Progression-free | 79 (87) | 44 (96) | 35 (78) | |
| Follow-up (mo) | 19 (7–33) | 18 (7–32) | 19 (7–33) | 0.708 |

*Statistically significant at $P < 0.05$.
EBV = Epstein–Barr virus.
Qualitative data are number and percentage; continuous data are median or mean and range.

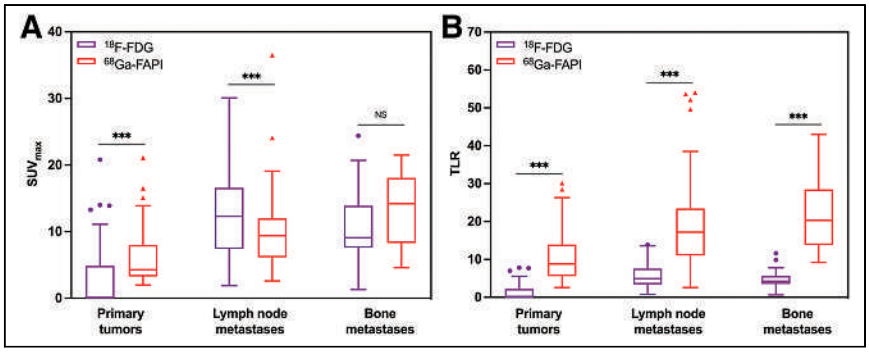


**FIGURE 1.** Box plots of $SUV_{max}$ (A) and TLR (B) detected on $^{18}$F-FDG and $^{68}$Ga-FAPI PET/CT. Primary tumors showed significantly higher semiquantitative uptake of $^{68}$Ga-FAPI than $^{18}$F-FDG ($P < 0.001$). $^{18}$F-FDG outperformed $^{68}$Ga-FAPI PET/CT in detecting lymph node metastases, with significantly higher $SUV_{max}$ ($P < 0.001$). In terms of TLR, lymph node and bone metastases presented more favorable uptake of $^{68}$Ga-FAPI than $^{18}$F-FDG ($P < 0.001$). ***$P < 0.001$. NS = no significance.

patients were pathologically negative but diagnosed clinically. Table 2 shows that the locations of primary tumors included the nasopharynx ($n = 14$; Supplemental Fig. 2), tonsil ($n = 21$; Supplemental Fig. 3), submandibular gland ($n = 3$), thyroid ($n = 3$), hypopharynx ($n = 2$), tongue ($n = 1$), laryngopharynx ($n = 1$), and palate ($n = 1$; Fig. 2; Supplemental Fig. 4). Among the 7 patients with the primary tumor diagnosed clinically, 4 patients were diagnosed as having nasopharyngeal carcinoma with metastatic cervical nonkeratinizing squamous cell carcinoma and Epstein–Barr virus infection, and the other 3 patients were diagnosed as having tonsil carcinoma with metastatic cervical squamous cell carcinoma and moderate to severe dysplasia of tonsil squamous epithelial cells.

Primary tumors in 17 of 91 (19%) patients were identified by $^{18}$F-FDG PET/CT. $^{68}$Ga-FAPI PET/CT showed a significantly higher detection rate (51%) of primary tumors than did $^{18}$F-FDG PET/CT ($P < 0.001$). Furthermore, $^{68}$Ga-FAPI PET/CT led to treatment changes in 22 of 91 (24%) patients compared with $^{18}$F-FDG PET/CT. Moreover, in terms of $SUV_{max}$ and TLR, primary tumors demonstrated significantly higher semiquantitative uptake of $^{68}$Ga-FAPI than $^{18}$F-FDG ($SUV_{max}$, $6.11 \pm 4.30$ and $3.16 \pm 5.11$, $P < 0.001$; TLR, $10.85 \pm 6.81$ and $1.45 \pm 2.31$, $P < 0.001$).

With regard to diagnostic performance in identifying primary tumors, contrast-enhanced MRI and $^{18}$F-FDG PET/CT showed similar sensitivity, positive predictive value, and accuracy, whereas contrast-enhanced CT showed the lowest sensitivity and accuracy (Table 3). $^{68}$Ga-FAPI PET/CT outperformed contrasted-enhanced CT, contrast-enhanced MRI, and $^{18}$F-FDG PET/CT in terms of sensitivity (51% vs. 17%, 27%, and 25%, respectively), positive predictive value (98% vs. 44%, 42%, and 43%, respectively), and accuracy (51% vs. 14%, 20%, and 19%, respectively).

### Survival Outcome

After PET/CT scans, the median follow-up time was 19 mo (range, 7–33 mo). Patients with identified primary tumors were managed with a specific regimen, whereas patients with unidentified primary tumors were treated by referring to the guidelines for HNCUP. The progression-free survival rate of patients with identified and unidentified primary tumors was 96% (44/46) and 78% (35/45), respectively. Moreover, the Kaplan–Meier curve (Fig. 3) illustrates that patients with unidentified primary tumors had a significantly worse prognosis than those with identified primary tumors (hazard ratio, 5.77; 95% CI, 1.86–17.94; $P = 0.0097$).

## DISCUSSION

To our knowledge, this study is the largest prospective study investigating the performance of $^{68}$Ga-FAPI PET/CT compared with $^{18}$F-FDG PET/CT in detecting primary tumors in patients with HNCUP. Our results demonstrated that $^{68}$Ga-FAPI PET/CT presented significantly higher diagnostic accuracy (51% vs. 19%, $P < 0.001$) and radioactive uptake ($SUV_{max}$, $6.11 \pm 4.30$ and

**TABLE 2**
Comparison of Primary Tumors Detected on $^{18}$F-FDG and $^{68}$Ga-FAPI PET/CT

| Primary tumor site | Total (*n*) | $^{18}$F-FDG | $^{68}$Ga-FAPI | Treatment change led by $^{68}$Ga-FAPI |
|---|---|---|---|---|
| Nasopharynx | 14 (4) | 6 | 14 (4) | 4 |
| Tonsil | 21 (3) | 5 | 21 (3) | 13 |
| Palatine tonsil | 13 (2) | 3 | 13 (2) | 8 |
| Lingual tonsil | 8 (1) | 2 | 8 (1) | 5 |
| Submandibular gland | 3 | 1 | 3 | 2 |
| Thyroid | 3 | 3 | 3 | 0 |
| Hypopharynx | 2 | 0 | 2 | 2 |
| Tongue | 1 | 1 | 1 | 0 |
| Laryngopharynx | 1 | 1 | 1 | 0 |
| Palate | 1 | 0 | 1 | 1 |
| Total, $n = 91$ | 46 (51%) | 17 (19%) | 46 (51%) | 22 (24%) |

Primary tumor site data in parentheses indicate primary tumor was pathologically negative but diagnosed clinically. Total tumor data are number and percentage ($P < 0.001$).

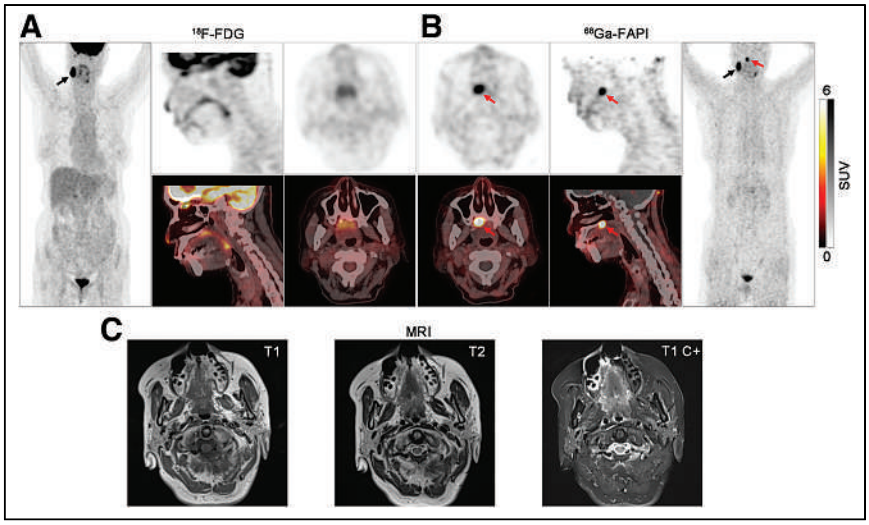


**FIGURE 2.** PET/CT and MR images of 72-y-old woman (patient 30) pathologically confirmed with metastatic squamous cell carcinoma of right neck. (A) $^{18}$F-FDG PET images (left and top) and PET/CT images (bottom), shown in coronal, sagittal, and axial views (from left to right), demonstrated metastatic lymph node of right neck with intensive metabolic activity (black arrow, $SUV_{max}$, 30.1) but presented no evidence for primary tumor. (B) $^{68}$Ga-FAPI PET images (top and right) and PET/CT images (bottom), shown in axial, sagittal, and coronal views (from left to right), also detected metastatic lymph node with high $^{68}$Ga-FAPI activity (black arrow, $SUV_{max}$, 16.3). There was intensive uptake of $^{68}$Ga-FAPI in palate (red arrow, $SUV_{max}$, 11.3). (C) T1-weighted, T2-weighted, and contrast-enhanced T1-weighted MRI also presented no evidence for primary tumor. Subsequent surgery confirmed mucoepidermoid carcinoma of palate. C+ = contrast-enhanced.

$3.16 \pm 5.11$, $P < 0.001$; TLR, $10.85 \pm 6.81$ and $1.45 \pm 2.31$, $P < 0.001$) in localizing primary tumors than did $^{18}$F-FDG PET/CT. Meanwhile, $^{68}$Ga-FAPI PET/CT led to treatment changes in 22 of 91 (24%) patients compared with $^{18}$F-FDG PET/CT. Furthermore, $^{68}$Ga-FAPI PET/CT outperformed $^{18}$F-FDG PET/CT in detecting lymph node and bone metastases in terms of TLR.

Our data also highlighted that the prognosis of patients was significantly improved by identifying the primary tumors ($P = 0.0097$; Fig. 3). Recent studies have shown that the 5-y overall survival of HNCUP patients is still dismal, approximately 55% (*21*). In addition, Faisal et al. (*22*) reported that the late detection of primary tumors in HNCUP patients after treatment may lead to significantly worse 5-y overall survival than that of HNCUP patients in whom primary tumors remain unidentified. Thus, accurate diagnosis of the primary tumor before treatment is crucial for patients with HNCUP.

Because the oropharynx is the most common primary location for HNCUP malignancies, diagnostic tonsillectomy is recommended for patients with metastatic squamous cell carcinoma of the neck when the primary tumor cannot be identified by noninvasive diagnostic methods, according to American Society of Clinical Oncology guidelines (*4*). However, only 18%–47% of patients with HNCUP could benefit from diagnostic tonsillectomy (*23–25*). $^{18}$F-FDG PET/CT, as a noninvasive, whole-body, and tumor-specific imaging modality, has been widely accepted for locating and clinically staging primary tumors before treatment (*26*). Significant visual differences between the tumor and the background on PET/CT images could effectively guide the biopsy of suspected malignant lesions. However, physiologic or inflammatory $^{18}$F-FDG uptake in the head and neck may hide small primary tumors, especially those in the oropharynx (*27*). In our current study, $^{18}$F-FDG PET/CT missed 16 of 21 primary tumors in the oropharynx, which is consistent with the research of Pencharz et al. (*27*). Surprisingly, $^{68}$Ga-FAPI PET/CT detected all 21 primary tumors in the oropharynx, with significantly higher uptake than in the contralateral normal oropharynx (Supplemental Fig. 3). In line with our research, Serfling et al. (*18*) demonstrated higher $^{68}$Ga-FAPI than $^{18}$F-FDG avidity within malignant primary tumors in the Waldeyer tonsillar ring. Furthermore, Mona et al. (*28*) reported stronger FAP expression in malignant oropharyngeal lesions than in nonmalignant tissue and a strong correlation between the uptake of $^{68}$Ga-FAPI and the FAP immunohistochemistry score. Therefore, our research further demonstrates that $^{68}$Ga-FAPI PET/CT could avoid invasive diagnostic tonsillectomy in patients with HNCUP.

In the current study, although $^{68}$Ga-FAPI PET/CT detected all 46 primary tumors, which were confirmed pathologically or clinically, the overall sensitivity and accuracy seemed unsatisfactory (51% for each characteristic). This may be because the other 45 patients presented with inconspicuous primary tumors on imaging and endoscopy. Even so, $^{68}$Ga-FAPI PET/CT could identify small, mucous, and adenoid carcinomas, which always presented non–$^{18}$F-FDG avidity (Table 1) (*10*). Kratochwil et al. (*29*) and Chen et al. (*13*) demonstrated that $^{68}$Ga-FAPI was a broad-spectrum tumor imaging probe that outperformed $^{18}$F-FDG in

**TABLE 3**
Diagnostic Performance of Contrast-Enhanced CT, Contrast-Enhanced MRI, $^{18}$F-FDG, and $^{68}$Ga-FAPI PET/CT in Identifying Primary Tumors

| Test characteristic | Contrast-enhanced CT | Contrast-enhanced MRI | $^{18}$F-FDG | $^{68}$Ga-FAPI |
|---|---|---|---|---|
| True-positive (*n*) | 12 | 15 | 17 | 46 |
| False-positive (*n*) | 15 | 21 | 23 | 1 |
| False-negative (*n*) | 60 | 40 | 51 | 44 |
| Sensitivity (%) | 17 | 27 | 25 | 51 |
| Positive predictive value (%) | 44 | 42 | 43 | 98 |
| Accuracy rate (%) | 14 | 20 | 19 | 51 |

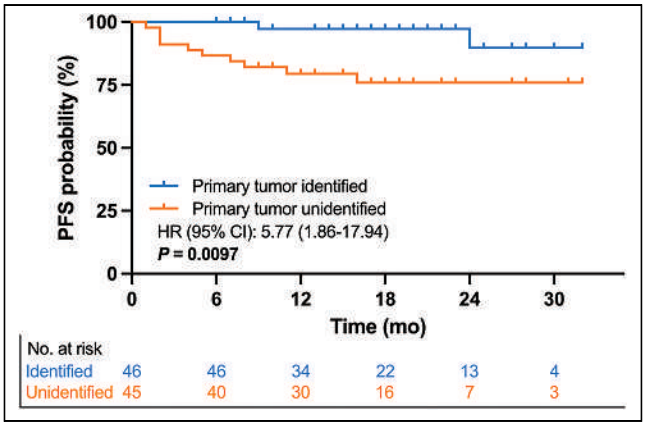


**FIGURE 3.** Kaplan–Meier curve for progression-free survival (PFS). HR = hazard rate.

delineating the primary and metastatic lesions in patients with head and neck cancers, gynecologic malignancies, and gastrointestinal cancers, among others. Furthermore, Chen et al. (*13*) demonstrated the superiority of $^{68}$Ga-FAPI PET/CT to $^{18}$F-FDG PET/CT in detecting very small (diameter $<$ 1.0 cm) malignant lesions. In line with the results of the Chen et al. (*13*) study, our results indicate the potential value of $^{68}$Ga-FAPI PET/CT in delineating small primary lesions (Supplemental Fig. 2).

The accurate detection of metastatic lesions is helpful in making treatment-related decisions, especially for HNCUP patients. Previous studies (*30*,*31*) have shown the apparent advantage of $^{68}$Ga-FAPI PET/CT over $^{18}$F-FDG PET/CT in detecting regional and distant metastatic lesions. Wang et al. (*30*) reported that $^{68}$Ga-FAPI PET/CT outperformed $^{18}$F-FDG PET/CT in the detection of advanced lung cancer metastases to the brain, lymph nodes, bone, and pleura. In another study (*31*), $^{68}$Ga-FAPI PET/CT revealed significantly higher accuracy than $^{18}$F-FDG PET/CT in the evaluation of the N0 neck status of oral squamous cell carcinoma patients (100% vs. 29%), which could overcome the potential false-positivity of $^{18}$F-FDG PET/CT. In our current study, dual-tracer PET/CT detected the same number of metastatic lesions (121 lymph node metastases and 15 bone metastases). In addition, more favorable uptake of $^{68}$Ga-FAPI than $^{18}$F-FDG in terms of TLR was presented by both lymph node metastases ($18.65 \pm 10.50$ and $5.64 \pm 2.81$, $P < 0.001$) and bone metastases ($21.99 \pm 9.70$ and $4.94 \pm 2.90$, $P < 0.001$), which indicates that FAP-targeted radioligand therapy may exert a strong antitumor effect with little damage to organs at risk (*32*).

The major limitation of this study is the absence of a histopathologic analysis of tissue samples from primary and metastatic lesions for FAP expression. Because some lesions were examined by fine-needle aspiration, there were no remaining specimens for further immunohistochemistry. Another limitation is that this trial was performed at a single center. In the future, a multicenter trial needs to be performed to verify our results.

## CONCLUSION

Our study demonstrated that $^{68}$Ga-FAPI PET/CT has higher sensitivity, positive predictive value, and accuracy in locating the primary tumors in HNCUP patients than does $^{18}$F-FDG PET/CT, which indicates that $^{68}$Ga-FAPI PET/CT could serve as a sensitive, reliable, and reproducible indicator of primary tumors in HNCUP patients.

## DISCLOSURE

This work was funded by the Special Clinical Research Project of Health Industry of the Shanghai Municipal Health Commission (grant 20224Y0238), the National Natural Science Foundation of China (grant 82272035), and the Talent development project of the Shanghai Public Health System Construction Three-Year Action Plan (GWVI-11.2-YQ49). Data generated or analyzed during this study are available from the corresponding author by request. No other potential conflict of interest relevant to this article was reported.

## ACKNOWLEDGMENT

We thank the head and neck cancer multidisciplinary team in Fudan University Shanghai Cancer Center for help with our work.

## KEY POINTS

**QUESTION:** What is the diagnostic accuracy of $^{68}$Ga-FAPI PET/CT imaging for localization of the primary tumor of HNCUP?

**PERTINENT FINDINGS:** In this prospective comparative imaging trial of 91 patients, $^{68}$Ga-FAPI PET/CT detected more primary lesions than did $^{18}$F-FDG PET/CT (46 vs. 17 primary tumors) and outperformed $^{18}$F-FDG PET/CT in sensitivity, positive predictive value, and accuracy for locating the primary tumor (51% vs. 25%, 98% vs. 43%, and 51% vs. 19%, respectively).

**IMPLICATIONS FOR PATIENT CARE:** $^{68}$Ga-FAPI PET/CT outperforms $^{18}$F-FDG PET/CT in detecting primary lesions and could serve as a sensitive, reliable, and reproducible imaging modality for HNCUP patients.

## REFERENCES

1. Ota I, Kitahara T. Cancer of unknown primary in the head and neck: diagnosis and treatment. *Auris Nasus Larynx.* 2021;48:23–31.
2. Piazza C, Incandela F, Giannini L. Unknown primary of the head and neck: a new entry in the TNM staging system with old dilemmas for everyday practice. *Curr Opin Otolaryngol Head Neck Surg.* 2019;27:73–79.
3. Pfister DG, Spencer S, Adelstein D, et al. Head and neck cancers, version 2.2020, NCCN clinical practice guidelines in oncology. *J Natl Compr Canc Netw.* 2020; 18:873–898.
4. Maghami E, Ismaila N, Alvarez A, et al. Diagnosis and management of squamous cell carcinoma of unknown primary in the head and neck: ASCO guideline. *J Clin Oncol.* 2020;38:2570–2596.
5. Lee MS, Sanoff HK. Cancer of unknown primary. *BMJ.* 2020;371:m4050.
6. Albertson M, Chandra S, Sayed Z, Johnson C. PET/CT evaluation of head and neck cancer of unknown primary. *Semin Ultrasound CT MR.* 2019;40: 414–423.
7. Schaarschmidt BM, Heusch P, Buchbender C, et al. Locoregional tumour evaluation of squamous cell carcinoma in the head and neck area: a comparison between MRI, PET/CT and integrated PET/MRI. *Eur J Nucl Med Mol Imaging.* 2016;43: 92–102.
8. Goel R, Moore W, Sumer B, Khan S, Sher D, Subramaniam RM. Clinical practice in PET/CT for the management of head and neck squamous cell cancer. *AJR.* 2017;209:289–303.
9. Szyszko TA, Cook GJR. PET/CT and PET/MRI in head and neck malignancy. *Clin Radiol.* 2018;73:60–69.
10. Gu B, Xu X, Zhang J, et al. The added value of $^{68}$Ga-FAPI PET/CT in patients with head and neck cancer of unknown primary with $^{18}$F-FDG-negative findings. *J Nucl Med.* 2022;63:875–881.

11. Alzahrani F, Sahovaler A, Mundi N, et al. Transoral robotic surgery for the identification of unknown primary head and neck squamous cell carcinomas: its effect on the wait and the weight. *Head Neck.* 2022;44:1206–1212.
12. Larsen MHH, Scott SI, Channir HI, et al. Days alive and out of hospital following transoral robotic surgery: cohort study of 262 patients with head and neck cancer. *Head Neck.* 2021;43:3866–3874.
13. Chen H, Pang Y, Wu J, et al. Comparison of [$^{68}$Ga]Ga-DOTA-FAPI-04 and [$^{18}$F]FDG PET/CT for the diagnosis of primary and metastatic lesions in patients with various types of cancer. *Eur J Nucl Med Mol Imaging.* 2020;47:1820–1832.
14. Gu B, Liu X, Wang S, et al. Head-to-head evaluation of [$^{18}$F]FDG and [$^{68}$Ga]Ga-DOTA-FAPI-04 PET/CT in recurrent soft tissue sarcoma. *Eur J Nucl Med Mol Imaging.* 2022;49:2889–2901.
15. Kuzet SE, Gaggioli C. Fibroblast activation in cancer: when seed fertilizes soil. *Cell Tissue Res.* 2016;365:607–619.
16. Pang Y, Zhao L, Luo Z, et al. Comparison of $^{68}$Ga-FAPI and $^{18}$F-FDG uptake in gastric, duodenal, and colorectal cancers. *Radiology.* 2021;298:393–402.
17. Guo W, Pang Y, Yao L, et al. Imaging fibroblast activation protein in liver cancer: a single-center post hoc retrospective analysis to compare [$^{68}$Ga]Ga-FAPI-04 PET/CT versus MRI and [$^{18}$F]-FDG PET/CT. *Eur J Nucl Med Mol Imaging.* 2021;48:1604–1617.
18. Serfling S, Zhi Y, Schirbel A, et al. Improved cancer detection in Waldeyer's tonsillar ring by $^{68}$Ga-FAPI PET/CT imaging. *Eur J Nucl Med Mol Imaging.* 2021;48:1178–1187.
19. Lindner T, Loktev A, Altmann A, et al. Development of quinoline-based theranostic ligands for the targeting of fibroblast activation protein. *J Nucl Med.* 2018;59:1415–1422.
20. Eisenhauer EA, Therasse P, Bogaerts J, et al. New response evaluation criteria in solid tumours: revised RECIST guideline (version 1.1). *Eur J Cancer.* 2009;45:228–247.
21. Pala M, Novakova P, Pechacova Z, et al. Long-term results of radio(chemo)therapy in metastatic carcinoma to cervical lymph nodes from an unknown primary: Adult Comorbidity Evaluation 27 score as a predictor of survival. *Strahlenther Onkol.* 2023;199:149–159.
22. Faisal M, Le NS, Grasl S, et al. Carcinoma of unknown primary (CUP) versus CUP turned to primary carcinoma of the head and neck-an analysis of diagnostic methods and the impact of primary tumor on clinical outcome. *Diagnostics (Basel).* 2022;12:894.
23. Kothari P, Randhawa PS, Farrell R. Role of tonsillectomy in the search for a squamous cell carcinoma from an unknown primary in the head and neck. *Br J Oral Maxillofac Surg.* 2008;46:283–287.
24. Cianchetti M, Mancuso AA, Amdur RJ, et al. Diagnostic evaluation of squamous cell carcinoma metastatic to cervical lymph nodes from an unknown head and neck primary site. *Laryngoscope.* 2009;119:2348–2354.
25. Waltonen JD, Ozer E, Schuller DE, Agrawal A. Tonsillectomy vs. deep tonsil biopsies in detecting occult tonsil tumors. *Laryngoscope.* 2009;119:102–106.
26. Ahmad S, Mair M, Haris PA, et al. Comparison of PET-CT, CT and MRI scan in initial staging and management of head and neck cancers. *Eur Arch Otorhinolaryngol.* 2022;279:2651–2656.
27. Pencharz D, Dunn J, Connor S, et al. Palatine tonsil SUVmax on FDG PET-CT as a discriminator between benign and malignant tonsils in patients with and without head and neck squamous cell carcinoma of unknown primary. *Clin Radiol.* 2019;74:165.e17–165.e23.
28. Mona CE, Benz MR, Hikmat F, et al. Correlation of $^{68}$Ga-FAPI-46 PET biodistribution with FAP expression by immunohistochemistry in patients with solid cancers: interim analysis of a prospective translational exploratory study. *J Nucl Med.* 2022;63:1021–1026.
29. Kratochwil C, Flechsig P, Lindner T, et al. $^{68}$Ga-FAPI PET/CT: tracer uptake in 28 different kinds of cancer. *J Nucl Med.* 2019;60:801–805.
30. Wang L, Tang G, Hu K, et al. Comparison of $^{68}$Ga-FAPI and $^{18}$F-FDG PET/CT in the evaluation of advanced lung cancer. *Radiology.* 2022;303:191–199.
31. Chen S, Chen Z, Zou G, et al. Accurate preoperative staging with [$^{68}$Ga]Ga-FAPI PET/CT for patients with oral squamous cell carcinoma: a comparison to 2-[$^{18}$F]FDG PET/CT. *Eur Radiol.* 2022;32:6070–6079.
32. Privé BM, Boussihmad MA, Timmermans B, et al. Fibroblast activation protein-targeted radionuclide therapy: background, opportunities, and challenges of first (pre)clinical studies. *Eur J Nucl Med Mol Imaging.* 2023;50:1906–1918.

# Diagnostic Accuracy of $^{68}$Ga-FAPI Versus $^{18}$F-FDG PET in Patients with Various Malignancies

Nader Hirmas[1], Rainer Hamacher[2], Miriam Sraieb[1], Lukas Kessler[1], Kim M. Pabst[1], Francesco Barbato[1], Helena Lanzafame[1], Stefan Kasper[2], Michael Nader[1], Claudia Kesch[3], Bastian von Tresckow[4], Hubertus Hautzel[1], Clemens Aigner[5], Martin Glas[6], Martin Stuschke[7], Sherko Kümmel[8,9], Philipp Harter[10], Celine Lugnier[11], Waldemar Uhl[12], Boris Hadaschik[3], Viktor Grünwald[3], Jens T. Siveke[13,14], Ken Herrmann[1], and Wolfgang P. Fendler[1]

*[1]Department of Nuclear Medicine, German Cancer Consortium–University Hospital Essen, University of Duisburg–Essen, Essen, Germany; [2]Department of Medical Oncology, West German Cancer Center, German Cancer Consortium–University Hospital Essen, University of Duisburg–Essen, Essen, Germany; [3]Department of Urology, German Cancer Consortium–University Hospital Essen, University of Duisburg–Essen, Essen, Germany; [4]Department of Hematology and Stem Cell Transplantation, West German Cancer Center, German Cancer Consortium–University Hospital Essen, University of Duisburg–Essen, Essen, Germany; [5]Department of Thoracic Surgery and Thoracic Endoscopy, German Cancer Consortium–University Hospital Essen, University of Duisburg–Essen, Essen, Germany; [6]Division of Clinical Neurooncology, Department of Neurology, German Cancer Consortium–University Hospital Essen, University of Duisburg–Essen, Essen, Germany; [7]Department of Radiation Therapy, German Cancer Consortium–University Hospital Essen, University of Duisburg–Essen, Essen, Germany; [8]Breast Unit, Kliniken Essen–Mitte, Essen, Germany; [9]Department of Gynecology with Breast Center, Charité–Universitätsmedizin Berlin, Berlin, Germany; [10]Department of Gynecology and Gynecologic Oncology, Evangelische Kliniken Essen-Mitte, Essen, Germany; [11]Department of Hematology and Oncology with Palliative Care, Ruhr University Bochum, Bochum, Germany; [12]Department of General and Visceral Surgery, Ruhr University Bochum, Bochum, Germany; [13]Bridge Institute of Experimental Tumor Therapy, West German Cancer Center, University Hospital Essen, Essen, Germany; and [14]Division of Solid Tumor Translational Oncology, German Cancer Consortium (DKTK partner site Essen), German Cancer Research Center, Heidelberg, Germany*

To assess the diagnostic accuracy of $^{68}$Ga-labeled fibroblast activation protein inhibitor (FAPI) and $^{18}$F-labeled FDG PET for the detection of various tumors, we performed a head-to-head comparison of both imaging modalities across a range of tumor entities as part of our ongoing $^{68}$Ga-FAPI PET observational trial. **Methods:** The study included 115 patients with 8 tumor entities who received imaging with $^{68}$Ga-FAPI for tumor staging or restaging between October 2018 and March 2022. Of those, 103 patients received concomitant imaging with $^{68}$Ga-FAPI and $^{18}$F-FDG PET and had adequate lesion validation for accuracy analysis. Each scan was evaluated for the detection of primary tumor, lymph nodes, and visceral and bone metastases. True or false positivity and negativity to detected lesions was assigned on the basis of histopathology from biopsies or surgical excision, as well as imaging validation. **Results:** $^{68}$Ga-FAPI PET revealed higher accuracy than $^{18}$F-FDG PET in the detection of colorectal cancer ($n$ = 14; per-patient, 85.7% vs. 78.6%; per-region, 95.6% vs. 91.1%) and prostate cancer ($n$ = 22; per-patient, 100% vs. 90.9%; per-region, 96.4% vs. 92.7%). $^{68}$Ga-FAPI PET and $^{18}$F-FDG PET had comparable per-patient accuracy in detecting breast cancer ($n$ = 16, 100% for both) and head and neck cancers ($n$ = 10, 90% for both modalities). $^{68}$Ga-FAPI PET had lower per-patient accuracy than $^{18}$F-FDG PET in cancers of the bladder ($n$ = 12, 75% vs. 100%) and kidney ($n$ = 10, 80% vs. 90%), as well as lymphoma ($n$ = 9, 88.9% vs. 100%) and myeloma ($n$ = 10, 80% vs. 90%). **Conclusion:** $^{68}$Ga-FAPI PET demonstrated higher diagnostic accuracy than $^{18}$F-FDG PET in the diagnosis of colorectal cancer and prostate cancer, as well as comparable diagnostic performance for cancers of the breast and head and neck. Accuracy and impact on management will be further assessed in an ongoing prospective interventional trial (NCT05160051).

**Key Words:** FAPI; FDG; PET; oncology; theranostic; accuracy

**J Nucl Med 2024; 65:372–378**
DOI: 10.2967/jnumed.123.266652

Imaging is fundamental in the treatment of malignancies, with varying detection rates depending on the tumor entity and diagnostic modality. PET of cancer cells using $^{18}$F-FDG PET acquires additional molecular information useful for the detection of disease recurrence and metastases, response assessment, disease management, and prognostication (*1–6*). However, drawbacks of $^{18}$F-FDG include false-positive findings due to physiologic uptake or inflammatory responses, as well as false-negative findings due to elevated serum blood glucose levels. As such, targeting of cancer cells using alternative radioisotopes has been an area of growing interest.

Cancer-associated fibroblasts, a constituent of the tumor microenvironment, are involved in tumor growth, migration, and progression (*7*). Fibroblast activation protein (FAP) α is expressed by cancer-associated fibroblasts, a marker associated with protumorigenic functions (*8–12*) and, therefore, a suitable target for diagnostic and therapeutic purposes. Multiple preclinical and clinical studies have shown the promise of FAP-directed therapies, including radiolabeled FAP inhibitors (FAPIs), which exhibit favorable properties in cancer diagnosis and therapy (*13–18*). These properties include, but are not limited to, fast imaging times, high contrast in tumor lesions, and no dietary requirements with regard to

Received Sep. 8, 2023; revision accepted Dec. 20, 2023.
For correspondence or reprints, contact Nader Hirmas (naderhirmas@gmail.com).
Published online Feb. 8, 2024.

imaging, as well as acceptable side effects and long tumor retention times with regard to therapy.

Because of the favorable characteristics of this imaging modality, patients were referred for clinical $^{68}$Ga-FAPI PET staging, both at initial diagnosis and for reevaluation, and were offered subsequent enrollment in our prospective observational $^{68}$Ga-FAPI registry.

In this report, we assess the diagnostic accuracy of $^{68}$Ga-FAPI compared with $^{18}$F-FDG PET separately for various tumor entities by analyzing sensitivity, specificity, positive predictive value (PPV), negative predictive value (NPV), and accuracy on per-patient and per-region bases.

## MATERIALS AND METHODS

### Study Design and Participants

Until March 2022, adult patients who underwent clinical $^{68}$Ga-FAPI PET were offered the possibility to consent to a prospective observational trial for correlation and clinical follow-up of PET findings (NCT04571086). Patients signed a written informed consent form, and evaluation of data was approved by the ethics committee of the University Duisburg–Essen (20-9485-BO and 19-8991-BO). We previously reported data on $^{68}$Ga-FAPI PET uptake and accuracy in sarcoma ($n$ = 47 (*19*)), as well as $^{68}$Ga-FAPI PET uptake in mixed cohorts ($n$ = 69 (*20*), $n$ = 91 (*21*), and $n$ = 324 (*22*)). Patients with sarcoma, pancreatic cancer, and pleural mesothelioma have been excluded from this analysis since the results have already been or will be published separately. Moreover, solid tumor entities with fewer than 10 patients per entity for $^{68}$Ga-FAPI PET accuracy assessment were excluded from this analysis.

Details of data collection (*23*,*24*), imaging and administration of radioligands (*20*,*25*,*26*), imaging analysis, lesion validation, follow-up (*27*), and statistical analysis are provided in the supplemental materials (available at http://jnm.snmjournals.org).

## RESULTS

### Patient Characteristics

We identified 133 patients, of whom 115 with adequate lesion validation were included in this analysis. In total, 8 tumor entities and 313 regions were analyzed; patient characteristics ($n$ = 115) are outlined in Table 1. The median age was 63 y (interquartile range, 17 y). The most common tumor entities were prostate cancer (22/115, 19%), head and neck cancers (18/115, 16%), breast cancer (16/115, 14%), colorectal cancer (15/115, 13%), and bladder cancer (12/115, 10%). Most patients (81/115, 70%) underwent $^{68}$Ga-FAPI PET imaging for restaging purposes. A total of 103 (90%) patients underwent concomitant imaging via $^{68}$Ga-FAPI and $^{18}$F-FDG PET and had adequate lesion validation for the accuracy analysis, and this set of patients was included in the composite analysis.

**TABLE 1**
Patient Characteristics ($n$ = 115)

| Variable | Data |
|---|---|
| Sex | |
| Male | 71 (62%) |
| Female | 44 (38%) |
| Median age at $^{68}$Ga-FAPI scan (y) | 63 (17) |
| Tumor entities | |
| Prostate | 22 (19%) |
| Head and neck | 18 (16%) |
| Breast | 16 (14%) |
| Colorectal | 15 (13%) |
| Bladder | 12 (10%) |
| Myeloma | 12 (10%) |
| Kidney | 10 (9%) |
| Lymphoma | 10 (9%) |
| Regional detection with $^{68}$Ga-FAPI scan* | |
| No evidence of disease | 15 (13%) |
| Primary or local disease detected | 42 (37%) |
| Lymph node metastases detected | 28 (24%) |
| Visceral metastases detected | 38 (33%) |
| Bone metastases detected | 24 (21%) |
| Scanning purposes | |
| Staging at initial diagnosis | 34 (30%) |
| Restaging after therapy | 81 (70%) |
| Prior therapy received* | |
| None | 35 (30%) |
| Surgery | 65 (57%) |
| Chemotherapy | 53 (46%) |
| Radiation therapy | 31 (27%) |
| Immune therapy | 20 (17%) |
| Hormone therapy | 16 (14%) |
| Radionuclide therapy | 3 (3%) |
| Median uptake time (min) | |
| $^{68}$Ga-FAPI | 15 (25) |
| $^{18}$F-FDG | 65 (21) |
| Median time between $^{68}$Ga-FAPI and $^{18}$F-FDG (d) | 0 (2) |

*Different combinations are possible; hence, values do not add to 100%.

Qualitative data are number and percentage; continuous data are median and interquartile range.

### Composite Analysis: Higher Diagnostic Accuracy with $^{68}$Ga-FAPI PET Than with $^{18}$F-FDG PET

$^{68}$Ga-FAPI PET showed higher diagnostic accuracy than $^{18}$F-FDG PET in the diagnosis of colorectal cancer and prostate cancer as listed in Table 2.

At a per-patient level in colorectal cancer, $^{68}$Ga-FAPI PET was superior to $^{18}$F-FDG PET in accuracy (85.7% vs. 78.6%), sensitivity (90.9% vs. 81.8%), and NPV (66.7% vs. 50%). At a per-region level, $^{68}$Ga-FAPI PET was superior to $^{18}$F-FDG PET in accuracy (95.6% vs. 91.1%), sensitivity (94.1% vs. 88.2%), and PPV (94.1% vs. 88.2%).

Furthermore, at a per-patient level in prostate cancer, $^{68}$Ga-FAPI PET was superior to $^{18}$F-FDG PET in accuracy (100% vs. 90.9%) and sensitivity (100% vs. 90.9%). At a per-region level, $^{68}$Ga-FAPI PET was superior to $^{18}$F-FDG PET in sensitivity (94.3% vs. 88.6%) and NPV (90.9% vs. 83.3%).

### Composite Analysis: Comparable Diagnostic Accuracy Between $^{68}$Ga-FAPI PET and $^{18}$F-FDG PET

$^{68}$Ga-FAPI PET was comparable to $^{18}$F-FDG PET in the diagnosis of breast cancer and head and neck cancers as listed in Table 3.

**TABLE 2**
Comparison of Diagnostic Efficacy Between $^{68}$Ga-FAPI and $^{18}$F-FDG PET (Per-Patient and Per-Region Analysis) for Tumors in Which $^{68}$Ga-FAPI Outperformed $^{18}$F-FDG PET

| Tumor entity | *n* | Stratification | PET-positive/total | Sensitivity | Specificity | PPV | NPV | Accuracy |
|---|---|---|---|---|---|---|---|---|
| $^{68}$Ga-FAPI PET | | | | | | | | |
| Colorectal | 14 | Per-patient | 11/14 | 90.9 (58.7–99.8) | 66.7 (9.4–99.2) | 90.9 (66.6–98) | 66.7 (20.8–93.9) | 85.7 (57.2–98.2) |
| | | Per-region | 17/45 | 94.1 (71.3–99.9) | 96.4 (81.7–99.9) | 94.1 (69.9–99.1) | 96.4 (80.1–99.5) | 95.6 (84.9–99.5) |
| Prostate | 22 | Per-patient | 22/22 | 100 (84.6–100) | — | 100 | — | 100 |
| | | Per-region | 33/55 | 94.3 (80.8–99.3) | 100 (83.2–100) | 100 | 90.9 (72.3–97.5) | 96.4 (87.5–99.6) |
| $^{18}$F-FDG PET | | | | | | | | |
| Colorectal | 14 | Per-patient | 10/14 | 81.8 (48.2–97.7) | 66.7 (9.43–99.2) | 90 (63.9–97.9) | 50 (18.4–81.6) | 78.6 (49.2–95.3) |
| | | Per-region | 17/45 | 88.2 (63.6–98.5) | 92.9 (76.5–99.1) | 88.2 (66.1–96.7) | 92.9 (77.9–98) | 91.1 (78.8–97.5) |
| Prostate | 22 | Per-patient | 20/22 | 90.9 (70.84–98.9) | — | 100 | — | 90.9 |
| | | Per-region | 31/55 | 88.6 (73.3–96.8) | 100 (83.2–100) | 100 | 83.3 (66.53–92.63) | 92.7 (82.41–97.98) |

Data in parentheses are 95% CI.

At a per-patient level in breast cancer, $^{68}$Ga-FAPI PET and $^{18}$F-FDG PET showed equal accuracy, sensitivity, specificity, PPV, and NPV (all 100%). At a per-region level, $^{68}$Ga-FAPI PET showed accuracy (97.9% vs. 100%) and sensitivity (96.6% vs. 100%) comparable to those of $^{18}$F-FDG PET but lower NPV (94.7% vs. 100%).

At a per-patient level in head and neck cancers, $^{68}$Ga-FAPI PET and $^{18}$F-FDG PET showed equal accuracy (90%), sensitivity (100%), and PPV (90%). At a per-region level, $^{68}$Ga-FAPI PET showed accuracy (90.3% vs. 93.6%) and specificity (86.7% for both) comparable to those of $^{18}$F-FDG PET but lower sensitivity (93.8% vs. 100%) and NPV (92.9% vs. 100%).

### Composite Analysis: Lower Diagnostic Accuracy with $^{68}$Ga-FAPI PET Than with $^{18}$F-FDG PET

$^{68}$Ga-FAPI PET showed lower accuracy than $^{18}$F-FDG PET in the diagnosis of bladder and kidney cancers, lymphoma, and myeloma as shown in Table 4.

At a per-patient level in bladder cancer, $^{68}$Ga-FAPI PET showed lower accuracy (75% vs. 100%), sensitivity (72.7% vs. 100%), and NPV (25% vs. 100%) than $^{18}$F-FDG PET. At a per-region level, $^{68}$Ga-FAPI PET showed lower accuracy (89.2% vs. 94.4%), sensitivity (78.6% vs. 92.3%), and NPV (88% vs. 95.7%) than $^{18}$F-FDG PET.

At a per-patient level in kidney cancer, $^{68}$Ga-FAPI PET showed sensitivity comparable to that of $^{18}$F-FDG PET (87.5% for both) but lower accuracy (80% vs. 90%), specificity (50% vs. 100%), and PPV (87.5% vs. 100%). At a per-region level, $^{68}$Ga-FAPI PET showed accuracy (90.3% vs. 93.6%), sensitivity (92.9% for both), and NPV (93.8% vs. 94.1%) comparable to those of $^{68}$Ga-FAPI PET but lower specificity (88.2% vs. 94.1%) and PPV (86.7% vs. 92.9%).

At a per-patient level in lymphoma, $^{68}$Ga-FAPI PET showed lower accuracy (88.9% vs. 100%), sensitivity (87.5% vs. 100%), and NPV (50% vs. 100%) than $^{18}$F-FDG PET. At a per-region level, $^{68}$Ga-FAPI PET showed lower accuracy (90% vs. 96.7%), sensitivity (78.6% vs. 100%), and NPV (84.2% vs. 100%) than $^{18}$F-FDG PET.

Finally, for myeloma at per-patient and per-region levels, accuracy (80% vs. 90%) and sensitivity (75% vs. 87.5%) were lower with $^{68}$Ga-FAPI PET than with $^{18}$F-FDG PET.

### Histopathology-Only Analysis

In a subgroup of 45 patients and 5 tumor entities, accuracy was assessed by histopathology validation only (Supplemental Table 1). In line with the findings of the composite analysis, $^{68}$Ga-FAPI PET demonstrated higher accuracy than $^{18}$F-FDG PET for prostate cancer, comparable accuracy for breast cancer and colorectal cancer, and lower accuracy for bladder and kidney cancers.

## DISCUSSION

Here, we compare the diagnostic accuracy of $^{68}$Ga-FAPI and $^{18}$F-FDG PET for various tumors. Tumor validation by a composite reference standard revealed that the diagnostic accuracy of $^{68}$Ga-FAPI PET was higher than that of $^{18}$F-FDG PET in colorectal cancer and prostate cancer, comparable in breast cancer and head and neck cancer, and lower in bladder and kidney cancers, lymphoma, and myeloma. Histopathology-only analysis revealed that the diagnostic accuracy of $^{68}$Ga-FAPI PET was higher than that of $^{18}$F-FDG PET in prostate cancer, comparable in breast and colorectal cancers, and lower in bladder and kidney cancers.

For cancers of the abdomen and pelvis, $^{68}$Ga-FAPI uptake was low in normal parenchyma, such as bowel ($SUV_{max}$ range, 0.08–3.56), liver ($SUV_{max}$ range, 0.47–2.91), and spleen ($SUV_{max}$ range, 0.64–2.81) (*15*,*28*,*29*). This improves tumor delineation,

**TABLE 3**
Comparison of Diagnostic Efficacy Between $^{68}$Ga-FAPI and $^{18}$F-FDG PET (Per-Patient and Per-Region Analysis) for Tumors in Which $^{68}$Ga-FAPI Was Comparable to $^{18}$F-FDG PET

| Tumor entity | *n* | Stratification | PET-positive/total | Sensitivity | Specificity | PPV | NPV | Accuracy |
|---|---|---|---|---|---|---|---|---|
| $^{68}$Ga-FAPI PET | | | | | | | | |
| Breast | 16 | Per-patient | 15/16 | 100 (78.2–100) | 100 (2.5–100) | 100 | 100 | 100 (79.4–100) |
| | | Per-region | 28/47 | 96.6 (82.2–100) | 100 (81.5–100) | 100 | 94.7 (72.4–99.2) | 97.9 (88.7–100) |
| Head and neck | 10 | Per-patient | 10/10 | 100 (66.4–100) | 0 (0–97.5) | 90 (90) | — | 90.0 (55.5–99.8) |
| | | Per-region | 17/31 | 93.8 (69.8–99.8) | 86.7 (59.5–98.3) | 88.2 (67.2–96.5) | 92.9 (65.9–98.9) | 90.3 (74.3–98) |
| $^{18}$F-FDG PET | | | | | | | | |
| Breast | 16 | Per-patient | 15/16 | 100 (78.2–100) | 100 (2.5–100) | 100 | 100 | 100 (79.4–100) |
| | | Per-region | 28/47 | 100 (88.1–100) | 100 (81.5–100) | 100 | 100 | 100 (92.5–100) |
| Head and neck | 10 | Per-patient | 10/10 | 100 (66.4–100) | — | 90 (90) | — | 90.0 (55.5–99.8) |
| | | Per-region | 18/31 | 100 (79.4–100) | 86.7 (59.5–98.3) | 88.9 (68.8–96.7) | 100 | 93.6 (78.6–99.2) |

Data in parentheses are 95% CI.

with absolute and tumor-to-liver uptakes being higher on $^{68}$Ga-FAPI PET than on $^{18}$F-FDG PET, which may lead to superior diagnostic accuracy (*22*). This is particularly relevant in abdominal surgery, for example, after which patients are required to take nothing by mouth until bowel recovery. Also, the prevalence of coexisting diabetes (≤15.5% in patients with colon cancer, for instance (*30*)) poses limitations for molecular imaging with $^{18}$F-FDG PET. $^{68}$Ga-FAPI PET in such a context has protocol advantages, given that no diet or fasting is required in preparation for imaging, and image acquisition can take place a few minutes after tracer application. $^{68}$Ga-FAPI PET, therefore, has the potential to replace $^{18}$F-FDG for abdominal staging.

Our findings are corroborated by other studies that have also shown $^{68}$Ga-FAPI PET to have diagnostic accuracy superior to that of $^{18}$F-FDG PET in breast cancer (*31–33*) and head and neck cancers (*34–36*). Moreover, reports have shown that $^{68}$Ga-FAPI PET can detect PSMA-negative prostate cancer lesions (*37–39*), which can aid in the diagnostic process, with potential therapeutic implications.

With regard to lymphoma and myeloma, several studies have shown that $^{68}$Ga-FAPI PET is inferior to (or at best, not superior to) $^{18}$F-FDG PET (*40–43*). For example, in comparison to colorectal cancer, lymphoma lesions show lower uptake with $^{68}$Ga-FAPI than with $^{18}$F-FDG PET (*22*,*41*,*44*), higher background uptake, and, thus, lower tumor-to-background values (e.g., median $SUV_{max}$ of 7.4 vs. 22.5 and median liver tumor-to-background ratio of 6.4 vs. 10.5 for $^{68}$Ga-FAPI vs. $^{18}$F-FDG PET, respectively (*22*)). Taking this a step further, using systematic lesion validation and follow-up, our study revealed $^{68}$Ga-FAPI to be less accurate than $^{18}$F-FDG PET in lymphoma and myeloma.

An ongoing prospective clinical trial at our department (NCT05160051) is exploring the diagnostic accuracy of $^{68}$Ga-FAPI-46 PET and its effect on patient management and interreader reproducibility for different tumor entities. An interim analysis of findings has shown that $^{68}$Ga-FAPI PET is associated with a lower rate of false-positive findings, especially in lymph node assessments (*44*).

With high tumor and low organ uptakes (*22*), as well as diagnostic accuracy across various tumor entities, $^{68}$Ga-FAPI PET has a role as a gatekeeper for FAP-directed radioligand therapy. Feasibility of FAP radioligand therapy has been reported for $^{90}$Y- and $^{153}$Sm-labeled compounds in breast (*13*) and ovarian (*45*) cancer, as well as sarcomas and pancreatic cancers (*17*,*46*). $^{177}$Lu-labeled compounds have also been used in multiple advanced and refractory tumors, including thyroid cancer (*16*,*47–49*). In patients with intense FAP expression on $^{68}$Ga-FAPI PET, $^{90}$Y-FAPI-46 radioligand therapy led to disease control in about one third of patients with initially progressive sarcomas, pancreatic cancer, and other cancers (*50*), and the novel dimeric $^{177}$Lu-labeled FAPI radioligand ($^{177}$Lu-DOTAGA.(SA.FAPi)$_2$) led to disease control in almost half the patients with radioiodine-refractory differentiated thyroid cancer who had progressed on tyrosine kinase inhibitors (*49*). FAPI imaging therefore has the potential to enhance drug development with targeted clinical applications.

One notable example of a FAP-targeting drug that has shown clinical promise is talabostat, which has demonstrated tumor control in 21% of patients with colorectal cancer (*51*). Moreover, targeting FAP with chimeric antigen receptor T cells has shown promise in preclinical studies and case reports (*52*,*53*), and there is potential for combination with cancer vaccines or immune checkpoint inhibitors (such as PD-1 inhibitors), which would lead to further blockade of immunosuppressive factors (*52*). Another promising approach is using cancer vaccines that successfully target FAP,

**TABLE 4**
Comparison of Diagnostic Efficacy Between $^{68}$Ga-FAPI and $^{18}$F-FDG PET (Per-Patient and Per-Region Analysis) for Tumors in Which $^{68}$Ga-FAPI Underperformed in Comparison to $^{18}$F-FDG PET

| Tumor entity | *n* | Stratification | PET-positive/total | Sensitivity | Specificity | PPV | NPV | Accuracy |
|---|---|---|---|---|---|---|---|---|
| $^{68}$Ga-FAPI PET | | | | | | | | |
| Bladder | 12 | Per-patient | 8/12 | 72.7 (39–94) | 100 (2.5–100) | 100 | 25 (11.3–46.7) | 75 (42.8–94.5) |
| | | Per-region | 12/37 | 78.6 (49.2–95.3) | 95.7 (78.1–99.9) | 91.7 (61.34–98.7) | 88 (72.8–95.3) | 89.2 (74.6–97) |
| Kidney | 10 | Per-patient | 8/10 | 87.5 (47.4–99.7) | 50 (1.26–98.7) | 87.5 (63.1–96.6) | 50 (9.13–90.9) | 80 (44.4–97.5) |
| | | Per-region | 15/31 | 92.9 (66.1–99.8) | 88.2 (63.6–98.5) | 86.7 (63.7–96) | 93.8 (69.2–99) | 90.3 (74.3–98) |
| Lymphoma | 9 | Per-patient | 7/9 | 87.5 (47.4–99.7) | 100 (2.5–100) | 100 | 50 (13.8–86.2) | 88.9 (51.8–99.7) |
| | | Per-region | 11/30 | 78.6 (49.2–95.3) | 100 (79.4–100) | 100 | 84.2 (66.2–93.6) | 90 (73.5–97.9) |
| Myeloma | 10 | Per-patient | 6/10 | 75 (34.9–96.8) | 100 (15.8–100) | 100 | 50 (23.1–76.9) | 80 (44.4–97.5) |
| | | Per-region | 6/10 | 75 (34.9–96.8) | 100 (15.8–100) | 100 | 50 (23.1–76.9) | 80 (44.4–97.5) |
| $^{18}$F-FDG PET | | | | | | | | |
| Bladder | 12 | Per-patient | 11/12 | 100 (71.5–100) | 100 (2.5–100) | 100 | 100 | 100 (73.5–100) |
| | | Per-region | 13/36 | 92.3 (64–99.8) | 95.7 (78.1–99.9) | 92.31 (63.7–98.8) | 95.7 (77–99.3) | 94.4 (81.3–99.3) |
| Kidney | 10 | Per-patient | 7/10 | 87.5 (47.4–99.7) | 100 (15.8–100) | 100 | 66.7 (24.2–92.6) | 90 (55.5–99.8) |
| | | Per-region | 14/31 | 92.9 (66.1–99.8) | 94.1 (71.3–99.9) | 92.9 (65.9–98.9) | 94.12 (70.7–99.1) | 93.55 (78.6–99.2) |
| Lymphoma | 9 | Per-patient | 8/9 | 100 (63.1–100) | 100 (2.5–100) | 100 | 100 | 100 (66.4–100) |
| | | Per-region | 15/30 | 100 (76.8–100) | 93.8 (69.8–99.8) | 93.33 (67.7–98.9) | 100 | 96.7 (82.8–99.9) |
| Myeloma | 10 | Per-patient | 7/10 | 87.5 (47.4–99.7) | 100 (15.8–100) | 100 | 66.7 (24.2–92.6) | 90 (55.5–99.8) |
| | | Per-region | 7/10 | 87.5 (47.4–99.7) | 100 (15.8–100) | 100 | 66.7 (24.2–92.6) | 90 (55.5–99.8) |

Data in parentheses are 95% CI.

particularly the genome of stromal fibroblasts (*54*). As such, future drug development and its potential clinical applications may be enhanced through $^{68}$Ga-FAPI imaging, which aids in selecting patients whose tumors exhibit high $^{68}$Ga-FAPI uptake and who would potentially benefit from FAP-directed therapy. This theranostic approach also has the potential to improve clinical trial design.

Our study is limited by its retrospective design and the small number of patients included per tumor entity. Histopathology was not available for all patients, as tissue sampling is not routinely performed, and biopsy of metastatic lesions may be difficult because they may be small or remote. Thus, most lesion follow-up was based on correlative or follow-up imaging with known intrinsic limitations. Despite these limitations, the study provided valuable systematic information on the diagnostic efficacy of $^{68}$Ga-FAPI PET from an ongoing registry study evaluating $^{68}$Ga-FAPI and $^{18}$F-FDG PET, using a composite reference standard with adequate follow-up time ($\leq\sim$6 mo) and across a wide range of tumor entities, thereby adding to the growing pool of theranostic data.

## CONCLUSION

When compared with $^{18}$F-FDG PET, $^{68}$Ga-FAPI PET demonstrated higher accuracy in the diagnosis of colorectal cancer and prostate cancer, as well as comparable diagnostic performance for cancers of the breast and head and neck. $^{68}$Ga-FAPI has the potential for improved staging or theranostic screening, particularly for these tumor entities.

## DISCLOSURE

Rainer Hamacher is supported by the Clinician Scientist Program of the University Medicine Essen Clinician Scientist Academy (UMEA) sponsored by the faculty of medicine and Deutsche Forschungsgemeinschaft (DFG) and has received travel grants from Lilly, Novartis, and Pharma Mar, as well as fees from Lilly and Pharma Mar. Lukas Kessler is a consultant for AAA and BTG and received fees from Sanofi. Kim Pabst is a consultant for Novartis, has received a Junior Clinician Scientist Stipend from the University Medicine Essen Clinician Scientist Academy (UMEA) sponsored by the Faculty of Medicine at the University of Duisburg–Essen and the Deutsche Forschungsgemeinschaft (DFG), and has received research funding from Bayer outside the submitted work. Stefan Kasper reports personal fees and grants from AstraZeneca, Merck Serone, Merck Sharpe & Dohme, Amgen, Bristol Myers Squibb, Roche, Lilly, Servier, Incyte, and SanofiAventis outside the submitted work. Claudia Kesch has received consultant fees from Apogepha, research funding from AAA/Novartis and Curie Therapeutics, and compensation for travel from Janssen R&D, Amgen, and Bayer. Bastian von Tresckow is an advisor or consultant for Allogene, BMS/Celgene, Cerus, Incyte, IQVIA, Gilead Kite, Lilly, Miltenyi, Novartis, Noscendo, Pentixapharm, Roche, Amgen, Pfizer, Takeda, Merck Sharp & Dohme, and Gilead Kite; has received honoraria from AstraZeneca, BMS, Incyte, Lilly, Novartis, Roche Pharma AG, Takeda, and Merck Sharp & Dohme; reports research funding from Novartis (to the institution), Merck Sharp & Dohme (to the institution), and Takeda (to the institution); and reports travel support from AbbVie, AstraZeneca, Gilead Kite, Lilly, Merck Sharp & Dohme, Pierre Fabre, Roche, Takeda, and Novartis. Hubertus Hautzel reports research funding and travel support from PARI GmbH outside the submitted work. Martin Glas reports honoraria from Roche, Novartis, UCB, Abbvie, Daiichi Sankyo, Novocure, Bayer, Janssen-Cilag, Medac, Merck, and Kyowa Kirin; travel support from Novocure and Medac; and a research grant from Novocure. Ken Herrmann reports personal fees from Bayer, SIRTEX, Adacap, Curium, Endocyte, IPSEN, Siemens Healthineers, GE Healthcare, Amgen, Novartis, ymabs, Aktis, Oncology, and Pharma15, as well as personal and other fees from SOFIE Biosciences, nonfinancial support from ABX, and grants and personal fees from BTG, all of which are outside the submitted work. Boris Hadaschik declares grants to the institution from Novartis, BMS, and the German Research Foundation; consulting fees from ABX, Amgen, AstraZeneca, Bayer, BMS, Janssen, Lightpoint Medical, Novartis, and Pfizer; payment for lectures from Janssen and Monrol; support for travel or meeting attendance from AstraZeneca, Bayer, and Janssen; and participation on data safety monitoring boards for Janssen, all outside the submitted work. Philipp Harter reports honoraria from Amgen, AstraZeneca, GSK, Roche, Sotio, Stryker, Zai Lab, MSD, Clovis, Eisai, Mersana, and Exscientia. He is on the advisory board for Astra Zeneca, Roche, GSK, Clovis, Immunogen, MSD, Miltenyi, Novartis, and Eisai. He has received research funding (to the institution) from AstraZeneca, Roche, GSK, Genmab, DFG, European Union, DKH, Immunogen, Seagen, Clovis, and Novartis. Jens Siveke received honoraria as a consultant or for continuing medical education presentations from AstraZeneca, Bayer, Bristol-Myers Squibb, Eisbach Bio, Immunocore, Novartis, Roche/Genentech, and Servier; his institution receives research funding from Bristol-Myers Squibb, Celgene, Eisbach Bio, and Roche/Genentech; and he holds ownership and serves on the board of directors of Pharma15, all outside the submitted work. Wolfgang P. Fendler reports fees from SOFIE Biosciences (research funding), Janssen (consultant, speaker), Calyx (consultant, image review), Bayer (consultant, speaker, research funding), Novartis (speaker, consultant), Telix (speaker), GE Healthcare (speaker), Eczacıbaşı Monrol (speaker), Abx (speaker), and Amgen (speaker) outside the submitted work. No other potential conflict of interest relevant to this article was reported.

**KEY POINTS**

**QUESTION:** How does $^{68}$Ga-FAPI compare with $^{18}$F-FDG PET in the diagnosis of various malignancies?

**PERTINENT FINDINGS:** We compared the diagnostic accuracy of $^{68}$Ga-FAPI and $^{18}$F-FDG PET for the detection of various tumors. Tumor validation by a composite reference standard revealed higher diagnostic accuracy for $^{68}$Ga-FAPI PET in colorectal and prostate cancers, comparable diagnostic performance for cancers of the breast and head and neck, and lower diagnostic accuracy for bladder and kidney cancers, lymphoma, and myeloma.

**IMPLICATIONS FOR PATIENT CARE:** $^{68}$Ga-FAPI PET is particularly suited for the diagnosis of colorectal cancer, prostate cancer, and cancers of the breast and head and neck. $^{68}$Ga-FAPI PET offers theranostic screening and has the potential for more precise staging and management of patients who have these entities than is possible with $^{18}$F-FDG PET.

## REFERENCES

1. van Tinteren H, Hoekstra OS, Smit EF, et al. Effectiveness of positron emission tomography in the preoperative assessment of patients with suspected non-small-cell lung cancer: the PLUS multicentre randomised trial. *Lancet.* 2002;359:1388–1393.

2. Ell PJ. The contribution of PET/CT to improved patient management. *Br J Radiol.* 2006;79:32–36.
3. Choi JY, Lee KH, Shim YM, et al. Improved detection of individual nodal involvement in squamous cell carcinoma of the esophagus by FDG PET. *J Nucl Med.* 2000;41:808–815.
4. Annovazzi A, Rea S, Zoccali C, et al. Diagnostic and clinical impact of $^{18}$F-FDG PET/CT in staging and restaging soft-tissue sarcomas of the extremities and trunk: mono-institutional retrospective study of a sarcoma referral center. *J Clin Med.* 2020;9:2549.
5. Grimer R, Judson I, Peake D, Seddon B. Guidelines for the management of soft tissue sarcomas. *Sarcoma.* 2010;2010:506182.
6. Ioannidis JPA, Lau J. $^{18}$F-FDG PET for the diagnosis and grading of soft-tissue sarcoma: a meta-analysis. *J Nucl Med.* 2003;44:717–724.
7. Erdogan B, Ao M, White LM, et al. Cancer-associated fibroblasts promote directional cancer cell migration by aligning fibronectin. *J Cell Biol.* 2017;216:3799–3816.
8. Chen WT, Kelly T. Seprase complexes in cellular invasiveness. *Cancer Metastasis Rev.* 2003;22:259–269.
9. Keane FM, Nadvi NA, Yao TW, Gorrell MD, Neuropeptide Y, B-type natriuretic peptide, substance P and peptide YY are novel substrates of fibroblast activation protein-alpha. *FEBS J.* 2011;278:1316–1332.
10. Huang Y, Wang S, Kelly T. Seprase promotes rapid tumor growth and increased microvessel density in a mouse model of human breast cancer. *Cancer Res.* 2004; 64:2712–2716.
11. Kelly T. Fibroblast activation protein-alpha and dipeptidyl peptidase IV (CD26): cell-surface proteases that activate cell signaling and are potential targets for cancer therapy. *Drug Resist Updat.* 2005;8:51–58.
12. Mueller SC, Ghersi G, Akiyama SK, et al. A novel protease-docking function of integrin at invadopodia. *J Biol Chem.* 1999;274:24947–24952.
13. Lindner T, Loktev A, Altmann A, et al. Development of quinoline-based theranostic ligands for the targeting of fibroblast activation protein. *J Nucl Med.* 2018;59:1415–1422.
14. Loktev A, Lindner T, Mier W, et al. A tumor-imaging method targeting cancer-associated fibroblasts. *J Nucl Med.* 2018;59:1423–1429.
15. Giesel FL, Kratochwil C, Lindner T, et al. $^{68}$Ga-FAPI PET/CT: biodistribution and preliminary dosimetry estimate of 2 DOTA-containing FAP-targeting agents in patients with various cancers. *J Nucl Med.* 2019;60:386–392.
16. Baum RP, Schuchardt C, Singh A, et al. Feasibility, biodistribution, and preliminary dosimetry in peptide-targeted radionuclide therapy of diverse adenocarcinomas using $^{177}$Lu-FAP-2286: first-in-humans results. *J Nucl Med.* 2022;63:415–423.
17. Ferdinandus J, Fragoso Costa P, Kessler L, et al. Initial clinical experience with $^{90}$Y-FAPI-46 radioligand therapy for advanced stage solid tumors: a case series of nine patients. *J Nucl Med.* 2022;63:727–734.
18. Kratochwil C, Flechsig P, Lindner T, et al. $^{68}$Ga-FAPI PET/CT: tracer uptake in 28 different kinds of cancer. *J Nucl Med.* 2019;60:801–805.
19. Kessler L, Ferdinandus J, Hirmas N, et al. $^{68}$Ga-FAPI as a diagnostic tool in sarcoma: data from the $^{68}$Ga-FAPI PET prospective observational trial. *J Nucl Med.* 2022;63:89–95.
20. Ferdinandus J, Kessler L, Hirmas N, et al. Equivalent tumor detection for early and late FAPI-46 PET acquisition. *Eur J Nucl Med Mol Imaging.* 2021;48:3221–3227.
21. Kessler L, Ferdinandus J, Hirmas N, et al. Pitfalls and common findings in $^{68}$Ga-FAPI-PET: a pictorial analysis. *J Nucl Med.* 2022;63:890–896.
22. Hirmas N, Hamacher R, Sraieb M, et al. Fibroblast activation protein positron emission tomography and histopathology in a single-center database of 324 patients and 21 tumor entities. *J Nucl Med.* 2023;64:711–716.
23. Harris PA, Taylor R, Minor BL, et al.; the REDCap consortium. Building an international community of software platform partners. *J Biomed Inform.* 2019;95:103208.
24. Harris PA, Taylor R, Thielke R, Payne J, Gonzalez N, Conde JG. Research electronic data capture (REDCap): a metadata-driven methodology and workflow process for providing translational research informatics support. *J Biomed Inform.* 2009;42:377–381.
25. Lindner T, Loktev A, Giesel F, Kratochwil C, Altmann A, Haberkorn U. Targeting of activated fibroblasts for imaging and therapy. *EJNMMI Radiopharm Chem.* 2019;4:16.
26. Loktev A, Lindner T, Burger EM, et al. Development of fibroblast activation protein-targeted radiotracers with improved tumor retention. *J Nucl Med.* 2019;60:1421–1429.
27. Eisenhauer EA, Therasse P, Bogaerts J, et al. New response evaluation criteria in solid tumours: revised RECIST guideline (version 1.1). *Eur J Cancer.* 2009;45:228–247.
28. Gündoğan C, Güzel Y, Can C, Kaplan İ, Kömek H. FAPI-04 uptake in healthy tissues of cancer patients in $^{68}$Ga-FAPI-04 PET/CT imaging. *Contrast Media Mol Imaging.* 2021;2021:9750080.
29. Giesel FL, Kratochwil C, Schlittenhardt J, et al. Head-to-head intra-individual comparison of biodistribution and tumor uptake of $^{68}$Ga-FAPI and $^{18}$F-FDG PET/CT in cancer patients. *Eur J Nucl Med Mol Imaging.* 2021;48:4377–4385.
30. Roderburg C, Loosen SH, Hoyer L, Luedde T, Kostev K. Prevalence of diabetes mellitus among 80,193 gastrointestinal cancer patients in five European and three Asian countries. *J Cancer Res Clin Oncol.* 2022;148:1057–1062.
31. Zheng S, Lin J, Zhu Y, et al. $^{68}$Ga-FAPI versus $^{18}$F-FDG PET/CT in evaluating newly diagnosed breast cancer patients: a head-to-head comparative study. *Clin Nucl Med.* 2023;48:e104–e109.
32. Kömek H, Can C, Güzel Y, et al. $^{68}$Ga-FAPI-04 PET/CT, a new step in breast cancer imaging: a comparative pilot study with the $^{18}$F-FDG PET/CT. *Ann Nucl Med.* 2021;35:744–752.
33. Ballal S, Yadav MP, Moon ES, et al. Biodistribution, pharmacokinetics, dosimetry of [$^{68}$Ga]Ga-DOTA.SA.FAPi, and the head-to-head comparison with [$^{18}$F]F-FDG PET/CT in patients with various cancers. *Eur J Nucl Med Mol Imaging.* 2021;48: 1915–1931.
34. Chen S, Chen Z, Zou G, et al. Accurate preoperative staging with [$^{68}$Ga]Ga-FAPI PET/CT for patients with oral squamous cell carcinoma: a comparison to 2-[$^{18}$F]FDG PET/CT. *Eur Radiol.* 2022;32:6070–6079.
35. Fu H, Wu J, Huang J, et al. $^{68}$Ga fibroblast activation protein inhibitor PET/CT in the detection of metastatic thyroid cancer: comparison with $^{18}$F-FDG PET/CT. *Radiology.* 2022;304:397–405.
36. Linz C, Brands RC, Kertels O, et al. Targeting fibroblast activation protein in newly diagnosed squamous cell carcinoma of the oral cavity: initial experience and comparison to [$^{18}$F]FDG PET/CT and MRI. *Eur J Nucl Med Mol Imaging.* 2021; 48:3951–3960.
37. Khreish F, Rosar F, Kratochwil C, Giesel FL, Haberkorn U, Ezziddin S. Positive FAPI-PET/CT in a metastatic castration-resistant prostate cancer patient with PSMA-negative/FDG-positive disease. *Eur J Nucl Med Mol Imaging.* 2020;47: 2040–2041.
38. Pang Y, Meng T, Xu W, Shang Q, Chen H. $^{68}$Ga-FAPI PET/CT detected non-PSMA/FDG-avid primary tumor in de novo metastatic prostate cancer. *Clin Nucl Med.* 2022;47:1108–1111.
39. Aryana K, Manafi-Farid R, Amini H, Divband G, Moghadam SZ. $^{68}$Ga-FAPI-46 PET/CT in a metastatic castration-resistant prostate cancer patient with low PSMA expression. *Clin Nucl Med.* 2022;47:972–973.
40. Lan L, Liu H, Wang Y, et al. The potential utility of [$^{68}$Ga]Ga-DOTA-FAPI-04 as a novel broad-spectrum oncological and non-oncological imaging agent: comparison with [$^{18}$F]FDG. *Eur J Nucl Med Mol Imaging.* 2022;49:963–979.
41. Chen X, Lin X, Yuan T, Wei M, Wang X. Head-to-head comparison between $^{68}$Ga-FAPI-04 and [$^{18}$F]-FDG-PET/CT in lymphomas: a preliminary analysis [abstract]. *J Nucl Med.* 2022;63(suppl 2):2272.
42. Elboga U, Sahin E, Cayirli YB, et al. Comparison of [$^{68}$Ga]-FAPI PET/CT and [$^{18}$F]-FDG PET/CT in multiple myeloma: clinical experience. *Tomography.* 2022; 8:293–302.
43. Jin X, Wei M, Wang S, et al. Detecting fibroblast activation proteins in lymphoma using $^{68}$Ga-FAPI PET/CT. *J Nucl Med.* 2022;63:212–217.
44. Fendler WP, Bartel T, Pabst KM, et al. $^{68}$Ga-FAPI-46 PET for cancer imaging: a prospective single-arm clinical trial [abstract]. *J Clin Oncol.* 2023;41(suppl):3064.
45. Lindner T, Altmann A, Kramer S, et al. Design and development of $^{99m}$Tc-labeled FAPI tracers for SPECT imaging and $^{188}$Re therapy. *J Nucl Med.* 2020;61:1507–1513.
46. Kratochwil C, Giesel FL, Rathke H, et al. [$^{153}$Sm]samarium-labeled FAPI-46 radioligand therapy in a patient with lung metastases of a sarcoma. *Eur J Nucl Med Mol Imaging.* 2021;48:3011–3013.
47. Kuyumcu S, Kovan B, Sanli Y, et al. Safety of fibroblast activation protein-targeted radionuclide therapy by a low-dose dosimetric approach using $^{177}$Lu-FAPI04. *Clin Nucl Med.* 2021;46:641–646.
48. Assadi M, Rekabpour SJ, Jafari E, et al. Feasibility and therapeutic potential of $^{177}$Lu-fibroblast activation protein inhibitor-46 for patients with relapsed or refractory cancers: a preliminary study. *Clin Nucl Med.* 2021;46:e523–e530.
49. Ballal S, Yadav MP, Moon ES, et al. Novel fibroblast activation protein inhibitor-based targeted theranostics for radioiodine-refractory differentiated thyroid cancer patients: a pilot study. *Thyroid.* 2022;32:65–77.
50. Fendler WP, Pabst KM, Kessler L, et al. Safety and efficacy of $^{90}$Y-FAPI-46 radioligand therapy in patients with advanced sarcoma and other cancer entities. *Clin Cancer Res.* 2022;28:4346–4353.
51. Narra K, Mullins SR, Lee HO, et al. Phase II trial of single agent Val-boroPro (talabostat) inhibiting fibroblast activation protein in patients with metastatic colorectal cancer. *Cancer Biol Ther.* 2007;6:1691–1699.
52. Bughda R, Dimou P, D'Souza RR, Klampatsa A. Fibroblast activation protein (FAP)-targeted CAR-T cells: launching an attack on tumor stroma. *ImmunoTargets Ther.* 2021;10:313–323.
53. Pircher M, Schuberth P, Gulati P, et al. FAP-specific re-directed T cells first in-man study in malignant pleural mesothelioma: experience of the first patient treated [abstract]. *J Immunother Cancer.* 2015;3(suppl 2):P120.
54. Busek P, Mateu R, Zubal M, Kotackova L, Sedo A. Targeting fibroblast activation protein in cancer: prospects and caveats. *Front Biosci (Landmark Ed).* 2018;23: 1933–1968.

# Diagnostic Performance of $^{68}$Ga-PSMA-11 PET/CT Versus Multiparametric MRI for Detection of Intraprostatic Radiorecurrent Prostate Cancer

Alexander Light[1,2], Stefan Lazic[3], Kate Houghton[3], Max Bayne[2], Martin J. Connor[1,2], Henry Tam[3], Hashim U. Ahmed[1,2], Taimur T. Shah*[1,2], and Tara D. Barwick*[3,4]

*[1]Imperial Prostate, Department of Surgery and Cancer, Imperial College London, London, United Kingdom; [2]Imperial Urology, Charing Cross Hospital, Imperial College Healthcare NHS Trust, London, United Kingdom; [3]Department of Imaging, Charing Cross Hospital, Imperial College Healthcare NHS Trust, London, United Kingdom; and [4]Department of Surgery and Cancer, Imperial College London, London, United Kingdom*

For men with prostate cancer who develop biochemical failure after radiotherapy, European guidelines recommend reimaging with $^{68}$Ga-PSMA-11 PET/CT and multiparametric MRI (mpMRI). However, the accuracy of $^{68}$Ga-PSMA-11 PET/CT for detecting intraprostatic recurrences is unclear, both with and without mpMRI. **Methods:** A single-center retrospective study of a series of patients investigated for radiorecurrence between 2016 and 2022 is described. All patients underwent $^{68}$Ga-PSMA-11 PET/CT, mpMRI, and prostate biopsy. PET/CT images were interpreted independently by 2 expert readers masked to other imaging and clinical data. The primary outcome was the diagnostic accuracy of PET/CT versus mpMRI and of PET/CT with mpMRI together versus mpMRI alone. The secondary outcome was the proportion of cancers missed by mpMRI but detected by PET/CT. Diagnostic accuracy analysis was performed at the prostate hemigland level using cluster bootstrapping. **Results:** Thirty-five men (70 hemiglands) were included. Cancer was confirmed by biopsy in 43 of 70 hemiglands (61%). PET/CT sensitivity and negative predictive values (NPVs) were 0.89 (95% CI, 0.78–0.98) and 0.79 (95% CI, 0.62–0.95), respectively, which were not significantly different from results by MRI (sensitivity of 0.72; 95% CI, 0.61–0.83; $P = 0.1$) (NPV of 0.59; 95% CI, 0.41–0.75; $P = 0.07$). Specificity and positive predictive values were not significantly different. When PET/CT and MRI were used together, the sensitivity was 0.98 (95% CI, 0.92–1.00) and NPV was 0.93 (95% CI, 0.75–1.00), both significantly higher than MRI alone ($P = 0.003$ and $P < 0.001$, respectively). Specificity and positive predictive values remained not significantly different. MRI missed 12 of 43 cancers (28%; 95% CI, 17%–43%), of which 11 of 12 (92%; 95% CI, 62%–100%) were detected by PET/CT. **Conclusion:** For detecting intraprostatic radiorecurrence, $^{68}$Ga-PSMA-11 PET/CT has high sensitivity that is not significantly different from mpMRI. When $^{68}$Ga-PSMA-11 PET/CT and mpMRI were used together, the results conferred a significantly greater sensitivity and NPV than with mpMRI alone. $^{68}$Ga-PSMA-11 PET/CT may therefore be a useful tool in the diagnosis of localized radiorecurrence.

**Key Words:** PSMA PET/CT; multiparametric MRI; prostate cancer; radiotherapy; recurrence

**J Nucl Med 2024; 65:379–385**
DOI: 10.2967/jnumed.123.266527

Over 13,000 men with prostate cancer undergo radiotherapy each year in the U.K. alone (*1*). However, 25% will develop biochemical failure within 10 y (*2*). Subsequent outcomes are poor; within 5 y, 50% develop metastases and 20%–30% die from their cancer (*3*). Approximately 10% of biochemical failure patients will develop prostate-confined recurrence, a state independently predictive of metastasis and cancer-specific death (*4*). Salvage treatments for localized recurrences have shown good medium-term oncologic outcomes and should be considered (*5*,*6*). However, patient selection is key, requiring accurate detection of any intraprostatic radiorecurrence (*7*).

On reaching biochemical failure, European guidelines recommend reimaging with prostate multiparametric MRI (mpMRI) and prostate-specific membrane antigen (PSMA) PET/CT (*8*). Although mpMRI is highly accurate in the untreated prostate, its interpretation after radiotherapy is challenging because of glandular atrophy, reduced zonal differentiation, and diffuse T2 hypointensity (*9*). Our group recently published the FORECAST U.K. prospective multicenter trial, which concluded that MRI and MRI-targeted biopsy had high sensitivity for radiorecurrent cancer detection, but systematic biopsies were also needed to identify MRI-invisible disease (*6*,*10*).

$^{68}$Ga-PSMA-11 PET/CT is increasingly used for whole-body imaging after previous treatment, with excellent specificity for identifying extraprostatic disease (*11*). However, data regarding detection of intraprostatic recurrences are fewer and less robust, with most studies omitting verification of findings against a histologic reference (*12*). This contrasts with the primary diagnostic setting; the recently published PRIMARY trial identified that $^{68}$Ga-PSMA-11 PET/CT and mpMRI used together significantly improve sensitivity and negative predictive values (NPVs) versus mpMRI alone for detecting clinically significant disease (*13*). We therefore hypothesized that $^{68}$Ga-PSMA-11 PET/CT, both with and without mpMRI, may be useful for detecting local failures after radiotherapy and identifying candidates for local salvage. We sought to address this using a robust biopsy reference standard.

## MATERIALS AND METHODS

### Study Design

This single-center retrospective study was approved by the local institutional review board, and the requirement to obtain informed consent was waived. All patients who had undergone $^{68}$Ga-PSMA-11

Received Aug. 10, 2023; revision accepted Oct. 4, 2023.
For correspondence or reprints, contact Tara Barwick (tara.barwick@nhs.net).
*Contributed equally to this work.
Published online Jan. 11, 2024.

PET/CT imaging were reviewed. Patients were included if they underwent both $^{68}$Ga-PSMA-11 PET/CT and mpMRI with prostate biopsy to investigate for radiorecurrence. No restrictions were placed on the type of radiotherapy or the use of androgen deprivation therapy. Other local treatment before imaging was prohibited.

### Index Tests

All $^{68}$Ga-PSMA-11 PET/CT examinations were performed on Siemens Healthineers scanners (Biograph 64 scanner, attenuation-corrected reconstruction, $n = 28$; Biograph 128 scanner, time-of-flight attenuation-corrected reconstruction, $n = 2$; Biograph Vision scanner; time-of-flight point-spread function reconstruction with 4.5-mm gaussian filter, $n = 5$). This comprised standard knees-to-vertex acquisitions (mean, 61 min after injection) and delayed postmicturition pelvic acquisitions (mean, 91 min after injection). Diuretics were not used. The mean activity of the administered radiotracer was 1.9 MBq/kg. Two expert readers, masked to clinical information and previous imaging, independently interpreted images using Hermia software (Hermes Medical Solutions). The prostate was divided into hemiglands (left/right). Suspicion of radiorecurrence within each hemigland was scored with a 5-point Likert system, with a score of 3–5 deemed suspicious (Fig. 1). Where there was a score discrepancy between the readers, the higher score was chosen for analysis. A 5-point Likert score was chosen as it aligned with E-PSMA guidance (*14*). Furthermore, the PRIMARY score had not been developed at the time of analysis and was designed for use in the untreated prostate (*15*).

MRI was performed per the Prostate Imaging–Reporting and Data System guidelines on a 1.5- or 3.0-T scanner with a multiparametric protocol incorporating T2-weighted images, diffusion-weighted images with apparent diffusion coefficient mapping and at least 1 high b-value acquisition, and dynamic contrast-enhanced images. Examinations were reported by specialist prostate MRI radiologists, who were not masked, and were interpreted binarily as either suspicious or nonsuspicious. A binary score was chosen to reflect simplified clinical decision-making on whether to recommend biopsy based on MRI. The new Prostate Imaging–Recurrence Reporting criteria were not used for interpretation as these had not been validated at the time of analysis (*16*).

### Reference Test

All patients underwent biopsy to confirm recurrence with a view to offering salvage local treatment. All had bilateral sampling of the peripheral zone as the minimum via targeted or systematic cores. Of 35 patients, 33 (94%) underwent biopsy via the transperineal route.

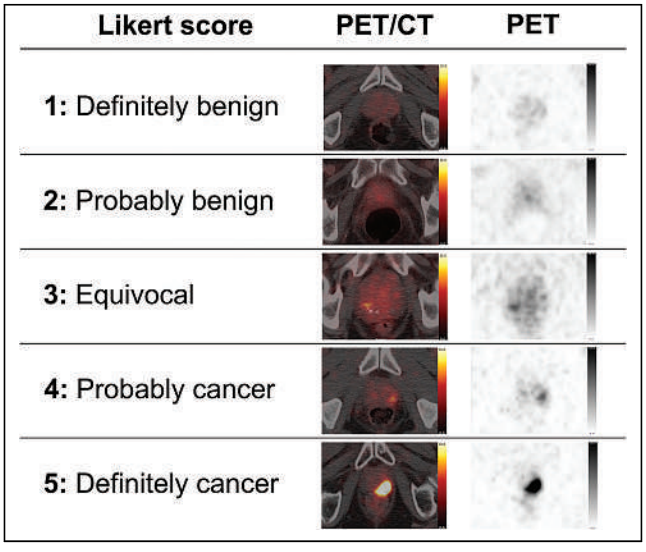


**FIGURE 1.** Explanation and examples for 5-point Likert system used for PET/CT interpretation.

### Outcomes

Analyses were performed at the prostate hemigland level. The primary outcomes were the diagnostic accuracy metrics of PET/CT versus MRI and of PET/CT with MRI compared with MRI alone. When PET/CT and MRI were used together, if either modality detected a suspicious lesion, the test was deemed positive. Figures 2–4 illustrate comparative examples.

Several secondary outcomes were analyzed. First, the proportion of hemiglands correctly classified by each modality, the proportion of cancers missed by each modality, and the number of cancers missed by MRI but detected by PET/CT were compared. Second, the characteristics of cancers detected by PET/CT versus undetected cancers were compared. Third, the optimal $SUV_{max}$ cut point was determined that would maximize sensitivity and specificity for detecting cancer. The accuracy of other $SUV_{max}$ cut points in 1.0 increments between 2.0 and 15.0 was also evaluated.

Because the role of Gleason grading after radiotherapy is not well established, analyses focused on detecting cancer of any grade and length (any cancer). Analyses were also performed with clinical significance definitions used in the primary diagnostic setting: a grade group of at least 3 or maximum cancer core length of at least 6 mm (definition 1), and a grade group of at least 2 or maximum cancer core length of at least 4 mm (definition 2) (*17*). Patients were excluded from calculations if an undeterminable grade or maximum cancer core length meant it was not possible to apply the definition.

As a sensitivity analysis, outcomes were recalculated using a Likert threshold of at least 4 for $^{68}$Ga-PSMA-11 PET/CT. Analyses were also performed at the whole-gland level (Appendix 1; Supplemental Tables 7–10; Supplemental Figs. 3 and 4 [supplemental materials are available at http://jnm.snmjournals.org]).

### Statistical Analysis

Interreader agreement for Likert scores was determined by calculating Cohen κ. For calculating diagnostic accuracy at the hemigland level, to account for nonindependent data among individual patients, cluster bootstrapping with 1,000 resamples was performed to generate a 95% CI. Sensitivity and specificity were compared between diagnostic tests using the McNemar test (*18*). Positive predictive values (PPVs) and NPVs were compared using a general estimating equation logistic regression model (*19*).

For comparison of proportions of hemiglands correctly classified and cancers missed, the Fisher exact test was used. The 95% CIs were calculated using the adjusted Wald method.

To compare characteristics between imaging-detected and -undetected cancers, the Fisher exact test was used for categoric variables, the Wilcoxon rank-sum test for continuous variables, and the $\chi^2$ test for trends in ordinal variables.

For determining optimal $SUV_{max}$ cut points, receiver-operating-characteristic curve analyses were performed and the curves plotted. Cluster bootstrapping was used to generate a 95% CI. Smoothed receiver-operating-characteristic curves were plotted from bootstrapped samples. $SUV_{max}$ here referred to the highest value of the standard and delayed acquisitions.

All analyses were performed with R version 4.2.2. Statistical significance was set as a $P$ value of less than 0.05.

## RESULTS

### Cohort Description

Thirty-five men (35 scans; 70 hemiglands) were included in this analysis. Figure 5 gives exclusion reasons. Table 1 describes cohort characteristics.

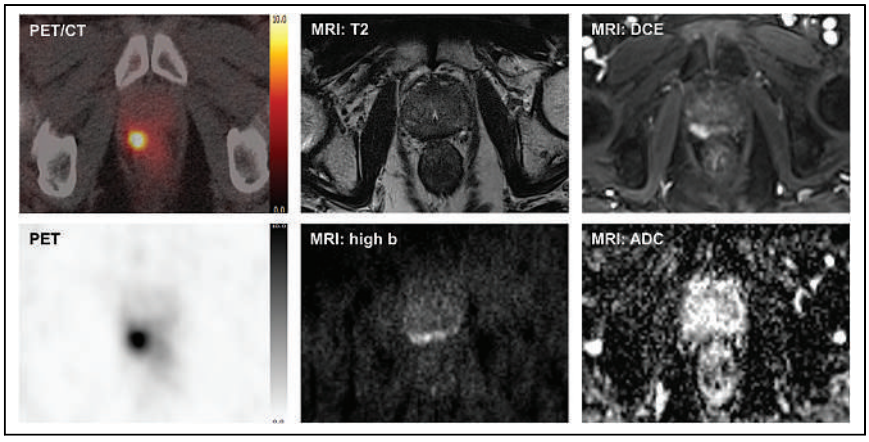


**FIGURE 2.** Comparison of $^{68}$Ga-PSMA-11 PET/CT (positive) and mpMRI (positive). Patient was reimaged 6.3 y after diagnosis, had current prostate-specific antigen of 3.1 ng/mL, and was previously treated with external-beam radiotherapy and neoadjuvant and adjuvant androgen deprivation therapy. On PET/CT, right apex demonstrated Likert score 5/5 lesion with $SUV_{max}$ of 11.1. MRI demonstrated corresponding restricted diffusion with intense contrast enhancement. Targeted biopsy revealed grade group 3 cancer with maximum cancer core length of 15 mm. ADC = apparent diffusion coefficient; DCE = dynamic contrast enhancement.

### Primary Outcomes

Cancer was confirmed by biopsy in 43 of 70 hemiglands (61%), with 37 of 65 (57%) and 40 of 67 (60%) harboring definition 1 and definition 2 cancer, respectively. Of the 70 (67%) hemiglands, 47 had a suspicious PET/CT (Likert score of 3–5) and 41 of 70 (59%) had a suspicious MRI. When both modalities were used together, 57 of 70 (79%) hemiglands were deemed suspicious.

On categorizing Likert scores as 1–2 versus 3–5, there was substantial interrater agreement ($\kappa = 0.65$; 95% CI, 0.48–0.83). Table 2 details the diagnostic accuracy metrics. For detection of any cancer, PET/CT sensitivity was 0.89 (95% CI, 0.78–0.98), which was not significantly different from MRI (0.72; 95% CI, 0.61–0.83; $P = 0.1$). Specificity was not significantly different between PET/CT (0.67; 95% CI, 0.48–0.86) and MRI (0.64; 95% CI, 0.44–0.83; $P = 0.8$). Furthermore, neither PPV nor NPV was significantly different between modalities.

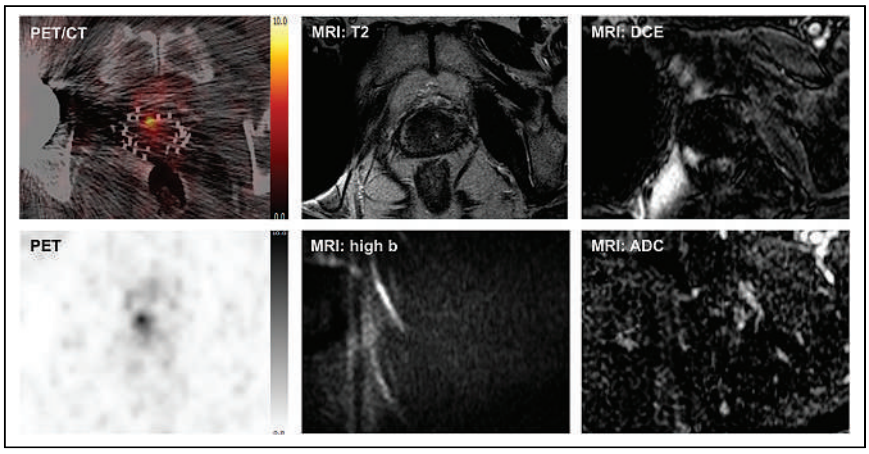


**FIGURE 3.** Comparison of $^{68}$Ga-PSMA-11 PET/CT (positive) and mpMRI (negative). Patient was reimaged 16.2 y after diagnosis, had current prostate-specific antigen of 4.6 ng/mL, and was previously treated with low–dose-rate brachytherapy. On PET/CT, right mid gland and base demonstrated Likert score 5/5 lesion with $SUV_{max}$ of 9.1. MRI interpretation was hindered by artifact from right hip replacement and brachytherapy seeds. Targeted biopsy revealed grade group 3 cancer with maximum cancer core length of 1 mm. ADC = apparent diffusion coefficient; DCE = dynamic contrast enhancement.

When both modalities were used together, sensitivity was 0.98 (95% CI, 0.92–1.00) and the NPV was 0.93 (95% CI, 0.75–1.00), both significantly higher than with MRI alone ($P = 0.003$ and $P < 0.001$, respectively). Specificity was 0.45 (95% CI, 0.27–0.67), and PPV was 0.74 (95% CI, 0.61–0.87), which were not significantly different from the results with MRI alone ($P = 0.07$ and 0.6, respectively).

For definition 1 and definition 2 cancers, the diagnostic metrics for each modality used alone were comparable to detection of any cancer, with no significant differences detected (Table 2). When modalities were used together, sensitivity and NPV were again significantly higher than with MRI alone. For definition 1 only, the specificity of the combined modalities (0.44; 95% CI, 0.27–0.63) was significantly reduced versus MRI (0.65; 95% CI, 0.46–0.84; $P = 0.04$). PPV estimates were not significantly different for either definition.

Supplemental Table 1 details the diagnostic accuracy metrics when the Likert score threshold was increased to at least 4. Substantial interrater agreement remained when categorizing Likert scores here as 1–3 versus 4–5 ($\kappa = 0.72$; 95% CI, 0.55–0.88). With this new threshold, 40 of 70 (57%) and 52 of 70 (74%) hemiglands were suspicious on PET/CT alone and on PET/CT with MRI, respectively. Similar to a Likert threshold of at least 3, diagnostic metrics were not significantly different between PET/CT alone and MRI. However, when used together, sensitivity and NPV were significantly higher than with MRI alone. These patterns were preserved for all cancer definitions.

### Secondary Outcomes

MRI missed 12 of 43 cancers (28%; 95% CI, 17%–43%), and PET/CT missed 5 of 43 (12%; 95% CI, 5%–25%), a nonsignificant difference ($P = 0.1$; Supplemental Table 2). Although 11 of 12 cancers (92%; 95% CI, 62%–100%) were missed by MRI, they were detected by PET/CT. For definition 1 and definition 2, 8 of 9 (89%; 95% CI, 54%–100%) and 9 of 10 (90%; 95% CI, 57%–100%) tumors undetected by MRI were detected by PET/CT. With a Likert threshold of at least 4, PET/CT detected 75%–80% of MRI-missed cancers (Supplemental Table 3).

Aside from $SUV_{max}$, there were no significant differences observed with regard to tumor characteristics for cancers detected and undetected by PET/CT (Supplemental Table 4). These results were consistent when a Likert threshold of at least 4 was used (Supplemental Table 5).

Supplemental Figure 1 details the characteristics of the 5 tumors undetected by PET/CT. All PET/CT examinations were performed on a Biograph 64 scanner. Three of these had cancer detected in the contralateral hemigland both on PET/CT

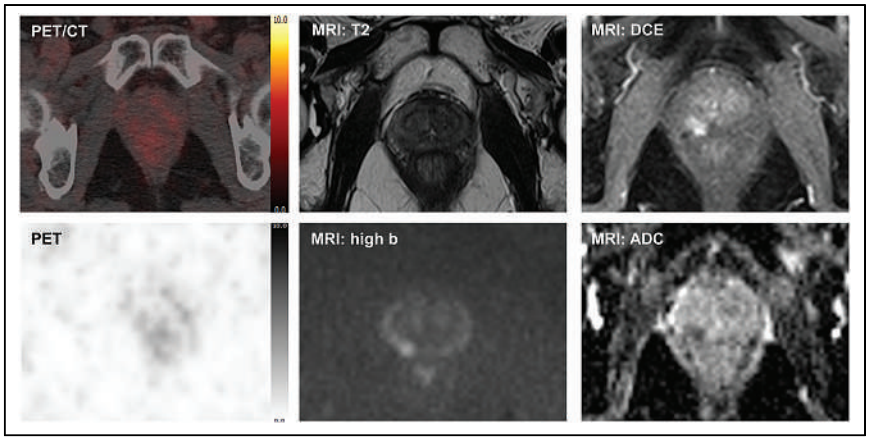


**FIGURE 4.** Comparison of $^{68}$Ga-PSMA-11 PET/CT (negative) and mpMRI (positive). Patient was reimaged 4.8 y after diagnosis, had current prostate-specific antigen of 2.4 ng/mL, and was previously treated with external-beam radiotherapy and neoadjuvant androgen deprivation therapy. MRI demonstrated restricted diffusion in right mid gland. In this region, PET/CT was scored as Likert 1/5, with $SUV_{max}$ of 2.1. Targeted biopsy revealed cancer with maximum cancer core length of 6 mm. Gleason grading was not possible because of irradiation effect. ADC = apparent diffusion coefficient; DCE = dynamic contrast enhancement.

and on biopsy, with 1 of these likely reflecting midline extension of a medial tumor contralaterally. All 5 undetected tumors fulfilled definition 1 criteria (grade group $\geq$ 3 or maximum cancer core length $\geq$ 6 mm), the most stringent clinical significance definition used. One patient had received adjuvant androgen deprivation therapy at the time of the PET/CT imaging; 2 patients had not, and for 2 patients, these data were not available. No tumor displayed neuroendocrine differentiation.

Figure 6 displays the receiver-operating-characteristic analysis to determine optimal $SUV_{max}$ cut points; Supplemental Table 6 and Supplemental Figure 2 detail the diagnostic accuracy metrics for these cut points. With $SUV_{max}$, the area under the curve for any cancer was 0.83 (95% CI, 0.71–0.92); for definition 1, it was 0.81 (95% CI, 0.69–0.90), and for definition 2, it was 0.82 (95% CI, 0.71–0.92). For all definitions, an $SUV_{max}$ of 4.4 yielded the greatest combination of sensitivity and specificity. With this cut point, across cancer definitions, sensitivity ranged from 0.84 to 0.86, specificity from 0.79 to 0.82, PPV from 0.85 to 0.88, and NPV from 0.48 to 0.78.

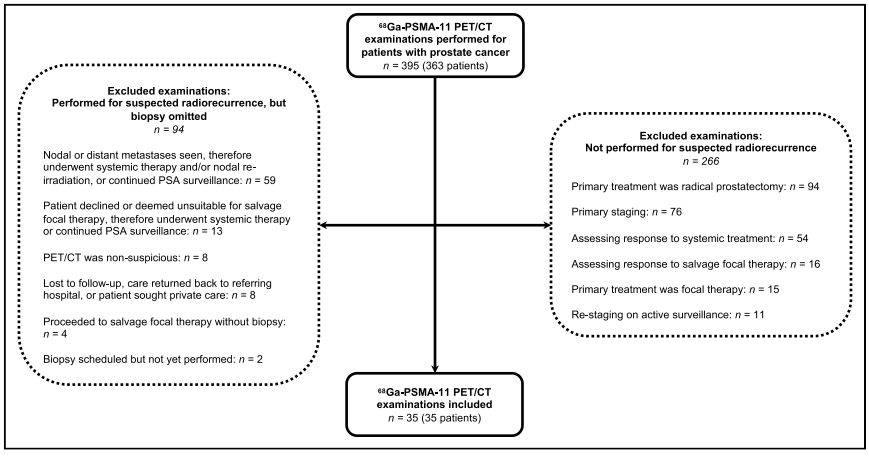


**FIGURE 5.** Flowchart outlining eligibility process. PSA = prostate-specific antigen.

## DISCUSSION

### Summary

$^{68}$Ga-PSMA-11 PET/CT has high sensitivity and modest specificity for detecting intraprostatic radiorecurrent cancer measured against biopsy. mpMRI also has good sensitivity with comparatively lower specificity, consistent with FORECAST findings (*6*). The use of both modalities together, however, conferred a significantly greater sensitivity and NPV than with MRI alone across all cancer definitions. Notably, 89%–92% of cancers missed by MRI were detected by PET/CT imaging. Within the limitations of our small, highly selected cohort, these data suggest that using $^{68}$Ga-PSMA-11 PET/CT and mpMRI together could be an excellent tool for ruling out local failure after radiotherapy. An inherent further advantage of $^{68}$Ga-PSMA-11 PET/CT is its established utility in detecting extraprostatic spread. A concern raised, in contrast, is that the low specificity across modalities indicates these tests do produce many false-positive results. PPV, however, was fair when both modalities were used together (0.70–0.74).

Pathologic characteristics were not significantly different between PET/CT-detected and -undetected tumors in this small cohort. This remains an area needing investigation in larger studies (*10*). Nonetheless, all 5 tumors that PET/CT missed satisfied definition 1 criteria and, at least in the primary diagnostic setting, would be deemed aggressive tumors.

An optimal $SUV_{max}$ cut point of 4.4 across each cancer definition conferred high sensitivity and specificity. This cut point could represent a useful metric for quantitative image assessment.

### Comparison to Literature

Our results are comparable to primary diagnostic data. For detection of cancer with a grade group of at least 2, the PRIMARY trial determined $^{68}$Ga-PSMA-11 PET/CT to have a sensitivity of 0.90, a specificity of 0.50, a PPV of 0.69, and an NPV of 0.80 (*13*). When combined with mpMRI, the sensitivity was 0.97, with a specificity of 0.40, a PPV of 0.67, and an NPV of 0.91. Sensitivity and NPV compared between PET/CT and MRI alone were not significantly different; however, the sensitivity and NPV of the combined modalities were significantly greater than with MRI alone.

PSMA PET/CT is increasingly used after radiotherapy and is advocated by the European guidelines (*8*). However, relevant data are mostly weak as many studies omit a histologic reference standard (*12*). This is problematic; false positives are common in the irradiated prostate as we also demonstrate in our own data, often due to faint-to-moderate prostatic uptake and inflammation (*20*). Furthermore, when histologic data are provided, these are frequently and inappropriately amalgamated

**TABLE 1**
Characteristics of Included Patients ($n$ = 35)

| Characteristic | Data |
|---|---|
| At original diagnosis | |
| Age (y) | 63.1 (58.9–68.3) |
| PSA known (ng/mL) | 16.9 (9.8–34.2) |
| PSA unknown | 9 |
| Grade group | |
| 1 | 7 (24%) |
| 2 | 9 (31%) |
| 3 | 5 (17%) |
| 4 | 5 (17%) |
| 5 | 3 (10%) |
| Unknown | 6 (17%) |
| Tumor stage | |
| T1 | 3 (12%) |
| T2 | 10 (42%) |
| T3 | 11 (46%) |
| Unknown | 11 (46%) |
| At time of PET/CT | |
| Age (y) | 72.4 (68.4–75.5) |
| Time between diagnosis and PET/CT (y) | 7.2 (5.9–10.7) |
| Primary radiotherapeutic treatment | |
| EBRT | 30 (86%) |
| HDR brachytherapy and EBRT | 2 (6%) |
| LDR brachytherapy | 3 (9%) |
| Hormone use during primary treatment | |
| Adjuvant | 8 (30%) |
| Neoadjuvant | 7 (26%) |
| Neoadjuvant and adjuvant | 9 (33%) |
| Nil | 3 (11%) |
| Unknown | 8 |
| Phoenix criteria met | 24 (83%) |
| Unknown whether Phoenix criteria met* | 6 |
| PSA (ng/mL) | 3.80 (2.60–5.53) |

*PSA nadir unavailable.

PSA = prostate-specific antigen; EBRT = external beam radiotherapy; HDR = high dose rate; LDR = low dose-rate.

Qualitative data are number and percentage; continuous data are median and interquartile range.

with histologic data from postprostatectomy patients or extraprostatic sites (*12*).

A 2022 review by our group identified just 3 studies presenting histology-verified prostatic imaging findings after PSMA PET/CT for radiorecurrence (*12*). Our findings are concordant, principally in that PSMA PET/CT with or without mpMRI has high sensitivity for detecting radiorecurrent disease. In a German retrospective $^{68}$Ga-PSMA-11 series of 50 patients undergoing salvage radical prostatectomy, sensitivity on a hemigland basis was 81% and specificity was 67% (*21*). The method of PET/CT interpretation, however, was not reported. In an Australian retrospective $^{68}$Ga-PSMA-11 series ($n$ = 267), 33 of 90 patients with isolated local recurrence on PET/CT underwent biopsy, conferring a sensitivity of 85% (*22*). Local recurrence here was defined as a moderately or intensely avid lesion with an $SUV_{max}$ of at least 3.0. A third, prospective, American $^{18}$F-DCFPyL series ($n$ = 30) reported positive intraprostatic lesions in 15 patients, defined as uptake above background. Three of the 15 patients underwent prostate biopsy, with recurrence confirmed in all (sensitivity, 100%) (*23*). Since this review, a Dutch group has published prospective data from 41 men undergoing biopsy for a suggestive focus on both $^{68}$Ga-PSMA-11 PET/CT and mpMRI (*24*). Using both modalities in conjunction, sensitivity was 100% at the whole-gland level with 1 false-positive reading (PPV, 98%). This study defined a positive intraprostatic lesion as focal increased uptake. Importantly, in all 4 studies, biopsy was performed only in patients with a positive PET/CT image. In contrast, our study included 4 patients with negative PET/CT, and the use of a hemigland analysis also increased the number of units for analysis with negative imaging. Furthermore, only the last study evaluated the performance of mpMRI alongside PET/CT, a central element of our analysis (*23*).

### Implications for Practice

Many patients with radiorecurrence are managed with watchful waiting or androgen deprivation therapy. The latter carries bothersome side effects and potentially serious adverse events, with castration-resistant disease developing after 2–3 y, necessitating expensive second- and third-line treatments (*25*).

One study of 128 radiorecurrent patients with positive $^{68}$Ga-PSMA-11 PET/CT imaging from 3 prospective trials observed that 36% had uptake confined to the prostate only (*26*). For these patients, some centers offer salvage radical prostatectomy or reirradiation. Though effective, these can have considerable toxicity. This is particularly the case for radical prostatectomy, which can lead to erectile dysfunction in nearly all patients, urinary incontinence in 80% of patients, and rectal injury in 5%–10% of patients (*5*,*27*). An emerging alternative is salvage focal ablation, for example, with high-intensity focused ultrasound or cryotherapy, which targets the recurrent lesion or lesions alone. Early data suggest that this approach provides good early disease control comparable to whole-gland treatments but with reduced toxicity (*5*,*6*).

Patient selection for focal ablation is crucial; beyond establishing the presence of localized recurrence, meticulous mapping of disease is needed for treatment planning (*7*). In this context, our findings suggest that $^{68}$Ga-PSMA-11 PET/CT and mpMRI, if both negative, can convincingly rule out intraprostatic recurrence. Furthermore, the FORECAST trial demonstrated that MRI and MRI-targeted biopsy misses 8% of cancers (*6*); our results show that $^{68}$Ga-PSMA-11 PET/CT does detect most tumors missed by MRI. Given that performing both mpMRI and $^{68}$Ga-PSMA-11 PET/CT is advocated by guidelines for restaging men with suspected radiorecurrence, we therefore recommend that intraprostatic findings from each imaging modality should be integrated to improve diagnostics (*8*).

### Limitations

Our study is a small, single-center retrospective cohort. However, our cohort does include patients referred from elsewhere for $^{68}$Ga-PSMA-11 PET/CT and salvage focal ablation. Furthermore, our cohort size is comparable to the aforementioned studies, reflecting the paucity of radiorecurrence patients undergoing

**TABLE 2**
Diagnostic Metrics for Imaging Modalities

| Metric | $^{68}$Ga-PSMA-11 PET/CT | mpMRI | $P^*$ | $^{68}$Ga-PSMA-11 PET/CT and mpMRI | $P^\dagger$ |
|---|---|---|---|---|---|
| Any cancer | | | | | |
| Sensitivity | 0.89 (0.78–0.98) | 0.72 (0.61–0.83) | 0.1 | 0.98 (0.92–1.00) | 0.003 |
| Specificity | 0.67 (0.48–0.86) | 0.64 (0.44–0.83) | 1 | 0.45 (0.27–0.67) | 0.07 |
| PPV | 0.81 (0.67–0.93) | 0.76 (0.62–0.90) | 0.4 | 0.74 (0.61–0.87) | 0.6 |
| NPV | 0.79 (0.62–0.95) | 0.59 (0.41–0.75) | 0.07 | 0.93 (0.75–1.00) | <0.001 |
| Definition 1 cancer | | | | | |
| Sensitivity | 0.87 (0.75–0.97) | 0.76 (0.64–0.86) | 0.4 | 0.97 (0.91–1.00) | 0.01 |
| Specificity | 0.65 (0.47–0.83) | 0.65 (0.46–0.84) | 1 | 0.44 (0.27–0.63) | 0.04 |
| PPV | 0.77 (0.60–0.90) | 0.74 (0.59–0.89) | 0.7 | 0.70 (0.54–0.84) | 0.3 |
| NPV | 0.79 (0.62–0.95) | 0.67 (0.48–0.83) | 0.3 | 0.93 (0.75–1.00) | 0.006 |
| Definition 2 cancer | | | | | |
| Sensitivity | 0.88 (0.77–0.97) | 0.75 (0.64–0.86) | 0.3 | 0.98 (0.92–1.00) | 0.007 |
| Specificity | 0.67 (0.48–0.86) | 0.64 (0.44–0.83) | 1 | 0.45 (0.27–0.67) | 0.07 |
| PPV | 0.80 (0.65–0.93) | 0.76 (0.61–0.90) | 0.5 | 0.73 (0.58–0.86) | 0.5 |
| NPV | 0.79 (0.62–0.95) | 0.63 (0.45–0.80) | 0.2 | 0.93 (0.75–1.00) | 0.002 |

*Comparison of PET/CT against MRI.
†Comparison of PET/CT and MRI combined against MRI alone.
Data in parentheses are 95% CI.

biopsy and the paucity of patients subsequently undergoing salvage focal ablation (*5*,*12*,*21*–*24*).

Although we have included patients with negative imaging, in contrast to previous studies, our use of a biopsied cohort does confer some selection bias. Ultimately, this cohort comprises patients in whom extraprostatic disease has been ruled out and who are both fit and willing to undergo salvage intervention, having already undergone radiotherapy several years previously. On a related note, biopsy protocols were not uniform, and therefore, bias may arise from this, although the majority were transperineal and all included bilateral sampling sufficient for prostate mapping.

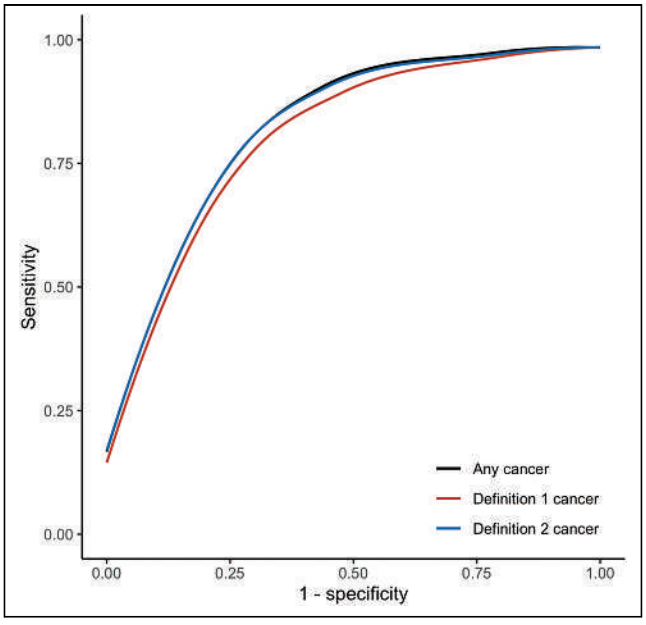


**FIGURE 6.** Smoothed receiver-operating-characteristic curves plotted for each cancer definition based on $SUV_{max}$.

### Further Research

Biopsy verification should be a core element of future studies, which should also be designed to overcome the aforementioned limitations (*12*). We believe our preliminary data encourage development of a well-designed, paired-cohort, multicenter prospective study that offers template biopsies to patients both with and without a positive PET/CT or MRI, similar to the FORECAST trial (*6*). This would be vital to establish confidence in PET/CT for ruling out local failures. Although we have included men undergoing biopsy with nonsuspicious PET/CT and MRI, previous studies have offered biopsy only to patients with positive imaging (*21*–*24*). Granular histologic data in larger cohorts will also enable better characterization of tumors that are not visible on imaging.

Other considerations also need investigation. First, work into the feasibility of PET/CT-targeted biopsies is needed. Second, $^{68}$Ga-PSMA-11 interpretation is not standardized. Validation of the recently published 5-point PRIMARY score in the radiorecurrence setting should be considered (*15*). Furthermore, small validation studies have shown the potential of the 5-point Prostate Imaging–Recurrence Reporting score in improving MRI interpretation after radiotherapy (*16*,*28*). Prostate Imaging–Recurrence Reporting validation was not the focus of our work but certainly warrants future study. Last, although research into hybrid PET/MRI remains at a preliminary stage, future work should aim to compare its performance against PET/CT and MRI in this setting.

## CONCLUSION

$^{68}$Ga-PSMA-11 PET/CT confers high sensitivity for detecting intraprostatic recurrences that are not significantly different from

mpMRI when measured against biopsy. However, using $^{68}$Ga-PSMA-11 PET/CT and mpMRI together leads to a significantly greater sensitivity and NPV than mpMRI alone. This may be a useful tool for the diagnosis of localized radiorecurrence and thus the selection of patients for salvage focal ablation.

## DISCLOSURE

Alexander Light acknowledges research funding from the U.K. National Institute for Heath and Care Research (NIHR) and Imperial Health Charity. Hashim Ahmed, Taimur Shah, and Tara Barwick receive infrastructure support from the NIHR Imperial Biomedical Research Centre. Hashim Ahmed and Taimur Shah also receive infrastructure support from the Imperial College Experimental Cancer Medicine Centre. Hashim Ahmed also receives research funding from Sonablate and Boston Scientific; is a paid scientific advisory board member for Francis Medical; has given lectures for Boston Scientific, Ipsen, and Janssen; and has received funding to attend scientific conferences from Janssen. No other potential conflict of interest relevant to this article was reported.

**KEY POINTS**

**QUESTION:** What is the diagnostic performance of $^{68}$Ga-PSMA-11 PET/CT compared with mpMRI for detecting intraprostatic radiorecurrent prostate cancer?

**PERTINENT FINDINGS:** $^{68}$Ga-PSMA-11 PET/CT alone had high sensitivity when measured against biopsy. However, combining findings from $^{68}$Ga-PSMA-11 PET/CT and mpMRI led to a significantly higher sensitivity and NPV than did mpMRI alone.

**IMPLICATIONS FOR PATIENT CARE:** Using $^{68}$Ga-PSMA-11 PET/CT and mpMRI together may be excellent for ruling out intraprostatic radiorecurrence.

## REFERENCES

1. Annual report 2021: results of the NPCA prospective audit in England and Wales for men diagnosed from 1 April 2019 to 31 March 2020 and the impact of COVID-19 in England during 2020. National Prostate Cancer Audit website. https://www.npca.org.uk/content/uploads/2022/01/NPCA-Annual-Report-2021_Final_13.01.22-1.pdf. Published January 2022. Accessed October 26, 2023.
2. Syndikus I, Griffin C, Philipps L, et al. 10-year efficacy and co-morbidity outcomes of a phase III randomised trial of conventional vs. hypofractionated high dose intensity modulated radiotherapy for prostate cancer (CHHiP; CRUK/06/016). *J Clin Oncol.* 2023;41:304.
3. Philipson RG, Romero T, Wong JK, et al. Patterns of clinical progression in radiorecurrent high-risk prostate cancer. *Eur Urol.* 2021;80:142–146.
4. Ma TM, Chu FI, Sandler H, et al. Local failure events in prostate cancer treated with radiotherapy: a pooled analysis of 18 randomized trials from the meta-analysis of randomized trials in cancer of the prostate consortium (LEVIATHAN). *Eur Urol.* 2022;82:487–498.
5. Valle LF, Lehrer EJ, Markovic D, et al. A systematic review and meta-analysis of local salvage therapies after radiotherapy for prostate cancer (MASTER). *Eur Urol.* 2021;80:280–292.
6. Shah TT, Kanthabalan A, Otieno M, et al. Magnetic resonance imaging and targeted biopsies compared to transperineal mapping biopsies before focal ablation in localised and metastatic recurrent prostate cancer after radiotherapy. *Eur Urol.* 2022;81:598–605.
7. Kanthabalan A, Arya M, Freeman A, et al. Intraprostatic cancer recurrence following radical radiotherapy on transperineal template mapping biopsy: implications for focal ablative salvage therapy. *J Urol.* 2020;204:950–955.
8. Prostate cancer: treatment. European Association of Urology website. https://uroweb.org/guidelines/prostate-cancer/chapter/treatment. Accessed October 31, 2023.
9. Gaur S, Turkbey B, Prostate MR. Imaging for posttreatment evaluation and recurrence. *Urol Clin North Am.* 2018;45:467–479.
10. Light A, Kanthabalan A, Otieno M, et al. The role of multiparametric MRI and MRI-targeted biopsy in the diagnosis of radiorecurrent prostate cancer: an analysis from the FORECAST trial. *Eur Urol.* September 29, 2023 [Epub ahead of print].
11. Perera M, Papa N, Roberts M, et al. Gallium-68 prostate-specific membrane antigen positron emission tomography in advanced prostate cancer: updated diagnostic utility, sensitivity, specificity, and distribution of prostate-specific membrane antigen-avid lesions—a systematic review and meta-analysis. *Eur Urol.* 2020;77:403–417.
12. Light A, Ahmed HU, Shah TT. The unclear role of PET-CT in localized radiorecurrent prostate cancer. *Nat Rev Urol.* 2022;19:573–574.
13. Emmett L, Buteau J, Papa N, et al. The additive diagnostic value of prostate-specific membrane antigen positron emission tomography computed tomography to multiparametric magnetic resonance imaging triage in the diagnosis of prostate cancer (PRIMARY): a prospective multicentre study. *Eur Urol.* 2021;80:682–689.
14. Ceci F, Oprea-Lager DE, Emmett L, et al. E-PSMA: the EANM standardized reporting guidelines v1.0 for PSMA-PET. *Eur J Nucl Med Mol Imaging.* 2021;48:1626–1638.
15. Emmett L, Papa N, Buteau J, et al. The PRIMARY score: using intraprostatic $^{68}$Ga-PSMA PET/CT patterns to optimize prostate cancer diagnosis. *J Nucl Med.* 2022;63:1644–1650.
16. Panebianco V, Villeirs G, Weinreb JC, et al. Prostate magnetic resonance imaging for local recurrence reporting (PI-RR): international consensus-based guidelines on multiparametric magnetic resonance imaging for prostate cancer recurrence after radiation therapy and radical prostatectomy. *Eur Urol Oncol.* 2021;4:868–876.
17. Ahmed HU, El-Shater Bosaily A, Brown LC, et al. Diagnostic accuracy of multiparametric MRI and TRUS biopsy in prostate cancer (PROMIS): a paired validating confirmatory study. *Lancet.* 2017;389:815–822.
18. Kim S, Lee W. Does McNemar's test compare the sensitivities and specificities of two diagnostic tests? *Stat Methods Med Res.* 2017;26:142–154.
19. Leisenring W, Alonzo T, Pepe MS. Comparisons of predictive values of binary medical diagnostic tests for paired designs. *Biometrics.* 2000;56:345–351.
20. Fendler WP, Calais J, Eiber M, et al. False positive PSMA PET for tumor remnants in the irradiated prostate and other interpretation pitfalls in a prospective multicenter trial. *Eur J Nucl Med Mol Imaging.* 2021;48:501–508.
21. Pfister D, Haidl F, Nestler T, et al. $^{68}$Ga-PSMA-PET/CT helps to select patients for salvage radical prostatectomy with local recurrence after primary radiotherapy for prostate cancer. *BJU Int.* 2020;126:679–683.
22. Raveenthiran S, Yaxley J, Gianduzzo T, et al. The use of $^{68}$Ga-PET/CT PSMA to determine patterns of disease for biochemically recurrent prostate cancer following primary radiotherapy. *Prostate Cancer Prostatic Dis.* 2019;22:385–390.
23. Song H, Harrison C, Duan H, et al. Prospective evaluation of $^{18}$F-DCFPyL PET/CT in biochemically recurrent prostate cancer in an academic center: a focus on disease localization and changes in management. *J Nucl Med.* 2020;61:546–551.
24. Rasing M, van Son M, Moerland M, et al. Value of targeted biopsies and combined PSMA PET/CT and mp-MRI imaging in locally recurrent prostate cancer after primary radiotherapy. *Cancers (Basel).* 2022;14:781.
25. Nguyen PL, Alibhai SMH, Basaria S, et al. Adverse effects of androgen deprivation therapy and strategies to mitigate them. *Eur Urol.* 2015;67:825–836.
26. Smith CP, Xiang M, Armstrong WR, et al. Patterns of failure in men with radiorecurrent prostate cancer: a post-hoc analysis of 3 prospective gallium 68 prostate-specific membrane antigen positron emission tomography/computed tomography imaging trials. *Int J Radiat Oncol Biol Phys.* 2023;116:1079–1084.
27. Marra G, Karnes RJ, Calleris G, et al. Oncological outcomes of salvage radical prostatectomy for recurrent prostate cancer in the contemporary era: a multicenter retrospective study. *Urol Oncol.* 2021;39:296.e21–296.e29.
28. Pecoraro M, Turkbey B, Purysko AS, et al. Diagnostic accuracy and observer agreement of the MRI prostate imaging for recurrence reporting assessment score. *Radiology.* 2022;304:342–350.

# First-in-Human Evaluation of Site-Specifically Labeled $^{89}$Zr-Pertuzumab in Patients with HER2-Positive Breast Cancer

Randy Yeh*[1,2], Joseph A. O'Donoghue*[3], Vetri Sudar Jayaprakasam[1,2], Audrey Mauguen[4], Ryan Min[1], Sue Park[5,6], Julia P. Brockway[5,6], Jacqueline F. Bromberg[5,6], W Iris Zhi[5], Mark E. Robson[5,6], Rachel Sanford[5,6], Shanu Modi[5,6], Brian J. Agnew[7], Serge K. Lyashchenko[1,2], Jason S. Lewis*[1,2,8], Gary A. Ulaner*[1,2,9,10], and Brian M. Zeglis*[1,2,11]

*[1]Department of Radiology, Memorial Sloan Kettering Cancer Center, New York, New York; [2]Department of Radiology, Weill Cornell Medical College, New York, New York; [3]Department of Medical Physics, Memorial Sloan Kettering Cancer Center, New York, New York; [4]Department of Biostatistics and Epidemiology, Memorial Sloan Kettering Cancer Center, New York, New York; [5]Department of Medicine, Memorial Sloan Kettering Cancer Center, New York, New York; [6]Department of Medicine, Weill Cornell Medical College, New York, New York; [7]Biosciences Division, Thermo Fisher Scientific, Eugene, Oregon; [8]Program in Molecular Pharmacology, Memorial Sloan Kettering Cancer Center, New York, New York; [9]Molecular Imaging and Therapy, Hoag Family Cancer Institute, Newport Beach, California; [10]Departments of Radiology and Translational Genomics, University of Southern California, Los Angeles, California; and [11]Department of Chemistry, Hunter College, New York, New York*

Radioimmunoconjugates targeting human epidermal growth factor receptor 2 (HER2) have shown potential to noninvasively visualize HER2-positive tumors. However, the stochastic approach that has been traditionally used to radiolabel these antibodies yields poorly defined and heterogeneous products with suboptimal in vivo performance. Here, we describe a first-in-human PET study on patients with HER2-positive breast cancer evaluating the safety, biodistribution, and dosimetry of $^{89}$Zr-site-specific (ss)-pertuzumab PET, a site-specifically labeled radioimmunoconjugate designed to circumvent the limitations of random stochastic lysine labeling. **Methods:** Six patients with HER2-positive metastatic breast cancer were enrolled in a prospective clinical trial. Pertuzumab was site-specifically modified with desferrioxamine (DFO) via a novel chemoenzymatic strategy and subsequently labeled with $^{89}$Zr. Patients were administered 74 MBq of $^{89}$Zr-ss-pertuzumab in 20 mg of total antibody intravenously and underwent PET/CT at 1 d, 3–4 d, and 5–8 d after injection. PET imaging, whole-body probe counts, and blood draws were performed to assess the pharmacokinetics, biodistribution, and dosimetry. **Results:** $^{89}$Zr-ss-pertuzumab PET/CT was used to assess HER2 status and heterogeneity to guide biopsy and decide the next line of treatment at progression. The radioimmunoconjugate was able to detect known sites of malignancy, suggesting that these tumor lesions were HER2-positive. The optimal imaging time point was 5–8 d after administration, and no toxicities were observed. Dosimetry estimates from OLINDA showed that the organs receiving the highest doses (mean ± SD) were kidney (1.8 ± 0.5 mGy/MBq), liver (1.7 ± 0.3 mGy/MBq), and heart wall (1.2 ± 0.1 mGy/MBq). The average effective dose for $^{89}$Zr-ss-pertuzumab was 0.54 ± 0.03 mSv/MBq, which was comparable to both stochastically lysine-labeled $^{89}$Zr-DFO-pertuzumab and $^{89}$Zr-DFO-trastuzumab. One patient underwent PET/CT with both $^{89}$Zr-ss-pertuzumab and $^{89}$Zr-DFO-pertuzumab 1 mo apart, with $^{89}$Zr-ss-pertuzumab demonstrating improved lesion detection and higher tracer avidity. **Conclusion:** This study demonstrated the safety, dosimetry, and potential clinical applications of $^{89}$Zr-ss-pertuzumab PET/CT. $^{89}$Zr-ss-pertuzumab may detect more lesions than $^{89}$Zr-DFO-pertuzumab. Potential clinical applications include real-time evaluation of HER2 status to guide biopsy and assist in treatment decisions.

**Key Words:** breast cancer; HER2; immuno-PET; radioimmunoconjugates

**J Nucl Med 2024; 65:386–393**
DOI: 10.2967/jnumed.123.266392

Over the past 2 decades, human epidermal growth factor receptor 2 (HER2) has emerged as a critical prognostic biomarker in patients with metastatic breast cancer (mBC), as well as a vital target for therapeutics such as trastuzumab and pertuzumab. HER2 status is traditionally determined via immunohistochemistry (IHC) for protein expression or in situ hybridization for gene amplification (*1*). Determining HER2 status via single-site biopsies is indeed useful and remains the gold standard for qualifying patients for HER2-targeted therapies. However, this approach inevitably fails to capture intertumoral HER2 expression heterogeneity, and biopsies from multiple lesions are not feasible or routinely performed in clinical practice. In fact, HER2 discordance between primary and metastatic tumors can be as high as 25% (*2*), and the limitations of single-site biopsies for heterogeneity may in part explain the mixed or discordant responses in some patients with HER2-positive mBC to HER2-targeted therapies.

To address these challenges, PET imaging with radiolabeled HER2-targeted antibodies was developed as a noninvasive approach to evaluate HER2 expression in both primary tumors and metastatic lesions, thereby providing a snapshot of receptor heterogeneity throughout the body. In 2010, Dijkers et al. from the University of Groningen introduced HER2 PET by evaluating $^{89}$Zr-trastuzumab PET in mBC patients (*3*). This group's pioneering work continued in subsequent studies, including investigating $^{89}$Zr-trastuzumab to assess HER2 heterogeneity and predict response to trastuzumab emtansine in the ZEPHIR trial (*4*) and to assist in clinical decision-making when HER2 status could not be determined (*5*). More recently, Dehdashti et al. showed that $^{89}$Zr-trastuzumab PET could

Received Jul. 21, 2023; revision accepted Dec. 4, 2023.
For correspondence or reprints, contact Randy Yeh (yehr@mskcc.org).
*Contributed equally to this work.
Published online Jan. 25, 2024.

discriminate between HER2-positive and HER2-negative lesions in mBC patients (*6*). Our group has performed several clinical trials to evaluate HER2-targeted PET radiotracers in both breast and gastroesophageal cancers (*7–12*), beginning with $^{89}$Zr-desferrioxamine (DFO)-trastuzumab (*7–9*,*12*) and then $^{89}$Zr-DFO-pertuzumab (*10*,*11*). These studies demonstrated the clinical potential of HER2 PET for detecting HER2-positive tumor lesions, evaluating HER2 heterogeneity, and identifying occult HER2-positive lesions in patients with HER2-negative breast cancer (*7–12*).

Several weaknesses of $^{89}$Zr-labeled HER2-targeting PET tracers have been elucidated over the last decade, including absent or low uptake in HER2-positive metastases (false negatives), as well as high background uptake in the liver and bone marrow that reduces sensitivity for detecting HER2-positive lesions. In addition, a high rate of false positives for HER2-positive tumor was observed in patients who subsequently underwent biopsy of tracer-avid lesions (*7*,*8*,*11*).

One possible route to improving the performance of $^{89}$Zr-labeled HER2-targeting PET tracers is site-specific (ss) modification. In general, radioimmunoconjugates are created by randomly attaching chelators, for example DFO, to lysines within the antibody and then labeling the resultant immunoconjugate with the radiometal of choice, for example $^{89}$Zr. However, because antibodies have upward of 40 lysines distributed through their macromolecular structure, this approach—although undeniably facile—inevitably produces poorly defined and complex heterogeneous mixtures of regioisomers that can exhibit suboptimal in vitro and in vivo behavior, including attenuated immunoreactivity and increased uptake in nontarget tissues (*13*,*14*). Although pertuzumab does contain lysine residues within its complementarity-determining regions (*15*), the antibody was chosen for this investigation because a stochastically labeled variant—$^{89}$Zr-DFO-pertuzumab—has already been clinically translated and thus could provide a point of reference for the clinical performance of the site-specifically modified radioimmunoconjugate.

Over the last several years, we have developed and validated a novel chemoenzymatic method for the synthesis of well-defined and homogeneous radioimmunoconjugates (*14*,*16*,*17*). This strategy relies on a pair of enzymes—EndoS and GalT(Y289L)—to incorporate azide-containing sugars into the heavy-chain glycans of the antibody's Fc region and then leverages the strain-promoted azide-alkyne cycloaddition click reaction to attach dibenzocyclooctyne-bearing chelators to these artificial sugars (*14*). Using this methodology, we have previously synthesized $^{89}$Zr-ss-pertuzumab in high yield and high specific activity and demonstrated its homogeneity, immunoreactivity, and stability. Furthermore, in preclinical models of HER2-positive breast cancer, $^{89}$Zr-ss-pertuzumab exhibited excellent in vivo behavior, in several cases surpassing that of its traditionally synthesized progenitor, stochastically lysine labeled $^{89}$Zr-DFO-pertuzumab (*16*). Yet despite these clear advantages, a site-specifically modified radioimmunoconjugate has never, to the best of our knowledge, been translated to the clinic. Here, we present the results of a first-in-human clinical trial of $^{89}$Zr-ss-pertuzumab in HER2-positive mBC patients focused on the safety, pharmacokinetic profile, dosimetry, and potential clinical applications of this site-specifically modified radioimmunoconjugate.

## MATERIALS AND METHODS

### Study Design

This study was a prospective, single-center, single-arm, and open-label imaging trial. The study protocol was approved by the Memorial Sloan Kettering Cancer Institutional Review Board and was registered with the National Library of Medicine (ClinicalTrials.gov identifier NCT04692831). All patients gave written informed consent.

### Patients

Patients with HER2-positive mBC were identified and recruited from the breast medical oncology clinics. HER2 status was defined according to American Society of Clinical Oncology/College of American Pathologist guidelines (*1*), with HER2-positive defined as an HER2 IHC score of 3+ or an IHC score of 2+ with HER2 amplification on fluorescence in situ hybridization (FISH) as defined by a HER2–to–CEP17 ratio of at least 2.0. Tumor samples with an IHC score of 0, 1+, or 2+ and FISH-negative were defined as HER2-negative. Inclusion criteria were adult patients (>18 y old) with biopsy-proven HER2-positive primary malignancy or metastatic disease; biopsy-proven metastatic disease; at least 5 malignant lesions on CT, MRI, or $^{18}$F-FDG PET/CT within 60 d of the protocol; and an Eastern Cooperative Oncology Group performance score of 0–2 (*18*). Exclusion criteria were creatinine more than 2 times the normal limit, aspartate transaminase or alkaline phosphatase more than 2 times the normal limit within 8 wk, life expectancy of less than 3 mo, pregnancy or lactation, and patients who could not undergo PET/CT.

### Preparation of $^{89}$Zr-ss-Pertuzumab

$^{89}$Zr-ss-pertuzumab was manufactured by the Memorial Sloan Kettering Radiochemistry and Molecular Imaging Probes Core Facility in compliance with a U.S. Food and Drug Administration Investigational New Drug application (investigational new drug 153644). Clinical-grade pertuzumab (Perjeta; Genentech) was site-specifically modified with DFO and then radiolabeled with $^{89}$Zr, a positron-emitting radiometal with a 78.4-h radioactive half-life. The conjugation was performed using a previously described methodology (*12*) in which a pair of enzymes, EndoS and GalT(Y289L) (Thermo Fisher Scientific), was used in conjunction with bioorthogonal click chemistry to append DFO to the heavy-chain glycans of the Fc region's CH2 domain (*14*). The final drug product, $^{89}$Zr-ss-pertuzumab, underwent quality control testing before batch release for patient administration, to ensure conformance with specifications for radiochemical purity, radioimmunoreactivity, endotoxin content, sterilizing filter integrity, pH, visual appearance, radionuclidic identity verification, and sterility testing.

### Administration of $^{89}$Zr-ss-Pertuzumab

All patients received 74 MBq ± 10% of $^{89}$Zr-ss-pertuzumab intravenously in 20 mg of total antibody mass with an approximate mass ratio of 18 mg of cold, nonradiolabeled antibody and 2 mg of $^{89}$Zr-labeled antibody. After placement of an intravenous line, nonradiolabeled and unmodified pertuzumab was administered over 5 min to help reduce nonspecific uptake as previously described for HER2-targeted PET tracers (*3*,*7*). Then, $^{89}$Zr-ss-pertuzumab was administered as an intravenous push. The line was primed and subsequently flushed with 5% human serum albumin solution. Patients were monitored for 2 h after administration and subsequently with a follow-up phone call by a study physician 1–3 d later. Any adverse effects were graded using the Common Terminology Criteria for Adverse Events (version 4).

### $^{89}$Zr-ss-Pertuzumab PET/CT Imaging

All patients returned for serial PET/CT imaging at 1, 3–4, and 5–8 d after administration. Patients underwent PET/CT from the top of the skull to the mid thigh on a dedicated research PET/CT scanner (Discovery PET/CT 710; GE Healthcare), with low-dose CT (80 mA) for attenuation correction and lesion localization. PET imaging was performed at 6–7 bed positions with a total imaging time of no more than 1 h (8 min/bed position). Images were reconstructed using our standard method with 3-dimensional ordered-subsets expectation maximization

with 2 iterations, 16 subsets, and a postreconstruction gaussian filter of 7 mm, as well as Q.clear reconstruction (GE Healthcare).

$^{89}$Zr-ss-pertuzumab PET/CT images were interpreted by a nuclear radiologist experienced in HER2-targeted PET. The interpreting radiologist knew the patient's clinical history and prior imaging results. Physiologic uptake of $^{89}$Zr-ss-pertuzumab was expected in the blood pool, liver, spleen, and kidneys on the basis of our experience with $^{89}$Zr-DFO-pertuzumab (*10*). Foci of radiotracer uptake in nonphysiologic areas and greater than adjacent background were considered positive for HER2-positive tumor. Three-dimensional volumes of interest were drawn on the PET/CT images using a dedicated workstation (Hermes Medical Solutions) over the cardiac blood pool, aortic arch, and normal liver, kidney, spleen, and lung. In addition, for patients with discernible uptake in the gastrointestinal tract or lesions, corresponding volumes of interest were generated for the whole gastrointestinal tract and up to 3 index lesions using a thresholding approach. SUVs normalized to lean body mass were quantified.

### Whole-Body and Serum Clearance Measurements

Whole-body clearance was determined by serial measurements of count rate using a 12.7-cm-thick NaI(Tl) scintillation detector at a fixed distance of 3 m from the patient. Background-corrected geometric mean counts were obtained before and after the first voiding and subsequently at the times of the PET scans. Count rates were normalized to the immediate postinfusion value (taken as 100%) to yield relative retained activities (as a percentage).

Serial blood samples were obtained before radiotracer administration and at approximately 30 min, 60 min, and 2 h after administration and on subsequent days of each PET scan ($n$ = 7 samples total). Counts in aliquots of serum were obtained using a well-type detector (Wallac Wizard 1480 γ-counter; Perkin Elmer) and expressed as percentage injected activity per liter.

Monoexponential functions were fitted to the whole-body probe data, and biexponential functions were fitted to the serum activity concentration data, using SAAM software (*19*). Time-integrated activity coefficients (TIACs) for the whole body and for serum were determined from these data. Serum data were also used to determine pharmacokinetic parameters, including concentration at time zero, the distribution volume of the central compartment, area under the curve (AUC), and systemic clearance. The total percentage injected activity initially present in the serum was estimated by multiplying the percentage injected activity per liter in serum at time zero by the patient's estimated plasma volume determined from a nomogram (*20*).

### Normal-Tissue Dosimetry

Normal-tissue dose estimates were derived as described previously (*9*,*21*). In brief, the AUCs of image-derived activity concentration per unit mass (kBq/g) were estimated by trapezoidal integration. Whole-organ AUCs were estimated by multiplying the activity concentration AUCs by the projected organ mass. TIACs were derived by dividing whole-organ AUCs by the administered activity. Corresponding values for heart contents and red marrow were estimated from the serum TIAC (*22*). TIACs for the remainder of the body were derived by subtracting all individually estimated TIACs from the whole-body TIAC. Thereafter, absorbed radiation doses to individual organs were estimated using the OLINDA/EXM software application (*23*). Normal-tissue dosimetry estimates for $^{89}$Zr-ss-pertuzumab were compared with published values for $^{89}$Zr-DFO-pertuzumab and $^{89}$Zr-DFO-trastuzumab.

### Statistics

Kinetic parameters and absorbed dose estimates were calculated for each patient and summarized using descriptive statistics including median or mean and SD.

## RESULTS

### Patient Characteristics

Between May 2021 and May 2022, 6 patients (5 female, 1 male; median age, 51 y; range, 41–69) with HER2-positive mBC completed the study protocol. All patients underwent serial imaging on days 1, 3–5, and 6–8 after injection of $^{89}$Zr-ss-pertuzumab. Table 1 summarizes the patient characteristics.

### Detection of Sites of Known Malignancy with $^{89}$Zr-ss-Pertuzumab PET

All patients had sites of malignancy determined on $^{18}$F-FDG PET/CT performed within 60 d of study enrollment. Known osseous metastatic disease was present in 5 patients, hepatic disease in 3 patients, nodal disease in 3 patients, lung disease in 2 patients, and primary breast malignancy in 1 patient. $^{89}$Zr-ss-pertuzumab PET scans were positive in 5 patients and negative in 1 patient. Of 5 patients with positive scans, complete concordance between $^{18}$F-FDG- and $^{89}$Zr-ss-pertuzumab–avid lesions at sites of known malignancy was observed in 2 patients. The 3 other patients demonstrated HER2 intertumoral heterogeneity, with 5% concordance, 20% concordance, and 80% concordance in patients 4, 5, and 6, respectively. Sites of known malignancy and $^{89}$Zr-ss-pertuzumab PET detection are summarized in Table 1.

### Adverse Events

All 6 patients underwent intravenous administration of $^{89}$Zr-ss-pertuzumab. No related side effects were observed or reported. The mean (±SD) of the administered mass of pertuzumab was 19.1 ± 0.375 mg (range, 18.5–19.5 mg). The mean administered activity was 73.1 MBq (range, 70.7–74.4 MBq). There were no

**TABLE 1**
Patient Characteristics

| Patient no. | Age (y) | Sex | Avidity | | Concordance |
|---|---|---|---|---|---|
| | | | $^{18}$F-FDG | $^{89}$Zr-ss-pertuzumab | |
| 1 | 50 | F | Nodal, hepatic, right lung | Nodal, hepatic, right lung | 100% |
| 2 | 48 | F | Osseous | Osseous | 100% |
| 3 | 41 | F | Right breast, nodal, hepatic, osseous | None (interval treatment response) | 0% |
| 4 | 57 | M | Hepatic, osseous | Osseous | 7.4% |
| 5 | 52 | F | Osseous, lung | Solitary osseous (sternum) | 20% |
| 6 | 69 | F | Osseous, nodal | Osseous | 80% |

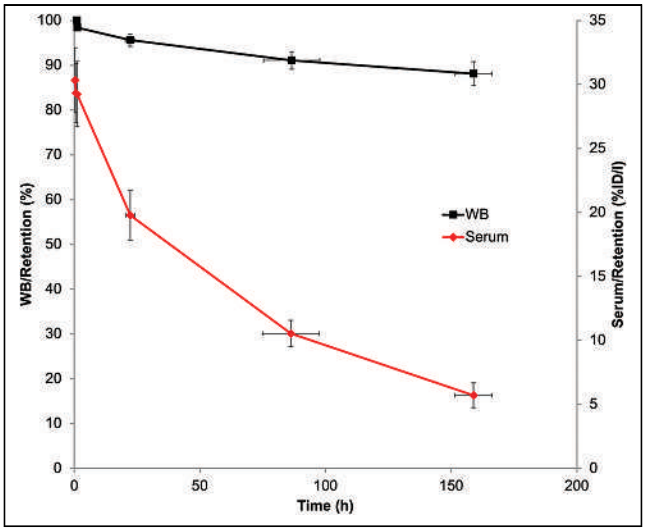


**FIGURE 1.** Summed whole-body and serum biologic clearance curves for $^{89}$Zr-ss-pertuzumab in 6 patients. Error bars indicate SE of mean. %ID/l = percentage injected dose per liter; WB = whole body.

adverse or clinically detectable pharmacologic effects in any of the 6 subjects. No significant changes in vital signs were observed.

### Pharmacokinetics

Whole-body and serum clearance conformed to mono- and biexponential kinetics, respectively. Summed biologic clearance data are shown in Figure 1, and summary statistics for the clearance parameters are provided in Supplemental Table 1 (supplemental materials are available at http://jnm.snmjournals.org).

### Biodistribution and Normal-Tissue Dose Estimates

Similar to other HER2-targeted PET radiotracers, the optimal imaging time point for tumor visualization was 5–8 d after administration, when the best contrast was observed between tumor foci and background uptake. The early images at 1 d after administration showed primarily blood pool, with little to no observable uptake in tumor lesions. Lesion uptake gradually increased with time and was highest at the last time point. Uptake in all normal tissues except kidney decreased with time. Kidney uptake continued to increase over the period of observation.

Absorbed dose estimates for normal tissues are summarized in Supplemental Table 2. The organs receiving the highest mean doses were kidney ($1.8 \pm 0.5$ mGy/MBq), liver ($1.7 \pm 0.3$ mGy/MBq), heart wall ($1.2 \pm 0.1$ mGy/MBq), and lung ($1.2 \pm 0.2$ mGy/MBq).

### Comparison of $^{89}$Zr-ss-Pertuzumab Dosimetry with $^{89}$Zr-DFO-Pertuzumab and $^{89}$Zr-Trastuzumab Dosimetry

The average effective dose was $0.54 \pm 0.03$ mSv/MBq, which is the same as that reported for $^{89}$Zr-DFO-pertuzumab ($0.54 \pm 0.07$ mSv/MBq; $P > 0.05$) (*10*) but higher than that reported for $^{89}$Zr-trastuzumab ($0.48 \pm 0.06$ mSv/MBq; $P < 0.05$) (*9*). The comparatively lower absorbed doses reported for $^{89}$Zr-trastuzumab are likely related to the large fraction of male vs. female patients (8 vs. 2) in the original esophagogastric cancer study. Figure 2 compares the biodistribution and absorbed dose estimates for the 3 HER2-targeting $^{89}$Zr-immuno-PET probes.

### Tumor Imaging with $^{89}$Zr-ss-Pertuzumab PET/CT

Patient 1 had an estrogen receptor (ER)–positive, progesterone receptor (PR)–positive, HER2-positive (IHC score, 2+; FISH ratio, 2.0) right-breast invasive ductal carcinoma (IDC) diagnosed in 2016 and underwent mastectomy followed by adjuvant therapy. In November 2020, she developed metastatic disease to the thoracic nodes and lungs. A subcarinal node was biopsied twice and found to be HER2-negative (first biopsy: IHC score, 0; second biopsy: IHC score, 2+; FISH ratio, 1.2). She started taking anastrozole and palbociclib but subsequently developed disease progression with new hepatic metastases. Given the discordant HER2 results between the breast primary and the metastatic disease, she was referred for $^{89}$Zr-ss-pertuzumab PET/CT to help select a liver lesion for biopsy to maximize the chances of HER2-positive disease and subsequent HER2-targeted therapy. She had thoracic nodes, liver lesions, and a right lung nodule avid for $^{18}$F-FDG at enrollment. There was gradually increasing $^{89}$Zr-ss-pertuzumab avidity of all lesions on days 3 and 6, with no avidity above the background level on day 1 (Fig. 3). Decreasing background blood pool and slightly decreasing liver uptake from days 1 to 6 allowed for optimal visualization of lesions on day 6. The liver lesions were the most avid, with a segment 4A/8 lesion demonstrating an $SUV_{max}$ of 11.4 (equal to liver background), 20.7, and 35.0, on days 1, 3, and 6, respectively. The second most avid liver lesion, in segment 6 ($SUV_{max}$, 30.0), was selected for biopsy given the ease of accessibility and high uptake. However, the biopsy found the lesion to be HER2-negative (IHC score, 1+).

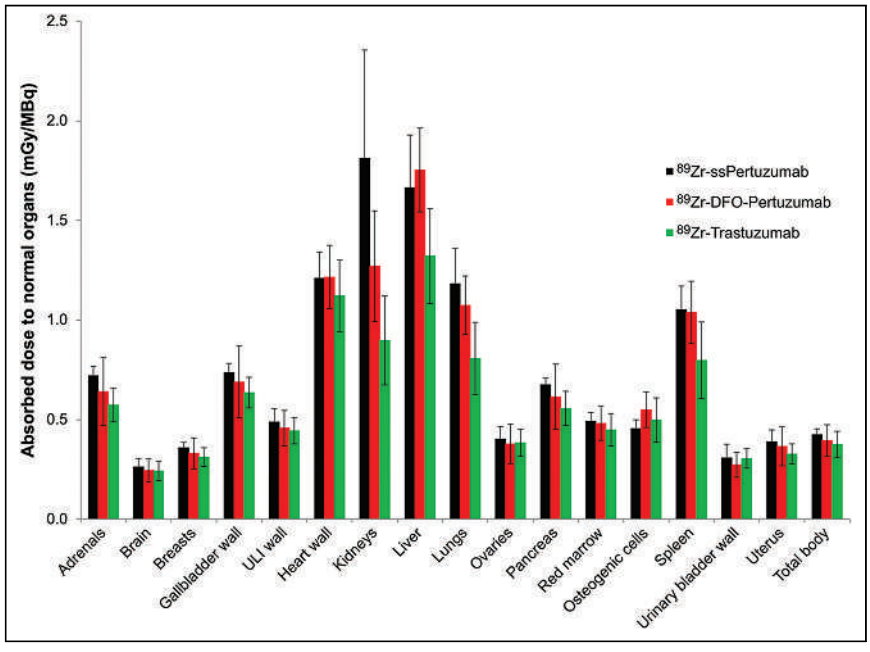


**FIGURE 2.** Comparison of radiation dosimetry for HER2 immuno-PET radiotracers. ULI = upper large intestinal.

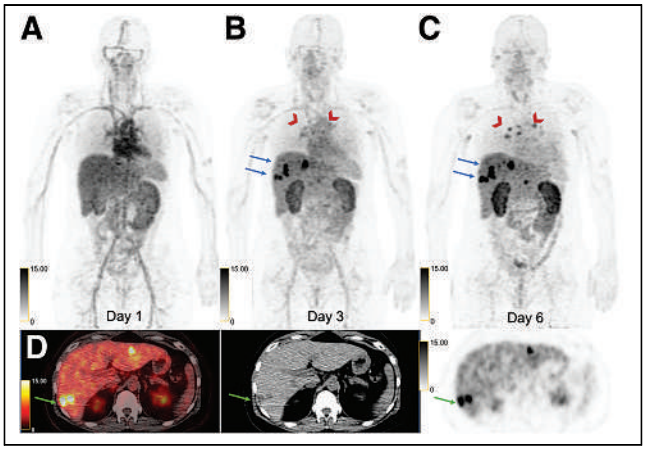


**FIGURE 3.** 50-y-old woman with HER2-positive mBC and known right lung, thoracic nodal, and liver metastases. (A–C) Sequential maximum-intensity projection PET images at 1 d (A), 3 d (B), and 6 d (C) after administration of $^{89}$Zr-ss-pertuzumab demonstrating gradually increasing uptake in thoracic nodes (arrowheads) and hepatic lesions (arrows) over time. Decreasing blood pool and slightly decreasing liver background uptake was observed on serial imaging, with increasing kidney uptake. (D) Axial $^{89}$Zr-ss-pertuzumab PET/CT, CT, and PET images at 6 d demonstrating a few avid hepatic lesions, of which segment 6 lesion (arrows) was selected for biopsy.

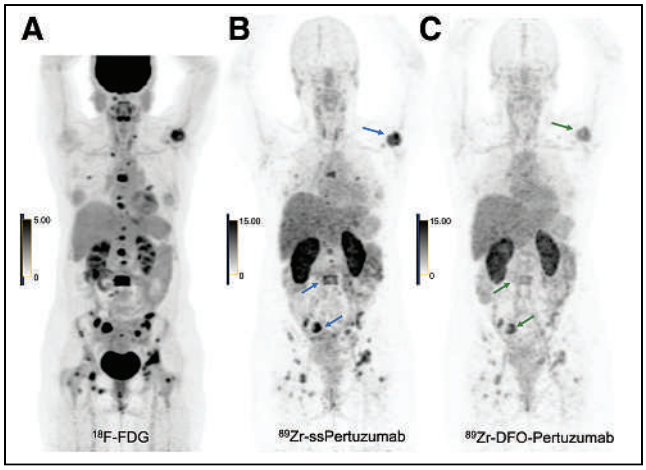


**FIGURE 4.** 46-y-old woman with HER2-positive mBC and known osseous metastases. (A) $^{18}$F-FDG maximum-intensity projection PET image demonstrating numerous avid osseous metastases. (B and C) Maximum-intensity projection PET images of $^{89}$Zr-ss-pertuzumab (B) and $^{89}$Zr-DFO-pertuzumab (C) at 5 d after injection showing uptake within osseous metastases; however, $^{89}$Zr-ss-pertuzumab detected more lesions and had higher lesion conspicuity and intensity of tracer uptake. The 3 hottest lesions with $^{89}$Zr-ss-pertuzumab and $^{89}$Zr-DFO-pertuzumab are denoted with arrows. $^{89}$Zr-ss-pertuzumab PET/CT was performed 1 mo before $^{89}$Zr-DFO-pertuzumab PET/CT.

Patient 2 had an ER-positive, PR-positive, HER2-positive (IHC score, 1–2+; FISH ratio, 3.0) right-breast IDC diagnosed in 2018 and underwent lumpectomy. The patient declined adjuvant therapy and developed right-breast, axilla, and bone recurrence in 2019, with HER2-negative disease (IHC score, 1+) in both breast and bone. The patient received paclitaxel, trastuzumab, and pertuzumab followed by maintenance trastuzumab and pertuzumab until progression of bone metastasis in 2021. She then received trastuzumab emtansine for a few months with further bony progression. Given the HER2 discordance, a repeat bone biopsy was planned, and the patient was referred for $^{89}$Zr-ss-pertuzumab PET/CT to help select a bone lesion. She had numerous $^{18}$F-FDG–avid osseous lesions at enrollment, all with increasing $^{89}$Zr-ss-pertuzumab avidity on days 1, 5, and 7. A right sacral lesion was the most avid ($SUV_{max}$, 6.5, 20.7, and 22.3 on days 1, 5, and 7, respectively) and was selected for biopsy. The sclerotic and most conspicuous component of this right sacral lesion had the least tracer avidity, and $^{89}$Zr-ss-pertuzumab PET/CT directed the CT-guided biopsy toward an adjacent more avid component without a CT correlate. However, biopsy showed HER2 negativity (IHC score, 1–2+; FISH ratio, 1.3), and as a result, the patient received palbociclib, letrozole, and leuprorelin instead of trastuzumab deruxtecan (T-DXd).

This patient also underwent both $^{89}$Zr-ss-pertuzumab PET/CT and $^{89}$Zr-DFO-pertuzumab PET/CT 1 mo apart during a treatment holiday, with $^{89}$Zr-ss-pertuzumab PET/CT performed first. Representative images (Fig. 4) show markedly improved lesion detection, conspicuity, and intensity of tracer uptake by numerous osseous lesions with $^{89}$Zr-ss-pertuzumab compared with $^{89}$Zr-DFO-pertuzumab. For example, the total number of tracer-avid osseous lesions visualized on $^{89}$Zr-ss-pertuzumab PET/CT was 55, versus 38 on $^{89}$Zr-DFO-pertuzumab PET/CT. For $^{89}$Zr-ss-pertuzumab versus $^{89}$Zr-DFO-pertuzumab, the $SUV_{max}$ of the 3 hottest lesions was 22.3 versus 12.2, respectively, in the right sacrum, 15.5 versus 6.9, respectively, in L3, and 19.7 versus 8.9, respectively, in the left humerus.

Patient 3 had an ER-positive, PR-positive, HER2-positive (IHC score, 3+) right-breast mixed ductal and lobular invasive carcinoma diagnosed in 2021, with de novo metastatic disease to the right axillary nodes, liver, and bones. A left iliac bone biopsy was ER-positive, PR-positive, and HER2-positve (IHC score equivocal because of crush artifact, but *ERBB2* amplification on next-generation sequencing). She had just completed her fourth cycle of paclitaxel, trastuzumab, and pertuzumab before $^{89}$Zr-ss-pertuzumab PET/CT. No tracer-avid lesions were visualized, and the lack of $^{89}$Zr-ss-pertuzumab uptake in known metastatic lesions was thought to be due to treatment response (as opposed to lack of HER2 expression), as an $^{18}$F-FDG PET/CT shortly afterward showed complete response with no $^{18}$F-FDG–avid disease.

Patient 4 had an ER-positive, PR-negative, HER2-positive (IHC score, 2+; FISH ratio, 2.6) left-breast IDC diagnosed in 2019, with metastatic disease to the bones. An L2 vertebral metastasis was biopsied as HER2-negative (IHC score, 1+). The patient was started on paclitaxel, trastuzumab, and pertuzumab, and the osseous metastasis progressed. Given the HER2 discordance, a repeat HER2 FISH was performed on the primary breast tumor and was HER2-negative (FISH ratio, 1.87). He underwent multiple lines of therapy and had recently progressed on trastuzumab and pertuzumab before being referred for $^{89}$Zr-ss-pertuzumab PET/CT to assess the current HER2 status of his disease and decide whether to continue HER2-targeted therapy or switch to chemotherapy. At enrollment, he had $^{18}$F-FDG–avid diffuse osseous metastases and multiple hepatic metastases. Of the diffuse osseous disease, only a few lesions demonstrated only mild $^{89}$Zr-ss-pertuzumab avidity, and there were no tracer-avid hepatic lesions. Since only a small percentage was HER2 PET–positive (concordance, 7.4%), he was

switched to chemotherapy with doxorubicin instead of HER2-targeted therapy.

Patient 5 had an ER-negative, PR-negative, HER2-positive (IHC score, 3+) right-breast IDC diagnosed in 2011 and underwent neoadjuvant chemotherapy and mastectomy followed by 1 y of adjuvant trastuzumab. In 2017, she was found to have pulmonary nodules, one of which was biopsied and found to be HER2-positive (IHC score, 3+). She received multiple lines of HER2-targeted therapy including paclitaxel, trastuzumab, and pertuzumab; trastuzumab emtansine; and capecitabine and neratinib but subsequently developed brain and bone metastases. She was started on T-DXd and had a partial response but was lost to follow-up for several months. She was restarted on T-DXd but developed progression of $^{18}$F-FDG–avid lung and bone metastases. The patient was referred for $^{89}$Zr-ss-pertuzumab PET/CT to assess her current HER2 status and help decide between further HER2-targeted therapy or chemotherapy. HER2 PET heterogeneity was observed with $^{89}$Zr-ss-pertuzumab avidity in a solitary sternal lesion on day 7 ($SUV_{max}$, 12.7), whereas the remaining bone and lung lesions were not tracer-avid. Since at least 1 lesion was tracer-avid, she was switched to another line of HER2-targeted therapy with trastuzumab, capecitabine, and tucatinib.

Patient 6 had an ER-positive, PR-positive, HER2-positive (IHC score, 2+; FISH ratio, 2.1) left-breast IDC diagnosed in 2016 and underwent neoadjuvant chemotherapy, lumpectomy, and radiation followed by adjuvant letrozole. She was subsequently diagnosed with metastases to the lung, neck and thoracic nodes, and sternum. A left neck node was biopsied and found to be HER2-positive (IHC score, 2+; FISH ratio, 2.34). She was treated with several lines of HER2-targeted therapy, with progression of the osseous metastases and a subcarinal node. The patient was referred for $^{89}$Zr-ss-pertuzumab PET/CT to assess her current HER2 status and help decide between further HER2-targeted therapy or chemotherapy. HER2 PET heterogeneity was observed, with gradually increasing $^{89}$Zr-ss-pertuzumab avidity in all bone lesions on days 1, 3, and 6 after injection ($SUV_{max}$ of the most avid sternal lesions, 11.7, 18.5, and 34.4) but no uptake in a mildly $^{18}$F-FDG–avid subcarinal nodal metastasis. Since most lesions demonstrated $^{89}$Zr-ss-pertuzumab avidity, she was switched to another line of HER2-targeted therapy with trastuzumab, capecitabine, and tucatinib.

## DISCUSSION

In this trial, we demonstrated the safety and investigated the biodistribution and dosimetry of $^{89}$Zr-ss-pertuzumab. We also showed that $^{89}$Zr-ss-pertuzumab successfully targets and visualizes metastatic lesions in patients with HER2-positive mBC. To our knowledge, this is first successful clinical translation of a site-specifically radiolabeled antibody.

Similar to two other HER2-targeted immuno-PET agents, $^{89}$Zr-DFO-trastuzumab and $^{89}$Zr-DFO-pertuzumab, the optimal imaging time point for $^{89}$Zr-ss-pertuzumab was 5–8 d. Tumor uptake increased over time, and concomitant decreases were seen in the blood pool and liver background. The mean effective dose of $^{89}$Zr-ss-pertuzumab (0.54 mSv/MBq) was equal to that of $^{89}$Zr-DFO-pertuzumab (0.54 mSv/MBq) (*10*) and comparable to that of $^{89}$Zr-DFO-trastuzumab (0.48 mSv/MBq) (*9*). The biodistribution and normal-tissue dosimetry of $^{89}$Zr-ss-pertuzumab were also similar; however, $^{89}$Zr-ss-pertuzumab had the highest uptake in the kidneys, whereas the other two had the highest uptake in the liver. Otherwise, the dosimetry profile was relatively similar among the 3 tracers. One patient (patient 2) underwent PET/CT with both $^{89}$Zr-ss-pertuzumab and $^{89}$Zr-DFO-pertuzumab 1 mo apart during a treatment break, allowing for a preliminary comparison between the site-specifically and stochastically lysine-labeled radioimmunoconjugates. $^{89}$Zr-ss-pertuzumab showed tumor lesion detection, conspicuity, and uptake superior to those of $^{89}$Zr-DFO-pertuzumab in this patient, in keeping with the superior imaging properties observed in preclinical models (*23*). Compared with trastuzumab, radiolabeling of pertuzumab has advantages since pertuzumab binds to a different site (extracellular domain II) on the HER2 receptor from trastuzumab (domain IV) (*24*), preventing the radioimmunoconjugate from interfering with drug binding in breast cancer patients treated with trastuzumab-based agents. However, radiolabeled pertuzumab may be limited in potential applications such as predicting response to trastuzumab-based therapy, including the newer HER2-targeted antibody–drug conjugates.

In our study, $^{89}$Zr-ss-pertuzumab PET/CT was used to assess the current HER2 status of metastatic lesions to guide biopsy and assist in deciding the next line of treatment. Although CT and $^{18}$F-FDG PET/CT are excellent in detecting tumor lesions in mBC (*25*), these imaging modalities provide information only on the presence or absence, size, and viability of tumor lesions, with no information on their current receptor status. Thus, a potential application of $^{89}$Zr-ss-pertuzumab PET/CT is to select a lesion to biopsy in patients with more than 1 metastatic lesion. Lesion selection is critically important, as one of the primary goals of tissue sampling is to maximize the chances of identifying HER2-positive disease so a patient can receive HER2-targeted therapy.

In the first 2 patients, $^{89}$Zr-ss-pertuzumab PET/CT helped select lesions to biopsy, as patient 1 had more than 5 hepatic lesions and patient 2 had more than 20 osseous lesions. In both patients, lesion selection was based on $^{89}$Zr-ss-pertuzumab avidity and biopsy feasibility. Surprisingly, both lesions were found to be HER2-negative on pathology despite clear and intense tracer avidity ($SUV_{max}$ range, 22.3–30.0). One possible explanation of this phenomenon is that $^{89}$Zr-ss-pertuzumab uptake does not necessarily align with the historical binary definition of HER2 status per the guidelines of the American Society of Clinical Oncology and the College of American Pathologists. Rather, $^{89}$Zr-ss-pertuzumab may be able to detect a wide array of HER2 expression levels and thus may visualize both HER2-positive tumors and HER2-low tumors (IHC score, 1+, or 2+ and FISH negative). This hypothesis is in line with the recent findings of the DESTINY-Breast04 trial, which showed for the first time that HER2-targeted therapy with T-DXd had efficacy in patients with HER2-low mBC (*26*), thereby establishing HER2-low patients as a new and distinct population (*26*,*27*). This detection of HER2-low tumors may also in part explain the false positives for HER2-positive malignancy in our prior HER2 PET studies (*7*,*8*,*11*).

Another potential application for $^{89}$Zr-ss-pertuzumab PET/CT is real-time assessment of intertumoral HER2 expression heterogeneity throughout all lesions to assist in deciding whether to continue HER2-targeted therapy or change to chemotherapy at disease progression. In our study, 3 patients—patients 4, 5, and 6—underwent $^{89}$Zr-ss-pertuzumab PET for this reason. Patient 4 had positive $^{89}$Zr-ss-pertuzumab PET findings, but only a small percentage of his diffuse disease was tracer-avid and thus he was switched to chemotherapy. Patients 5 and 6 had positive $^{89}$Zr-ss-pertuzumab PET findings with at least 1 tracer-avid lesion and were thus switched to another line of HER2-targeted therapy. Interestingly,

whereas both patients had positive HER2 PET findings, different degrees of HER2 intertumoral heterogeneity were observed on a lesion-by-lesion basis: patient 5 had only 1 $^{89}$Zr-ss-pertuzumab–avid lesion of 5 total (20% concordance), whereas patient 6 had 4 $^{89}$Zr-ss-pertuzumab–avid lesions of 5 total (80% concordance).

It remains unclear at this point whether patients with more homogeneous and uniform HER2 expression will respond better to HER2-targeted therapy than patients with more heterogeneous and discordant HER2 expression. Mechanistically, however, this hypothesis is certainly plausible, especially in light of the growing evidence supporting the theranostic utility of other PET tracers such as $^{68}$Ga-DOTATATE (*28*) and $^{68}$Ga-PSMA-617 (*29*). Along these lines, the ZEPHIR trial demonstrated that $^{89}$Zr-DFO-trastuzumab PET/CT predicted treatment response to trastuzumab emtansine in mBC patients with a positive predictive value of 72% and negative predictive value of 88%. In addition, 29% of patients in this study had negative HER2 PET findings and 46% of patients had intertumoral heterogeneity, further highlighting how single-site biopsies may underestimate underlying HER2 heterogeneity. In this study, $^{89}$Zr-DFO-trastuzumab PET/CT results were classified as positive if more than 50% of the tumor load was tracer-avid and as negative if otherwise (*4*). However, no clear method has yet been established for HER2 PET interpretation or defining HER2 PET heterogeneity.

$^{89}$Zr-ss-pertuzumab is a promising HER2 immuno-PET agent. Further exploration is necessary, and we plan to continue this work through an ongoing pancancer trial investigating $^{89}$Zr-ss-pertuzumab PET/CT in patients with different HER2-positive primary cancers. Other areas of investigation include whether $^{89}$Zr-ss-pertuzumab can detect brain metastases, since the rate of brain metastasis is higher in patients with HER2-positive mBC than in those with HER2-negative disease (*30*). Finally, the landmark approval of T-DXd, a HER2-targeted antibody–drug conjugate, for patients with HER2-low mBC may portend yet another clinical application for $^{89}$Zr-ss-pertuzumab PET, potentially as a predictive biomarker for this novel antibody–drug conjugate.

## CONCLUSION

This study demonstrated the safety, dosimetry, and tumor targeting of $^{89}$Zr-ss-pertuzumab PET and represents the first translation of a site-specifically radiolabeled antibody to the clinic. Potential clinical applications include assessment of current HER2 status and the heterogeneity of metastatic lesions throughout the body to guide biopsy and treatment decisions.

## DISCLOSURE

Funding was received from National Institutes of Health (NIH) grant R01 CA204167 (to Brian Agnew, Gary Ulaner, Jason Lewis, and Brian Zeglis) and from the Memorial Sloan Kettering Cancer Center Radiochemistry and Molecular Imaging Probe Core (NIH grant P30 CA08748) for additional support. Jason Lewis is supported in part by R35 CA232130. Shanu Modi serves as a scientific advisor/consultant for Genentech, Daiichi Sankyo, AstraZeneca, Seagen, Gilead, Macrogenics, Zymeworks, and Novartis; receives honoraria from Daiichi Sankyo, AstraZeneca, and Seagen; and has institutional grants for research from Genentech, Daiichi Sankyo, AstraZeneca, and Seagen. No other potential conflict of interest relevant to this article was reported.

**KEY POINTS**

**QUESTION:** What are the safety, radiation dosimetry, and potential imaging characteristics of site-specifically radiolabeled $^{89}$Zr-pertuzumab, and how does it compare with prior HER2-targeted immuno-PET probes?

**PERTINENT FINDINGS:** In a first-in-humans clinical trial on 6 patients with HER2-positive mBC, $^{89}$Zr-ss-pertuzumab PET/CT was safe and demonstrated biodistribution and dosimetry profiles similar to those of $^{89}$Zr-DFO-pertuzumab and $^{89}$Zr-DFO-trastuzumab. $^{89}$Zr-ss-pertuzumab PET/CT was able to detect known malignant lesions, indicating that they are HER2-positive, and may detect more lesions than $^{89}$Zr-DFO-pertuzumab.

**IMPLICATIONS FOR PATIENT CARE:** HER2 PET with $^{89}$Zr-ss-pertuzumab could enable real-time evaluation of HER2 status to guide biopsy and treatment decisions.

## REFERENCES

1. Wolff AC, Hammond ME, Hicks DG, et al. Recommendations for human epidermal growth factor receptor 2 testing in breast cancer: American Society of Clinical Oncology/College of American Pathologists clinical practice guideline update. *J Clin Oncol.* 2013;31:3997–4013.
2. Niikura N, Liu J, Hayashi N, et al. Loss of human epidermal growth factor receptor 2 (HER2) expression in metastatic sites of HER2-overexpressing primary breast tumors. *J Clin Oncol.* 2012;30:593–599.
3. Dijkers EC, Oude Munnink TH, Kosterink JG, et al. Biodistribution of $^{89}$Zr-trastuzumab and PET imaging of HER2-positive lesions in patients with metastatic breast cancer. *Clin Pharmacol Ther.* 2010;87:586–592.
4. Gebhart G, Lamberts LE, Wimana Z, et al. Molecular imaging as a tool to investigate heterogeneity of advanced HER2-positive breast cancer and to predict patient outcome under trastuzumab emtansine (T-DM1): the ZEPHIR trial. *Ann Oncol.* 2016;27:619–624.
5. Bensch F, Brouwers AH, Lub-de Hooge MN, et al. $^{89}$Zr-trastuzumab PET supports clinical decision making in breast cancer patients, when HER2 status cannot be determined by standard work up. *Eur J Nucl Med Mol Imaging.* 2018;45:2300–2306.
6. Dehdashti F, Wu N, Bose R, et al. Evaluation of [$^{89}$Zr]trastuzumab-PET/CT in differentiating HER2-positive from HER2-negative breast cancer. *Breast Cancer Res Treat.* 2018;169:523–530.
7. Ulaner GA, Hyman DM, Ross DS, et al. Detection of HER2-positive metastases in patients with HER2-negative primary breast cancer using $^{89}$Zr-trastuzumab PET/CT. *J Nucl Med.* 2016;57:1523–1528.
8. Ulaner GA, Hyman DM, Lyashchenko SK, Lewis JS, Carrasquillo JA. $^{89}$Zr-trastuzumab PET/CT for detection of human epidermal growth factor receptor 2-positive metastases in patients with human epidermal growth factor receptor 2-negative primary breast cancer. *Clin Nucl Med.* 2017;42:912–917.
9. O'Donoghue JA, Lewis JS, Pandit-Taskar N, et al. Pharmacokinetics, biodistribution, and radiation dosimetry for $^{89}$Zr-trastuzumab in patients with esophagogastric cancer. *J Nucl Med.* 2018;59:161–166.
10. Ulaner GA, Lyashchenko SK, Riedl C, et al. First-in-human human epidermal growth factor receptor 2-targeted imaging using $^{89}$Zr-pertuzumab PET/CT: dosimetry and clinical application in patients with breast cancer. *J Nucl Med.* 2018;59:900–906.
11. Ulaner GA, Carrasquillo JA, Riedl CC, et al. Identification of HER2-positive metastases in patients with HER2-negative primary breast cancer by using HER2-targeted $^{89}$Zr-pertuzumab PET/CT. *Radiology.* 2020;296:370–378.
12. Lumish MA, Maron SB, Paroder V, et al. Noninvasive assessment of human epidermal growth factor receptor 2 (HER2) in esophagogastric cancer using $^{89}$Zr-trastuzumab PET: a pilot study. *J Nucl Med.* 2023;64:724–730.

13. Agarwal P, Bertozzi CR. Site-specific antibody-drug conjugates: the nexus of bioorthogonal chemistry, protein engineering, and drug development. *Bioconjug Chem.* 2015;26:176–192.
14. Zeglis BM, Davis CB, Abdel-Atti D, et al. Chemoenzymatic strategy for the synthesis of site-specifically labeled immunoconjugates for multimodal PET and optical imaging. *Bioconjug Chem.* 2014;25:2123–2128.
15. Spanov B, Olaleye O, Mesurado T, et al. Pertuzumab charge variant analysis and complementarity-determining region stability assessment to deamidation. *Anal Chem.* 2023;95:3951–3958.
16. Vivier D, Fung K, Rodriguez C, et al. The influence of glycans-specific bioconjugation on the FcγRI binding and in vivo performance of $^{89}$Zr-DFO-pertuzumab. *Theranostics.* 2020;10:1746–1757.
17. Zeglis BM, Davis CB, Aggeler R, et al. Enzyme-mediated methodology for the site-specific radiolabeling of antibodies based on catalyst-free click chemistry. *Bioconjug Chem.* 2013;24:1057–1067.
18. Oken MM, Creech RH, Tormey DC, et al. Toxicity and response criteria of the Eastern Cooperative Oncology Group. *Am J Clin Oncol.* 1982;5:649–655.
19. Barrett PH, Bell BM, Cobelli C, et al. SAAM II: simulation, analysis, and modeling software for tracer and pharmacokinetic studies. *Metabolism.* 1998;47:484–492.
20. Retzlaff JA, Tauxe WN, Kiely JM, Stroebel CF. Erythrocyte volume, plasma volume, and lean body mass in adult men and women. *Blood.* 1969;33:649–661.
21. Pandit-Taskar N, O'Donoghue JA, Beylergil V, et al. $^{89}$Zr-huJ591 immuno-PET imaging in patients with advanced metastatic prostate cancer. *Eur J Nucl Med Mol Imaging.* 2014;41:2093–2105.
22. Sgouros G, Stabin M, Erdi Y, et al. Red marrow dosimetry for radiolabeled antibodies that bind to marrow, bone, or blood components. *Med Phys.* 2000;27:2150–2164.
23. Stabin MG, Sparks RB, Crowe E. OLINDA/EXM: the second-generation personal computer software for internal dose assessment in nuclear medicine. *J Nucl Med.* 2005;46:1023–1027.
24. Capelan M, Pugliano L, De Azambuja E, et al. Pertuzumab: new hope for patients with HER2-positive breast cancer. *Ann Oncol.* 2013;24:273–282.
25. Ulaner GA. PET/CT for patients with breast cancer: where is the clinical impact? *AJR.* 2019;213:254–265.
26. Modi S, Jacot W, Yamashita T, et al. Trastuzumab deruxtecan in previously treated HER2-low advanced breast cancer. *N Engl J Med.* 2022;387:9–20.
27. Hurvitz SA. DESTINY-changing results for advanced breast cancer. *N Engl J Med.* 2022;387:75–76.
28. Strosberg J, El-Haddad G, Wolin E, et al. Phase 3 trial of $^{177}$Lu-dotatate for midgut neuroendocrine tumors. *N Engl J Med.* 2017;376:125–135.
29. Sartor O, de Bono J, Chi KN, et al. Lutetium-177–PSMA-617 for metastatic castration-resistant prostate cancer. *N Engl J Med.* 2021;385:1091–1103.
30. Pasquier D, Darlix A, Louvel G, et al. Treatment and outcomes in patients with central nervous system metastases from breast cancer in the real-life ESME MBC cohort. *Eur J Cancer.* 2020;125:22–30.

# Design, Preclinical Evaluation, and Clinical Translation of $^{68}$Ga-FAPI-LM3, a Heterobivalent Molecule for PET Imaging of Nasopharyngeal Carcinoma

Liang Zhao*[1–3], Yizhen Pang*[1–3], Jianyang Fang*[4], Jianhao Chen[1–3], Yangfan Zhou[1–3], Long Sun[1], Hua Wu[1], Zhide Guo[4], Qin Lin[2,3], and Haojun Chen[1,5]

*[1]Department of Nuclear Medicine and Minnan PET Center, Xiamen Key Laboratory of Radiopharmaceuticals, First Affiliated Hospital of Xiamen University, School of Medicine, Xiamen University, Xiamen, China; [2]School of Clinical Medicine, Fujian Medical University, Fuzhou, China; [3]Xiamen Key Laboratory of Radiation Oncology, Department of Radiation Oncology, Xiamen Cancer Center, First Affiliated Hospital of Xiamen University, School of Medicine, Xiamen University, Xiamen, China; [4]State Key Laboratory of Molecular Vaccinology and Molecular Diagnostics and Center for Molecular Imaging and Translational Medicine, School of Public Health, Xiamen University, Xiamen, China; and [5]Xiamen Key Laboratory of Rare Earth Photoelectric Functional Materials, Xiamen Institute of Rare Earth Materials, Haixi Institute, Chinese Academy of Sciences, Xiamen, China*

Extensive research has been conducted on radiolabeled fibroblast activation protein (FAP) inhibitors (FAPIs) and p-Cl-Phe-cyclo(D-Cys-Tyr-D-4-amino-Phe(carbamoyl)-Lys-Thr-Cys)D-Tyr-$NH_2$ (LM3) peptides for imaging of FAP and somatostatin receptor 2 (SSTR2)–positive tumors. In this study, we designed and synthesized a FAPI-LM3 heterobivalent molecule radiolabeled with $^{68}$Ga and evaluated its effectiveness in both tumor xenografts and patients with nasopharyngeal carcinoma (NPC). **Methods:** The synthesis of FAPI-LM3 was based on the structures of FAPI-46 and LM3. After radiolabeling with $^{68}$Ga, its dual-receptor–binding affinity was evaluated in vitro and in vivo. Preclinical studies, including small-animal PET and biodistribution evaluation, were conducted on HT-1080-FAP and HT-1080-SSTR2 tumor xenografts. The feasibility of $^{68}$Ga-FAPI-LM3 PET/CT in a clinical setting was evaluated in patients with NPC, and the results were compared with those of $^{18}$F-FDG. **Results:** $^{68}$Ga-FAPI-LM3 showed high affinity for both FAP and SSTR2. The tumor uptake of $^{68}$Ga-FAPI-LM3 was significantly higher than that of $^{68}$Ga-FAPI-46 and $^{68}$Ga-DOTA-LM3 in HT-1080-FAP–plus–HT-1080-SSTR2 tumor xenografts. In a clinical study involving 6 NPC patients, $^{68}$Ga-FAPI-LM3 PET/CT showed significantly higher uptake than did $^{18}$F-FDG in primary and metastatic lesions, leading to enhanced lesion detectability and tumor delineation. **Conclusion:** $^{68}$Ga-FAPI-LM3 exhibited FAPI and SSTR2 dual-receptor–targeting properties both in vitro and in vivo, resulting in improved tumor uptake and retention compared with that observed with monomeric $^{68}$Ga-FAPI and $^{68}$Ga-DOTA-LM3. This study highlights the clinical feasibility of $^{68}$Ga-FAPI-LM3 PET/CT for NPC imaging.

**Key Words:** fibroblast activation protein; somatostatin receptor 2; heterobivalent molecule; nasopharyngeal carcinoma; PET

**J Nucl Med 2024; 65:394–401**
DOI: 10.2967/jnumed.123.266183

The tumor microenvironment encompasses multiple types of nontumor cells, including cancer-associated fibroblasts, immune cells, and endothelial cells. The tumor microenvironment has attracted significant attention in research on tumor occurrence and development (*1*). Regarding nasopharyngeal carcinoma (NPC), the Epstein–Barr virus can promote fibrosis and NPC progression by activating signaling of YAP1/fibroblast activation protein (FAP) α in fibroblasts (*2*). Cancer-associated fibroblasts enhance the survival of irradiated NPC cells through the NF-κB pathway, leading to increased radioresistance (*3*). Therefore, diagnostic and therapeutic approaches focusing on the tumor microenvironment could be crucial frontiers in NPC. The use of the FAP-targeting inhibitor (FAPI), small ligand (oncoFAP), and cyclic peptide (FAP-2286) has achieved impressive results in tumor diagnosis. However, further improvement is needed to enhance their efficacy in radioligand therapy (*4–6*).

Within the domain of nuclear medicine, several targets, such as somatostatin receptor 2 (SSTR2), prostate-specific membrane antigen, and FAP, have emerged as prominent subjects of research (*7*,*8*). Epstein–Barr virus latent membrane protein 1 can upregulate SSTR2 expression via the NF-κB pathway (*9*). Both FAP and SSTR2 are important markers in the biology of NPC, as evidenced by the plethora of such PET radiopharmaceuticals, including $^{68}$Ga-FAPI for imaging cancer-associated fibroblasts and $^{68}$Ga-DOTATATE for imaging SSTR2 (*10*,*11*). For example, over 80% of patients showed positive expression of SSTR2 in both primary and metastatic NPCs (*11*). In addition to NPC, SSTR2 is expressed in other malignancies, including neuroendocrine tumor, thyroid carcinoma, breast cancer, and meningioma, expanding its potential applications in tumor theranostics (*12–14*). Apart from agonists, antagonists such as p-Cl-Phe-cyclo(D-Cys-Tyr-D-4-amino-Phe(carbamoyl)-Lys-Thr-Cys)D-Tyr-$NH_2$

Received Jun. 14, 2023; revision accepted Nov. 9, 2023.
For correspondence or reprints, contact Haojun Chen (leochen0821@foxmail.com) or Qin Lin (linqin05@163.com).
*Contributed equally to this work.
Published online Jan. 4, 2024.

(LM3) and JR11 are undergoing extensive research for their SSTR2-targeting properties. Unlike SSTR2 agonists, which exhibit a high internalization rate, the antagonist LM3 possesses a high binding affinity to SSTR2 but a low internalization rate (*15*). Notably, LM3, characterized by low liver uptake and superior lesion-to-background contrast, shows promising potential for peptide-receptor radionuclide therapy (*15*).

Therefore, developing a heterobivalent molecule targeting both SSTR2 and FAP holds significant importance. In this study, we designed a heterobivalent molecule called FAPI-LM3 and evaluated its preliminary application in preclinical models and patients with NPC. We hypothesized that this heterobivalent peptide can effectively combine the merits of SSTR2 and FAP, resulting in favorable pharmacokinetic characteristics and initial clinical effects.

## MATERIALS AND METHODS

### Chemistry and Radiochemistry

Information regarding the reagents, chemicals, high-performance liquid chromatography, liquid chromatography–mass spectrometry, and flow diagram of the synthesis of FAPI-LM3 are provided in the supplemental materials (available at http://jnm.snmjournals.org (*16*)). The radiolabeling of FAPI-46, DOTA-LM3, and FAPI-LM3 precursors with $^{68}$Ga was performed following similar procedures. In brief, 25 nmol of the precursor in 1 mL of sodium acetate buffer (0.25 M, pH 8.2–8.3) was allowed to react with 4 mL of $^{68}$Ga solution (1.3 GBq in 0.6 M HCl) at 100°C for 15 min. For clinical imaging, the final product was passed through a 0.22-μm Millipore filter for sterilization in each $^{68}$Ga-FAPI-LM3 preparation process. The stability of $^{68}$Ga-FAPI-LM3 was determined by incubating the product in phosphate-buffered saline and fetal bovine serum at 37°C and analyzing it via radio–high-performance liquid chromatography after 1 and 2 h of incubation.

### In Vitro Characterization of FAPI-LM3

HT-1080-FAP and HT-1080-SSTR2 cell lines were derived from HT-1080 cells (obtained from the China National Infrastructure of Cell Line Resource) and stably transfected with human FAP and SSTR2, respectively, following our previously established protocol (*17*). Information on cell resources, transfection, and culture is provided in the supplemental materials. For in vitro studies, the cells were seeded in 24-well plates and cultured in a routine medium until they reached approximately 80% confluence. During the experiment, the medium was replaced with a fetal bovine serum–free medium. In the cellular uptake test, different cells (HT-1080-FAP, HT-1080-SSTR2, HT-1080-FAP–plus–HT-1080-SSTR2, C666-1, or U87 cells) were treated with $^{68}$Ga-FAPI-LM3 with or without 10 nmol of unlabeled precursor (FAPI-46, DOTA-LM3, or FAPI-46 plus DOTA-LM3) and incubated for 60 min. For FAP radioligand binding assays, HT-1080-FAP cells were incubated with unlabeled FAPI-LM3 or FAPI-46 ($8.16 \times 10^{-5}$ to $10^{-13}$ M, $n = 3$) using $^{68}$Ga-FAPI-46 as the radioligand. Similarly, for the SSTR2 receptor binding assay, HT-1080-SSTR2 cells were incubated with unlabeled FAPI-LM3 or DOTA-LM3 ($8.16 \times 10^{-5}$ to $10^{-13}$ M, $n = 3$) using $^{68}$Ga-DOTA-LM3. After a 60-min incubation period, the free tracer was removed using phosphate-buffered saline before measurement. The cells were lysed with 0.5 mL of 1 M NaOH, and radioactivity was subsequently gauged using a γ-counter (Wizard 2480; PerkinElmer Inc.).

### Small-Animal PET Imaging and Biodistribution Studies

The Animal Care and Use Committee of Xiamen University approved all animal studies. Six-week-old BALB/c nude mice were obtained from Beijing Vital River Laboratory Animal Technology Co. In total, $5 \times 10^6$ tumor cells ($2.5 \times 10^6$ HT-1080-FAP and $2.5 \times 10^6$ HT-1080-SSTR2) in 100 μL of phosphate-buffered saline were subcutaneously injected into the right shoulder of each mouse. Tumor-bearing mice (3/group) were intravenously injected with approximately 7.4 MBq of $^{68}$Ga-FAPI-LM3, $^{68}$Ga-FAPI-46, or $^{68}$Ga-DOTA-LM3. Subsequent static PET scans were obtained at intervals of 0.5, 1, 2, and 4 h after injection using an Inveon small-animal PET scanner (Siemens). In the blocking experiment, approximately 60 nmol of the unlabeled precursor (FAPI-46, DOTA-LM3, or FAPI-46 plus DOTA-LM3) were simultaneously injected with $^{68}$Ga-FAPI-LM3. The PET images were reconstructed iteratively using 3-dimensional OpMAP 256 (PET reconstruction protocol [.pPetRcn]; Siemens Healthineers AG) and converted to percentage injected dose per gram of tissue (%ID/g) by delineating the regions of interest. For the biodistribution studies, approximately 1.48 MBq of $^{68}$Ga-FAPI-LM3, $^{68}$Ga-FAPI-46, $^{68}$Ga-DOTA-LM3, or $^{68}$Ga-FAPI-LM3 with unlabeled precursor were injected into tumor-bearing mice (3/group), and different groups of mice were euthanized at the scheduled time points after injection.

### PET/CT Imaging in Healthy Volunteers and Patients with NPC

The clinical study was approved by the institutional review board of the First Affiliated Hospital of Xiamen University and registered at ClinicalTrials.gov (NCT05873777). Written informed consent was obtained from all healthy volunteers and patients. Selection of the voluntary cohort was based on a set of inclusion and exclusion criteria. The inclusion criteria were adults (>18 y) with no known history of chronic disease or cancer. The exclusion criteria were pregnancy or breastfeeding. Each participant received a 3.0–3.7 MBq/kg dose of $^{68}$Ga-FAPI-LM3 on the basis of our prior study related to another heterobivalent agent (*18*). Adverse events were monitored for 4 h after the injection of $^{68}$Ga-FAPI-LM3. The PET/CT scans and reconstruction protocols are presented in the supplemental materials. Doses were calculated using OLINDA/EXM software (version 1.1) (*19*). Six patients underwent paired $^{68}$Ga-FAPI-LM3 and $^{18}$F-FDG PET/CT imaging for comparison, whereas 1 patient underwent paired $^{68}$Ga-FAPI-LM3 and $^{68}$Ga-FAPI-46 PET/CT imaging for comparison. For quantitative analysis, $SUV_{max}$ and $SUV_{mean}$ were used to measure uptake by normal organs and tumor tissues. Delayed $^{68}$Ga-FAPI-LM3 PET/CT scans were obtained at 3 h after injection in 6 patients to analyze the in vivo distribution pattern. For our PET/CT study, the inclusion of a healthy cohort was pivotal in understanding the tracer's normal biodistribution, which helps in distinguishing pathologic from physiologic uptake. Furthermore, we attempted to test both tracers in a single patient to generate head-to-head comparison data, aiding in the direct comparison of their diagnostic efficacies.

### FAP and SSTR2 Immunohistochemistry in NPC

Tissue microarrays of human NPC (HNasN110su01) were purchased from Shanghai Outdo Biotech Co. The Ethics Committee of the Shanghai Outdo Biotech Co. approved the study. Continuous sections of tumor tissue microarrays were used to ensure consistency in verifying different biomarkers in immunohistochemistry experiments. For immunohistochemistry analysis of paraffin-embedded areas, the BenchMark ULTRA (Ventana Medical Systems) automated slide stainer was used to stain cells with the anti-FAP antibody (ab218164; Abcam) or anti-SSTR2 antibody (ZA-0587; ZAGB-BIO) according to the manufacturer's recommendation. The sections were visualized, and images were captured using a Leica microscope. FAP and SSTR2 expression was semiquantitatively evaluated using the H-score method (*20*). Negative expression was defined as an H-score of less than 10.

### Statistical Analysis

All statistical analyses were conducted using SPSS 22.0 software (IBM). Mean values were compared using the Student *t*-test, whereas SUVs derived from $^{18}$F-FDG and $^{68}$Ga-FAPI-LM3 PET/CT were

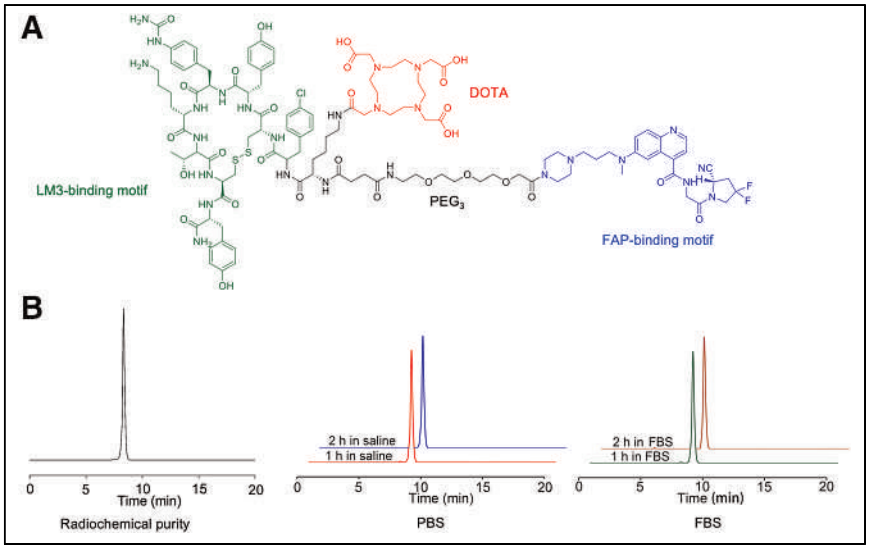


**FIGURE 1.** (A) Chemical structure of FAPI-LM3. (B) Radiochemical purity and stability of $^{68}$Ga-FAPI-LM3 via radio–high-performance liquid chromatography analysis. FBS = fetal bovine serum; PBS = phosphate-buffered saline; $PEG_3$ = polyethylene glycol 3.

compared using the Wilcoxon matched-pairs signed-rank test. Differences were considered statistically significant at a $P$ value of less than 0.05 in a 2-tailed test.

## RESULTS

### Synthesis and Radiolabeling

Polyethylene glycol 3 groups incorporating a heterobivalent of FAPI-46 and LM3 and the chelator DOTA were synthesized (Fig. 1A; Supplemental Fig. 1). Radiolabeling of $^{68}$Ga-FAPI-LM3 was achieved at an activity concentration of approximately 74 MBq/mL (molar activity, 29 GBq/μmol), with over 95% radiochemical purity after purification (Fig. 1B). High-performance liquid chromatography analysis showed that $^{68}$Ga-FAPI-LM3 exhibited high stability for up to 2 h, with no significant demetallation observed in the presence of phosphate-buffered saline and fetal bovine serum (>99%) (Fig. 1B).

### Selective Binging of Heterobivalent Peptide FAPI-LM3 to Human FAP and SSTR2

In the cell uptake study, the heterobivalent peptide $^{68}$Ga-FAPI-LM3 exhibited effective binding to all cell types (Fig. 2). In double-target–positive cells (HT-1080-FAP plus HT-1080-SSTR2), FAP-positive cells (HT-1080-FAP and U87MG), and SSTR2-positive cells (HT-1080-SSTR2 and C666-1), the binding of $^{68}$Ga-FAPI-LM3 to FAP or SSTR2 was significantly blocked by the corresponding unlabeled agent (all $P < 0.05$, shown in Supplemental Table 1), indicating the specificity of targeting both human FAP and SSTR2. Additional cellular uptake studies were conducted using a standard sample (precursor labeled with natural gallium). Blocking experiments with either natural gallium–labeled or unlabeled precursors showed similar trends (Supplemental Fig. 2).

The binding affinities of FAPI-46 and FAPI-LM3 for FAP were evaluated in HT-1080-FAP cells, whereas the SSTR2-binding affinities of DOTA-LM3 and FAPI-LM3 were evaluated in HT-1080-SSTR2 cells. Comparative analysis of half-maximal inhibitory concentrations indicates that FAPI-LM3 has lower FAP (11.72 vs. 4.39 nM) and SSTR2 (13.21 vs. 1.30 nM; Fig. 2B) binding affinities than does its corresponding counterpart.

### Better Tumor Uptake and Retention with Heterobivalent Molecule FAPI-LM3 Than with Corresponding Monomer in Mice

Small-animal PET imaging was performed on a HT-1080-FAP–plus–HT-1080-SSTR2 tumor xenograft model, which is dual-receptor–positive. $^{68}$Ga-FAPI-LM3 rapidly accumulated in FAP and SSTR2 dual-positive tumors at 0.5 h after injection (14.03 ± 0.47 %ID/g) and remained steady until 4 h after injection (2 h, 14.37 ± 0.68 %ID/g; 4 h, 13.77 ± 0.68 %ID/g)

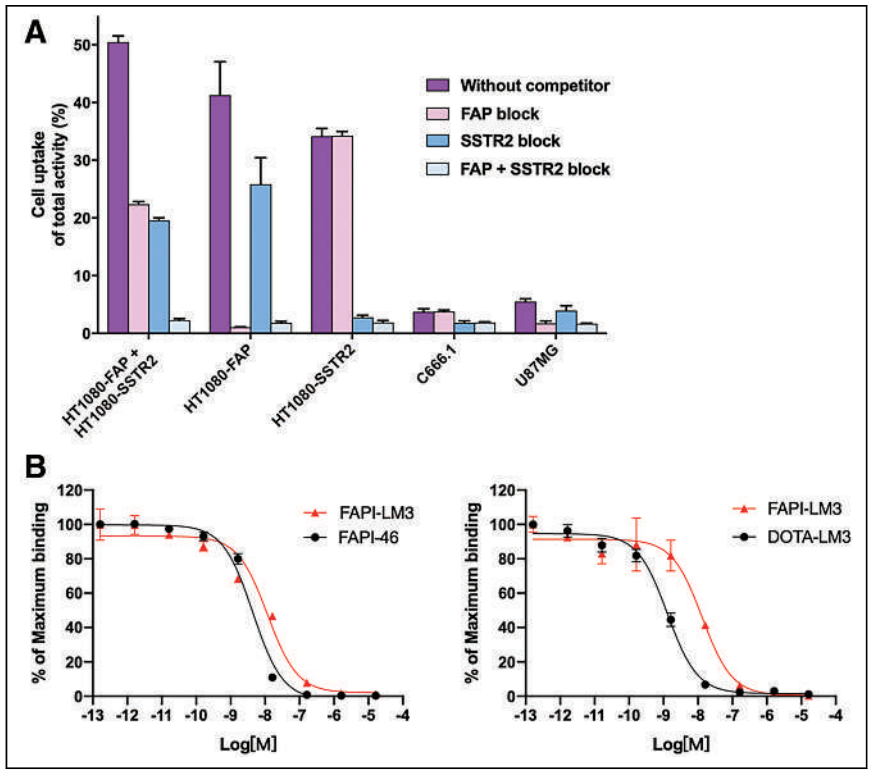


**FIGURE 2.** (A) Cell uptake assay of $^{68}$Ga-FAPI-LM3 and blocking experiments on HT1080-FAP, 1080-SSTR2, HT1080-FAP–plus–1080-SSTR2, C666-1, and U87MG cells. (B) Inhibition of $^{68}$Ga-FAPI-46 binding to FAP on HT1080-FAP cells by unlabeled FAPI-LM3 and unlabeled FAPI-46 ($8.16 \times 10^{-5}$ to $10^{-13}$ M, $n = 3$, left); inhibition of $^{68}$Ga-DOTA-LM3 binding to SSTR2 on HT-1080-SSTR2 cells by unlabeled FAPI-LM3 and unlabeled DOTA-LM3 ($8.16 \times 10^{-5}$ to $10^{-13}$ M, $n = 3$, right).

(Fig. 3). The tumor accumulation of $^{68}$Ga-FAPI-46 remained stable for up to 2 h after injection (5.43 ± 0.91 %ID/g) and then decreased at 4 h after injection (4.33 ± 0.80 %ID/g), whereas tumor uptake of $^{68}$Ga-DOTA-LM3 decreased from 1 to 4 h (5.93 ± 0.50 vs. 4.46 ± 0.57 %ID/g). Quantitative PET data revealed that tumor uptake of $^{68}$Ga-FAPI-LM3 was significantly higher than that of $^{68}$Ga-FAPI-46 and $^{68}$Ga-DOTA-LM3 at all examined time points. Uptake of $^{68}$Ga-FAPI-LM3 in the main organs was relatively low and decreased over time. Therefore, $^{68}$Ga-FAPI-LM3 PET imaging yielded favorable tumor-to-background ratios over time.

The receptor specificity of $^{68}$Ga-FAPI-LM3 was evaluated through several blocking studies, wherein $^{68}$Ga-FAPI-LM3 was administered simultaneously with unlabeled FAPI-46, DOTA-LM3, or FAPI-46 plus DOTA-LM3 (Fig. 4). At 1 h after injection, tumor uptake (14.43 ± 0.67 %ID/g) was mostly suppressed when FAPI-46 and DOTA-LM3 were coadministered with $^{68}$Ga-FAPI-LM3 (1.07% ± 0.06%, 93% blockade). Tumor uptake could be partially blocked by unlabeled FAPI-46 (5.30 ± 1.27 %ID/g, 63% blockade) and DOTA-LM3 (5.43 ± 0.61 %ID/g, 62% blockade).

The ex vivo biodistribution of $^{68}$Ga-FAPI-LM3 was evaluated in HT-1080-FAP–plus–HT-1080-SSTR2 xenografts at different time points, with results similar to those of the PET studies. $^{68}$Ga-FAPI-LM3 accumulated mainly in the tumor tissue and remained stable from 1 to 4 h after injection (14.78 ± 0.76 %ID/g at 1 h; 17.68 ± 2.46 %ID/g at 4 h). Biodistribution studies of $^{68}$Ga-FAPI-46 and $^{68}$Ga-DOTA-LM3 were also performed for comparison (Supplemental Fig. 3). At 1 h after injection, tumor uptake of $^{68}$Ga-FAPI-LM3 was significantly higher than that of $^{68}$Ga-FAPI-46 (14.78 ± 0.76 vs. 8.48 ± 1.75 %ID/g; $P < 0.001$) and $^{68}$Ga-DOTA-LM3 (14.78 ± 0.76 vs. 7.88 ± 1.10 %ID/g; $P < 0.001$). In addition, high $^{68}$Ga-FAPI-LM3 uptake was observed in blood. The blocking data in the biodistribution experiment exhibited the same tendency as those of the PET studies (Fig. 4).

### Safety and Radiation Dosimetry of $^{68}$Ga-FAPI-LM3 in Healthy Volunteers

No adverse events were observed with $^{68}$Ga-FAPI-LM3 in any healthy volunteers or patients during the injection or at the 4-h follow-up. Supplemental Figure 4

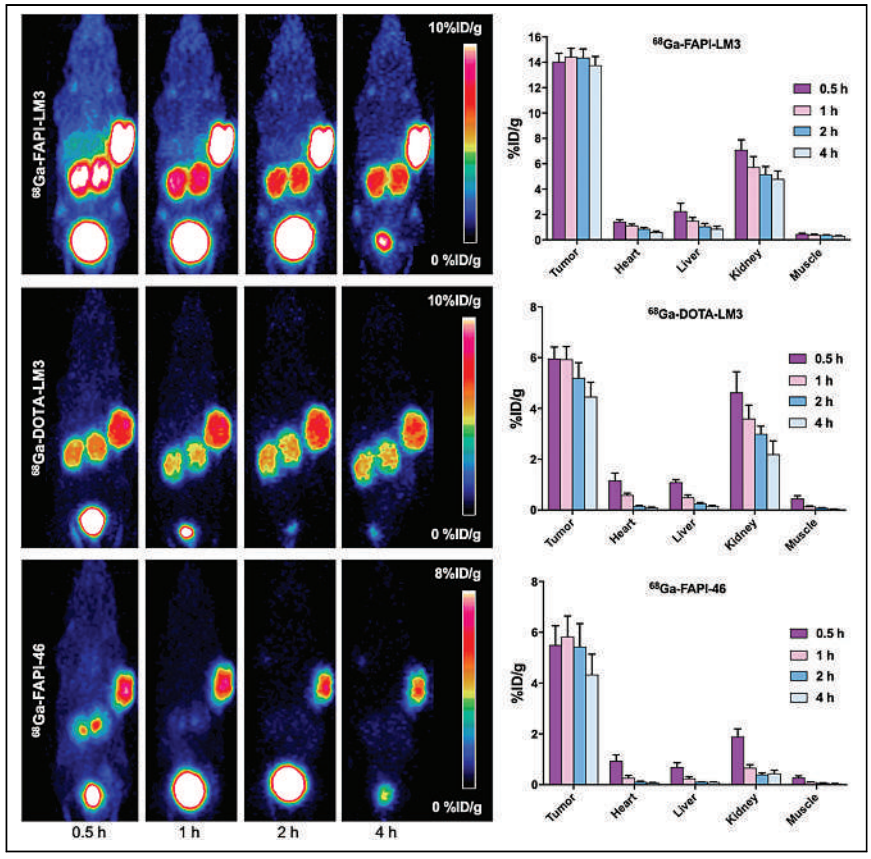


**FIGURE 3.** Representative static PET imaging and quantification results in HT1080-FAP–plus–HT1080-SSTR2 tumor-bearing mice with $^{68}$Ga-FAPI-LM3, $^{68}$Ga-FAPI-46, and $^{68}$Ga-DOTA-LM3.

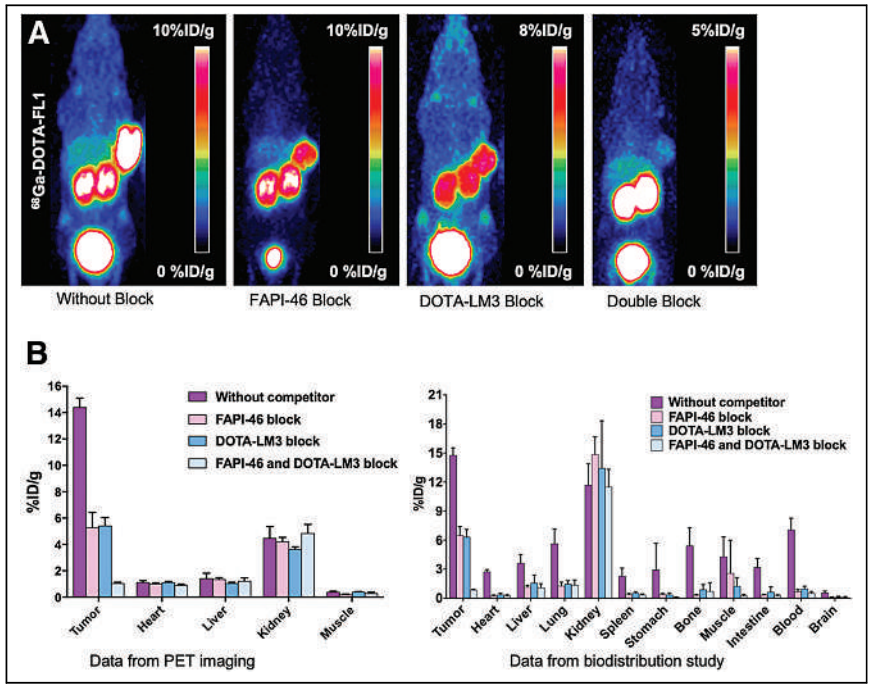


**FIGURE 4.** (A) Representative PET imaging of $^{68}$Ga-FAPI-LM3 and blocking with FAPI-46, DOTA-LM3, or FAPI-46 plus DOTA-LM3 in HT1080-FAP–plus–1080-SSTR2 tumor model. (B) Quantification results of PET imaging and biodistribution studies of $^{68}$Ga-FAPI-LM3 at 1 h with or without simultaneous injection of unlabeled inhibitors after administration.

**TABLE 1**
$^{68}$Ga-FAPI-LM3 Dosimetry Summary of Effective Doses Using OLINDA/EXM

| Target organ | Mean (mSv/MBq) | SD (mSv/MBq) |
|---|---|---|
| Adrenal glands | 5.98E–05 | 2.35E–05 |
| Brain | 1.63E–06 | 4.45E–07 |
| Breasts | 3.47E–05 | 4.15E–06 |
| Gallbladder wall | — | — |
| LLI wall | 4.34E–04 | 1.01E–04 |
| Small intestine | 2.71E–05 | 1.21E–05 |
| Stomach wall | 4.04E–04 | 4.13E–05 |
| ULI wall | 1.53E–05 | 7.73E–06 |
| Heart wall | — | — |
| Kidneys | 1.08E–04 | 3.45E–05 |
| Liver | 1.28E–03 | 3.52E–04 |
| Lungs | 7.68E–04 | 1.91E–04 |
| Muscle | 1.57E–05 | 9.87E–06 |
| Ovaries | 3.66E–04 | 1.87E–05 |
| Pancreas | 1.23E–04 | 5.03E–05 |
| Red marrow | 7.62E–04 | 8.49E–05 |
| Osteogenic cells | 4.22E–05 | 4.00E–06 |
| Skin | 6.29E–06 | 8.34E–07 |
| Spleen | 1.23E–04 | 3.57E–05 |
| Thymus | — | — |
| Thyroid | 3.68E–06 | 1.85E–06 |
| Urinary bladder wall | 2.14E–03 | 9.87E–05 |
| Uterus | 2.19E–04 | 7.60E–05 |
| Effective dose equivalent | 1.20E–03 | 1.03E–03 |
| Effective dose | 1.49E–02 | 2.55E–03 |

LLI = lower large intestine; ULI = upper large intestine.

displays representative PET maximum-intensity projection images of a healthy volunteer and biodistribution data on 3 volunteers' normal organs.

According to the results from OLINDA/EXM, the effective dose of $^{68}$Ga-FAPI-LM3 was determined to be $1.49 \times 10^{-2}$ mSv/MBq (Table 1), which was comparable to that of $^{68}$Ga-FAPI-46 ($1.80 \times 10^{-2}$ mSv/MBq) (*21*) but lower than that of $^{68}$Ga-DOTA-LM3 ($2.50 \times 10^{-2}$ mSv/MBq) (*15*).

### $^{68}$Ga-FAPI-LM3 PET/CT Imaging in Patients with NPC

In this study, 6 patients were enrolled for initial staging (4 patients) or relapsed detection (2 patients), and their detailed clinical information is provided in Supplemental Table 2. $^{68}$Ga-FAPI-LM3 and $^{18}$F-FDG PET/CT imaging was conducted with a median interval of 3 d (range, 1–7 d). $^{68}$Ga-FAPI-LM3 exhibited durable retention in all lesions up to 3 h after injection. When tumor uptake was compared between the 2 time points, $SUV_{max}$ at the delayed time point (3 h) was significantly higher than that at the routine time point (1 h) for regional lymph node (11.4 vs. 10.1; $P = 0.031$), liver (16.5 vs. 14.3; $P = 0.046$), bone (11.2 vs. 10.4; $P = 0.003$), and distant lymph node (16.9 vs. 14.5; $P = 0.028$) metastases. However, there was no statistical difference in $SUV_{max}$ between 3 and 1 h for primary tumors (Supplemental Table 3).

In the paired $^{68}$Ga-FAPI-LM3 and $^{18}$F-FDG PET/CT scans, 5 primary tumors, 34 metastatic lymph nodes, and 37 bone or visceral metastatic lesions were evaluated. The $SUV_{max}$ derived from $^{68}$Ga-FAPI-LM3 PET/CT was significantly higher than that derived from $^{18}$F-FDG in the primary tumors (13.8 vs. 9.3, $P = 0.043$), regional lymph node metastases (11.4 vs. 6.6, $P < 0.001$), and distant metastases (14.6 vs. 5.6, $P < 0.001$) (Table 2). Specifically, the $SUV_{max}$ obtained from $^{68}$Ga-FAPI-LM3 PET/CT was approximately 2–4 times greater than that from $^{18}$F-FDG PET/CT in liver (16.5 vs. 3.7, $P = 0.028$) and bone (11.2 vs. 4.6, $P = 0.001$) metastases. As a result, $^{18}$F-FDG missed several metastatic lesions, including regional lymph node ($n = 3$), liver ($n = 4$), bone ($n = 1$), peritoneal ($n = 2$), and retroperitoneal lymph node ($n = 1$) metastases. Interestingly, these $^{18}$F-FDG–negative lesions could be visualized by $^{68}$Ga-FAPI-LM3 PET/CT. Representative images from $^{18}$F-FDG and $^{68}$Ga-FAPI-LM3 PET/CT are shown in Figure 5A and Supplemental Figure 5. Additionally, 1 patient underwent paired $^{68}$Ga-FAPI-LM3 and $^{68}$Ga-FAPI-46 PET/CT for comparison. $^{68}$Ga-FAPI-LM3 PET/CT showed more lesions than $^{68}$Ga-FAPI-46 for lymph node, liver, and bone metastases, with higher uptake (Fig. 5B; Supplemental Fig. 6).

### FAP and SSTR2 Expression in Tissue Microarrays of NPC

We excluded 1 human NPC sample because of inadequate tumor cells. The tissue microarrays were positive for FAP or SSTR2 expression (H-score, ≥10) in most NPC samples. Remarkably, more than 77.98% of these NPC samples exhibited positivity for both markers. However, in 19.26% of the cases, discordant expression of FAP and SSTR2 was observed. This included 13.76% of cases that were FAP-negative but SSTR2-positive and 5.50% of cases that were FAP-positive but SSTR2-negative (Fig. 6).

## DISCUSSION

FAP is expressed in a wide range of tumor types, making it a promising target for cancer imaging and radionuclide therapy in recent years (*4*,*5*). Apart from neuroendocrine tumors, most other cancers, such as NPC, thyroid cancer, and breast cancer, express SSTR2 (*9*,*14*,*22*,*23*). Both proteins are located on the cell surface, reinforcing their potential as theranostic targets. This study focused on synthesis, preclinical evaluation, and pilot PET imaging of $^{68}$Ga-FAPI-LM3, a heterobivalent tracer designed to target both FAP and SSTR2. Our results demonstrated that this tracer exhibits a favorable safety profile and diagnostic utility in preclinical and clinical trials.

To be a good dual-targeting tracer, each binding motif of the heterobivalent molecule must retain its biologic activity. In the receptor-binding assay, the FAPI-LM3 yielded high half-maximal inhibitory concentrations for both proteins, indicating its ability to target both FAP and SSTR2 receptors. In the cell uptake and blocking assays, $^{68}$Ga-FAPI-LM3 showed strong binding to FAP and SSTR2. Additionally, the varied tumor internalization rates of the different compounds may influence their tumor uptake patterns (*24*), which necessitates further validation and warrants exploration in subsequent studies. In this study, unlabeled FAPI and DOTA-LM3 successfully blocked the binding of $^{68}$Ga-FAPI-LM3 to FAP and SSTR2, respectively. This result further supports the dual functionality of our tracer in specifically targeting both proteins.

**TABLE 2**
Comparison of $SUV_{max}$ on $^{68}$Ga-FAPI-LM3 and $^{18}$F-FDG PET/CT Images in Primary and Metastatic Tumors

| Tumor | *n* | Median size (cm) | $^{68}$Ga-FAPI-LM3 PET/CT | | $^{18}$F-FDG PET/CT | | *P* for median $SUV_{max}$* |
|---|---|---|---|---|---|---|---|
| | | | Positive tumors (*n*) | Median $SUV_{max}$ | Positive tumors (*n*) | Median $SUV_{max}$ | |
| Primary | 5 | NA | 5 | 13.8 (10.0–21.1) | 5 | 9.3 (6.6–18.4) | 0.043 |
| Regional LN mets | 34 | 1.4 (0.8–3.1) | 34 | 11.4 (4.5–19.0) | 31 | 6.6 (2.1–16.0) | <0.001 |
| Liver mets | 6 | 1.7 (1.3–4.0) | 6 | 16.5 (8.6–26.3) | 2 | 3.7 (3.1–10.8) | 0.028 |
| Bone mets | 15 | 1.2 (0.8–2.2) | 15 | 11.2 (7.4–18.0) | 14 | 4.6 (2.0–8.2) | 0.001 |
| Pleural mets | 5 | 2.3 (1.1–4.0) | 5 | 17.3 (14.6–21.1) | 5 | 7.2 (3.7–12.0) | 0.043 |
| Peritoneal mets | 4 | 0.9 (0.7–3.2) | 4 | 13.1 (7.0–18.7) | 2 | 3.4 (1.5–8.6) | 0.068 |
| Distant LN mets | 7 | 2.3 (0.9–4.1) | 7 | 16.9 (10.8–22.5) | 6 | 8.2 (2.0–9.0) | 0.018 |
| Total† | 37 | 1.4 (0.7–4.1) | 37 | 14.6 (7.0–26.3) | 29 | 5.6 (1.5–12.0) | <0.001 |

*$^{68}$Ga-FAPI-LM3 vs. $^{18}$F-FDG.
†Included liver (*n* = 6), bone (*n* = 15), pleura (*n* = 5), peritoneum (*n* = 4), and distant (*n* = 7) lymph node metastases.
NA = not applicable (lesion size cannot be calculated because of diffuse type of peritoneal metastasis [irregular shape]); LN = lymph node; mets = metastases.
Data in parentheses are ranges.

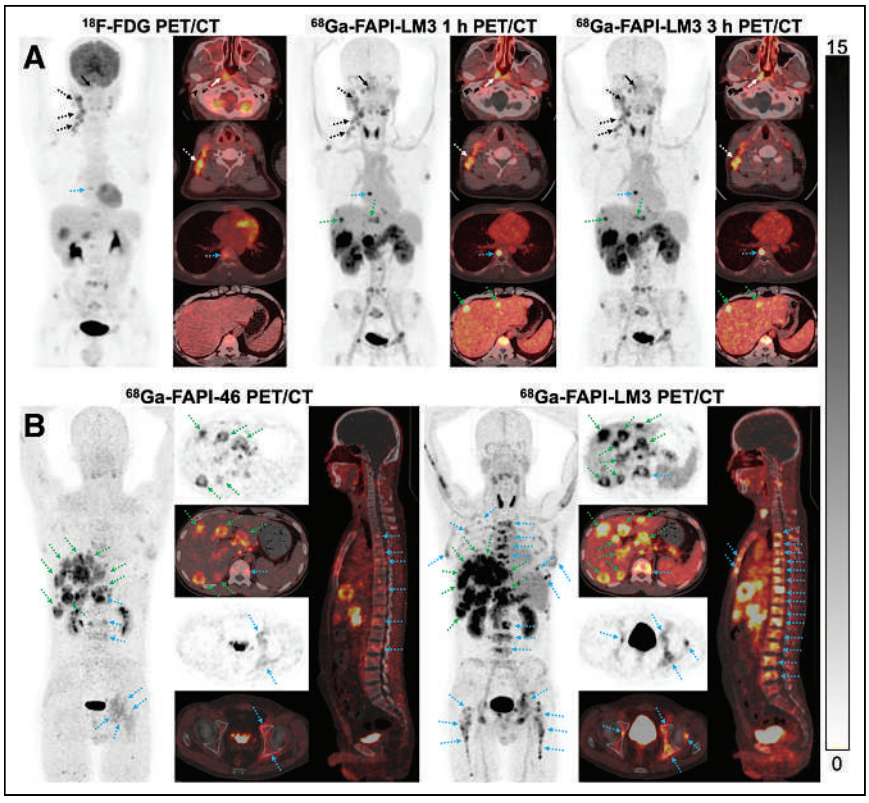


**FIGURE 5.** (A) PET/CT imaging findings in 32-y-old treatment-naïve patient with NPC. Both $^{18}$F-FDG and $^{68}$Ga-FAPI-LM3 PET/CT showed abnormal activity in primary tumor (solid white arrows), regional lymph node (dotted white arrows), and bone (dotted blue arrows). Additional liver metastases with intense activity (dotted green arrows) were observed on $^{68}$Ga-FAPI-LM3 PET/CT. However, these lesions were not visualized on $^{18}$F-FDG PET/CT. (B) PET/CT imaging findings in 44-y-old patient with metastatic NPC. $^{68}$Ga-FAPI-LM3 PET/CT revealed more lesions than did $^{68}$Ga-FAPI-46 for lymph node, liver (dotted green arrows), and bone (dotted blue arrows) metastases, with higher uptake.

In vivo experiments were conducted using small-animal PET to evaluate the performance of $^{68}$Ga-FAPI-LM3 in HT-1080-FAP–plus–HT-1080-SSTR2 double-positive tumor xenografts. Tumor uptake of $^{68}$Ga-FAPI-LM3 was significantly higher than that of $^{68}$Ga-FAPI and $^{68}$Ga-DOTA-LM3. This enhanced uptake could be attributed to an increased binding resulting from the dual-receptor targeting.

The preclinical findings suggest that the dual-receptor specificity of $^{68}$Ga-FAPI-LM3 allows for detecting tumors with either FAP or SSTR2 expression patterns, offering a potentially valuable tool in the diagnosis of NPC. In our preliminary clinical PET study with $^{68}$Ga-FAPI-LM3, it exhibited intense physiologic uptake in the blood, thyroid, pancreas, liver, kidney, and spleen. The existence of a soluble FAP form in plasma may explain the slow blood clearance in our preclinical and clinical data (*25*,*26*). Moreover, we speculate that the slow blood clearance may also be explained by the change in structure (from a monovalent to a divalent ligand) and the increase in molecular weight, which might affect the polarity of FAP/SSTR2-binding molecules (leading to increased lipophilicity). As for the high uptake in the thyroid and pancreas, similar findings were reported with $^{68}$Ga-labeled FAPI dimer (*27*,*28*). The reason for the increased

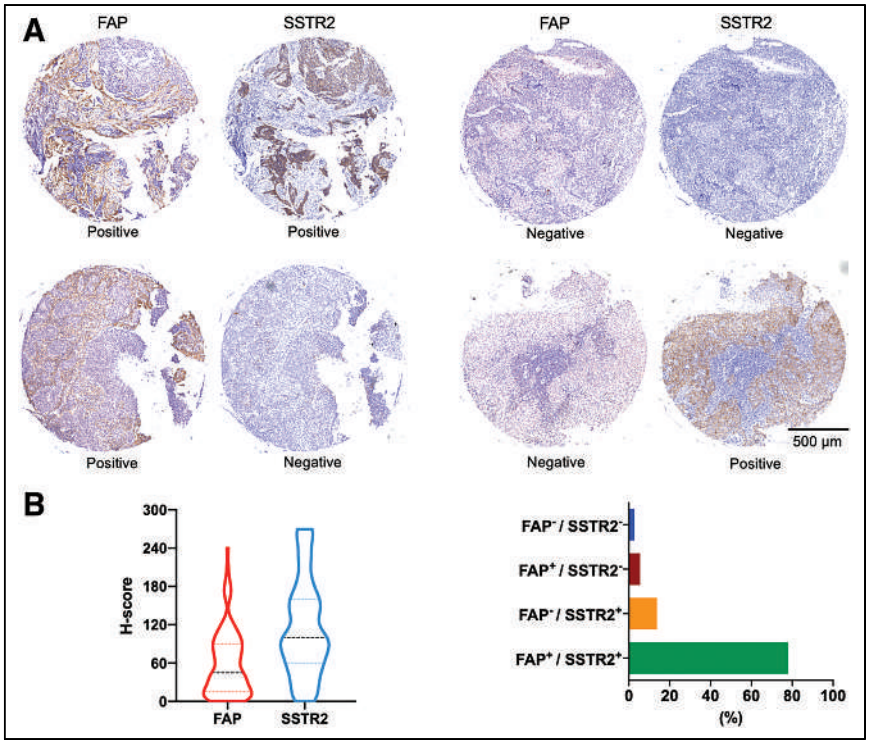


**FIGURE 6.** (A) Representative imaging of paired immunohistochemical staining of 110 human NPC specimens using anti-FAP and anti-SSTR2 antibodies. (B) Proportion of different H-score levels for FAP and SSTR2 expression.

physiologic uptake in these normal organs is still unclear. However, it should be noted that after covalent conjugation, the heterobivalent molecule is a new compound, which would show different in vivo pharmacokinetics from the monomers. Thus, it is not surprising that within normal organs and tissues, FAPI-LM3 showed distribution patterns different from either FAPI or LM3 alone.

Additionally, the uptake of $^{68}$Ga-FAPI-LM3 in most tumor lesions demonstrated an trend to increase from 1 to 3 h after injection. Therefore, delayed $^{68}$Ga-FAPI-LM3 PET/CT imaging could offer optimal lesion contrast. When $^{68}$Ga-FAPI-LM3 was compared with $^{18}$F-FDG, the standard-of-care PET tracer in oncology, we observed significantly higher uptake with $^{68}$Ga-FAPI-LM3 than with $^{18}$F-FDG in primary tumors, regional lymph node metastases, and distant metastases. As a result, $^{68}$Ga-FAPI-LM3 showed superiority over $^{18}$F-FDG in diagnosing NPC, especially in detecting lymph node, liver, bone, and peritoneal metastases. Interestingly, $^{68}$Ga-FAPI-LM3 also showed superiority over $^{68}$Ga-FAPI-46 in detecting liver and bone metastases in 1 patient with metastatic NPC.

FAP was expressed mainly on cancer-associated fibroblasts within the tumor stroma, whereas SSTR2 was expressed predominantly on tumor cells. It is also unlikely that there is dual binding because of the distance between the 2 targets: tumor cell and tumor microenvironment. There is no indication that the bivalent tracer binds simultaneously to both targets. The primary advantage of this heterobivalent molecule over its counterparts is the multivalency effect, resulting in improved tumor uptake and an increased number of effective receptors. For instance, recent research on bispecific antibodies such as PD-1/CTLA4 and PD-L1/CTLA-4 has demonstrated their potential in enhancing the effectiveness of immunotherapy (*29*,*30*). Our previous work demonstrated improved tumor uptake and retention in clinical PET studies using the heterobivalent FAPI-Arg-Gly-Asp (*31*). A similar strategy with heterobivalent FAPI–prostate-specific membrane antigen showed significant tumor uptake enhancement (*32*). In the present study, we focused on 2 promising oncologic receptors, FAP and SSTR2, which are highly expressed in most NPCs (*9*–*11*,*33*). The PET and biodistribution data obtained for $^{68}$Ga-FAPI-LM3 indicated that tumor uptake and retention were significantly improved when both targets were positively expressed in preclinical models. Compared with the monomer, which rapidly washes out from tumors, the bivalent monocular exhibits a lower dissociation rate.

The heterobivalent FAPI-LM3 comprises 2 motifs that target 2 distinct types of receptors and are covalently linked. Even if the primary motif of the heterobivalent agent detaches from the target, the secondary binding motif can still attach to the corresponding target within the tumor (*34*). From the perspective of clinical investigations, the main objective of the divalent molecule FAPI-LM3 was to provide a better detection rate for primary lesions and metastases of NPC instead of knowledge of FAP and SSTR2 receptor level. From this point of view, the study was successful because FAPI-LM3 PET is better than FAPI-46 PET in lesion detection. Therefore, well-designed prospective trials are needed to further investigate the diagnostic accuracy of $^{68}$Ga-FAPI-LM3 in primary and metastatic NPC. Additionally, the improved tumor uptake and prolonged tumor retention of FAPI-LM3 make it a suitable candidate for theranostic applications after labeling with β- or α-emitting radioisotopes for endoradiotherapy.

The dynamic nature of the tumor microenvironment and interlesion heterogeneity can, however, result in low or no expression for a specific receptor. As shown in this study using tissue microarray samples, discordant expression of FAP and SSTR2 was observed in 19.26% of NPC samples, with 13.76% of the samples being FAP-negative but SSTR2-positive and 5.50% being FAP-positive but SSTR2-negative. Under these circumstances, the heterobivalent FAPI-LM3 is superior to its monomeric counterpart for imaging of NPC. However, this superiority requires further validation through clinical data in a direct comparison of $^{68}$Ga-FAPI-LM3 with $^{68}$Ga-FAPI/$^{68}$Ga-DOTA-LM3 PET/CT.

This study had some limitations. First, the preclinical tumor model involved transfected cell lines with extremely high FAP/SSTR2 expression. Second, the clinical study included a limited number of patients, which restricted the statistical power needed to calculate the diagnostic accuracy of $^{68}$Ga-FAPI-LM3 precisely. Additionally, our study lacked direct comparisons between $^{68}$Ga-FAPI-LM3, $^{68}$Ga-FAPI, and $^{68}$Ga-DOTA-LM3. Further investigations involving larger patient cohorts are required.

## CONCLUSION

This study demonstrated the feasibility and efficacy of $^{68}$Ga-FAPI-LM3, a divalent molecule for PET imaging of FAP and SSTR2,

emphasizing its clinical utility for tumor detection and staging in patients with NPC. The findings contribute to understanding of dual-receptor targeting and suggest future directions for more extensive clinical studies and comparisons with other tracers.

## DISCLOSURE

This work was funded by the National Natural Science Foundation of China (82071961, 82272037), Fujian Research and Training Grants for Young and Middle-Aged Leaders in Healthcare, the Key Scientific Research Program for Young Scholars in Fujian (2021ZQNZD016), the Fujian Natural Science Foundation for Distinguished Young Scholars (2022D005), the Natural Science Foundation of Fujian Province (grant 2020J011220), Key Medical and Health Projects in Xiamen (grant 3502Z20209002), the Xiamen Key Laboratory of Radiation Oncology, the Xiamen Clinical Research Center for Head and Neck Cancer, and the 2021 National Clinical Key Specialty Grant (oncology, grant 3210013). Liang Zhao was partially funded by the China Scholarship Council (CSC). No other potential conflict of interest relevant to this article was reported.

**KEY POINTS**

**QUESTION:** Does a heterobivalent molecule that recognizes both FAP and SSTR2 demonstrate improved efficacy in tumor-targeting and in vivo pharmacokinetics compared with those of its corresponding monomers?

**PERTINENT FINDINGS:** $^{68}$Ga-FAPI-LM3 showed FAP- and LM3-binding affinity both in vitro and in vivo. This study further revealed significantly higher tumor uptake of $^{68}$Ga-FAPI-LM3 than of $^{18}$F-FDG in patients with NPC.

**IMPLICATIONS FOR PATIENT CARE:** The dual-receptor–targeting property of $^{68}$Ga-FAPI-LM3 results in improved tumor uptake and retention compared with those of its monomeric counterparts, enabling PET imaging of tumors expressing either one or both receptor types.

## REFERENCES

1. Ho WJ, Jaffee EM, Zheng L. The tumour microenvironment in pancreatic cancer: clinical challenges and opportunities. *Nat Rev Clin Oncol.* 2020;17:527–540.
2. Lee PJ, Sui YH, Liu TT, et al. Epstein-Barr viral product-containing exosomes promote fibrosis and nasopharyngeal carcinoma progression through activation of YAP1/FAPalpha signaling in fibroblasts. *J Exp Clin Cancer Res.* 2022;41:254.
3. Huang W, Zhang L, Yang M, et al. Cancer-associated fibroblasts promote the survival of irradiated nasopharyngeal carcinoma cells via the NF-kappaB pathway. *J Exp Clin Cancer Res.* 2021;40:87.
4. Zhao L, Chen J, Pang Y, et al. Fibroblast activation protein-based theranostics in cancer research: a state-of-the-art review. *Theranostics.* 2022;12:1557–1569.
5. Hirmas N, Hamacher R, Sraieb M, et al. Fibroblast-activation protein PET and histopathology in a single-center database of 324 patients and 21 tumor entities. *J Nucl Med.* 2023;64:711–716.
6. Backhaus P, Gierse F, Burg MC, et al. Translational imaging of the fibroblast activation protein (FAP) using the new ligand [$^{68}$Ga]Ga-OncoFAP-DOTAGA. *Eur J Nucl Med Mol Imaging.* 2022;49:1822–1832.
7. Herrmann K, Schwaiger M, Lewis JS, et al. Radiotheranostics: a roadmap for future development. *Lancet Oncol.* 2020;21:e146–e156.
8. Kratochwil C, Flechsig P, Lindner T, et al. $^{68}$Ga-FAPI PET/CT: tracer uptake in 28 different kinds of cancer. *J Nucl Med.* 2019;60:801–805.
9. Lechner M, Schartinger VH, Steele CD, et al. Somatostatin receptor 2 expression in nasopharyngeal cancer is induced by Epstein Barr virus infection: impact on prognosis, imaging and therapy. *Nat Commun.* 2021;12:117.
10. Zhao L, Pang Y, Zheng H, et al. Clinical utility of [$^{68}$Ga]Ga-labeled fibroblast activation protein inhibitor (FAPI) positron emission tomography/computed tomography for primary staging and recurrence detection in nasopharyngeal carcinoma. *Eur J Nucl Med Mol Imaging.* 2021;48:3606–3617.
11. Zhao L, Pang Y, Wang Y, et al. Somatostatin receptor imaging with [$^{68}$Ga]Ga-DOTATATE positron emission tomography/computed tomography (PET/CT) in patients with nasopharyngeal carcinoma. *Eur J Nucl Med Mol Imaging.* 2022;49:1360–1373.
12. Waldmann CM, Stuparu AD, van Dam RM, Slavik R. The search for an alternative to [$^{68}$Ga]Ga-DOTA-TATE in neuroendocrine tumor theranostics: current state of $^{18}$F-labeled somatostatin analog development. *Theranostics.* 2019;9:1336–1347.
13. Conry BG, Papathanasiou ND, Prakash V, et al. Comparison of $^{68}$Ga-DOTATATE and $^{18}$F-fluorodeoxyglucose PET/CT in the detection of recurrent medullary thyroid carcinoma. *Eur J Nucl Med Mol Imaging.* 2010;37:49–57.
14. Dalm SU, Haeck J, Doeswijk GN, de Blois E, de Jong M, van Deurzen CHM. SSTR-mediated imaging in breast cancer: is there a role for radiolabeled somatostatin receptor antagonists? *J Nucl Med.* 2017;58:1609–1614.
15. Zhu W, Cheng Y, Jia R, et al. A prospective, randomized, double-blind study to evaluate the safety, biodistribution, and dosimetry of $^{68}$Ga-NODAGA-LM3 and $^{68}$Ga-DOTA-LM3 in patients with well-differentiated neuroendocrine tumors. *J Nucl Med.* 2021;62:1398–1405.
16. Breckpot K, Aerts JL, Thielemans K. Lentiviral vectors for cancer immunotherapy: transforming infectious particles into therapeutics. *Gene Ther.* 2007;14:847–862.
17. Zhao L, Chen J, Pang Y, et al. Development of fibroblast activation protein inhibitor-based dimeric radiotracers with improved tumor retention and antitumor efficacy. *Mol Pharm.* 2022;19:3640–3651.
18. Zhao L, Wen X, Xu W, et al. Clinical evaluation of $^{68}$Ga-FAPI-RGD for imaging of fibroblast activation protein and integrin $\alpha_v\beta_3$ in various cancer types. *J Nucl Med.* 2023;64:1210–1217.
19. Stabin MG, Sparks RB, Crowe E. OLINDA/EXM: the second-generation personal computer software for internal dose assessment in nuclear medicine. *J Nucl Med.* 2005;46:1023–1027.
20. Mazières J, Brugger W, Cappuzzo F, et al. Evaluation of EGFR protein expression by immunohistochemistry using H-score and the magnification rule: re-analysis of the SATURN study. *Lung Cancer.* 2013;82:231–237.
21. Giesel FL, Kratochwil C, Lindner T, et al.$^{68}$Ga-FAPI PET/CT: biodistribution and preliminary dosimetry estimate of 2 DOTA-containing FAP-targeting agents in patients with various cancers. *J Nucl Med.* 2019;60:386–392.
22. Fonti R, Panico M, Pellegrino S, et al. Heterogeneity of SSTR2 expression assessed by $^{68}$Ga-DOTATOC PET/CT using coefficient of variation in patients with neuroendocrine tumors. *J Nucl Med.* 2022;63:1509–1514.
23. Carmona Matos DM, Jang S, Hijaz B, et al. Characterization of somatostatin receptors (SSTRs) expression and antiproliferative effect of somatostatin analogues in aggressive thyroid cancers. *Surgery.* 2019;165:64–68.
24. Sancey L, Garanger E, Foillard S, et al. Clustering and internalization of integrin alphavbeta3 with a tetrameric RGD-synthetic peptide. *Mol Ther.* 2009;17:837–843.
25. Escudero-Castellanos A, Kurth J, Imlimthan S, et al. Translational assessment of a DATA-functionalized FAP inhibitor with facile $^{68}$Ga-labeling at room temperature. *Eur J Nucl Med Mol Imaging.* 2023;50:3202–3213.
26. Lee KN, Jackson KW, Christiansen VJ, Lee CS, Chun JG, McKee PA. Antiplasmin-cleaving enzyme is a soluble form of fibroblast activation protein. *Blood.* 2006;107:1397–1404.
27. Moon ES, Ballal S, Yadav MP, et al. Fibroblast activation protein (FAP) targeting homodimeric FAP inhibitor radiotheranostics: a step to improve tumor uptake and retention time. *Am J Nucl Med Mol Imaging.* 2021;11:476–491.
28. Zhao L, Niu B, Fang J, et al. Synthesis, preclinical evaluation, and a pilot clinical PET imaging study of $^{68}$Ga-labeled FAPI dimer. *J Nucl Med.* 2022;63:862–868.
29. Burton EM, Tawbi HA. Bispecific antibodies to PD-1 and CTLA4: doubling down on T cells to decouple efficacy from toxicity. *Cancer Discov.* 2021;11:1008–1010.
30. Jiang C, Zhang L, Xu X, et al. Engineering a smart agent for enhanced immunotherapy effect by simultaneously blocking PD-L1 and CTLA-4. *Adv Sci (Weinh).* 2021;8:e2102500.
31. Zhao L, Wen X, Xu W, et al. Clinical evaluation of $^{68}$Ga-FAPI-RGD for imaging of fibroblast activation protein and integrin $\alpha_v\beta_3$ in various cancer types. *J Nucl Med.* 2023;64:1210–1217.
32. Boinapally S, Lisok A, Lofland G, et al. Hetero-bivalent agents targeting FAP and PSMA. *Eur J Nucl Med Mol Imaging.* 2022;49:4369–4381.
33. Qin C, Liu F, Huang J, et al. A head-to-head comparison of $^{68}$Ga-DOTA-FAPI-04 and $^{18}$F-FDG PET/MR in patients with nasopharyngeal carcinoma: a prospective study. *Eur J Nucl Med Mol Imaging.* 2021;48:3228–3237.
34. Chittasupho C. Multivalent ligand: design principle for targeted therapeutic delivery approach. *Ther Deliv.* 2012;3:1171–1187.

# Effectiveness of $^{225}$Ac-Labeled Anti-EGFR Radioimmunoconjugate in EGFR-Positive Kirsten Rat Sarcoma Viral Oncogene and BRAF Mutant Colorectal Cancer Models

Anjong Florence Tikum[1], Jessica P. Ketchemen[1], Alireza Doroudi[1], Anand K. Nambisan[1], Hanan Babeker[1,2], Fabrice Ngoh Njotu[1], and Humphrey Fonge[1,3]

[1]*Department of Medical Imaging, College of Medicine, University of Saskatchewan, Saskatoon, Saskatchewan, Canada;* [2]*Department of Pathology and Laboratory Medicine, College of Medicine, University of Saskatchewan, Saskatoon, Saskatchewan, Canada; and* [3]*Department of Medical Imaging, Royal University Hospital Saskatoon, Saskatoon, Saskatchewan, Canada*

Eighty percent of colorectal cancers (CRCs) overexpress epidermal growth factor receptor (EGFR). Kirsten rat sarcoma viral oncogene (KRAS) mutations are present in 40% of CRCs and drive de novo resistance to anti-EGFR drugs. BRAF oncogene is mutated in 7%–10% of CRCs, with even worse prognosis. We have evaluated the effectiveness of [$^{225}$Ac]Ac-macropa-nimotuzumab in KRAS mutant and in KRAS wild-type and BRAF$^{V600E}$ mutant EGFR-positive CRC cells in vitro and in vivo. Anti-CD20 [$^{225}$Ac]Ac-macropa-rituximab was developed and used as a nonspecific radioimmunoconjugate. **Methods:** Anti-EGFR antibody nimotuzumab was radiolabeled with $^{225}$Ac via an 18-membered macrocyclic chelator *p*-SCN-macropa. The immunoconjugate was characterized using flow cytometry, radioligand binding assay, and high-performance liquid chromatography, and internalization was studied using live-cell imaging. In vitro cytotoxicity was evaluated in 2-dimensional monolayer EGFR-positive KRAS mutant DLD-1, SW620, and SNU-C2B; in KRAS wild-type and BRAF$^{V600E}$ mutant HT-29 CRC cell lines; and in 3-dimensional spheroids. Dosimetry was studied in healthy mice. The in vivo efficacy of [$^{225}$Ac]Ac-macropa-nimotuzumab was evaluated in mice bearing DLD-1, SW620, and HT-29 xenografts after treatment with 3 doses of 13 kBq/dose administered 10 d apart. **Results:** In all cell lines, in vitro studies showed enhanced cytotoxicity of [$^{225}$Ac]Ac-macropa-nimotuzumab compared with nimotuzumab and controls. The inhibitory concentration of 50% in the DLD-1 cell line was 1.8 nM for [$^{225}$Ac]Ac-macropa-nimotuzumab versus 84.1 nM for nimotuzumab. Similarly, the inhibitory concentration of 50% was up to 79-fold lower for [$^{225}$Ac]Ac-macropa-nimotuzumab than for nimotuzumab in KRAS mutant SNU-C2B and SW620 and in KRAS wild-type and BRAF$^{V600E}$ mutant HT-29 CRC cell lines. A similar trend was observed for 3-dimensional spheroids. Internalization peaked 24–48 h after incubation and depended on EGFR expression. In the [$^{225}$Ac]Ac-macropa-nimotuzumab group, 3 of 7 mice bearing DLD-1 tumors had complete remission. Median survival was 40 and 34 d for mice treated with phosphate-buffered saline and [$^{225}$Ac]Ac-macropa-rituximab (control), respectively, whereas it was not reached for the [$^{225}$Ac]Ac-macropa-nimotuzumab group (>90 d). Similarly, median survival of mice bearing HT-29 xenografts was 16 and 12.5 d for those treated with [$^{225}$Ac]Ac-macropa-rituximab and phosphate-buffered saline, respectively, and was not reached for those treated with [$^{225}$Ac]Ac-macropa-nimotuzumab (>90 d). One of 7 mice bearing HT-29 xenografts and treated using [$^{225}$Ac]Ac-macropa-nimotuzumab had complete remission. Compared with untreated mice, [$^{225}$Ac]Ac-macropa-nimotuzumab more than doubled (16 vs. 41 d) the median survival of mice bearing SW620 xenografts. **Conclusion:** [$^{225}$Ac]Ac-macropa-nimotuzumab is effective against KRAS mutant and BRAF$^{V600E}$ mutant CRC models.

**Key Words:** radiopharmaceuticals; alpha particle; BRAFV600E mutation; colorectal cancer; EGFR; KRAS mutation

**J Nucl Med 2024; 65:402–408**
DOI: 10.2967/jnumed.123.266204

Overexpression of epidermal growth factor receptor (EGFR) I is associated with most aggressive cancers of epithelial origin, particularly in 80%–85% of colorectal cancers (CRCs) (*1*). Mutations in EGFR, such as Kirsten rat sarcoma viral oncogene (KRAS), lead to constitutive overactivation of the receptor and hence resistance to anti-EGFR treatments. KRAS is an intracellular effector molecule that routes ligand-bound EGFR to the nucleus, where it stimulates proliferation (*2–4*). B-rapidly accelerated fibrosarcoma murine sarcoma viral oncogene homolog B (BRAF) is a serine–threonine protein kinase that causes enhanced proliferation in EGFR-positive CRC cells (*5,6*). BRAF$^{V600E}$ is the most common BRAF mutation in EGFR-positive CRC cells (*5,6*).

Metastatic CRC (mCRC) is the second leading cause of death from cancer, with a 5-y survival rate of less than 10% (stage IV) (*7*), likely because more than 45% of CRC patients have metastatic disease at initial diagnosis. Surgery, which is a primary treatment option, is contraindicated in patients with advanced disease, and even when it is possible, the local recurrence rate is high (38%–88%) (*8*). In EGFR-positive mCRC patients with KRAS wild-type mutation, the addition of anti-EGFR antibodies (e.g., cetuximab) to chemotherapy results in small—albeit significant—improvements in survival, but there is no benefit in patients with KRAS and BRAF mutations (*9*). Mutations in KRAS occur in up to 40% of CRCs, whereas BRAF mutations are present in 7%–10% of CRCs (*5*). The concurrent presence of KRAS and BRAF$^{V600E}$ mutations has not been observed in the same patient (*10*). However, BRAF$^{V600E}$ and other BRAF mutations occur in patients with KRAS wild-type cancers and have been associated with even worse

Received Jun. 28, 2023; revision accepted Jan. 5, 2024.
For correspondence or reprints, contact Humphrey Fonge (humphrey.fonge@usask.ca).
Published online Feb. 15, 2024.

prognosis in CRCs (*11*). EGFR-positive mCRCs (especially those with KRAS and BRAF mutations) represent an unmet clinical need.

Anti-EGFR antibodies—for example, cetuximab, panitumumab, and nimotuzumab—are used to treat EGFR-positive cancers, including CRC. With the exception of nimotuzumab, anti-EGFR antibodies have been associated with significant cutaneous toxicity in 45%–100% of patients (*12*). In contrast, nimotuzumab is better tolerated and has low skin toxicities, because its affinity-optimized binding characteristics ensure low transient binding to low EGFR–expressing healthy tissues, such as the skin and intestinal mucosa.

High linear energy transfer makes α-emitting radionuclides the ideal isotopes for targeted radiopharmaceutical therapy of metastatic disease. α-emitters such as $^{213}$Bi- and $^{225}$Ac-labeled agents have shown promising results in preclinical and clinical studies in ovarian cancer, neuroendocrine tumors, breast cancer, and prostate cancer (*13–16*). The characteristics of $^{225}$Ac—a half-life of 10.0 d, energy range of 6–8 MeV (cumulative emission of 28 MeV/decay) with the emission of 4 αs (range, 50–80 μm), and 3 $\beta^-$ emissions with linear energy transfer of up to 0.16 MeV/μm—make it an ideal isotope for radioimmunotherapy.

We describe the use of [$^{225}$Ac]Ac-macropa-nimotuzumab for radioimmunotherapy of KRAS mutant and of KRAS wild-type and BRAF$^{V600E}$ mutant CRC models. We evaluate the in vitro (2-dimensional [2D] cell culture and 3-dimensional [3D] spheroid models) and in vivo characteristics and the in vivo effectiveness of [$^{225}$Ac]Ac-macropa-nimotuzumab in these models with different numbers of EGFR copies per cell.

## MATERIALS AND METHODS

### Conjugation, Quality Control of Immunoconjugates, and Internalization

The conjugation and in vitro characterization of nimotuzumab and of nonspecific control IgG anti-CD20 rituximab to 6-((16-((6-carboxypyridin-2-yl)methyl)-1,4,10,13-tetraoxa-7,16-diazacyclooctadecan-7-yl)methyl)-4-isothiocyanatopicolinic acid (*p*-SCN-macropa) are provided in supplemental materials (supplemental materials are available at http://jnm.snmjournals.org) (*17*). All cell lines were obtained from the American Type Culture Collection. DLD-1, SNU-C2B, and SW620 are KRAS mutant cells with KRAS$^{G13D}$, KRAS$^{G12D}$, and KRAS$^{G12V}$ mutations, respectively, whereas HT-29 is a KRAS wild-type but BRAF$^{V600E}$ mutant CRC cell line (*18,19*).

### Radiolabeling and Quality Control

*p*-SCN-macropa–conjugated nimotuzumab or rituximab was radiolabeled using $^{225}$Ac-nitrate dissolved in 0.1 M hydrogen chloride (Optima grade; Fisher Scientific) at a targeted specific activity of 10 kBq/μg, as reported (*20*). Quality control and purification were done after labeling, following lab standard operating procedures (*20*). Radioligand binding assay was studied in DLD-1 cells as described previously (*20*).

### Cytotoxicity in 2D Monolayer and 3D Spheroids

The in vitro cytotoxicity of [$^{225}$Ac]Ac-macropa-nimotuzumab was studied in 2D monolayer cultures and 3D spheroids using the Incucyte S3 live-cell imaging system (Essen BioScience) in DLD-1, SNU-C2B, HT-29, and SW620 CRC cell lines. The details are provided in the supplemental materials (*21*).

### Biodistribution, Dosimetry, and In Vivo Toxicity

To estimate radiation dose to organs, healthy BALB/c mice were administered 13 kBq of $^{225}$Ac-nimotuzumab via a tail vein and euthanized 1, 24, 48, 120, or 264 h after injection, followed by biodistribution studies. Carcasses were collected and analyzed using a γ-counter, and activity was expressed as percentage injected activity (%IA) and %IA per gram organ weight (%IA/g). The mouse biodistribution (%IA/g) data were extrapolated to human data (%IA) using the following formula: %IA (human) = %IA/g (mouse) × total body weight of mouse (in kilograms) × mass of human organ (in grams) per total body weight of human (in kilograms). For each organ, this was plotted against sampling time and used to obtain an estimate of the residence time (in megabecquerel hours per megabecquerel) of the agent in the organ, represented by the area under the time–activity function integrated to infinity (complete decay) of the $^{225}$Ac. The residence time was fitted into the OLINDA kinetics model (OLINDA/EXM version 2.2; Hermes Medical Solutions) to generate absorbed doses in units of centigray per millicurie of $^{225}$Ac administered.

Biodistribution of $^{225}$Ac-nimotuzumab was also studied in athymic nude BALB/c mice bearing EGFR-positive DLD-1 xenografts. Animals ($n$ = 4/group) were administered 13 kBq of [$^{225}$Ac]Ac-macropa-nimotuzumab and euthanized 24, 72, 120, or 288 h after injection. Organs were harvested for biodistribution studies and expressed as %IA/g. Toxicity was also studied in healthy BALB/c mice and is reported in the supplemental materials.

### Radioimmunotherapy

Biodistribution of [$^{225}$Ac]Ac-macropa-nimotuzumab showed clearance from almost all organs after 10 d, with retention in tumors. For in vivo α-particle therapy, mice were divided into 3 groups ($n \geq 5$/group): [$^{225}$Ac]Ac-macropa-nimotuzumab, [$^{225}$Ac]Ac-macropa-rituximab, and phosphate-buffered saline (PBS). Mice received 3 doses of 13 kBq (39 kBq in total) administered on days 0, 10, and 20 via a tail vein. Tumor growth was monitored by measuring the greatest length and width of each tumor using a digital caliper. Tumor volume was calculated using the following formula: volume = (length × width$^2$)/2. At the start of the study, tumor volumes for DLD-1, HT-29, and SW620 were not statistically different among the groups treated with [$^{225}$Ac]Ac-macropa-nimotuzumab, [$^{225}$Ac]Ac-macropa-rituximab, and PBS ($P > 0.05$). Initial tumor volumes ± SEM for the [$^{225}$Ac]Ac-macropa-nimotuzumab, [$^{225}$Ac]Ac-macropa-rituximab, and PBS groups were 153.2 ± 73.3, 67.9 ± 3.8, and 149.3 ± 19.3 mm$^3$ for DLD-1 xenografts; 129.2 ± 40.3, 188 ± 86, and 119.8 ± 65.9 mm$^3$ for HT-29 xenografts; and 39.2 ± 21.3, 73.4 ± 63.9, and 33.8 ± 58.67 mm$^3$ for SW620 xenografts, respectively. The study was terminated when tumor volume reached at least 1,500 mm$^3$, and then survival was determined using a Kaplan–Meier curve. The individual body weights of mice were recorded during the study period.

### Statistical Analysis

All data were expressed as the mean ± SEM of at least 3 independent experiments. Comparisons between groups were performed via either Student $t$ test with Welch correction (2-group comparison) or 1-way ANOVA with Bonferroni multiple comparison post hoc test (multiple-group comparison). Graphs were prepared and $P$ values were calculated using GraphPad Prism (version 9; GraphPad Software).

### Ethics Statement

All animal studies were approved by the University of Saskatchewan Animal Care and Use Committee protocol 20220021.

## RESULTS

### Quality Control

The conjugation of *p*-SCN-macropa to nimotuzumab or control antibody rituximab was obtained as a clear solution with no particulate matter or milky appearance. The high-performance liquid chromatography purity of macropa-nimotuzumab and macropa-rituximab was at least 98%. Immunoconjugates were further characterized for

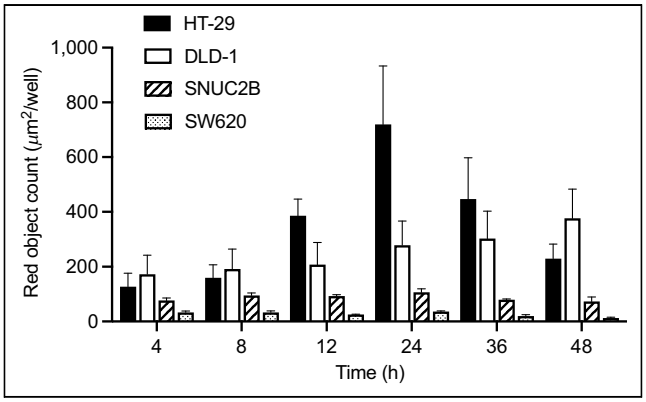


**FIGURE 1.** Internalization of nimotuzumab in DLD-1, SNU-C2B, HT-29, and SW620 cell lines at different time points after incubation using live-cell imaging. All data shown are mean of 3 wells ± SEM.

binding to EGFR, aggregation, and size (Supplemental Figs. 1 and 2; Supplemental Table 1). Bioanalyzer showed that macropa-nimotuzumab was more than 86% pure, with a molecular weight of 162.8 kDa (vs. 161.2 kDa for nimotuzumab). This indicates that there were an estimated 3 macropa per antibody molecule. Saturation binding of nimotuzumab to EGFR on DLD-1, SNU-C2B, HT-29, and SW620 cells was studied using flow cytometry (Supplemental Fig. 3). The dissociation constant and the maximum specific binding were 5.6 ± 0.06 nM and 610,576 for DLD-1, 20.1 ± 0.73 nM and 321,040 for SNU-C2B, 6.4 ± 1.6 nM and 1,484,086 for HT-29, and 5.4 ± 2.4 nM and 43,518 for SW620 cell lines, respectively.

#### Radiolabeling, Characterization, and Internalization

Macropa-nimotuzumab and control immunoconjugate macropa-rituximab were quantitatively radiolabeled using $^{225}$Ac (>90% radiochemical yield) and in high radiochemical purity (>99% in each case) at a specific activity of 10 kBq/μg. The purity was confirmed by instant thin-layer chromatography and high-performance liquid chromatography (Supplemental Figs. 2C and 2D).

Internalization efficiency of nimotuzumab compared with control IgG was estimated by total red counts observed at the end of 48 h after treatment. In all cell lines except for DLD-1, internalization peaked at 24 h and depended on EGFR expression on the surface of the cell (Fig. 1). At 48 h after incubation, the internalization of nimotuzumab in DLD-1 (376.82 ± 106.5, high EGFR expression) was 30.9 times greater than in SW620 (12.18 ± 3.28, low EGFR expression). Similarly, at 24 h, nimotuzumab was 20 times more internalized in HT-29 (719.21 ± 213.5, high EGFR expression) than in SW620 (35.98 ± 3.095, low EGFR expression).

The binding of [$^{225}$Ac]Ac-macropa-nimotuzumab to the EGFR-positive DLD-1 cell line was studied using radioligand binding assay. The estimated dissociation constant and maximum specific binding were 14.8 ± 41.7 nM and 10,050, respectively (Supplemental Fig. 4).

#### In Vitro Cytotoxicity (2D and 3D Spheroids)

Live-cell imaging was used to study the in vitro cytotoxicity (2D cells) of nimotuzumab and [$^{225}$Ac]Ac-macropa-nimotuzumab in DLD-1, SW620, SNU-C2B, and HT-29 mCRC cells (Table 1; Supplemental Figs. 5 and 6). Despite the low specific activity, [$^{225}$Ac]Ac-macropa-nimotuzumab was more potent than unlabeled nimotuzumab. In DLD-1 cells, the inhibitory concentration of 50% ($IC_{50}$) of [$^{225}$Ac]Ac-macropa-nimotuzumab (1.8 ± 1.0 nM) was 46.7-fold lower than that of cold (unlabeled) nimotuzumab (84.1 ± 0.3 nM; $P < 0.001$). Similar trends were observed for SNU-C2B and SW620 cell lines (Table 1). Phase contrast images showed a higher concentration of cell death with [$^{225}$Ac]Ac-macropa-nimotuzumab than with unlabeled nimotuzumab. Unlabeled nimotuzumab had no effect on HT-29, but [$^{225}$Ac]Ac-macropa-nimotuzumab was cytotoxic ($IC_{50}$, 10.1 nM) to the cell.

Live-cell imaging was used to study the in vitro cytotoxicity of nimotuzumab and [$^{225}$Ac]Ac-macropa-nimotuzumab in DLD-1, SW620, SNU-C2B, and HT-29 mCRC 3D spheroids (Table 2; Supplemental Figs. 7 and 8). In DLD-1 spheroids, the $IC_{50}$ of [$^{225}$Ac]Ac-macropa-nimotuzumab (10.6 ± 0.6 nM) was 32.4 times lower than that of nimotuzumab (342.4 ± 0.1 nM). Similar differences were observed in SNU-C2B and SW620 spheroids (Table 2). Phase contrast images displayed a decrease in spheroid sizes after treatment with [$^{225}$Ac]Ac-macropa-nimotuzumab (Supplemental Fig. 7), indicating the enhanced cytotoxic effect of [$^{225}$Ac]Ac-macropa-nimotuzumab compared with nimotuzumab. In HT-29 spheroids, unlabeled nimotuzumab had no effects. Enhanced cytotoxicity was observed with [$^{225}$Ac]Ac-macropa-nimotuzumab ($IC_{50}$, 41.5 ± 1.4 nM).

#### Biodistribution, Dosimetry, and In Vivo Toxicity

Biodistribution of [$^{225}$Ac]Ac-macropa-nimotuzumab was studied in healthy BALB/c mice and in athymic nude BALB/c mice bearing EGFR-positive DLD-1 xenografts. In healthy BALB/c mice, the uptake of [$^{225}$Ac]Ac-macropa-nimotuzumab was high in the kidney, liver, and blood at early time points, but only the liver (11.5 ± 0.6 %IA/g) and the blood (8.1 ± 1.1 %IA/g) had high uptake 11 d after injection (Fig. 2; Supplemental Table 2). Projected human radiation dose estimates were calculated with OLINDA/EXM version 2.2 using the human scaling factor and biodistribution data obtained from healthy BALB/c mice (Table 3). As expected, the liver received the highest organ dose of [$^{225}$Ac]Ac-macropa-nimotuzumab, followed by the spleen. In mice bearing DLD-1 xenografts, uptake of [$^{225}$Ac]Ac-macropa-nimotuzumab was higher in the tumor at all time points than in other organs, with a maximum at 120 h (DLD-1 tumor, 32.0 ± 13.8 %IA/g; liver, 4.0 ± 2.9 %IA/g; kidney, 3.2 ± 2.2 %IA/g;

**TABLE 1**
$IC_{50}$ Values of Immunoconjugates in KRAS Wild-Type and $BRAF^{V600E}$ HT-29 and KRAS Mutant DLD-1, SW620, and SNU-C2B CRC Monolayer Cells with Different Levels of EGFR Expression

| Parameter | DLD-1 | SNU-C2B | SW620 | HT-29 |
|---|---|---|---|---|
| $IC_{50}$ (nM) | | | | |
| Nimotuzumab | 84 ± 0.3 | 101.7 ± 0.3 | 362.8 ± 2.3 | — |
| [$^{225}$Ac]Ac-macropa-nimotuzumab | 1.8 ± 1.0 | 3.3 ± 1.3 | 4.6 ± 0.6 | 10.1 ± 1.3 |
| $IC_{50}$ (kBq/mL) | 2.8 ± 0.0 | 5.1 ± 0.3 | 7.2 ± 0.2 | 15.4 ± 0.6 |

**TABLE 2**
$IC_{50}$ Values of Immunoconjugates in KRAS Wild-Type and $BRAF^{V600E}$ HT-29 and Mutant CRC DLD-1, SW620, and SNU-C2B Spheroids with Different Levels of EGFR Expression

| Parameter | DLD-1 | SNU-C2B | SW620 | HT-29 |
|---|---|---|---|---|
| $IC_{50}$ (nM) | | | | |
| Nimotuzumab | 342.4 ± 0.1 | 363.2 ± 0.0 | 414.3 ± 0.1 | — |
| [$^{225}$Ac]Ac-macropa-nimotuzumab | 10.6 ± 0.6 | 14.7 ± 2.5 | 19.5 ± 1.7 | 41.5 ± 1.4 |
| $IC_{50}$ (kBq/mL) | 15.9 ± 0.6 | 22.0 ± 2.5 | 37.0 ± 1.7 | 62.3 ± 1.4 |

blood, 5.1 ± 4.3 %IA/g; Supplemental Table 3). There were no changes in most hematopoietic parameters after administration of 11.1 kBq of [$^{225}$Ac]Ac-macropa-nimotuzumab in healthy mice (Supplemental Table 4).

### Efficacy of [$^{225}$Ac]Ac-Macropa-Nimotuzumab

We evaluated the efficacy of [$^{225}$Ac]Ac-macropa-nimotuzumab and control [$^{225}$Ac]Ac-macropa-rituximab in mCRC KRAS mutant DLD-1 (high EGFR expression) and in KRAS wild-type and $BRAF^{V600E}$ mutant HT-29 (high EGFR expression) and SW620 (low EGFR expression) mouse xenograft models (Figs. 3–5). Tumor growth inhibition was evaluated using a digital caliper. In mice bearing DLD-1 xenografts treated with 3 doses of [$^{225}$Ac]Ac-macropa-nimotuzumab, 3 of 7 mice had complete tumor regression on days 13, 100, and 130, whereas tumor volume reached 1,500 $mm^3$ for a partially responding mouse on day 76. The remaining 3 mice in this group had tumor volumes of less than 100 $mm^3$ at the end of the study. Two of 7 mice treated with 3 doses of control [$^{225}$Ac]Ac-macropa-rituximab reached 1,500 $mm^3$ on day 30, and the rest reached 1,500 $mm^3$ by day 64. In the PBS group, all 8 mice reached the study endpoint (1,500 $mm^3$) by day 42. In HT-29 mice treated with [$^{225}$Ac]Ac-macropa-nimotuzumab, 1 of 7 mice had complete tumor regression and 4 mice showed a partial response to therapy, evidenced by reduction in tumor growth (75, 57, 200, and 550.4 $mm^3$ on day 90). However, 1 mouse from this group reached the tumor endpoint on day 35. In the $^{225}$Ac-rituximab group, 3 of 4 mice reached the endpoint on day 16. In KRAS mutant SW620 mice (low EGFR copies per cell) treated with [$^{225}$Ac]Ac-macropa-nimotuzumab, 2 of 8 mice showed a partial response to therapy, whereas the others reached 1,500 $mm^3$ by days 16, 21, 35, 38, and 41. All mice in the [$^{225}$Ac]Ac-macropa-rituximab and PBS groups reached the endpoint of this study within 33 and 47 d, respectively.

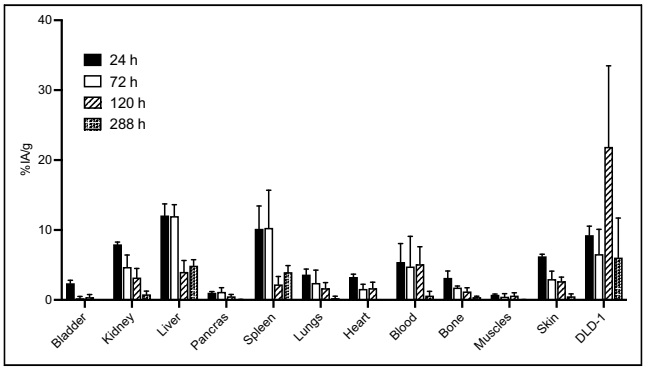


**FIGURE 2.** Biodistribution of [$^{225}$Ac]Ac-macropa-nimotuzumab in selected healthy organs in athymic nude BALB/c mice ($n \geq 3$/group) bearing DLD-1 xenografts at different time points after injection, expressed as %IA/g.

The Kaplan–Meier survival curves of DLD-1, HT-29, and SW620 xenografts are presented in Figures 3, 4, and 5, respectively. Compared with the control [$^{225}$Ac]Ac-macropa-rituximab and PBS groups, $^{225}$Ac-nimotuzumab significantly extended survival in all models ($P < 0.01$). For KRAS mutant DLD-1 xenografts, median survival was 34 and 27 d for the [$^{225}$Ac]Ac-macropa-rituximab and PBS groups, respectively, but was not reached for the $^{225}$Ac-nimotuzumab group after 130 d. For KRAS wild-type and $BRAF^{V600E}$ mutant HT-29 xenografts, median survival was 16 and 12.5 d for the [$^{225}$Ac]Ac-macropa-rituximab and PBS groups, respectively, but was not reached for the [$^{225}$Ac]Ac-macropa-nimotuzumab group (>90 d). For SW620 xenografts, median survival was 16, 24.5, and 41 d for the [$^{225}$Ac]Ac-macropa-rituximab, PBS, and [$^{225}$Ac]Ac-macropa-nimotuzumab groups, respectively. There was no gross toxicity in $^{225}$Ac-treated groups compared with control, as evidenced by the body weights of the mice (Supplemental Fig. 10).

## DISCUSSION

Continuous activation of EGFR by oncogenic KRAS and BRAF abrogates antitumor activity of anti-EGFR targeted therapeutics (*2*). Because of their decay properties, $^{225}$Ac-targeted radioimmunoconjugates are considered molecular nanogenerators and can be ideal in the setting of KRAS and BRAF mutant CRC. To our knowledge, no prior study has evaluated an α-particle–labeled anti-EGFR agent in KRAS or BRAF wild-type and mutant CRC models. Others have evaluated the anti-EGFR antibodies [$^{212}$Pb]Pb-TCMC-panitumumab and [$^{212}$Pb]Pb-TCMC-cetuximab,

**TABLE 3**
Human Radiation Dose Estimates for Women Estimated Using OLINDA/EXM Version 2.2

| Organ | Dose (mSv/MBq) |
|---|---|
| Brain | 2.77E+00 |
| Small intestine | 2.14E−02 |
| Stomach wall | 8.1E−03 |
| Right colon | 1.02E−02 |
| Heart wall | 4.08E+01 |
| Kidneys | 1.29E+02 |
| Liver | 2.44E+02 |
| Lungs | 7.42E+01 |
| Pancreas | 7.66E+00 |
| Spleen | 1.59E+02 |
| Urinary bladder wall | 2.5E−04 |
| Total body | 8.05E+00 |

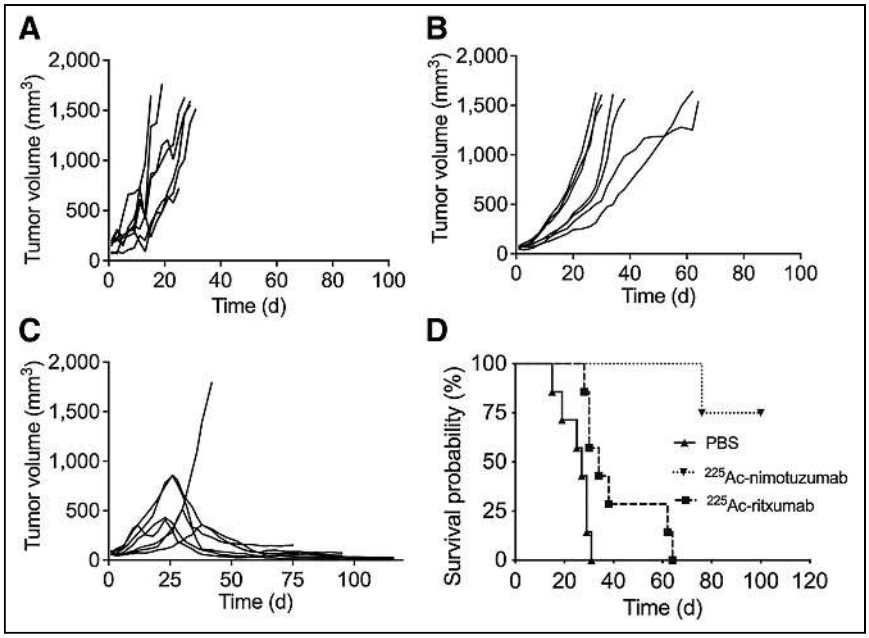


**FIGURE 3.** Efficacy of $^{225}$Ac-labeled radioimmunoconjugates in mice bearing EGFR-positive KRAS mutant ($KRAS^{G13D}$) DLD-1 colorectal xenografts. Mice were treated using saline (A), three 13-kBq doses (39 kBq total, administered 10 d apart) of control anti-CD20 antibody [$^{225}$Ac]Ac-macropa-rituximab (B), and three 13-kBq doses (39 kBq total, administered 10 d apart) of anti-EGFR antibody [$^{225}$Ac]Ac-macropa-nimotuzumab (C). (D) Kaplan–Meier survival curves of different groups. Study endpoint was when xenografts reached ≥1,500 $mm^3$.

or [$^{213}$Bi]Bi-CHX-A″-DTPA-cetuximab preclinically in other disease models (*22*,*23*). Hence, this study was undertaken to explore the effectiveness of an $^{225}$Ac-labeled anti-EGFR radioimmunoconjugate in KRAS and BRAF mutant CRC. CRC has 4 major types of KRAS mutations, namely, $KRAS^{G12D}$ (34.2%), $KRAS^{G12V}$ (21%), $KRAS^{G13D}$ (20%), and $KRAS^{G12C}$ (8.4%) (*24*). Compared with other mutations that show no sensitivity to anti-EGFR agents, $KRAS^{G13D}$ shows some sensitivity to cetuximab, albeit less than the wild type (*9*).

We found that internalization depended on receptor density rather than KRAS status and was lowest in SW620, with the lowest EGFR expression, but similar between HT-29 and DLD-1, both with high EGFR copies per cell. Similarly, the binding (dissociation constant) of anti-EGFR antibodies observed in this and previous studies depended not on KRAS but on EGFR copies per cell (*25*). In vitro cytotoxicity was studied using Incucyte S3 live-cell imaging and a Cytotox red agent (Essen BioScience), which allows the quantification of dead cells (Table 1) in real time. Unlabeled nimotuzumab had no effect on the survival of $BRAF^{V600E}$ mutant HT-29 cells despite high EGFR expression, confirming the same observations by others (*26*,*27*). However, [$^{225}$Ac]Ac-macropa-nimotuzumab was effective against 2D monolayer and 3D spheroids of HT-29 cells, albeit at a higher dose than for DLD-1 with similar EGFR copies per cell (Tables 1 and 2). DLD-1 with $KRAS^{G13D}$ mutation is a bit responsive to unlabeled anti-EGFR antibodies and antibody–drug conjugates (*27*). We previously showed that nimotuzumab antibody–drug conjugate (nimotuzumab-$PEG_6$-DM1, with a drug-to-antibody ratio of 3:4) (*27*) was cytotoxic to DLD-1, with $IC_{50}$ of 32.6 nM (compared with 1.8 nM for [$^{225}$Ac]Ac-macropa-nimotuzumab in this study), but was not cytotoxic to HT-29. Hence, the in vitro potency of [$^{225}$Ac]Ac-macropa-nimotuzumab was severalfold more than the naked antibody or antibody–drug conjugate in the HT-29 model. In vitro cytotoxicity was also observed in SW620 with KRAS mutation and low EGFR copies per cell. Hence, [$^{225}$Ac]Ac-macropa-nimotuzumab is advantageous over antibody–drug conjugates or other anti-EGFR inhibitors.

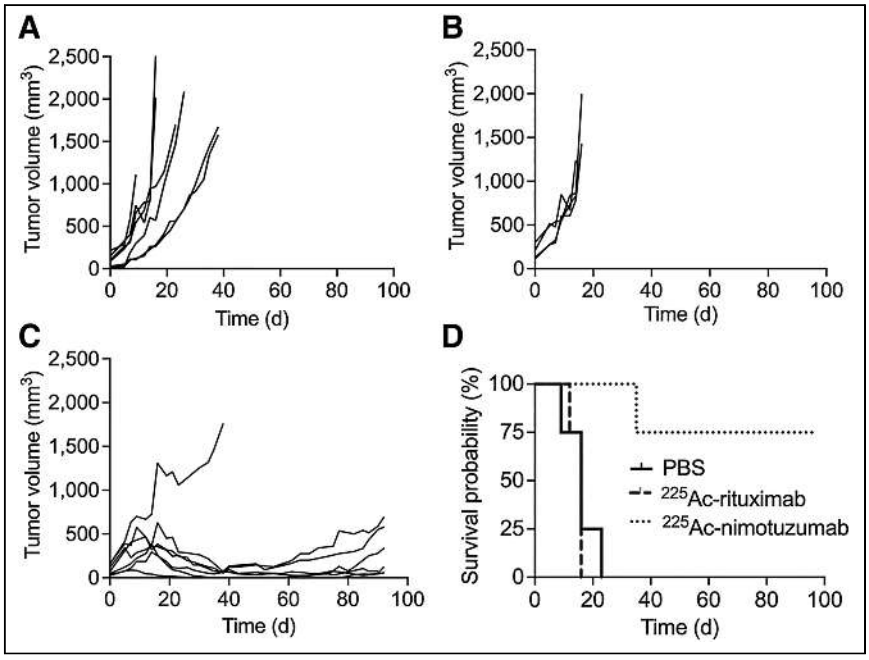


**FIGURE 4.** Efficacy of $^{225}$Ac-labeled radioimmunoconjugates in mice bearing EGFR-positive $BRAF^{V600E}$ mutant HT-29 colorectal xenografts. Mice were treated using saline (A), three 13-kBq doses (39 kBq total, administered 10 d apart) of control anti-CD20 antibody [$^{225}$Ac]Ac-macropa-rituximab (B), and three 13-kBq doses (39 kBq total, administered 10 d apart) of anti-EGFR antibody [$^{225}$Ac]Ac-macropa-nimotuzumab (C). (D) Kaplan–Meier survival curves of different groups. Study endpoint was when xenografts reached ≥1,500 $mm^3$.

3D spheroids are a more relevant in vitro model than monolayer cells when studying in vitro cytotoxicity, particularly because they more accurately mimic micrometastatic lesions. Spheroid diameters for DLD-1, HT-29, SNU-C2B, and SW620 were in the range of 200–650 mM. In all spheroids tested, [$^{225}$Ac]Ac-macropa-nimotuzumab was 22- to 33-fold more potent than the unlabeled nimotuzumab. These results suggest that [$^{225}$Ac]Ac-macropa-nimotuzumab is potent against both KRAS and $BRAF^{V600E}$ mutant spheroids and would be effective in micrometastatic lesions in vivo.

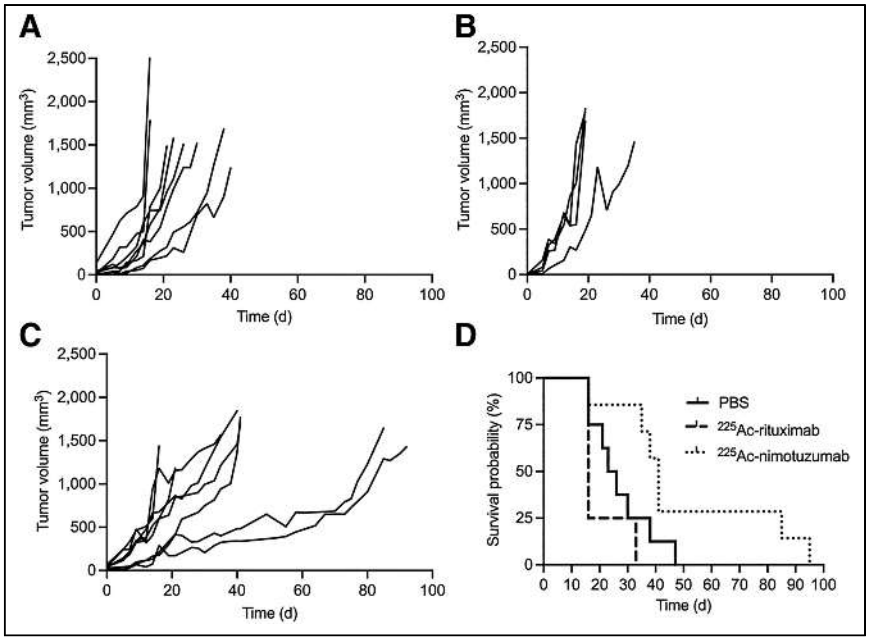


**FIGURE 5.** Efficacy of $^{225}$Ac-labeled radioimmunoconjugates against EGFR-positive SW620 colorectal xenografts. Mice were treated using saline (A), three 13-kBq doses (39 kBq total, administered 10 d apart) of control anti-CD20 antibody [$^{225}$Ac]Ac-macropa-rituximab (B), and three 13-kBq doses (39 kBq total, administered 10 d apart) of anti-EGFR antibody [$^{225}$Ac]Ac-macropa-nimotuzumab (C). (D) Kaplan–Meier survival curves of different groups. Study endpoint was when xenografts reached ≥1,500 mm$^3$.

We previously showed that the effective organ dose of $^{89}$Zr-nimotuzumab was more than 2-fold lower than that of $^{89}$Zr-cetuximab (*25*). Organ doses in this study showed similar trends compared with work using other anti-EGFR antibody conjugates, such as [$^{213}$Bi]Bi-CHX-A″-DTPA-cetuximab (*28*), as well as our previous study using [$^{89}$Zr]Zr-DFO-nimotuzumab (*25*). [$^{225}$Ac]Ac-macropa-nimotuzumab was cleared from almost all organs after 10 d and was retained in tumors, hence the justification for dose fractionation every 10 d. We recently showed using anti-EGFR antibody [$^{89}$Zr]Zr-DFO-matuzumab that tumor uptake of CRC xenografts depended on EGFR expression rather than KRAS and BRAF mutational status, with a similar uptake in DLD-I and HT-29 xenografts, both with high EGFR density, that was more than 3-fold higher than in SW620 xenografts, with low EGFR density (*29*). In addition, the high internalization rate of nimotuzumab likely contributed to the prolonged retention of $^{225}$Ac in the tumor and hence the effectiveness. These characteristics make [$^{225}$Ac]Ac-macropa-nimotuzumab a potentially effective molecular nanogenerator with continuous delivery of high linear energy transfer radiation doses to the tumor. A few BRAF inhibitors, including vemurafenib, dabrafenib, and encorafenib, are approved for treating BRAF mutant melanomas and show significant benefits in this population (*30–32*). However, these inhibitors show no benefits in CRC patients with BRAF$^{V600E}$ mutation, confirming preclinical data that showed the activation of this pathway is different for both cancer types (*33*). KRAS mutant DLD-1 xenografts and BRAF mutant HT-29 xenografts showed a similar response to [$^{225}$Ac]Ac-macropa-nimotuzumab. However, [$^{225}$Ac]Ac-macropa-nimotuzumab had less of an effect on KRAS mutant SW620 xenografts, likely because of its low EGFR expression. In all cell lines, [$^{225}$Ac]Ac-macropa-rituximab showed no significant response. Therefore, the benefits (>6-fold improvement in survival, including complete remission) of [$^{225}$Ac]Ac-macropa-nimotuzumab in mice bearing HT-29, as demonstrated in this study, could have a significant clinical implication in CRC patients with BRAF$^{V600E}$ mutation when translated. In addition, we demonstrated enhancement in survival in KRAS mutant xenografts, including some complete remissions of DLD-1 tumors, and more than 2-fold enhancement in median survival of mice bearing KRAS mutant SW620 xenografts, despite low EGFR expression.

## CONCLUSION

This work showed the benefits of α-particle [$^{225}$Ac]Ac-macropa-nimotuzumab as an anti-EGFR molecular nanogenerator against KRAS and BRAF$^{V600E}$ mutant xenografts. [$^{225}$Ac]Ac-macropa-nimotuzumab was more effective in KRAS$^{G13D}$ DLD-1 and BRAF$^{V600E}$ HT-29, with high EGFR expression, than in KRAS$^{G12V}$ SW620, with low EGFR expression. This effectiveness results from its high internalization rate in these cells and high tumor retention. Preliminary hematopoietic studies showed that [$^{225}$Ac]Ac-macropa-nimotuzumab was safe, and animals tolerated 3 doses of the agent. These promising data warrant further investigation and potential clinical translation.

## DISCLOSURE

This work was funded by a Canadian Institute for Health Research project grant (437660) to Humphrey Fonge. No other potential conflict of interest relevant to this article was reported.

**KEY POINTS**

**QUESTION:** Can an anti-EGFR antibody radiolabeled with an α-emitting radioisotope ($^{225}$Ac) be effective against EGFR-positive CRC xenografts that are irresponsive to naked antibodies, such as cetuximab?

**PERTINENT FINDINGS:** Anti-EGFR radioimmunotherapeutic [$^{225}$Ac]Ac-macropa-nimotuzumab was effective in prolonging the survival of mice bearing EGFR-positive CRC xenografts that harbor KRAS and BRAF$^{V600E}$ mutations.

**IMPLICATIONS FOR PATIENT CARE:** [$^{225}$Ac]Ac-macropa-nimotuzumab could result in significant survival improvements in patients with EGFR-positive CRC with or without KRAS or BRAF$^{V600E}$ mutations, which represent up to 80% of patients, when or if translated in clinical trial.

## REFERENCES

1. Cunningham D, Humblet Y, Siena S, et al. Cetuximab monotherapy and cetuximab plus irinotecan in irinotecan-refractory metastatic colorectal cancer. *N Engl J Med.* 2004;351:337–345.
2. van Houdt WJ, Hoogwater FJ, de Bruijn MT, et al. Oncogenic KRAS desensitizes colorectal tumor cells to epidermal growth factor receptor inhibition and activation. *Neoplasia.* 2010;12:443–452.

3. McCubrey JA, Steelman LS, Chappell WH, et al. Ras/Raf/MEK/ERK and PI3K/PTEN/Akt/mTOR cascade inhibitors: how mutations can result in therapy resistance and how to overcome resistance. *Oncotarget.* 2012;3:1068–1111.
4. McCubrey JA, Steelman LS, Chappell WH, et al. Mutations and deregulation of Ras/Raf/MEK/ERK and PI3K/PTEN/Akt/mTOR cascades which alter therapy response. *Oncotarget.* 2012;3:954–987.
5. Yaeger R, Chatila WK, Lipsyc MD, et al. Clinical sequencing defines the genomic landscape of metastatic colorectal cancer. *Cancer Cell.* 2018;33:125–136.e3.
6. Corcoran RB, Andre T, Atreya CE, et al. Combined BRAF, EGFR, and MEK inhibition in patients with $BRAF^{V600E}$-mutant colorectal cancer. *Cancer Discov.* 2018; 8:428–443.
7. O'Connell JB, Maggard MA, Ko CY. Colon cancer survival rates with the new American Joint Committee on Cancer sixth edition staging. *J Natl Cancer Inst.* 2004;96:1420–1425.
8. Sadahiro S, Suzuki T, Ishikawa K, et al. Recurrence patterns after curative resection of colorectal cancer in patients followed for a minimum of ten years. *Hepatogastroenterology.* 2003;50:1362–1366.
9. De Roock W, De Vriendt V, Normanno N, Ciardiello F, Tejpar S. KRAS, BRAF, PIK3CA, and PTEN mutations: implications for targeted therapies in metastatic colorectal cancer. *Lancet Oncol.* 2011;12:594–603.
10. Yaeger R, Kotani D, Mondaca S, et al. Response to anti-EGFR therapy in patients with BRAF non-V600-mutant metastatic colorectal cancer. *Clin Cancer Res.* 2019; 25:7089–7097.
11. Yokota T, Ura T, Shibata N, et al. BRAF mutation is a powerful prognostic factor in advanced and recurrent colorectal cancer. *Br J Cancer.* 2011;104:856–862.
12. Lacouture ME. Mechanisms of cutaneous toxicities to EGFR inhibitors. *Nat Rev Cancer.* 2006;6:803–812.
13. Poty S, Francesconi LC, McDevitt MR, Morris MJ, Lewis JS. α-emitters for radiotherapy: from basic radiochemistry to clinical studies—part 1. *J Nucl Med.* 2018; 59:878–884.
14. Zacherl MJ, Gildehaus FJ, Mittlmeier L, et al. First clinical results for PSMA-targeted α-therapy using $^{225}$Ac-PSMA-I&T in advanced-mCRPC patients. *J Nucl Med.* 2021;62:669–674.
15. Yadav MP, Ballal S, Sahoo RK, Tripathi M, Seth A, Bal C. Efficacy and safety of $^{225}$Ac-PSMA-617 targeted alpha therapy in metastatic castration-resistant prostate cancer patients. *Theranostics.* 2020;10:9364–9377.
16. Ballal S, Yadav MP, Bal C, Sahoo RK, Tripathi M. Broadening horizons with $^{225}$Ac-DOTATATE targeted alpha therapy for gastroenteropancreatic neuroendocrine tumour patients stable or refractory to $^{177}$Lu-DOTATATE PRRT: first clinical experience on the efficacy and safety. *Eur J Nucl Med Mol Imaging.* 2020;47:934–946.
17. Thiele NA, Brown V, Kelly JM, et al. An eighteen-membered macrocyclic ligand for actinium-225 targeted alpha therapy. *Angew Chem Int Ed Engl.* 2017;56:14712–14717.
18. Khan S, Cameron S, Blaschke M, et al. Differential gene expression of chemokines in KRAS and BRAF mutated colorectal cell lines: role of cytokines. *World J Gastroenterol.* 2014;20:2979–2994.
19. Wang G, Huang Y, Wu Z, et al. KRAS-mutant colon cancer cells respond to combined treatment of ABT263 and axitinib. *Biosci Rep.* 2019;39:BSR20181786.
20. Solomon VR, Barreto K, Bernhard W, et al. Nimotuzumab site-specifically labeled with $^{89}$Zr and $^{225}$Ac using SpyTag/SpyCatcher for PET imaging and alpha particle radioimmunotherapy of epidermal growth factor receptor positive cancers. *Cancers (Basel).* 2020;12:3449.
21. Solomon VR, Alizadeh E, Bernhard W, et al. $^{111}$In- and $^{225}$Ac-labeled cixutumumab for imaging and α-particle radiotherapy of IGF-1R positive triple-negative breast cancer. *Mol Pharm.* 2019;16:4807–4816.
22. Milenic DE, Baidoo KE, Kim YS, Barkley R, Brechbiel MW. Targeted α-particle radiation therapy of HER1-positive disseminated intraperitoneal disease: an investigation of the human anti-EGFR monoclonal antibody, panitumumab. *Transl Oncol.* 2017;10:535–545.
23. Milenic DE, Baidoo KE, Kim YS, Brechbiel MW. Evaluation of cetuximab as a candidate for targeted α-particle radiation therapy of HER1-positive disseminated intraperitoneal disease. *MAbs.* 2015;7:255–264.
24. Thangaiyan R, Aljahdali IA, Lent-Moore KY, Liao J, Ling X, Li F. Kras mutation subtypes distinctly affect colorectal cancer cell sensitivity to FL118, a novel inhibitor of survivin, Mcl-1, XIAP, cIAP2 and MdmX. *Am J Transl Res.* 2021;13: 7458–7474.
25. Chekol R, Solomon VR, Alizadeh E, et al. $^{89}$Zr-nimotuzumab for immunoPET imaging of epidermal growth factor receptor I. *Oncotarget.* 2018;9:17117–17132.
26. Zhi J, Li Z, Lv J, et al. Effects of PHA-665752 and vemurafenib combination treatment on in vitro and murine xenograft growth of human colorectal cancer cells with $BRAF^{V600E}$ mutations. *Oncol Lett.* 2018;15:3904–3910.
27. Hartimath SV, El-Sayed A, Makhlouf A, et al. Therapeutic potential of nimotuzumab PEGylated-maytansine antibody drug conjugates against EGFR positive xenograft. *Oncotarget.* 2019;10:1031–1044.
28. Song H, Hedayati M, Hobbs RF, et al. Targeting aberrant DNA double-strand break repair in triple-negative breast cancer with alpha-particle emitter radiolabeled anti-EGFR antibody. *Mol Cancer Ther.* 2013;12:2043–2054.
29. Tikum AF, Nambisan AK, Ketchemen JP, et al. Simultaneous imaging and therapy using epitope-specific anti-epidermal growth factor receptor (EGFR) antibody conjugates. *Pharmaceutics.* 2022;14:1917.
30. Chapman PB, Hauschild A, Robert C, et al. Improved survival with vemurafenib in melanoma with $BRAF^{V600E}$ mutation. *N Engl J Med.* 2011;364:2507–2516.
31. Hauschild A, Grob JJ, Demidov LV, et al. Dabrafenib in BRAF-mutated metastatic melanoma: a multicentre, open-label, phase 3 randomised controlled trial. *Lancet.* 2012;380:358–365.
32. Dummer R, Ascierto PA, Gogas HJ, et al. Encorafenib plus binimetinib versus vemurafenib or encorafenib in patients with BRAF-mutant melanoma (COLUMBUS): a multicentre, open-label, randomised phase 3 trial. *Lancet Oncol.* 2018;19: 603–615.
33. Prahallad A, Sun C, Huang SD, et al. Unresponsiveness of colon cancer to $BRAF^{V600E}$ inhibition through feedback activation of EGFR. *Nature.* 2012;483:100–103.

# The Impact of Posttreatment Imaging in Peptide Receptor Radionuclide Therapy

Surekha Yadav[1], Courtney Lawhn-Heath[1], Alan Paciorek[2], Sheila Lindsay[1,3], Rebecca Mirro[1], Emily K. Bergsland[3,4], and Thomas A. Hope[1,4,5]

*[1]Department of Radiology and Biomedical Imaging, University of California San Francisco, San Francisco, California; [2]Department of Epidemiology and Biostatistics, University of California San Francisco, San Francisco, California; [3]Department of Medicine, Division of Medical Oncology, University of California San Francisco, San Francisco, California; [4]Helen Diller Family Comprehensive Cancer Center, University of California San Francisco, San Francisco, California; and [5]Department of Radiology, San Francisco VA Medical Center, San Francisco, California*

Posttreatment imaging of γ-emissions after peptide receptor radionuclide therapy (PRRT) can be used to perform quantitative dosimetry as well as assessment response using qualitative measures. We aimed to assess the impact of qualitative posttreatment imaging on the management of patients undergoing PRRT. **Methods:** In this retrospective study, we evaluated 100 patients with advanced well-differentiated neuroendocrine tumors undergoing PRRT, who had posttreatment SPECT/CT imaging at 24 h. First, we evaluated the qualitative assessment of response at each cycle. Then using a chart review, we determined the impact on management from the posttreatment imaging. The changes in management were categorized as major or minor, and the cycles at which these changes occurred were noted. Additionally, tumor grade was also evaluated. **Results:** Of the 100 sequential patients reviewed, most (80% after cycle 2, 79% after cycle 3, and 73% after cycle 4) showed qualitatively stable disease during PRRT. Management changes were observed in 27% ($n$ = 27) of patients; 78% of those ($n$ = 21) were major, and 30% ($n$ = 9) were minor. Most treatment changes occurred after cycle 2 (33% major, 67% minor) and cycle 3 (62% major, 33% minor). Higher tumor grade correlated with increased rate of changes in management ($P$ = 0.006). **Conclusion:** In this retrospective study, qualitative analysis of posttreatment SPECT/CT imaging informed changes in management in 27% of patients. Patients with higher-grade tumors had a higher rate of change in management, and most of the management changes occurred after cycles 2 and 3. Incorporating posttreatment imaging into standard PRRT workflows could potentially enhance patient management.

**Key Words:** neuroendocrine; radionuclide therapy; SPECT/CT; $^{177}$Lu-DOTATATE; posttreatment imaging

**J Nucl Med 2024; 65:409–415**
DOI: 10.2967/jnumed.123.266614

Neuroendocrine neoplasms encompass a diverse range of tumors, primarily originating in the lungs and gastroenteropancreatic sites. The classification of gastroenteropancreatic neuroendocrine neoplasms by the World Health Organization into different histopathologic subgroups provides prognostic insights based primarily on differentiation status, mitotic rate, or Ki-67 proliferation index; well-differentiated tumors are subclassified into G1 (Ki-67, <3%), G2 (Ki-67, 3%–20%), and G3 (Ki-67, >20%) neuroendocrine tumors (NETs), which exhibit increasing aggressiveness as the proliferation rate increases; poorly differentiated neuroendocrine carcinomas represent the most aggressive subset and include large and small cell subtypes (*1*). Despite the relatively low incidence of each individual subtype, the global burden of neuroendocrine neoplasms is on the rise (*2,3*).

Peptide receptor radionuclide therapy (PRRT) using $^{177}$Lu-DOTATATE has become a standard treatment for well-differentiated NETs (*4–8*) and is given clinically as 4 cycles of 7.4 GBq every 8 wk. However, with increased clinical experience, adapting standard treatment protocols to specific patients has become more common. For example, in patients who experience bone marrow toxicity, administered activity can be decreased or the interval between PRRT treatments can be increased (*9*).

Although somatostatin receptor (SSTR) PET is used to select patients and follow patients after treatment (*10*), there are currently no guidelines for how to use posttreatment imaging of the administered $^{177}$Lu-DOTATATE (referred to as posttreatment imaging here) during PRRT, and most treatment centers in the United States do not routinely perform immediate posttreatment imaging. Similarly, the latest published guidelines from the North American Neuroendocrine Tumor Society and the Society of Nuclear Medicine and Molecular Imaging regarding administration of $^{177}$Lu-DOTATATE PRRT do not specifically address the utility of performing posttreatment imaging (*4*).

Posttreatment imaging can be used in 2 major ways: the first is to perform quantitative dosimetry of tumors and normal organs, and the second is to qualitatively evaluate the patient's response to treatment. Quantitative dosimetry has been shown to correlate with radiographic response in gastroenteropancreatic NETs but not overall survival (*11,12*). Although there is a relationship between lesion absorbed dose and response, it is unclear how to apply this quantitative data to change management on a patient level. In terms of the role of qualitative interpretation of posttreatment imaging, there is no evidence of its current role or value. A study evaluating the practice of radiopharmaceutical therapies across European countries revealed that each one of them performed posttreatment imaging for $^{177}$Lu-DOTATATE PRRT (*13*). The study highlighted that the impact of posttreatment imaging on clinical decision-making remains uncertain.

Received Sep. 5, 2023; revision accepted Dec. 20, 2023.
For correspondence or reprints, contact Thomas A. Hope (thomas.hope@ucsf.edu).

**TABLE 1**
Patient Demographic and Tumor Features or Patient Clinical and Demographic Features

| Parameter | *n* |
|---|---|
| Sex | |
| Female | 58 (58) |
| Male | 42 (42) |
| Functional syndrome | 71 (71) |
| Carcinoid syndrome | 64 (90) |
| Other syndrome | 7 (10) |
| Prior therapies | |
| Previous chemotherapy | 36 (36) |
| Targeted therapy (everolimus, sunitinib) or immunotherapy | 37 (37) |
| Liver-directed therapy | 38 (38) |
| External-beam radiation therapy | 21 (21) |
| Somatostatin analog therapies | 89 (89) |
| Surgery | 64 (64) |
| Previous PRRT | 5 (2) |
| Primary site | |
| Small bowel | 55 (55) |
| Pancreas | 26 (26) |
| Bronchial tube | 6 (6) |
| Unknown | 5 (5) |
| Others | 8 (8) |
| Ki-67 index at diagnosis | |
| Known | 8.6 (9.1) |
| Unknown | 9 (9) |
| Grade of tumor differentiation | |
| 1 | 36 (36) |
| 2 | 59 (59) |
| 3 | 5 (5) |

Data are number and percentage. Mean age was 69.2 y (±11.1 y).

The role of qualitative posttreatment imaging–based response and its impact on management is not clearly understood, and therefore, we aimed to investigate the impact of posttreatment imaging on changes in management in patients undergoing $^{177}$Lu-DOTATATE PRRT at our institution.

## MATERIALS AND METHODS

### Study Population

We conducted a retrospective study of the first 107 patients who underwent $^{177}$Lu-DOTATATE PRRT for well-differentiated NETs at our institution between 2018 and 2020. The patient cohort included individuals who had received a minimum of 2 cycles of PRRT as per standard treatment guidelines (*4*). Anatomic imaging was performed as a part of our institutional protocol after cycle 2, and characterization of pseudoprogression was based on these images. The institutional review board approved this retrospective study, and the requirement to obtain informed consent was waived.

### Posttherapy Scan Acquisition

Whole-body planar and SPECT/CT imaging were performed 1 d after each cycle in the context of routine clinical care using a dual-head γ-camera Infinia Hawkeye (GE Healthcare) system with the following acquisition parameters: 208% ± 10% keV photopeak, 170% ± 10% keV scatter window, 128 × 128 matrix, 30 s per projection, 60 projections in total using 2 detectors, medium-energy general-purpose collimators, and a low-dose CT for attenuation correction. A Xeleris workstation (GE Healthcare) was used for reconstruction with the following reconstruction parameters: ordered-subset expectation maximization, 10 iterations, 6 subsets, and a Butterworth filter, with scatter correction and attenuation correction. The imaging duration was approximately 60 min, consisting of 1 whole-body planar acquisition and two 20-min SPECT/CT bed positions covering the kidneys and most of the tumor.

### Posttherapy Scan Analysis

Consecutive posttreatment scans were compared with the baseline scan performed after cycle 1. Response was qualitatively assessed using both SPECT/CT and planar images and was divided into 4 subtypes: marked reduction in tumor volume, reduction in tumor volume but with significant residual disease, stable disease, and development of new lesions. After each cycle, the clinical management for each patient was evaluated to determine whether the posttreatment imaging influenced the treatment plan. Patients whose posttreatment imaging resulted in a change in their management were further analyzed to identify the extent of the impact, which was broken down into either major or minor changes. Major changes included early discontinuation of PRRT (before completion of 4 cycles); for example, stoppage of PRRT because of progressive disease or because of marked response, delay or deferral of PRRT with a recommendation for targeted treatment of a new or growing lesion based on posttherapy imaging, or stoppage of PRRT because of developing hematologic toxicities with substantial imaging response. Minor changes included changes that resulted in tailoring of PRRT cycles to specific occurrences; for example, continuation of PRRT despite development of borderline hematologic toxicities, pseudoprogression, or hydronephrosis leading to stent placement. Additionally, we divided these changes into subgroups (objective vs. subjective changes), with objective changes indicating management changes that would be considered within the standard of practice.

**TABLE 2**
Qualitative Response Assessment on Posttreatment Imaging After Each PRRT Cycle

| SPECT/CT imaging | Total patients | Marked response | Response | Stable disease | Progression |
|---|---|---|---|---|---|
| After cycle 2 | 100 (100) | 2 (2) | 16 (16) | 80 (80) | 2 (2) |
| After cycle 3 | 85 (85) | 4 (5) | 12 (14) | 67 (79) | 2 (2) |
| After cycle 4 | 64 (64) | 4 (6) | 10 (16) | 47 (73) | 3 (5) |

Data are number and percentage.

**TABLE 3**
Types of Change in Management Based on Posttreatment Imaging and Cycles After Which Change Was Noted

| Type of management change | *n* | Cycle 2 | Cycle 3 | Cycle 4 |
|---|---|---|---|---|
| Any type | 30 | 13 | 16 | 1 |
| Major changes in management | 21 | 7 | 13 | 1 |
| Objective decisions | | | | |
| PRRT stopped because of progressive disease | 3 | 1 | 2 | 0 |
| PRRT delayed/deferred and recommendation of additional treatment for targeted treatment of new/growing lesion | 6 | 3 | 2 | 1 |
| PRRT stopped because of developing hematologic toxicities with imaging response | 7 | 1 | 6 | 0 |
| Subjective decisions* | | | | |
| PRRT stopped because of marked response | 5 | 2 | 3 | 0 |
| Minor changes in management† | 9 | 6 | 3 | 0 |
| Objective decisions | | | | |
| Hydronephrosis noted leading to stent placement | 1 | 0 | 1 | 0 |
| Subjective decisions* | | | | |
| PRRT continued despite borderline development of hematologic toxicities | 2 | 0 | 2 | 0 |
| Characterization of pseudoprogression | 6 | 6 | 0 | 0 |

*In 3 patients, more than one type of subjective or objective decisions was noted.
†Three patients had one major and one minor change in management.

### Statistical Analysis

Descriptive statistics in the form of mean, median, SD, and ranges were used to describe quantitative variables from the clinical data. Categoric variables were reported as counts and percentages. A Pearson $\chi^2$ test was conducted to assess the relationship between the grade of tumor and the rate of changes in management at a predetermined significance level of less than 0.05. If more than one type of change in management was noted in a single patient, major changes usurped minor changes and objective changes usurped subjective changes for analysis.

## RESULTS

### Patient Characteristics

In total, 107 sequential patients with well-differentiated NETs underwent PRRT from May 2016 to April 2021. Seven patients did not receive posttreatment imaging and were not included in the analysis. Patient and demographic data are provided in Table 1.

*Qualitative Response Assessment.* All 100 patients had posttreatment imaging performed after cycles 1 and 2, 85% of patients had imaging after cycle 3, and 64% of patients had imaging after cycle 4. The most common imaging response was stable disease, which was seen in 73%–80% of the posttreatment images depending on the cycle. Ten patients had a marked response seen on posttreatment imaging (Table 2).

*Change in Management Based on Posttreatment Imaging.* Posttreatment imaging resulted in a change in management in 27% (27/100) of patients, with 78% (21/27) experiencing a major change and 33% (9/27) having a minor change. When broken down on the basis of subjective or objective changes in management, 59% (16/27) experienced an objective change and 44% (12/27) experienced a

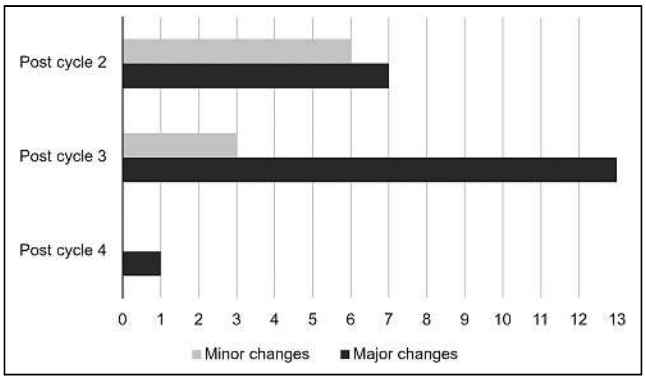


**FIGURE 1.** Impact of posttreatment imaging on management, broken down by cycle when change in management occurred.

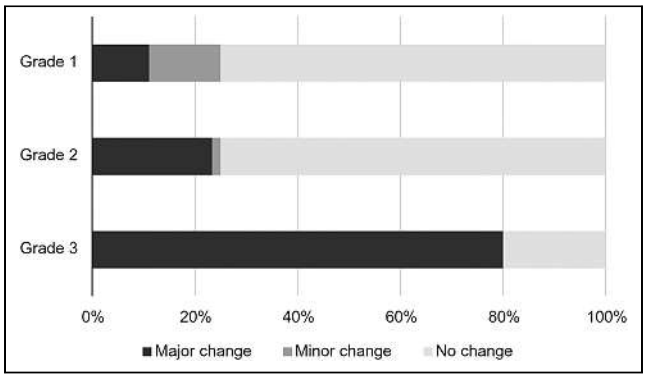


**FIGURE 2.** Change in management based on grade of tumor.

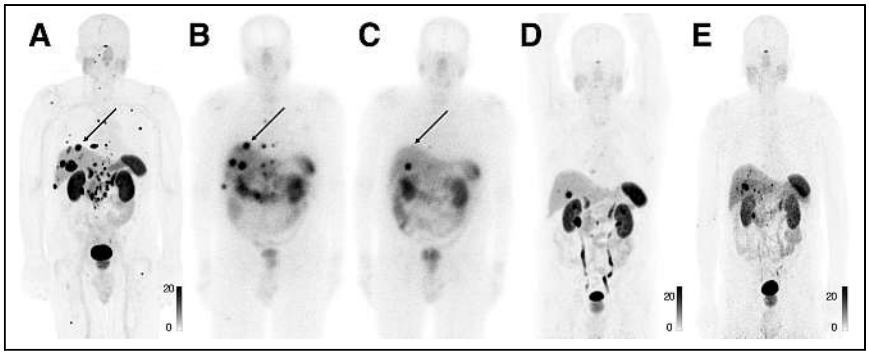


**FIGURE 3.** 80-y-old man with grade 2 small-bowel NET treated with 2 cycles of $^{177}$Lu-DOTATATE, demonstrating major change in management with stopping of PPRT in setting of marked response. (A) Pretreatment $^{68}$Ga-DOTATATE PET demonstrates SSTR-positive disease (arrow). (B) Postcycle 1 planar imaging demonstrates uptake in osseous and hepatic disease (arrow). (C) Postcycle 2 planar imaging demonstrates reduction in uptake in previously visualized disease (arrow). Treatment was stopped because of marked response, and disease progressed after 41 mo since start of treatment. (D) $^{68}$Ga-DOTATATE PET demonstrates no evidence of progression after 12 mo of PRRT. (E) $^{64}$Cu-DOTATATE PET demonstrates SSTR-positive disease on progression; however, tumor volume decreased compared with baseline.

subjective change in management. Within the 27 patients, 30 major or minor management changes were observed, with 3 patients experiencing multiple changes in management (Table 3).

Among the 21 patients exhibiting major changes, 3 had further PRRT cycles stopped because disease progression was found on posttreatment imaging, 5 had discontinuation of further cycles because of a marked response to PRRT, 6 had subsequent PRRT cycles delayed to allow for targeted treatment of a new or growing lesion, and 7 had further PRRT cycles deferred because of hematologic toxicity in the setting of imaging response to PRRT (Table 3; Supplemental Tables 1 and 2; supplemental materials are available at http://jnm.snmjournals.org). Among the patients with major changes, the change was made after cycle 2 for 7 patients (33%), after cycle 3 for 13 patients (62%), and after cycle 4 for 1 patient (5%) (Fig. 1).

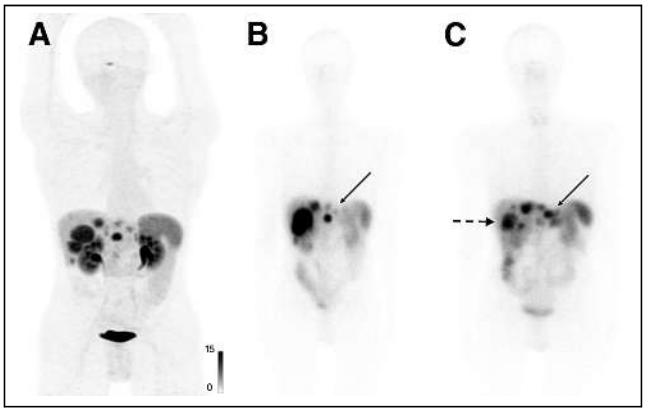


**FIGURE 4.** 43-y-old man with grade 3 pancreatic NET (Ki-67, 40%) treated with 3 cycles of $^{177}$Lu-DOTATATE, demonstrating major change in management with stopping of PRRT because of progressive disease on posttreatment imaging. (A) Pretreatment $^{68}$Ga-DOTATATE PET demonstrates liver-dominant disease. (B) Postcycle 1 planar imaging demonstrates uptake in nodal and hepatic disease (arrow). (C) Postcycle 3 planar imaging demonstrates mixed response to treatment, with increase in SSTR-avid tumor volume in midline (arrow) but slight reduction in right lobe liver disease (dotted arrowhead). Although there was partial response in some lesions, cycle 4 was not administered because of evidence of progression, and patient was converted to treatment with chemotherapy.

Of the 9 patients who had minor changes, 2 had PRRT continued for 4 cycles despite borderline hematologic toxicities, 1 had a stent placed for hydronephrosis, and 6 had pseudoprogression detected on conventional imaging and characterized on posttreatment imaging (Table 3). Among the patients with minor changes, the change was made after cycle 2 in 6 patients (67%) and after cycle 3 in 3 patients (33%); no minor change in management was noted after cycle 4 (Fig. 1).

In 3 patients, both major and minor changes were noted: in 2 patients, pseudoprogression was characterized after cycle 2 and treatment was stopped early because of a marked response after cycle 3; in 1 patient, treatment was stopped in the setting of developing hematologic toxicity with partial response, and a renal stent was placed because of marked hydronephrosis.

*Tumor Grade and Change in Management.* Patients with a higher tumor grade had a higher rate of change in management. A significant relationship was noted between the tumor grade and the change in management. Of the patients with grade 1 and 2 tumors, 23 of 95 had a change in management, whereas in patients with grade 3 tumors, 4 of 5 patients had a change in management ($P = 0.006$; Fig. 2).

*Case Examples.* Six cases are provided to highlight how posttreatment imaging results in changes in management.

The first case demonstrates a patient with a marked response. This patient was an 80-y-old man with a grade 2 pancreatic NET for whom treatment was stopped after 2 cycles because of marked response. His disease progressed 41 mo after the initiation of PRRT (Fig. 3).

The second case demonstrates a patient with progressive disease. This patient was a 43-y-old man with a grade 3 pancreatic NET for whom treatment was stopped after 3 cycles because of evidence of disease progression on posttreatment imaging. The patient was converted to treatment with chemotherapy (Fig. 4).

The third case demonstrates a patient with a major change in management due to a new lesion on posttreatment imaging. This was a 68-y-old woman with a grade 2 pancreatic NET in which a new lesion was detected on the L4 vertebra on imaging after cycle 4. The patient was given stereotactic body radiation therapy for the new vertebral lesion immediately after PRRT (Fig. 5).

The fourth case demonstrates a patient for whom treatment was halted after cycle 2 to treat a SSTR-negative lesion. This was a 76-y-old man with a grade 2 bronchial carcinoid who had a growing SSTR-negative hepatic lesion after cycle 2. The patient underwent transarterial chemoembolization for this lesion before resuming cycle 3 of PRRT (Fig. 6).

The fifth case demonstrates a patient with minor change in management with characterization of pseudoprogression after cycle 2. This was a 68-y-old woman with a grade 1 small-bowel NET treated with 4 cycles of $^{177}$Lu-DOTATATE, in which a growing hepatic lesion on MRI was characterized as pseudoprogression on posttreatment imaging at cycle 2 (Fig. 7).

The sixth case demonstrates a patient for whom PRRT was stopped because of developing hematologic toxicities in the setting of imaging response. This was a 60-y-old man with a grade 3 pancreatic NET who had a good response to PRRT except for bulky

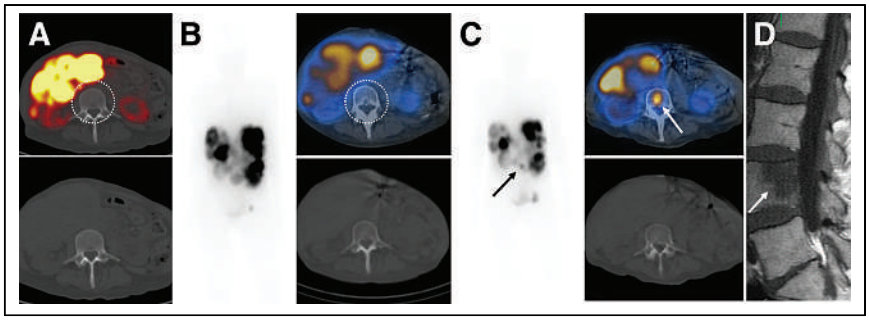


**FIGURE 5.** 68-y-old woman with grade 2 pancreatic NET treated with 4 cycles of $^{177}$Lu-DOTATATE, demonstrating major change in management with treatment of new lesion detected on posttreatment imaging. Pretreatment $^{68}$Ga-DOTATATE PET/CT (A, fused SPECT/CT [top] and CT from PET/CT [bottom]) and postcycle 1 images (B, whole-body planar image [left], fused SPECT/CT [top], CT from SPECT/CT [bottom]) demonstrate no evidence of lesion in L4 vertebra (dashed circles). (C, whole-body planar image [left], fused SPECT/CT [top], and CT from SPECT/CT [bottom]) Postcycle 4 planar and SPECT/CT imaging demonstrates uptake in L4 vertebrae with no corresponding CT abnormality (white and black arrows). Patient developed back pain at cycle 4, and MRI demonstrates new lesion (D, arrow). Patient was treated with stereotactic body radiation therapy to L4 lesion immediately after cycle 4.

pancreatic disease after cycle 3. There was an impending risk of hematotoxicity with grade 2 toxicity per the Common Terminology Criteria for Adverse Events, and PRRT was discontinued given the partial response on posttreatment imaging. SSTR-positive pancreatic disease was subsequently managed surgically after his liver disease was stable over a period of 3 mo after PRRT cycles (Supplemental Fig. 1)

## DISCUSSION

We demonstrated that 27% of patients with NETs being treated with PRRT underwent a change in management based on posttreatment SPECT/CT imaging. Patients with higher-grade tumors had a higher rate of change in management. Most of the changes in management occurred after cycles 2 and 3.

To our knowledge, this is the first description of the qualitative impact of posttreatment SPECT/CT imaging on the management of patients undergoing PRRT. Although most prior work has focused on the role of quantitative dosimetry for the management of patients, there is a growing interest in the qualitative impact of posttreatment scans as well. A previous study found that thoracoabdominal SPECT/CT imaging is the preferred method for post-PRRT imaging and that all accompanying CT images should be reviewed for additional findings, such as ascites (*14*). Although our study builds on the existing body of literature, our results demonstrate that posttreatment SPECT/CT imaging can have significant value as a qualitative marker of response, which can directly impact patient management.

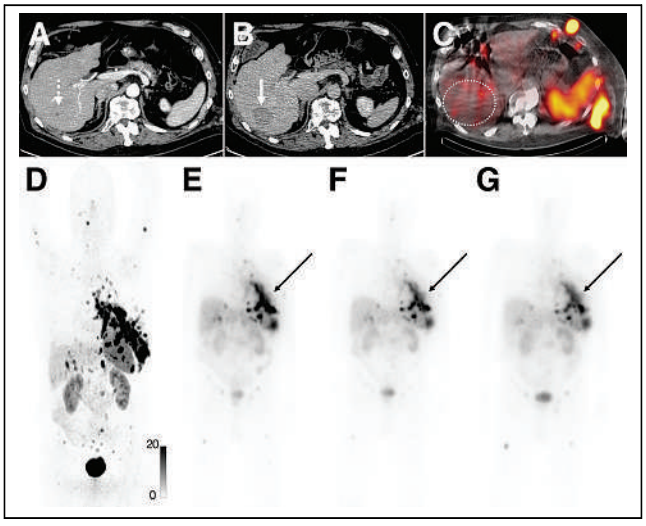


**FIGURE 6.** 78-y-old man with grade 2 bronchial carcinoid treated with 3 cycles of $^{177}$Lu-DOTATATE, demonstrating major change with delay of cycle 3 to manage growing SSTR-negative hepatic lesion after cycle 2. Pretreatment CT (A, dotted arrow) and $^{68}$Ga-DOTATATE PET (D) done within month of cycle 1 of PRRT demonstrate no evidence of hepatic lesion. CT imaging done after cycle 2 of treatment (B) demonstrates lesion in segment VI of liver (arrow). Postcycle 2 imaging (C, dotted circle) demonstrates no uptake in this hepatic lesion, although posttreatment $^{68}$Ga-DOTATATE PET from cycle 1 to cycle 3 demonstrates reduction in SSTR-positive chest wall disease (E–G, arrow). Cycle 4 was abandoned because patient had worsening of clinical symptoms.

Current guidelines do not include recommendations for performing posttreatment imaging, primarily because there is currently little direct impact of quantitative dosimetry on patient management. Our results demonstrate that qualitative posttreatment imaging is critical to patient management. Baseline imaging after cycle 1 should be obtained for comparison of future posttreatment images. Given that most changes in management occurred after cycles 2 and 3, images should be considered after these 2 cycles. The role of postcycle 4 images is unclear, but the images may be valuable for comparison to future imaging studies in patients. On the basis of our analysis, it is evident that for grade 3 tumors, posttreatment imaging should be performed after each cycle because these patients exhibit a high rate of change in management.

Although our practice is to stop PRRT early in patients with marked response, it is unclear if this is the appropriate way to manage patients. The average time to disease progression after PRRT in the subgroup in which PRRT was halted early was 27 mo. These results suggest that it is safe to stop treatment early and save the remaining cycles of treatment for subsequent use; however, further research is warranted to understand the appropriate management.

In the future, we hope that quantitative dosimetry will lead to patient-specific adjustments in treatment. There is currently extensive interest in understanding and using quantitative dosimetry in radioligand therapies (*11,12,15–17*). Obtaining posttreatment imaging for qualitative assessment allows for the accumulation of data that can be later used to understand the role of quantitative dosimetry. Although the absorbed dose in grays can be used for response assessment, our result suggests that qualitative evaluation has an important impact on patient management, and therefore, other quantitative measures such as SPECT-based SUVs may be useful as response markers without needing to be converted to grays. Although we did not evaluate SUV in our paper, our results suggest that this quantitative approach, rather than a dosimetric quantitative approach, may be a valuable tool for evaluation response to PRRT in the future. Currently, significant ongoing work implementing SPECT-based quantitative uptake will enable

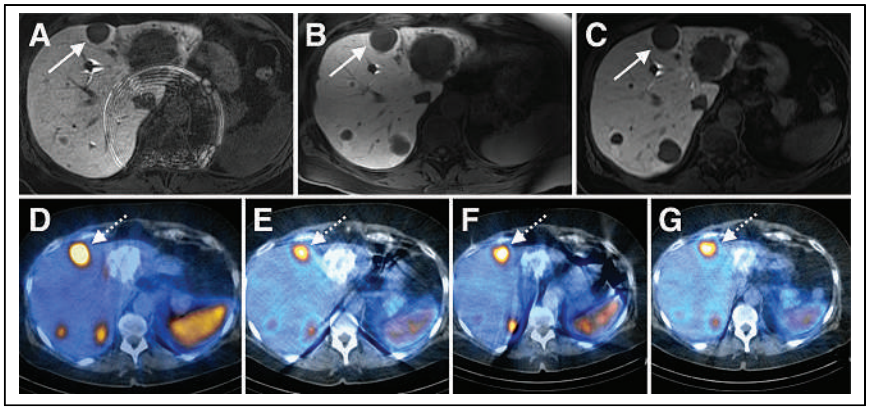


**FIGURE 7.** 68-y-old woman with grade 1 small-bowel NET (Ki-67, 1%) treated with 4 cycles of $^{177}$Lu-DOTATATE, demonstrating minor change in management with characterization of pseudoprogression after cycle 2. Pretreatment MRI (A) done 3 wk before cycle 1 demonstrates hepatic lesion with increase in size on subsequent MRI (B) done after cycle 2 of PRRT (arrow). Growth was characterized as pseudoprogression on posttreatment SPECT/CT after cycle 2 given unchanged appearance from cycle 1 (D and E, dotted arrows). Posttreatment SPECT/CT after cycles 3 and 4 (F and G, dotted arrows) demonstrates reduction in uptake of lesion from cycle 1 to cycle 4. Postcycle 4 MRI demonstrates reduction in size of hepatic lesion (C, arrow).

this approach in the future (*18,19*). An important consideration while assessing response with SUV is to consider the tumor sink effect and its impact on SUV measurements as patients start responding to PRRT (*20*).

There is controversy about when to acquire conventional imaging (CT and MRI) or functional imaging (SSTR PET) during and after PRRT. Currently, anatomic imaging remains the backbone for disease assessment, but anatomic imaging often lags functional imaging response. We identified a subgroup of patients who demonstrated progression on structural imaging but were characterized as pseudoprogression on posttreatment imaging, which suggests that posttreatment imaging may be a better approach for response assessment than anatomic imaging. Additionally, posttreatment SPECT may be able to replace SSTR PET for response evaluation. Having said this, how conventional imaging and posttreatment imaging complement each other remains an open question. Moving forward, we hope that guidelines will embrace posttreatment imaging because of its impact on patient management, as we continue to learn how to leverage the qualitative dosimetry data acquired on the images. SPECT/CT scanners are widely available in nuclear medicine departments, and most centers offering PRRT would have access to SPECT/CT scanners.

There are many limitations with this study, in particular, the small cohort of patients in which a change in management based on posttreatment imaging was noted. Second, this study is retrospective in nature, and prospective evaluation would help validate the results. Third, in the subgroup in which PRRT was stopped early because of impending hematotoxity (Common Terminology Criteria for Adverse Events grade 2 and above) in the setting of stable or partial response on posttreatment imaging, the contribution of posttreatment scans alone remains unclear because of multiple factors causing early discontinuation of PRRT. Lastly, performing mid-cycle CT or MRI is not yet standardized, and characterization of pseudoprogression may not be relevant at other institutions where these scans are not routinely performed. The cost implications and frequent visits associated with posttreatment imaging are worth considering in this context. However, a point to note is that 4 SPECT/CT scans are approximately the same cost as 1 SSTR PET scan. Additionally, we chose the 24-h time point because it is convenient for patients who might be traveling for PRRT, not to mention the benefit of not undergoing additional radionuclide injection.

## CONCLUSION

In this retrospective study, qualitative analysis of posttreatment SPECT/CT led to changes in management in 27% of patients. Patients with higher-grade tumors had a higher rate of change in management, and most of the changes in management occurred after cycles 2 and 3. It may be valuable to incorporate posttreatment imaging in the standard PRRT workflow to aid in patient management.

## DISCLOSURE

Thomas Hope has grant funding to the institution from Clovis Oncology, GE Healthcare, Lantheus, Janssen, the Prostate Cancer Foundation, Telix, and the National Cancer Institute (R01CA235741 and R01CA212148). He received personal fees from Bayer, BlueEarth Diagnostics, and Lantheus and received fees from and has an equity interest in RayzeBio and Curium. No other potential conflict of interest relevant to this article was reported.

**KEY POINTS**

**QUESTION:** What is the clinical role of posttreatment imaging during PRRT?

**PERTINENT FINDINGS:** Qualitative posttreatment imaging triggered a change in management in 27% of patients undergoing PRRT, with most changes occurring after cycle 2 (37%) and cycle 3 (59%). Higher tumor grade was associated with a higher rate of change in management.

**IMPLICATIONS FOR PATIENT CARE:** Incorporating posttreatment SPECT/CT imaging into standard PRRT workflows could potentially facilitate personalized patient management.

## REFERENCES

1. Nagtegaal ID, Odze RD, Klimstra D, et al. The 2019 WHO classification of tumours of the digestive system. *Histopathology.* 2020;76:182–188.
2. Rindi G, Klimstra DS, Abedi-Ardekani B, et al. A common classification framework for neuroendocrine neoplasms: an International Agency for Research on Cancer (IARC) and World Health Organization (WHO) expert consensus proposal. *Mod Pathol.* 2018;31:1770–1786.
3. Leoncini E, Boffetta P, Shafir M, Aleksovska K, Boccia S, Rindi G. Increased incidence trend of low-grade and high-grade neuroendocrine neoplasms. *Endocrine.* 2017;58:368–379.
4. Hope TA, Abbott A, Colucci K, et al. NANETS/SNMMI procedure standard for somatostatin receptor–based peptide receptor radionuclide therapy with $^{177}$Lu-DOTATATE. *J Nucl Med.* 2019;60:937–943.
5. Bodei L, Cremonesi M, Grana CM, et al. Peptide receptor radionuclide therapy with $^{177}$Lu-DOTATATE: the IEO phase I-II study. *Eur J Nucl Med Mol Imaging.* 2011;38:2125–2135.
6. Kong G, Thompson M, Collins M, et al. Assessment of predictors of response and long-term survival of patients with neuroendocrine tumour treated with peptide

receptor chemoradionuclide therapy (PRCRT). *Eur J Nucl Med Mol Imaging.* 2014;41:1831–1844.
7. Strosberg J, Wolin E, Chasen B, et al. Health-related quality of life in patients with progressive midgut neuroendocrine tumors treated with $^{177}$Lu-Dotatate in the phase III NETTER-1 trial. *J Clin Oncol.* 2018;36:2578–2584.
8. Strosberg J, El-Haddad G, Wolin E, et al. Phase 3 trial of $^{177}$Lu-Dotatate for midgut neuroendocrine tumors. *N Engl J Med.* 2017;376:125–135.
9. De Vries-Huizing DMV, Versleijen MWJ, Sinaasappel M, et al. Haematotoxicity during peptide receptor radionuclide therapy: baseline parameters differences and effect on patient's therapy course. *PLoS ONE.* 2021;16:e0260073.
10. Hope TA, Allen-Auerbach M, Bodei L, et al. SNMMI procedure standard/EANM practice guideline for SSTR PET: imaging neuroendocrine tumors. *J Nucl Med.* 2023;64:204–210.
11. Ilan E, Sandström M, Wassberg C, et al. Dose response of pancreatic neuroendocrine tumors treated with peptide receptor radionuclide therapy using $^{177}$Lu-DOTATATE. *J Nucl Med.* 2015;56:177–182.
12. Alipour R, Jackson P, Bressel M, et al. The relationship between tumour dosimetry, response, and overall survival in patients with unresectable neuroendocrine neoplasms (NEN) treated with $^{177}$Lu DOTATATE (LuTate). *Eur J Nucl Med Mol Imaging.* 2023;50:2997–3010.
13. Sjögreen Gleisner K, Spezi E, Solny P, et al. Variations in the practice of molecular radiotherapy and implementation of dosimetry: results from a European survey. *EJNMMI Phys.* 2017;4:28.
14. Aalbersberg EA, De Vries-Huizing DMV, Tesselaar MET, Stokkel MPM, Versleijen MWJ. Post-PRRT scans: which scans to make and what to look for. *Cancer Imaging.* 2022;22:29.
15. Jahn U, Ilan E, Sandström M, Lubberink M, Garske-Román U, Sundin A. Peptide receptor radionuclide therapy (PRRT) with $^{177}$Lu-DOTATATE: differences in tumor dosimetry, vascularity and lesion metrics in pancreatic and small intestinal neuroendocrine neoplasms. *Cancers (Basel).* 2021;13:962.
16. Del Prete M, Buteau F-A, Arsenault F, et al. Personalized $^{177}$Lu-octreotate peptide receptor radionuclide therapy of neuroendocrine tumours: initial results from the P-PRRT trial. *Eur J Nucl Med Mol Imaging.* 2019;46:728–742.
17. Garske-Román U, Sandström M, Fröss Baron K, et al. Prospective observational study of $^{177}$Lu-DOTA-octreotate therapy in 200 patients with advanced metastasized neuroendocrine tumours (NETs): feasibility and impact of a dosimetry-guided study protocol on outcome and toxicity. *Eur J Nucl Med Mol Imaging.* 2018;45:970–988.
18. Thuillier P, Maajem M, Schick U, et al. Clinical assessment of $^{177}$Lu-DOTATATE quantification by comparison of SUV-based parameters measured on both post-PRRT SPECT/CT and $^{68}$Ga-DOTATOC PET/CT in patients with neuroendocrine tumors: a feasibility study. *Clin Nucl Med.* 2021;46:111–118.
19. Wong KK, Frey KA, Niedbala J, et al. Differences in tumor-to-normal organ SUV ratios measured with $^{68}$Ga-DOTATATE PET compared with $^{177}$Lu-DOTATATE SPECT in patients with neuroendocrine tumors. *Nucl Med Commun.* 2022;43:892–900.
20. Beauregard J-M, Hofman MS, Kong G, Hicks RJ. The tumour sink effect on the biodistribution of $^{68}$Ga-DOTA-octreotate: implications for peptide receptor radionuclide therapy. *Eur J Nucl Med Mol Imaging.* 2012;39:50–56.

# Somatostatin Receptor Imaging with [$^{18}$F]FET-βAG-TOCA PET/CT and [$^{68}$Ga]Ga-DOTA-Peptide PET/CT in Patients with Neuroendocrine Tumors: A Prospective, Phase 2 Comparative Study

Suraiya Dubash*[1], Tara D. Barwick*[1,2], Kasia Kozlowski[1], Andrea G. Rockall[1], Sairah Khan[2], Sameer Khan[2], Siraj Yusuf[3], Angela Lamarca[4,5], Juan W. Valle[4,5], Richard A. Hubner[4,5], Mairéad G. McNamara[4,5], Andrea Frilling[1], Tricia Tan[6], Florian Wernig[6], Jeannie Todd[6], Karim Meeran[6], Bhavesh Pratap[1], Saleem Azeem[7], Michael Huiban[7], Nicholas Keat[7], Jingky P. Lozano-Kuehne[1,8], Eric O. Aboagye[1], and Rohini Sharma[1]

*[1]Department of Surgery and Cancer, Imperial College London, London, United Kingdom; [2]Department of Imaging, Imperial College Healthcare NHS Trust, London, United Kingdom; [3]Radiology and Nuclear Medicine Department, Royal Marsden NHS Foundation Trust, London, United Kingdom; [4]Division of Cancer Sciences, University of Manchester, Manchester, United Kingdom; [5]Department of Medical Oncology, The Christie NHS Foundation Trust, Manchester, United Kingdom; [6]Department of Endocrinology, Imperial College Healthcare NHS Trust, London, United Kingdom; [7]Invicro-London, Imperial College London, London, United Kingdom; and [8]Population Health Sciences Institute, Faculty of Medical Sciences, University of Newcastle, Newcastle, United Kingdom*

There is a clinical need for $^{18}$F-labeled somatostatin analogs for the imaging of neuroendocrine tumors (NET), given the limitations of using [$^{68}$Ga]Ga-DOTA-peptides, particularly with regard to widespread accessibility. We have shown that [$^{18}$F]fluoroethyl-triazole-[Tyr$^3$]-octreotate ([$^{18}$F]FET-βAG-TOCA) has favorable dosimetry and biodistribution. As a step toward clinical implementation, we conducted a prospective, noninferiority study of [$^{18}$F]FET-βAG-TOCA PET/CT compared with [$^{68}$Ga]Ga-DOTA- peptide PET/CT in patients with NET. **Methods:** Forty-five patients with histologically confirmed NET, grades 1 and 2, underwent PET/CT imaging with both [$^{18}$F]FET-βAG-TOCA and [$^{68}$Ga]Ga-peptide performed within a 6-mo window (median, 77 d; range, 6–180 d). Whole-body PET/CT was conducted 50 min after injection of 165 MBq of [$^{18}$F]FET-βAG-TOCA. Tracer uptake was evaluated by comparing $SUV_{max}$ and tumor-to-background ratios at both lesion and regional levels by 2 unblinded, experienced readers. A randomized, blinded reading of both scans was also then undertaken by 3 experienced readers, and consensus was assessed at a regional level. The ability of both tracers to visualize liver metastases was also assessed. **Results:** A total of 285 lesions were detected on both imaging modalities. An additional 13 tumor deposits were seen in 8 patients on [$^{18}$F]FET-βAG-TOCA PET/CT, and [$^{68}$Ga]Ga-DOTA-peptide PET/CT detected an additional 7 lesions in 5 patients. Excellent correlation in $SUV_{max}$ was observed between both tracers ($r = 0.91$; $P < 0.001$). No difference was observed between median $SUV_{max}$ across regions, except in the liver, where the median tumor-to-background ratio of [$^{18}$F]FET-βAG-TOCA was significantly lower than that of [$^{68}$Ga]Ga-DOTA-peptide ($2.5 \pm 1.9$ vs. $3.5 \pm 2.3$; $P < 0.001$). **Conclusion:** [$^{18}$F]FET-βAG-TOCA was not inferior to [$^{68}$Ga]Ga-DOTA-peptide in visualizing NET and may be considered in routine clinical practice given the longer half-life and availability of the cyclotron-produced fluorine radioisotope.

**Key Words:** [$^{18}$F]FET-βAG-TOCA; [$^{68}$Ga]Ga-DOTA-peptide; PET; neuroendocrine tumors; somatostatin receptor

**J Nucl Med 2024; 65:416–422**
DOI: 10.2967/jnumed.123.266601

Neuroendocrine neoplasms (NEN) are a heterogeneous group of malignancies arising from cells of the diffuse neuroendocrine system. Accurate diagnosis of primary lesion and staging the extent of disease dictates both management and prognosis, whereby patients with limited disease can undergo radical locoregional therapy, including surgery or ablation with curative intent, whereas systemic therapy is reserved for those with metastatic disease given with palliative intent (*1*). Accurate imaging is crucial. As 20%–50% of patients with NEN will have metastatic disease at presentation (*2*), there is a need for an imaging methodology that is both sensitive and widely accessible.

A unique characteristic of NEN is the expression of somatostatin receptors (SSTRs) on the tumor surface (*3*). The presence of SSTRs has long been exploited for imaging NEN initially with planar or SPECT imaging using [$^{111}$In]In-diethylenetriaminepentaacetic acid-octreotide and, more recently, with PET/CT using radiolabeled somatostatin analogs (SSAs). PET imaging has greater sensitivity, enhanced resolution, and better accuracy in detecting NEN compared with SPECT imaging (*4*,*5*). The most commonly used PET tracers used for the visualization of NEN are SSAs labeled with [$^{68}$Ga]Ga-DOTA-peptides, including [$^{68}$Ga]Ga-DOTA-0-Tyr3-octreotate ([$^{68}$Ga]Ga-DOTATATE) and [$^{68}$Ga]Ga-DOTA-0-Phe1-Tyr3-octreotide ([$^{68}$Ga]Ga-DOTATOC). Defining the presence of SSTRs on the tumor surface is also important for therapeutic decision making, whereby patients with SSTR-positive NEN on [$^{68}$Ga]Ga-DOTA PET may be candidates for [$^{177}$Lu]Lu-

Received Sep. 22, 2023; revision accepted Dec. 19, 2023.
For correspondence or reprints, contact Rohini Sharma (r.sharma@imperial.ac.uk).
*Contributed equally to this work.
Published online Feb. 8, 2024.

DOTA0-Tyr3-octreotate ([$^{177}$Lu]Lu-DOTATATE), a targeted radiotherapeutic that significantly improves progression-free survival in patients with metastatic disease (*6*).

Although [$^{68}$Ga]Ga-DOTA analogs have good resolution, the availability and scalability of production is limited due to the necessity of an on-site generator pertaining to the short half-life of [$^{68}$Ga]Ga. Furthermore, the [$^{68}$Ga]Ga-radiometal may accumulate within the uncinate process of the pancreas, leading to a false-positive diagnosis (*7*). Clinically, a [$^{18}$F]F-radioligand would overcome the limited capacity of [$^{68}$Ga]Ga-DOTA production while exploiting existing worldwide cyclotron manufacturing. We developed a novel [$^{18}$F]F-octreotate radioligand, [$^{18}$F]fluoroethyl-triazole-[Tyr$^3$]-octreotate ([$^{18}$F]FET-βAG-TOCA) (*8*), to obviate these limitations of [$^{68}$Ga]Ga-DOTA ligands. Previously, we showed that tumor uptake of [$^{18}$F]FET-βAG-TOCA was superior to that of [$^{68}$Ga]Ga-DOTATATE in vivo with good spatial resolution (*9*). Clinically, [$^{18}$F]FET-βAG-TOCA has favorable dosimetry and biodistribution (*8*). We therefore performed a prospective study, the primary objective of which was to assess uptake of [$^{18}$F]FET-βAG-TOCA both at lesion and regional levels. Evaluation of interreader agreement between [$^{18}$F]FET-βAG-TOCA and [$^{68}$Ga]Ga-DOTA-peptide PET was assessed as a secondary endpoint.

## MATERIALS AND METHODS

### Study Design and Participants

A prospective, multicenter, open-label, single-arm comparative imaging study consisting of an initial safety run phase (part A) followed by a noninferiority phase (part B) was conducted. The safety and biodistribution study (part A) has been reported (*8*). Patients from part A ($n = 9$) were included in the noninferiority analysis. Key eligibility criteria include histologically confirmed diagnosis of locally advanced or metastatic grade 1 or 2 neuroendocrine tumors (NET), measurable disease with at least 1 lesion with longest diameter ≥ 10 mm on conventional imaging, and positive SSTR imaging within 6 mo of study enrollment with [$^{68}$Ga]Ga-DOTA-peptide PET. Patients were not required to stop SSAs before either PET scan. Patients were recruited from 2 U.K. European Neuroendocrine Tumor Society Centers of Excellence, Imperial College Health Care NHS Trust and Christie NHS Foundation Trust, Manchester. All diagnostic tissue samples underwent central pathology review to assess eligibility. The study was approved by the Leeds East, Yorkshire and Humber National Research Committee (13/YH/0281). The administration of radioactivity was approved by the Administration of Radioactive Substances Advisory Committee (United Kingdom) (RPC 630/2892/30595). The Medicines and Health Care Products Regulatory Agency (United Kingdom) gave permission to administer the investigational medicinal product (European Clinical Trials no. 2013-003152-20). All patients provided written informed consent. The study was conducted in accordance with the Declaration of Helsinki and registered with EudraCT (2013-003152-20).

### Procedures

*PET Imaging Protocol.* At Imperial College Health Care NHS Trust, clinical PET/CT imaging was performed using [$^{68}$Ga]Ga-DOTATATE, as previously described (*10*) (mean dose injected, 134.1 MBq; mean uptake period, 37.7 min [range, 27–82 min]). At Christie NHS Foundation Trust, imaging was performed using [$^{68}$Ga]Ga-DOTANOC PET (mean dose injected: 136.2 MBq and mean uptake period of 65.2 min (range, 30–82 min) and a single case [$^{68}$Ga]Ga-DOTATOC (dose, 143 MBq; uptake time, 75 min). No clinically significant differences in DOTA tracers have been reported (*11*,*12*), and these patients were all included for the primary analysis. Imaging with [$^{18}$F]FET-βAG-TOCA was conducted after [$^{68}$Ga]Ga-DOTA-peptide PET in most cases.

[$^{18}$F]FET-βAG-TOCA was synthesized by Invicro-London (*8*); the mean dose injected was 157.7 MBq, with a mean uptake period of 37.4 min (range, 30–51 min). Images were acquired on a Siemens Biograph 6 TruePoint PET/CT scanner (with TrueV; extended field of view) at 50 min after injection (*8*). An attenuation CT scan was obtained from vertex to midthigh, immediately followed by a PET emission study at 4 min per bed position (CT settings: tube potential, 130 kV; exposure, 15 effective mAs; pitch, 1.5; slice thickness, 5 mm; rotation time, 0.6 s). Images were reconstructed using the ordered-subsets expectation maximization algorithm (4 iterations and 8 subsets) with corrections for dead time, scatter, attenuation, and radioactive decay. All images were viewed on a dedicated PET workstation (Hermes Medical Solutions).

*Image Interpretation.* Images were reviewed by 2 observers: a radiation oncologist with greater than 15 y of experience in imaging and tumor outlining and an experienced radiologist (with dual accreditation in radiology and nuclear medicine) with greater than 20 y of experience. To ensure a methodical and consistent approach, comparison of [$^{18}$F]FET-βAG-TOCA with [$^{68}$Ga]Ga-DOTA-peptide PET/CT on a patient-by-patient and lesion-by-lesion analysis was performed. Due to the large number of metastases, lesions were analyzed within the context of anatomic regions. Seven regions were defined as being the most common sites for both primary tumors and metastases: head and neck, lung, liver, pancreas, abdomen/pelvis, bone and lymph nodes. Any organ with greater than 5 lesions were truncated at 5 target lesions as in previous studies (*13*,*14*). SUV measurements ($SUV_{max}$, $SUV_{mean}$, and tumor-to-background ratio [TBR]) were obtained for lesion-by-lesion analysis by manually outlining whole tumor volumes on side-by-side analysis of both studies to ensure, in cases with innumerable lesions, that the same lesions were selected for comparative quantitative analysis. For comparative SUV analysis, only those lesions that were visible on both [$^{18}$F]FET-βAG-TOCA and [$^{68}$Ga]Ga-DOTA-peptide PET/CT were included reference (normal background) tissue were outlined using a spheric reference volume of interest (3 $cm^3$ for background liver; 2 $cm^3$ for spleen, bone, and mediastinal blood pool); 1 $cm^3$ for spheric volumes in the pancreas and sum of 3 slices manually drawn around each adrenal gland). TBR was calculated using tumor lesion $SUV_{max}$/background tissue $SUV_{mean}$ using background liver for liver metastases, background bone marrow for bone metastases, and background mediastinal blood pool for soft-tissue, nodal, and pulmonary metastases.

As the presence of liver metastases is an independent prognostic factor (*15*), subgroup analysis of SUV and TBR measurements of the liver lesions based on tumor size was performed.

*Independent Reader Evaluations.* PET/CT scans were reviewed by 3 independent imaging experts to obtain an objective interreader lesion detection rate between [$^{18}$F]FET-βAG-TOCA PET/CT and [$^{68}$Ga]Ga-DOTA-peptide PET/CT scans. To avoid recall bias, [$^{18}$F]FET-βAG-TOCA PET/CT and [$^{68}$Ga]Ga-DOTA-peptide PET/CT scans for each subject were reviewed at least 4 wk apart in random order. Readers were blinded to clinical details, type of scan and results of other imaging modalities. Readers documented the presence or absence of lesions in each of the 7 previously defined areas. Comparison was made between individual readers across both imaging modalities for interobserver agreement. After locking findings, readers then performed a final side-by-side visual analysis of the 2 sets of scans to document any discordant lesions

detected on 1 scan and not the other, to arrive at consensus between the 3 readers.

Clinical cross-sectional imaging (contrast-enhanced CT or MRI) performed within 3 mo of [$^{18}$F]FET-βAG-TOCA was reviewed by a single experienced observer with more than 20 y of experience.

### Statistical Analysis

A total of 56 patients were required based on a hypothesized 90% sensitivity, a noninferiority margin of 10%, power of 80%, and a level of significance of 5%. Descriptive statistics such as the median and interquartile range were calculated for numeric outcomes. Wilcoxon test was used for comparison of results. Pearson linear correlation test was used to evaluate correlation between $SUV_{max}$ values. Groups were compared using the $\chi^2$ test. The Cohen κ and the Fleiss κ were used to determine the level of agreement among 2 and more than 2 readers of [$^{18}$F]FET-βAG-TOCA and [$^{68}$Ga]Ga-DOTA-peptide PET/CT, respectively. A *P* value lower than 0.05 was taken to be significant. All statistical analyses were performed using SPSS version 27.0 (IBM Inc.) and Stata 16 (StataCorp LLC).

## RESULTS

### Baseline Characteristics

A total of 56 patients were enrolled to the study. Eleven patients were excluded from the primary analysis: 2 patients underwent octreotide scan, 6 patients did not have a [$^{68}$Ga]Ga-DOTA-peptide PET/CT within 6 mo of [$^{18}$F]FET-βAG-TOCA PET/CT and in a further 3 patients, central pathology review after [$^{68}$Ga]Ga-DOTA-peptide and [$^{18}$F]FET-βAG-TOCA imaging reported high-grade neuroendocrine carcinoma. A total of 45 patients were included in the final analysis. Four patients had a [$^{68}$Ga]Ga-DOTANOC PET/CT and 1 patient had [$^{68}$Ga]Ga-DOTATOC PET/CT. All remaining patients underwent [$^{68}$Ga]Ga-DOTATATE PET/CT. The median age of the enrolled population was 57 y (range, 29–81 y) and most had a diagnosis of small-bowel (44%) NET. All patients had either locally advanced (9%) or metastatic disease (91%), the commonest site of metastases being the liver (58%). Demographics and clinical characteristics of the study population are presented in Table 1. The median interval between [$^{18}$F]FET-βAG-TOCA and [$^{68}$Ga]Ga-DOTA PET/CT was 77 d (range, 6–180 d).

### Comparison of [$^{18}$F]FET-βAG-TOCA and [$^{68}$Ga]Ga-DOTA-Peptide PET

*Lesion Analysis.* On per-lesion analysis, 285 lesions were seen both on [$^{18}$F]FET-βAG-TOCA PET/CT and [$^{68}$Ga]Ga-DOTA-peptide PET/CT. Most lesions were within the liver (38.6% for both imaging modalities) followed by nodal involvement (16.8%) and bone metastases (17.1%). After unblinding of readers, side-by-side visual analysis illustrated 20 discordant lesions in 11 patients; in 6 patients additional lesions were detected on [$^{18}$F]FET-βAG-TOCA in comparison to [$^{68}$Ga]Ga-DOTA-peptide, conversely additional lesions were detected on [$^{68}$Ga]Ga-DOTA-peptide in 3 patients compared with [$^{18}$F]FET-βAG-TOCA and in 2 patients there was a mixture with some lesions detected by 1 tracer and not the other and vice versa (Table 2). [$^{18}$F]FET-βAG-TOCA detected an additional 13 lesions (6 liver metastases, 4 bone metastases, 2 nodes, and 1 small-bowel lesion) in 8 patients and [$^{68}$Ga]DOTA-peptide PET/CT detected an additional 7 lesions (4 liver, 1 bone, 1 pancreas, and 1 node) in 5 patients (Fig. 1B).

**TABLE 1**
Baseline Characteristics of Patient Cohort ($n$ = 45)

| Variable | Value* |
|---|---|
| Age (y) | |
| Median | 57 |
| Range | 29–81 |
| Sex | |
| Male | 23 (51) |
| Female | 22 (49) |
| Stage | |
| Locally advanced | 4 (9) |
| Metastatic | 41 (91) |
| Site of primary tumor | |
| Pancreas | 15 (33) |
| Small bowel | 20 (44) |
| Lung | 3 (7) |
| Other | 7 (16) |
| Grade | |
| 1 | 15 (33) |
| 2 | 21 (47) |
| Unknown | 9 (20) |
| Site of metastatic disease | |
| Liver | 27 (60) |
| Bone | 12 (27) |
| Nodes | 10 (22) |
| Lung | 3 (7) |
| Other | 17 (38) |
| Median Ki-67 (%) | 3 (7)† |
| Chromogranin A (ng/mL) | 72 (92)† |
| Previous treatment | |
| Surgery | 24 (53) |
| Somatostatin analogs | 20 (44) |
| Chemotherapy | 9 (20) |
| PRRT | 7 (16) |
| RFA | 6 (13) |
| Other | 3 (7) |

*Data are reported as numbers of patients, with percentages of patients in parentheses.
†Value in parentheses is interquartile range.
PRRT = peptide receptor radiotherapy; RFA = radiofrequency ablation.

For comparative SUV analysis, 285 lesions were included. Excellent correlation in lesion $SUV_{max}$ between imaging modalities was observed ($r$ = 0.91; $P < 0.001$) (Fig. 2). We then assessed the impact of the use of SSAs on tracer uptake. Twenty-three patients (51%) were receiving monthly injections with SSAs. No difference was observed in median $SUV_{max}$ (± SD) of [$^{18}$F]FET-βAG-TOCA of those receiving SSAs (19.2 ± 21.1) compared with those who were not (15.8 ± 15.9) ($P$ = 0.06).

*Regional Analysis.* No significant difference was noted in the median $SUV_{max}$ across all tumor regions between the 2 imaging

**TABLE 2**
Discordant Lesions Between [$^{18}$F]FET-βAG-TOCA (FETO) and [$^{68}$Ga]Ga-DOTA-peptide (DOTA) PET/CT

| Patient | Time between scans (mo) | Congruent site(s) | Lesion | Discordant lesion site | Lesion size (mm) | Scan |
|---|---|---|---|---|---|---|
| 1 | 4.6 | Liver | 1 | Liver | 7 | FETO |
| 2 | 0.2 | Liver, nodal | 2 | Node | 5 | FETO |
| | | | 3 | Node | 5 | FETO |
| 3 | 4.8 | Liver, peritoneal | 4 | Liver | 7 | FETO |
| 4 | 0.6 | Bone | 5 | Bone | 3 | FETO |
| 5 | 4.3 | Liver, nodal | 6 | Liver | 10 | DOTA |
| 6 | 2.5 | Gastric, liver | 7 | Liver | 8 | DOTA |
| | | | 8 | Liver | 8 | DOTA |
| 7 | 0.2 | Liver, nodal | 9 | Liver | 12 | DOTA |
| | | | 10 | Pancreas | 13 | DOTA |
| 8 | 1.6 | Bone, nodal | 11 | Bone | 10 | FETO |
| | | | 12 | Bone | 4 | FETO |
| | | | 13 | Bone | 4 | FETO |
| | | | 14 | Small bowel | 5 | FETO |
| | | | 15 | Node | 15 | DOTA |
| 9 | 1.1 | Liver | 16 | Liver | 9 | FETO |
| | | | 17 | Liver | 9 | FETO |
| 10 | 3.7 | Liver, nodal | 18 | Liver | 5 | FETO |
| 11 | 4.4 | Liver, bone | 19 | Bone | 3 | DOTA |
| | | | 20 | Liver | 8 | FETO |

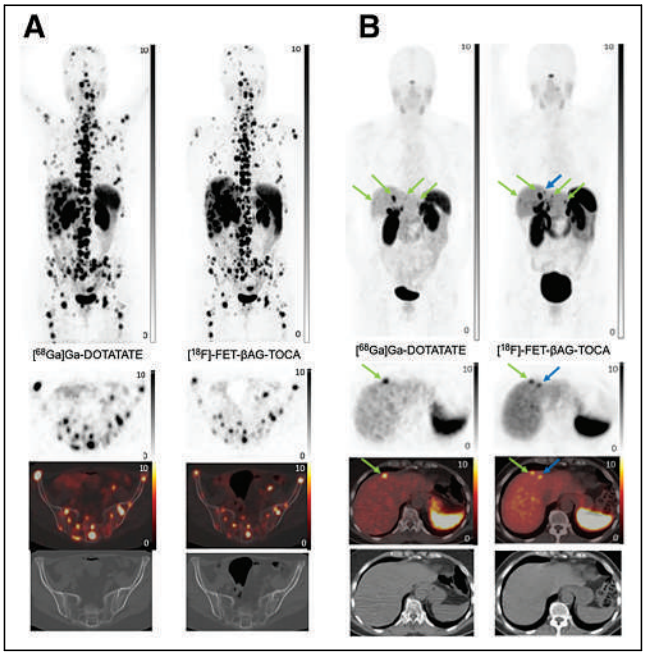


**FIGURE 1.** (A) Congruent imaging: [$^{68}$Ga]Ga-DOTATATE imaging and [$^{18}$F]FET-βAG-TOCA imaging (maximum-intensity projection [MIP], axial PET, fused and CT images) in metastatic small-bowel NEN with widespread liver and bone metastases. (B) Incongruent imaging: [$^{68}$Ga]Ga-DOTATATE imaging and [$^{18}$F]FET-βAG-TOCA imaging (MIP, axial PET, fused and CT images) performed 4 wk apart in metastatic ileal NEN with liver metastases (green arrows), which are more visible on [$^{18}$F]FET-βAG-TOCA. Additional lesion is detected on [$^{18}$F]FET-βAG-TOCA (blue arrow).

modalities (Table 3). The highest median [$^{18}$F]FET-βAG-TOCA $SUV_{max}$ was observed in pancreatic lesions (median $SUV_{max}$, $24.5 \pm 24.9$) and the lowest was observed in bone (median $SUV_{max}$, $9.7 \pm 8.8$).

Both tracers demonstrated comparable distribution in background organs (spleen, pancreas, adrenals, bone) except for increased background hepatic activity on [$^{18}$F]FET-βAG-TOCA PET/CT (Supplemental Fig. 1) (supplemental materials are available at http://jnm.snmjournals.org). Low physiologic uptake of [$^{18}$F]FET-βAG-TOCA was observed, as previously described in the pituitary, salivary glands, spleen and thyroid gland (*8*). There

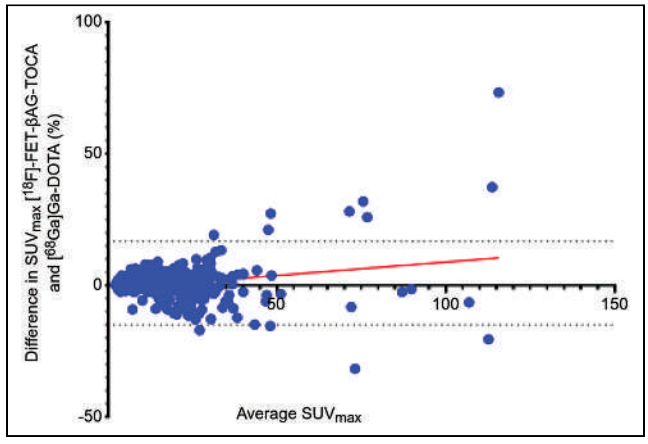


**FIGURE 2.** Bland–Altman plot of difference in $SUV_{max}$ between [$^{18}$F]FET-βAG-TOCA and [$^{68}$Ga]Ga-DOTA-peptide.

**TABLE 3**
Median Tumor Uptake ($SUV_{max}$) and Tumor-to-Background Ratio (TBR) of [$^{18}$F]FET-βAG-TOCA and [$^{68}$Ga]Ga-DOTA-peptide per Anatomic Region

| Region | No. of lesions | [$^{18}$F]FET-βAG-TOCA | | [$^{68}$Ga]Ga-DOTA-peptide | | | Median TBR with: | | |
|---|---|---|---|---|---|---|---|---|---|
| | | Median $SUV_{max}$ | Range | Median $SUV_{max}$ | Range | *P* | [$^{18}$F]FET-βAG-TOCA | [$^{68}$Ga]Ga-DOTA-peptide | *P* |
| Head and neck | 3 | 12.4 | 10.4–27.7 | 6.9 | 6.4–23.4 | 0.5 | 29.8 | 12.2 | 0.3 |
| Liver | 110 | 19.59 | 7.2–132.4 | 20.6 | 6.7–95.1 | 0.5 | 2.5 | 3.5 | <0.001 |
| Bone | 49 | 9.7 | 2.2–37.0 | 7.2 | 1.9–38.8 | 0.5 | 12.5 | 10.1 | 0.5 |
| Lung | 11 | 10.4 | 5.3–42.1 | 9.4 | 2.2–38.0 | 0.9 | 14.6 | 15.4 | 0.4 |
| Pancreas | 28 | 24.5 | 4.2–85.8 | 21.9 | 6.4–88.4 | 0.8 | 35.2 | 36.6 | 0.6 |
| Abdomen/pelvis | 36 | 18.8 | 2.7–152.3 | 21.2 | 4.1–110.3 | 0.6 | 23.5 | 23.6 | 0.1 |
| Lymph nodes | 48 | 18.0 | 3.4–102.4 | 17.0 | 3.1–122.9 | 0.7 | 21.1 | 29.7 | 0.5 |

was a statistical difference observed in median TBR for liver lesions with [$^{18}$F]FET-βAG-TOCA compared with [$^{68}$Ga]Ga-DOTA-peptide PET/CT (2.52 ± 1.88 vs. 3.50 ± . 2.35; $P <$ 0.001). No other differences in regional TBR were observed (Table 3).

### Interreader Agreement

Interreader agreement across tumor sites was considered. It was possible to estimate with 95% confidence a κ-agreement of 86% with an SE of 10% assuming 90% positive ratings among raters for a total of 45 subjects. Agreement was significantly higher in the liver with [$^{68}$Ga]Ga-DOTA-peptide (κ = 0.3) than with [$^{18}$F]FET-βAG-TOCA (κ = 0.05) ($P <$ 0.001). In particular, when considering the liver, discrepancies in reads were noted in 4 patients on [$^{18}$F]FET-βAG-TOCA imaging, 3 of whom did not have liver metastases but were thought to be present by 1 of the 3 readers. In contrast, only 1 patient was felt to have liver metastases on [$^{68}$Ga]Ga-DOTA-peptide PET, where none were present by 1 of the 3 readers. No significant differences in agreement were observed across other sites (Table 4).

### Liver Metastases

As the presence of liver metastases is an independent prognostic factor, we performed subgroup analysis of uptake in the liver lesions based on lesion size (<1 cm, 1.0–2 cm, >2.1 cm). Of the 110 liver metastases, 28 lesions were smaller than 1 cm, 52 were 1–2 cm, and 30 were larger than 2.1 cm. When considering $SUV_{max}$, no significant difference in uptake was observed with [$^{18}$F]FET-βAG-TOCA in lesions smaller than 1 cm (15.1 ± 7.9) and those 1–2 cm (22.7 ± 19.9) compared with [$^{68}$Ga]Ga-DOTATATE (<1 cm, 12.2 ± 6.9 [$P$ = 0.2]; 1–2 cm, 22.4 ± 14.5 [$P$ = 0.4]). A significantly lower median TBR was observed for lesions 1–2 cm with [$^{18}$F]FET-βAG-TOCA (3.3 ± 2.1) compared with [$^{68}$Ga]Ga-DOTA-peptide (4.5 ± 2.4) ($P$ = 0.050. No difference was observed in median TBR for lesions smaller than 1 cm ([$^{18}$F]FET-βAG-TOCA, 1.9 ± 0.8; [$^{68}$Ga]Ga-DOTA-peptide, 2.3 ± 1.3) ($P$ = 0.4). Overall, the [$^{18}$F]FET-βAG-TOCA median TBR was significantly lower in the liver than the [$^{68}$Ga]Ga-DOTA-peptide median TBR (2.5 ± 1.9 vs. 3.5 ± 2.3; $P <$ 0.001).

## DISCUSSION

The superiority of [$^{68}$Ga]Ga-DOTA-peptide PET/CT over [$^{111}$In]In-octreotide SPECT/CT and contrast CT imaging for the visualization of NET is well established (*4*,*5*). However, the use of [$^{68}$Ga]Ga necessitates the presence of an onsite (limited life span) generator, limiting the scalability and availability of [$^{68}$Ga]Ga-DOTA-peptide radioligands, such that many patients are not able to access [$^{68}$Ga]Ga-DOTA-peptide for diagnosis, treatment planning or assessment of disease progression. To alleviate these issues, we developed a GMP compliant [$^{18}$F]F-octreotate radiopharmaceutical, [$^{18}$F]FET-βAG-TOCA. We have previously reported [$^{18}$F]FET-βAG-TOCA to be safe, with good dosimetry and biodistribution, that highlights tumor lesions with high contrast (*8*). In this prospective study, we have shown that [$^{18}$F]FET-βAG-TOCA is excellent in detecting lesions and is not inferior to [$^{68}$Ga]Ga-DOTA-peptide- PET/CT for the detection of NET. We have also shown the ability of [$^{18}$F]FET-βAG-TOCA in detecting small liver lesions, an important consideration given the prognostic impact of liver metastases (*15*).

We observed no significant difference in tumoral $SUV_{max}$ both on lesion and regional bases between scan types confirming the noninferiority of [$^{18}$F]FET-βAG-TOCA for imaging NET. Observed $SUV_{max}$ values of [$^{18}$F]FET-βAG-TOCA are consistent with the high affinity of [$^{18}$F]FET-βAG-TOCA for SSTR2 binding ($IC_{50}$,1.6 ± 0.2 nM) (*16*). The use of SSAs had no impact on [$^{18}$F]FET-βAG-TOCA $SUV_{max}$, an important consideration, given the widespread use of these agents. Moreover, there was excellent correlation between the 2 tracers as confirmed by interobserver agreement across most regions.

The liver is the commonest site of metastases and is an independent prognostic factor in patients with NET (*15*). Background liver uptake was significantly lower with [$^{18}$F]FET-βAG-TOCA compared with [$^{68}$Ga]Ga-DOTA-peptide. This difference in uptake can be attributed to differences in elimination. [$^{18}$F]FET-βAG-TOCA is eliminated by both the biliary and renal system, whereas [$^{68}$Ga]Ga-DOTA-peptide is eliminated predominantly through the kidneys. Hepatic clearance and slow clearance through the common bile duct may contribute to the higher background uptake observed on [$^{18}$F]FET-βAG-TOCA imaging. As a result of this difference in background uptake, a significant difference in TBR in the liver between the 2 tracers was observed. The higher liver background activity may have contributed to the difference observed on interreader agreement within the liver, whereby observers were less confident in 3 cases about the absence of metastases in "normal liver", a concept that needs exploring in future work. However, of the 20 discordant lesions, 10 were in the

**TABLE 4**
Interrater Agreement for [$^{18}$F]FET-βAG-TOCA and [$^{68}$Ga]Ga-DOTA-peptide per Anatomic Region Between All 4 Raters

| Scan site | Agreement between raters 1, 2, 3, and 4 for: | | | | | | P for [$^{18}$F]FET-βAG-TOCA vs. [$^{68}$Ga]Ga-DOTA-peptide |
|---|---|---|---|---|---|---|---|
| | [$^{18}$F]FET-βAG-TOCA | | | [$^{68}$Ga]Ga-DOTA-peptide | | | |
| | Agreement (%) | κ* | P | Agreement (%) | κ* | P | |
| Head and neck | 97.4 | 0.2 (−0.01 to 0.3) | <0.001 | 97.8 | −0.01 (−0.02 to −0.006) | 0.6 | 0.04 |
| Lung | 97.8 | −0.01 (−0.02 to −0.01) | 0.6 | 98.9 | −0.01 (NC) | 0.5 | NC |
| Liver | 94.4 | −0.03 (−0.05 to −0.006) | 0.7 | 98.5 | 0.3 (NC) | <0.001 | <0.001 |
| Pancreas | 89.3 | 0.2 (0.1 to 0.3) | <0.001 | 91.5 | 0.1 (−0.03 to 0.3) | 0.05 | 0.2 |
| Abdomen/pelvis | 88.5 | 0.0005 (−0.07 to 0.2) | 0.5 | 95.2 | 0.1 (−0.02 to 0.3) | 0.04 | 0.3 |
| Bone | 98.5 | 0.3 (NC) | <0.001 | 100.0 | NC | NC | NC |
| Lymph nodes | 97.4 | 0.3 (−0.01 to 0.3) | <0.001 | 96.3 | 0.2 (−0.02 to 0.3) | 0.008 | 0.7 |

*Values in parentheses are 95% CIs.
NC = noncalculable.

liver, 6 were only detected on [$^{18}$F]FET-βAG-TOCA and 4 with [$^{68}$Ga]Ga-DOTA-peptide imaging. The management in these cases did not change as the patients already had multiple liver metastases.

Since $^{18}$F has a shorter positron range and higher positron yield than $^{68}$Ga, one might postulate that [$^{18}$F]FET-βAG-TOCA imaging could detect smaller lesions compared with [$^{68}$Ga]Ga-DOTA-peptide imaging. On the 20 discordant lesions, 13 were detected only on [$^{18}$F]FET-βAG-TOCA, and all were less than or equal to 10 mm in size, whereas 7 were detected only on[$^{68}$Ga]Ga-DOTA-peptide imaging, of which all were greater than or equal to 8 mm in size except for 1 (Table 2). The latest digital PET detector technology may improve detection of small lesions.

The use of [$^{18}$F]FET-βAG-TOCA PET/CT may be considered in the clinical setting where difficulties accessing [$^{68}$Ga]Ga-DOTA-peptide have led to longer waiting times for patients, particularly where delivery of [$^{68}$Ga]Ga-DOTA-peptide is limited to those centers within close proximity to the gallium generator. Delivery of low yields of [$^{68}$Ga]Ga-DOTA-peptide is also a common problem and can lead to last minute cancellation of scanning slots with an ever-increasing burden on nuclear medicine departments. Recent work has explored the utility of [$^{18}$F]F-AIF-1,4,7-triazacyclononane-1,4,7-tri-acetate-octreotide ([$^{18}$F]F-AIF-NOTA-octreotide compared with [$^{68}$Ga]Ga-DOTATATE/NOC in patients with NET (*17*). In this study the noninferiority of $^{18}$F-labeled AIF-NOTA-octreotide was illustrated; the authors reported high physiologic uptake in the pancreas, necessitating the need for additional cross-sectional imaging to delineate any pancreatic lesion, a feature not observed with [$^{18}$F]FET-βAG-TOCA (*8*). Moreover, $SUV_{max}$ was lower than [$^{68}$Ga]Ga-DOTATATE and TBR within the bone was particularly lower, which may have implications in assessing disease response to therapy within the bone. [$^{64}$Cu]Cu-DOTATATE has also recently been studied, with comparable results to [$^{68}$Ga]Ga-DOTATOC, albeit with a higher radiation burden, which may not be acceptable to users, particularly as patients typically undergo multiple PET/CT studies during their disease journey (*18*).

However, there are some key limitations. As [$^{18}$F]FET-βAG-TOCA imaging was performed after [$^{68}$Ga]Ga-DOTA-peptide imaging in most patients, potential sequence effects cannot be excluded, but most were performed within 6 mo and no change in treatment occurred between both scans. Moreover, due to the variation in time interval between the 2 scans, changes in tumor composition or size and the possible change in SSTR density cannot be excluded (*14*). Although most patients underwent [$^{68}$Ga]Ga-DOTATATE imaging, a number were imaged with other [$^{68}$Ga]Ga-DOTA-peptide radioligands, the impact of which remains unclear. Finally, PET findings were not validated by a reference imaging standard such that sensitivity or specificity cannot be established.

## CONCLUSION

In this prospective head-to-head comparison of [$^{18}$F]FET-βAG-TOCA PET/CT and [$^{68}$Ga]Ga-DOTA-peptide PET/CT we have shown excellent tumoural uptake and noninferiority at both lesion and regional levels. [$^{18}$F]FET-βAG-TOCA could potentially be used clinically as an alternate to [$^{68}$Ga]Ga-DOTA-peptide. Further developments could lead to its use as a theranostic agent in locally advanced and metastatic NET.

## DISCLOSURE

This work was funded by Medical Research Council Developmental Clinical Studies grant MR/J007986/1. The authors acknowledge

infrastructure support from the National Institute for Health Research Imperial Biomedical Research Centre and the Imperial College Experimental Cancer Medicine Centre. Rohini Sharma received grant funding from Incyte, AAA, Boston Scientific, and Terumo. Mairéad McNamara received research grant support from Servier, Ipsen, NuCana, and AstraZeneca, travel and accommodation support from AAA, Ipsen, and AstraZeneca, and speaker honoraria from AAA and AstraZeneca and is on the advisory boards for Incyte and AstraZeneca. Andrea Frilling received grants from Novartis, AAA, Ipsen, Sirtex, and Clifton, all unrelated to the submitted work. Angela Lamarca received travel and educational support from Ipsen, Pfizer, Bayer, AAA, SirtEx, Novartis, Mylan, Delcath Advanz Pharma, and Roche, speaker honoraria from Merck, Pfizer, Ipsen, Incyte, AAA/Novartis, QED, Servier, AstraZeneca, EISAI, Roche, Advanz Pharma, and MSD, advisory and consultancy honoraria from EISAI, Nutricia, Ipsen, QED, Roche, Servier, Boston Scientific, Albireo Pharma, AstraZeneca, Boehringer Ingelheim, GENFIT, TransThera Biosciences, Taiho, and MSD, and principal investigator–associated institutional funding from QED, Merck, Boehringer Ingelheim, Servier, AstraZeneca, GenFit, Albireo Pharma, Taiho, TransThera, and Roche and is a member of the Knowledge Network and NETConnect Initiatives funded by Ipsen. Juan Valle received personal fees from Agios, AstraZeneca, Baxter, Genoscience Pharma, Hutchison Medipharma, Imaging Equipment Ltd (AAA), Incyte, Ipsen, QED, Servier, Sirtex, and Zymeworks and grants, personal fees, and nonfinancial support from NuCana, all outside the submitted work. Richard Hubner received consultancy fees from Beigene, Ipsen, and Novartis and travel and accommodation support from Roche. The views expressed are those of the authors and not necessarily those of the NIHR or the Department of Health and Social Care. No other potential conflict of interest relevant to this article was reported.

**KEY POINTS**

**QUESTION:** How does the novel fluorine-labeled PET tracer [$^{18}$F]FET-βAG-TOCA compare with [$^{68}$Ga]Ga-DOTA-peptide PET/CT for the detection of NET?

**PERTINENT FINDINGS:** In a prospective, noninferiority study in 45 patients with histologically confirmed NET, we observed excellent correlations between both tracers with no difference across median $SUV_{max}$.

**IMPLICATIONS FOR PATIENT CARE:** [$^{18}$F]FET-βAG-TOCA may be considered in routine clinical practice for imaging NET.

## REFERENCES


1. Pavel M, Oberg K, Falconi M, et al. Gastroenteropancreatic neuroendocrine neoplasms: ESMO Clinical Practice Guidelines for diagnosis, treatment and follow-up. *Ann Oncol.* 2020;31:844–860.
2. Yao JC, Hassan M, Phan A, et al. One hundred years after "carcinoid": epidemiology of and prognostic factors for neuroendocrine tumors in 35,825 cases in the United States. *J Clin Oncol.* 2008;26:3063–3072.
3. Klöppel G, Couvelard A, Perren A, et al. ENETS Consensus Guidelines for the Standards of Care in Neuroendocrine Tumors: towards a standardized approach to the diagnosis of gastroenteropancreatic neuroendocrine tumors and their prognostic stratification. *Neuroendocrinology.* 2009;90:162–166.
4. Sadowski SM, Neychev V, Millo C, et al. Prospective study of $^{68}$Ga-DOTATATE positron emission tomography/computed tomography for detecting gastro-enteropancreatic neuroendocrine tumors and unknown primary sites. *J Clin Oncol.* 2016; 34:588–596.
5. Krausz Y, Freedman N, Rubinstein R, et al. $^{68}$Ga-DOTA-NOC PET/CT imaging of neuroendocrine tumors: comparison with $^{111}$In-DTPA-octreotide (OctreoScan®). *Mol Imaging Biol.* 2011;13:583–593.
6. Strosberg J, El-Haddad G, Wolin E, et al. Phase 3 trial of $^{177}$Lu-Dotatate for midgut neuroendocrine tumors. *N Engl J Med.* 2017;376:125–135.
7. Mapelli P, Tam HH, Sharma R, Aboagye EO, Al-Nahhas A. Frequency and significance of physiological versus pathological uptake of $^{68}$Ga-DOTATATE in the pancreas: validation with morphological imaging. *Nucl Med Commun.* 2014;35:613–619.
8. Dubash SR, Keat N, Mapelli P, et al. Clinical translation of a click-labeled $^{18}$F-octreotate radioligand for imaging neuroendocrine tumors. *J Nucl Med.* 2016;57: 1207–1213.
9. Iddon L, Leyton J, Indrevoll B, et al. Synthesis and in vitro evaluation of [$^{18}$F]fluoroethyl triazole labelled [Tyr3]octreotate analogues using click chemistry. *Bioorg Med Chem Lett.* 2011;21:3122–3127.
10. Sharma R, Wang WM, Yusuf S, et al. $^{68}$Ga-DOTATATE PET/CT parameters predict response to peptide receptor radionuclide therapy in neuroendocrine tumours. *Radiother Oncol.* 2019;141:108–115.
11. Koopmans KP, de Vries EG, Kema IP, et al. Staging of carcinoid tumours with $^{18}$F-DOPA PET: a prospective, diagnostic accuracy study. *Lancet Oncol.* 2006;7:728–734.
12. Wild D, Bomanji JB, Benkert P, et al. Comparison of $^{68}$Ga-DOTANOC and $^{68}$Ga-DOTATATE PET/CT within patients with gastroenteropancreatic neuroendocrine tumors. *J Nucl Med.* 2013;54:364–372.
13. Koopmans KP, Neels ON, Kema IP, et al. Molecular imaging in neuroendocrine tumors: molecular uptake mechanisms and clinical results. *Crit Rev Oncol Hematol.* 2009;71:199–213.
14. Poeppel TD, Binse I, Petersenn S, et al. $^{68}$Ga-DOTATOC versus $^{68}$Ga-DOTATATE PET/CT in functional imaging of neuroendocrine tumors. *J Nucl Med.* 2011;52:1864–1870.
15. Dasari A, Shen C, Halperin D, et al. Trends in the incidence, prevalence, and survival outcomes in patients with neuroendocrine tumors in the United States. *JAMA Oncol.* 2017;3:1335–1342.
16. Leyton J, Iddon L, Perumal M, et al. Targeting somatostatin receptors: preclinical evaluation of novel $^{18}$F-fluoroethyltriazole-Tyr3-octreotate analogs for PET. *J Nucl Med.* 2011;52:1441–1448.
17. Pauwels E, Cleeren F, Tshibangu T, et al. $^{18}$F-AlF-NOTA-octreotide outperforms $^{68}$Ga-DOTATATE/NOC PET in neuroendocrine tumor patients: results from a prospective, multicenter study. *J Nucl Med.* 2023;64:632–638.
18. Johnbeck CB, Knigge U, Loft A, et al. Head-to-head comparison of $^{64}$Cu-DOTATATE and $^{68}$Ga-DOTATOC PET/CT: a prospective study of 59 patients with neuroendocrine tumors. *J Nucl Med.* 2017;58:451–457.

# Prostate-Specific Membrane Antigen–Targeted Radioguided Pelvic Lymph Node Dissection in Newly Diagnosed Prostate Cancer Patients with a Suspicion of Locoregional Lymph Node Metastases: The DETECT Trial

Melline G.M. Schilham[1–3], Diederik M. Somford[2,3], Heidi V.N. Küsters-Vandevelde[4], Rick Hermsen[5], Jean Paul A. van Basten[2,3], Robert J. Hoekstra[2,6], Tom W.J. Scheenen[1], Martin Gotthardt[1], J.P. Michiel Sedelaar[2,7], and Mark Rijpkema[1]

*[1]Department of Medical Imaging, Radboud University Medical Center, Nijmegen, The Netherlands; [2]Prosper Prostate Cancer Clinics, Nijmegen/Eindhoven, The Netherlands; [3]Department of Urology, Canisius Wilhelmina Hospital, Nijmegen, The Netherlands; [4]Department of Pathology, Canisius Wilhelmina Hospital, Nijmegen, The Netherlands; [5]Department of Nuclear Medicine, Canisius Wilhelmina Hospital, Nijmegen, The Netherlands; [6]Department of Urology, Catharina Hospital, Eindhoven, The Netherlands; and [7]Department of Urology, Radboud University Medical Center, Nijmegen, The Netherlands*

Prostate-specific membrane antigen (PSMA)–targeted radioguided surgery (RGS) aims to optimize the peroperative detection and removal of PSMA-avid lymph node (LN) metastases (LNMs) and has been described in patients with recurrent prostate cancer (PCa). In newly diagnosed PCa patients undergoing pelvic LN dissections, PSMA RGS could guide the urologist toward PSMA-expressing LNMs as identified on preoperative $^{18}$F-PSMA PET/CT imaging. The objective was to evaluate the safety and feasibility of $^{111}$In-PSMA RGS in primary PCa patients with one or more suggestive LNs on preoperative $^{18}$F-PSMA PET/CT. **Methods:** This prospective, phase I/II study included 20 newly diagnosed PCa patients with at least 1 suggestive LN on preoperative $^{18}$F-PSMA PET/CT. PSMA RGS was performed 24 h after $^{111}$In-PSMA-I&T administration, and postoperative $^{18}$F-PSMA PET/CT was performed to verify successful removal of the suggestive lesions. The primary endpoint was determination of the safety and feasibility of $^{111}$In-PSMA RGS. Safety was assessed by monitoring adverse events. Feasibility was described as the possibility to peroperatively detect suggestive LNs as identified on preoperative imaging. Secondary outcomes included the accuracy of $^{111}$In-PSMA RGS compared with histopathology, tumor- and lesion-to-background ratios, and biochemical recurrence. **Results:** No tracer-related adverse events were reported. In 20 patients, 43 of 49 (88%) $^{18}$F-PSMA PET–suggestive lesions were successfully removed. $^{111}$In-PSMA RGS facilitated peroperative identification and resection of 29 of 49 (59%) RGS-target lesions, of which 28 (97%) contained LNMs. Another 14 of 49 (29%) resected LNs were not detected with $^{111}$In-PSMA RGS, of which 2 contained metastases. **Conclusion:** $^{111}$In-PSMA RGS is a safe and feasible procedure that allows peroperative detection of $^{18}$F-PSMA PET/CT–suggestive lesions in newly diagnosed PCa patients. The use of a radioactive PSMA tracer and a detection device (γ-probe) during surgery helps in identifying LNs that were suggestive of PCa metastases on the $^{18}$F-PSMA PET/CT before surgery and thus may improve the peroperative identification and removal of these LNs.

Received Aug. 10, 2023; revision accepted Nov. 7, 2023.
For correspondence or reprints, contact Melline G.M. Schilham (melline.schilham@radboudumc.nl).
Published online Jan. 4, 2024.


**Key Words:** lymph node dissection; prostate cancer; PSMA; radioguided surgery

**J Nucl Med 2024; 65:423–429**
DOI: 10.2967/jnumed.123.266495

In newly diagnosed prostate cancer (PCa) patients, determination of the presence and localization of lymph node (LN) metastases (LNMs) is crucial for clinical decision-making and treatment planning, as nodal involvement correlates with recurrence and these patients could benefit from adjuvant therapies (*1*,*2*). To date, extended pelvic LN dissection (ePLND) is still considered the best available tool for nodal staging. Although the therapeutic impact of ePLND remains controversial, some evidence suggests that removal of all LNMs could maximize locoregional disease control and potentially impact oncologic outcomes in selected patients (*3*). The radicality of ePLND depends on the template's extent and resection adequacy, and research indicated that up to one third of the nodes, including 13% with LNMs, can be missed (*4*,*5*).

Conventional imaging modalities have been of limited value in nodal staging, because of low sensitivity (<40%) (*6*). The introduction of PET tracers targeting the cell-surface glycoprotein prostate-specific membrane antigen (PSMA) has significantly altered imaging strategies in PCa (*7*). The overexpression of PSMA on most PCa cells makes it a valuable target for PSMA PET/CT, which is currently increasingly used to preoperatively detect and map potential LNMs. Although PSMA PET/CT improved the detection of potential LNMs compared with conventional imaging, its sensitivity remains insufficient (13%–85%) to completely replace ePLND (*8*–*10*). Nevertheless, recent studies have shown that the presence of suggestive LNs on preoperative PSMA PET/CT is associated with an increased risk of biochemical persistence and biochemical recurrence after robot-assisted radical prostatectomy combined with ePLND (*2*,*11*). This could to some extent be associated with inadequate detection and subsequent resection of all LNMs during surgery.

PSMA-targeted radioguided surgery (RGS) is a novel technique with the aim of optimizing peroperative detection and removal of

PCa lesions. This technique uses PSMA ligands labeled with a γ-emitting radionuclide (e.g., $^{111}$In or $^{99m}$Tc) to facilitate peroperative detection of PSMA-expressing PCa tissue, that is, LNM. Several studies have shown the safety and feasibility of PSMA RGS using different PSMA ligands in patients with recurrent PCa (*12*–*17*). Hence, the question was raised of whether $^{111}$In-PSMA RGS could also optimize ePLND in the primary setting. If so, $^{111}$In-PSMA RGS could increase the probability of complete removal and subsequent accurate staging and thus potentially improve prognosis in a selected group of pN1 patients with limited nodal involvement (*3*,*18*).

In this prospective study, we evaluated the safety and feasibility of $^{111}$In-PSMA-I&T RGS in 20 newly diagnosed PCa patients with at least 1 suggestive LN on preoperative $^{18}$F-PSMA PET/CT imaging, with the aim of peroperatively detecting the $^{18}$F-PSMA PET–suggestive lesions.

## MATERIALS AND METHODS

### Study Design and Patient Population

This investigator-initiated prospective study was approved by the Institutional Review Board (CMO-Arnhem-Nijmegen) and registered at ClinicalTrials.gov (NCT04300673). Between September 2020 and April 2022, 20 patients with histopathologically proven PCa were included. Written informed consent was obtained from all. We selected patients without prior active PCa treatment who were scheduled for ePLND with robot-assisted radical prostatectomy or ePLND before radiotherapy on the prostate and who had at least 1 PSMA-suggestive LN within the ePLND template on $^{18}$F-PSMA PET/CT. Exclusion criteria were unequivocal evidence of metastatic disease outside the pelvic region and prior pelvic nodal surgery. Adjuvant therapy (i.e., radiotherapy or androgen deprivation therapy) was applied in accordance with local guidelines.

### Preoperative Procedure

Preoperative $^{18}$F-PSMA PET/CT was part of preoperative staging according to local protocols. Scans were reviewed by experienced nuclear medicine physicians. For suggestive lesions, anatomic location and level of suspicion were systematically reported. Level of suspicion was defined on a 5-point Likert scale expressing the probability of metastasis presence in a LN, based on tracer uptake, LN size, and location as described in the PSMA reporting and data system classification by Rowe et al. (*19*). LNs with a level of suspicion of at least 3 were defined as RGS-target lesions. One day before scheduled ePLND, a single dose of 157 MBq (range, 151.8–164.2 MBq) of $^{111}$In-PSMA-I&T was intravenously injected.

### Surgical Procedure

All procedures were performed via a transperitoneal approach using the Da Vinci Xi robotic surgical system (Intuitive Surgical), and images were available in the operating theater (Figs. 1A and 1B). Radioguidance was achieved using a laparoscopic γ-probe (SOE-311-AL; Eurorad SA) connected to the Europrobe 3.2 control unit (Eurorad SA). The γ-probe was covered with a sterile sleeve and inserted in the abdominal peritoneal cavity through a 12-mm assistant's port via the Alexis laparoscopic system (Applied Medical Corp.), placed above the right iliac crest. Real-time feedback of γ-probe measurements in response to $^{111}$In activity was provided both acoustically and numerically by the control unit. Background measurements at the lateral abdominal wall muscle served as a reference. Additionally, radiosignals were measured for structures near RGS-target lesions (ureters, iliac arteries, bladder, prostate, and intestines) to assess nonspecific tracer uptake.

Standard bilateral ePLND was performed, including obturator fossa, external iliac, internal iliac, common iliac, and, at the surgeon's discretion, presacral and mesorectal regions. γ-probe measurements were taken in regions of interest in vivo to identify the RGS-target lesions (Fig. 1C). A lesion was considered positive if counts per second were at least twice the counts per second of the background reference. Directly after resection, ex vivo benchtop measurements were taken (Fig. 1D). Ex vivo, a lesion with at least 10 cps was considered suggestive and subsequently marked with a suture. If ex vivo measurements showed no activity (<10 cps), in vivo measurements were repeated. All resected specimens were assessed using the γ-probe ex vivo and likewise marked if at least 10 cps were measured. Specimens were collected separately according to the anatomic resection site.

### Postoperative Histopathologic Analysis and Imaging

All specimens were fixed in formaldehyde (10%) and processed for paraffin embedding. The tissue blocks were cut at a 3-μm thickness, and slides were stained with hematoxylin and eosin (Figs. 1E and 1F). The total number and size of LNs (macroscopically) and LNMs (microscopically) per specimen per anatomic region were reported. PSMA staining was applied on the marked LNs and on LNs that showed metastases on hematoxylin and eosin staining. PSMA expression was classified according to the percentage of PSMA-positive tumor cells (0%, <10%, 10%–50%, 51%–80%, >80%) and staining intensity (none, 0; mild, 1; moderate, 2; strong, 3).

Postoperative $^{18}$F-PSMA PET/CT was used to confirm or reject successful removal of RGS-target lesions (Figs. 1G and 1H) and was performed approximately 6 wk after surgery (robot-assisted radical prostatectomy plus ePLND) or 2 wk after surgery (ePLND only), before adjuvant treatment (i.e., radiotherapy or androgen deprivation therapy).

### Safety and Follow-up

During administration of $^{111}$In-PSMA-I&T, safety was assessed by clinical observation of the patients for 1 h after injection. Vital parameters (temperature, blood pressure, heart rate) were measured before and 5, 30, and 60 min after injection. Long-term safety was assessed by monitoring adverse events for 12 mo, including analysis of

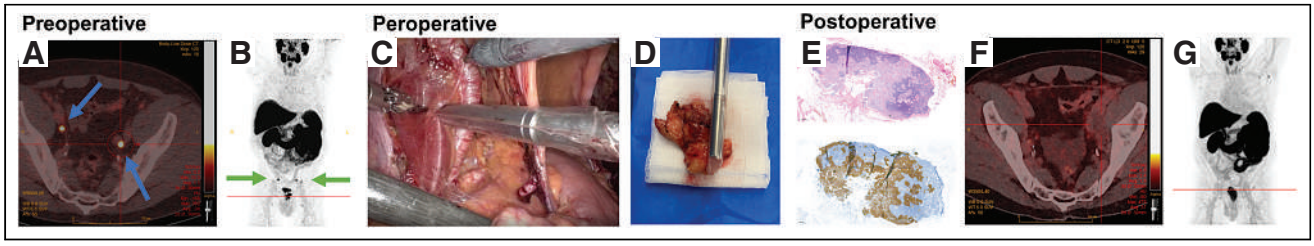


**FIGURE 1.** (A and B) $^{18}$F-PSMA PET/CT 11 wk before surgery demonstrates presence of suggestive LNs in left and right obturator fossa in transversal plane (blue arrows, A) and on maximum-intensity projection (green arrows, B). (C) Laparoscopic γ-probe is inserted via Alexis laparoscopic system to make in vivo measurements to detect suggestive LNs. (D) Resected specimens are measured ex vivo at benchtop examination. (E) Histopathologic examination shows LNM on hematoxylin and eosin staining and strong PSMA expression. (F and G) $^{18}$F-PSMA PET/CT (F) and maximum-intensity projection (G) 11 wk after surgery show successful removal of both suggestive LNs.

laboratory results from blood samples taken at baseline, 10 d, and 3 mo after tracer administration. Adverse events were reported according to the Common Terminology Criteria for Adverse Events version 5.0. Surgical complications were assessed according to the Clavien–Dindo classification. Follow-up consisted of clinical examination and PSA measurements at 6 wk and 3, 6, 9, and 12 mo after surgery.

### Study Endpoints

The primary endpoint of this study was determination of the safety and feasibility of the RGS procedure with $^{111}$In-PSMA-I&T. Feasibility was defined as the ability to peroperatively detect the RGS-target lesions preoperatively identified on $^{18}$F-PSMA PET/CT. Secondary outcomes included the accuracy of $^{111}$In-PSMA RGS compared with histopathology, lesion-to-background ratios (LBRs) of identified RGS-target lesions, and tumor-to-background ratios (TBRs) of histopathologically proven LNMs. Ratios were calculated for identified RGS-target lesions and retrospectively histopathologically confirmed LNMs. Adjuvant treatment strategies and biochemical recurrence within 1 y were descriptively reported as they were not part of the primary aim of this study.

### Statistical Analyses

All clinical data were collected in the Castor Electronic Data Capture system (https://castoredc.com). Quantitative data describing the feasibility of the procedure are presented as medians with interquartile ranges (IQRs) or means with total ranges and numbers with frequencies within groups, as appropriate. The sensitivity, specificity, positive predictive value, and negative predictive value on a per-lesion analysis of $^{111}$In-PSMA RGS compared with histopathology were derived from $2 \times 2$ contingency tables. LBRs and TBRs were compared using unpaired *t* tests. Statistical analyses were performed using the SPSS statistical software package (version 27.0; IBM Corp.) and Prism (version 9.0; GraphPad Software). A *P* value of less than 0.05 was considered statistically significant.

**TABLE 1**
Demographics and Clinical Characteristics of Study Population at Diagnosis ($n$ = 20)

| Characteristic | Data |
|---|---|
| Age at time of surgery (y) | 69 (57–79) |
| Body mass index | 25.6 (20.9–32.9) |
| iPSA (ng/L) | 22.2 (2.9–117) |
| EAU risk classification | |
| Intermediate | 7 (35%) |
| High | 13 (65%) |
| $^{18}$F-PSMA PET–suggestive (LoS ≥ 3) LNs per patient | |
| 1 | 3 (15%) |
| 2 | 9 (45%) |
| 3 | 6 (30%) |
| >3 | 2 (10%) |
| LoS of $^{18}$F-PSMA PET–suggestive LNs | |
| 3 | 17 (35%) |
| 4 | 13 (27%) |
| 5 | 19 (39%) |
| Location of $^{18}$F-PSMA PET–suggestive LNs | |
| Obturator fossa | 15 (31%) |
| External iliac | 17 (35%) |
| Internal iliac | 9 (18%) |
| Common iliac | 5 (10%) |
| Pararectal and presacral | 3 (6%) |

iPSA = initial prostate-specific antigen level; EAU = European Association of Urology; LoS = level of suspicion.

Qualitative data are number and percentage; continuous data are mean and range.

## RESULTS

### Primary Outcomes

*Patient and Surgical Characteristics.* The characteristics of the included patients ($n$ = 20) are summarized in Table 1. In total, 49 suggestive LNs were identified on preoperative $^{18}$F-PSMA PET/CT and defined as RGS-target lesions. Surgical characteristics are described in Table 2. In total, 523 LNs were resected. Final histopathology concluded pN1 in 16 patients (80%).

*Safety of $^{111}$In-PSMA-I&T RGS.* No adverse events were recorded after the administration of $^{111}$In-PSMA-I&T (Table 2). Temperature,

**TABLE 2**
Peroperative Surgical and Oncologic Characteristics

| Characteristic | Data |
|---|---|
| Time between $^{18}$F-PSMA PET/CT and surgery (wk) | 8 (3–24) |
| Injected dose of $^{111}$In-PSMA-I&T (MBq) | 157.0 (151.8–164.2) |
| Time between tracer administration and surgery (h) | 22.5 (19.4–26.5) |
| Complications related to $^{111}$In-PSMA-I&T administration (CTCAE version 5.0) | 0 (0%) |
| RARP + ePLND | 11 (55%) |
| ePLND only | 9 (45%) |
| Blood loss (mL) | 118 (0–350) |
| Duration (min) | |
| RARP + ePLND | 237 (206–286) |
| ePLND only | 110 (67–162) |
| Complications related to surgery (Clavien–Dindo classification) | |
| No complications | 19 (95%) |
| Grade 1* | 1 (5%) |
| Histopathologic N-stage | |
| pN0 | 4 (20%) |
| pN1 | 14 (70%) |
| pM1a | 2 (10%) |
| Resected LNs per patient | 26 (16–45) |
| Resected LNMs per patient | 2 (0–6) |
| Total resected LNs | 523 |
| Total resected LNMs | 45 (8%) |

*Urinary leakage at anastomosis.

CTCAE = Common Terminology Criteria for Adverse Events; RARP = robot-assisted radical prostatectomy.

Qualitative data are number and percentage; continuous data are mean and range.

blood pressure, and heart rate remained stable in the hour after tracer injection (Supplemental Table 1; supplemental materials are available at http://jnm.snmjournals.org). One surgical complication (Clavien–Dindo grade 1) was observed and was managed conservatively (urinary leakage at the anastomosis of the bladder). No study-related adverse events were observed within 1 y of follow-up (Supplemental Table 2).

*Feasibility of $^{111}$In-PSMA-I&T RGS: Peroperative Detection of $^{18}$F-PSMA PET–Suggestive Lesions.* Twenty-nine of the 49 RGS-target lesions (59%) were identified with the γ-probe (in vivo or ex vivo), and successful removal was confirmed (Table 3). Of those, 28 LNs (97%) contained LNMs, with a mean size of 7.9 mm (range, 0.8–20.0 mm). One LN peroperatively measured an absolute count of 15 cps ex vivo yet was confirmed benign after complete sectioning. This 24-mm LN correlated with an RGS-target lesion with a level of suspicion of 3. Fourteen (of 49; 29%) RGS-target lesions could not be detected peroperatively, whereas postoperative imaging concluded successful surgical removal. Of those 14 LNs, 2 (14%) contained LNMs, both of which were no larger than 3 mm and were mild to moderate in PSMA expression. Those LNMs were matched on the basis of corresponding anatomic regions. The remaining 6 (of 49; 12%) RGS-target lesions could not be detected by PSMA RGS and were still visible and suggestive on postoperative $^{18}$F-PSMA PET/CT. Those lesions were located in surgically challenging regions (deep internal iliac regions and presacral regions).

Figure 2 depicts the in vivo and ex vivo LBRs of the RGS-target lesions. The in vivo and ex vivo median LBRs of detected RGS-target lesions (i.e., irrespective of histopathology) were 2.05 (IQR, 1.2–3.0) and 36 (IQR, 3.8–71), respectively ($P = 0.0004$). An overview of background measurements is provided in Supplemental Table 3.

### Secondary Outcomes

*$^{111}$In-PSMA RGS: Concordance Between Peroperative γ-Probe Findings and Histopathology.* $^{111}$In-PSMA RGS identified 2 lesions with increased counts per second that did not correlate with RGS-target lesions. Both contained LNMs on final histopathology (>3 mm and strong PSMA expression). Furthermore, histopathology identified 13 LNMs that were not identified on preoperative imaging or during $^{111}$In-PSMA RGS. These LNs were located at anatomic levels different from those of potentially missed RGS-target lesions. The mean size of those LNMs was 2.2 mm (range, 0.5–5.5 mm), and they showed strong, moderate, and no PSMA expression in 8 (62%), 4 (31%), and 1 (8%) cases, respectively.

The sensitivity, specificity, positive predictive value, and negative predictive value of $^{111}$In-PSMA RGS (in vivo and ex vivo combined) compared with histopathology on a per-lesion analysis were 66.7%, 99.8%, 96.8%, and 97.0%, respectively. The in vivo median TBR of LNMs was 2.3 (IQR, 1.3–3.1). The ex vivo median TBR of LNMs and benign LNs were 42 (IQR, 1.1–71) and 0 (IQR, 0.0–0.0), respectively ($P = 0.0002$) (Fig. 3).

*Oncologic Outcomes and Follow-up.* Although not part of the primary aim of this study, a description of oncologic outcomes and treatment strategies per patient up to 1 y is provided in Supplemental Table 4. A distinction was made between patients undergoing

**TABLE 3**
Peroperative γ-Probe Detection (In Vivo and Ex Vivo) and Characteristics of RGS-Target Lesions

| Characteristic | Probe-positive and resected ($n = 29$) | Probe-negative | |
|---|---|---|---|
| | | Resected ($n = 14$) | Not resected* ($n = 6$) |
| LoS of lesion on $^{18}$F-PSMA PET | | | |
| 5 | 15 (52%) | 1 (7%) | 3 (50%) |
| 4 | 9 (31%) | 4 (29%) | 0 (0%) |
| 3 | 5 (17%) | 9 (64%) | 3 (50%) |
| Location on $^{18}$F-PSMA PET/CT | | | |
| Obturator fossa | 13 (45%) | 2 (14%) | 0 (0%) |
| External iliac | 11 (38%) | 6 (43%) | 0 (0%) |
| Internal iliac | 3 (10%) | 1 (7%) | 5 (83%) |
| Common iliac | 0 (0%) | 5 (36%) | 0 (0%) |
| Pararectal and presacral | 2 (7%) | 0 (0%) | 1 (17%) |
| Histopathology | | | |
| Number of LNMs | 28 (97%) | 2 (14%) | |
| Size (mm) | 7.9 (0.8–20.0) | 1.8 (0.6–3.0) | |
| Strong PSMA expression | 26 (93%) | 0 (0%) | |
| Moderate PSMA expression | 2 (7%) | 1 (50%) | |
| Mild PSMA expression | 0 (0%) | 1 (50%) | |
| No PSMA expression | 0 (0%) | 0 (0%) | |

*Still present and suggestive on postoperative $^{18}$F-PSMA PET/CT.
LoS = level of suspicion.
Qualitative data are number and percentage; continuous data are mean and range.

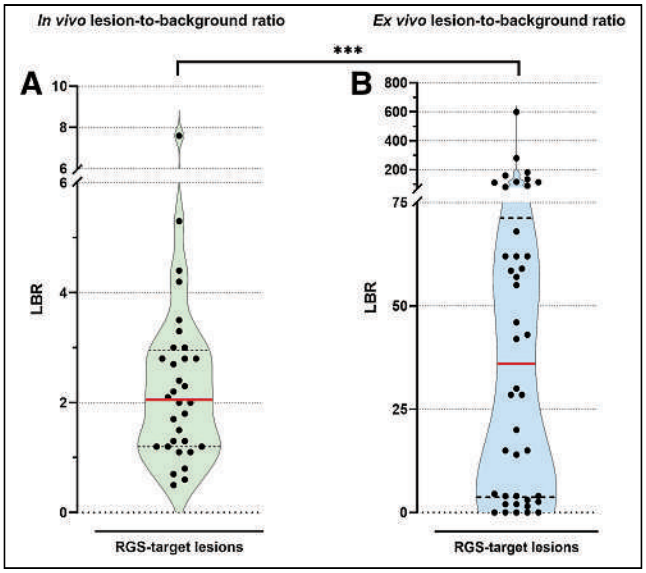


**FIGURE 2.** In vivo and ex vivo LBRs of RGS-target lesions and comparison (unpaired *t* test) between in vivo and ex vivo ratios. Identification of RGS-target lesions during procedure was based on anatomic landmarks as indicated by preoperative imaging. To calculate LBR, maximum counts per second of identified RGS-target lesions were measured and divided by background counts per second both in vivo (A) and ex vivo (B). RGS-target lesion was considered γ-probe–positive if LBR > 2 in vivo or maximum counts per second ≥ 10 ex vivo. Results depicted in both A and B describe peroperative measurements, irrespective of histopathologic conclusions. ***$P$ = 0.0004.

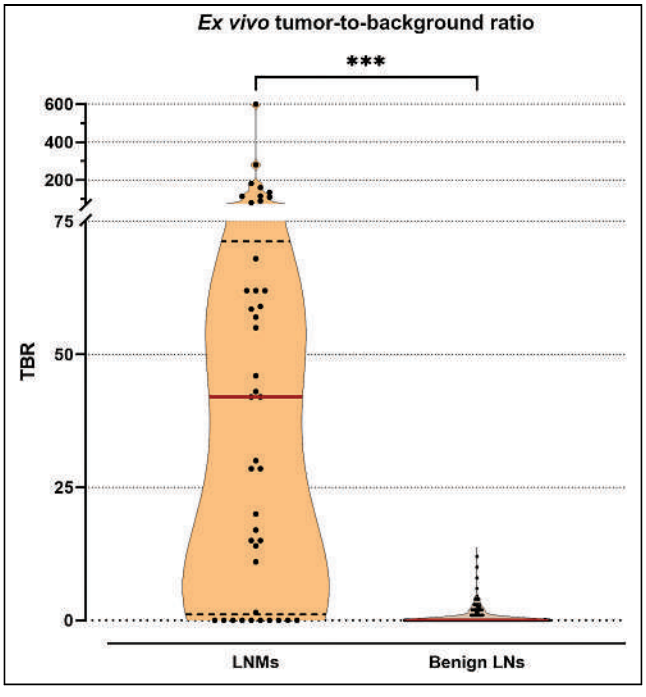


**FIGURE 3.** Comparison of ex vivo TBRs between histopathologically proven metastatic LNs and nonmetastatic LNs (unpaired *t* test). To calculate TBR, maximum counts per second of all resected LNs were measured and divided by background counts per second. Results depicted in this figure are thus irrespective of whether lesion was RGS-target lesion. ***$P$ = 0.0002.

robot-assisted radical prostatectomy plus ePLND ($n$ = 11) and patients undergoing ePLND before radiotherapy ($n$ = 9). Of the 11 patients undergoing robot-assisted radical prostatectomy plus ePLND, 8 were staged pN1, yet 5 of those patients had undetectable PSA levels at 6 wk after surgery, of whom 2 patients eventually demonstrated biochemical recurrence, both 9 mo after surgery. The other 3 patients remained free of biochemical recurrence during 1 y of follow-up. Eight of 9 patients who underwent ePLND before radiotherapy were staged pN1, and all 8 received adjuvant radiotherapy to the pelvis and concomitant androgen deprivation therapy.

## DISCUSSION

Whereas thus far the potential of PSMA RGS has been evaluated mainly for PCa patients undergoing salvage surgery for nodal recurrences, evidence regarding its feasibility in the primary setting is scarce. During ePLND in primary intermediate- and high-risk PCa patients, removal of PSMA PET–suggestive lesions is most likely to determine the presence of LNM. With this aim, $^{111}$In-PSMA RGS was evaluated in this phase I/II study on newly diagnosed PCa patients and showed that the administration of $^{111}$In-PSMA-I&T is safe and facilitates peroperative detection of $^{18}$F-PSMA PET–suggestive lesions. Overall, 88% of $^{18}$F-PSMA PET–suggestive RGS-target lesions were successfully removed. $^{111}$In-PSMA RGS facilitated peroperative identification of 59% of RGS-target lesions but missed 29% within the ePLND template. Successfully detected RGS-target lesions contained LNMs in 97% of cases, whereas the incidence of LNMs in the nondetected RGS-target lesions was considerably lower (14%). The critical role of patient selection for the PSMA RGS procedure is underlined by the fact that the majority (64%) of the surgically nondetected RGS-target lesions were level-of-suspicion 3 on preoperative $^{18}$F-PSMA PET/CT.

Another important finding from this study is the difference between in vivo and ex vivo performance of the γ-probe (Figs. 2 and 3), a finding that was also reported in previous series (*14*,*20*,*21*). The limited TBR in vivo is likely due to interfering physiologic tracer accumulation in the surrounding organs (i.e., the intestines, ureters, bladder, vasculature, and primary prostate tumor) (Supplemental Table 3); a longer interval between tracer administration and surgery could hypothetically improve TBR. As a result, γ-probe measurements in vivo are sensitive to the orientation toward an RGS-target lesion in relation to its surroundings (*22*).

Two series investigating PSMA RGS in the primary setting based feasibility on the diagnostic accuracy of probe measurements compared with histopathology (*20*,*21*). In the current study, accuracy of $^{111}$In-PSMA RGS was assessed as a secondary outcome. When our results are being compared with those series, the use of different tracers, incubation times, and γ-probes has to be kept in mind. Gondoputro et al. (*20*) reported a higher sensitivity (76%) and positive predictive value (89%) than we did, but they used a lower threshold for PSMA RGS positivity (LBR > 1.5, vs. 2 in our study). Preliminary results of Gandaglia et al. (*21*) were similar to our results (sensitivity, specificity, positive predictive value, and negative predictive value of 63%, 99%, 83%, and 96%, respectively).

From a clinical perspective, we focused specifically on $^{18}$F-PSMA PET–suggestive LNs, and the primary objective was to detect those lesions during $^{111}$In-PSMA RGS, irrespective of histopathologic results. A similar objective was recently described by Lunger

et al. (*23*), who reported that PSMA RGS successfully facilitated resection of 70 of 78 (90%) $^{18}$F-PSMA PET–suggestive lesions in 35 patients. Of note, the reported $SUV_{max}$ for $^{18}$F-PSMA PET–suggestive target lesions was considerably higher than in our series. Moreover, in our study postoperative imaging was applied in all patients to assess LN removal, whereas in the other studies postoperative imaging was not systematically applied and conclusions regarding LN removal were drawn indirectly on the basis of postoperative PSA levels only. Furthermore, resected $^{111}$In-PSMA RGS–suggestive lesions were marked during the procedure to ensure correlation between PSMA RGS findings and pathology on a node-to-node level. This more reliably indicates successful removal of specific lesions and justifies lesion-specific conclusions.

Most PSMA RGS feasibility studies (including ours) equally report the presence of additional microscopic LNMs found by histopathology that were missed by both $^{18}$F-PSMA PET/CT and PSMA RGS (*13*,*20*,*21*). This suggests that PSMA RGS, like PSMA PET/CT (*24*), underestimates the nodal burden in miN1 patients and that, at this point, sensitivity is not yet sufficient to facilitate omission of routine ePLND. However, some technical aspects that affect tracer retention in target tissue and interfering background tissue (e.g., optimal tracer dose and incubation time) could be further optimized to improve LBRs (*25*). At the same time, the high specificity of PSMA RGS regarding suggestive lesions, especially ex vivo, justifies use of the technique to directly confirm successful removal of suggestive lesions. Negative findings on ex vivo γ-probe measurements should trigger surgeons toward more extensive resection, especially in PSMA PET–suggestive regions. Furthermore, our results strengthen the suggestion as proposed by Gandaglia et al. (*21*) and Gondoputro et al. (*20*) that PSMA RGS in the primary setting is likely most productive for PSMA PET–suggestive lesions. This endorses the in vivo utility of PSMA RGS specifically to detect PMSA-avid LNs outside the standard ePLND template or in surgically challenging regions (e.g., pararectal and presacral), aiming to identify LNMs that would have been missed otherwise. Whether improved peroperative detection and resection of suggestive LNs using $^{111}$In-PSMA RGS leads to superior oncologic outcomes has yet to be determined by prospective trials.

Limitations of our study comprise the limited cohort size, which included both patients treated with ePLND combined with robot-assisted radical prostatectomy and patients treated with PLND only. In this proof-of-concept evaluation, our endpoint was defined as successful removal of suggestive lesions, whereas oncologic outcomes are more significant and should be considered in future prospective trials. Ideally, a comparison with standard-of-care ePLND should be made.

## CONCLUSION

$^{111}$In-PSMA RGS is a safe procedure that aids peroperative detection of lesions identified as suggestive on preoperative $^{18}$F-PSMA PET/CT in newly diagnosed PCa patients. This image-guided approach to detecting potential LNMs at ePLND may potentially improve nodal staging.

## DISCLOSURE

No potential conflict of interest relevant to this article was reported.

**KEY POINTS**

**QUESTION:** Is PSMA RGS feasible and safe in primary PCa with suggestive nodes on PSMA PET/CT?

**PERTINENT FINDINGS:** PSMA RGS facilitated peroperative identification and resection of 59% of PSMA PET–suggestive lesions, of which 97% contained LNMs in a total of 20 PCa patients. Only 2 metastases were found in $^{18}$F-PSMA PET–suggestive lesions that were not detected by PSMA RGS.

**IMPLICATIONS FOR PATIENT CARE:** PSMA RGS may improve nodal staging by peroperative identification and confirmation of successful removal of PSMA PET–suggestive lesions.

## REFERENCES


1. Marra G, Valerio M, Heidegger I, et al. Management of patients with node-positive prostate cancer at radical prostatectomy and pelvic lymph node dissection: a systematic review. *Eur Urol Oncol.* 2020;3:565–581.
2. Baas DJH, Schilham M, Hermsen R, et al. Preoperative PSMA-PET/CT as a predictor of biochemical persistence and early recurrence following radical prostatectomy with lymph node dissection. *Prostate Cancer Prostatic Dis.* 2022; 25:65–70.
3. Abdollah F, Gandaglia G, Suardi N, et al. More extensive pelvic lymph node dissection improves survival in patients with node-positive prostate cancer. *Eur Urol.* 2015;67:212–219.
4. Lestingi JFP, Guglielmetti GB, Trinh Q-D, et al. Extended versus limited pelvic lymph node dissection during radical prostatectomy for intermediate- and high-risk prostate cancer: early oncological outcomes from a randomized phase 3 trial. *Eur Urol.* 2021;79:595–604.
5. Joniau S, Van den Bergh L, Lerut E, et al. Mapping of pelvic lymph node metastases in prostate cancer. *Eur Urol.* 2013;63:450–458.
6. Hövels AM, Heesakkers RA, Adang EM, et al. The diagnostic accuracy of CT and MRI in the staging of pelvic lymph nodes in patients with prostate cancer: a meta-analysis. *Clin Radiol.* 2008;63:387–395.
7. Bukavina L, Luckenbaugh AN, Hofman MS, et al. Incorporating prostate-specific membrane antigen positron emission tomography in management decisions for men with newly diagnosed or biochemically recurrent prostate cancer. *Eur Urol.* 2023;83:521–533.
8. Hofman MS, Lawrentschuk N, Francis RJ, et al. Prostate-specific membrane antigen PET-CT in patients with high-risk prostate cancer before curative-intent surgery or radiotherapy (proPSMA): a prospective, randomised, multicentre study. *Lancet.* 2020;395:1208–1216.
9. Stabile A, Pellegrino A, Mazzone E, et al. Can negative prostate-specific membrane antigen positron emission tomography/computed tomography avoid the need for pelvic lymph node dissection in newly diagnosed prostate cancer patients? A systematic review and meta-analysis with backup histology as reference standard. *Eur Urol Oncol.* 2022;5:1–17.
10. van Kalmthout LWM, van Melick HHE, Lavalaye J, et al. Prospective validation of gallium-68 prostate specific membrane antigen-positron emission tomography/computerized tomography for primary staging of prostate cancer. *J Urol.* 2020; 203:537–545.
11. van Leeuwen PJ, Donswijk M, Nandurkar R, et al. Gallium-68-prostate-specific membrane antigen ($^{68}$Ga-PSMA) positron emission tomography (PET)/computed tomography (CT) predicts complete biochemical response from radical prostatectomy and lymph node dissection in intermediate- and high-risk prostate cancer. *BJU Int.* 2019;124:62–68.
12. Robu S, Schottelius M, Eiber M, et al. Preclinical evaluation and first patient application of $^{99m}$Tc-PSMA-I&S for SPECT imaging and radioguided surgery in prostate cancer. *J Nucl Med.* 2017;58:235–242.
13. Maurer T, Robu S, Schottelius M, et al. $^{99m}$Technetium-based prostate-specific membrane antigen-radioguided surgery in recurrent prostate cancer. *Eur Urol.* 2019;75:659–666.
14. de Barros HA, van Oosterom MN, Donswijk ML, et al. Robot-assisted prostate-specific membrane antigen-radioguided salvage surgery in recurrent prostate cancer using a DROP-IN gamma probe: the first prospective feasibility study. *Eur Urol.* 2022;82:97–105.
15. Schottelius M, Wirtz M, Eiber M, Maurer T, Wester HJ. [$^{111}$In]PSMA-I&T: expanding the spectrum of PSMA-I&T applications towards SPECT and radioguided surgery. *EJNMMI Res.* 2015;5:68.

16. Maurer T, Weirich G, Schottelius M, et al. Prostate-specific membrane antigen-radioguided surgery for metastatic lymph nodes in prostate cancer. *Eur Urol.* 2015; 68:530–534.
17. Jilg CA, Reichel K, Stoykow C, et al. Results from extended lymphadenectomies with [$^{111}$In]PSMA-617 for intraoperative detection of PSMA-PET/CT-positive nodal metastatic prostate cancer. *EJNMMI Res.* 2020;10:17.
18. Maurer T, Graefen M, van der Poel H, et al. Prostate-specific membrane antigen-guided surgery. *J Nucl Med.* 2020;61:6–12.
19. Rowe SP, Pienta KJ, Pomper MG, Gorin MA. Proposal for a structured reporting system for prostate-specific membrane antigen-targeted PET imaging: PSMA-RADS version 1.0. *J Nucl Med.* 2018;59:479–485.
20. Gondoputro W, Scheltema MJ, Blazevski A, et al. Robot-assisted prostate-specific membrane antigen-radioguided surgery in primary diagnosed prostate cancer. *J Nucl Med.* 2022;63:1659–1664.
21. Gandaglia G, Mazzone E, Stabile A, et al. Prostate-specific membrane antigen radioguided surgery to detect nodal metastases in primary prostate cancer patients undergoing robot-assisted radical prostatectomy and extended pelvic lymph node dissection: results of a planned interim analysis of a prospective phase 2 study. *Eur Urol.* 2022;82:411–418.
22 Dell'Oglio P, Meershoek P, Maurer T, et al. A DROP-IN gamma probe for robot-assisted radioguided surgery of lymph nodes during radical prostatectomy. *Eur Urol.* 2021;79:124–132.
23. Lunger L, Steinhelfer L, Korn P, et al. Prostate-specific membrane antigen–radio-guided surgery facilitates pelvic lymph node dissection during radical prostatectomy for the treatment of locally advanced prostate cancer with regional lymph node metastases. *Eur Urol Oncol.* 2023;6:95–98.
24. Fossati N, Scarcella S, Gandaglia G, et al. Underestimation of positron emission tomography/computerized tomography in assessing tumor burden in prostate cancer nodal recurrence: head-to-head comparison of $^{68}$Ga-PSMA and $^{11}$C-choline in a large, multi-institutional series of extended salvage lymph node dissections. *J Urol.* 2020;204:296–302.
25. Privé BM, Derks YHW, Rosar F, et al. $^{89}$Zr-labeled PSMA ligands for pharmacokinetic PET imaging and dosimetry of PSMA-617 and PSMA-I&T: a preclinical evaluation and first in man. *Eur J Nucl Med Mol Imaging.* 2022;49:2064–2076.

# The DETECT Trial: Are We on the Verge of Precision Surgery in Primary Prostate Cancer?

Tobias Maurer[1,2], Christian Thomas[3], and Boris Hadaschik[4]

[1]*Martini-Klinik Prostate Cancer Center, University Hospital Hamburg–Eppendorf, Hamburg, Germany;* [2]*Department of Urology, University Hospital Hamburg–Eppendorf, Hamburg, Germany;* [3]*Department of Urology, University Hospital Dresden, Dresden, Germany; and* [4]*Department of Urology, University Hospital Essen, Essen, Germany*

The DETECT trial presented by Schilham et al. in *The Journal of Nuclear Medicine* constitutes one of the first prospective trials on prostate-specific membrane antigen (PSMA) radioguided surgery (RGS) in primary prostate cancer patients (*1*). Thus, we first would like to congratulate the authors for their efforts in the design, execution, and subtle analysis of this study that proved the feasibility and safety of this still-novel approach during robotic pelvic lymphadenectomy with or without primary prostatectomy in patients with prostate cancer and evidence of lymphatic spread on preoperative PSMA PET imaging. However, in this context and especially concerning the role of lymph node dissection, some aspects deserve further discussion.

The intricate lymphatic drainage pathways of the prostate pose a challenge in the treatment of prostate cancer because cancer cells might disseminate to atypical regions not covered in established surgical templates. Traditional extended lymph node dissection often falls short in addressing spread to locations such as the bladder pedicle and the deep internal, pararectal, or presacral regions. Sentinel procedures have been proposed to make up for this shortcoming and may detect slight atypical lymphatic spread; however, the tracers used for these approaches are not tumor-specific and often are even combined with an extended pelvic lymph node dissection rather than replacing it (*2*).

Pelvic lymph node dissection causes morbidity while remaining of inconclusive oncologic value, as robust evidence from long-term studies, even in primary high-risk disease, is lacking (*3*). Although pelvic lymph node dissection represents a diagnostic tool and may conciliate patients, this uncertainty about its oncologic value is even more troublesome in patients without evidence of lymphatic spread on final histopathology postoperatively. Thus, there is still much controversy on the value of and indications for lymph node dissection in prostate cancer patients. Increased use of modern imaging with PSMA PET has led some countries to omit lymphadenectomy in patients without evidence of lymph node metastases, whereas other guidelines still emphasize the value of extended lymph node dissection in patients with an elevated risk of metastasis in preoperative clinical nomograms.

The advent of PSMA PET imaging in primary prostate cancer has substantially augmented our ability to discern lymphatic involvement compared with conventional cross-sectional imaging (*4*). Still, the challenge remains to intraoperatively detect those tumor-infested lymph nodes reliably. The development and introduction of PSMA RGS into clinical practice may at least partly close this gap by enabling real-time molecular detection of prostate cancer lesions during surgery through in vivo and ex vivo γ-probe measurements (*5*). Undoubtedly, this technique holds promise in improving surgical accuracy and completeness.

Despite these advancements, PSMA PET lacks sensitivity for small metastases, and PSMA RGS may still overlook small lymph node metastases, as Schilham et al. accurately analyzed using postoperative PSMA PET imaging (*1*). Particularly, in patients with PSMA PET–positive pelvic lymph node metastases at primary diagnosis, there is a risk of further additional slight lymphatic spread. This understaging may be substantially higher than in the setting of biochemical recurrence, when, additionally, the prostate-specific antigen value, its dynamics, and other clinical parameters can be taken into consideration and correlated with the PSMA PET–positive tumor volume. This ability enables careful patient selection to avoid early treatment failure.

Patients with PSMA PET–positive lymph nodes at primary staging harbor a considerable risk of aggressive tumor biology requiring additional treatments besides surgery (*6*). In this clinical scenario, a renaissance of neoadjuvant treatment strategies may be expected. Several studies are investigating such neoadjuvant treatment strategies in prostate cancer patients with an elevated risk profile. First, emerging data suggest an oncologic benefit (*7,8*), but data from registration trials are still pending. Neoadjuvant treatment approaches lead to shrinkage of lymph node metastases, impeding detectability by molecule-targeted PSMA RGS and rendering such surgical approaches futile. At present, evidence for an oncologic benefit is best for radiotherapy in combination with androgen receptor pathway inhibition in patients with pelvic lymph node metastases.

At the same time, PSMA PET leads to more sensitive detection of lymph node metastases, and this early oligometastatic stage might be an opportunity for surgery alone. For sure, the primary setting offers an opportune environment for surgeons to familiarize themselves with the intricacies of the PSMA RGS procedure, especially in learning its limitations and in navigating to anatomically challenging locations, as compared with the setting of biochemical recurrence after primary radical prostatectomy or radiation therapy, in which surgery might be even more complicated. Recent developments in hardware technology, such as the design of novel γ-probes

Received Dec. 21, 2023; revision accepted Jan. 23, 2024.
For correspondence or reprints, contact Tobias Maurer (t.maurer@uke.de).
Published online Feb. 15, 2024.

DOI: 10.2967/jnumed.123.267187

for robotic surgery as compared with rigid laparoscopic γ-probes, might further facilitate those surgical procedures within the confined space of the small pelvis (*9*). Furthermore, advancements in tracer design and labeling, such as with $^{99m}$Tc instead of $^{111}$In, will expand its availability because $^{99m}$Tc is an inexpensive and readily available radiotracer with a favorable half-life and less radiation exposure than $^{111}$In (*10*).

Besides these limitations and open questions regarding patient selection and the oncologic benefits of surgery, the presented DETECT trial and its thoughtful evaluation underscore the potential of PSMA RGS, and we thus want to applaud the authors again for conducting this important clinical trial. Challenges persist, and they urge us as a scientific community to delve more deeply into refining the technique of PSMA-targeted surgery, exploring alternative tracers, and conducting rigorous trials to decipher the true impact of this technique on long-term oncologic outcomes to ultimately improve patient outcomes and shape the future landscape of surgical prostate cancer management.

## DISCLOSURE

Tobias Maurer reports personal fees from ABX, Astellas, Bayer, Phillips, and Sanofi-Aventis (speakers' bureau) and consultation fees from ABX, Applications International S.A., Astellas, Axiom, Blue Earth Diagnostics, GEMoAb, Novartis, ROTOP Pharma, and Telix within the last 5 y. Christian Thomas reports personal fees from Astellas, AstraZeneca, Bayer, BMS, Janssen, MSD, Novartis, and Pfizer and has been an invited speaker for Astellas, Janssen, and MSD. Boris Hadaschik reports personal fees from ABX, Amgen, Astellas, AstraZeneca, Bayer, Janssen, Lightpoint Ltd., MSD, Novartis, and Pfizer; has been an invited speaker for Accord, Astellas, and Janssen R&D; has received research funding from AAA/Novartis, Bristol Myers Squibb, and German Research Foundation; and has been in leadership roles for DKG AUO, and DGU. No other potential conflict of interest relevant to this article was reported.

## REFERENCES


1. Schilham MGM, Somford DM, Küsters-Vandevelde HVN, et al. Prostate-specific membrane antigen–targeted radioguided pelvic lymph node dissection in newly diagnosed prostate cancer patients with a suspicion of locoregional lymph node metastases: the DETECT trial. *J Nucl Med.* 2024;65:423–429.
2. van Leeuwen FWB, Winter A, van Der Poel HG, et al. Technologies for image-guided surgery for managing lymphatic metastases in prostate cancer. *Nat Rev Urol.* 2019;16:159–171.
3. Fossati N, Willemse PM, Van den Broeck T, et al. The benefits and harms of different extents of lymph node dissection during radical prostatectomy for prostate cancer: a systematic review. *Eur Urol.* 2017;72:84–109.
4. Hofman MS, Lawrentschuk N, Francis RJ, et al. Prostate-specific membrane antigen PET-CT in patients with high-risk prostate cancer before curative-intent surgery or radiotherapy (proPSMA): a prospective, randomised, multicentre study. *Lancet.* 2020;395:1208–1216.
5. Knipper S, Mehdi Irai M, Simon R, et al. Cohort study of oligorecurrent prostate cancer patients: oncological outcomes of patients treated with salvage lymph node dissection via prostate-specific membrane antigen-radioguided surgery. *Eur Urol.* 2023;83:62–69.
6. Amiel T, Würnschimmel C, Heck M, et al. Regional lymph node metastasis on prostate specific membrane antigen positron emission tomography correlates with decreased biochemical recurrence-free and therapy-free survival after radical prostatectomy: a retrospective single-center single-arm observational study. *J Urol.* 2021;205:1663–1670.
7. Devos G, Tosco L, Baldewijns M, et al. ARNEO: a randomized phase II trial of neoadjuvant degarelix with or without apalutamide prior to radical prostatectomy for high-risk prostate cancer. *Eur Urol.* 2023;83:508–518.
8. Ravi P, Kwak L, Xie W, et al. Neoadjuvant novel hormonal therapy followed by prostatectomy versus up-front prostatectomy for high-risk prostate cancer: a comparative analysis. *J Urol.* 2022;208:838–845.
9. Dell'Oglio P, Meershoek P, Maurer T, et al. A DROP-IN gamma probe for robot-assisted radioguided surgery of lymph nodes during radical prostatectomy. *Eur Urol.* 2021;79:124–132.
10. Maurer T, Robu S, Schottelius M, et al. $^{99m}$Technetium-based prostate-specific membrane antigen-radioguided surgery in recurrent prostate cancer. *Eur Urol.* 2019;75:659–666.

# First Safety and Efficacy Data with the Radiohybrid $^{177}$Lu-rhPSMA-10.1 for the Treatment of Metastatic Prostate Cancer

Alexander Dierks[1], Alexander Gäble[1], Andreas Rinscheid[2], Georgine Wienand[1], Christian H. Pfob[1], Malte Kircher[1], Johanna S. Enke[1], Tilman Janzen[2], Marianne Patt[1], Martin Trepel[3], Dorothea Weckermann[4], Ralph A. Bundschuh*[1], and Constantin Lapa*[1]

[1]*Nuclear Medicine, Faculty of Medicine, University of Augsburg, Augsburg, Germany;* [2]*Medical Physics and Radiation Protection, University Hospital Augsburg, Augsburg, Germany;* [3]*Internal Medicine and Oncology, Faculty of Medicine, University of Augsburg, Augsburg, Germany; and* [4]*Urology, Faculty of Medicine, University of Augsburg, Augsburg, Germany*

We recently published the first dosimetry data, to our knowledge, for the radioligand therapy agent $^{177}$Lu-rhPSMA-10.1, providing an intrapatient comparison with $^{177}$Lu-PSMA-I&T in patients with metastatic prostate cancer. Here, we report efficacy and safety findings from these patients. **Methods:** Four consecutive patients with prostate-specific membrane antigen (PSMA)–positive metastatic prostate cancer received up to 6 cycles of $^{177}$Lu-rhPSMA-10.1 (7.4–7.7 GBq per cycle). Efficacy (prostate-specific antigen response according to Prostate Cancer Working Group 3 criteria and the Response Evaluation Criteria in PSMA PET/CT), progression-free survival, and overall survival were evaluated. Adverse events were recorded from the first dose until 16–24 mo after treatment. **Results:** The patients received a total activity of 29.6–59.4 GBq (4–6 cycles). Prostate-specific antigen was reduced by 100%, 99%, 88%, and 35%. Progression-free survival was not reached for 2 patients at 24 and 18 mo of follow-up and was 15 and 12 mo for the other 2 patients. One patient had a sustained complete response with 2 y of follow up. All patients were alive at the last time point of data collection. No serious adverse events were reported. **Conclusion:** $^{177}$Lu-rhPSMA-10.1 demonstrated encouraging preliminary efficacy and was well tolerated. Formal clinical trials are now under way to evaluate its potential prospectively (NCT05413850).

**Key Words:** prostate cancer; radioligand therapy; prostate-specific membrane antigen; therapeutic response

**J Nucl Med 2024; 65:432–437**
DOI: 10.2967/jnumed.123.266741

A recently developed radiohybrid technology platform has enabled engineering of prostate-specific membrane antigen (PSMA)–targeted ligands (rhPSMA) that can be labeled with $^{18}$F for diagnostic imaging or with α- or β-emitting radiometals for systemic radiation therapy (*1*). The lead diagnostic rhPSMA, $^{18}$F-flotufolastat ($^{18}$F-rhPSMA-7.3), was recently approved by the U.S. Food and Drug Administration for diagnostic imaging in patients with newly diagnosed and recurrent prostate cancer (*2,3*). A pharmacokinetically tuned $^{177}$Lu-labeled rhPSMA therapeutic candidate for patients with metastatic prostate cancer, $^{177}$Lu-rhPSMA-10.1, has shown encouraging results in a series of preclinical assessments (*4,5*).

We recently reported the first clinical data, to our knowledge, comparing pretherapeutic dosimetry of $^{177}$Lu-rhPSMA-10.1 with $^{177}$Lu-PSMA-I&T (*6*). In an intrapatient comparison in patients with metastatic prostate cancer, we were able to show that $^{177}$Lu-rhPSMA-10.1 delivers an increased radiation dose to the tumor compared with $^{177}$Lu-PSMA-I&T, reaching an up to 8-fold improvement in tumor dose in one of the patients (*6*). Data on the recently approved $^{177}$Lu-labeled vipivotide tetraxetan ($^{177}$Lu-PSMA-617) suggest that the greater the radiation dose delivered to the tumor, the better the response observed (*7,8*). Additionally, data from the use of external-beam radiation therapy in over 30,000 patients with prostate cancer are highly supportive of longer survival in patients receiving higher radiation doses to their tumor (*9*). Furthermore, we were able to demonstrate a more favorable tumor-to-kidney therapeutic index (TI), defined as the mean absorbed radiation dose to tumors divided by the absorbed dose to kidneys, for $^{177}$Lu-rhPSMA-10.1 than for $^{177}$Lu-PSMA-I&T. This is of clinical importance because the kidneys are a significant organ at risk in patients undergoing radioligand therapy (RLT) (*10*) and because as the use of such compounds moves earlier in the disease timeline, possibly even into the curative setting, the risk of a delayed radiation nephropathy may increase.

As a result of the favorable TI of $^{177}$Lu-rhPSMA-10.1, and in the absence of an approved RLT in Germany at that time, all 4 patients in our analysis ultimately proceeded to receive RLT with $^{177}$Lu-PSMA-10.1. Here, we report the efficacy and safety findings among these 4 patients who, to the best of our knowledge, were the first globally to receive RLT with $^{177}$Lu-rhPSMA-10.1.

## MATERIALS AND METHODS

### Radiopharmaceutical Preparation and Approval

As previously reported (*6*), all investigations were conducted in accordance with the Helsinki Declaration and with national regulations. The local institutional review board (review board of the Ludwig-Maximilians-Universität München) approved this analysis (permit 22-1011). $^{177}$Lu-rhPSMA-10.1 was prepared in compliance with the German Medicinal Products Act, Arzneimittelgesetz §13 2b,

Received Sep. 23, 2023; revision accepted Nov. 7, 2023.
For correspondence or reprints, contact Constantin Lapa (constantin.lapa@uk-augsburg.de).
*Contributed equally to this work.
Published online Dec. 21, 2023.

and after informing the responsible regulatory body. All patients gave written informed consent to the imaging and therapeutic procedures.

### Patients and Lesions

Four consecutive patients with metastatic prostate cancer were included in this retrospective analysis. All subjects were previously treated with a spectrum of prostate cancer therapies including surgery, radiation therapy, androgen deprivation, novel androgen-axis drugs, and chemotherapy. To be eligible, the patients were required to have PSMA-positive metastatic prostate cancer, defined by the presence of at least 1 PSMA-positive metastatic lesion and no PSMA-negative lesions. The presence of PSMA-positive lesions was determined with $^{68}$Ga-PSMA-I&T PET/CT and defined in accordance with the criteria used in the VISION trial (*11*). PSMA expression was also assessed using the PSMA PET tumor–to–salivary gland ratio (*12*).

The $SUV_{max}$ of the most avid metastasis was measured with $^{68}$Ga-PSMA-I&T PET/CT. Additionally, each PET scan was analyzed with a semiautomatic tumor segmentation algorithm (LIFEx software (*13*)). The total PSMA-positive tumor volume was estimated as previously described using an absolute SUV threshold of at least 3 for segmentation (*14*). Physiologic uptake sites, such as salivary glands, liver, spleen, kidneys, intestine, ureters, and urinary bladder, were manually excluded.

After sufficient PSMA expression was confirmed, the patients underwent dosimetry with both $^{177}$Lu-rhPSMA-10.1 and $^{177}$Lu-PSMA-I&T to determine the TI (*6*). All 4 patients went on to receive treatment with $^{177}$Lu-rhPSMA-10.1 because it was determined to provide the more favorable TI (*6*).

### Therapeutic Dosimetry of First Treatment Cycle

Therapeutic dosimetry in 3 of 4 patients (patient 4 was excluded because of claustrophobia) was conducted after the first treatment cycle as previously described (*6*).

### $^{177}$Lu-rhPSMA-10.1 Therapy and Response Assessment

The patients received up to 6 cycles of $^{177}$Lu-rhPSMA-10.1 (7.4–7.7 GBq), with an interval of 6 wk between cycles.

Efficacy, or serum prostate-specific antigen (PSA) response, was evaluated using Prostate Cancer Working Group 3 criteria (*15*) and the Response Evaluation Criteria in PSMA PET/CT (*16*). In addition, estimations of progression-free survival and overall survival were calculated until the last evaluated time point (July 2023).

### Safety

All patients were monitored for the frequency of adverse events and treatment-related adverse events graded according to version 5.0 of

**TABLE 1**
Clinical Characteristics

| Characteristic | Patient 1 | Patient 2 | Patient 3 | Patient 4 |
|---|---|---|---|---|
| ECOG performance score | 1 | 1 | 1 | 1 |
| Site of disease | | | | |
| Lung | No | No | No | No |
| Liver | No | No | No | No |
| Lymph node | No | No | Yes | Yes |
| Bone | Yes | Yes | No | Yes |
| PSA level (ng/mL) | 0.9 | 9.9 | 15 | 20 |
| Alkaline phosphate level (U/L)* | 85 | 66 | 95 | 82 |
| LDH (U/L)† | 208 | 190 | 183 | 180 |
| Median time since diagnosis (y) | 10 | 3 | 12 | 8 |
| Gleason score at diagnosis | 8 | 9 | 7 | 9 |
| Prior treatment | | | | |
| Prostatectomy | Yes | No | Yes | Yes |
| Androgen receptor pathway | None | 1 | 3 | 2 |
| Inhibitor | | Abiraterone | Abiraterone, enzalutamide, apalutamide | Enzalutamide, abiraterone |
| Taxane therapy | None | Docetaxel | Docetaxel | Docetaxel |
| PSMA expression | | | | |
| PROMISE V2 score | 2 | 2 | 3 | 3 |
| PSMA status (VISION criteria) | Positive | Positive | Positive | Positive |
| $SUV_{max}$ (most avid lesion) | 17.4 | 10.1 | 97.1 | 68.0 |
| Metastases: PSMA-positive TV ($cm^3$) | 19.1 | 7.9 | 47.7 | 118.3 |

*Reference range, 40–130 U/L.
†Reference range, 0–250 U/L.
ECOG = Eastern Cooperative Oncology Group; LDH = lactate dehydrogenase; PROMISE V2 = Prostate Cancer Molecular Imaging Standardized Evaluation, version 2; TV = tumor volume.

the Common Terminology Criteria for Adverse Events (*17*) from the first dose of treatment to 24 mo after treatment.

Blood samples for monitoring of hemoglobin, white blood cells, platelets, creatinine, glomerular filtration rate, alkaline phosphatase, and liver parameters were obtained directly before RLT and every 2–4 wk thereafter.

### Statistics

Most of the reported data are descriptive. All continuous data are reported as mean, SD, and range.

## RESULTS

### Patients

Four patients aged between 65 and 80 y were included in the analysis. Three of 4 patients presented with bone metastases, and 2 presented with lymph node involvement. Their clinical characteristics are shown in Table 1.

### PSMA Expression

All patients were positive for PSMA according to the VISION criteria (*11*), with the $SUV_{max}$ of the most avid metastasis ranging between 10.1 and 97.1. Two patients were rated 2, and 2 patients were rated 3, using the PSMA PET tumor–to–salivary gland ratio (*12*). The PSMA-positive tumor volume varied greatly across patients (range, 7.9–118.3 $cm^3$). Pretherapeutic $^{68}$Ga-PSMA-I&T scans of patients 1 and 4 can be found in Figure 1.

### Therapy

Three of the 4 patients had previously undergone prostatectomy. The patients' treatment before and during $^{177}$Lu-rhPSMA-10.1 is presented in Figure 2. The patients received 4–6 cycles of $^{177}$Lu-rhPSMA-10.1 (Table 2). In posttherapeutic dosimetry for the first treatment cycle, tumor-absorbed doses for reference lesions varied between 0.23 and 0.87 mGy/MBq injected dose of $^{177}$Lu-rhPSMA-10.1 in patient 1, 0.93–1.24 mGy/MBq in patient 2, and 5.5–8.9 mGy/MBq in patient 3, whereas in patient 4, no dosimetry could be performed because of claustrophobia (*6*).

All 4 patients showed a PSA response while receiving $^{177}$Lu-rhPSMA-10.1 as presented in Figure 3. Progression-free survival was not reached for 2 patients at 24 and 18 mo of follow up and was 12 and 15 mo in the other 2 patients.

As of July 2023, all patients were alive, with 1 patient showing an ongoing complete response more than 2 y after starting RLT. Two patients had a partial response, with one having residual lesions in the pelvic lymph nodes and the other having residual disease in the local tumor, thoracic lymph node, and bone. The remaining patient showed disease progression according to the Response Evaluation Criteria in PSMA PET/CT (*16*).

### Safety

No serious or treatment-related adverse events were reported. All reported events are listed in Table 3 and Supplemental Table 1 (supplemental materials are available at http://jnm.snmjournals.org).

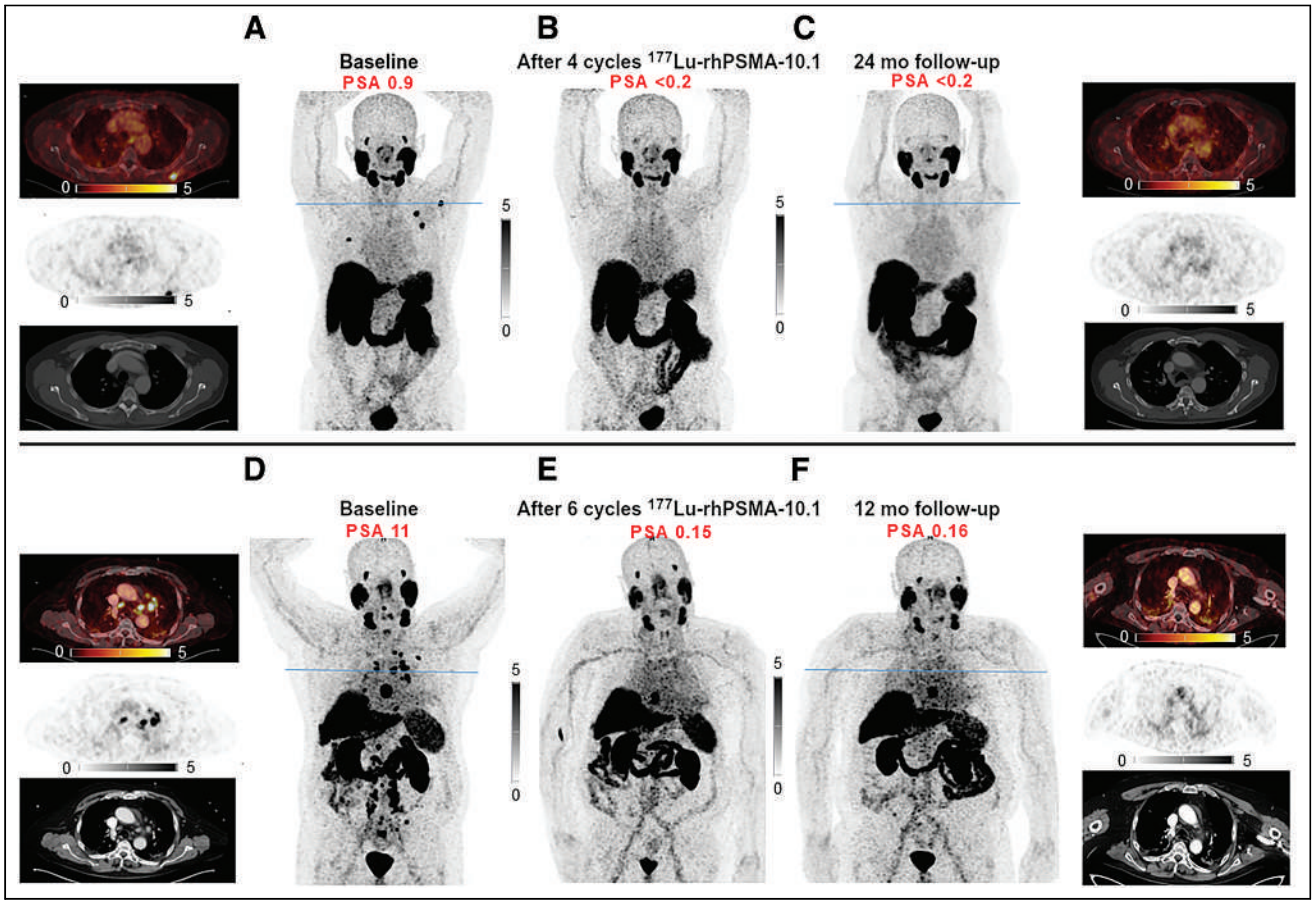


**FIGURE 1.** Example of tumor response to RLT with $^{177}$Lu-rhPSMA-10.1: $^{68}$Ga-PSMA-I&T PET/CT at baseline (A and D), at end of treatment with $^{177}$Lu-rhPSMA-10.1 (B and E), and during follow-up (C and F) of patients 1 (top) and 4 (bottom).

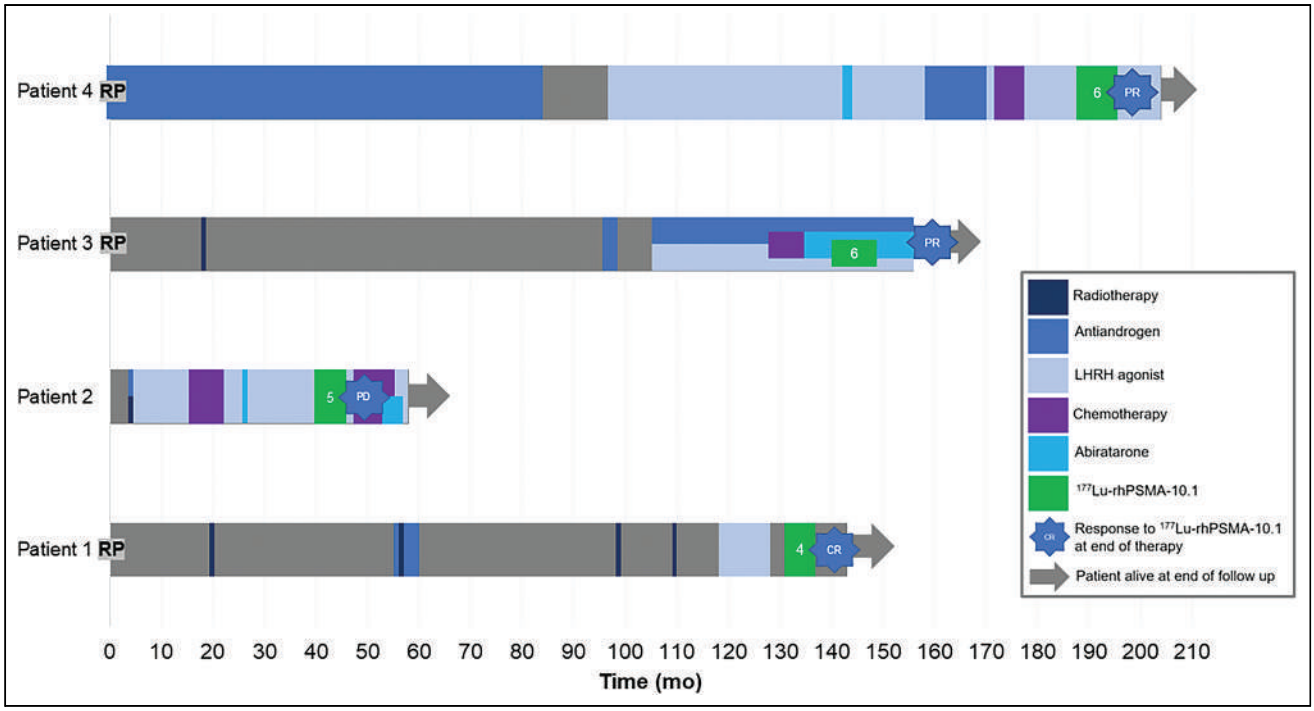


**FIGURE 2.** Patients' treatment before and during $^{177}$Lu-rhPSMA-10.1. All 4 patients were followed up until July 2023. Number of $^{177}$Lu-rhPSMA-10.1 cycles is indicated by number in green bar. CR = complete response; PD = progressive disease; PR = partial response; RP = radical prostatectomy.

All events were mild and graded 1 or 2 according to version 5.0 of the Common Terminology Criteria for Adverse Events (*17*).

## DISCUSSION

Here, we present efficacy and safety data from the clinical use of $^{177}$Lu-rhPSMA-10.1 RLT in 4 patients with metastatic prostate cancer. Our data show that $^{177}$Lu-rhPSMA-10.1 was well tolerated and induced a profound PSA response in 3 of 4 patients, with a smaller PSA response in the fourth patient.

We previously showed that, in the same 4 patients, $^{177}$Lu-rhPSMA-10.1 provided a high TI, indicating a high dose to tumors relative to the absorbed dose to the kidneys. The present data extend these findings to demonstrate that this was able to bring about a remarkable complete response in 1 patient that was still ongoing after more than 2 y of follow-up, with 2 further patients showing partial responses that comprised a 99% and 88% decrease in PSA. The patients received therapeutic $^{177}$Lu-rhPSMA-10.1 activities of between 7.4 and 7.7 GBq per cycle. The favorable TI with $^{177}$Lu-rhPSMA-10.1 raises the possibility that the administered therapeutic activities of $^{177}$Lu-rhPSMA-10.1 could be optimized according to patient need—maximizing tumor-absorbed doses in patients with significantly shortened life expectancy while tolerating higher kidney-absorbed radiation doses. For patients who are earlier in the disease timeline and have a longer life expectancy, the radiation exposure to the kidneys could be reduced while still achieving an effective dose to the tumor (*6*).

**TABLE 2**
$^{177}$Lu-rhPSMA-10.1 Treatment and Response

| $^{177}$Lu-rhPSMA-10.1 | Patient 1 | Patient 2 | Patient 3 | Patient 4 |
|---|---|---|---|---|
| Number of cycles | 4 | 5 | 6 | 6 |
| Cumulative dose (GBq) | 29.6 | 37.6 | 44.4 | 44.7 |
| Greatest PSA decrease in response to $^{177}$Lu-rhPSMA-10.1 (%) | 100 | 35 | 88 | 99 |
| Best response to $^{177}$Lu-rhPSMA-10.1 (RECIP) | Complete response | Stable disease | Partial response | Partial response |
| Response to $^{177}$Lu-rhPSMA-10.1 at end of therapy (RECIP) | Complete response | Progressive disease | Partial response | Partial response |
| Progression-free survival (mo) | 24 (not reached) | 12 | 15 | 18 (not reached) |
| Overall survival | Alive | Alive | Alive | Alive |

RECIP = Response Evaluation Criteria in PSMA PET/CT.

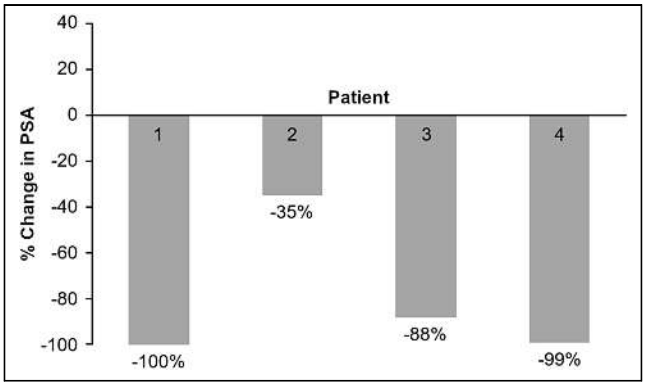


**FIGURE 3.** Waterfall plot to show each patient's response to $^{177}$Lu-rhPSMA-10.1

Our previous data from these patients show that the dose to the tumor varied by patient and by lesion. Data derived with $^{177}$Lu-PSMA-617 in patients with metastatic castration-resistant prostate cancer suggest that efficacy increases when a higher radiation dose is delivered to the tumor (*7,18*). In the present study, we used the criteria applied in the VISION study to determine the PSMA positivity of lesions before initiating RLT (i.e., SUV greater than liver) (*11*). Notably, the patient showing the lowest SUV ($SUV_{max}$, 10.1; patient 2) and a highly variable tumor-absorbed dose was the only patient who showed any disease progression. Despite a 35% reduction in PSA during his 5 cycles of $^{177}$Lu-rhPSMA-10.1, this patient was determined to have progressive disease at the end of treatment. This perhaps highlights the importance of identifying predictive factors that may help select patients with the best chance of success before initiation of $^{177}$Lu-PSMA–based RLT. Recent studies have proposed nomograms that include pretherapeutic imaging with $^{68}$Ga- or $^{18}$F-labeled PSMA ligands to help predict outcomes from $^{177}$Lu-PSMA–based RLT (*19,20*). In addition, the use of radiomics features and artificial intelligence applied on pretherapeutic PET has been suggested (*21*). On the other hand, it has to be acknowledged that in subjects with lower tracer uptake but no other therapeutic options, PSMA therapy may still be preferable to no treatment at all.

**TABLE 3**
Frequency and Severity of Adverse Events

| Adverse event category | Grade 1 | Grade 2 | Grade 3 | Grade 4 |
|---|---|---|---|---|
| Anemia | 4 | 0 | 0 | 0 |
| Leukopenia | 1 | 0 | 0 | 0 |
| Thrombocytopenia | 1 | 0 | 0 | 0 |
| Salivary gland toxicity | 4 | 0 | 0 | 0 |
| Decline in kidney function | 2 | 2* | 0 | 0 |
| Hepatotoxicity | 0 | 0 | 0 | 0 |

*One patient had grade 2 chronic kidney disease at baseline and did not deteriorate.

Data are number of patients (total $n = 4$). All events were graded according to Common Terminology Criteria for Adverse Events version 5.0 (*17*).

Although $^{177}$Lu-labeled radiopharmaceuticals are generally well tolerated, the kidneys remain one of the most important normal organs to consider when planning RLT because of the risk of delayed radiation nephropathy (*22,23*). Although this is less concerning in patients with heavily pretreated disease and a short life expectancy, several years from now it is entirely plausible that this class of agents could be used as neoadjuvant or adjuvant therapies in men with high-risk newly diagnosed prostate cancer undergoing radical primary therapy. Therefore, understanding the exposure to normal organs and the long-term safety is critical. Our data show that there were only minimal adverse events in these patients receiving $^{177}$Lu-rhPSMA-10.1, including grade 1 (mild) chronic kidney disease (*17*). However, our data are limited by a maximum follow-up period of 24 mo, and data extending many years might be necessary to detect a safety signal.

There are some limitations to the present work. Whereas the follow-up period of up to 24 mo after treatment is longer than for most other studies, even longer-term safety data are needed to accurately quantify the risk to normal-organ function. We report data from only a small number of patients who were the first to receive $^{177}$Lu-rhPSMA-10.1 RLT at our clinic. The encouraging findings, however, show $^{177}$Lu-labeled rhPSMA compounds to be suitable candidates for clinical translation, and the results of the ongoing phase 1/2 clinical trial of $^{177}$Lu-rhPSMA-10.1 in patients with metastatic castration-resistant prostate cancer (NCT05413850) are eagerly anticipated.

## CONCLUSION

These clinical data from patients with metastatic castration-resistant prostate cancer undergoing $^{177}$Lu-rhPSMA-10.1 RLT show $^{177}$Lu-rhPSMA-10.1 to be well tolerated and, in all 4 patients evaluated, to bring about PSA responses accompanied by durable radiologic responses to therapy.

## DISCLOSURE

Constantin Lapa reports prior consulting activities for Blue Earth Diagnostics Ltd. and Novartis. Ralph Bundschuh is a consultant for and has received speaker honoraria from Bayer Healthcare, Novartis, and Eisai GmbH and has received travel expenses from Blue Earth Diagnostics Ltd. No other potential conflict of interest relevant to this article was reported.

## ACKNOWLEDGMENT

Medical writing support was provided by Dr. Catriona Turnbull (Blue Earth Diagnostics Ltd.).

**KEY POINTS**

**QUESTION:** Does $^{177}$Lu-rhPSMA-10.1 provide a therapeutic response in patients with metastatic prostate cancer?

**PERTINENT FINDINGS:** In these 4 patients who received RLT with $^{177}$Lu-rhPSMA-10.1, no serious adverse events were noted. All 4 patients showed a PSA response, with 1 patient showing a complete biochemical and radiologic response that was maintained for the 2 y until last follow-up.

**IMPLICATIONS FOR PATIENT CARE:** $^{177}$Lu-rhPSMA-10.1 is well tolerated and brought about decreases in PSA levels ranging from 33% to 100% in all patients evaluated. Prospective clinical studies are under way to confirm these findings (NCT05413850).

## REFERENCES


1. Wurzer A, DiCarlo D, Schmidt A, et al. Radiohybrid ligands: a novel tracer concept exemplified by $^{18}$F- or $^{68}$Ga-labeled rhPSMA inhibitors. *J Nucl Med.* 2020;61:735–742.
2. Surasi DS, Eiber M, Maurer T, et al. Diagnostic performance and safety of positron emission tomography with $^{18}$F-rhPSMA-7.3 in patients with newly diagnosed unfavourable intermediate to very high-risk prostate cancer: results from a phase 3, prospective, multicentre study (LIGHTHOUSE). *Eur Urol.* 2023;84:361–370.
3. Jani AB, Ravizzini G, Gartrell BA, et al. Diagnostic performance and safety of $^{18}$F-rhPSMA-7.3 PET in men with suspected prostate cancer recurrence: results from a phase 3, prospective, multicenter study (SPOTLIGHT). *J Urol.* 2023;210:299–311.
4. Foxton C, Grønlund RV, Simon J, et al. Preclinical evaluation of a novel radioligand therapy for patients with prostate cancer: biodistribution and efficacy of $^{177}$Lu-rhPSMA-10.1 in comparison with $^{177}$Lu-PSMA-I&T [abstract]. *J Nucl Med.* 2022;63(suppl 2):2567.
5. Vassileva V, Grønlund RV, Waldron B, Gauden DE, Stevens DJ, Foxton C. Enhanced therapeutic response to $^{177}$Lu-rhPSMA-10.1 in pre-clinical models of prostate cancer [abstract]. *J Nucl Med.* 2023;64(suppl 1):P621.
6. Rinscheid A, Gäble A, Wienand G, et al. An intrapatient dosimetry comparison of $^{177}$Lu-rhPSMA-10.1 and $^{177}$Lu-PSMA-I&T in patients with metastatic castration-resistant prostate cancer. *J Nucl Med.* 2023;64:1918–1924.
7. Kuo P, Hesterman J, Rahbar K, et al. [$^{68}$Ga]Ga-PSMA-11 PET baseline imaging as a prognostic tool for clinical outcomes to [$^{177}$Lu]Lu-PSMA-617 in patients with mCRPC: a VISION substudy [abstract]. *J Clin Oncol.* 2022;40(suppl):5002.
8. Violet J, Jackson P, Ferdinandus J, et al. Dosimetry of $^{177}$Lu-PSMA-617 in metastatic castration-resistant prostate cancer: correlations between pretherapeutic imaging and whole-body tumor dosimetry with treatment outcomes. *J Nucl Med.* 2019;60:517–523.
9. Kalbasi A, Li J, Berman A, et al. Dose-escalated irradiation and overall survival in men with nonmetastatic prostate cancer. *JAMA Oncol.* 2015;1:897–906.
10. Okamoto S, Thieme A, Allmann J, et al. Radiation dosimetry for $^{177}$Lu-PSMA I&T in metastatic castration-resistant prostate cancer: absorbed dose in normal organs and tumor lesions. *J Nucl Med.* 2017;58:445–450.
11. Sartor O, de Bono J, Chi KN, et al. Lutetium-177–PSMA-617 for metastatic castration-resistant prostate cancer. *N Engl J Med.* 2021;385:1091–1103.
12. Hotta M, Gafita A, Murthy V, et al. PSMA PET tumor-to-salivary glands ratio (PSG score) to predict response to Lu-177 PSMA radioligand therapy: an international multicenter retrospective study [abstract]. *J Nucl Med.* 2022;63(suppl 2):P3040.
13. Nioche C, Orlhac F, Boughdad S, et al. LIFEx: a freeware for radiomic feature calculation in multimodality imaging to accelerate advances in the characterization of tumor heterogeneity. *Cancer Res.* 2018;78:4786–4789.
14. Ferdinandus J, Violet J, Sandhu S, et al. Prognostic biomarkers in men with metastatic castration-resistant prostate cancer receiving [$^{177}$Lu]-PSMA-617. *Eur J Nucl Med Mol Imaging.* 2020;47:2322–2327.
15. Scher HI, Morris MJ, Stadler WM, et al. Trial design and objectives for castration-resistant prostate cancer: updated recommendations from the Prostate Cancer Clinical Trials Working Group 3. *J Clin Oncol.* 2016;34:1402–1418.
16. Gafita A, Rauscher I, Weber M, et al. Novel framework for treatment response evaluation using PSMA PET/CT in patients with metastatic castration-resistant prostate cancer (RECIP 1.0): an international multicenter study. *J Nucl Med.* 2022;63:1651–1658.
17. *Common Terminology Criteria for Adverse Events (CTCAE) Version 5.0.* U.S. Department of Health and Human Services; 2017; https://ctep.cancer.gov/protocolDevelopment/electronic_applications/docs/CTCAE_v5_Quick_Reference_5x7.pdf#search=%22CTCAE%20version%205%22.
18. Hohberg M, Reifegerst M, Drzezga A, Wild M, Schmidt M. Prediction of response to $^{177}$Lu-PSMA therapy based on tumor-to-kidney ratio on pretherapeutic PSMA PET/CT and posttherapeutic tumor-dose evaluation in mCRPC. *J Nucl Med.* 2023;64:1758–1764.
19. Gafita A, Calais J, Grogan TR, et al. Nomograms to predict outcomes after $^{177}$Lu-PSMA therapy in men with metastatic castration-resistant prostate cancer: an international, multicentre, retrospective study. *Lancet Oncol.* 2021;22:1115–1125.
20. Rauscher I, Hansen K, Gafita A, et al. Extension of a $^{68}$Ga-PSMA PET-based nomogram for outcome prediction of $^{177}$Lu-PSMA radioligand therapy for the use of $^{18}$F-rhPSMA-7.3 [abstract]. *J Nucl Med.* 2023;63(suppl 1):P400.
21. Moazemi S, Erle A, Khurshid Z, et al. Decision-support for treatment with $^{177}$Lu-PSMA: machine learning predicts response with high accuracy based on PSMA-PET/CT and clinical parameters. *Ann Transl Med.* 2021;9:818.
22. Tagawa ST, Sartor O, Saad F, et al. 647TiP PSMAddition: a phase III trial to compare treatment with $^{177}$Lu-PSMA-617 plus standard of care (SOC) versus SOC alone in patients with metastatic hormone-sensitive prostate cancer. *Ann Oncol.* 2021;32(suppl 5):S673–S675.
23. Schäfer H, Mayr S, Buttner-Herold M, et al. Extensive $^{177}$Lu-PSMA radioligand therapy can lead to radiation nephropathy with a renal thrombotic microangiopathy-like picture. *Eur Urol.* 2023;83:385–390.

# Differences and Common Ground in $^{177}$Lu-PSMA Radioligand Therapy Practice Patterns: International Survey of 95 Theranostic Centers

Andrea Farolfi[1,2], Wesley R. Armstrong[1], Loic Djaileb[1,3], Andrei Gafita[1,4], Masatoshi Hotta[1], Martin Allen-Auerbach[1], Lena M. Unterrainer[1,5], Wolfgang P. Fendler[6], Matthew Rettig[7,8], Matthias Eiber[9], Michael S. Hofman[10], Boris Hadaschik[11], Ken Herrmann[6], Johannes Czernin[1], Jeremie Calais[1], and Matthias R. Benz[1,6,12]

*[1]Ahmanson Translational Theranostics Division, Department of Molecular and Medical Pharmacology, UCLA, Los Angeles, California; [2]Nuclear Medicine, IRCCS Azienda Ospedaliero–Universitaria di Bologna, Bologna, Italy; [3]LRB, Nuclear Medicine Department, CHU Grenoble Alpes, University of Grenoble Alpes, INSERM, Grenoble, France; [4]Division of Nuclear Medicine and Molecular Imaging, Russell H. Morgan Department of Radiology and Radiological Science, Johns Hopkins University School of Medicine, Baltimore, Maryland; [5]Department of Nuclear Medicine, Ludwig-Maximilian University, Munich, Germany; [6]Department of Nuclear Medicine, University of Duisburg–Essen and German Cancer Consortium–University Hospital Essen, Essen, Germany; [7]Department of Medicine and Urology, UCLA, Los Angeles, California; [8]Department of Medicine, VA Greater Los Angeles, Los Angeles, California; [9]Department of Nuclear Medicine, Klinikum Rechts Der Isar, Technical University of Munich, Munich, Germany; [10]Prostate Cancer Theranostics and Imaging Centre of Excellence, Molecular Imaging and Therapeutic Nuclear Medicine, Cancer Imaging, Peter MacCallum Cancer Centre, and Sir Peter MacCallum Department of Oncology, University of Melbourne, Melbourne, Victoria, Australia; [11]Department of Urology, University of Duisburg–Essen and German Cancer Consortium–University Hospital Essen, Essen, Germany; and [12]Department of Radiological Sciences, UCLA, Los Angeles, California*

$^{177}$Lu-labeled prostate-specific membrane antigen (PSMA) radioligand therapy effectively treats metastatic castration-resistant prostate cancer. Patients requiring treatment, and consequently the number of theranostic centers, are expected to increase significantly after Food and Drug Administration and European Medicines Agency approval. This requires standardization or harmonization among theranostic centers. The aim of this study was to assess operational differences and similarities among $^{177}$Lu-PSMA treatment centers. **Methods:** A questionnaire comprising 62 items, designed by a core team of 5 physicians and externally reviewed by international experts, was developed. Study participants were asked to provide answers about their center, patient selection, radiopharmaceuticals, clinical assessment before and after $^{177}$Lu-PSMA treatments, laboratory values, treatment discontinuation, posttreatment imaging, and general information. An invitation e-mail to participate in the study was sent in June 2022. Duplicates were removed to allow for only one valid response per center. **Results:** Ninety-five of 211 (45%) contacted centers completed the questionnaire. Most participating centers were in Europe (51%), followed by America (22%) and Asia (22%). During the 12 mo before this study, a total of 5,906 patients received $^{177}$Lu-PSMA therapy at the 95 participating centers. Most of these patients were treated in Europe (2,840/5,906; 48%), followed by Asia (1,313/5,906; 22%) and Oceania (1,225/5,906; 21%). PSMA PET eligibility for $^{177}$Lu-PSMA was determined most frequently using $^{68}$Ga-PSMA-11 (77%). Additional pretherapy imaging included $^{18}$F-FDG PET/CT, CT, renal scintigraphy, and bone scintigraphy at 41 (49%), 27 (32%), 25 (30%), and 13 (15%), respectively, of the 84 centers for clinical standard of care, compassionate care, or local research protocols and 11 (26%), 25 (60%), 9 (21%), and 28 (67%), respectively, of the 42 centers for industry-sponsored trials. PSMA PET eligibility criteria included subjective qualitative assessment of PSMA positivity at 33% of centers, VISION criteria at 23%, and TheraP criteria at 13%. The mean standard injected activity per cycle was 7.3 GBq (range, 5.5–11.1 GBq). Sixty-two (65%) centers applied standardized response assessment criteria, and PSMA PET Progression Criteria were the most applied (37%). **Conclusion:** Results from this international survey revealed interinstitutional differences in several aspects of $^{177}$Lu-PSMA radionuclide therapy, including patient selection, administered activity, and the response assessment strategy. Standardization or harmonization of protocols and dedicated training are desirable in anticipation of increasing numbers of patients and theranostic centers.

**Key Words:** PET/CT; radionuclide therapy; $^{177}$Lu-PSMA; prostate cancer; survey; theranostic

**J Nucl Med 2024; 65:438–445**
DOI: 10.2967/jnumed.123.266391

Prospective single-arm (*1–3*), randomized (*4,5*) clinical trials have shown $^{177}$Lu-labeled prostate-specific membrane antigen (PSMA) radioligand therapy (RLT) to be effective for treating metastatic castration-resistant prostate cancer (CRPC). It received U.S Food and Drug Administration and European Medicines Agency approval in 2022 and was swiftly adopted into prostate cancer management guidelines (*6–8*). PSMA PET imaging and $^{177}$Lu-PSMA RLT are gaining momentum globally, but treatment delivery has faced several obstacles limiting its widespread accessibility. Patient numbers are expected to increase significantly, with an estimated 34,000 prostate cancer patients requiring approximately 120,000 $^{177}$Lu-PSMA treatment cycles per year in the United States alone (*9,10*). Approximately 140 U.S. centers are needed to satisfy this demand, assuming the administration of 4 cycles per center per day (*9*).

Received Jul. 19, 2023; revision accepted Nov. 18, 2023.
For correspondence or reprints, contact Matthias R. Benz (mbenz@mednet.ucla.edu).
Guest Editor: David A. Mankoff, University of Pennsylvania
Published online Jan. 18, 2024.

Besides the limited number of treatment centers, challenges include radiopharmaceutical production and delivery, with demand–supply imbalance, lack of medical provider training and competence, and the need for additional workforce, including nuclear medicine physicians and nursing staff (*11*). Despite a widely varying regulatory, financial, and medical landscape, the nuclear medicine community has been spearheading efforts to meet the need for this new standard-of-care (SOC) treatment (*12*). Joint guidelines were recently proposed by the European Association of Nuclear Medicine, Society of Nuclear Medicine and Molecular Imaging, and International Atomic Energy Agency to establish an overarching framework helping practitioners understand what is required to set up a theranostics center (*13,14*). Further guidance is provided by joint procedure guidelines of the European Association of Nuclear Medicine and Society of Nuclear Medicine and Molecular Imaging (*15*). Moreover, the nuclear medicine community has engaged with urooncology experts to incorporate PSMA imaging and radionuclide therapy into clinical practice consensus guidelines (*16,17*).

$^{177}$Lu-vipivotide tetraxetan, also known as $^{177}$Lu-PSMA-617, is Food and Drug Administration–approved for treatment of adults with PSMA-positive metastatic CRPC who have been treated with androgen receptor pathway inhibitor and taxane-based chemotherapy. The prescribing information suggests patient selection based on PSMA imaging and the administration of 7.4 GBq (200 mCi) every 6 wk for up to 6 doses, as the registrational VISION trial proposed (*4*). However, criteria defining $^{177}$Lu-PSMA RLT eligibility by PSMA PET, therapy protocols, therapy response assessment, and parameters for treatment discontinuation all differ between established theranostic centers and countries. Therefore, the aim of this international questionnaire study was to assess operational differences and similarities between $^{177}$Lu-PSMA treatment centers.

## MATERIALS AND METHODS

The survey comprised 62 questions including multiple-choice and free-text answers and was prepared using Qualtrics XM in a web-based design (Supplemental Fig. 1; supplemental materials are available at http://jnm.snmjournals.org). The questions were drafted by UCLA investigators and externally reviewed by 5 international experts in the field of PSMA theranostics. Once the final version of the questionnaire was outlined, an official invitation e-mail to participate in the study was sent in June 2022. The invitation was sent to all centers involved in patient recruitment for the TheraP and VISION trials (*4,5*), the corresponding authors on clinical $^{177}$Lu-PSMA publications (screened through PubMed), and international contacts of the investigators. Duplicates were removed to allow for only one valid response per center. The survey was closed in late September 2022.

### Survey Structure

The questionnaire involved general physician and center-specific questions; questions on patient selection, radiopharmaceuticals, clinical assessment before and after $^{177}$Lu-PSMA treatments, laboratory values, treatment discontinuation, and posttreatment imaging; and general questions (Supplemental Fig. 1).

### Data Analysis

Survey answers were exported in an Excel (Microsoft) spreadsheet, and the data were analyzed. Descriptive analysis was performed using SPSS software (IBM).

## RESULTS

### Geographic Location of Participating Centers

In total, 95 of 211 (45%) contacted centers completed the questionnaire (Fig. 1). Most participating centers were in Europe (48; 51%), followed by North and South America (21; 22%), Asia (21; 22%), Oceania (3; 3%), and Africa (2; 2%). On a national level, Germany (22%), France (12%), Brazil (8%), the United States (7%), India (6%), and China (5%) provided the highest number of participating centers (Fig. 2A).

### Population Characteristics

During the 12 mo before the study, a total of 5,906 patients received $^{177}$Lu-PSMA therapy at the 95 participating centers. Most patients were treated in Europe (2,840/5,906; 48%), followed by Asia (1,313/5,906; 22%) and Oceania (1,225/5,906; 21%) (Fig. 2B). Most centers were actively involved in $^{177}$Lu-PSMA through different models of care: $^{177}$Lu-PSMA was given at 84 (88%) centers as SOC treatment or compassionate-care access (CCA), at 42 (44%) centers as part of industry-sponsored clinical trials, and at 21 (22%) centers as part of locally approved research protocols (LARPs) not sponsored by industry (multiple options of care possible per center; therefore, number exceeds 100%; Fig. 3; Supplemental Fig. 2). Forty-six (48%) centers treated patients only with metastatic CRPC, whereas 47 (49%) centers treated patients

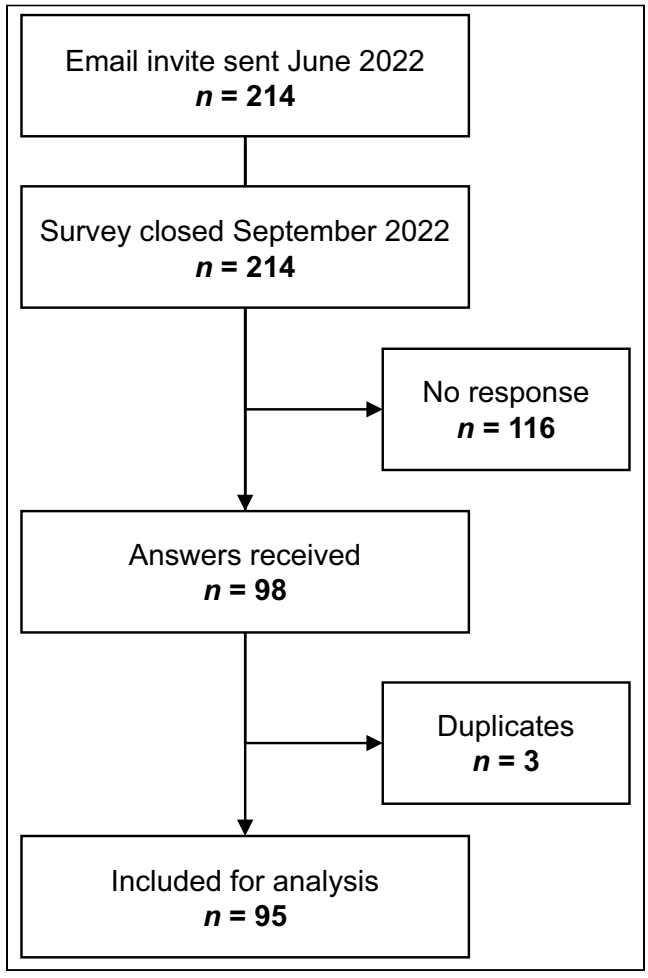


**FIGURE 1.** Diagram of number of participating centers.

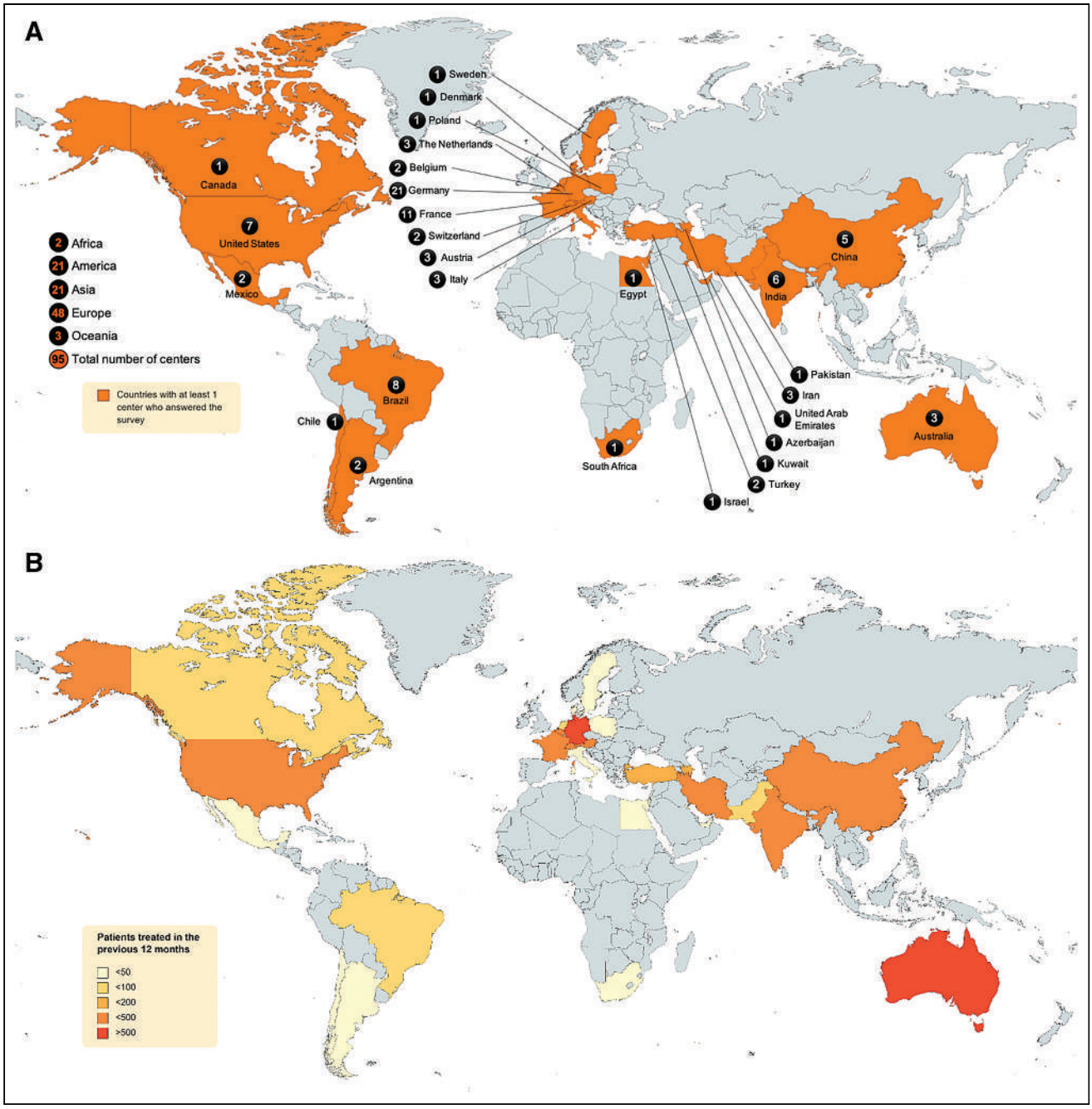


**FIGURE 2.** Geographic location of participating centers (A), and heat map of number of patients treated between June 2021 and September 2022 (B).

with metastatic CRPC and hormone-sensitive prostate cancer (HSPC). Two (2%) centers treated only HSPC.

### Initiation of PSMA RLT

Ten (11%) centers started PSMA RLT before 2015, 64 (67%) between 2015 and 2020, and 21 (22%) between 2021 and 2022. The earliest $^{131}$I-MIP-1095 had been used was 2011. Overall, 50% of centers were already treating patients before 2018. Supplemental Figure 3 shows increments of PSMA RLT centers per continent.

### Pretreatment Imaging and PSMA PET Eligibility Criteria

*Pretreatment PSMA Imaging.* PSMA PET or PSMA SPECT was performed at all participating centers to assess patient eligibility for $^{177}$Lu-PSMA RLT (Fig. 4). $^{68}$Ga-PSMA-11 was the most frequently used PET radiotracer (73; 77%), followed by $^{18}$F-PSMA-1007 (39; 41%), $^{68}$Ga-PSMA-I&T (21; 22%), and $^{18}$F-DCFPyL (18; 19%) (continent-based analysis in Supplemental Fig. 4). At 12 (13%) centers, $^{99m}$Tc-labeled PSMA for SPECT imaging was sufficient to assess $^{177}$Lu-PSMA RLT eligibility, and these locations were predominantly in Germany (5/12), Iran (2/12), and Mexico (2/12).

*Additional Pretreatment Imaging.* $^{18}$F-FDG PET/CT was performed at 49% of centers when $^{177}$Lu-PSMA therapy was provided as SOC, CCA, or LARP not sponsored by industry and at 26% of centers when patients were enrolled in industry-sponsored clinical trials (Fig. 4). Additional pretherapy imaging included CT

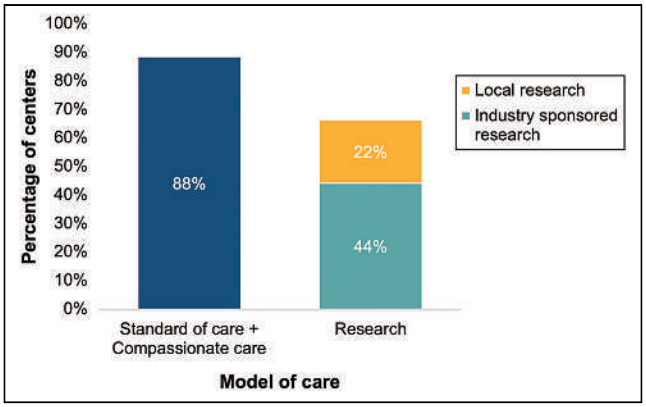


**FIGURE 3.** $^{177}$Lu-PSMA model of care among participating centers (multiple answers allowed).

(SOC + CCA + LARP, 32%; industry-sponsored trials, 60%), bone scintigraphy (SOC + CCA + LARP, 15%; industry-sponsored trials, 67%), renal scintigraphy (SOC + CCA + LARP, 30%; industry-sponsored trials, 21%), and others (Fig. 4). Geographic differences were evident mainly for pretherapy renal scintigraphy (e.g., as part of the eligibility process at 15 of 21 centers in Germany) and for choline PET (e.g., performed at 9 of 11 centers in France).

*PSMA PET Eligibility Criteria.* The most frequently applied PSMA PET eligibility criterion for $^{177}$Lu-PSMA RLT was a subjective visual whole-body tumor PSMA positivity evaluation (33%), followed by assessment of tumor PSMA uptake in comparison to liver (defined as >50% of tumor lesions with uptake more than in the liver) (26%), VISION criteria (23%), and TheraP criteria (13%) (Fig. 5). No significant differences among continents were observed for applied eligibility criteria.

*Performance Status and Quality of Life.* To be eligible for $^{177}$Lu-PSMA RLT, patients had to have an Eastern Cooperative Oncology Group performance status no higher than 1 at 2 centers (2%), 2 at 65 (68%), 3 at 22 (23%), and 4 at 6 (6%). Pretreatment quality-of-life assessment using validated questionnaires was not performed routinely at 67 (71%) centers. Among quality-of-life tools, European Organisation for Research and Treatment of Cancer Quality of Life Questionnaire Core 30 was the most commonly used, that is, at 14 (15%) centers.

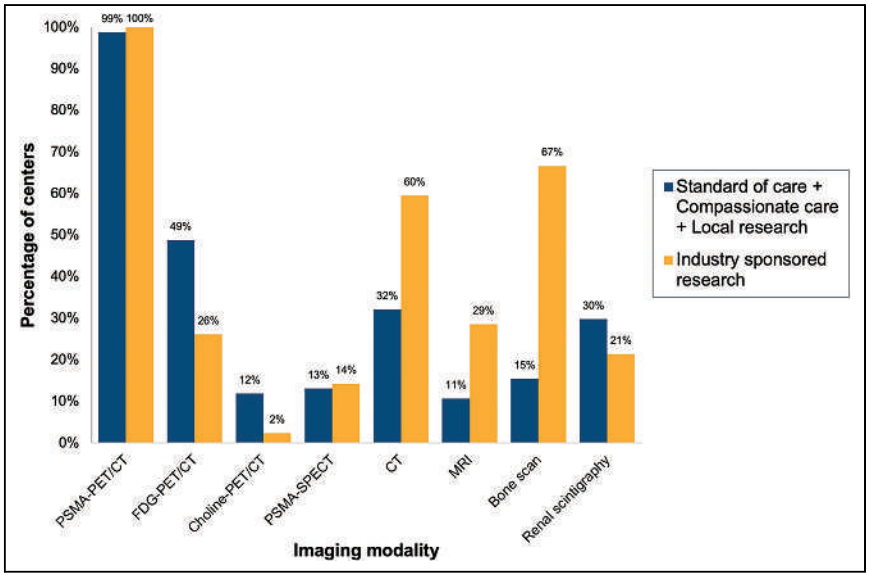


**FIGURE 4.** Imaging modalities performed to assess patient eligibility classified by model of care (multiple answers allowed).

## Treatment

*Administered Radiopharmaceuticals.* For RLT agents, 48 (51%) centers use $^{177}$Lu PSMA-617 only, 21 (22%) $^{177}$Lu PSMA-I&T only, and 26 (27%) both $^{177}$Lu PSMA-617 and $^{177}$Lu PSMA-I&T. Additionally, 7 (7%) were also using other labeled PSMA-targeting agents such as $^{225}$Ac-PSMA.

*Therapy Dose and Interval Between Treatment Cycles.* Mean standard injected radioactivity per cycle for $^{177}$Lu-PSMA RLT was 7.3 GBq (range, 5.5–11.1 GBq). Continent-based subanalysis showed an average injected radioactivity (GBq) per cycle of $7.5 \pm 0.1$, $7.3 \pm 0.4$, $7.5 \pm 1.1$, $7.1 \pm 0.7$, and $8.2 \pm 0.3$ for Africa, America, Asia, Europe, and Oceania, respectively. Dose deescalation was performed at 10 (11%) centers. Injected activity was adapted on the basis of bone marrow, salivary gland, kidney, or liver function at 50 (53%) centers; the patients' PSMA-positive tumor volume at 12 (13%); patient weight at 9 (9%); and dosimetry measurements at 6 (6%).

The most frequent intervals between $^{177}$Lu-PSMA RLT cycles was 6 wk at 57 centers (60%) and 8 wk at 26 (27%). Six (7%) centers adapted the intervals between cycles on the basis of prostate-specific antigen (PSA) levels and clinical parameters.

## Response Assessment

*Imaging Response Criteria.* The PSMA PET Progression Criteria were most frequently applied (35; 37%), followed by RECIST 1.1 (23; 24%), the Prostate Cancer Working Group Criteria (PCWG3) (21; 22%), the Response Evaluation Criteria in Prostate Cancer (RECIP) 1.0 (10; 11%), and PERCIST (7; 7%) (Fig. 6; Supplemental Fig. 5). Multiple answers were allowed for this question. Thirty-three (35%) centers did not apply standardized radiographic criteria for response assessment.

*Timing of Radiographic Response Assessment.* PSMA PET was performed for response assessment at 83 (87%) centers. PSMA PET was performed before the third treatment cycle at 48 (51%) centers and after completion of therapy at 63 (66%) centers. Twenty-four (25%) centers indicated that the timing of imaging response assessment was variable, depending on biochemical parameters and clinical status.

*Clinical Assessment During Therapy.* Parameters systematically evaluated by most (≥80%) centers throughout the course of $^{177}$Lu-PSMA RLT included pain, fatigue, xerostomia, appetite, weight, and quality of life, at 99%, 95%, 88%, 85%, 83%, and 83% of centers, respectively.

## Laboratory Parameters

Blood was drawn most frequently 2 and 3 wk after each therapy cycle at 45 (47%) and 20 (21%) centers, respectively. Blood was drawn most frequently 1 and 2 wk

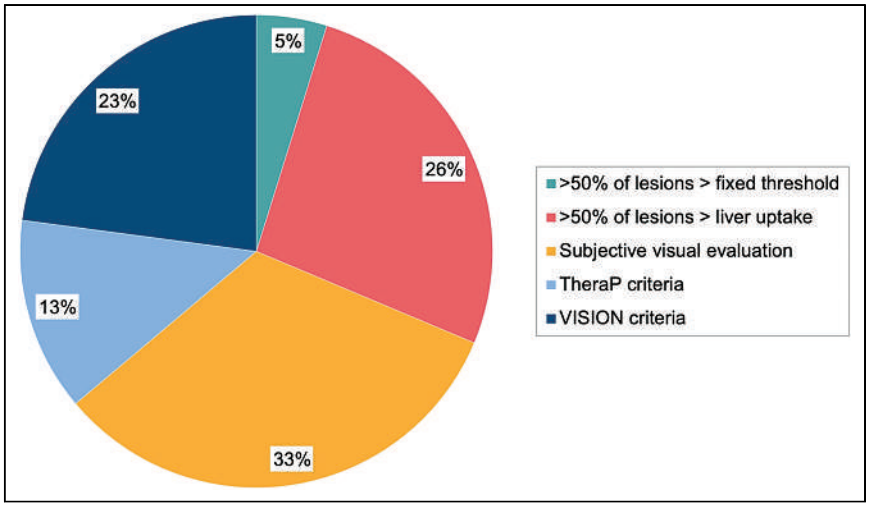


**FIGURE 5.** PSMA PET eligibility criteria for $^{177}$Lu-PSMA RLT.

before the next therapy cycle at 62 (65%) and 24 (25%) centers, respectively.

At least 98% of centers measured platelets, erythrocytes, hemoglobin, and total white cell count before treatment initiation and between cycles. Some discrepancies were found between the blood tests requested at treatment initiation and between treatment cycles, including PSA (99% vs. 94%), neutrophils (92% vs. 83%), creatinine (99% vs. 91%), glomerular filtration rate (87% vs. 73%), liver enzymes (94% vs 82%), alkaline phosphatase (92% vs. 77%), and lactate dehydrogenase (74% vs. 57%) (Fig. 7).

### $^{177}$Lu-PSMA γ-Imaging

Posttreatment $^{177}$Lu-PSMA γ-imaging was performed at 90 (95%) of centers. Regarding each treatment cycle, 94% of centers performed $^{177}$Lu-PSMA γ-imaging after the first cycle, 87% after the second, and 85% after the third and fourth cycles. Whole-body planar acquisition was most frequently used (77%), followed by semiquantitative SPECT with 2 or more bed positions (37%). The time of $^{177}$Lu-PSMA γ-image acquisition was 4, 24, 48, and 72 h after injection at 18%, 62%, 32%, and 12% of centers, respectively. Ten (11%) stated that they always acquire images at at least 2 different time points.

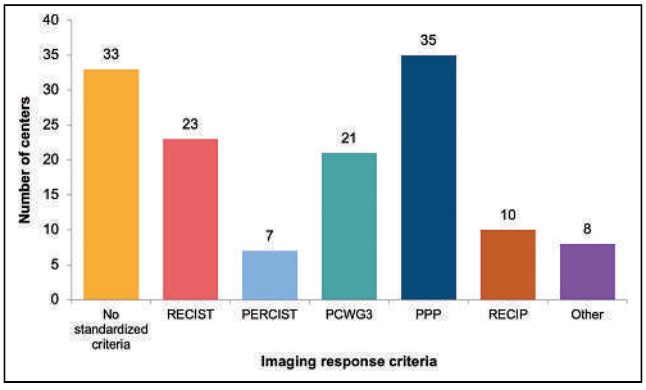


**FIGURE 6.** Imaging response criteria for $^{177}$Lu-PSMA (multiple answers allowed). PPP = PSMA PET Progression Criteria.

### Discontinuation

Treatment discontinuation was more frequent after the second treatment cycle (54; 57%) than after the third treatment cycle (37; 39%). A rising PSA required confirmation before $^{177}$Lu-PSMA RLT discontinuation, with a second PSA sample obtained at 14 (15%) centers, whereas confirmatory imaging in conjunction with a second PSA sample was a requirement for discontinuation at 65 (68%) centers. Parameters leading alone to treatment discontinuation were low platelets at 61 centers (64%), low neutrophils at 58 (61%), and low hemoglobin at 31 (33%). A rise in PSA alone led to treatment discontinuation at 21 (22%) centers.

### Role of Nuclear Medicine Physician

The responders were nuclear medicine physicians at 88 (93%) centers, medical oncologists at 2 (2%), radiation oncologists at 2 (2%), and others at 3 (3%) (1 radiologist, 1 internal medicine physician, and 1 radiochemist). At 94 (99%) centers, nuclear medicine physicians were involved in at least one aspect of $^{177}$Lu-PSMA RLT, namely evaluation of the treatment indication (89; 94%), assessment of patient eligibility (86; 91%), and management between cycles (87; 92%). Patients were followed up for posttherapy outcomes by nuclear medicine physicians at 74% of centers. At 23 (24%) centers, the nuclear medicine physician was not involved in the discussion of treatment discontinuation. At the 72 (76%) centers where the nuclear medicine physician was involved in the discussion of treatment discontinuation, it was the nuclear medicine physician's responsibility to bring the treatment discontinuation discussion to a multidisciplinary team at 65 of 72 (90%) centers.

### $^{177}$Lu-PSMA RLT Reimbursement

$^{177}$Lu-PSMA RLT was completely covered by the health care system at 51 (54%) centers, whereas 19 (20%) centers reported only partial coverage. No insurance coverage was reported at 25 (26%) centers.

$^{177}$Lu-PSMA RLT was performed as an outpatient procedure at 46 (48%) centers and as a 1-, 2-, and 3-d inpatient procedure at 19 (20%), 16 (17%), and 14 (15%) centers, respectively (Supplemental Fig. 6).

## DISCUSSION

The rapid increase in use of theranostics is being addressed by scientific societies supporting theranostic centers with treatment guidelines (*13–15,18*). The current study demonstrated interinstitutional differences in $^{177}$Lu-PSMA RLT operations, including patient selection, dosing, response assessment, and treatment discontinuation. In part, these differences reflect variations in accepted standards of practice as reflected in guidelines and the evidence base. The survey also, however, identifies some areas of concern. Although data on the effectiveness of $^{177}$Lu-PSMA RLT in HSPC are still lacking, 49% of participating centers were treating both CRPC and HSPC, which is remarkably higher than was found in a previous survey reporting 20% of centers treating CRPC and HSPC (*19*). This difference may, in part, reflect increased participation in trials investigating the effectiveness of $^{177}$Lu-PSMA RLT in HSPC, such as the LuTectomy

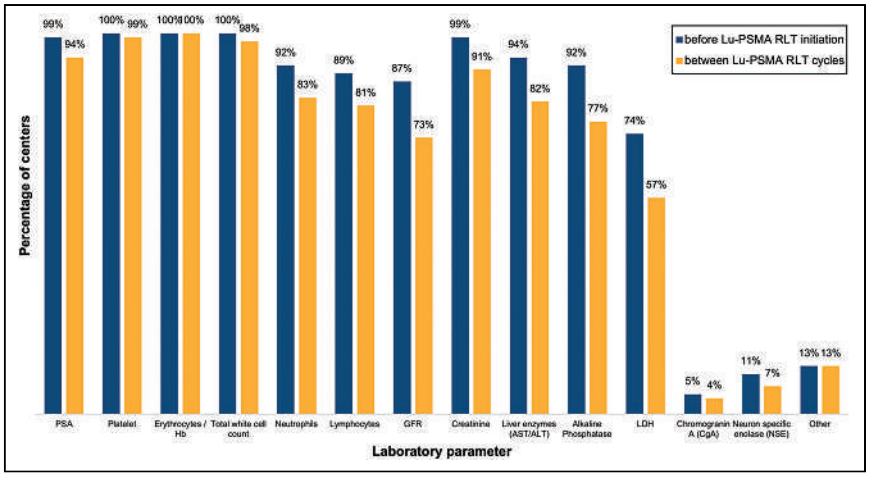


**FIGURE 7.** Laboratory parameters assessed before and between $^{177}$Lu-PSMA RLT cycles. AST/ALT = aspartate transaminase/alanine transaminase; GFR = glomerular filtration rate; Hb = hemoglobin; LDH = lactate dehydrogenase.

(NCT04430192), UpFrontPSMA (NCT04343885), and PSMAddition (NCT04720157) trials. However, sufficient data are still missing to entirely justify $^{177}$Lu-PSMA RLT in HSPC patient outside prospective studies.

Interestingly, at 68% of centers, an Eastern Cooperative Oncology Group score of 2 was the highest performance status accepted for $^{177}$Lu-PSMA therapy, whereas 29% of centers accepted an Eastern Cooperative Oncology Group score of up to 3 or 4. This might reflect differences in the training and competence of physician and nonphysician staff in providing appropriate care to patients with poor functional status.

The survey highlights variations in patient selection. The Food and Drug Administration advised that selection of patients for treatment using an approved PSMA imaging agent be based on PSMA expression in tumors. Several PSMA PET eligibility criteria have been proposed, including criteria published in reports of previous prospective trials (*4,5*). However, we found that, most commonly, a subjective visual whole-body tumor PSMA positivity evaluation (33%) was performed to assess treatment eligibility. In several studies investigating predictive PSMA PET imaging for assessing response to $^{177}$Lu-PSMA RLT, the biomarkers differed from those in previously published prospective trials and require further investigation (*20–22*).

Even though the mean standard injected activity per cycle for $^{177}$Lu-PSMA RLT was almost similar to what is recommended by the Food and Drug Administration (7.3 vs. 7.4 GBq), the administered doses in our survey ranged between 5.5 and 11.1 GBq. More than half the centers (53%) adapted the injected dose on the basis of the patient's bone marrow, salivary gland, kidney, or liver function. Further trials are needed to better understand the morbidity and mortality of adapted versus fixed-dose protocols. Also, dose deescalation or adaptation based on patient weight or dosimetry was performed at fewer than 12% of centers.

In the European Association of Urology–European Association of Nuclear Medicine Consensus Statement, the experts achieved consensus on the use of PSMA PET/CT in the evaluation of response to $^{177}$Lu-PSMA RLT even though no consensus on the timing of PSMA PET/CT was reached (*23*). This reflects the heterogeneity of our findings, with centers applying PET at different intervals after treatment. The panelists discussed neither the specific radiographic response criteria nor the possibility of assessing treatment response using posttreatment $^{177}$Lu-PSMA γ-imaging, a method that around 30% of centers participating in our survey use. In this context, the PROMISE V2 guidelines also provide a framework for response criteria (*24*). In metastatic prostate cancer, treatment response was traditionally evaluated using CT/MRI and bone scanning according to the PCWG3 criteria (*25*). Nevertheless, neither PCWG3 nor RECIST 1.1 (*26*) or PERCIST 1.0 (*27*) was designed to include PSMA PET/CT imaging. The PSMA PET Progression Criteria (*28*) and RECIP 1.0 (*29*) were just recently introduced but had already been applied at 37% and 11% of participating centers, respectively. A recent study investigated the accuracy of RECIST 1.1, adapted PCWG3, adapted PERCIST 1.0, the PSMA PET Progression Criteria, and RECIP 1.0 for response evaluation using PSMA PET/CT in men with metastatic CRPC treated with $^{177}$Lu-PSMA RLT (*30*). Among the assessed frameworks, RECIP 1.0 were found to have the highest prognostic value and interreader reliability. However, one third (35%) of centers do not apply any standardized imaging criteria for therapy response evaluation. RECIP originally integrated software-based quantitative assessment of total tumor volume (quantitative RECIP), but wide clinical implementation of such software is not expected soon. Recently, RECIP—determined using visual reads by nuclear medicine physicians (visual RECIP)—showed 95% agreement with quantitative RECIP (*31*). Hence, RECIP can immediately be implemented in daily practice.

Since a large number of metastatic CRPC patients might not benefit from $^{177}$Lu-PSMA RLT (*1–3*), criteria for treatment discontinuation need to be discussed. Our results suggest that the clinical complexity does not allow for easy establishment of criteria or definite cutoffs. There is agreement that a single post–$^{177}$Lu-PSMA RLT PSA increase alone is not sufficient to justify $^{177}$Lu-PSMA RLT discontinuation but that confirmation by a second PSA sample or radiologic progression is required.

All participating centers stated that PSMA imaging, that is, PET or SPECT, was mandatory to assess $^{177}$Lu-PSMA RLT eligibility. On the basis of the European Association of Urology–European Association of Nuclear Medicine consensus statement, PSMA PET/CT should be performed on any candidate before $^{177}$Lu-PSMA RLT (*23*), whereas in our results 13% of centers affirmed that they also use PSMA SPECT imaging. Evaluation of PSMA expression is crucial to assess $^{177}$Lu-PSMA RLT eligibility, but limiting evaluation of PSMA receptor expression to PET imaging might potentially exclude countries and centers without established access to PET imaging. Use of additional pretreatment imaging was variable, especially among patients participating in sponsored trials versus protocols outside industry-sponsored trials, including SOC. Patients participating in industry-sponsored trials were more likely to undergo additional bone scanning and CT, whereas protocols outside industry-sponsored trials more often included $^{18}$F-FDG PET/CT to assess patient eligibility. These differences might be explained by the use of the PCWG3 criteria for response assessment in clinical trials.

The need for a robust supply chain for $^{177}$Lu-PSMA is crucial to meet the increasing demand for $^{177}$Lu-PSMA RLT (*9*). A previous study highlighted that 5% of the patients died while waiting for a supply of $^{177}$Lu-PSMA (*32*).

This study had several limitations. First, a high number of responses were received from Europe, given the early use and high number of treatment centers. Second, countries with a small number of centers but high patient volumes might be underrepresented since the data do not account for the number of treated patients per center. Third, Food and Drug Administration approval of $^{177}$Lu-PSMA in 2022 in part changed the practice of U.S. centers from treating patients as part of research protocols to SOC. Fourth, national regulatory differences impact several aspects of $^{177}$Lu-PSMA RLT.

## CONCLUSION

Results from this international survey revealed significant interinstitutional differences regarding multiple aspects of $^{177}$Lu-PSMA RLT, such as eligibility assessment, administered activity, and response assessment strategies. In part, this variation reflects differences in accepted practice standards supported by evolving clinical practice guidelines. Some responses, however, raise concern and highlight the need for theranostic centers, specific training, and an improved evidence base as theranostics is widely adopted.

## DISCLOSURE

Andrea Farolfi reports fees from Telix (speaker) and Calyx (image review). Wesley Armstrong is supported by the UCLA–Caltech Medical Scientist Training Program (NIGMS T32 GM008042). Lena Unterrainer reports fees from Astellas (speaker) and Novartis (consultant, speaker) outside the submitted work. Michael Hofman acknowledges philanthropic/government grant support from the Prostate Cancer Foundation (PCF) funded by Canica, the Peter MacCallum Foundation, the Medical Research Future Fund (MRFF), an NHMRC investigator grant, Movember, and the Prostate Cancer Foundation of Australia (PCFA); acknowledges research grant support (to the institution) from Novartis (including AAA and Endocyte), ANSTO, Bayer, Isotopia, and MIM; and declares personal consulting fees for lectures or advisory boards from Astellas and AstraZeneca in the last 2 y. Matthias Eiber reports fees from Blue Earth Diagnostics Ltd. (consultant, research funding), Novartis/AAA (consultant, speaker), Telix (consultant), Bayer (consultant, research funding), RayzeBio (consultant), Point Biopharma (consultant), Eckert-Ziegler (speaker), Janssen Pharmaceuticals (consultant, speakers bureau), Parexel (image review), and Bioclinica (image review) outside the submitted work and a patent application for rhPSMA. Wolfgang Fendler reports fees from SOFIE Biosciences (research funding), Janssen (consultant, speaker), Calyx (consultant, image review), Bayer (consultant, speaker, research funding), Novartis (speaker, consultant), Telix (speaker), GE Healthcare (speaker), and Eczacıbaşı Monrol (speaker) outside the submitted work. Boris Hadaschik reports the following: advisory board (Janssen, Bayer, ABX, Lightpoint, Amgen, MSD, Pfizer, Novartis), invited speaker (Astellas, Janssen R&D), institutional royalties (Uromed), institutional funding (AAA/Novartis, BMS, German Research Foundation), an advisory role (German Cancer Aid), and a leadership role/speaker (DKG AUO). Ken Herrmann reports personal fees from Bayer, personal fees and other from SOFIE Biosciences, personal fees from SIRTEX, nonfinancial support from ABX, personal fees from Adacap, personal fees from Curium, personal fees from Endocyte, grants and personal fees from BTG, personal fees from IPSEN, personal fees from Siemens Healthineers, personal fees from GE Healthcare, personal fees from Amgen, personal fees from Fusion, personal fees from Immedica, personal fees from Onkowissen.de, personal fees from Novartis, personal fees from ymabs, personal fees from Aktis Oncology, personal fees from Theragnostics, personal fees from Pharma15, personal fees from Debiopharm, personal fees from AstraZeneca, and personal fees from Janssen. No other potential conflict of interest relevant to this article was reported.

**KEY POINTS**

**QUESTION:** How is $^{177}$Lu-PSMA RLT organized around the world?

**PERTINENT FINDINGS:** A questionnaire was developed, and 95 theranostic centers around the globe answered. The aim was to assess operational differences and similarities between $^{177}$Lu-PSMA treatment centers. We found significant interinstitutional differences regarding multiple aspects of $^{177}$Lu-PSMA RLT, such as eligibility assessment, administered activity, and response assessment strategies.

**IMPLICATIONS FOR PATIENT CARE:** There is a need for specific training and an improved evidence base because theranostics is being widely adopted.

## REFERENCES

1. Hofman MS, Violet J, Hicks RJ, et al. [$^{177}$Lu]-PSMA-617 radionuclide treatment in patients with metastatic castration-resistant prostate cancer (LuPSMA trial): a single-centre, single-arm, phase 2 study. *Lancet Oncol.* 2018;19:825–833.
2. Violet J, Sandhu S, Iravani A, et al. Long-term follow-up and outcomes of retreatment in an expanded 50-patient single-center phase II prospective trial of $^{177}$Lu-PSMA-617 theranostics in metastatic castration-resistant prostate cancer. *J Nucl Med.* 2020;61:857–865.
3. Calais J, Czernin J, Thin P, et al. Safety of PSMA-targeted molecular radioligand therapy with $^{177}$Lu-PSMA-617: results from the prospective multicenter phase 2 trial RESIST-PC (NCT03042312). *J Nucl Med.* 2021;62:1447–1456.
4. Sartor O, de Bono J, Chi KN, et al. Lutetium-177-PSMA-617 for metastatic castration-resistant prostate cancer. *N Engl J Med.* 2021;385:1091–1103.
5. Hofman MS, Emmett L, Sandhu S, et al. [$^{177}$Lu]Lu-PSMA-617 versus cabazitaxel in patients with metastatic castration-resistant prostate cancer (TheraP): a randomised, open-label, phase 2 trial. *Lancet.* 2021;397:797–804.
6. FDA approves $^{18}$F-DCFPyL PET agent in prostate cancer. *J Nucl Med.* 2021; 62(8):11N.
7. FDA approves Pluvicto/Locametz for metastatic castration-resistant prostate cancer. *J Nucl Med.* 2022;63(5):13N.
8. Prostate cancer. European Association of Urology website. https://uroweb.org/guidelines/prostate-cancer. Published 2023. Accessed December 21, 2023.
9. Czernin J, Calais J. How many theranostics centers will we need in the United States? *J Nucl Med.* 2022;63:805–806.
10. Czernin J, Calais J. The $^{177}$Lu-PSMA-617 (Pluvicto) supply problem will be solved by competition [editorial]. *J Nucl Med.* 2023;64:343.
11. Pomykala KL, Würker M, Herrmann K. Tackling the last mile: a major component to successfully establish radioligand therapy. *J Nucl Med.* 2023;64:347–348.
12. Lee ST, Emmett LM, Pattison DA, et al. The importance of training, accreditation, and guidelines for the practice of theranostics: the Australian perspective. *J Nucl Med.* 2022;63:819–822.
13. Herrmann K, Giovanella L, Santos A, et al. Joint EANM, SNMMI and IAEA enabling guide: how to set up a theranostics centre. *Eur J Nucl Med Mol Imaging.* 2022;49:2300–2309.
14. Herrmann K, Giovanella L, Santos A, et al. Joint EANM, SNMMI, and IAEA enabling guide: how to set up a theranostics center. *J Nucl Med.* 2022;63:1836–1843.

15. Kratochwil C, Fendler WP, Eiber M, et al. Joint EANM/SNMMI procedure guideline for the use of $^{177}$Lu-labeled PSMA-targeted radioligand-therapy ($^{177}$Lu-PSMA-RLT). *Eur J Nucl Med Mol Imaging.* 2023;50:2830–2845.
16. Gillessen S, Bossi A, Davis ID, et al. Management of patients with advanced prostate cancer: metastatic and/or castration-resistant prostate cancer—report of the Advanced Prostate Cancer Consensus Conference (APCCC) 2022. *Eur J Cancer.* 2023;185:178–215.
17. Gillessen S, Bossi A, Davis ID, et al. Management of patients with advanced prostate cancer. Part I: intermediate-/high-risk and locally advanced disease, biochemical relapse, and side effects of hormonal treatment: report of the Advanced Prostate Cancer Consensus Conference 2022. *Eur Urol.* 2023;83:267–293.
18. Kratochwil C, Fendler WP, Eiber M, et al. EANM procedure guidelines for radionuclide therapy with $^{177}$Lu-labelled PSMA-ligands ($^{177}$Lu-PSMA-RLT). *Eur J Nucl Med Mol Imaging.* 2019;46:2536–2544.
19. Beyer T, Czernin J, Freudenberg L, et al. A 2022 international survey on the status of prostate cancer theranostics. *J Nucl Med.* 2023;64:47–53.
20. Gafita A, Marcus C, Kostos L, Schuster DM, Calais J, Hofman MS. Predictors and real-world use of prostate-specific radioligand therapy: PSMA and beyond. *Am Soc Clin Oncol Educ Book.* 2022;42:1–17.
21. Hotta M, Gafita A, Murthy V, et al. PSMA PET tumor-to-salivary gland ratio to predict response to [$^{177}$Lu]PSMA radioligand therapy: an international multicenter retrospective study. *J Nucl Med.* 2023;64:1024–1029.
22. Buteau JP, Martin AJ, Emmett L, et al. PSMA and FDG-PET as predictive and prognostic biomarkers in patients given [$^{177}$Lu]Lu-PSMA-617 versus cabazitaxel for metastatic castration-resistant prostate cancer (TheraP): a biomarker analysis from a randomised, open-label, phase 2 trial. *Lancet Oncol.* 2022;23:1389–1397.
23. Fanti S, Briganti A, Emmett L, et al. EAU-EANM consensus statements on the role of prostate-specific membrane antigen positron emission tomography/computed tomography in patients with prostate cancer and with respect to [$^{177}$Lu]Lu-PSMA radioligand therapy. *Eur Urol Oncol.* 2022;5:530–536.
24. Seifert R, Emmett L, Rowe SP, et al. Second version of the prostate cancer molecular imaging standardized evaluation framework including response evaluation for clinical trials (PROMISE V2). *Eur Urol.* 2023;83:405–412.
25. Scher HI, Morris MJ, Stadler WM, et al. Trial design and objectives for castration-resistant prostate cancer: updated recommendations from the Prostate Cancer Clinical Trials Working Group 3. *J Clin Oncol.* 2016;34:1402–1418.
26. Eisenhauer EA, Therasse P, Bogaerts J, et al. New response evaluation criteria in solid tumours: revised RECIST guideline (version 1.1). *Eur J Cancer.* 2009;45:228–247.
27. Wahl RL, Jacene H, Kasamon Y, Lodge MA. From RECIST to PERCIST: evolving considerations for PET response criteria in solid tumors. *J Nucl Med.* 2009;50:122S–150S.
28. Fanti S, Hadaschik B, Herrmann K. Proposal for systemic-therapy response-assessment criteria at the time of PSMA PET/CT imaging: The PSMA PET progression criteria. *J Nucl Med.* 2020;61:678–682.
29. Gafita A, Rauscher I, Weber M, et al. Novel framework for treatment response evaluation using PSMA PET/CT in patients with metastatic castration-resistant prostate cancer (RECIP 1.0): an international multicenter study. *J Nucl Med.* 2022;63:1651–1658.
30. Gafita A, Rauscher I, Fendler WP, et al. Measuring response in metastatic castration-resistant prostate cancer using PSMA PET/CT: comparison of RECIST 1.1, aPCWG3, aPERCIST, PPP, and RECIP 1.0 criteria. *Eur J Nucl Med Mol Imaging.* 2022;49:4271–4281.
31. Gafita A, Djaileb L, Rauscher I, et al. Response evaluation criteria in PSMA PET/CT (RECIP 1.0) in metastatic castration-resistant prostate cancer. *Radiology.* 2023;308:e222148.
32. Ravi P, Whelpley B, Kelly E, et al. Clinical implementation of $^{177}$Lu-PSMA-617 in the United States: lessons learned and ongoing challenges. *J Nucl Med.* 2023;64:349–350.

# Dopamine Transporter SPECT with 12-Minute Scan Duration Using Multiple-Pinhole Collimators

Ralph Buchert[1], Balazs Szabo[2], Akos Kovacs[2], Thomas Buddenkotte[1], Franziska Mathies[1], Amir Karimzadeh[1], Wencke Lehnert[1], Susanne Klutmann[1], Attila Forgacs[2], and Ivayla Apostolova[1]

[1]*Department of Diagnostic and Interventional Radiology and Nuclear Medicine, University Medical Center Hamburg–Eppendorf, Hamburg, Germany; and* [2]*Mediso Medical Imaging Systems, Budapest, Hungary*

This study evaluated the potential to reduce the scan duration in dopamine transporter (DAT) SPECT when using a second-generation multiple-pinhole (MPH) collimator designed for brain SPECT with improved count sensitivity and improved spatial resolution compared with parallel-hole and fanbeam collimators. **Methods:** The retrospective study included 640 consecutive clinical DAT SPECT studies that had been acquired in list mode with a triple-head SPECT system with MPH collimators and a 30-min net scan duration after injection of 181 ± 10 MBq of [$^{123}$I]FP-CIT. Raw data corresponding to scan durations of 20, 15, 12, 8, 6, and 4 min were obtained by restricting the events to a proportionally reduced time interval of the list-mode data for each projection angle. SPECT images were reconstructed iteratively with the same parameter settings irrespective of scan duration. The resulting 5,120 SPECT images were assessed for a neurodegeneration-typical reduction in striatal signal by visual assessment, conventional specific binding ratio analysis, and a deep convolutional neural network trained on 30-min scans. **Results:** Regarding visual interpretation, image quality was considered diagnostic for all 640 patients down to a 12-min scan duration. The proportion of discrepant visual interpretations between 30 and 12 min (1.2%) was not larger than the proportion of discrepant visual interpretations between 2 reading sessions of the same reader at a 30-min scan duration (1.5%). Agreement with the putamen specific binding ratio from the 30-min images was better than expected for 5% test–retest variability down to a 10-min scan duration. A relevant change in convolutional neural network–based automatic classification was observed at a 6-min scan duration or less. **Conclusion:** The triple-head SPECT system with MPH collimators allows reliable DAT SPECT after administration of about 180 MBq of [$^{123}$I]FP-CIT with a 12-min scan duration.

**Key Words:** dopamine transporter; SPECT; ioflupane; multipinhole; scan duration

**J Nucl Med 2024; 65:446–452**
DOI: 10.2967/jnumed.123.266276

SPECT of striatal dopamine transporter (DAT) availability with *N*-ω-fluoropropyl-2β-carbomethoxy-3β-(4-$^{123}$I-iodophenyl)-nortropane ([$^{123}$I]FP-CIT) is widely used to support the diagnostic work-up in patients with a clinically uncertain parkinsonian syndrome or suspicion of dementia with Lewy bodies (*1–6*).

Received Jul. 2, 2023; revision accepted Nov. 28, 2023.
For correspondence or reprints, contact Ralph Buchert (r.buchert@uke.de).
Published online Jan. 18, 2024.


Multiple-pinhole (MPH) collimator technology has the potential to concurrently improve spatial resolution and count sensitivity compared with imaging with conventional parallel-hole and fanbeam collimators in clinical SPECT of small organs (*7*), including DAT SPECT with [$^{123}$I]FP-CIT (*8–15*).

A recent prospective study showed that MPH collimators improve intra- and interreader agreement and the certainty of the visual interpretation of DAT SPECT compared with low-energy, high-resolution, high-sensitivity collimators (*16*). A technical performance evaluation of the triple-head camera with MPH collimators used in this previous (and in the current) study found a peak system sensitivity of 675 cps/MBq, which is about 3 times higher than the typical system sensitivity of double-head cameras with conventional parallel-hole or fanbeam collimators (*7*,*15*). This finding suggests that the triple-head camera equipped with MPH collimators allows a considerable reduction in scan duration in DAT SPECT. This reduction is desirable for better patient comfort, reduced risk of motion artifacts, and reduced costs (in terms of camera occupancy).

Against this background, the current study evaluated the impact of scan duration on MPH DAT SPECT with respect to visual interpretation, conventional semiquantitative analysis, and automatic classification with a deep convolutional neural network. The study retrospectively included 640 MPH DAT SPECT studies from clinical routine that had been acquired in list mode and therefore allowed realistic simulation of reduced scan duration.

## MATERIALS AND METHODS

### Patients

MPH DAT SPECT with [$^{123}$I]FP-CIT had been performed on 665 consecutive patients with a clinically uncertain parkinsonian syndrome or suspected dementia with Lewy bodies. Thirteen patients were excluded because the [$^{123}$I]FP-CIT dose was less than 150 MBq. Twelve patients were excluded because of relevant structural or vascular lesions in the striata or midbrain on MRI. The remaining 640 patients were included (age, 67.2 ± 11.4 y; range, 26–91 y; 44.2% women). To guarantee that the included patient sample was representative of the clinical routine at our site, no further eligibility criteria were applied.

A waiver of informed consent for the retrospective analysis of the anonymized data was obtained from the ethics review board of the general medical council of the state of Hamburg, Germany.

### SPECT Imaging

The SPECT acquisition started 203 ± 25 min (range, 135–335 min) after intravenous injection of 181 ± 10 MBq (range, 156–215 MBq) of [$^{123}$I]FP-CIT. In total, 90 projection views (30 per head, 120° scan

arc) at angular steps of 4° were acquired in list mode with an AnyScan Trio (Mediso) triple-head, general-purpose camera equipped with second-generation, general-purpose brain MPH collimators designed for high count sensitivity at the center of the field of view with a rather broad peak of the sensitivity profile for improved stability with respect to off-center positioning (*16*). A detailed description of the MPH collimator is given in the supplemental materials ("Multiple-Pinhole Collimator"; Supplemental Fig. 1; supplemental materials are available at http://jnm.snmjournals.org) (*15*,*17*,*18*).

The acquisition time per projection was 60 s, resulting in a 30-min total net scan duration. The energy window was set to 143–175 keV. The distance between the center-of-rotation axis and the pinhole focal plane was fixed to 140 mm. A helical acquisition mode with a 40-mm total table displacement was used to avoid axial undersampling (*19*,*20*).

Projection data corresponding to reduced scan durations of 20, 15, 12, 8, 6, and 4 min were obtained by restricting the events to a proportionally reduced time interval of the list-mode data for each projection angle. For each projection, the earliest sequential decay events were selected (rather than random selection from all events). Projection data were sorted into 256 × 256 matrices with a 2.13 × 2.13 mm pixel size, separately for each scan duration.

Transaxial images of 128 × 128 cubic pixels with a 1.8-mm edge length were reconstructed with the Monte Carlo photon simulation engine and iterative 1-step-late maximum-a-posteriori expectation maximization implemented in the camera software (24 iterations, 2 subsets) (*15*,*21*). Attenuation and scatter correction do not affect the ability of DAT SPECT to discriminate between a normal striatal signal and a neurodegeneration-typical reduction (*22*). Hence, correction for photon attenuation and scatter was not performed to avoid variability of no interest between images of the same patient with different scan durations, as might be caused by variability in the outer contour of the head for postreconstruction attenuation and scatter correction.

### Image Preprocessing

Individual DAT SPECT images were stereotactically normalized (affine) to the anatomic space of the Montreal Neurologic Institute using the Normalize tool of the Statistical Parametric Mapping software package (version SPM12) and a set of custom DAT SPECT templates representative of normal and different levels of a neurodegeneration-typical reduction in striatal uptake as the target (*23*). For each of the 640 patients, stereotactic normalization was performed first for the SPECT image from the full 30-min projection data. The images corresponding to shorter scan durations from the same raw data were stereotactically normalized using the same transformation as for the 30-min images.

Intensity was normalized by voxelwise scaling to the individual 75th percentile of the voxel intensity in a reference region comprising the whole brain without striata, thalamus, medial temporal lobe, brain stem, cerebellum, and ventricles (*24*). The reference value for intensity scaling was obtained separately for each scan duration. The scaled images are semiquantitative images representing the distribution volume ratio.

### Visual Interpretation

A standardized display (Fig. 1) was used for visual interpretation of the DAT SPECT distribution-volume-ratio images, similar to the display used in clinical routine at our site. Visual interpretation was performed by a reader with about 20 y of experience in clinical DAT SPECT reading (≥3,000 cases). The reader was unaware of any clinical data and was asked to use a 3-step approach to visual interpretation. In the first step, the reader decided whether statistical image quality was adequate for visual interpretation or whether the image was too noisy (Fig. 1). If statistical image quality was adequate, the reader decided in the second step whether there was an artificial reduction in striatal [$^{123}$I]FP-CIT uptake such as a more prominent reduction in the caudate nucleus than in the putamen or a barbell-shaped appearance of the striatum (Fig. 1), the rationale being that artificial reduction most likely indicated an artifact, because patients with relevant lesions on MRI had been excluded. If there was no artificial reduction, the reader was asked to categorize the case as showing a neurodegeneration-typical reduction or normal striatal [$^{123}$I]FP-CIT uptake (Fig. 1).

The 5,120 cases (640 patients × 8 scan durations) were presented in randomized order in a 5,120-page Portable Document Format file with 1 case per page. Visual interpretation was performed by clicking 1 of the 4 buttons in the display (Fig. 1). To assess intrareader variability (as a benchmark for variability between different scan durations), all 5,120 cases were interpreted a second time by the same reader using a second 5,120-page Portable Document Format file with the cases randomized differently. The time between the 2 reading sessions was 2 wk.

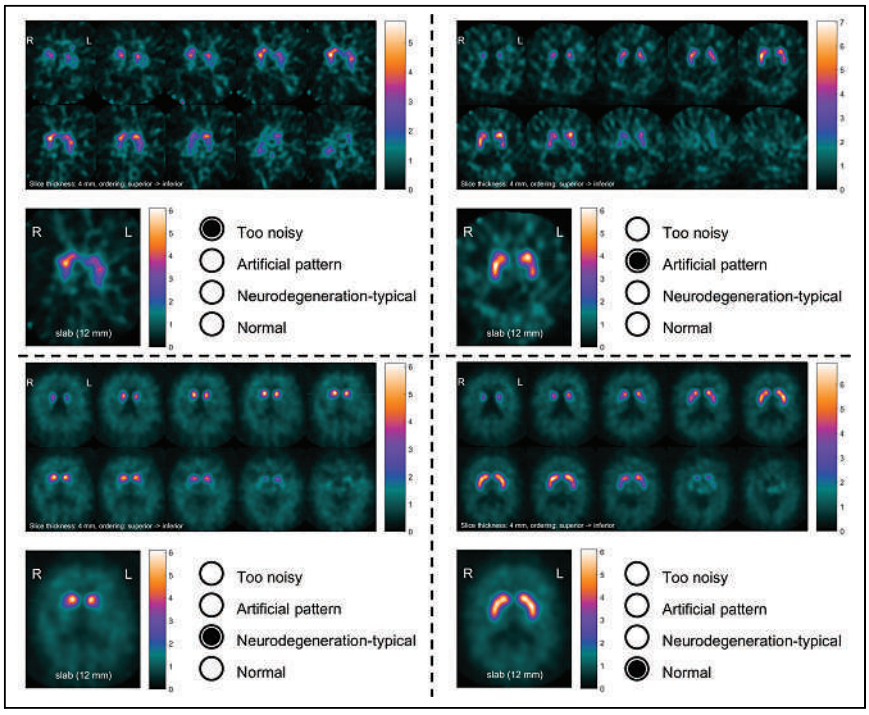


**FIGURE 1.** Standardized display for visual interpretation of 4 cases: 4-min scan considered too noisy for visual interpretation (upper left), 4-min scan interpreted as artificial because of barbell shape of left striatum (upper right), and two 30-min scans interpreted as neurodegeneration-typical reduction (lower left) and normal (lower right). Top of each panel shows 10 transversal distribution-volume-ratio slices of 4-mm thickness from superior to inferior edge of striatum with maximum of color table individually scaled to maximum intensity in 10 images. Bottom of each panel shows transversal distribution-volume-ratio image of 12-mm thickness through center of striatum with maximum of color table scaled to fixed upper distribution-volume-ratio threshold optimized previously.

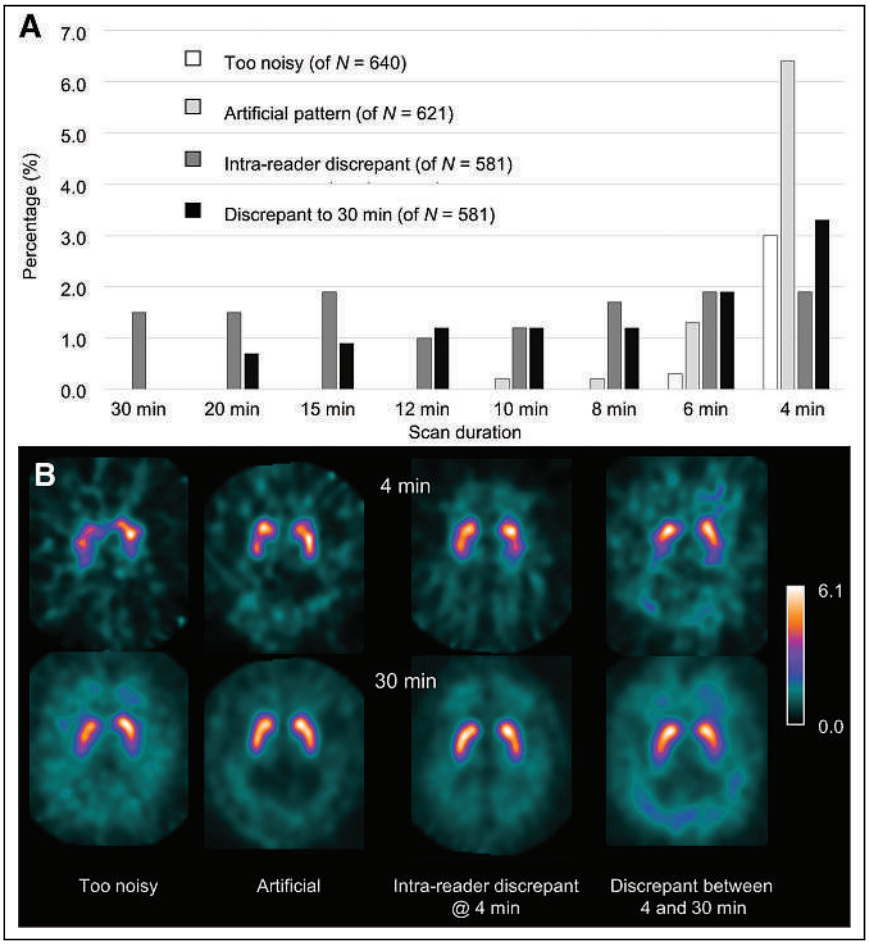


**FIGURE 2.** (A) Results of visual interpretation. (B) Transversal 12-mm SPECT images with 4-min vs. 30-min scan durations for 4 representative cases: too noisy on 4-min scan (male, 83 y, 175 MBq, 210-min uptake period), artificial on 4-min scan (male, 81 y, 182 MBq, 188-min uptake period), intrareader discrepancy (normal vs. reduced) on 4-min scan (male, 68 y, 183 MBq, 177-min uptake period), and discrepant classification between 4-min (reduced) and 30-min (normal) scans (female, 77 y, 196 MBq, 268-min uptake period).

Cases whose interpretation was discrepant between the 2 reading sessions were read a third time by the same reader to obtain an intrareader consensus.

### Semiquantitative Analysis

A detailed description of the semiquantitative analysis is given in the supplemental materials ("Specific Binding Ratio Analysis" (*23*–*30*)). In brief, the unilateral [$^{123}$I]FP-CIT specific binding ratio (SBR) in the left and right putamina was obtained by hottest-voxels analysis of the stereotactically normalized distribution-volume-ratio image using large unilateral putamen masks predefined in the space of the Montreal Neurologic Institute as described previously (*30*).

### Automatic Classification by Deep Convolutional Neural Network

A randomly selected subset of 427 (=2/3) of the DAT SPECT scans with a 30-min duration and visual interpretation by the experienced reader (intrareader consensus) was used to train a convolutional neural network for automatic binary classification of DAT SPECT scans. Details are given in the supplemental materials ("Convolutional Neural Network"; Supplemental Fig. 2 (*31*–*33*)).

The performance of the network was first tested in the remaining 213 DAT SPECT scans with a 30-min duration. To assess the impact of scan duration on the network's performance, the same network was applied to the same 213 test cases but with a reduced scan duration. No attempt was made to optimize the network for scan durations of less than 30 min.

Semiquantitative analyses and network-based classification included all cases; neither too-noisy nor artificial cases (according to visual interpretation) were excluded.

### Statistical Analysis

The Cochran Q test for related samples was used to test for an impact of scan duration on the proportion of too-noisy cases according to visual inspection in the whole dataset, on the proportion of artificial cases among cases with adequate statistical image quality, on the proportion of cases with discrepant visual interpretation between the 2 reading sessions, and on the proportion of cases with a discrepant intrareader consensus at a reduced scan duration compared with the intrareader consensus on the 30-min image. If the Cochran Q test demonstrated a significant effect of scan duration ($P < 0.05$), pairwise comparisons of scan durations were performed with Bonferroni adjustment for multiple tests (28 pairs from 8 different scan durations). IBM SPSS (version 27) was used for these analyses.

The impact of scan duration on the unilateral putamen SBR ($n$ = 1,280) was assessed by scatterplots and regression analysis to determine the coefficient of determination ($R^2$) of the SBR from the full 30-min scan by the SBR from a reduced scan duration. The threshold on $R^2$ for the impact of a reduced scan duration on the SBR to be relevant was fixed at 0.98, which would be expected alone because of the 5% variability in putamen SBR in short-term test–retest DAT SPECT of the same patient ("Relevant Loss of SBR Determination" in the supplemental materials; Supplemental Fig. 3 (*34*)). Thus, the impact of a reduced scan duration was considered relevant if $R^2$ was below 0.98.

The impact of scan duration on the discriminative power of the putamen SBR was tested as described previously (*22*). In brief, the distribution of the putamen SBR (minimum of both hemispheres, $n$ = 640) was characterized by a histogram with a 0.1 bin width. The resulting histogram was fitted by the sum of 2 gaussians:

$$\text{histogram}\,(\text{SBR}) = A_1 \exp\left(-\frac{(\text{SBR}-M_1)^2}{2\text{SD}_1^2}\right) + A_2 \exp\left(-\frac{(\text{SBR}-M_2)^2}{2\text{SD}_2^2}\right), \quad \text{Eq. 1}$$

where $A_1$ and $A_2$ are the amplitudes, $M_1$ and $M_2$ are the mean values, and $\text{SD}_1$ and $\text{SD}_2$ are the SD of the gaussian functions. The MATLAB routine fminsearch with default parameter settings was used for this purpose.

The power of the SBR to differentiate between normal and reduced DAT SPECT was estimated by the effect size $d$ of the distance between the 2 gaussians computed as the differences between the mean values scaled to the pooled SD:

$$d = (M_2 - M_1)/\sqrt{\frac{SD_1^2 + SD_2^2}{2}}. \quad \text{Eq. 2}$$

The cutoff $c$ for differentiation between normal and reduced SBRs was selected halfway between $M_1$ and $M_2$ in units of SD, that is

$$c = (SD_2 M_1 + SD_1 M_2)/(SD_1 + SD_2). \quad \text{Eq. 3}$$

The histogram analysis was performed separately for each scan duration.

## RESULTS

None of the DAT SPECT images were considered too noisy for visual interpretation down to an 8-min scan duration (Fig. 2A). The proportion of too-noisy images was 0.3% at a 6-min scan duration and 3.0% at a 4-min scan duration. The impact of scan duration on the proportion of too-noisy images was highly significant ($P < 0.0005$). Pairwise testing showed that the proportion of too-noisy images was significantly higher at 4 min than at any of the longer scan durations (all $P < 0.0005$). The difference between the 6-min scan duration and the longer scan durations was not significant (all $P = 1.000$).

Among the 621 DAT SPECT images with sufficient statistical quality at all scan durations, the proportion with an artificial pattern was no more than 0.2% for any scan duration down to 8 min (Fig. 2A). It was 1.3% at a 6-min scan duration and 6.4% at a 4-min scan duration. The impact of scan duration on the proportion of artificial images was highly significant ($P < 0.0005$). Pairwise testing showed that the proportion of artificial images was significantly higher at 4 min than at any of the longer scan durations (all $P < 0.0005$). The difference between the 6-min scan duration and the longer scan durations was not significant (all $P \geq 0.575$).

Among the 581 DAT SPECT images that were neither too noisy nor artificial at any scan duration, the proportion of cases with discrepant visual categorization between the 2 reading sessions ranged between 1.0% and 1.9%, without a significant effect of scan duration ($P = 0.822$, Fig. 2A).

The proportion of cases with a discrepant visual intrareader consensus at a reduced scan time compared with the intrareader consensus on the 30-min image among these 581 DAT SPECT images ranged between 0.7% and 1.2% for scan durations from 20 to 8 min (Fig. 2A). The proportion increased to 1.9% and 3.3% at 6- and 4-min scan durations, respectively. The impact of scan duration on the rate of discrepant consensus interpretation was highly significant ($P < 0.0005$). Pairwise testing showed that the proportion of discrepant interpretations compared with the 30-min image was significantly higher at 4 min than at 8 min or more (all $P < 0.0005$). The proportion of discrepant cases at a 6-min scan duration did not differ from the proportion at a 4-min scan duration ($P = 0.093$) or longer ($P \geq 0.268$).

Representative examples of too-noisy, artificial, intrareader-discrepant, and between-scan-duration–discrepant cases are shown in Figure 2B. Retrospective inspection of the cases with a concordant visual interpretation across all scan durations revealed only minor differences in the visual appearance of the SPECT images down to a 4-min scan duration in most cases (Fig. 3).

Scatterplots of the putamen SBR with a reduced scan duration versus a 30-min scan duration are shown in Figure 4. $R^2$ decreased with reduced scan durations from 0.998 at a 20-min duration to 0.853 at a 4-min duration. It dropped below the threshold of 0.98 for clinical relevance at an 8-min duration.

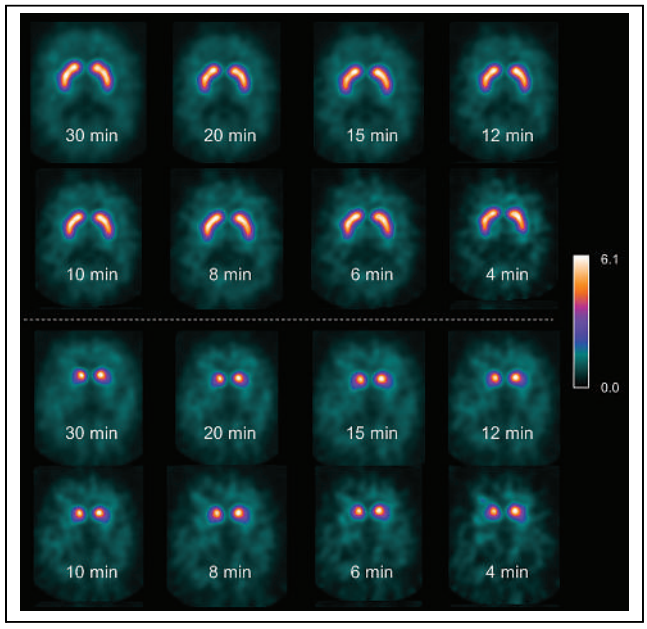


**FIGURE 3.** Representative examples in which scan duration had no relevant impact down to 4 min (transversal 12-mm images; top: female, 44 y, 200 MBq, 186-min uptake period; bottom: female, 72 y, 200 MBq, 220-min uptake period).

The histograms of the putamen SBR at different scan durations and their fit by the sum of 2 gaussians are shown in Figure 5. The parameters obtained by the fit are given in Supplemental Table 1. The effect size $d$ of the distance between the 2 gaussians was stable from a 30-min to a 6-min scan duration and then dropped by about 20% at a 4-min scan duration.

The results of the automatic network-based classification are summarized in Figure 6. A relevant loss of accuracy was observed for scan durations of 6 min or less.

## DISCUSSION

The primary finding of this study is that the triple-head SPECT camera equipped with MPH collimators allows reliable DAT SPECT after administration of the standard dose of about 180 MBq of [$^{123}$I]FP-CIT with a 12-min scan duration, independent of the interpretation method (visual, conventional semiquantitative analysis, or deep learning–based automatic classification). This scan duration represents a reduction of at least 50% compared with the typical 25–40 min according to the European Association of Nuclear Medicine/Society of Nuclear Medicine practice guideline for DAT SPECT when using a double-head camera with conventional collimators (*5*).

Regarding visual interpretation, none of the 640 DAT SPECT images was considered too noisy or artificial at a 12-min scan duration (Fig. 2). The proportion of cases with a discrepant visual interpretation between the 2 reading sessions of the same reader was not larger at a 12-min scan duration than at a 30-min scan duration (1.0% vs. 1.5%). The proportion of cases with a discrepant visual classification between a 12-min and a 30-min scan duration (1.2%) was similar to the proportion of intrareader-discrepant cases at 30 min (1.5%). Thus, the reduction of scan duration from 30 to 12 min had no impact on visual interpretation. Regarding semiquantitative analysis, a relevant impact was observed only at a scan duration of 8 min or less (Figs. 4 and 5). Automatic

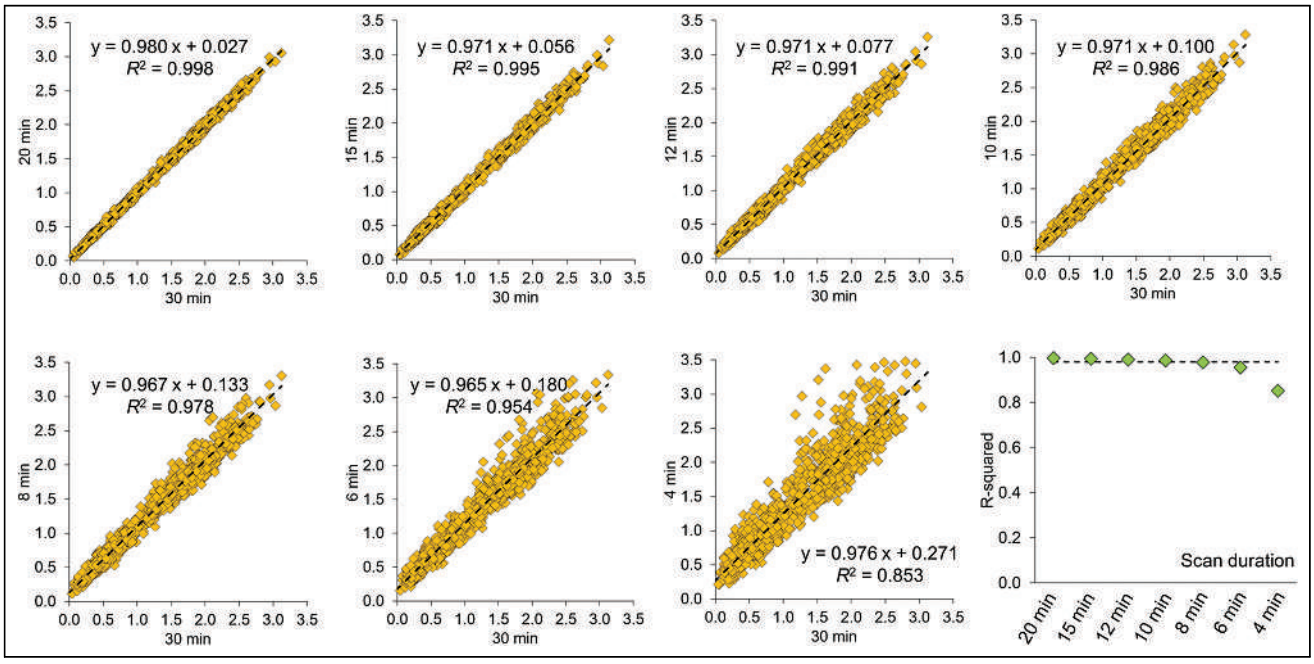


**FIGURE 4.** Scatterplots of unilateral putamen SBR ($n$ = 1,280) with reduced vs. 30-min scan duration, and plot of $R^2$. Dashed lines indicate $R^2$ expected for putamen SBR from 2 short-term repeat DAT SPECT scans of same patient with 5% test–retest variability.

classification with the convolutional neural network showed a relevant impact only at a scan duration of 6 min or less (Fig. 6).

The current study provides strong evidence against an impact of reduced scan duration down to 12 min with MPH SPECT, given the rather large sample size ($n$ = 640) and that no specific eligibility criteria were imposed. In response to this finding, the scan duration of clinical DAT SPECT with the triple-head SPECT camera equipped with MPH collimators and the standard dose of about 180 MBq of [$^{123}$I]FP-CIT was reduced to 12 min at our site.

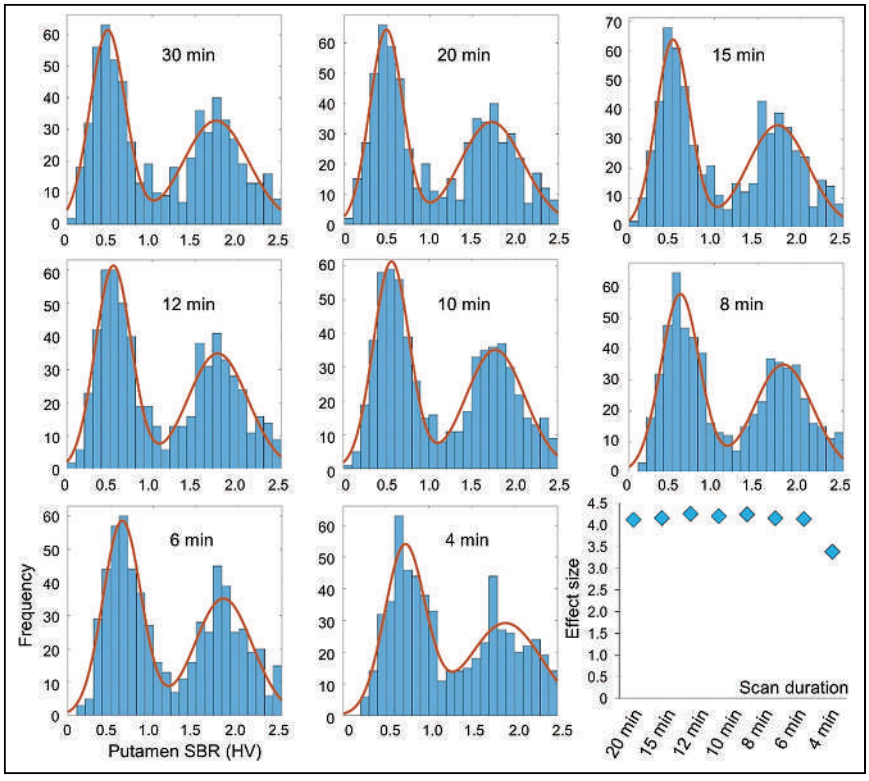


**FIGURE 5.** Histograms of putamen SBR (minimum of both hemispheres, $n$ = 640), and effect size $d$ of distance between 2 gaussian functions (according to Eq. 2). Fit by sum of 2 gaussians is indicated by continuous line. Remaining fit parameters are given in Supplemental Table 1. HV = hottest-voxels.

Further reduction of the scan duration to 6 min did not impact DAT SPECT image interpretation in most cases (≥95%, Figs. 2–6). Thus, a 12-min scan duration can be considered a safe choice. Under difficult conditions (e.g., patients with severe pain when lying on the examination table or agitated patients with dementia with Lewy bodies), an attempt at a 6-min duration might be made. If the resulting image quality appears adequate visually (neither too noisy nor artificial), the risk of misinterpretation is only marginally increased (Fig. 2). If the resulting image quality does not appear adequate, the scan might be repeated with a longer duration.

Reduction of scan duration with MPH collimators is based on their increased count sensitivity compared with conventional collimators (*7–15*,*35*). More precisely, the total number of striatal counts detected with the triple-head SPECT camera with MPH collimators with a 12-min scan duration is about the same as detected with a double-head SPECT camera with conventional parallel-hole or fanbeam collimators during a 25- to 30-min scan (*16*). Thus, novel software approaches such as deep learning–based image enhancement

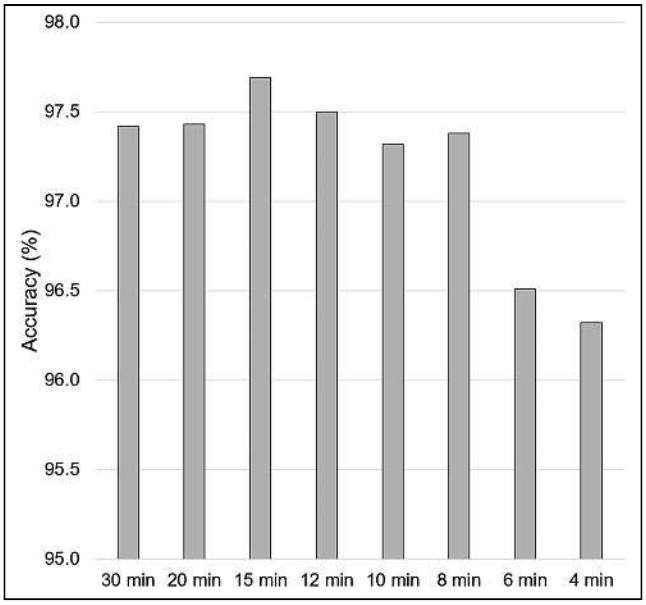


**FIGURE 6.** Balanced accuracy of network trained for automatic classification of MPH DAT SPECT with 30-min scan duration in same 213 test cases with varying scan duration.

or denoising (*36*) might be added to further reduce the scan duration in DAT SPECT with MPH collimators.

Reduction of scan duration to 12 min or even lower might allow early-phase SPECT imaging after injection of [$^{123}$I]FP-CIT to provide a surrogate image of regional cerebral blood flow (e.g., to discriminate between different neurodegenerative parkinsonian syndromes) as described for PET with [$^{123}$I]FP-CIT (*37*). However, this possibility needs to be tested in future studies, since system sensitivity with MPH collimators decreases toward the edges of the field of view and, therefore, improvement in sensitivity is lower for cortical brain regions than for the striata (*16*).

A limitation of the current study is that the reduced scan duration was simulated by restricting the events used for image reconstruction to a proportionally reduced time interval of the list-mode data for each projection angle. As a consequence, the current study does not allow testing for potential improvement of diagnostic performance by less involuntary head motion during a reduced scan duration. Another limitation is that the visual interpretation was performed by only a single experienced reader. However, at the safe choice of a 12-min scan duration, close inspection of the images was required to see any effect of reduced scan duration at all (Fig. 3). There was no change in image quality at a 12-min scan duration that might affect interpretation by less experienced readers. This was further supported by imagewise correlation analyses described in the supplemental materials ("Imagewise Correlation"; Supplemental Fig. 4). Finally, images with reduced scan durations were stereotactically normalized using the transformation derived for the corresponding 30-min image. This might have caused overly optimistic performance estimates (the 30-min scan is not available in clinical practice with a reduced scan duration). Repeat analyses in which the affine transformation into the anatomic standard space was estimated from the image with a reduced scan duration itself (i.e., without reference to the 30-min images) resulted in an $R^2$ (of the 30-min SBR by the 12-min SBR) that was slightly lower (0.98 vs. 0.99) but still compatible with the nonrelevance threshold. Thus, additional variability by independent stereotactic normalization did not have a relevant impact on the diagnostic performance of MPH DAT SPECT with a 12-min scan duration. The same might be assumed for attenuation and scatter correction, particularly when the delineation of the outer contour of the head (required for postreconstruction uniform attenuation and scatter correction) is based on the transformation used for stereotactic normalization (*38*).

## CONCLUSION

The triple-head SPECT system with MPH collimators allows reliable DAT SPECT with a 12-min scan duration when a standard dose of about 180 MBq of [$^{123}$I]FP-CIT is administered. The improved count sensitivity might also be used to reduce the radioactivity dose administered to patients.

## DISCLOSURE

Balazs Szabo, Akos Kovacs, and Attila Forgacs are employees of Mediso Medical Imaging Systems, Budapest, Hungary. However, the nonemployee authors had full control of the data and information that might present a conflict of interest for the employee authors. No other potential conflict of interest relevant to this article was reported.

**KEY POINTS**

**QUESTION:** What is the minimum scan duration for DAT SPECT with a general-purpose triple-head camera equipped with brain-specific MPH collimators?

**PERTINENT FINDINGS:** The retrospective study included 640 MPH DAT SPECT images that had been acquired at a 30-min duration in list mode and therefore allowed realistic simulation of reduced scan duration. Reduction of scan duration to 12 min had no impact on the interpretation of the SPECT images independent of the interpretation method (visual, conventional semiquantitative analysis, or deep learning–based automatic classification).

**IMPLICATIONS FOR PATIENT CARE:** The triple-head SPECT system equipped with MPH collimators allows reliable DAT SPECT with a 12-min scan duration when a standard 180-MBq dose of [$^{123}$I]FP-CIT is administered.

## REFERENCES

1. Jreige M, Kurian GK, Perriraz J, et al. The diagnostic performance of functional dopaminergic scintigraphic imaging in the diagnosis of dementia with Lewy bodies: an updated systematic review. *Eur J Nucl Med Mol Imaging.* 2023;50:1988–2035.
2. Bega D, Kuo PH, Chalkidou A, et al. Clinical utility of DaTscan in patients with suspected Parkinsonian syndrome: a systematic review and meta-analysis. *NPJ Parkinsons Dis.* 2021;7:43.
3. Berardelli A, Wenning G, Antonini A, et al. EFNS/MDS-ES recommendations for the diagnosis of Parkinson's disease. *Eur J Neurol.* 2013;20:16–34.
4. Kaasinen V, Kankare T, Joutsa J, Vahlberg T. Presynaptic striatal dopaminergic function in atypical parkinsonism: a metaanalysis of imaging studies. *J Nucl Med.* 2019;60:1757–1763.
5. Morbelli S, Esposito G, Arbizu J, et al. EANM practice guideline/SNMMI procedure standard for dopaminergic imaging in Parkinsonian syndromes 1.0. *Eur J Nucl Med Mol Imaging.* 2020;47:1885–1912.
6. Wallert ED, van de Giessen E, Knol RJJ, Beudel M, de Bie RMA, Booij J. Imaging dopaminergic neurotransmission in neurodegenerative disorders. *J Nucl Med.* 2022;63(suppl 1):27S–32S.

7. Van Audenhaege K, Van Holen R, Vandenberghe S, Vanhove C, Metzler SD, Moore SC. Review of SPECT collimator selection, optimization, and fabrication for clinical and preclinical imaging. *Med Phys.* 2015;42:4796–4813.
8. Auer B, Zeraatkar N, Goding JC, et al. Inclusion of quasi-vertex views in a brain-dedicated multi-pinhole SPECT system for improved imaging performance. *Phys Med Biol.* 2021;66:035007.
9. Beekman FJ, van der Have F, Goorden MC, et al. G-SPECT-I: a full ring high sensitivity and ultra-fast clinical molecular imaging system with < 3mm resolution [abstract]. *Eur J Nucl Med Mol Imaging.* 2015;42(suppl 1):S209.
10. Chen Y, Vastenhouw B, Wu C, Goorden MC, Beekman FJ. Optimized image acquisition for dopamine transporter imaging with ultra-high resolution clinical pinhole SPECT. *Phys Med Biol.* 2018;63:225002.
11. King MA, Mukherjee JM, Konik A, Zubal IG, Dey J, Licho R. Design of a multi-pinhole collimator for I-123 DaTscan imaging on dual-headed SPECT systems in combination with a fan-beam collimator. *IEEE Trans Nucl Sci.* 2016;63:90–97.
12. Könik A, Zeraatkar N, Kalluri KS, et al. Improved performance of a multipinhole SPECT for DAT imaging by increasing number of pinholes at the expense of increased multiplexing. *IEEE Trans Radiat Plasma Med Sci.* 2021;5:817–825.
13. Lee TC, Ellin JR, Huang Q, Shrestha U, Gullberg GT, Seo Y. Multipinhole collimator with 20 apertures for a brain SPECT application. *Med Phys.* 2014;41:112501.
14. Ozsahin I, Chen L, Konik A, King MA, Beekman FJ, Mok GSP. The clinical utilities of multi-pinhole single photon emission computed tomography. *Quant Imaging Med Surg.* 2020;10:2006–2029.
15. Tecklenburg K, Forgacs A, Apostolova I, et al. Performance evaluation of a novel multi-pinhole collimator for dopamine transporter SPECT. *Phys Med Biol.* 2020; 65:165015.
16. Mathies F, Apostolova I, Dierck L, et al. Multiple-pinhole collimators improve intra- and between-rater agreement and the certainty of the visual interpretation in dopamine transporter SPECT. *EJNMMI Res.* 2022;12:51.
17. Van Audenhaege K, Vanhove C, Vandenberghe S, Van Holen R. The evaluation of data completeness and image quality in multiplexing multi-pinhole SPECT. *IEEE Trans Med Imaging.* 2015;34:474–486.
18. Lin J. On artifact-free projection overlaps in multi-pinhole tomographic imaging. *IEEE Trans Med Imaging.* 2013;32:2215–2229.
19. Meikle SR, Kench PL, Lin J. Design considerations of small-animal SPECT cameras. In: Zaidi H, ed. *Molecular Imaging of Small Animals: Instrumentation and Application.* Springer; 2014:135–162.
20. Tuy HK. An inversion-formula for cone-beam reconstruction. *SIAM J Appl Math.* 1983;43:546–552.
21. Magdics M, Szirmay-Kalos L, Szlavecz A, et al. TeraTomo project: a fully 3D GPU based reconstruction code for exploiting the imaging capability of the NanoPET$^{TM}$/CT system. Presented at: World Molecular Imaging Congress; September 9, 2010; Kyoto, Japan.
22. Schiebler T, Apostolova I, Mathies FL, Lange C, Klutmann S, Buchert R. No impact of attenuation and scatter correction on the interpretation of dopamine transporter SPECT in patients with clinically uncertain parkinsonian syndrome. *Eur J Nucl Med Mol Imaging.* 2023;50:3302–3312.
23. Apostolova I, Schiebler T, Lange C, et al. Stereotactical normalization with multiple templates representative of normal and Parkinson-typical reduction of striatal uptake improves the discriminative power of automatic semi-quantitative analysis in dopamine transporter SPECT. *EJNMMI Phys.* 2023;10:25.
24. Kupitz D, Apostolova I, Lange C, et al. Global scaling for semi-quantitative analysis in FP-CIT SPECT. *Nuklearmedizin.* 2014;53:234–241.
25. Aylward EH, Li QA, Habbak R, et al. Basal ganglia volume in adults with Down syndrome. *Psychiatry Res.* 1997;74:73–82.
26. Buchert R, Kluge A, Tossici-Bolt L, et al. Reduction in camera-specific variability in [$^{123}$I]FP-CIT SPECT outcome measures by image reconstruction optimized for multisite settings: impact on age-dependence of the specific binding ratio in the ENC-DAT database of healthy controls. *Eur J Nucl Med Mol Imaging.* 2016;43: 1323–1336.
27. Hall H, Halldin C, Guilloteau D, et al. Visualization of the dopamine transporter in the human brain postmortem with the new selective ligand [$^{125}$I]PE2I. *Neuroimage.* 1999;9:108–116.
28. Tossici-Bolt L, Hoffmann SMA, Kemp PM, Mehta RL, Fleming JS. Quantification of [$^{123}$I]FP-CIT SPECT brain images: an accurate technique for measurement of the specific binding ratio. *Eur J Nucl Med Mol Imaging.* 2006;33:1491–1499.
29. Tzourio-Mazoyer N, Landeau B, Papathanassiou D, et al. Automated anatomical labeling of activations in SPM using a macroscopic anatomical parcellation of the MNI MRI single-subject brain. *Neuroimage.* 2002;15:273–289.
30. Wenzel M, Milletari F, Krueger J, et al. Automatic classification of dopamine transporter SPECT: deep convolutional neural networks can be trained to be robust with respect to variable image characteristics. *Eur J Nucl Med Mol Imaging.* 2019; 46:2800–2811.
31. He K, Zhang X, Ren S, Sun J. Deep residual learning for image recognition. Presented at: IEEE Conference on Computer Vision and Pattern Recognition; Las Vegas, NV, June 27–30, 2016. https://arxiv.org/abs/1512.03385. Published December 10, 2015. Accessed January 8, 2024.
32. Isensee F, Jaeger PF, Kohl SAA, Petersen J, Maier-Hein KH. nnU-Net: a self-configuring method for deep learning-based biomedical image segmentation. *Nat Methods.* 2021;18:203–211.
33. Sutskever I, Martens J, Dahl G, Hinton G. On the importance of initialization and momentum in deep learning. Proceedings of the 30th International Conference on Machine Learning. Atlanta, GA, June 16–21, 2013;28:1139–1147.
34. Matsuoka K, Yasuno F, Shinkai T, et al. Test-retest reproducibility of extrastriatal binding with $^{123}$I-FP-CIT SPECT in healthy male subjects. *Psychiatry Res Neuroimaging.* 2016;258:10–15.
35. Könik A, De Beenhouwer J, Mukherjee JM, et al. Simulations of a multi-pinhole SPECT collimator for clinical dopamine transporter (DAT) imaging. *IEEE Trans Radiat Plasma Med Sci.* 2018;2:444–451.
36. Daveau RS, Law I, Henriksen OM, et al. Deep learning based low-activity PET reconstruction of [C-11]PiB and [F-18]FE-PE2I in neurodegenerative disorders. *Neuroimage.* 2022;259:119412.
37. Jin S, Oh M, Oh SJ, et al. Additional value of early-phase $^{18}$F-FP-CIT PET image for differential diagnosis of atypical parkinsonism. *Clin Nucl Med.* 2017;42: e80–e87.
38. Lange C, Kurth J, Seese A, et al. Robust, fully automatic delineation of the head contour by stereotactical normalization for attenuation correction according to Chang in dopamine transporter scintigraphy. *Eur Radiol.* 2015;25:2709–2717.

# One-Year Longitudinal Changes in Tau Accumulation on [$^{18}$F]PI-2620 PET in the Alzheimer Spectrum

Minyoung Oh[1], Seung Jun Oh[1], Sang Ju Lee[1], Jungsu S. Oh[1], Seung Yeon Seo[1,2], Soorack Ryu[3], Jee Hoon Roh[4–6], Jae-Hong Lee[4], and Jae Seung Kim[1]

*[1]Department of Nuclear Medicine, Asan Medical Center, University of Ulsan College of Medicine, Seoul, Korea; [2]Department of Electrical and Electronic Engineering, Yonsei University, Seoul, Korea; [3]Biostatistical Consulting and Research Laboratory, Medical Research Collaborating Center, Hanyang University, Seoul, Korea; [4]Department of Neurology, Asan Medical Center, University of Ulsan College of Medicine, Seoul, Korea; [5]Departments of Biomedical Sciences and Physiology, Korea University College of Medicine, Seoul, Korea; and [6]Department of Neurology, Anam Hospital, Korea University College of Medicine, Seoul, Korea*

We investigated the longitudinal changes in cortical tau accumulation and their association with cognitive decline in patients in the Alzheimer disease (AD) continuum using 2-(2-([$^{18}$F]fluoro)pyridin-4-yl)-9*H*-pyrrolo[2,3-b:4,5c′]dipyridine ([$^{18}$F]PI-2620) PET. **Methods:** We prospectively enrolled 52 participants (age, 69.7 ± 8.4 y; 18 men and 34 women): 7 with normal cognition, 28 with mild cognitive impairment, and 17 with AD. They all completed the [$^{18}$F]PI-2620 and [$^{18}$F]florbetaben PET, MRI, and neuropsychologic tests at baseline and, excepting the [$^{18}$F]florbetaben PET, at the 1-y follow-up. Amyloid-β (Aβ) PET images were visually scored as positive (+) or negative (−). Patients on the AD continuum, including Aβ+ mild cognitive impairment and AD, were classified into early-onset (EO+) (<65 y old) or late-onset (LO+) (≥65 y old) groups. [$^{18}$F]PI-2620 PET SUV ratios (SUVRs) were determined by calculating the cerebral–to–inferior cerebellar ratio. Cortical volumes were calculated using 3-dimensional T1-weighted MRI. The correlation between tau accumulation progression and cognitive decline was also investigated. **Results:** The global [$^{18}$F]PI-2620 PET SUVRs were 1.04 ± 0.07 in 15 Aβ− patients, 1.18 ± 0.21 in 20 LO+ patients (age, 76.7 ± 3.8 y), and 1.54 ± 0.38 in 17 EO+ patients (age, 63.4 ± 5.4 y; $P < 0.001$) at baseline. The global SUVR increased over 1 y by 0.05 ± 0.07 (3.90%) and 0.13 ± 0.22 (8.41%) in the LO+ and EO+ groups, respectively, whereas in the Aβ− groups, it remained unchanged. The EO+ group showed higher global and regional tau deposition than did the Aβ− and LO+ groups ($P < 0.05$ for each) and rapid accumulation in Braak stage V (0.15 ± 0.25; 9.10% ± 12.27%; $P = 0.016$ and 0.008), Braak stage VI (0.08 ± 0.12; 7.16% ± 10.06%; $P < 0.006$ and 0.005), and global SUVR ($P = 0.013$) compared with the Aβ− group. In the EO+ group, the changes in SUVR in Braak stages II–VI were strongly correlated with the baseline and changes in verbal memory ($P < 0.03$). The LO+ group showed higher tau accumulation in Braak stage I–IV areas than did the Aβ− group ($P < 0.001$ for each). In the LO+ group, the change in SUVR in Braak stages III and IV moderately correlated with the change in attention ($P < 0.05$), and the change in SUVR in Braak stages V and VI moderately correlated with the change in visuospatial function ($P < 0.005$). **Conclusion:** These findings suggest that [$^{18}$F]PI-2620 PET can be a biomarker to provide regional and chronologic information about tau pathology in the AD continuum.

**Key Words:** tau PET; Alzheimer disease; neurodegenerative disease; longitudinal study

**J Nucl Med 2024; 65:453–461**
DOI: 10.2967/jnumed.123.265893

Dementia is a heterogeneous group of progressive and degenerative brain pathologies clinically characterized by deterioration in memory, learning, orientation, language, comprehension, and judgment. Alzheimer disease (AD) is the most common cause of dementia (*1*). Age is the most prominent biologic risk factor. Patients with AD are often classified into early-onset AD (EOAD) and late-onset AD (LOAD) groups, with 65 y as the cutoff age (*2*). EOAD occurs in approximately 10% of the patients with AD, with the first symptoms appearing in the age range of 30–65 y (*3*).

The neuropathologic hallmarks of AD brains include extracellular accumulation of diffuse and neuritic amyloid-β (Aβ) plaques, frequently surrounded by dystrophic neurites, and intraneuronal accumulation of hyperphosphorylated tau protein neurofibrillary tangles (*4*). Although some studies report widespread pathology extending outside the medial temporal lobe in younger patients (*5*), the overall pathology of EOAD and LOAD patients is similar, making it difficult to distinguish between the two.

The tau radiotracers for PET imaging developed in the past decade enable in vivo visualization and quantification of pathologic tau protein in AD. Cross-sectional tau PET imaging revealed tracer accumulation patterns similar to those reported in postmortem studies (*6*). Patients with EOAD typically show an extensive tau pathology distribution and burden when presenting with Aβ-positive (+) PET, whereas patients with LOAD yield a distinct tau retention pattern, predominantly confined to the temporal lobe (*7*). These preliminary findings indicated that the onset age might be an important contributor to AD heterogeneity, highlighting the potential that tau PET has in capturing phenotypic variations across patients with AD.

Longitudinally, patients with EOAD showed a faster cognitive decline than those with LOAD and faster widespread thinning of association cortices (*8*), took longer for an AD diagnosis to be reached, and had a higher frequency of 2 apolipoprotein ε4 alleles. However, both groups showed similar cognitive and global responses to cholinesterase inhibitor treatment and longitudinal outcomes, including activities-of-daily-living capacities and time from diagnosis to nursing home placement (*9*). However, studies on how longitudinal tau accumulation influences these changes are lacking.

Received May 21, 2023; revision accepted Dec. 8, 2023.
For correspondence or reprints, contact Jae Seung Kim (jaeskim@amc.seoul.kr).
Published online Feb. 1, 2024.

Cross-sectionally, 2-(2-([$^{18}$F]fluoro)pyridin-4-yl)-9*H*-pyrrolo[2,3-b:4,5-c′]dipyridine ([$^{18}$F]PI-2620), a second-generation tau PET tracer, demonstrated a high tau aggregate image quality and excellent signal-to-noise ratio in patients with AD (*7*,*10*). This tracer has the pyrrolo[2,3-b:4,5-c′]dipyridine core that strongly binds to aggregated tau and significantly reduces monoamine oxidase A binding properties compared with pyrido[4,3-b]indole derivatives. Its negative log of half-maximal inhibitory concentration was 8.5 ± 0.1 in the competition assay to tau aggregates, but it showed low binding properties to Aβ, monoamine oxidase A, and monoamine oxidase B as off-target binding tests. An autoradiography study showed specific binding to pathologic misfolded tau on AD brain sections but no specific tracer binding in the brain slices from nondemented donors (*11*). The tracer demonstrated no nonspecific binding in the basal ganglia and showed no uptake in non–tau-driven neurodegenerative disorders, including semantic variant primary progressive aphasia (*12*). [$^{18}$F]PI-2620 accumulation in the globus pallidus internus can detect progressive supranuclear palsy in patients (*13*,*14*). [$^{18}$F]PI-2620 showed higher distribution volume ratios in patients with Aβ+ corticobasal syndrome than in the controls in several cortical target regions and could serve as a differential diagnosis tool (*15*).

This study tracked longitudinal tau accumulation in patients with EOAD and LOAD using [$^{18}$F]PI-2620 PET to better understand the dynamic interactions between tau accumulation and Aβ, neurodegeneration, and cognitive decline over time.

## MATERIALS AND METHODS

### Eligibility and Overall Study Design

We prospectively enrolled cognitively normal controls (NCs) and patients with mild cognitive impairment (MCI) or AD. NCs were 40–85 y old with no evidence of cognitive impairment by history and the Seoul Neuropsychological Screening Battery (SNSB), which is one of the standardized neuropsychologic test batteries widely used in Korea and assesses 5 cognitive domains: attention, memory, language, visuospatial function, and frontal/executive function (*16*), with a Mini-Mental State Examination (MMSE) score within 1 SD of the sex-, age-, and education-specific norm and a score of 0 on the clinical dementia rating (CDR). Patients with MCI met the criteria of Petersen et al. (*17*). Patients with AD were more than 40 y old and met the probable AD criteria following the National Institute on Aging–Alzheimer's Association guidelines (*18*). Subjects with structural lesions such as territorial infarctions, intracranial hemorrhage, psychologic disease, non-AD tauopathy, Parkinson disease, or cerebrovascular disease were excluded. Subjects with at least 2 immediate family members diagnosed with AD were also excluded. Subjects treated before the screening visit with any investigational medicinal product, including tau-targeted treatment, were excluded.

The subjects underwent [$^{18}$F]PI-2620 PET to evaluate tau accumulation, [$^{18}$F]florbetaben PET to establish Aβ status (Aβ+ or Aβ negative [−]), MRI, neuropsychiatric testing, and safety evaluations at baseline. All tests were repeated after 1 y except [$^{18}$F]florbetaben PET. We collectively classified Aβ+ MCI and Aβ+ AD into late-onset (LO) and early-onset (EO) groups with the cutoff at the age of 65 y (*19*–*21*).

This study was approved by the Institutional Review Board of Asan Medical Center before it began, and all subjects signed an informed consent form. The study was registered at http://www.clinicaltrials.gov (NCT 03903211).

### Radiopharmaceutical Synthesis of [$^{18}$F]PI-2620

[$^{18}$F]PI-2620 synthesis was described before (*12*); briefly, it was synthesized using a modified Trasis AllinOne automatic chemistry module according to published methods (*11*) with minor modifications (*22*). The overall radiochemical non–decay-corrected yield was 8.0% ± 5.2% ($n$ = 39), and the total preparation time was 75 ± 5.0 min, including high-performance liquid chromatography purification and formulation. The radiochemical purity and molar activity were 99.9% ± 0.2% and 91.8 ± 45.7 GBq/μmol, respectively.

### PET Imaging

We acquired brain PET scans for all participants using a Discovery 690, 710, or 690 Elite PET/CT scanner (GE Healthcare). The same scanner was used at baseline and after 1 y for [$^{18}$F]PI-2620 PET imaging. Scans were performed 60–90 min after intravenous injection of 259 ± 25.9 MBq of [$^{18}$F]PI-2620 for tau detection and 90–110 min after intravenous injection of 300 ± 30 MBq of [$^{18}$F]florbetaben for Aβ detection. The 3-dimensional PET images were reconstructed with a voxel size of 2.0 × 2.0 × 3.27 mm using the ordered-subsets expectation maximization algorithm (iterations, 4; subsets, 16; postreconstruction smoothing applied using a gaussian kernel of 4 mm in full width at half maximum).

### Quantitative Analysis for PET

[$^{18}$F]florbetaben PET scans were assessed visually by 2 nuclear medicine physicians (who were masked to the clinical information) using a binary classification (+ or −) as recommended (*23*).

For [$^{18}$F]PI-2620 PET, each participant's PET image was rigidly coregistered to that participant's magnetization-prepared rapid gradient-echo data using Statistical Parametric Mapping software, version SPM12 (Wellcome Trust Centre for Neuroimaging, University College London), in MATLAB R2013a (MathWorks). Cortical gray matter/white matter parcellation was performed using FreeSurfer, version 6.0 (Harvard University; http://surfer.nmr.mgh.harvard.edu), as described by Thomas et al. (*24*). The Desikan–Killiany–Tourville atlas was used to define the regions of interest for the PET Braaklike stages (*25*) and to perform high-resolution gyral parcellation using FreeSurfer (*26*). The global SUV ratio (SUVR) was calculated by combining all of the volumes of interest of Braak stages I–VI. The ratio of region-based voxelwise (*24*) partial-volume effect (PVE) to 7-mm smoothed PET (*27*) coregistered onto MR images was used for quantification and voxel-based PVE correction of the PET images. PVE correction was performed using the symmetric geometric transfer matrix approach (*28*) in PETsurfer, a submodule of FreeSurfer (*29*,*30*). The region-based voxelwise PVE correction method, which requires high-resolution anatomic segmentation and accurate point-spread function measurements, combines the advantages of the geometric transfer matrix method and voxelwise corrections to generate accurate PVE-corrected images.

The mean SUVR of [$^{18}$F]PI-2620 PET was calculated for each volume of interest and normalized to the inferior cerebellum (cerebellar crus b–X) as a reference. To better measure the mean uptake in the reference, we conducted spatial normalization of the coregistered [$^{18}$F]PI-2620 PET images as mentioned above (coregistered onto T1-weighted MR images) to the Montreal Neurological Institute space, which is achieved using the spatial normalization parameters that align the corresponding MR image with the Montreal Neurological Institute T1-weighted MRI template and FreeSurfer-based cerebellum gray matter mask, combined with a spatially unbiased atlas template of the cerebellum (SUIT; MATLAB), to generate an individual FreeSurfer mask-based gray matter–specific inferior cerebellum mask (using the SUIT mask), as defined on the template space of Baker et al. (*31*). Finally, we applied morphologic erosion to this cerebellum gray matter mask to better handle the potential tissue misclassification in volumetric MRI as well as misalignment (or misregistration) between PET and volumetric MR images.

**TABLE 1**
Clinical and Cognitive Assessments

| Parameter | Analysis standard | Test stage | *n* | Aβ− | LO+ | EO+ | Aβ− M | Aβ− SD | LO+ M | LO+ SD | EO+ M | EO+ SD | Group *F** | Group *P* | Time *F*† | Time *P* | Group × time *F*‡ | Group × time *P* | Post hoc *P*: Aβ− vs. LO+ | Post hoc *P*: Aβ− vs. EO+ | Post hoc *P*: LO+ vs. EO+ |
|---|---|---|---|---|---|---|---|---|---|---|---|---|---|---|---|---|---|---|---|---|---|
| CDR | | BL | 48 | 15 | 18 | 15 | 0.3 | 0.3 | 0.7 | 0.4 | 0.5 | 0.0 | 10.54 | <0.001¶ | 3.29 | 0.073 | 0.27 | 0.765 | <0.001¶ | 0.010¶ | 0.082 |
| | | FU | 48 | 15 | 18 | 15 | 0.4 | 0.3 | 0.8 | 0.5 | 0.7 | 0.4 | | | | | | | | | |
| | | Diff | 48 | 15 | 18 | 15 | 0.1 | 0.3 | 0.1 | 0.3 | 0.2 | 0.4 | 0.46 | 0.635 | | | | | | | |
| CDR-SB | | BL | 48 | 15 | 18 | 15 | 0.9 | 1.0 | 4.2 | 2.5 | 3.2 | 0.8 | 23.85 | <0.001¶ | 3.61 | 0.061 | 0.48 | 0.623 | <0.001¶ | <0.001¶ | 0.142 |
| | | FU | 48 | 15 | 18 | 15 | 1.1 | 1.6 | 5.3 | 3.3 | 4.5 | 2.0 | | | | | | | | | |
| | | Diff | 48 | 15 | 18 | 15 | 0.3 | 1.1 | 1.1 | 1.1 | 1.3 | 1.9 | 2.16 | 0.130 | | | | | | | |
| MMSE | | BL | 50 | 15 | 18 | 17 | 26.6 | 2.2 | 22.9 | 3.9 | 21.2 | 2.8 | 20.65 | <0.001¶ | 2.96 | 0.090 | 0.11 | 0.892 | <0.001¶ | <0.001¶ | 0.058 |
| | | FU | 50 | 15 | 18 | 17 | 25.8 | 3.8 | 21.4 | 3.8 | 19.6 | 3.5 | | | | | | | | | |
| | | Diff | 50 | 15 | 18 | 17 | −0.8 | 2.9 | −1.5 | 2.6 | −1.6 | 3.5 | 0.28 | 0.754 | | | | | | | |
| Attention | Digit span backward | BL | 47 | 14 | 17 | 16 | −0.3 | 1.3 | −0.2 | 1.7 | −0.7 | 0.7 | 2.19 | 0.119 | 0.47 | 0.495 | 1.08 | 0.344 | | | |
| | | FU | 47 | 14 | 17 | 16 | 0.4 | 1.2 | −0.5 | 1.5 | −0.6 | 1.0 | | | | | | | | | |
| | | Diff | 47 | 14 | 17 | 16 | 0.7 | 1.2 | −0.3 | 1.6 | 0.2 | 0.8 | 2.34 | 0.110 | | | | | | | |
| Language | K-BNT | BL | 47 | 15 | 17 | 15 | −0.3 | 1.1 | −1.0 | 1.3 | −1.6 | 1.3 | 9.59 | <0.001¶ | 0.47 | 0.494 | 0.56 | 0.571 | 0.016 | <0.001¶ | 0.046¶ |
| | | FU | 47 | 15 | 17 | 15 | −0.1 | 1.1 | −1.2 | 1.9 | −2.2 | 1.8 | | | | | | | | | |
| | | Diff | 47 | 15 | 17 | 15 | 0.2 | 0.6 | −0.2 | 0.8 | −0.7 | 1.2 | 3.03 | 0.060 | | | | | | | |
| Visuospatial function | RCFT copy | BL | 49 | 15 | 18 | 16 | 0.0 | 0.7 | −1.4 | 2.7 | −1.6 | 3.9 | 5.11 | 0.008¶ | 1.72 | 0.193 | 1.15 | 0.322 | 0.040¶ | 0.002¶ | 0.255 |
| | | FU | 49 | 15 | 18 | 16 | 0.3 | 0.7 | −2.1 | 3.2 | −4.2 | 6.5 | | | | | | | | | |
| | | Diff | 49 | 15 | 18 | 16 | 0.2 | 0.8 | −0.7 | 1.7 | −2.6 | 4.7 | 3.20 | 0.052 | | | | | | | |
| Memory | SVLT-DR | BL | 50 | 14 | 19 | 17 | −1.2 | 1.3 | −2.3 | 0.6 | −2.7 | 0.6 | 25.99 | <0.001¶ | 0.02 | 0.893 | 0.28 | 0.759 | <0.001¶ | <0.001¶ | 0.124 |
| | | FU | 50 | 14 | 19 | 17 | −0.9 | 1.3 | −2.4 | 0.6 | −2.8 | 0.7 | | | | | | | | | |
| | | Diff | 50 | 14 | 19 | 17 | 0.2 | 1.0 | −0.1 | 0.4 | −0.1 | 0.6 | 0.96 | 0.392 | | | | | | | |
| | RCFT-DR | BL | 49 | 15 | 18 | 16 | −1.1 | 0.9 | −2.1 | 1.0 | −2.3 | 1.1 | 21.16 | <0.001¶ | 0.25 | 0.620 | 1.22 | 0.302 | <0.001¶ | <0.001¶ | 0.334 |
| | | FU | 49 | 15 | 18 | 16 | −0.5 | 1.1 | −2.1 | 0.9 | −2.5 | 0.8 | | | | | | | | | |
| | | Diff | 49 | 15 | 18 | 16 | 0.6 | 0.9 | 0.0 | 0.6 | −0.2 | 0.6 | 4.31 | 0.021¶ | | | | | 0.028¶ | 0.009¶ | 0.585 |
| Frontal/executive function | COWAT: supermarket | BL | 49 | 15 | 18 | 16 | −0.6 | 1.1 | −1.5 | 0.6 | −1.4 | 0.9 | 7.52 | 0.001¶ | 1.26 | 0.266 | 0.69 | 0.503 | 0.003¶ | 0.001¶ | 0.487 |
| | | FU | 49 | 15 | 18 | 16 | −0.5 | 1.1 | −1.0 | 0.9 | −1.4 | 0.9 | | | | | | | | | |
| | | Diff | 49 | 15 | 18 | 16 | 0.2 | 0.9 | 0.5 | 1.0 | 0.0 | 0.8 | 1.45 | 0.247 | | | | | | | |

*Degrees of freedom for BL are *F*(2,77) and for Diff are *F*(2,38).
†Degrees of freedom are *F*(1,77).
‡Degrees of freedom are *F*(2,77)
¶Statistically significant at $P < 0.05$.
M = mean; BL = baseline; FU = follow-up; Diff = difference; SB = sum of boxes; K-BNT = K-Boston Naming Test; RCFT = Rey Complex Figure Test; SVLT-DR = Seoul Verbal Learning Test–Delayed Recall; COWAT = Controlled Oral Word Association Test.
All scores are *z* scores except CDR, CDR–sum of boxes, and MMSE.

### Acquisition and Analysis of MRI

MRI was performed with a 3.0-T system (Achieva; Philips). To evaluate the cortical volume, a high-resolution anatomic 3-dimensional volume image was obtained using a 3-dimensional gradient-echo T1-weighted sequence with the following parameters: repetition time, 9.9 ms; echo time, 4.6 ms; flip angle, 8°; field of view, 224 mm; matrix, 224 × 224; and slice thickness, 1 mm with no gaps. Images were analyzed using FreeSurfer software, and MRI parcellation was performed as described above.

### Statistical Analysis

SPSS Statistics version 21.0 (IBM) and SAS version 9.4 (SAS Institute Inc.) were used for statistical analysis of the demographic data. The ×2 test and a correction for multiple comparisons with the Bonferroni method were used to compare categoric variables. For the comparisons of continuous demographic data and SNSB, we used an ANOVA model with a Bonferroni post hoc test. The performance on SNSB was compared between groups using a linear mixed model with sex as a covariate and the Bonferroni method for correcting multiple comparisons. We primarily analyzed longitudinal changes in SNSB and the global and regional (Braak stages I–VI) SUVRs with linear mixed-effect models with sex and the time interval between baseline and follow-up as fixed factors and subject as a random factor under the assumption that the intercepts can differ between subjects. A generalized linear mixed-effect repeated-measures analysis was performed with 1 fixed factor, a Braak stage region, and a random subject effect to account for within-subject correlations. The response variable was the annual percentage of change in SUVR. We present bar plots with the mean percentage of change in the SUVR across Braak stages and indicate the statistical significance derived from the paired difference tests from the repeated-measures model. The annual change in [$^{18}$F]PI-2620 SUVR was calculated as the difference between the values at follow-up and baseline, and the annual percentage of the change was calculated as [SUVR follow-up − SUVR baseline]/SUVR baseline × 100. Multiple linear regression analysis was performed for the Aβ+ group versus the Aβ− group and age for the difference in the SUVR. Partial correlation analyses between CDR–sum of boxes, MMSE, cognitive function of attention, memory, language, visuospatial function, and frontal/executive function and the SUVR of [$^{18}$F]florbetaben and [$^{18}$F]PI-2620 and the cortical volume were performed with sex as a covariate.

*P* values of less than 0.05 were considered statistically significant.

## RESULTS

### Participants

Sixty-nine participants underwent baseline [$^{18}$F]PI-2620 PET scans (11 NC, 33 with MCI, and 25 with AD), of which 46 were Aβ+ (1 NC, 23 with MCI, and 22 with AD). Fifty-five participants completed both baseline and 1-y follow-up [$^{18}$F]PI-2620 PET scans. One patient was excluded because the MRI was of insufficient quality to be analyzed by FreeSurfer. Of the remaining 54 participants (age, 69.7 ± 8.4 y; 15 men and 39 women), 52 were categorized as Aβ− (15; 7 NC and 8 MCI), LO+ (20; 9 MCI and 11 AD), or EO+ (17; 11 MCI and 6 AD) for analysis. One Aβ+ NC and 1 Aβ− AD patient were excluded. The participants' demographic, clinical, and imaging characteristics are summarized in Table 1.

### SNSB

As shown in Table 2, both the LO+ and EO+ participants showed a significant deterioration in global cognitive function as determined by CDR, CDR–sum of boxes, and MMSE and deterioration in language (K-Boston Naming Test), visuospatial function

**TABLE 2**
Baseline Demographics and Clinical Characteristics

| Parameter | Aβ− (*n* = 15) | | LO+ (*n* = 20) | | EO+ (*n* = 17) | | Others (*n* = 2) | | *P* | | | |
|---|---|---|---|---|---|---|---|---|---|---|---|---|
| | Aβ− CN | Aβ− MCI | Aβ+ MCI | Aβ+ AD | Aβ+ MCI | Aβ+ AD | Aβ+ CN | Aβ− AD | All | Aβ− vs. LO+ | Aβ− vs. EO+ | LO+ vs. EO+ |
| *n* | 7 | 8 | 9 | 11 | 11 | 6 | 1 | 1 | | | | |
| Age (y) | 64.0 ± 10.1 | 72.6 ± 7.1 | 75. 1 ± 3.8 | 78.0 ± 3.9 | 61.8 ± 5.3 | 65.8 ± 6.0 | 72 | 65 | <0.001* | 0.002* | 0.073 | <0.001* |
| Age at onset (y) | | | 70.4 ± 4.5 | 73.2 ± 4.0 | 57.9 ± 5.4 | 57.7 ± 5.3 | | 64 | <0.001* | | <0.001* | <0.001* |
| Education (y) | 11.1 ± 2.9 | 10.9 ± 3.9 | 11.6 ± 2.4 | 12.5 ± 4.3 | 11.6 ± 4.8 | 10.2 ± 3.9 | 7 | 16 | 0.631 | | | |
| Male-to-female ratio | 2:5 | 4:4 | 3:6 | 5:6 | 3:8 | 1:5 | 0:1 | 0:1 | 0.504 | | | |
| HTN (%) | 57.1 | 62.5 | 44.4 | 72.7 | 27.3 | 50 | 0 | 0 | 0.247 | | | |
| DM (%) | 0 | 0 | 11.1 | 36.4 | 18.2 | 0 | 0 | 0 | 0.097 | | | |
| Hyperlipidemia (%) | 42.9 | 50 | 44.4 | 27.3 | 18.2 | 33.3 | 100 | 0 | 0.389 | | | |
| ApoE ε4 carrier (%) | 57.1 | 12.5 | 55.6 | 63.6 | 72.7 | 66.7 | 0 | 0 | 0.094 | | | |
| FU interval (mo) | 11.6 ± 1.1 | 12.1 ± 0.8 | 12.2 ± 1.1 | 11.7 ± 0.7 | 12.1 ± 0.9 | 11.8 ± 0.1 | 12 | 12 | 0.913 | | | |

*Statistically significant at $P < 0.05$.
HTN = hypertension; DM = diabetes mellitus; ApoE = apolipoprotein E; FU = follow-up.
Data are shown as mean ± SD for continuous variables and percentages for categoric variables.

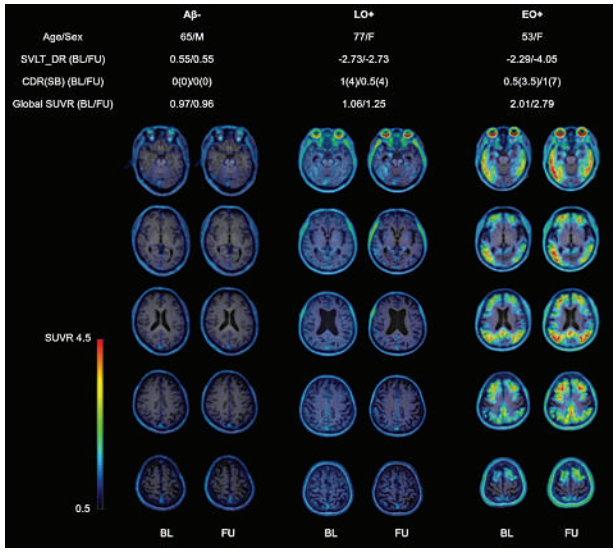


**FIGURE 1.** Representative [$^{18}$F]PI-2620 PET images of Aβ−, LO+, and EO+ at baseline (BL) and at 1-y follow-up (FU). SB = sum of boxes; SVLT-DR = Seoul Verbal Learning Test–Delayed Recall.

(Rey Complex Figure Test copy), verbal (Seoul Verbal Learning Test–Delayed Recall) and visual (Rey Complex Figure Test–Delayed Recall) memory, and frontal/executive function (Controlled Oral Word Association Test: supermarket) compared with Aβ− participants ($P < 0.001$ vs. $P = 0.040$).

Compared with LO+, EO+ showed worse performance on language ($P = 0.046$). Both LO+ and EO+ participants were stable on visual memory at the follow-up, whereas the Aβ− participants showed improvement ($P = 0.028$ and 0.009, respectively).

### Baseline [$^{18}$F]florbetaben Uptake in Aβ−, LO+, and EO+

The global [$^{18}$F]florbetaben SUVRs in the Aβ−, LO+, and EO+ groups were $1.23 \pm 0.11$, $1.72 \pm 0.22$, and $1.77 \pm 0.20$, respectively. LO+ and EO+ groups showed similar global Aβ deposition, but the deposition was higher than that of the Aβ− group ($P < 0.001$). A moderate correlation between the SUVR of the baseline Aβ ([$^{18}$F]florbetaben) and that of tau ([$^{18}$F]PI-2620) is present in the Aβ− group ($r = 0.581$; $P = 0.04$) but not in the LO+ and EO+ groups, as presented in Supplemental Table 1a (supplemental materials are available at http://jnm.snmjournals.org).

### Baseline and Longitudinal Changes in [$^{18}$F]PI-2620 Uptake

Some examples of baseline and follow-up [$^{18}$F]PI-2620 PET images are shown in Figure 1. Baseline and 1-y follow-up [$^{18}$F]PI-2620 SUVRs of the Aβ−, LO+, and EO+ groups are shown in Table 3 (the data were not corrected for a PVE [non-PVE]). Data corrected for PVE are presented in Supplemental Table 2.

The baseline global [$^{18}$F]PI-2620 SUVRs in the Aβ−, LO+, and EO+ groups were $1.04 \pm 0.07$, $1.18 \pm 0.21$, and $1.54 \pm 0.38$, respectively ($P < 0.001$). The LO+ group showed higher tau accumulation in Braak stage I–IV areas than did the Aβ− group ($P < 0.001$ for each). The EO+ group showed higher tau accumulation in the Braak stage I–VI areas than did the Aβ− group ($P < 0.001$ for each).

During the 1-y follow-up, the global cortical SUVRs of the LO+ and EO+ groups increased by $0.05 \pm 0.07$ (3.90% ± 6.30%) and $0.13 \pm 0.22$ (8.41% ± 11.89%), respectively. The EO+ group showed a statistically significant increase during follow-up in Braak stage V ($0.15 \pm 0.25$; 9.10% ± 12.27%; $P = 0.01$), Braak stage VI ($0.08 \pm 0.12$; 7.16% ± 10.06%; $P < 0.001$), and global SUVR ($P = 0.01$) compared with the Aβ− group. The annual SUVR changes by Braak staging are shown in Figure 2 for non-PVE and in Supplemental Figure 1 for PVE. Absolute and relative 1-y regional changes in the [$^{18}$F]PI-2620 SUVR are shown in Figure 3 for non-PVE.

Longitudinal change in the [$^{18}$F]PI-2620 SUVR in the cerebellum and off-target binding on the putamen and pallidum are shown in Supplemental Table 3. There were no significant differences in [$^{18}$F]PI-2620 in the cerebellum ($P = 0.265$). The pallidum showed an increased uptake in the LO+ group compared with the EO+ group ($1.22 \pm 0.19$ vs. $1.11 \pm 0.12$; $P = 0.003$) but with no significant longitudinal change.

### [$^{18}$F]PI-2620 Uptake, Age, Cognition, and Atrophy

Multiple linear regression analysis showed that the changes in [$^{18}$F]PI-2620 SUVR were significantly associated with Aβ+ and age globally (unstandardized coefficients, 0.092 for Aβ+ and −0.005 for age; $P = 0.029$ and 0.017, respectively) and in Braak stages IV–VI (Fig. 4).

In the Aβ− group, the baseline [$^{18}$F]PI-2620 SUVR of Braak stages III and IV correlated with visuospatial function ($r = 0.616$ and 0.682; $P < 0.05$ for each). The baseline SUVR of Braak stage VI correlated with the change in MMSE, language, and visual memory ($r = 0.663$, 0.645, and 0.687; $P < 0.05$ for each). The changes in SUVR in Braak stages I–VI and the global SUVR correlated with baseline attention, visuospatial function, and the changes in attention and frontal/executive function, as shown in Supplemental Table 1a. The baseline hippocampal volume (Braak stage II) correlated with the baseline CDR–sum of boxes ($r = -0.594$; $P < 0.05$). The baseline cortical volume of Braak stages IV–VI and the global cortical volume strongly correlated with the baseline verbal and visual memory ($P < 0.05$). The progression of hippocampal atrophy (Braak stage II) moderately to strongly correlated with the change in MMSE, language, and visual memory ($P < 0.05$).

In the LO+ group, the baseline SUVR of Braak stages IV–VI moderately correlated with the difference in MMSE ($P < 0.05$) as shown in Supplemental Table 1b. The change in SUVR of Braak stages III and IV moderately correlated with the change in attention ($P < 0.05$). The change in SUVR of Braak stages V and VI moderately correlated with the change in visuospatial function ($P < 0.05$). The baseline hippocampal volume moderately correlated with the baseline SUVR of Braak stages III and V ($P < 0.05$).

In the EO+ group, the baseline SUVR of Braak stage VI and the global SUVR moderately to strongly correlated with the baseline visuospatial and frontal/executive functions ($P < 0.05$) as shown in Supplemental Table 1c. The change in SUVR of Braak stages V and VI strongly correlated with the baseline and change in verbal memory ($P < 0.005$). The baseline cortical volume of Braak stage I moderately to strongly correlated with the baseline SUVR of Braak stages III and V and the global SUVR ($P < 0.05$). The differences in the cortical volume of Braak stages V and VI and the global cortical volume strongly correlated with the baseline frontal/executive function and the baseline SUVR of Braak stage IV.

## DISCUSSION

This study used [$^{18}$F]PI-2620 PET to identify a tau deposition pattern and longitudinal accumulation, which differed between the

**TABLE 3**
SUVRs of [$^{18}$F]PI-2620 in Aβ−, LO+, and EO+ Groups

| | | Aβ− | | LO+ | | EO+ | | Group | | Time | | Group × time | | Post hoc *P* | | |
|---|---|---|---|---|---|---|---|---|---|---|---|---|---|---|---|---|
| Braak stage | Test stage | M | SD | M | SD | M | SD | *F** | *P* | *F*† | *P* | *F*‡ | *P* | Aβ− vs. LO+ | Aβ− vs. EO+ | LO+ vs. EO+ |
| I | BL | 1.30 | 0.24 | 1.78 | 0.39 | 2.03 | 0.34 | 36.68 | <0.001¶ | 0.24 | 0.628 | 0.19 | 0.829 | <0.001 | <0.001 | 0.017¶ |
| | FU | 1.28 | 0.30 | 1.85 | 0.47 | 2.08 | 0.38 | | | | | | | | | |
| | Diff (F − B) | −0.03 | 0.15 | 0.07 | 0.15 | 0.05 | 0.27 | 1.15 | 0.325 | | | | | | | |
| | Diff (%) | −2.15 | 9.68 | 3.64 | 8.19 | 2.95 | 13.02 | 1.42 | 0.252 | | | | | | | |
| II | BL | 1.06 | 0.12 | 1.29 | 0.27 | 1.40 | 0.20 | 20.26 | <0.001¶ | 0.38 | 0.537 | 0.00 | 0.998 | <0.001 | <0.001 | 0.045¶ |
| | FU | 1.08 | 0.15 | 1.31 | 0.28 | 1.43 | 0.19 | | | | | | | | | |
| | Diff (F − B) | 0.02 | 0.05 | 0.03 | 0.09 | 0.03 | 0.13 | 0.04 | 0.964 | | | | | | | |
| | Diff (%) | 1.93 | 4.65 | 2.03 | 7.22 | 2.72 | 10.13 | 0.00 | 0.997 | | | | | | | |
| III | BL | 1.12 | 0.13 | 1.36 | 0.28 | 1.69 | 0.46 | 25.81 | <0.001¶ | 1.03 | 0.312 | 0.21 | 0.812 | 0.001 | <0.001 | <0.001¶ |
| | FU | 1.13 | 0.19 | 1.43 | 0.33 | 1.80 | 0.46 | | | | | | | | | |
| | Diff (F − B) | 0.01 | 0.09 | 0.07 | 0.10 | 0.11 | 0.27 | 1.23 | 0.300 | | | | | | | |
| | Diff (%) | 0.50 | 6.66 | 4.84 | 6.89 | 7.53 | 12.95 | 2.01 | 0.145 | | | | | | | |
| IV | BL | 1.06 | 0.10 | 1.30 | 0.32 | 1.64 | 0.36 | 29.77 | <0.001¶ | 1.44 | 0.234 | 0.30 | 0.744 | 0.001¶ | <0.001¶ | <0.001¶ |
| | FU | 1.07 | 0.16 | 1.37 | 0.38 | 1.78 | 0.44 | | | | | | | | | |
| | Diff (F − B) | 0.02 | 0.07 | 0.07 | 0.10 | 0.14 | 0.23 | 2.36 | 0.106 | | | | | | | |
| | Diff (%) | 1.22 | 5.39 | 4.95 | 6.91 | 8.61 | 11.91 | 2.50 | 0.093 | | | | | | | |
| V | BL | 1.03 | 0.06 | 1.14 | 0.20 | 1.59 | 0.47 | 31.10 | <0.001¶ | 1.03 | 0.312 | 0.41 | 0.667 | 0.090 | <0.001¶ | <0.001¶ |
| | FU | 1.03 | 0.08 | 1.19 | 0.25 | 1.73 | 0.57 | | | | | | | | | |
| | Diff (F − B) | 0.00 | 0.04 | 0.05 | 0.07 | 0.15 | 0.25 | 3.34 | 0.044¶ | | | | | 0.408 | 0.016¶ | 0.073 |
| | Diff (%) | 0.34 | 4.12 | 3.80 | 6.42 | 9.10 | 12.27 | 3.93 | 0.026¶ | | | | | 0.229 | 0.008¶ | 0.090 |
| VI | BL | 1.01 | 0.07 | 1.06 | 0.16 | 1.18 | 0.22 | 12.89 | <0.001¶ | 1.09 | 0.300 | 0.53 | 0.590 | 0.069 | <0.001¶ | 0.001¶ |
| | FU | 1.00 | 0.07 | 1.10 | 0.19 | 1.26 | 0.21 | | | | | | | | | |
| | Diff (F − B) | −0.01 | 0.05 | 0.04 | 0.06 | 0.08 | 0.12 | 4.16 | 0.022¶ | | | | | 0.120 | 0.006¶ | 0.147 |
| | Diff (%) | −0.75 | 4.51 | 3.03 | 5.63 | 7.16 | 10.06 | 4.43 | 0.017¶ | | | | | 0.129 | 0.005¶ | 0.114 |
| Global | BL | 1.04 | 0.07 | 1.18 | 0.21 | 1.54 | 0.38 | 32.97 | <0.001¶ | 1.24 | 0.268 | 0.42 | 0.660 | 0.016¶ | <0.001¶ | <0.001¶ |
| | FU | 1.04 | 0.10 | 1.23 | 0.25 | 1.67 | 0.45 | | | | | | | | | |
| | Diff (F − B) | 0.00 | 0.05 | 0.05 | 0.07 | 0.13 | 0.22 | 2.96 | 0.061 | | | | | | | |
| | Diff (%) | 0.34 | 4.64 | 3.90 | 6.30 | 8.41 | 11.89 | 3.37 | <0.001¶ | | | | | 0.209 | 0.013¶ | 0.148 |

*Degrees of freedom for BL are *F*(2,97) and for Diff (F − B) and Diff (%) are *F*(2,48).
†Degrees of freedom are *F*(1,97).
‡Degrees of freedom are *F*(2,97).
¶Statistically significant at $P < 0.05$.
M = mean; BL = baseline; FU = follow-up; Diff = difference; (F − B) = follow-up – baseline.
Data were not corrected for PVE.

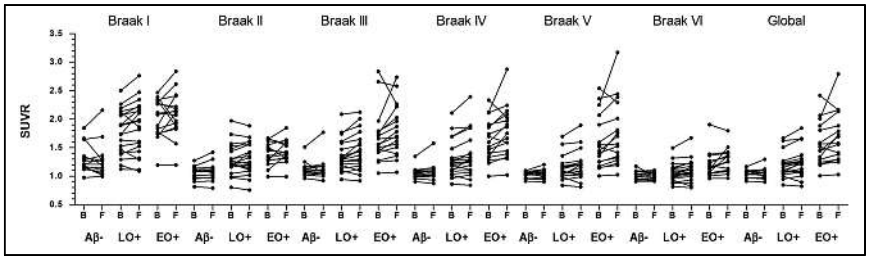


**FIGURE 2.** One-year changes in [$^{18}$F]PI-2620 SUVR by Braak staging region (data were not corrected for PVE). Aβ− is NC and MCI; LO−, Aβ+ is LO MCI and AD (≥65 y); EO+, Aβ+ is EO MCI and AD (<65 y). B = baseline; F = follow-up.

LO+ and EO+ groups. This study identified tau accumulation by [$^{18}$F]PI-2620 PET, with the EO+ group showing rapid accumulation globally and in Braak stage V and VI areas, correlating with the patients' verbal memory deterioration. At the 1-y follow-up, global SUVRs of the LO+ and EO+ groups increased by $0.05 \pm 0.07$ (3.90% ± 6.30%) and $0.13 \pm 0.22$ (8.41% ± 11.89%), respectively. These results are comparable with previous longitudinal tau accumulation studies in patients with AD (*32*,*33*).

Previously reported uncorrected $^{18}$F-flortaucipir ([$^{18}$F]AV-1451) PET values for annual global tau accumulation changes ranged between 0.02 (0.8%) in Aβ+ MCI patients and 0.04 (2.5%) in Aβ+ AD patients (*32*). The non-PVE 6-(fluoro-$^{18}$F)-3-(1*H*-pyrrolo[2,3-c]pyridin-1-yl)isoquinolin-5-amine ([$^{18}$F]MK-6240) PET values increased at the 1-y follow-up by 0.05 in Aβ+ MCI patients and 0.12 in Aβ+ AD patients (*33*).

[$^{18}$F]AV-1451 and [$^{18}$F]MK-6240 PET detected a more widespread tau accumulation in the parietooccipital cortex and hippocampus of patients with Aβ+ EOAD than with Aβ+ LOAD, compatible with results of this study (*19*,*34*,*35*). We showed a more rapid tau accumulation in the Braak stage III–V areas in the EO+ group than in the LO+ group. Although longitudinal changes in tau accumulation in this group were not yet established for autosomal dominant AD, it was reported that tau accumulation rates among carriers were most rapid in the parietal neocortex (~9%/y), as seen by [$^{18}$F]AV-1451 PET in the COLBOS biomarker study (*36*). These results support the different contributions of tau and amyloid to the onset and progression of EOAD and LOAD. LOAD is believed to affect complex, heterogeneous groups and to be caused by multiple genetic and environmental factors through diverse pathways (*37*–*39*).

The higher proportion of hypertension, diabetes mellitus, and hyperlipidemia in the LO+ group than in the EO+ group in this study partly explains the LOAD diverse pathologic processes other than Aβ. The LO+ and EO+ groups had similar global or regional Aβ SUVRs. However, the groups differed in their baseline global and regional (Braak stage I–VI areas) tau. These results suggested that tau might be a better biomarker than Aβ to explain the pathophysiology and progression in the EO+ group. Unlike EOAD and LOAD, studies with [$^{18}$F]AV-1451 showed no difference in cortical tau binding between EO and LO MCI (*19*). It is currently unknown whether these differences are due to the small samples studied or differences between the tau tracers used.

On the basis of this fact, we hypothesized that the interaction between amyloid and tau would differ between EO MCI and EOAD because EO MCI precedes EOAD and progresses to it. Tábuas-Pereira et al. reported that the clinical presentation, apolipoprotein E subtype, and cerebrospinal fluid biomarkers of EO and LO MCI were biologically indistinguishable (*21*). Furthermore, they found no difference in their conversion rates to AD. However, the patients' amyloid status was not evaluated, and that study was conducted before tau PET became available, so its interpretation was limited. The CREDOS study revealed that the visuospatial memory scores of EO MCI and verbal memory scores of LO MCI were significant predictors of AD conversion, suggesting a right-predominant pathology in EO MCI and a left-predominant pathology in LO MCI (*20*). Studies with PET biomarkers showed differences between these 2 groups, with EO MCI showing hypometabolism in brain regions vulnerable to mild AD (*40*). Therefore, we divided the Aβ+ participants into LO+ and EO+ groups on the basis of the age of memory impairment onset.

The changes in [$^{18}$F]PI-2620 SUVR were significantly associated with Aβ+ and age on multiple linear regression analysis. This association suggested that not only Aβ presence but also age is associated with longitudinal tau accumulation, especially in advanced Braak stages, although the small number of subjects in the Aβ−, LO+, and EO+ groups prevented us from confirming this possibility.

As in previous work, [$^{18}$F]PI-2620 maintained a high-quality PET image and an excellent signal-to-noise ratio when imaging tau deposition in AD (*7*,*10*). In this study, [$^{18}$F]PI-2620 SUVR indicated longitudinal tau accumulation in Braaklike regions in the LO+ and EO+ groups without significant off-target binding in the basal ganglia, cerebellum, choroid plexus, or meninges. As shown in Supplemental

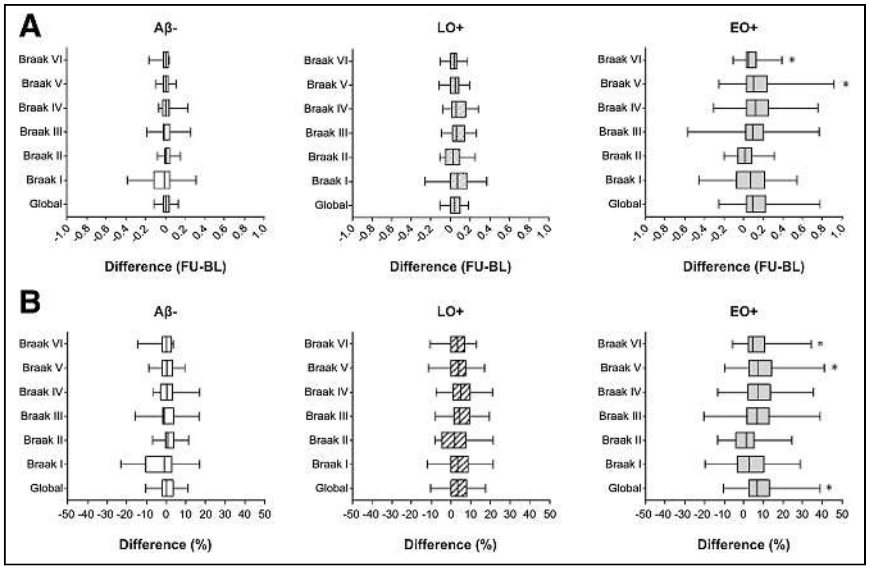


**FIGURE 3.** Absolute (A) and relative (B) 1-y regional changes in [$^{18}$F]PI-2620 SUVR. *$P < 0.05$ between Aβ− and EO+. FU = follow-up; BL = baseline.

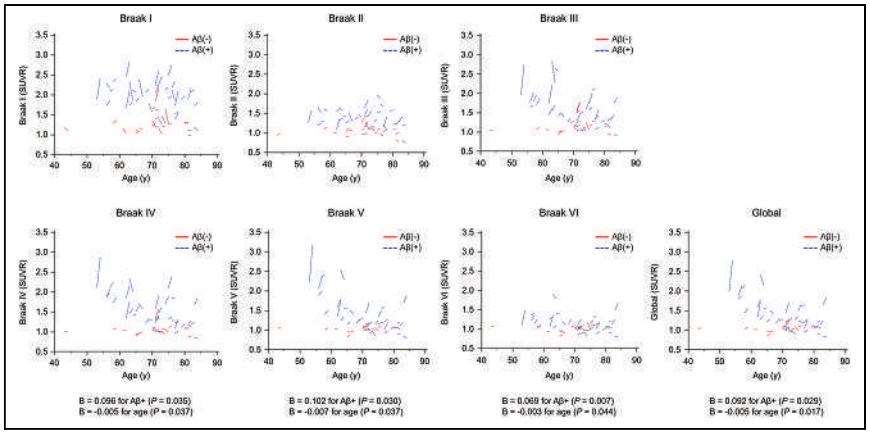


**FIGURE 4.** Individual trajectories of age and SUVR change. Multiple linear regression analysis of Aβ+ group vs. Aβ− group and age shows change in [$^{18}$F]PI-2620 SUVRs. B = unstandardized coefficients.

Table 3, uptake in the putamen, pallidum, and cerebellum was low, with no significant longitudinal accumulation. This could be an advantage over [$^{18}$F]MK-6240, which is limited in longitudinal assessments because of the highly variable signal in the meninges at the subject level, and [$^{18}$F]AV-1451, which has difficulties in quantifying hippocampal uptake due to choroid plexus uptake (*32*,*41*).

This study had several limitations. First, the classification criteria for EO+ and LO+ groups were not well established. The age-at-onset criterion to classify EOAD and LOAD is well known, but using it to define EO and LO MCI has not yet been well established. Second, the follow-up might have been too short to detect significant changes in cognitive function, cortical volume, and conversion to AD in patients with MCI. However, at the same time, it is also advantageous to be able to show differences between groups with only a short follow-up of 1 y. Third, conducting the study during the coronavirus disease 2019 pandemic caused patients to drop out and made follow-up visits challenging. Last, tau distribution and accumulation changes were not confirmed pathologically.

## CONCLUSION

This study identified tau accumulation by [$^{18}$F]PI-2620 PET, with the EO+ patients showing rapid accumulation globally and in Braak stage V and VI areas, correlating with their verbal memory deterioration. The LO+ patients showed tau deposition within Braak stage IV and relatively slow progression, which correlated with their attention and visuospatial functions. These findings suggest that [$^{18}$F]PI-2620 could be a potential biomarker for selecting tau-targeted therapies and monitoring their effects.

**KEY POINTS**

**QUESTION:** Does age at onset affect tau accumulation?

**PERTINENT FINDINGS:** Compared with the Aβ− group, the EO MCI and AD groups showed rapid accumulation globally and in Braak stage V and VI areas on [$^{18}$F]PI-2620 PET.

**IMPLICATIONS FOR PATIENT CARE:** These findings suggest that [$^{18}$F]PI-2620 could be a potential biomarker for selecting tau-targeted therapies and monitoring their effects.

## DISCLOSURE

This research was supported by Life Molecular Imaging GmbH (formerly Piramal Imaging GmbH), Berlin, Germany, and grants from the Korea Health Technology R&D Project through the Korea Health Industry Development Institute (KHIDI), funded by the Ministry of Health & Welfare, Republic of Korea (grants HI14C2768, HR18C0016, and HU22C0031). No other potential conflict of interest relevant to this article was reported.

## REFERENCES

1. Zeisel J, Bennett K, Fleming R. World Alzheimer report 2020: design, dignity, dementia—dementia-related design and the built environment. https://www.alzint.org/resource/world-alzheimer-report-2020/. Published September 21, 2020. Accessed January 3, 2024.
2. Seltzer B, Sherwin I. A comparison of clinical features in early- and late-onset primary degenerative dementia: one entity or two? *Arch Neurol.* 1983;40:143–146.
3. Cooper S, Greene J. The clinical assessment of the patient with early dementia. *J Neurol Neurosurg Psychiatry.* 2005;76(suppl 5):v15–v24.
4. Braak H, Braak E. Demonstration of amyloid deposits and neurofibrillary changes in whole brain sections. *Brain Pathol.* 1991;1:213–216.
5. van der Flier WM, Pijnenburg YA, Fox NC, Scheltens P. Early-onset versus late-onset Alzheimer's disease: the case of the missing *APOE* ε4 allele. *Lancet Neurol.* 2011;10:280–288.
6. Maruyama M, Shimada H, Suhara T, et al. Imaging of tau pathology in a tauopathy mouse model and in Alzheimer patients compared to normal controls. *Neuron.* 2013;79:1094–1108.
7. Mueller A, Bullich S, Barret O, et al. Tau PET imaging with $^{18}$F-PI-2620 in patients with Alzheimer disease and healthy controls: a first-in-humans study. *J Nucl Med.* 2020;61:911–919.
8. Cho H, Jeon S, Kang SJ, et al. Longitudinal changes of cortical thickness in early- versus late-onset Alzheimer's disease. *Neurobiol Aging.* 2013;34:1921.e9–1921.e15.
9. Wattmo C, Wallin ÅK. Early- versus late-onset Alzheimer's disease in clinical practice: cognitive and global outcomes over 3 years. *Alzheimers Res Ther.* 2017;9:70.
10. Bullich S, Mueller A, De Santi S, et al. Evaluation of tau deposition using $^{18}$F-PI-2620 PET in MCI and early AD subjects: a MissionAD tau sub-study. *Alzheimers Res Ther.* 2022;14:105.
11. Kroth H, Oden F, Molette J, et al. Discovery and preclinical characterization of [$^{18}$F]PI-2620, a next-generation tau PET tracer for the assessment of tau pathology in Alzheimer's disease and other tauopathies. *Eur J Nucl Med Mol Imaging.* 2019;46:2178–2189.
12. Oh M, Oh SJ, Lee SJ, et al. Clinical evaluation of $^{18}$F-PI-2620 as a potent PET radiotracer imaging tau protein in Alzheimer disease and other neurodegenerative diseases compared with $^{18}$F-THK-5351. *Clin Nucl Med.* 2020;45:841–847.
13. Song M, Scheifele M, Barthel H, et al. Feasibility of short imaging protocols for [$^{18}$F]PI-2620 tau-PET in progressive supranuclear palsy. *Eur J Nucl Med Mol Imaging.* 2021;48:3872–3885.
14. Brendel M, Barthel H, van Eimeren T, et al. Assessment of $^{18}$F-PI-2620 as a biomarker in progressive supranuclear palsy. *JAMA Neurol.* 2020;77:1408–1419.
15. Palleis C, Brendel M, Finze A, et al. Cortical [$^{18}$F]PI-2620 binding differentiates corticobasal syndrome subtypes. *Mov Disord.* 2021;36:2104–2115.
16. Ahn HJ, Chin J, Park A, et al. Seoul Neuropsychological Screening Battery-dementia version (SNSB-D): a useful tool for assessing and monitoring cognitive impairments in dementia patients. *J Korean Med Sci.* 2010;25:1071–1076.
17. Petersen RC, Smith GE, Waring SC, Ivnik RJ, Kokmen E, Tangelos EG. Aging, memory, and mild cognitive impairment. *Int Psychogeriatr.* 1997;9:65–69.
18. McKhann GM, Knopman DS, Chertkow H, et al. The diagnosis of dementia due to Alzheimer's disease: recommendations from the National Institute on Aging–Alzheimer's Association workgroups on diagnostic guidelines for Alzheimer's disease. *Alzheimers Dement.* 2011;7:263–269.
19. Cho H, Choi JY, Lee SH, et al. Excessive tau accumulation in the parieto-occipital cortex characterizes early-onset Alzheimer's disease. *Neurobiol Aging.* 2017;53:103–111.

20. Ye BS, Seo SW, Lee Y, et al. Neuropsychological performance and conversion to Alzheimer's disease in early- compared to late-onset amnestic mild cognitive impairment: CREDOS study. *Dement Geriatr Cogn Disord.* 2012;34:156–166.
21. Tábuas-Pereira M, Baldeiras I, Duro D, et al. Prognosis of early-onset vs. late-onset mild cognitive impairment: comparison of conversion rates and its predictors. *Geriatrics.* 2016;1:11.
22. Lee SJ, Oh SJ, Cho EH, et al. Full automatic synthesis of [$^{18}$F]THK-5351 for tau protein PET imaging in Alzheimer's disease patients: 1 year experience. *J Radioanal Nucl Chem.* 2017;314:1587–1593.
23. Minoshima S, Drzezga AE, Barthel H, et al. SNMMI procedure standard/EANM practice guideline for amyloid PET imaging of the brain 1.0. *J Nucl Med.* 2016;57:1316–1322.
24. Thomas BA, Erlandsson K, Modat M, et al. The importance of appropriate partial volume correction for PET quantification in Alzheimer's disease. *Eur J Nucl Med Mol Imaging.* 2011;38:1104–1119.
25. Schöll M, Lockhart SN, Schonhaut DR, et al. PET imaging of tau deposition in the aging human brain. *Neuron.* 2016;89:971–982.
26. Desikan RS, Ségonne F, Fischl B, et al. An automated labeling system for subdividing the human cerebral cortex on MRI scans into gyral based regions of interest. *Neuroimage.* 2006;31:968–980.
27. Son HJ, Oh JS, Roh JH, et al. Differences in gray and white matter $^{18}$F-THK5351 uptake between behavioral-variant frontotemporal dementia and other dementias. *Eur J Nucl Med Mol Imaging.* 2019;46:357–366.
28. Sattarivand M, Kusano M, Poon I, Caldwell C. Symmetric geometric transfer matrix partial volume correction for PET imaging: principle, validation and robustness. *Phys Med Biol.* 2012;57:7101–7116.
29. Greve DN, Svarer C, Fisher PM, et al. Cortical surface-based analysis reduces bias and variance in kinetic modeling of brain PET data. *Neuroimage.* 2014;92:225–236.
30. Greve DN, Salat DH, Bowen SL, et al. Different partial volume correction methods lead to different conclusions: an $^{18}$F-FDG-PET study of aging. *Neuroimage.* 2016;132:334–343.
31. Baker SL, Maass A, Jagust WJ. Considerations and code for partial volume correcting [$^{18}$F]-AV-1451 tau PET data. *Data Brief.* 2017;15:648–657.
32. Cho H, Choi JY, Lee HS, et al. Progressive tau accumulation in Alzheimer disease: 2-year follow-up study. *J Nucl Med.* 2019;60:1611–1621.
33. Pascoal TA, Benedet AL, Tudorascu DL, et al. Longitudinal $^{18}$F-MK-6240 tau tangles accumulation follows Braak stages. *Brain.* 2021;144:3517–3528.
34. Rabinovici GD, Iaccarino L, La Joie R, et al. Amyloid and tau PET in sporadic early-onset Alzheimer's disease: preliminary results from LEADS. *Alzheimers Dement.* 2020;16(suppl S4):e041613.
35. Malarte M-L, Nordberg A, Lemoine L. Characterization of MK6240, a tau PET tracer, in autopsy brain tissue from Alzheimer's disease cases. *Eur J Nucl Med Mol Imaging.* 2021;48:1093–1102.
36. Sanchez JS, Hanseeuw BJ, Lopera F, et al. Longitudinal amyloid and tau accumulation in autosomal dominant Alzheimer's disease: findings from the Colombia–Boston (COLBOS) biomarker study. *Alzheimers Res Ther.* 2021;13:27.
37. Efthymiou AG, Goate AM. Late onset Alzheimer's disease genetics implicates microglial pathways in disease risk. *Mol Neurodegener.* 2017;12:43.
38. Profenno LA, Porsteinsson AP, Faraone SV. Meta-analysis of Alzheimer's disease risk with obesity, diabetes, and related disorders. *Biol Psychiatry.* 2010;67:505–512.
39. Chishiki Y, Hirano S, Li H, et al. Different patterns of gray matter volume reduction in early-onset and late-onset Alzheimer disease. *Cogn Behav Neurol.* 2020;33:253–258.
40. Kim SH, Seo SW, Yoon DS, et al. Comparison of neuropsychological and FDG-PET findings between early- versus late-onset mild cognitive impairment: a five-year longitudinal study. *Dement Geriatr Cogn Disord.* 2010;29:213–223.
41. Fu JF, Lois C, Sanchez J, et al. Kinetic evaluation and assessment of longitudinal changes in reference region and extracerebral [$^{18}$F]MK-6240 PET uptake. *J Cereb Blood Flow Metab.* 2022;43:581–594.

# First-in-Human Study of $^{18}$F-SynVesT-2: An SV2A PET Imaging Probe with Fast Brain Kinetics and High Specific Binding

Lindsey R. Drake, Yanjun Wu, Mika Naganawa, Ruth Asch, Chao Zheng, Soheila Najafzadeh, Richard Pracitto, Marcel Lindemann, Songye Li, Jim Ropchan, David Labaree, Paul R. Emery, Mark Dias, Shannan Henry, Nabeel Nabulsi, David Matuskey, Ansel T. Hillmer, Jean-Dominique Gallezot, Richard E. Carson, Zhengxin Cai, and Yiyun Huang

*Yale PET Center, New Haven, Connecticut*

PET imaging of synaptic vesicle glycoprotein 2A allows for noninvasive quantification of synapses. This first-in-human study aimed to evaluate the kinetics, test–retest reproducibility, and extent of specific binding of a recently developed synaptic vesicle glycoprotein 2A PET ligand, (*R*)-4-(3-($^{18}$F-fluoro)phenyl)-1-((3-methylpyridin-4-yl)methyl)-pyrrolidine-2-one ($^{18}$F-SynVesT-2), with fast brain kinetics. **Methods:** Nine healthy volunteers participated in this study and were scanned on a High Resolution Research Tomograph scanner with $^{18}$F-SynVesT-2. Five volunteers were scanned twice on 2 different days. Five volunteers were rescanned with preinjected levetiracetam (20 mg/kg, intravenously). Arterial blood was collected to calculate the plasma free fraction and generate the arterial input function. Individual MR images were coregistered to a brain atlas to define regions of interest for generating time–activity curves, which were fitted with 1- and 2-tissue-compartment (1TC and 2TC) models to derive the regional distribution volume ($V_T$). The regional nondisplaceable binding potential ($BP_{ND}$) was calculated from 1TC $V_T$, using the centrum semiovale (CS) as the reference region. **Results:** $^{18}$F-SynVesT-2 was synthesized with high molar activity (187 ± 69 MBq/nmol, $n$ = 19). The parent fraction of $^{18}$F-SynVesT-2 in plasma was 28% ± 8% at 30 min after injection, and the plasma free fraction was high (0.29 ± 0.04). $^{18}$F-SynVesT-2 entered the brain quickly, with an $SUV_{peak}$ of 8 within 10 min after injection. Regional time–activity curves fitted well with both the 1TC and the 2TC models; however, $V_T$ was estimated more reliably using the 1TC model. The 1TC $V_T$ ranged from 1.9 ± 0.2 mL/cm$^3$ in CS to 7.6 ± 0.8 mL/cm$^3$ in the putamen, with low absolute test–retest variability (6.0% ± 3.6%). Regional $BP_{ND}$ ranged from 1.76 ± 0.21 in the hippocampus to 3.06 ± 0.29 in the putamen. A 20-min scan was sufficient to provide reliable $V_T$ and $BP_{ND}$. **Conclusion:** $^{18}$F-SynVesT-2 has fast kinetics, high specific uptake, and low nonspecific uptake in the brain. Consistent with the nonhuman primate results, the kinetics of $^{18}$F-SynVesT-2 is faster than the kinetics of $^{11}$C-UCB-J and $^{18}$F-SynVesT-1 in the human brain and enables a shorter dynamic scan to derive physiologic information on cerebral blood flow and synapse density.

**Key Words:** SV2A; brain PET; $^{18}$F-SynVesT-2; first-in-human; kinetic modeling; dosimetry

**J Nucl Med 2024; 65:462–469**
DOI: 10.2967/jnumed.123.266470

The ability of synapses to adapt and change is essential for learning and memory, and the capacity for synaptic plasticity can be influenced by environmental factors (*1*). Synaptic vesicle glycoprotein 2A (SV2A) is ubiquitously expressed in presynaptic vesicles throughout the central nervous system and thus considered to be a useful indirect measure of synaptic density. PET with radiotracers targeting SV2A therefore provides a minimally invasive method that is suitable for the longitudinal and quantitative assessment of synaptic density, making possible investigations of synapse dynamics during disease pathogenesis and in response to treatment with experimental drugs (*2–9*). In a SV2A PET imaging study in Alzheimer disease patients and healthy controls, the team of Chen et al. demonstrated that a single dynamic SV2A PET scan provides information on both cerebral blood flow, which is related to neuronal activity, and synaptic density (*10–12*). The commonly used SV2A PET ligands (*R*)-1-((3-[$^{11}$C]methylpyridin-4-yl)methyl)-4-(3,4,5-trifluorophenyl)pyrrolidin-2-one ($^{11}$C-UCB-J) and (*R*)-4-(3-fluoro-5-(fluoro-$^{18}$F)phenyl)-1-((3-methylpyridin-4-yl)methyl)pyrrolidin-2-one ($^{18}$F-SynVesT-1) (formerly referred to as $^{18}$F-SDM-8) need 60-min dynamic scans to reliably generate parameters related to cerebral blood flow and synaptic density (*3–5*). It is desirable to maximize the information gained through 1 dynamic PET scan with a shorter scan duration, as shorter scans would improve subject compliance and imaging throughput, reduce motion effects, and enable the study of broader patient populations. One common strategy to improve kinetics without compromising specific binding signal in the brain is to lower the binding affinity and increase the nondisplaceable brain free fraction ($f_{ND}$) by fine-tuning the physicochemical properties of the imaging ligands. The $^{18}$F-labeled monofluorinated UCB-J analog, (*R*)-4-(3-($^{18}$F-fluoro)phenyl)-1-((3-methylpyridin-4-yl)methyl)-pyrrolidine-2-one ($^{18}$F-SynVesT-2, formerly referred to as $^{18}$F-SDM-2), with slightly reduced binding affinity and hydrophobicity, exhibited faster brain kinetics, lower nonspecific binding, and high specific binding in nonhuman primate brains (*13*). Therefore, we hypothesized that $^{18}$F-SynVesT-2 would allow for shorter dynamic scanning for reliable estimation of both synapse density and cerebral blood flow index, with high specific binding in the human brain. We tested this hypothesis in this first-in-human study of $^{18}$F-SynVesT-2 on healthy volunteers at baseline and under blocking conditions using levetiracetam.

## MATERIALS AND METHODS

### Radiotracer Synthesis

$^{18}$F-SynVesT-2 was synthesized following a previously published protocol with minor modifications (*13*). The supplemental

Received Jul. 31, 2023; revision accepted Dec. 19, 2023.
For correspondence or reprints, contact Yiyun (Henry) Huang (henry.huang@yale.edu) or Zhengxin Cai (jason.cai@yale.edu).
Published online Feb. 15, 2024.

materials provide more details (available at http://jnm.snmjournals.org) (*14–23*).

### Radiation Dosimetry Study on Nonhuman Primates

The study was performed under a protocol approved by the Yale University Institutional Animal Care and Use Committee.

### Healthy Volunteers

Nine healthy volunteers participated (6 men and 3 women; age, 43 ± 12 y [range, 27–56 y]; weight, 77 ± 14 kg [range, 52–111 kg]). Two of the subjects underwent 3 PET scans, that is, 2 baseline scans and 1 blocking scan. All participants underwent a medical assessment including screening laboratory values and were free of present or past major medical illnesses, including significant neurologic and psychiatric disorders. Additionally, they reported no history of substance use and had no contraindications to MRI scans. The subject demographics and tracer injection parameters are shown in Supplemental Table 1. This PET imaging study was performed under a protocol approved by the Yale University Human Investigation Committee (approval 2000025929), the Yale Radiation Safety Committee, and the Yale MRI Safety Committee and was in accordance with U.S. federal policy for the protection of human research subjects contained in Title 45, part 46, of the *Code of Federal Regulations*. We obtained written informed consent from all participants after they had received a complete explanation of the study procedure.

### Human Brain Imaging Studies

*MRI.* Each subject underwent T1-weighted MRI for coregistration with the PET images.

*Human Brain PET Imaging.* Human brain PET scans were performed on a High Resolution Research Tomograph (Siemens Medical Systems) and followed a previously published scanning protocol (*3,5*).

*Blood Analysis.* Blood analysis experiments followed a previously published scanning protocol (*3–5*).

*Image Registration and Definitions of Regions of Interest (ROIs).* Image registration and definitions of ROIs followed previously published scanning protocols (*3–5*). The ROI for the centrum semiovale (CS) was based on a 2-$cm^3$ CS region defined in Montreal Neurologic Institute space, as previously described (*2*).

### Quantitative Analysis

Two outcome measures—distribution volume ($V_T$) and $K_1$—were calculated with the 1-tissue-compartment (1TC) model and the 2-tissue-compartment (2TC) model, without the cerebral blood fraction parameter. The relative performance of the 1TC and 2TC models was based on the Akaike information criterion (AIC), *F* tests, and comparison of $V_T$ and $K_1$ and their reproducibility. Percentage SE (%SE) was estimated from the theoretic parameter covariance matrix. Comparison of $K_1$ and $V_T$ calculated by different models was limited to those that were reliably estimated—for example, with %SE less than 10%. The time stability of 1TC $V_T$ and $K_1$ was evaluated, with or without counting for the fitted blood volume in the brain. Guo plot analysis was used to compare the in vivo $K_d$ of the SV2A PET tracers (*23*).

The CS was used as the reference region to compute regional nondisplaceable binding potential ($BP_{ND}$) from $V_T$. The Lassen plot was applied to compute levetiracetam occupancy and nondisplaceable distribution volume ($V_{ND}$). $V_{ND}$ was compared with the $V_T$ of the CS at baseline to test the suitability of the CS as a reference region, as previously done with $^{18}$F-SynVesT-1 (*4,5*). The minimum scan duration for $V_T$ was evaluated by fitting the regional time–activity curves for PET data with truncated acquisition times ranging from 20 to 90 min. The ratio of the regional $V_T$ from the truncated scan to that from the 90-min measurement was computed for each ROI. The minimum scan duration for $BP_{ND}$ was evaluated with truncated scan times ranging from 20 to 90 min in 10-min increments. The minimum acceptable acquisition time was assessed for each region according to the following criteria: an average ratio of 95%–105%, and an interindividual SD of less than 10% for the ratio.

An additional, simplified, outcome measure—the SUV ratio (SUVR)—was evaluated. Static SUVR–1, equivalent to $BP_{ND}$ at equilibrium, was computed for 7 time windows of 30-min duration (0–30, 10–40, 20–50, 30–60, 40–70, 50–80, and 60–90) and compared with $BP_{ND}$ calculated from the regional $V_T$ ratio (target/reference) − 1.

### Test–Retest Evaluation

The reproducibility of the obtained outcome parameters was examined by calculation of the relative test–retest variability (TRV) and absolute TRV (aTRV). TRV was calculated as 2 × (retest − test)/(test + retest), and aTRV was calculated as 2 × |retest − test|/(test + retest).

## RESULTS

### PET Tracer Synthesis and Quality Control

The synthesis process of $^{18}$F-SynVesT-2 was validated in 3 consecutive validation runs, and the final products met the preset quality control criteria (Supplemental Table 2 shows the quality control results of 3 validation runs). The production of $^{18}$F-SynVesT-2 for human use followed the same protocol as used in the validation runs, and the final product quality was consistent. The radiochemical purity of $^{18}$F-SynVesT-2 was over 99%. The molar activity at the end of synthesis was 187 ± 69 MBq/nmol ($n$ = 19).

### Dosimetry Calculation

The injected activity in the nonhuman primate dosimetry scans was 138.8 ± 57.7 MBq ($n$ = 4). The maximum permissible single-study dose of $^{18}$F-SynVesT-2 was calculated from the averaged organ radiation exposure levels to remain below the limit in title 21, part 361.1, of the *Code of Federal Regulations* (for a single study, 50 mSv per organ or 30 mSv to selected organs undergoing rapid cell division, whichever is less). The urinary bladder wall was determined to be the dose-limiting organ for both men and women, with a maximum permissible single-study dose of 257.9 MBq for a woman and 322.6 MBq for a man using the no-bladder-void model. Using the voiding model with a 3.5-h voiding interval, the maximum single-study doses for men and women were 719.6 and 414.4 MBq, respectively, with the urinary bladder wall as the dose-limiting organ (Supplemental Tables 3 and 4).

### Human Injection Parameters

The injected radioactivity of $^{18}$F-SynVesT-2 was 178.9 ± 4.2 MBq (range, 172.8–183.9 MBq; $n$ = 5) for the test PET scans, 181.7 ± 5.1 MBq (range, 175.4–186.1 MBq; $n$ = 5) for the retest PET scans, and 184.0 ± 3.9 MBq (range, 179.1–188.0 MBq; $n$ = 5) for the blocking PET scans (Supplemental Table 1). The injected mass dose of SynVesT-2 was 0.40 ± 0.19 μg (range, 0.20–0.99 μg; $n$ = 19), corresponding to 5.4 ± 3.6 ng/kg ($n$ = 19). There was no statistically significant difference in the injected radioactivity dose, molar activity, or injected mass between the test and retest conditions.

### Safety

No significant clinical changes were observed with the administration of $^{18}$F-SynVesT-2 in this study. There were no adverse events or clinically detectable pharmacologic effects reported in any of the subjects. No significant changes in vital signs were observed. The subjects completed their scans without reporting discomfort that would warrant secession from scanning.

### Blood Analysis

The mean extraction efficiency and high-performance liquid chromatography fraction recovery value were more than 97% at all time points. Representative high-performance liquid radiochromatograms from plasma samples obtained at 8, 15, 60, and 120 min after injection of $^{18}$F-SynVesT-2 in 1 volunteer are displayed in Figure 1A. After injection of $^{18}$F-SynVesT-2, only 1 major radiometabolite fraction was detected during the course of the PET measurement. The radiometabolite fraction had a retention time of about 7.5 min, eluting earlier than $^{18}$F-SynVesT-2 (~11 min). This is similar to $^{18}$F-SynVesT-1, which also features 1 major plasma radiometabolite peak (*5*). Figure 1B displays the parent fractions of $^{18}$F-SynVesT-2 over the time course of the baseline and blocking PET measurements. There was a trend toward slightly higher parent fractions during the blocking scans than during the baseline scans, albeit the differences were not statistically significant after correction for multiple comparisons. However, there was a significant difference in the mean area under the curve of the $^{18}$F-SynVesT-2 plasma concentration from 0 to 90 min after injection at baseline (area under the curve, 52.4 ± 1.3 SUV × min; $n$ = 14) and under blocking conditions (area under the curve, 69.0 ± 1.8 SUV × min; $n$ = 5; 2-tailed $P < 0.005$, paired $t$ test) (Figs. 1C and 1D). The observed higher area under the curve of plasma concentration under blocking conditions is not uncommon among brain PET tracers. The plasma free fraction ($f_p$) of $^{18}$F-SynVesT-2 was high and could be reliably measured at 0.29 ± 0.04 (range, 0.24–0.39; $n$ = 19). The $f_p$ of $^{18}$F-SynVesT-2 was not changed during the baseline and blocking scans ($P$ = 0.33, paired $t$ test; $n$ = 3 pairs).

### Brain Distribution and Kinetics

The regional brain distribution of $^{18}$F-SynVesT-2 was similar to that of $^{18}$F-SynVesT-1 and $^{11}$C-UCB-J, with high uptake in gray matter and low uptake in white matter. Typical time–activity curves from a representative subject as the 1TC model fitted curves are shown in Figure 2. SUV in brain regions peaked at 5–10 min after injection and ranged from 5 to 9 in gray matter. Uptake in white matter (CS) was considerably lower than that in gray matter. A steady decline in regional radioactivity was observed from 10 to 20 min after injection. The summed SUV images from 40 to 60 min after injection showed high-resolution mapping of SV2A in the human brain (Fig. 3).

The 1TC model described the regional time–activity curves well, and kinetic parameters (both $K_1$ and $V_T$) were reliably estimated (%SE < 10% for 418/418 ROIs). On the basis of the AIC and $F$ test results, the 2TC model fits the time–activity curves better than 1TC model does (for the $F$ test, $P < 0.05$ in 126/209 ROIs; the 2TC AIC value was lower than the 1TC AIC value, $P < 0.001$). However, using 2TC modeling, the $K_1$ could not be reliably estimated for 19% of the analyzed ROIs (%SE > 100% for 39/209 ROIs), and the $V_T$ could not be reliably estimated for 28% of the analyzed ROIs (%SE > 100% for 58/209 ROIs). This finding is consistent with previous $^{11}$C-UCB-J data (*3*). Similarly, the 1TC model with blood volume correction fits the time–activity curves better than the 1TC model does without blood volume correction (for the $F$ test, $P < 0.05$ in 80/209 ROIs; the 1TC with blood volume correction AIC value was lower than the 1TC without blood volume correction AIC value, $P < 0.001$). However, adding blood volume correction slightly degraded the reliability of the $V_T$ estimates (%SE > 100% for 21/209 ROIs), and $V_T$ estimates were similar with and without blood volume correction ($V_T$ estimates were only −2% ± 3% lower with blood volume correction, $n$ = 209). Therefore, the 1TC model without blood volume correction was used as the preferred model for the analysis of 90-min datasets. The mean $K_1$ (mL/cm$^3$/min) estimated from 1TC ranged from 0.11 ± 0.02 in the CS to 0.38 ± 0.06 in the putamen (Table 1). These $K_1$ (mL/cm$^3$/min) values are similar to those

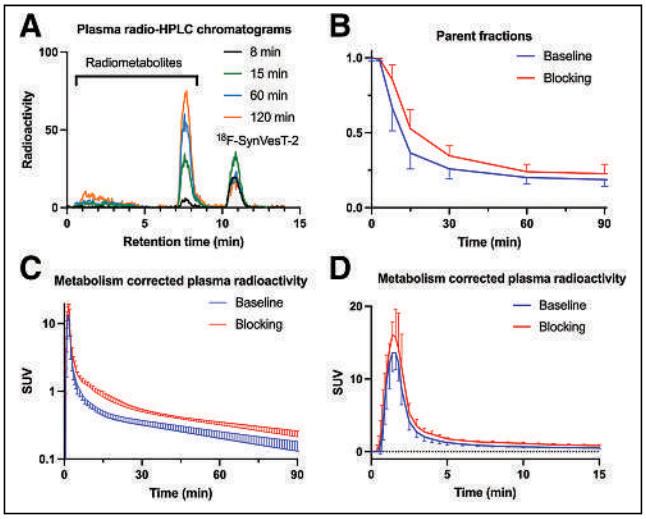


**FIGURE 1.** Representative radio–high-performance liquid chromatograms of plasma content at 8, 15, 60, and 120 min after intravenous injection of $^{18}$F-SynVesT-2 in humans, showing radiometabolite peaks with higher hydrophilicity (A), parent fraction of $^{18}$F-SynVesT-2 in plasma over time under baseline ($n$ = 14) and blocking ($n$ = 5) conditions (B), and concentration of $^{18}$F-SynVesT-2 (mean ± SD) in plasma over time under baseline ($n$ = 14) and blocking conditions ($n$ = 5) from 0 to 90 min after injection (C) and from 0 to 15 min after injection (D). HPLC = high-performance liquid chromatography.

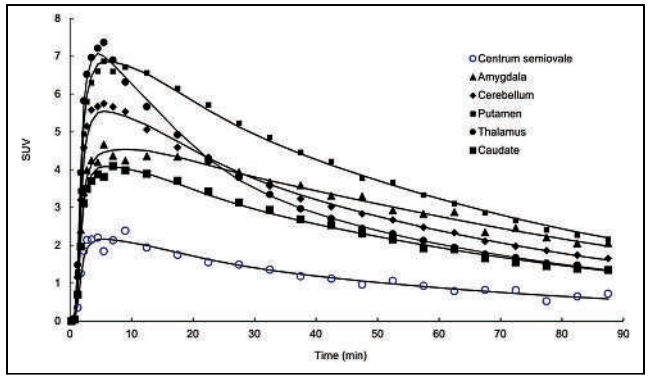


**FIGURE 2.** Time–activity curves derived from single representative $^{18}$F-SynVesT-2 baseline scan. Time–activity curves for amygdala, cerebellum, putamen, thalamus, caudate nucleus, and CS are displayed with 1TC model fitted curves (black solid lines).

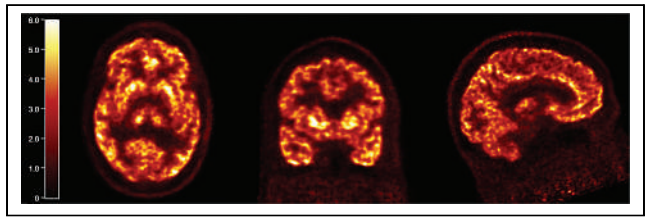

**FIGURE 3.** Summed SUV PET images of representative $^{18}$F-SynVesT-2 baseline scan, from 40 to 60 min after injection.

**TABLE 1**
Kinetic Parameters of $^{18}$F-SynVesT-2 Under Baseline and Blocking Conditions Derived with 1TC Model from 90-Minute Time–Activity Curves

| | $K_1$ (mL/cm$^3$/min) | | $K_2$ (min$^{-1}$) | | $V_T$ (mL/cm$^3$) | |
|---|---|---|---|---|---|---|
| Region | Baseline | Blocking | Baseline | Blocking | Baseline | Blocking |
| Amygdala | 0.25 ± 0.05 | 0.24 ± 0.05 | 0.037 ± 0.006 | 0.12 ± 0.02 | 6.72 ± 0.74 | 2.06 ± 0.26 |
| CS | 0.11 ± 0.02 | 0.09 ± 0.01 | 0.059 ± 0.009 | 0.07 ± 0.01 | 1.88 ± 0.23 | 1.44 ± 0.14 |
| Caudate nucleus | 0.28 ± 0.06 | 0.26 ± 0.06 | 0.050 ± 0.007 | 0.15 ± 0.03 | 5.64 ± 0.75 | 1.80 ± 0.22 |
| Cerebellum | 0.29 ± 0.04 | 0.26 ± 0.03 | 0.052 ± 0.005 | 0.14 ± 0.02 | 5.69 ± 0.65 | 1.80 ± 0.21 |
| Frontal lobe | 0.36 ± 0.05 | 0.3 ± 0.05 | 0.053 ± 0.006 | 0.15 ± 0.03 | 6.74 ± 0.85 | 2.02 ± 0.27 |
| Hippocampus | 0.24 ± 0.03 | 0.23 ± 0.03 | 0.046 ± 0.006 | 0.13 ± 0.02 | 5.17 ± 0.54 | 1.81 ± 0.20 |
| Occipital lobe | 0.35 ± 0.06 | 0.33 ± 0.05 | 0.050 ± 0.008 | 0.16 ± 0.03 | 6.96 ± 0.79 | 2.10 ± 0.28 |
| Parietal lobe | 0.35 ± 0.06 | 0.31 ± 0.05 | 0.050 ± 0.007 | 0.15 ± 0.03 | 6.91 ± 0.85 | 2.05 ± 0.30 |
| Putamen | 0.38 ± 0.06 | 0.35 ± 0.06 | 0.051 ± 0.008 | 0.16 ± 0.03 | 7.60 ± 0.78 | 2.27 ± 0.29 |
| Temporal lobe | 0.33 ± 0.05 | 0.30 ± 0.05 | 0.045 ± 0.007 | 0.14 ± 0.03 | 7.43 ± 0.87 | 2.18 ± 0.30 |
| Thalamus | 0.36 ± 0.05 | 0.32 ± 0.04 | 0.065 ± 0.007 | 0.17 ± 0.03 | 5.57 ± 0.63 | 1.91 ± 0.20 |

$n$ = 9 subjects.

of $^{18}$F-SynVesT-1 (range, 0.11–0.37) and $^{11}$C-UCB-J (range, 0.13–0.39) (*3,5*). The mean $k_2$ (min$^{-1}$) ranged from 0.037 ± 0.006 in the amygdala to 0.065 ± 0.007 in the thalamus (Table 1). $^{18}$F-SynVesT-2 features faster kinetics as evidenced by the higher washout rate than for $^{18}$F-SynVesT-1 (mean $k_2$ [min$^{-1}$], 0.014 in the amygdala to 0.032 in the CS) (*5*). The mean $k_2$ ratios of $^{18}$F-SynVesT-2 to those of $^{18}$F-SynVest-1 and $^{11}$C-UCB-J were 2.5 ± 0.2 and 2.8 ± 0.2, respectively, indicating that the brain kinetics of $^{18}$F-SynVesT-2 is 2.5-fold and 2.8-fold faster than the brain kinetics of $^{18}$F-SynVesT-1 and $^{11}$C-UCB-J, respectively. Correspondingly, the mean $V_T$ (mL/cm$^3$) ranged from 1.9 in the CS to 7.6 in the putamen (Table 1), which are lower than those of $^{18}$F-SynVesT-1 (3.5 in the CS to 19 in the putamen) (*5*) and $^{11}$C-UCB-J (5.3–22) (*3*), as expected from the faster washout rate constant, $k_2$.

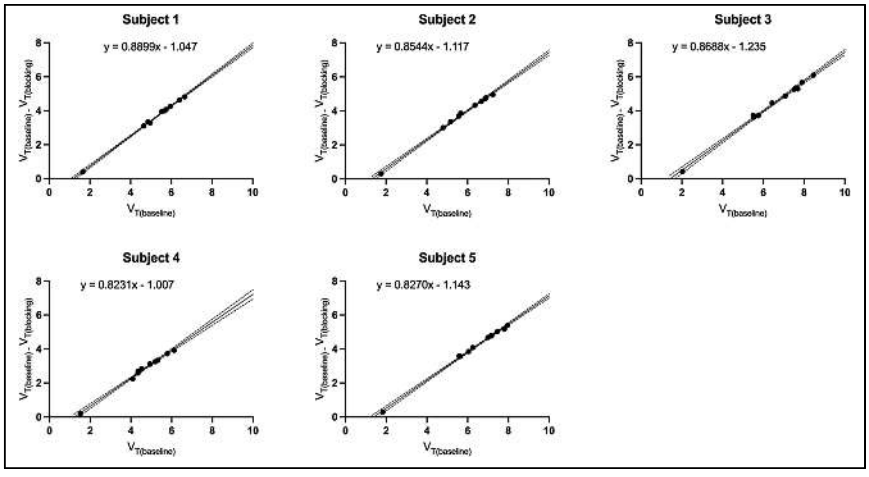


**FIGURE 4.** Lassen plots of $^{18}$F-SynVesT-2 in 5 subjects with baseline and levetiracetam (20 mg/kg, intravenously) blocking PET scans. Data are in mL/cm$^3$.

Blocking studies with levetiracetam (20 mg/kg intravenously, 3 h before tracer injection) were performed on 5 individuals to demonstrate the in vivo specific binding of $^{18}$F-SynVesT-2 to SV2A. Reduction in $^{18}$F-SynVesT-2 uptake was noticeable across brain regions, with the least change in the CS. The mean $V_T$ values (mL/cm$^3$) for the blocking scans were 1.44 ± 0.14 in the CS to 2.27 ± 0.29 in the putamen (Table 1). On the basis of the Lassen plots, SV2A occupancy by levetiracetam was 85% ± 3% (Fig. 4 Supplemental Tables 5 and 6). This level of occupancy is similar to that measured with $^{18}$F-SynVesT-1 (85.3%) or $^{11}$C-UCB-J (82.5%) under identical blocking conditions (*5*). The $V_{ND}$ determined as the x-intercepts from the Lassen plots was 1.30 ± 0.10 mL/cm$^3$ ($n$ = 5), which is significantly lower than those of $^{11}$C-UCB-J and $^{18}$F-SynVesT-1 (3.13 ± 0.41 mL/cm$^3$, $n$ = 4, and 2.38 ± 0.33 mL/cm$^3$, $n$ = 4, respectively; $P < 0.0001$, 1-way ANOVA), presumably because of the higher hydrophilicity of $^{18}$F-SynVesT-2 (*5*). The $V_{ND}$ of gray matter was lower than the baseline CS $V_T$ by 26% ± 4% for $^{18}$F-SynVesT-2 ($n$ = 5), which is lower than those for $^{18}$F-SynVesT-1 (32% ± 16%, $n$ = 4) and $^{11}$C-UCB-J (29% ± 13%, $n$ = 4) but not significantly different among the 3 tracers ($P$ = 0.74, 1-way ANOVA), likely because of the small sample sizes.

When the baseline CS $V_T$ was used as the reference value, the $BP_{ND}$ ranged from 1.76 ± 0.21 in the hippocampus to 3.06 ± 0.29 in the putamen for $^{18}$F-SynVesT-2 (Table 2). This range is lower than those of $^{18}$F-SynVesT-1 (2.7 ± 0.4 in the hippocampus to 4.5 ± 0.5 in the putamen: Supplemental Fig. 1) and $^{11}$C-UCB-J (2.1 in the hippocampus to 3.7 in the putamen).

**TABLE 2**
$BP_{ND}$ of $^{18}$F-SynVesT-2 Under Baseline and Blocking Conditions, and TRV of $BP_{ND}$

| | $BP_{ND}$ | | Test–retest | |
|---|---|---|---|---|
| Region | Baseline ($n$ = 9 subjects, 14 scans) | Blocking ($n$ = 5) | TRV ($n$ = 5) | aTRV ($n$ = 5) |
| Amygdala | 2.59 ± 0.31 | 0.43 ± 0.08 | 0.26% ± 9.90% | 7.38% ± 5.09% |
| Caudate nucleus | 2.03 ± 0.41 | 0.25 ± 0.1 | −2.73% ± 14.87% | 13.34% ± 5.12% |
| Cerebellum | 2.03 ± 0.18 | 0.25 ± 0.04 | −2.62% ± 10.93% | 9.77% ± 4.93% |
| Frontal lobe | 2.59 ± 0.34 | 0.4 ± 0.06 | −0.71% ± 11.78% | 9.96% ± 5.29% |
| Hippocampus | 1.76 ± 0.21 | 0.26 ± 0.07 | 3.08% ± 15.18% | 12.40% ± 5.09% |
| Occipital lobe | 2.72 ± 0.36 | 0.46 ± 0.09 | 0.74% ± 13.34% | 10.42% ± 5.27% |
| Parietal lobe | 2.69 ± 0.37 | 0.42 ± 0.09 | −0.33% ± 15.38% | 13.12% ± 6.88% |
| Putamen | 3.06 ± 0.29 | 0.58 ± 0.1 | −1.28% ± 10.59% | 9.36% ± 4.17% |
| Temporal lobe | 2.97 ± 0.37 | 0.51 ± 0.1 | 0.46% ± 12.72% | 10.69% ± 5.44% |
| Thalamus | 1.97 ± 0.24 | 0.33 ± 0.07 | −0.47% ± 17.23% | 14.15% ± 8.50% |

Data are mean ± SD.

This finding is consistent with the prediction from the Guo plots. A global decrease (~85%) in $BP_{ND}$ was observed in the blocking studies, consistent with the Lassen plot analysis results. Blocking $BP_{ND}$ ranged from 0.25 ± 0.10 in the caudate nucleus to 0.58 ± 0.1 in the putamen.

The time stability of $K_1$ and $V_T$ was investigated in shorter scan increments ranging from 20 to 90 min. Both $K_1$ and $V_T$ estimates were stable down to 20 min of scan time and were within 10% of the 90-min data (Fig. 5). The minimum dynamic scan time for stable $V_T$ estimates was 60 min for $^{11}$C-UCB-J and $^{18}$F-SynVesT-1, consistent with the faster kinetics and higher $k_2$ for $^{18}$F-SynVesT-2 in the human brain. The time stability of $V_T$ estimates would be slightly further improved by including blood volume correction in the model, whereas the time stability of $K_1$ estimates would be degraded slightly (Supplemental Fig. 2). The time stability of $BP_{ND}$ was also investigated, and $BP_{ND}$ derived from the minimum scan time of 20 min deviated by only –0.9% ± 9.0% from values estimated using the full 90-min dynamic imaging dataset (Fig. 6). This is an obvious improvement over $^{11}$C-UCB-J and $^{18}$F-SynVesT-1, both of which require longer dynamic scan times (Supplemental Figs. 3 and 4).

To evaluate the measurement robustness of the baseline scans using $^{18}$F-SynVesT-2, we calculated the TRV and aTRV of the key 1TC modeling parameters from the test–retest scans of 5 subjects. Table 3 lists the test–retest reproducibility results for each region for 1TC $K_1$ and $V_T$. The global mean aTRV of $V_T$ for $^{18}$F-SynVesT-2 was 6.0% (range, 4.7%–7.2%), which was similar to the values for $^{18}$F-SynVesT-1 (global mean, 5.8%; range, 4%–8%) and $^{11}$C-UCB-J (global mean, 4.4%; range, 3%–9%) (*3,4*). The mean regional aTRV for $^{18}$F-SynVesT-2 $BP_{ND}$ was 10.8% ± 1.9%, ranging from 7.8% to 13.7% (Table 2), which is also comparable to the values for $^{11}$C-UCB-J and $^{18}$F-SynVesT-1 (*4*). Note that the test–retest scans for $^{18}$F-SynVesT-2 and $^{18}$F-SynVesT-1 were performed on different days, whereas the test–retest scans for $^{11}$C-UCB-J were on the same day.

To determine the suitable imaging window for static scans using SUVR–1 as a surrogate of $BP_{ND}$ from dynamic scans, we compared the averaged SUVR–1 using CS as the reference region at different 30-min time windows with the $BP_{ND}$ calculated using 90 min of dynamic scan data (Fig. 7). An optimal imaging window from 20 to 50 min after injection was found to provide SUVR–1 s nearly identical to $BP_{ND}$, with a mean difference of −0.3% ± 2.6% from the $BP_{ND}$. This optimal static imaging window is earlier than that for $^{11}$C-UCB-J and $^{18}$F-SynVesT-1 (60–90 min after injection), as expected from the faster kinetics of $^{18}$F-SynVesT-2. Analysis of individual brain regions indicated that for brain regions other than the thalamus, the averaged SUVR–1 of early time windows underestimated $BP_{ND}$, whereas the SUVR–1 of late time windows overestimated $BP_{ND}$ (Supplemental Fig. 5).

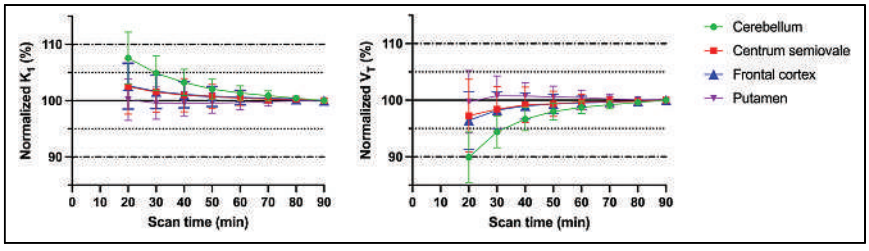


**FIGURE 5.** Time stability analyses of outcome parameters $K_1$ and $V_T$ of $^{18}$F-SynVesT-2. $K_1$ and $V_T$ were calculated using 1TC model on data from different scan times and divided by corresponding values measured using 90 min of PET data.

## DISCUSSION

After the discovery and development of the PET ligand $^{11}$C-UCB-J, which binds specifically to SV2A, researchers in the field of brain PET imaging have studied SV2A changes noninvasively in a variety of neurodegenerative and neuropsychiatric diseases (*11,12,24–32*). However, the currently used SV2A PET ligands, $^{11}$C-UCB-J and $^{18}$F-SynVesT-1 ($^{18}$F-SDM-8), need at least 60–90 min of dynamic scan data to reliably derive the index of the cerebral blood

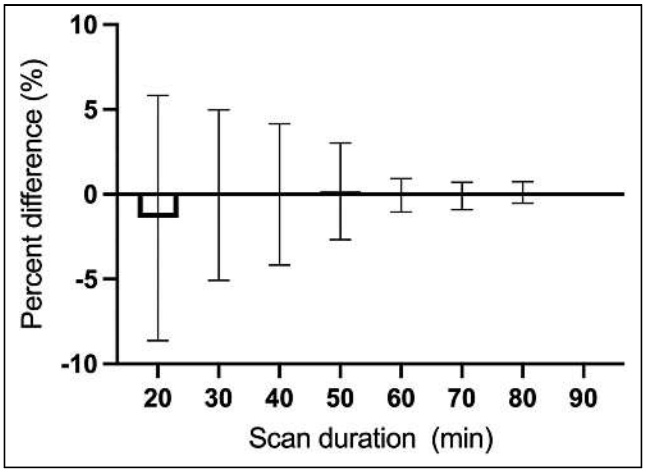


**FIGURE 6.** Time stability of $^{18}$F-SynVesT-2 baseline $BP_{ND}$ using CS as reference region. Shown are percentage differences between $BP_{ND}$ calculated using different scan durations at 10-min increments and $BP_{ND}$ calculated using 90 min of scan data. Data are mean and SD for 9 subjects and 14 scans.

flow and synaptic density. We discovered a new SV2A PET ligand, $^{18}$F-SynVesT-2 ($^{18}$F-SDM-2), which has faster kinetics in nonhuman primate brains (*13*). The aim of this study was to evaluate $^{18}$F-SynVesT-2 in healthy human subjects in comparison with $^{11}$C-UCB-J and $^{18}$F-SynVesT-1 to see whether it is possible to use $^{18}$F-SynVesT-2 to shorten the scanning time required for dynamic SV2A PET while getting quantitative information on synapse density and cerebral blood flow index.

Similar to $^{11}$C-UCB-J and $^{18}$F-SynVesT-1, the brain time–activity curves of $^{18}$F-SynVesT-2 are well described by the simple 1TC model, without counting for the cerebral blood fraction. The test–retest repeatability of $^{18}$F-SynVesT-2 $V_T$ is excellent, with aTRV below 8% for all brain regions analyzed. Because of the faster clearance from the brain, the 1TC $V_T$ of $^{18}$F-SynVesT-2 is consistently lower than that of $^{11}$C-UCB-J and $^{18}$F-SynVesT-1. Though we did not identify the major radiometabolite of $^{18}$F-SynVesT-2 in the plasma, it is likely to be its *N*-oxide pyridine derivative, which is probably not brain-penetrant, in view of the structural similarity of $^{18}$F-SynVesT-2 to $^{11}$C-UCB-J and $^{18}$F-SynVesT-1. The Food and Drug Administration–approved SV2A ligand levetiracetam blocked 85% of the specific binding of $^{18}$F-SynVesT-2 in the human brain at an intravenous dose of 20 mg/kg. The extent of blockade is similar to that for $^{11}$C-UCB-J and $^{18}$F-SynVesT-1 (*5*). Interestingly, the estimated $V_{ND}/f_p$ is 4.86 mL/cm$^3$, indicating that about 20% of the tracer uptake in CS at baseline is attributable to specific uptake, which is lower than the 35%–40% for $^{11}$C-UCB-J (*2*). Note that the CS ROI we used has been optimized to minimize the spill-in effects from the surrounding gray matter (*2*). The source of the specific binding in CS remains elusive for the SV2A PET tracers. The volume changes in CS need to be accounted for in neurodegenerative diseases at advanced stages.

Because of the lower tracer uptake of $^{18}$F-SynVesT-2 in CS, the lower 1TC $V_T$ in gray matter did not lead to a dramatically lower $BP_{ND}$. We correlated the baseline $V_T$ of $^{18}$F-SynVesT-2 with that of $^{11}$C-UCB-J and $^{18}$F-SynVesT-1 in the same subjects. By assuming the same maximum available binding sites ($B_{max}$) for the 3 SV2A PET tracers in the same subjects, the in vivo $K_d$ ratios of $^{18}$F-SynVesT-2 to $^{11}$C-UCB-J and $^{18}$F-SynVesT-1 are 3 (Supplemental Fig. 6), which is similar to the in vitro $K_d$ ratios measured using postmortem human brain tissue (*33*). Taken together, this indicates that the $f_{ND}$ of $^{18}$F-SynVesT-2 is higher than that of $^{11}$C-UCB-J and $^{18}$F-SynVesT-1. Though we did not experimentally measure the $f_{ND}$ of these tracers, using the $V_{ND}$ estimated from the baseline-blocking studies in 5 subjects and the corresponding $f_p$, we calculated the $f_{ND}$ of $^{18}$F-SynVesT-2 to be $0.17 \pm 0.05$ ($n = 6$), which is indeed higher than the calculated $f_{ND}$ of $^{11}$C-UCB-J (0.086) and $^{18}$F-SynVesT-1 (0.13) (*5*).

**TABLE 3**
Test–Retest Reproducibility of Kinetic Parameters of $^{18}$F-SynVesT-2 Derived with 1TC Model from 90 Minutes of Time–Activity Curves

| | $K_1$ (mL/cm$^3$/min) | | | | $V_T$ (mL/cm$^3$) | | | |
|---|---|---|---|---|---|---|---|---|
| | TRV | | aTRV | | TRV | | aTRV | |
| Region | Mean | SD | Mean | SD | Mean | SD | Mean | SD |
| Amygdala | 0.50 | 9.69 | 6.63 | 6.27 | −1.97 | 7.06 | 5.73 | 3.71 |
| CS | 2.88 | 8.62 | 7.71 | 3.22 | −2.05 | 10.18 | 7.17 | 6.68 |
| Caudate nucleus | −2.78 | 14.99 | 12.90 | 5.13 | −4.29 | 6.83 | 6.14 | 4.75 |
| Cerebellum | −3.72 | 12.91 | 10.28 | 7.20 | −3.96 | 6.07 | 5.96 | 3.48 |
| Frontal lobe | −1.32 | 12.14 | 8.81 | 7.26 | −2.74 | 7.69 | 6.07 | 4.74 |
| Hippocampus | −0.29 | 10.55 | 8.31 | 5.00 | −0.31 | 6.69 | 5.35 | 3.03 |
| Occipital lobe | 1.20 | 12.82 | 8.76 | 8.37 | −1.75 | 8.72 | 6.95 | 4.41 |
| Parietal lobe | −1.47 | 11.93 | 9.59 | 5.50 | −2.61 | 6.32 | 4.83 | 4.39 |
| Putamen | −5.27 | 13.85 | 12.02 | 6.76 | −3.11 | 7.03 | 6.39 | 3.23 |
| Temporal lobe | −1.41 | 11.81 | 8.16 | 7.66 | −1.90 | 8.16 | 6.12 | 4.93 |
| Thalamus | −6.04 | 14.59 | 13.47 | 5.64 | −2.56 | 5.31 | 4.69 | 2.97 |

Data are percentages. $n = 5$.

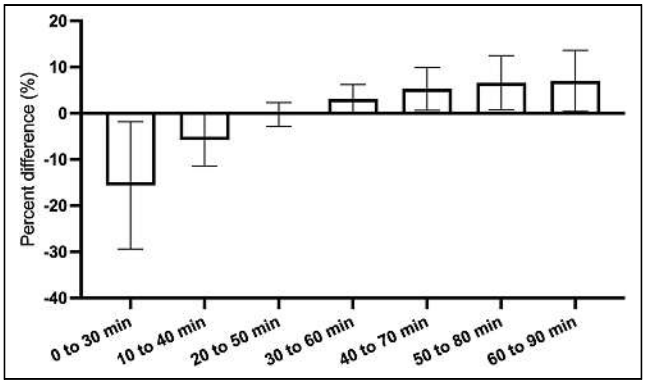


**FIGURE 7.** Percentage differences of SUVR–1 of $^{18}$F-SynVesT-2 in different scan time windows from $BP_{ND}$, represented as mean and SD for each 30-min time window. Mean percentage difference for each imaging window is for 10 brain regions in 14 baseline scans. SD reflects variability of averaged percentage differences for different brain regions.

Shortening of the dynamic scan time from 2 h to 30 min had negligible impact (−0.3% ± 4.3%) on the $BP_{ND}$ estimation for $^{18}$F-SynVesT-2. This is significantly shorter than the 60 min required for $^{11}$C-UCB-J and $^{18}$F-SynVesT-1 (*5*). To simplify the scan protocol as static scanning that is easier to execute in multicenter clinical trials, we opted to use SUVR–1 as a surrogate for $BP_{ND}$ by comparing the averaged SUVR–1 from different imaging windows with the $BP_{ND}$ from the full 90-min dataset. We found that the optimal static imaging window is 20–50 min after injection, with −0.3% ± 2.6% difference between SUVR–1 from 20 to 50 min and $BP_{ND}$. Therefore, the fast pharmacokinetics of $^{18}$F-SynVesT-2 requires only a 30-min dynamic scan to reliably derive $K_1$, $V_T$, and $BP_{ND}$, or a 30-min static scan (20–50 min after injection) to calculate the SUVR–1 as a surrogate of $BP_{ND}$. $^{18}$F-FDG PET, as a surrogate measure of neuronal activity, has been extensively used in the early detection of Alzheimer disease (*34*). The kinetic parameter $K_1$ is proportional to the blood flow and extraction fraction and serves as an index of blood flow for tracers with high brain permeability and a constant extraction fraction throughout the brain (no leakage in the blood–brain barrier, and no active influx or efflux). Indeed, Chen et al. have previously demonstrated a strong correlation between the $^{11}$C-UCB-J $K_1$ and $^{18}$F-FDG $K_i$ in 14 Alzheimer disease subjects and 11 cognitively normal controls ($R^2$ = 0.21–0.66) (*10*). Also, in another study on 7 healthy subjects, the $K_1$ of $^{11}$C-UCB-J in the visual cortex was sensitive to changes in cerebral blood flow and correlated well with the functional MRI blood oxygenation level–dependent response, whereas the $V_T$ and $BP_{ND}$ were unchanged during visual stimulations (*35*). Use of a relatively short 30-min dynamic $^{18}$F-SynVesT-2 PET scan to gather information on a patient's cerebral blood flow and synapse density, in lieu of a $^{18}$F-FDG PET scan and an SV2A PET scan, is expected to have clinical practicality.

In the literature, SV2A PET has been associated with synaptic density measurement. However, as the function of SV2A remains elusive, the validity of using SV2A PET as a quantification method for synaptic density needs to be validated for each application scenario.

## CONCLUSION

The newly developed SV2A PET tracer $^{18}$F-SynVesT-2 has faster brain kinetics than $^{11}$C-UCB-J and $^{18}$F-SynVesT-1 and similarly excellent test–retest reliability. Although lower than that of $^{11}$C-UCB-J and $^{18}$F-SynVesT-1, the specific binding of $^{18}$F-SynVesT-2 in the human brain remains high, as evidenced by a $BP_{ND}$ in the range of 1.76 to 3.06. The fast kinetics and high specific binding of $^{18}$F-SynVesT-2 in the brain allows shortened dynamic scans to get information related to both cerebral blood flow ($K_1$) and synapse density ($V_T$ or $BP_{ND}$), which could potentially lead to improved imaging throughput and expanded patient populations.

## DISCLOSURE

This research was supported by grants R01AG052560, R01AG065474, R01AG058773, and R01NS123183 from the National Institutes of Health and by research grants from the Michael J. Fox Foundation and the Archer Foundation. We thank the staff at the Yale PET Center for expert technical assistance. This publication was also made possible by CTSA grant UL1 RR024139 awarded jointly by the National Center for Research Resources (NCRR) and the National Center for Advancing Translational Sciences (NCATS), components of the National Institutes of Health (NIH). The contents of this publication are solely the responsibility of the authors and do not necessarily represent the official view of NIH. The radioligand $^{18}$F-SynVesT-2 (formerly referred to as $^{18}$F-SDM-2) is contained in the patent US11518754B2, "Radiolabeled Pharmaceuticals and Methods of Making and Using Same," filed on February 15, 2018, and granted on December 6, 2022 (Inventors: Yiyun Huang, Zhengxin Cai, Songye Li, Nabeel Nabulsi, and Richard Carson). No other potential conflict of interest relevant to this article was reported.

## KEY POINTS

**QUESTION:** Do the fast kinetics and high specific binding of $^{18}$F-SynVesT-2 in nonhuman primates translate to human brain PET?

**PERTINENT FINDINGS:** With high specific binding and fast and reversible kinetics in the human brain, $^{18}$F-SynVesT-2 allows for shortened imaging protocols, higher imaging throughput, and expanded patient populations.

**IMPLICATIONS FOR PATIENT CARE:** With simplified and shortened scan protocols, $^{18}$F-SynVesT-2 is expected to improve patient compliance while maximizing information obtained from a single dynamic PET scan.

## REFERENCES

1. Takeuchi T, Duszkiewicz AJ, Morris RGM. The synaptic plasticity and memory hypothesis: encoding, storage and persistence. *Philos Trans R Soc Lond B Biol Sci.* 2013;369:20130288.
2. Rossano S, Toyonaga T, Finnema SJ, et al. Assessment of a white matter reference region for $^{11}$C-UCB-J PET quantification. *J Cereb Blood Flow Metab.* 2020;40:1890–1901.
3. Finnema SJ, Nabulsi NB, Mercier J, et al. Kinetic evaluation and test-retest reproducibility of [$^{11}$C]UCB-J, a novel radioligand for positron emission tomography imaging of synaptic vesicle glycoprotein 2A in humans. *J Cereb Blood Flow Metab.* 2017;0:271678X17724947.
4. Li S, Naganawa M, Pracitto R, et al. Assessment of test-retest reproducibility of [$^{18}$F]SynVesT-1, a novel radiotracer for PET imaging of synaptic vesicle glycoprotein 2A. *Eur J Nucl Med Mol Imaging.* 2021;48:1327–1338.
5. Naganawa M, Li S, Nabulsi N, et al. First-in-human evaluation of $^{18}$F-SynVesT-1, a radioligand for PET imaging of synaptic vesicle glycoprotein 2A. *J Nucl Med.* 2021;62:561–567.

6. Bahri MA, Plenevaux A, Aerts J, et al. Measuring brain synaptic vesicle protein 2A with positron emission tomography and [$^{18}$F]UCB-H. *Alzheimers Dement (N Y).* 2017;3:481–486.
7. Cai Z, Li S, Matuskey D, Nabulsi N, Huang Y. PET imaging of synaptic density: a new tool for investigation of neuropsychiatric diseases. *Neurosci Lett.* 2019;691:44–50.
8. Finnema SJ, Li S, Cai Z, et al. PET imaging of synaptic vesicle protein 2A. In: Dierckx RAJO, Otte A, de Vries EFJ, van Waarde A, Lammertsma AA, eds. *PET and SPECT of Neurobiological Systems.* Springer International Publishing; 2021:993–1019.
9. Spurrier J, Nicholson L, Fang XT, et al. Reversal of synapse loss in Alzheimer mouse models by targeting mGluR5 to prevent synaptic tagging by C1Q. *Sci Transl Med.* 2022;14:eabi8593.
10. Chen MK, Mecca AP, Naganawa M, et al. Comparison of [$^{11}$C]UCB-J and [$^{18}$F]FDG PET in Alzheimer's disease: a tracer kinetic modeling study. *J Cereb Blood Flow Metab.* 2021;0:271678X211004312.
11. Mecca AP, Chen M-K, O'Dell RS, et al. In vivo measurement of widespread synaptic loss in Alzheimer's disease with SV2A PET. *Alzheimers Dement.* 2020;16:974–982.
12. Chen MK, Mecca AP, Naganawa M, et al. Assessing synaptic density in Alzheimer disease with synaptic vesicle glycoprotein 2A positron emission tomographic imaging. *JAMA Neurol.* 2018;75:1215–1224.
13. Cai Z, Li S, Zhang W, et al. Synthesis and preclinical evaluation of an $^{18}$F-labeled synaptic vesicle glycoprotein 2A PET imaging probe: [$^{18}$F]SynVesT-2. *ACS Chem Neurosci.* 2020;11:592–603.
14. Cristy M, Eckerman KF, Marietta M, Systems E. *Specific Absorbed Fractions of Energy at Various Ages from Internal Photon Sources.* Oak Ridge National Laboratory; 1987:1–110.
15. Stabin MG, Sparks RB, Crowe E. OLINDA/EXM: the second-generation personal computer software for internal dose assessment in nuclear medicine. *J Nucl Med.* 2005;46:1023–1027.
16. Carson RE, Barker WC, Liow J-S, Johnson CA. Design of a motion-compensation OSEM list-mode algorithm for resolution-recovery reconstruction for the HRRT. In: *2003 IEEE Nuclear Science Symposium. Conference Record*; IEEE; 2003:3281–3285.
17. Jin X, Mulnix T, Gallezot JD, Carson RE. Evaluation of motion correction methods in human brain PET imaging: a simulation study based on human motion data. *Med Phys.* 2013;40:102503.
18. Hilton J, Yokoi F, Dannals RF, Ravert HT, Szabo Z, Wong DF. Column-switching HPLC for the analysis of plasma in PET imaging studies. *Nucl Med Biol.* 2000;27:627–630.
19. Gallezot JD, Esterlis I, Bois F, et al. Evaluation of the sensitivity of the novel α4β2* nicotinic acetylcholine receptor PET radioligand 18F-(−)-NCFHEB to increases in synaptic acetylcholine levels in rhesus monkeys. *Synapse.* 2014;68:556–564.
20. Holmes CJ, Hoge R, Collins L, Woods R, Toga AW, Evans AC. Enhancement of MR images using registration for signal averaging. *J Comput Assist Tomogr.* 1998;22:324–333.
21. Tzourio-Mazoyer N, Landeau B, Papathanassiou D, et al. Automated anatomical labeling of activations in SPM using a macroscopic anatomical parcellation of the MNI MRI single-subject brain. *Neuroimage.* 2002;15:273–289.
22. Pajevic S, Daube-Witherspoon ME, Bacharach SL, Carson RE. Noise characteristics of 3-D and 2-D PET images. *IEEE Trans Med Imaging.* 1998;17:9–23.
23. Guo Q, Owen DR, Rabiner EA, Turkheimer FE, Gunn RN. A graphical method to compare the in vivo binding potential of PET radioligands in the absence of a reference region: application to [$^{11}$C]PBR28 and [$^{18}$F]PBR111 for TSPO imaging. *J Cereb Blood Flow Metab.* 2014;34:1162–1168.
24. Onwordi EC, Halff EF, Whitehurst T, et al. Synaptic density marker SV2A is reduced in schizophrenia patients and unaffected by antipsychotics in rats. *Nat Commun.* 2020;11:246.
25. Matuskey D, Tinaz S, Wilcox KC, et al. Synaptic changes in Parkinson disease assessed with in vivo imaging. *Ann Neurol.* 2020;87:329–338.
26. Finnema SJ, Toyonaga T, Detyniecki K, et al. Reduced synaptic vesicle protein 2A binding in temporal lobe epilepsy: a [$^{11}$C]UCB-J positron emission tomography study. *Epilepsia.* 2020;61:2183–2193.
27. Delva A, Van Weehaeghe D, Koole M, Van Laere K, Vandenberghe W. Loss of presynaptic terminal integrity in the substantia nigra in early Parkinson's disease. *Mov Disord.* 2020;35:1977–1986.
28. D'Souza DC, Radhakrishnan R, Naganawa M, et al. Preliminary in vivo evidence of lower hippocampal synaptic density in cannabis use disorder. *Mol Psychiatry.* 2021;26:3192–3200.
29. Holmes SE, Scheinost D, Finnema SJ, et al. Lower synaptic density is associated with depression severity and network alterations. *Nat Commun.* 2019;10:1529.
30. Finnema SJ, Nabulsi NB, Eid T, et al. Imaging synaptic density in the living human brain. *Sci Transl Med.* 2016;8:348ra96.
31. Wilson H, Pagano G, de Natale ER, et al. Mitochondrial complex 1, sigma 1, and synaptic vesicle 2A in early drug-naive Parkinson's disease. *Mov Disord.* 2020;35:1416–1427.
32. O'Dell RS, Mecca AP, Chen M-K, et al. Association of Aβ deposition and regional synaptic density in early Alzheimer's disease: a PET imaging study with [$^{11}$C]UCB-J. *Alzheimers Res Ther.* 2021;13:11.
33. Patel S, Knight A, Krause S, et al. Preclinical in vitro and in vivo characterization of synaptic vesicle 2A-targeting compounds amenable to F-18 labeling as potential PET radioligands for imaging of synapse integrity. *Mol Imaging Biol.* 2020;22:832–841.
34. Mosconi L. Glucose metabolism in normal aging and Alzheimer's disease: methodological and physiological considerations for PET studies. *Clin Transl Imaging.* 2013;1:10.1007/s40336-013-0026-y.
35. Smart K, Liu H, Matuskey D, et al. Binding of the synaptic vesicle radiotracer [$^{11}$C]UCB-J is unchanged during functional brain activation using a visual stimulation task. *J Cereb Blood Flow Metab.* 2021;41:1067–1079.

# Triggered Seizures for Ictal SPECT Imaging: A Case Series and Feasibility Study

Sabry L. Barlatey[1], Camille G. Mignardot[2], Cecilia Friedrichs-Maeder[2], Kaspar Schindler[2], Roland Wiest[3], Andreas Nowacki[1], Matthias Haenggi[4], Werner J. Z'Graggen[1], Claudio Pollo[1], Axel Rominger[5], Thomas Pyka*[5], and Maxime O. Baud*[2]

[1]*Department of Neurosurgery, University Hospital of Bern, Bern, Switzerland;* [2]*Sleep-Wake-Epilepsy Center and NeuroTec, Center for Experimental Neurology, Department of Neurology, University Hospital of Bern, Bern, Switzerland;* [3]*Support Center for Advanced Neuroimaging, University Institute of Diagnostic and Interventional Neuroradiology, University Hospital of Bern, Bern, Switzerland;* [4]*Department of Intensive Care Medicine, University Hospital of Bern, Bern, Switzerland; and* [5]*Department of Nuclear Medicine, University Hospital of Bern, Bern, Switzerland*

Ictal SPECT is an informative seizure imaging technique to tailor epilepsy surgery. However, capturing the onset of unpredictable seizures is a medical and logistic challenge. Here, we sought to image planned seizures triggered by direct stimulation of epileptic networks via stereotactic electroencephalography (sEEG) electrodes. **Methods:** In this case series of 3 adult participants with left temporal epilepsy, we identified and stimulated sEEG contacts able to trigger patient-typical seizures. We administered $^{99m}$Tc-HMPAO within 12 s of ictal onset and acquired SPECT images within 40 min without any adverse events. **Results:** Ictal hyperperfusion maps partially overlapped concomitant sEEG seizure activity. In both participants known for periictal aphasia, SPECT imaging revealed hyperperfusion in the speech cortex lacking sEEG coverage. **Conclusion:** Triggering of seizures for ictal SPECT complements discrete sEEG sampling with spatially complete images of early seizure propagation. This readily implementable method revives interest in seizure imaging to guide resective epilepsy surgery.

**Key Words:** human epilepsy; seizure imaging; ictal SPECT; seizure triggering; stereotactic electroencephalography

**J Nucl Med 2024; 65:470–474**
DOI: 10.2967/jnumed.123.266515

Delineating brain areas of seizure onset and propagation is a necessary step toward tailoring surgery for focal epilepsy (*1*). Ictal SPECT is a key method to capture a spatially complete view of propagating seizures by imaging areas of accompanying parenchymal hyperperfusion (*1–3*). However, the unpredictable timing of fleeting seizures renders ictal SPECT acquisitions logistically challenging and resource-intensive.

In practice, neurologists reduce antiseizure medications to hasten the occurrence of seizures. Their prompt detection requires continuous visual monitoring of the electroencephalogram. Until then, nuclear medicine staff must stand ready to inject a radiotracer, critically within seconds of seizure onset, which rarely succeeds without delay (*4*). Moreover, maintaining ready-to-inject radiotracer over days incurs issues with isotope production, transport and storage, as well as radioprotection (*5*). Thus, because of growing cost and time constraints in health care, most epilepsy centers, including ours, abandoned this informative technique (*6*).

Here, we conducted a feasibility study modifying the original ictal SPECT method to address these practical issues. In most patients with epilepsy undergoing invasive stereotactic electroencephalography (sEEG) monitoring, patient-typical seizures can be triggered using direct electric stimulation (*7*). This procedure contributes to localizing ictogenic tissue but also offers temporal control over the occurrence of seizures. We used this untapped opportunity to image planned seizures.

## MATERIALS AND METHODS

### Participants

Three male participants undergoing invasive sEEG investigations for the clinical purpose of localizing their seizures gave their written informed consent in accordance with the Declaration of Helsinki. The Ethics Committee of the Canton Bern, Switzerland, approved this prospective feasibility study (KEK 2021-01337).

### Electrophysiology

sEEG leads (DIXI Medical) were implanted under general anesthesia in cerebral areas of interest for recording (Natus Quantum), mapping, and stimulation (ISIS neurostimulator; Inomed Medizintechnik GmbH). We systematically screened all gray-matter sEEG contacts for minimal stimulation parameters able to trigger the patient-typical seizure (biphasic 1-ms square pulses; frequency, 60 Hz; duration, 1–4 s; intensity, 2–6 mA; Table 1). Epileptiform discharges without symptoms and symptoms without epileptiform discharges were disregarded.

### Seizure Triggering and SPECT Acquisition

One day after triggering a first patient-typical seizure (confirmed as such against spontaneous seizures), stimulation was repeated at the identified trigger site with a connected syringe containing the freshly produced $^{99m}$Tc-hexamethylpropyleneamine oxime (HMPAO) (medeo AG; Table 1). Upon the onset of an electroclinical seizure, the radiotracer was injected, followed by SPECT imaging within 21–39 min on a prebooked Symbia Intevo Bold system (Siemens Healthineers) (Fig. 1A). Potential spillover was assessed with a Geiger counter.

### Imaging Data

Postoperative CT images were coregistered to a preoperative T1-weighted MRI scan using the Lead-DBS toolbox (version 2.5.2) in

Received Aug. 7, 2023; revision accepted Dec. 4, 2023.
For correspondence or reprints, contact Maxime O. Baud (maxime.baud.neuro@gmail.com).
*Contributed equally to this work.
Published online Jan. 11, 2024.

**TABLE 1**
Characteristics of Participants, Trigger Parameters, SPECT Acquisition Data, and Clinical Value

| Category | Characteristic | Participant 1 | Participant 2 | Participant 3 |
|---|---|---|---|---|
| Participants and their epilepsy | Age and sex | 20-y-old man | 50-y-old man | 48-y-old man |
| | Epilepsy | Left mesiotemporal | Left mesiotemporal | Left laterotemporal |
| | Etiology | Hippocampal sclerosis | Hippocampal sclerosis | Posthemorragic |
| | Seizure onset zone from sEEG | Entorhinal cortex, anterior and posterior hippocampus | Anterior hippocampus | Temporal pole |
| | Spontaneous seizure symptoms* | Gustatory aura → oral and manual automatisms → aphasia | Rising epigastric sensation → déjà-vu → aphasia | Paresthesia in neck → familiar voices and music → tunnel vision → aphasia |
| Triggered seizures | Symptoms | Identical up to aphasia | Identical up to aphasia | Identical up to tunnel vision |
| | Antiseizure medication | Half-dose | None | Full-dose |
| | Triggering bipole | Entorhinal cortex | Entorhinal cortex | Temporal pole |
| | Stimulation intensity | 2 mA | 2 mA | 6 mA |
| | Stimulation duration | 1 s | 2 s | 4 s |
| | Loss of awareness | Yes | No | No |
| | Seizure duration | 151 s | 94 s | 188 s |
| | Seizure aborted | No | No | Yes, clonazepam, 1 mg |
| | Propagation* | Entorhinal → anterior and posterior hippocampus → amygdala → temporal pole | Amygdala → anterior and posterior hippocampus | Temporal pole → anterior hippocampus → insula → fusiform gyrus |
| SPECT | Delay | | | |
| | Seizure onset to injection | 12 s | 9 s | 7 s |
| | Injection to image | 21 min | 22 min | 39 min |
| | Radiotracer production to image | 3 h 13 min | 2 h 26 min | 1 h 38 min |
| | Dose | 406 MBq | 489 MBq | 511 MBq |
| | Hyperperfusion | Mesiotemporal, superior temporal, frontobasal | Mesiotemporal, superior temporal | Temporal pole, hippocampus, insula anterior |
| Surgery | Resection | Selective amygdalohippocampectomy, left | None because of cognitive risk | Selective polectomy and amygdalectomy |
| | Seizure outcome | Engel class ID at 1 y | NA | Engel class IV at 1 y |
| | Cognitive outcome | Improved | NA | Unchanged |

*Arrows indicate sequence of symptoms or involved areas, which can be complete or partial across seizures in same participant.
NA = not applicable.

MATLAB 2020a (The MathWorks) to compute the coordinates of sEEG contacts. We computed a SPECT deviation map for each participant and detected volumes with a z-value of at least 2.25 as hyperperfusion clusters using a normal database (*8*)—that is, normalization to whole-brain activity—provided by the Hermes BRASS software (version 6.1.3; Hermes Medical Solutions; Fig. 1B) as a reference. We computed patient-specific cortical reconstruction with FreeSurfer (Harvard) for covisualization with the hyperperfusion clusters and sEEG contacts (Fig. 2).

### Electrophysiologic Data

We computed bipolar traces of adjacent contacts and filtered signals with a 1- to 410-Hz bandpass filter. To estimate seizure power per bipolar contact, a z-value was calculated as follows: $(\overline{LL}_{post} - \overline{LL}_{pre})/(SD(LL_{pre}))$, where LL is the line length of the sEEG signal over a running window of 1 s, averaged over 60 s before (pre) and after (post) seizure onset (*9*). Seizure-triggering stimulation was excluded from this calculation.

## RESULTS

Within a few attempts over 3–8 min, we successfully triggered seizures in 3 participants, replicating the patient-typical seizure semiology and electrographic pattern on sEEG (Table 1). In each case, we injected $^{99m}$Tc-HMPAO (<520 MBq) within 9–12 s of

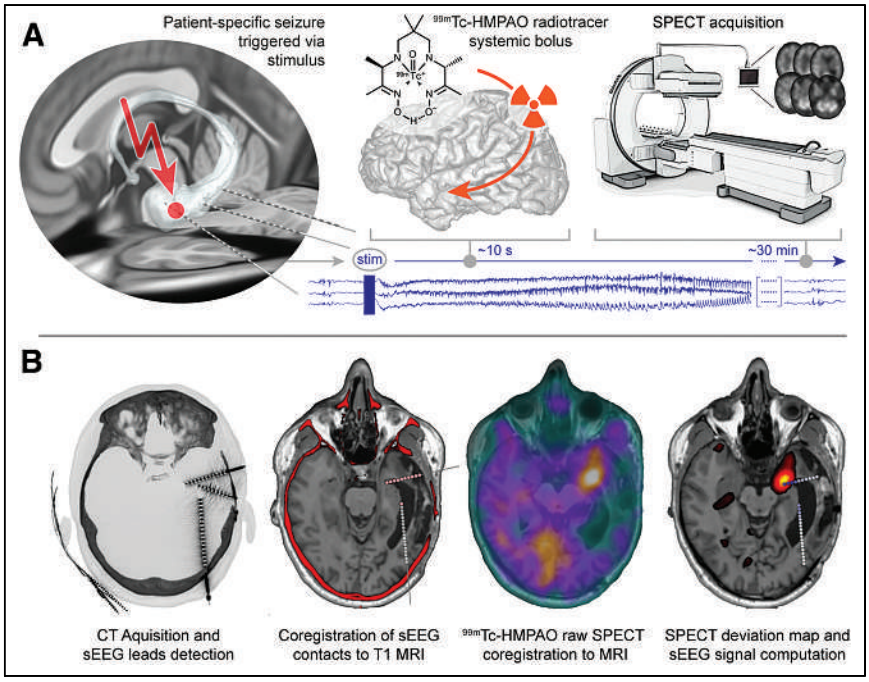


**FIGURE 1.** Schematic of triggered ictal SPECT and data processing. (A) Previously screened and selected sEEG bipolar contact is stimulated to trigger patient-typical seizure. Directly after seizure onset, confirmed through sEEG signals and semiology, systemic bolus of radiotracer ($^{99m}$Tc-HMPAO) is administered. Planned SPECT is acquired within less than 1 h. (B) Raw data processing from left to right (dataset from participant 3 as example). Postimplantation CT and preimplantation T1-weighted MRI are coregistered for sEEG lead localization. Raw SPECT images are coregistered to T1-weighted MRI sequence. SPECT deviation map is computed and anatomically colocalized with sEEG signals.

unequivocal seizure onset (Fig. 1), enabling a planned ictal SPECT acquisition with a prebooked γ-camera. The participants did not have any adverse events: triggered seizures were controlled and without secondary generalization, and radioprotection was ensured (absence of radiotracer spillover). In all 3 participants, the ictal SPECT contributed to characterizing periictal aphasia (Fig. 2).

Participant 1 reported his typical gustatory aura and showed oral and manual automatisms followed by loss of awareness and postictal aphasia. sEEG revealed a seizure onset zone in the left entorhinal cortex and posterior hippocampus. Hyperperfusion involved the ipsilateral posterior temporal lobe and contralateral mesiotemporal lobe (Fig. 2A). Participant 2 reported his typical rising epigastric sensation and had ictal aphasia without loss of awareness. sEEG located the seizure onset zone in the left anterior hippocampus. Hyperperfusion involved the same structure and the ipsilateral posterior temporal lobe (Fig. 2B). Participant 3 reported his typical paresthesia in the neck followed by familiar voices and tunnel vision, but the seizure did not progress to his occasional ictal aphasia. sEEG located the seizure onset zone in the left temporal pole. Hyperperfusion was restricted to this structure, without any additional early propagation (Fig. 2C).

Thus, despite stimulation in the same brain area (left mesiotemporal), each triggered seizure was patient-specific and the imaged early seizure propagation unique. In the first 2 cases, ictal SPECT offered complementary information to sEEG and revealed early involvement of brain areas lacking electrode coverage to limit the risk of complications in potentially eloquent cortex. In the third case, sEEG and ictal SPECT provided overlapping information.

## DISCUSSION

To our knowledge, this is the first study establishing the feasibility of triggering ictal SPECT on demand with direct electric stimulation of the epileptic cortex. Triggering seizures for SPECT imaging was previously explored in psychiatric patients undergoing electroconvulsive therapy (*10*) and epileptic patients receiving pentylenetetrazole (*11*). However, these prior methods did not generalize, given the unclear clinical utility and safety of these procedures. With this case series, we show that triggering of seizures with direct electric stimulation for ictal SPECT imaging is convenient, spares resources, and can be clinically useful.

The presented method is limited to patients with epilepsy undergoing invasive sEEG monitoring. As such, it cannot guide electrode placement but may contribute to the planning of resective surgery. Of note, we used a normal non–age-matched database for the calculation of deviation maps. Although we could identify ictal hyperperfusion areas, further optimization with the subtraction of patient-specific interictal SPECT is required. To establish the clinical value, future studies should compare triggered and spontaneous ictal SPECT as predictors of postsurgical outcomes, as well as delineate their added value over $^{18}$F-FDG PET (*12*) or electroencephalography/functional MRI (*13*). Moreover, the advent of digital SPECT using 360° cadmium-zinc-telluride detectors offers a promising opportunity to enhance the performance of ictal SPECT imaging with greater sensitivity and improved quantitation (*14*).

As proposed by previous retrospective work (*15,16*), the maximum ictal hyperperfusion did not overlap perfectly with the seizing parenchyma (Fig. 2), suggesting a potential regional impairment of neurovascular coupling (*17*) and potential ictal hypoperfusion areas (*16*). As shown here, delineating ictogenic parenchyma with high temporal resolution (sEEG) and spatial continuity (ictal SPECT) may offer a deeper understanding of seizure propagation pathways and help plan resections around eloquent cortex.

## CONCLUSION

Nuclear medicine and sEEG for recording and stimulation are broadly available at specialized epilepsy centers. In our opinion, SPECT imaging of seizures can be rapidly readopted in controlled conditions that mitigate its previous logistic drawbacks. Novel data generated with this technique in larger cohorts could contribute to refinement of resection planning, improving seizure and cognitive outcomes in epilepsy surgery.

## DISCLOSURE

Maxime Baud holds shares with Epios, Ltd., a medical device company based in Geneva. No other potential conflict of interest relevant to this article was reported.

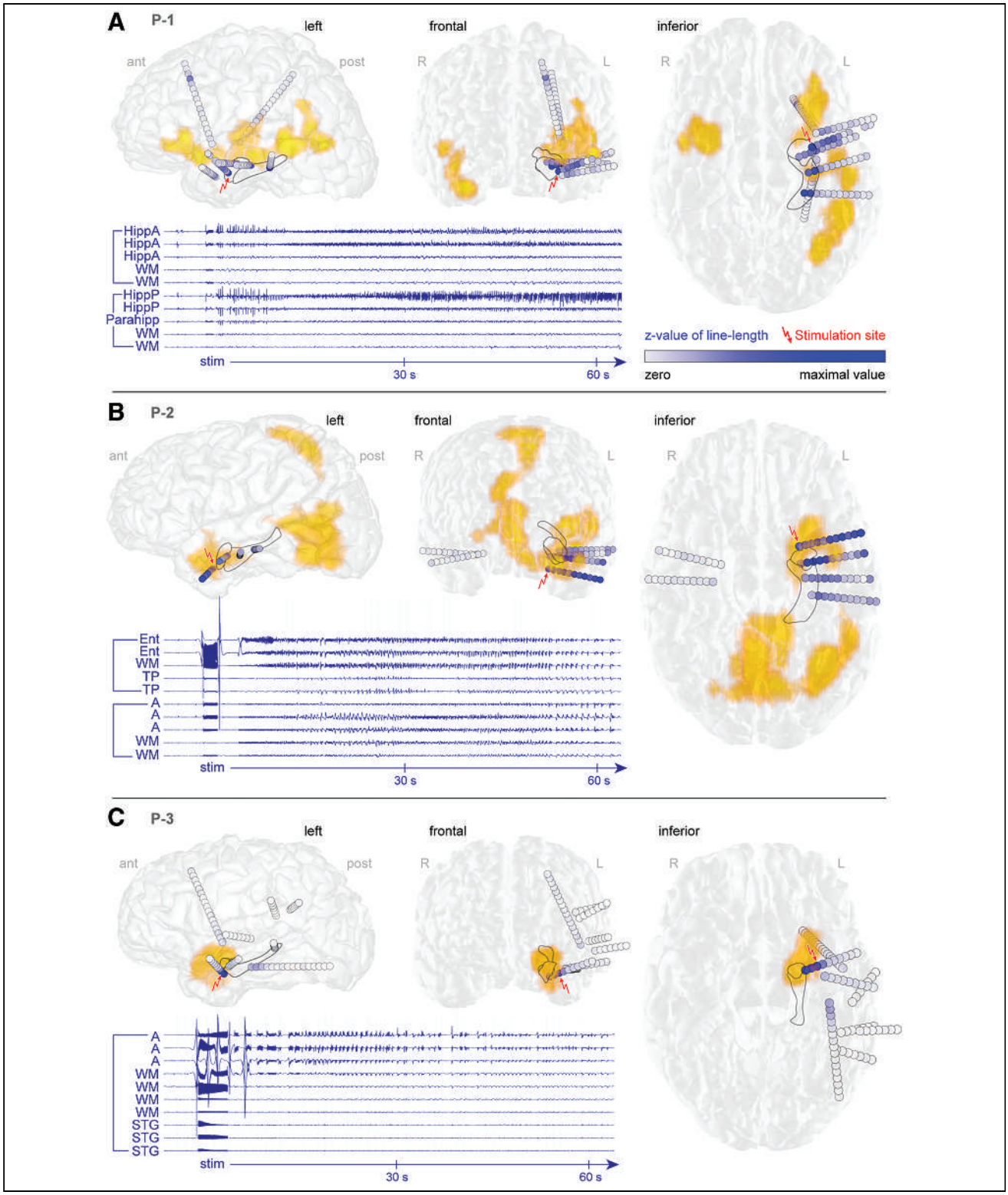


**FIGURE 2.** sEEG–SPECT comparison: patient-specific cortex reconstruction (FreeSurfer, left-hemisphere, frontal and inferior view) with sEEG bipolar contacts and SPECT deviation map (orange to yellow, more intense) for participants 1 (A), 2 (B), and 3 (C). Amygdala and hippocampus contours (adapted from FreeSurfer) are shown as dark gray overlays. sEEG bipolar contacts (plotted at anatomic centers of bipoles) are color-coded from white to blue according to amount of ictal activity recorded over 1 min (line length relative to baseline). Red bolt depicts stimulated bipole. sEEG traces are shown for selected channels of interest with their anatomic location. Brackets regroup channels from same lead. Note relationship between stimulus artifacts and direct beginning of epileptic discharges. A = amygdala; Ent = entorhinal cortex; HippA = hippocampus anterior; HippP = hippocampus posterior; P-1 = participant 1; P-2 = participant 2; P-3 = participant 3; Parahipp = parahippocampal gyrus; STG = superior temporal gyrus; TP = temporal pole; WM = white matter.

## ACKNOWLEDGMENT

We thank Sandy Feruglio for setting up the clinical database for this study.

**KEY POINTS**

**QUESTION:** Is ictal SPECT able to map seizures triggered by direct electric stimulation?

**PERTINENT FINDINGS:** We successfully triggered and imaged patient-typical seizures with SPECT in a prospective case series of 3 participants with left temporal epilepsy. Our combined sEEG/SPECT approach revealed early seizure propagation pathways, beyond discrete electrophysiologic exploration.

**IMPLICATIONS FOR PATIENT CARE:** Triggering of patient-typical seizures for on-demand ictal SPECT may broadly reinstate this often-abandoned imaging technique and help tailor resective epilepsy surgeries.

## REFERENCES

1. Zijlmans M, Zweiphenning W, van Klink N. Changing concepts in presurgical assessment for epilepsy surgery. *Nat Rev Neurol.* 2019;15:594–606.
2. Van Paesschen W. Ictal SPECT. *Epilepsia.* 2004;45(suppl 4):35–40.
3. von Oertzen TJ. PET and ictal SPECT can be helpful for localizing epileptic foci. *Curr Opin Neurol.* 2018;31:184–191.
4. Van Paesschen W, Dupont P, Van Heerden B, et al. Self-injection ictal SPECT during partial seizures. *Neurology.* 2000;54:1994–1997.
5. Rogeau A, Lilburn DML, Kaplar Z, et al. Identifying and troubleshooting the pitfalls of ictal/interictal brain perfusion SPECT studies. *Nucl Med Commun.* 2023;44:1053–1058.
6. Baud MO, Perneger T, Racz A, et al. European trends in epilepsy surgery. *Neurology.* 2018;91:e96–e106.
7. Cuello Oderiz C, von Ellenrieder N, Dubeau F, et al. Association of cortical stimulation-induced seizure with surgical outcome in patients with focal drug-resistant epilepsy. *JAMA Neurol.* 2019;76:1070–1078.
8. Radau PE, Slomka PJ, Julin P, Svensson L, Wahlund LO. Evaluation of linear registration algorithms for brain SPECT and the errors due to hypoperfusion lesions. *Med Phys.* 2001;28:1660–1668.
9. Schindler K, Leung H, Elger CE, Lehnertz K. Assessing seizure dynamics by analysing the correlation structure of multichannel intracranial EEG. *Brain.* 2007;130:65–77.
10. Enev M, McNally KA, Varghese G, Zubal IG, Ostroff RB, Blumenfeld H. Imaging onset and propagation of ECT-induced seizures. *Epilepsia.* 2007;48:238–244.
11. Barba C, Barbati G, Di Giuda D, et al. Diagnostic yield and predictive value of provoked ictal SPECT in drug-resistant epilepsies. *J Neurol.* 2012;259:1613–1622.
12. Steinbrenner M, Duncan JS, Dickson J, et al. Utility of $^{18}$F-fluorodeoxyglucose positron emission tomography in presurgical evaluation of patients with epilepsy: a multicenter study. *Epilepsia.* 2022;63:1238–1252.
13. Iannotti GR, Grouiller F, Centeno M, et al. Epileptic networks are strongly connected with and without the effects of interictal discharges. *Epilepsia.* 2016;57:1086–1096.
14. Bordonne M, Chawki MB, Marie PY, et al. High-quality brain perfusion SPECT images may be achieved with a high-speed recording using 360 degrees CZT camera. *EJNMMI Phys.* 2020;7:65.
15. Krishnan B, Tousseyn S, Nayak CS, et al. Neurovascular networks in epilepsy: correlating ictal blood perfusion with intracranial electrophysiology. *Neuroimage.* 2021;231:117838.
16. Lee HW, Hong SB, Tae WS. Opposite ictal perfusion patterns of subtracted SPECT. Hyperperfusion and hypoperfusion. *Brain.* 2000;123:2150–2159.
17. Prager O, Kamintsky L, Hasam-Henderson LA, et al. Seizure-induced microvascular injury is associated with impaired neurovascular coupling and blood-brain barrier dysfunction. *Epilepsia.* 2019;60:322–336.

# It's a Trap! Aldolase-Prescribed $C_4$ Deoxyradiofluorination Affords Intracellular Trapping and the Tracing of Fructose Metabolism by PET

Alexia Kirby[1,2], Dominic Graf[2,3], Mojmír Suchý[2,3], Nicholas D. Calvert[2,3], Thomas A. Charlton[2], Robert N. Ben[2], Christina L. Addison[4–6], and Adam Shuhendler[1,2,3,7]

[1]*Department of Biology, University of Ottawa, Ottawa, Ontario, Canada;* [2]*Heart Institute, University of Ottawa, Ottawa, Ontario, Canada;* [3]*Department of Chemistry and Biomolecular Sciences, University of Ottawa, Ottawa, Ontario, Canada;* [4]*Program for Cancer Therapeutics, Ottawa Hospital Research Institute, Ottawa, Ontario, Canada;* [5]*Department of Medicine, University of Ottawa, Ottawa, Ontario, Canada;* [6]*Department of Biochemistry, Microbiology, and Immunology, University of Ottawa, Ottawa, Ontario, Canada; and* [7]*Brain and Mind Research Institute, University of Ottawa, Ottawa, Ontario, Canada*

Fructose metabolism has been implicated in various diseases, including metabolic disorders, neurodegenerative disorders, cardiac disorders, and cancer. However, the limited availability of a quantitative imaging radiotracer has hindered its exploration in pathology and diagnostic imaging. **Methods:** We adopted a molecular design strategy based on the catalytic mechanism of aldolase, a key enzyme in fructolysis. We successfully synthesized a radiodeoxyfluorinated fructose analog, [$^{18}$F]4-fluoro-4-deoxyfructose ([$^{18}$F]4-FDF), in high molar activity. **Results:** Through heavy isotope tracing by mass spectrometry, we demonstrated that $C_4$-deoxyfluorination of fructose led to effective trapping as fluorodeoxysorbitol and fluorodeoxyfructose-1-phosphate in vitro, unlike $C_1$- and $C_6$-fluorinated analogs that resulted in fluorolactate accumulation. This observation was consistent in vivo, where [$^{18}$F]6-fluoro-6-deoxyfructose displayed substantial bone uptake due to metabolic processing whereas [$^{18}$F]4-FDF did not. Importantly, [$^{18}$F]4-FDF exhibited low uptake in healthy brain and heart tissues, known for their high glycolytic activity and background levels of [$^{18}$F]FDG uptake. [$^{18}$F]4-FDF PET/CT allowed for sensitive mapping of neuro- and cardioinflammatory responses to systemic lipopolysaccharide administration. **Conclusion:** Our study highlights the significance of aldolase-guided $C_4$ radiodeoxyfluorination of fructose in enabling effective radiotracer trapping, overcoming limitations of $C_1$ and $C_6$ radioanalogs toward a clinically viable tool for imaging fructolysis in highly glycolytic tissues.

**Key Words:** molecular imaging; fructose; inflammation; metabolic tracing; PET; radiofluorination

**J Nucl Med 2024; 65:475–480**
DOI: 10.2967/jnumed.123.266905

The use of fructose as an energy source (i.e., fructolysis) during the onset and progression of a variety of diseases is a continued area of both fundamental and clinical investigation, with inflammation-induced energy crises activating a fructolytic state in the affected tissues. In the heart, the switch from glycolysis to fructolysis has been identified in cardiac hypertrophy (*1*,*2*) and myocardial infarction (*3*), with data supporting a hypoxia-driven activation of this aberrant metabolic program. In the brain, fructolysis is thought to be a putative driver of Alzheimer disease (*4*) and has been shown to be proinflammatory, with negative implications after traumatic or stroke injury and in psychologic health (*5*). The switch from glucose to fructose as an energy source may also be a key oncologic driver, promoting the progression of a variety of solid tumors through the concerted transcriptional activation of transport and metabolic machinery (*6–10*). Excessive fructose consumption has also been associated with a liver-centered metabolic syndrome thought to drive obesity and diabetes (*11*) and to be a major player in the related cardiovascular (*11*,*12*), ocular (*13*), and degenerative (*12*) outcomes. The fundamental importance of fructolysis in a range of diseases has encouraged the development of methods to noninvasively map fructose metabolism, a challenge that is currently an unsolved problem.

Canonic fructose metabolism begins with glucose transporter 5–mediated transport into the cell and ketohexokinase-mediated trapping of the sugar as fructose-1-phosphate (Fig. 1A) (*11*). Phosphorylation is followed by carbon chain scission through the activity of aldolase enzymes and the subsequent formation of glyceraldehyde-3-phosphate, which continues to be metabolized downstream. This metabolic cascade has been followed using noninvasive in vivo imaging in preclinical models, taking advantage of the spectroscopic capabilities of deuterium and hyperpolarized MRI (*14*,*15*). Toward the clinical translational use of fructolysis as a quantitative imaging biomarker, previous work has attempted to trace fructose metabolism by PET by installing radiofluorine ($^{18}$F) at the $C_1$ or $C_6$ positions (*16–20*). The early metabolic trapping of fructose would lend itself to tracing of aberrant metabolism similarly to [$^{18}$F]FDG, the most extensively applied PET nuclear diagnostic used in the clinic. However, the significant bone-derived radioactivity observed by PET from previous radiodeoxyfluorofructose analogs suggests that cellular trapping was not achieved (Fig. 1A).

To produce a radiofluorinated fructose analog that is trapped in cells as its phosphorylated metabolite, we closely examined the catalytic mechanism of aldolase, the enzyme for which fructose-1-phosphate is a substrate (Fig. 1B) (*21*). Within the aldolase active site, the initial Schiff base formation with the $C_2$-carbonyl is immediately followed by a base-mediated proton abstraction from the $C_4$-hydroxyl moiety to induce C–C bond scission. Given the critical role of the $C_4$-OH in the catalytic mechanism, we hypothesized that the

Received Oct. 19, 2023; revision accepted Dec. 6, 2023.
For correspondence or reprints, contact Adam Shuhendler (adam.shuhendler@uottawa.ca).
Published online Jan. 25, 2024.

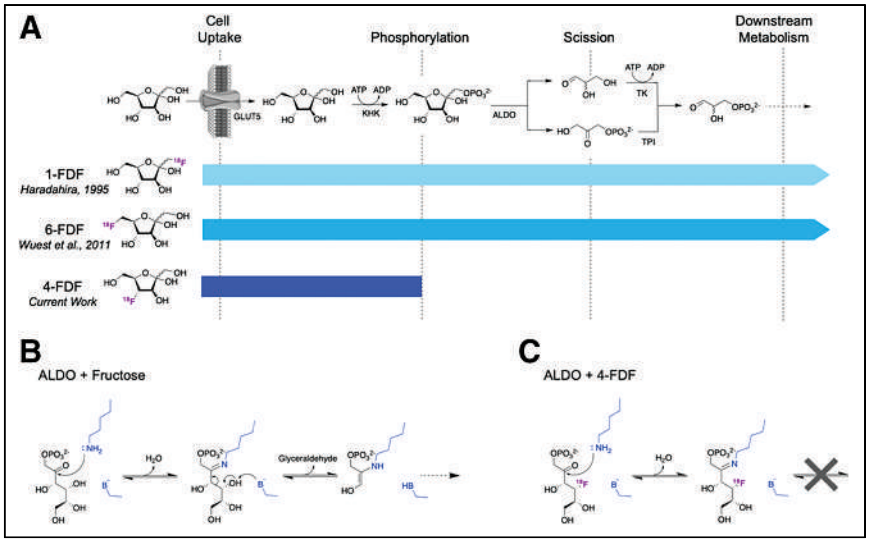


**FIGURE 1.** Fructose metabolism tracing, then and now. (A) Initial metabolism of fructose comprises cell uptake, phosphorylation, and scission steps mediated by glucose transporter 5, ketohexokinase, and aldolase, respectively. Proposed progression of existing fructose-derived radiotracers, 1-FDF and 6-FDF, as well as hypothesized trapping of proposed 4-FDF, are shown. (B) First 2 steps of aldolase-mediated scission of fructose. (C) Proposed effect of $C_4$ deoxyfluorination on aldolase mechanism. ADP = adenosine diphosphate; ALDO = aldolase; ATP = adenosine triphosphate; $B^-$ = basic residue; blue = aldolase active site residue; GLUT = glucose transporter; KHK = ketohexokinase; TK = triose kinase; TPI = triosephosphate isomerase.

deoxyfluorination of the $C_4$ position would prevent aldolase-mediated scission (Fig. 1C), resulting in the trapping of 4-fluoro-4-deoxyfructose (4-FDF) within the metabolic cell of origin (Fig. 1A). In the current work, we generated 4-FDF, evaluated its metabolic flux in vitro relative to 1-fluoro-1-deoxyfructose (1-FDF) and 6-fluoro-6-deoxyfructose (6-FDF), and compared the PET imaging of [$^{18}$F]4-FDF with that of [$^{18}$F]6-FDF and [$^{18}$F]FDG in tracing metabolism in mouse models of cancer and systemic inflammation.

## MATERIALS AND METHODS

### Synthesis

All synthetic procedures are described in detail in the supplemental materials (available at http://jnm.snmjournals.org).

### In Vitro Metabolic Tracing

All procedures for metabolic tracing of [U$^{13}$C]-fructose analogs are provided in the supplemental materials.

### Animal Models

All animal research was approved by the institutional animal care and use committee of the University of Ottawa under animal use protocols SCe-3254-R3 (tumor study) and SCe-4019-A1 (inflammation study). Mice were housed in standard cages, kept on a 12-h light–dark cycle, and provided standard rodent chow and water ad libitum.

Eight-week-old female nu/nu mice were inoculated, subcutaneously under the left shoulder, with $10 \times 10^6$ HepG2 cells suspended in 50% Matrigel (Corning)–50% Dulbecco modified Eagle medium. Within 3 wk of implantation, the mice were imaged by PET/CT.

Eight-week-old male C57BL/6 mice received a 5 mg/kg dose of lipopolysaccharide through intraperitoneal injection 24 h before planned PET/CT imaging. For 12 h after receiving the injection, they were kept warm, given fluids subcutaneously, monitored, and scored for severity of response to lipopolysaccharide as published previously (*22*).

### PET/CT Imaging

PET/CT imaging was performed on an Si78PET/CT scanner with a 4-position hotel having adjustable isoflurane and respiratory monitoring for each position (Bruker USA). Tail veins were catheterized, and an anatomic CT scan was acquired over the whole of the mouse bodies using the rat settings. The PET acquisition was started just before a bolus intravenous injection of approximately 7.4 MBq of radiotracer. Dynamic scans were acquired in list mode over 45 min and sorted into sixteen 0.5-mm sinogram bins for image reconstruction ($4 \times 15$ s, $4 \times 60$ s, and $8 \times 300$ s). Iterative reconstruction was performed using 3-dimensional ordered-subsets expectation maximization followed by fast maximum a posteriori estimation using Paravision 360 software, version 3.4 (Bruker). Four-mouse images were split into individual mice, and the bed was removed using PMOD (Bruker). VivoQuant, version 2022 (InviCRO), was used to visualize tissue uptake, for definition of 3-dimensional volumes of interest, and to visualize in 3 dimensions for volume rendering. The count densities were averaged for all volumes of interest at each time point to obtain a time–activity curve. Tumor and tissue time–activity curves were normalized to injected dose, measured by a CRC-15 PET dose calibrator (Capintec, Inc.), and expressed as percentage injected dose per cubic centimeter of tissue.

### Statistical Analyses

Statistical analyses were performed using Prism (version 9.5.0; GraphPad, Inc.). Comparisons across more than 2 groups were performed by 1-way ANOVA followed by the Tukey test for honestly significant differences. Normality was assumed when appropriate for all datasets. Before ANOVA, the Levene test was used to confirm equal variance, and visual quantile–quantile plot analysis was used to confirm homoscedasticity.

## RESULTS

To characterize the structure–activity effect of fructose deoxyfluorination on metabolic flux, we evaluated the metabolism of isotopically labeled [U$^{13}$C]-fructose and of [U$^{13}$C]-1-FDF, [U$^{13}$C]-6-FDF, and [U$^{13}$C]-4-FDF deoxyfluorinated fructose analogs in vitro in HepG2 human hepatocarcinoma cells by mass spectrometry (Fig. 2). HepG2 was chosen as a model cell line because of a recent report by Tee et al. outlining its propensity for fructolysis (*23*). [U$^{13}$C]-1-FDF and [U$^{13}$C]-6-FDF were synthesized according to previously published methods (*16*,*17*), and [U$^{13}$C]-4-FDF was synthesized as described in the supplemental materials. After confirming that [U$^{13}$C]-fructose was metabolized as expected through both fructolytic and polyol pathways to establish a baseline for tracing fructose metabolism (Fig. 2A), we next examined the relative flux of the deoxyfluorinated analogs (Fig. 2B). [U$^{13}$C]-1-FDF showed limited metabolism through the polyol pathway, with most of the $^{13}$C-labeled cellular product being [U$^{13}$C]-deoxyfluorolactate (Fig. 2B). Of critical importance, however, is that although [U$^{13}$C]-6-FDF metabolism produced a substantial amount of [U$^{13}$C]-deoxyfluorolactate through scission and downstream metabolism (Fig. 2B), [U$^{13}$C]-4-FDF metabolism halted at [U$^{13}$C]-4-fluorodeoxy-1-phosphate, the fructolytic metabolite that

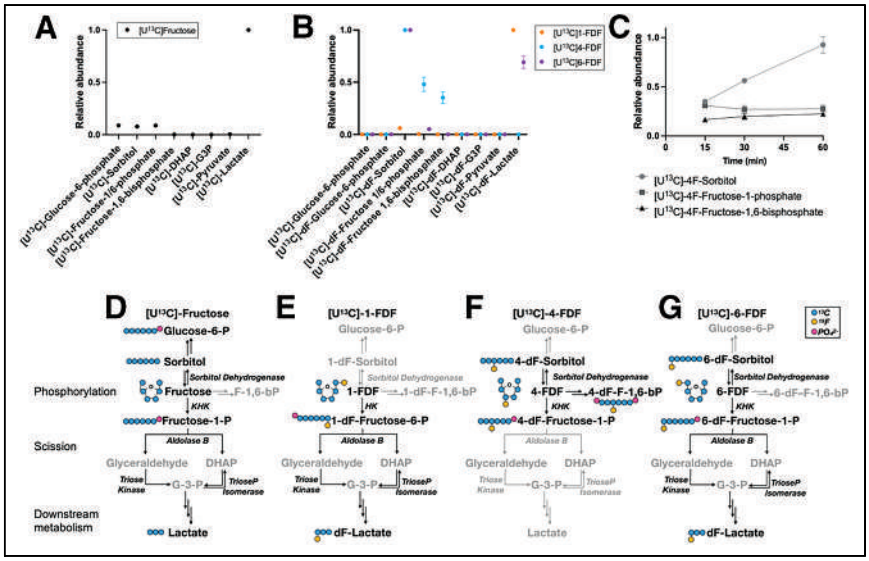


**FIGURE 2.** Decoding positional effects of fructose deoxyfluorination on its metabolism in vitro in HepG2 cells by mass spectrometry. (A and B) Relative abundance of metabolites from isotopically labeled [U$^{13}$C]-fructose (A) and [U$^{13}$C]-1-FDF, [U$^{13}$C]-4-FDF, and [U$^{13}$C]-6-FDF (B). (C) Time course of metabolite generation from [U$^{13}$C]-4-FDF. (D–G) Metabolism schemes based on mass spectrometry results for [U$^{13}$C]-fructose (D), [U$^{13}$C]-1-FDF (E), [U$^{13}$C]-4-FDF (F), and [U$^{13}$C]-6-FDF (G). Black text = detected metabolite or pathway; blue circle = $^{13}$C; dF = deoxyfructose; DHAP = dihydroxyacetone phosphate; G3P = glyceraldehyde-3-phosphate; gray text = undetected metabolite or pathway; HK = hexokinase; KHK = ketohexokinase; pink circle = $PO_4^{2-}$; yellow circle = $^{19}$F.

is the substrate for aldolase-mediated scission (Fig. 2B). Uniquely, [U$^{13}$C]-4-FDF metabolism also resulted in the accumulation of [U$^{13}$C]-4-fluorodeoxyfructose-1,6-bisphophate. A key outcome of this experiment was the confirmation that all deoxyfluorinated analogs of fructose entered the cells rapidly (within 30 min). To validate the observed metabolite trapping, a time course evaluation of [U$^{13}$C]-4-FDF metabolism was performed over 60 min, demonstrating the steady-state accumulation of [U$^{13}$C]-4-fluorodeoxyfructose-1-phosphate and [U$^{13}$C]-4-fluorodeoxyfructose-1,6-bisphosphate and the increase in [U$^{13}$C]-4-fluorodeoxysorbitol throughout the 60 min of incubation (Fig. 2C). The results of this study support our hypothesis that, like native fructose (Fig. 2D), neither [U$^{13}$C]-1-FDF (Fig. 2E) nor [U$^{13}$C]-6-FDF is metabolically trapped (Fig. 2G) but that the deoxyfluorination of fructose at $C_4$ prevents aldolase-mediated hexose scission and traps the deoxyfluorinated fructose analog in the cell (Fig. 2F). By rethinking the site of deoxyfluorination to afford metabolic trapping as informed by the catalytic mechanism of the enzyme immediately ensuing to the intended trapped metabolite, we uncovered the chemical requirements for mapping fructolysis.

To proceed toward fructolysis mapping in vivo by PET, a radiodeoxyfluorination approach was designed to afford nucleophilic substitution at the $C_4$ position using standard radiochemical techniques somewhat related to the routine production of [$^{18}$F]FDG. Details of the synthesis of compounds **1–4** have been reported previously (*24*), and further synthetic steps and chemical characterization for compounds **5, 6,** and [$^{18}$F]4-FDF are provided in the supplemental materials (Supplemental Schemes 1–5; Supplemental Figs. 3–232). The precursor synthesis began with $C_1$-OH methylation and dimethyl ketalation of $C_2$-OH and $C_3$-OH, followed by the protection of $C_6$-OH with chloromethyl methyl ether in order to isolate the $C_4$-OH (Fig. 3A). The stereochemistry at $C_4$ was then inverted in 2 steps and was converted to the tosylated precursor **5** (Fig. 3A). The $C_4$ stereoinversion was necessary to allow the subsequent radiodeoxyfluorination step to restore the $C_4$-D-enantiomer after the [$^{18}$F]tetraethylammonium fluoride–mediated nucleophilic attack (Fig. 3B, **6**). Rapid on-module deprotection resulted in [$^{18}$F]4-FDF in good radiochemical yield (25%–30%) and molar activity (25.3 ± 0.6 GBq/nmol) comparable to that resulting from the routine production of [$^{18}$F]FDG (*25*).

With the confirmation of cell uptake and intracellular trapping of [U$^{13}$C]4-FDF, and the successful production of the radiofluorinated analog, the biodistribution of [$^{18}$F]4-FDF was evaluated in a heterotopic HepG2 xenograft mouse model and compared with the biodistribution of [$^{18}$F]6-FDF and [$^{18}$F]FDG (Fig. 4). [$^{18}$F]1-FDF was not evaluated in vivo since it was already demonstrated to be poorly retained in cells in vitro and in vivo (*18*). After intravenous injection, [$^{18}$F]4-FDF was found to accumulate in the tumor, with renal exceeding hepatobiliary excretion (Fig. 4A). This pattern of radiotracer retention was similarly observed for [$^{18}$F]6-FDF, with a key difference, however, being bone uptake (Fig. 4B). Although any bone uptake was limited to less than 2% injected dose/mL for [$^{18}$F]4-FDF (Fig. 4A; Supplemental Fig. 2), bone uptake was 3.69-fold higher (>7% injected dose/mL) after [$^{18}$F]6-FDF imaging (Fig. 4B and 4D). This extensive bone uptake, which continues to increase over time (Supplemental Fig. 2), was reported previously for [$^{18}$F]6-FDF (*17*) and is supported by the metabolic flux outcomes of [U$^{13}$C]6-FDF demonstrating the production of [U$^{13}$C]fluorodeoxylactate (Figs. 2B and 2G).

Overall, the accumulation of [$^{18}$F]4-FDF in normal mouse tissues was lower than that of [$^{18}$F]FDG (Figs. 4A vs. 4C). Notably, the area under the time–activity curve in the brain and heart was 6.01- and 5.29-fold greater, respectively, for [$^{18}$F]FDG than for [$^{18}$F]4-FDF (Fig. 4D), suggesting that healthy brain and heart have a limited dependence on fructolysis for energy production. To further investigate whether a fructolytic switch occurs in inflammatory neural and cardiac tissues, as previously proposed (*1–5,12*), a mouse model of systemic inflammation was examined (Fig. 5). Mice receiving saline vehicle (Fig. 5A) or intraperitoneal bacterial cell wall lipopolysaccharide, as previously described (Fig. 5B) (*22*), were imaged by [$^{18}$F]4-FDF PET/CT 24 h after injection. A significant increase in cardiac (Figs. 5D and 5F) and brain (Figs. 5C and 5F) uptake of [$^{18}$F]4-FDF was observed after lipopolysaccharide treatment in all mice evaluated. Both the brain and the heart demonstrated inflammatory responses to lipopolysaccharide stimulation within 24 h of its systemic introduction, mediated through toll-like receptor engagement on microglia or cardiac adrenergic cells (*26,27*). The low uptake of [$^{18}$F]4-FDF in healthy brain and heart contributed to an increased signal-to-noise ratio for the mapping of cardio- and neuroinflammation (Figs. 5C and 5D).

## DISCUSSION

Although the pathologic switch to fructose metabolism has been implicated in a variety of metabolic, neurodegenerative, and cardiac diseases, as well as being a driver or consequence of

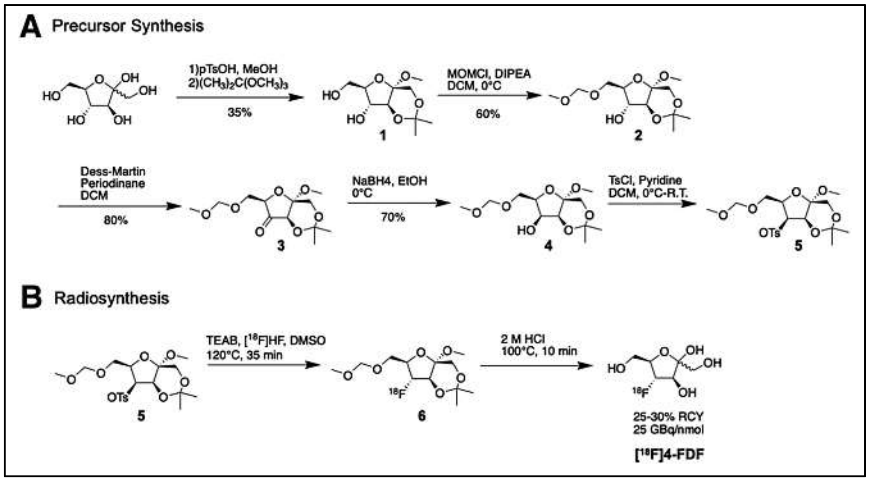


**FIGURE 3.** Syntheses of radiochemical precursor (A) and final radiofluorinated [$^{18}$F]4-FDF (B). pTsOH = *para*-toluenesulfonic acid; MeOH = methanol; MOMCl = chloromethyl methyl ether; DIPEA = *N,N*-diisopropylethylamine; DCM = dichloromethane; EtOH = ethanol; TsCl = *para*-toluenesulfonyl chloride; R.T. = room temperature; TEAB = tetraethylammonium bromide.; DMSO = dimethylsulfoxide; RCY = radiochemical yield.

malignancy, the evaluation of fructolysis in fundamental mechanisms of pathology and its implementation as a diagnostic imaging biomarker has been limited by the lack of a quantitative tracer for imaging-based analysis. Taking a molecular design approach informed by the catalytic mechanism of aldolase, the fructolytic enzyme whose activity must be blocked in order to afford metabolic trapping, we synthesized a radiodeoxyfluorinated analog of fructose: [$^{18}$F]4-FDF. Radiosynthesis was realized on a standard radiofluorination module in good yield and molar activity, mimicking the nucleophilic radiofluorination and acid-catalyzed deprotection used for the preparation of [$^{18}$F]FDG (Fig. 3).

As compared with previously reported $C_1$ and $C_6$ radioanalogs of fructose, using heavy-isotope tracing by mass spectrometry we demonstrated that the $C_4$ deoxyfluorination of fructose led to trapping as fluorodeoxysorbitol and fluorodeoxyfructose-1-phosphate in vitro (Fig. 2). Key differences in polyol pathway flux were also observed between the different fluorinated positional isomers. The limited polyol flux observed for $C_1$ fluorodeoxyfructose is likely the result of improper substrate positioning in the sorbitol dehydrogenase active site by the deoxyfluorination of $C_1$, which prevents a critical $C_1$-OH–to–zinc interaction (*28*). In contrast, both [U$^{13}$C]-6-FDF and [U$^{13}$C]-4-FDF were capable of proceeding through the polyol pathway but did not form detectable amounts of glucose-6-phosphate (Fig. 2B). The arrest at [U$^{13}$C]-4/6-fluorodeoxysorbitol could be the result of the reduction of aldose reductase activity either through active-site water displacement or through catalytically detrimental interactions with the active-site–adjacent specificity pocket (*29*,*30*). Notably, neither the $C_1$- nor the $C_6$-fluorinated analog led to trapping, but rather there was a procession through fructolysis to produce fluorolactate. This result was recapitulated in vivo, with [$^{18}$F]6-FDF showing significant bone uptake that was a result of metabolic processing but was not observed using [$^{18}$F]4-FDF (Fig. 4).

Our metabolic tracing studies suggest that the bone uptake observed with [$^{18}$F]6-FDF imaging in vivo (Fig. 4) may be the result not of tumor cell–induced defluorination but of lactate formation (Fig. 2). Lactate is actively pumped out of tumor cells by influx–efflux monocarboxylate transporters 1 and 4, which contribute to the acidic tumor microenvironment that is a hallmark of solid tumors (*31*,*32*). The direct mechanism of radiofluorinated metabolite uptake by bone remains to be uncovered; however, it is known that osteoblasts express monocarboxylate transporter 1 and actively take up lactate (*33*–*35*). Additionally, extratumoral metabolism may also contribute to radioactivity uptake in the bone, as hepatic lactate metabolism through lactate dehydrogenase can produce pyruvate with a potential for defluorination (*36*). By any mechanism, both in vitro and in vivo data demonstrate that radiodeoxyfluorination of fructose at $C_4$, but not at $C_6$, can subvert cellular radiometabolite loss and bone accumulation.

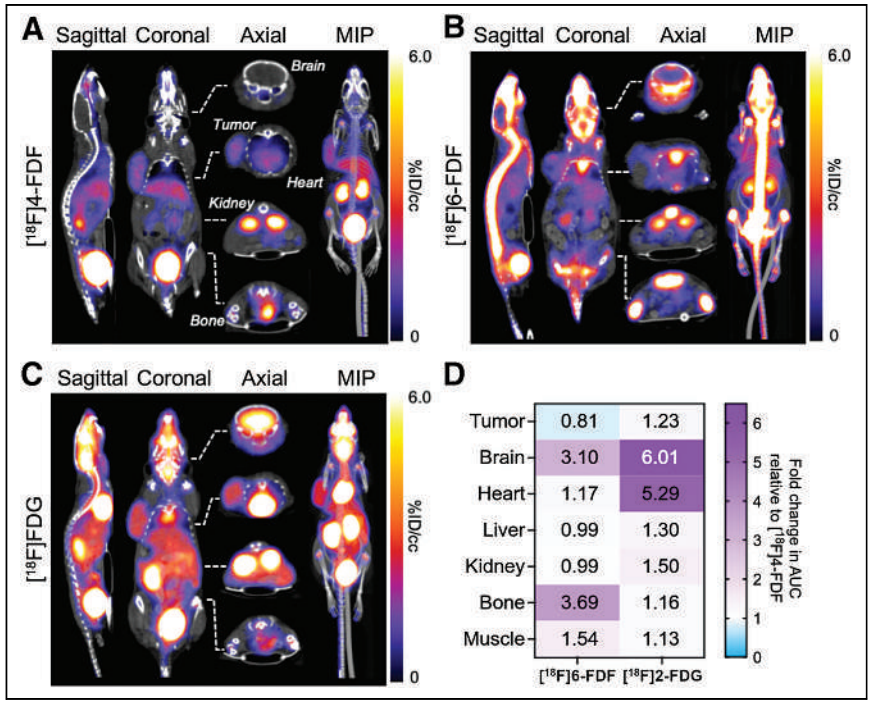


**FIGURE 4.** Comparative PET/CT imaging in heterotopic HepG2 xenograft mouse model. (A–C) Summed PET/CT images from 20 to 45 min after intravenous injection of [$^{18}$F]4-FDF (A), [$^{18}$F]6-FDF (B), or [$^{18}$F]FDG (C). Sagittal sections, coronal sections, and maximum-intensity projections are shown, in addition to axial sections at level of brain, heart, liver/kidneys, and hips. (D) Fold change in area under curve for entire time–activity curve in Supplemental Figure 2 for [$^{18}$F]6-FDF and [$^{18}$F] FDG normalized to values for [$^{18}$F]4-FDF. Purple represents increase in AUC, and blue represents decrease in area under curve. %ID = percentage injected dose; AUC = area under curve; MIP = maximum-intensity projection.

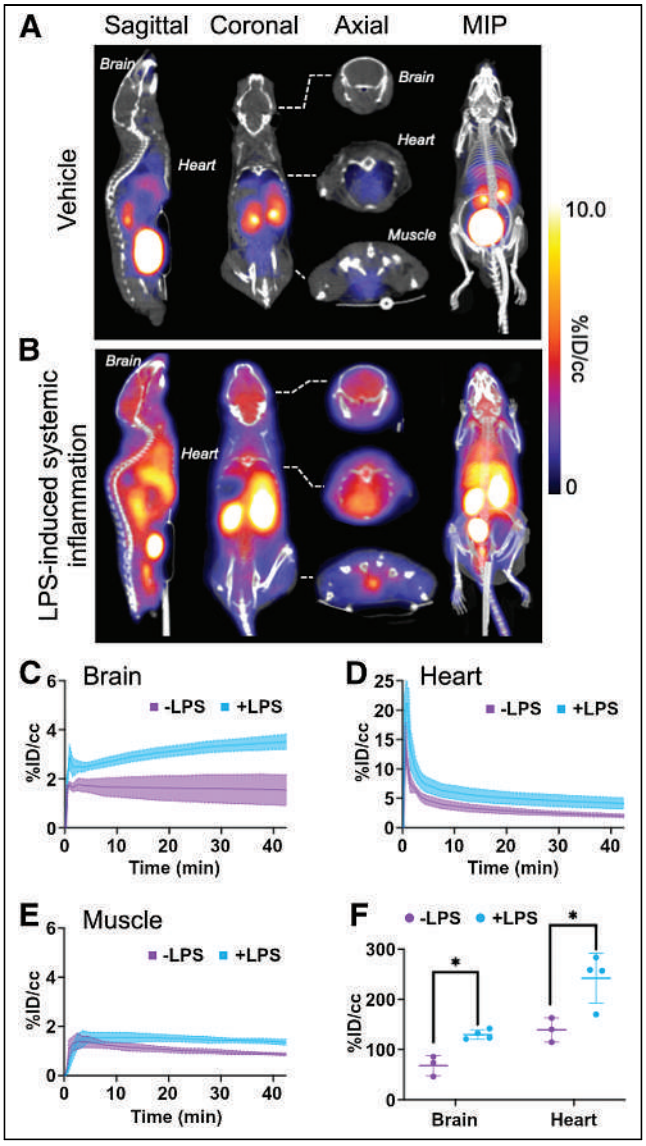


**FIGURE 5.** Imaging of inflammation in brain and heart. [$^{18}$F]4-FDF PET/CT was performed on mice receiving vehicle (A) or bacterial cell wall lipopolysaccharide (B) 24 h after injection. Sagittal, coronal, maximum-intensity projection, and axial sections of brain, heart, and muscle are shown. (C–E) Time–activity curves for brain (C), heart (D), and muscle (E) for mice receiving vehicle (−LPS, purple) or lipopolysaccharide (+LPS, blue). Solid lines are means, and shaded region are SDs. (F) Comparison of time–activity areas under curve for brain and heart regions of interest for mice receiving vehicle (−LPS, purple) or lipopolysaccharide (+LPS, blue). Plots show individual data points (circles), mean (long line), and SD (vertical line). *$P < 0.05$ by ANOVA followed by Tukey test. %ID = percentage injected dose; LPS = lipopolysaccharide; MIP = maximum-intensity projection.

An important outcome of the stable tracing of fructolysis afforded by [$^{18}$F]4-FDF was the observation of low uptake in healthy brain and heart (Fig. 5), tissues that are highly glycolytic and associated with high background levels of [$^{18}$F]FDG uptake (Fig. 4). The low fructolytic background rates in these tissues afforded the sensitive mapping of the neuro- and cardioinflammatory response to systemic lipopolysaccharide administration by [$^{18}$F]4-FDF (Fig. 5). Therefore, the aldolase-prescribed $C_4$ radiodeoxyfluorination of fructose resulted in radiotracer trapping on intracellular uptake and phosphorylation (Fig. 1), overcoming limitations to fructolysis tracing by $C_1$ and $C_6$ radioanalogs.

Although [$^{18}$F]FDG is used clinically to map glucose uptake for diagnostic imaging of traumatic brain injury (*37*), dementia (*38*), and Alzheimer disease (*39*), the estimation of neuroinflammation by [$^{18}$F]FDG PET is difficult because physiologic glucose uptake may obscure inflammation-specific signal. The presence of inflammatory cells can mask metabolic deficits in neurodegenerative diseases, hindering the use of glucose consumption as a biomarker in these cases (*40*). Neuronal [$^{18}$F]FDG uptake in a lipopolysaccharide-treated mouse therefore does not necessarily reflect metabolic state or neuronal damage, as microglial activation and immune cell infiltration confound uptake (*41*). [$^{18}$F]FDG PET may also be used for diagnostic imaging of cardiopulmonary inflammation (*42*), cardiopulmonary infection (*43*), and atherosclerosis; however, efforts must be made to minimize myocardial glucose metabolism before imaging to reduce the false-positive rate due to the low signal-to-noise ratio (*44*,*45*). These efforts rely on a diet-based metabolic switch from glucose to free fatty acids, relying heavily on patient compliance. The low brain and heart uptake in healthy, nonfasting mice described here makes fructose metabolism an attractive biomarker in tissues that are otherwise highly glycolytic and have high [$^{18}$F]FDG uptake in the absence of disease.

## CONCLUSION

The metabolic flux of deoxyfluorofructose was characterized by heavy-isotope labeling. [U$^{13}$C]-1-FDF exhibited limited polyol metabolism, whereas both [U$^{13}$C]-6-FDF and [U$^{13}$C]-4-FDF showed polyol pathway involvement. Only [U$^{13}$C]-4-FDF metabolism halted at [U$^{13}$C]-4-fluorodeoxyfructose-1-phosphate, supporting its unique ability to be trapped within cells. [$^{18}$F]4-FDF was synthesized with good molar activity and radiochemical yield. In a HepG2 xenograft mouse model, [$^{18}$F]4-FDF exhibited tumor accumulation with minimal bone uptake, whereas [$^{18}$F]6-FDF displayed substantial bone retention. [$^{18}$F]4-FDF displayed lower accumulation in normal mouse tissues than did [$^{18}$F]FDG, notably in the brain and heart. As a result, a significant increase in [$^{18}$F]4-FDF uptake in cardiac and brain tissues was observed after lipopolysaccharide treatment, highlighting the potential of [$^{18}$F]4-FDF PET/CT for sensitive mapping of cardio- and neuroinflammation in highly glycolytic tissues. Overall, this research provides critical insights into the metabolic fate of deoxyfluorinated fructose analogs and demonstrates the potential of [$^{18}$F]4-FDF for mapping disease or injury involving cardio- and neuroinflammation. With the ability to safely and effectively map fructolysis in mice, and low uptake in healthy tissues compared with [$^{18}$F]FDG, [$^{18}$F]4-FDF offers a clinically viable tool for diagnostic imaging of tissues with a high baseline glycolytic index. As dosimetry is not expected to be limiting, the clinical translation of this biosimilar radiotracer is feasible.

## DISCLOSURE

Funding was received from NSERC (RGPIN-2021-03387, to Adam Shuhendler), the Canada Research Chairs Program (950-230754, to Adam Shuhendler), and the Canadian Cancer Society (grant 707503 to Christina Addison and Adam Shuhendler). Metabolites were analyzed at the University of Ottawa Metabolomics Core Facility. This facility is supported by the Terry Fox Foundation and Ottawa University. No other potential conflict of interest relevant to this article was reported.

**KEY POINTS**

**QUESTION:** Can fructose metabolism accurately be mapped by PET?

**PERTINENT FINDINGS:** By installation of radiofluorine at the $C_4$ position of fructose, fructose metabolism can be accurately mapped because of intracellular trapping of the phosphorylated metabolite. Fructose use was low in the healthy brain and heart but elevated in disease, providing an opportunity for imaging neuro- and cardioinflammation.

**IMPLICATIONS FOR PATIENT CARE:** The introduction of [$^{18}$F]4-FDF opens new doors for mapping inflammation in cardiac and neural diseases with a biosimilar radiotracer based on a modified dietary sugar.

## REFERENCES


1. Mirtschink P, Krishnan J, Grimm F, et al. HIF-driven SF3B1 induces KHK-C to enforce fructolysis and heart disease. *Nature.* 2015;522:444–449.
2. Mirtschink P, Jang C, Arany Z, Krek W. Fructose metabolism, cardiometabolic risk, and the epidemic of coronary artery disease. *Eur Heart J.* 2018;39:2497–2505.
3. Williams AL, Khadka V, Tang M, et al. HIF1 mediates a switch in pyruvate kinase isoforms after myocardial infarction. *Physiol Genomics.* 2018;50:479–494.
4. Johnson RJ, Gomez-Pinilla F, Nagel M, et al. Cerebral fructose metabolism as a potential mechanism driving Alzheimer's disease. *Front Aging Neurosci.* 2020;12:560865.
5. Spagnuolo MS, Iossa S, Cigliano L. Sweet but bitter: focus on fructose impact on brain function in rodent models. *Nutrients.* 2020;13:1.
6. Chen C, Zhang Z, Liu C, et al. ATF4-dependent fructolysis fuels growth of glioblastoma multiforme. *Nat Commun.* 2022;13:6108.
7. Liu H, Huang D, McArthur DL, Boros LG, Nissen N, Heaney AP. Fructose induces transketolase flux to promote pancreatic cancer growth. *Cancer Res.* 2010; 70:6368–6376.
8. Helsley RN, Park SH, Vekaria HJ, et al. Ketohexokinase-C regulates global protein acetylation to decrease carnitine palmitoyltransferase 1a-mediated fatty acid oxidation. *J Hepatol.* 2023;79:25–42.
9. Ward PS, Thompson CB. Metabolic reprogramming: a cancer hallmark even Warburg did not anticipate. *Cancer Cell.* 2012;21:297–308.
10. Song A, Mao Y, Wei H. GLUT5: structure, functions, diseases and potential applications. *Acta Biochim Biophys Sin (Shanghai).* 2023;55:1519–1538.
11. Hannou SA, Haslam DE, McKeown NM, Herman MA. Fructose metabolism and metabolic disease. *J Clin Invest.* 2018;128:545–555.
12. Kolderup A, Svihus B. Fructose metabolism and relation to atherosclerosis, type 2 diabetes, and obesity. *J Nutr Metab.* 2015;2015:823081.
13. Harder JM, Guymer C, Wood JPM, et al. Disturbed glucose and pyruvate metabolism in glaucoma with neuroprotection by pyruvate or rapamycin. *Proc Natl Acad Sci USA.* 2020;117:33619–33627.
14. Keshari KR, Wilson DM, Chen AP, et al. Hyperpolarized [2-$^{13}$C]-fructose: a hemiketal DNP substrate for in vivo metabolic imaging. *J Am Chem Soc.* 2009;131: 17591–17596.
15. Zhang G, Cullen Q, Berishaj M, Deh K, Kim N, Keshari KR. [6,6′-2H2] fructose as a deuterium metabolic imaging probe in liver cancer. *NMR Biomed.* 2023;36:e4989.
16. Haradahira T, Tanaka A, Maeda M, Kanazawa Y, Ichiya YI, Masuda K. Radiosynthesis, rodent biodistribution, and metabolism of 1-deoxy-1-[$^{18}$F]fluoro-D-fructose. *Nucl Med Biol.* 1995;22:719–725.
17. Wuest M, Trayner BJ, Grant TN, et al. Radiopharmacological evaluation of 6-deoxy-6-[$^{18}$F]fluoro-D-fructose as a radiotracer for PET imaging of GLUT5 in breast cancer. *Nucl Med Biol.* 2011;38:461–475.
18. Wuest M, Hamann I, Bouvet V, et al. Molecular imaging of GLUT1 and GLUT5 in breast cancer: a multitracer positron emission tomography imaging study in mice. *Mol Pharmacol.* 2018;93:79–89.
19. Bouvet V, Jans HS, Wuest M, et al. Automated synthesis and dosimetry of 6-deoxy-6-[$^{18}$F]fluoro-D-fructose (6-[$^{18}$F]FDF): a radiotracer for imaging of GLUT5 in breast cancer. *Am J Nucl Med Mol Imaging.* 2014;4:248.
20. Boyle AJ, Murrell E, Tong J, et al. PET imaging of fructose metabolism in a rodent model of neuroinflammation with 6-[$^{18}$F]fluoro-6-deoxy-D-fructose. *Molecules.* 2022;27:8529.
21. Fushinobu S, Nishimasu H, Hattori D, Song HJ, Wakagi T. Structural basis for the bifunctionality of fructose-1,6-bisphosphate aldolase/phosphatase. *Nature.* 2011; 478:538–541.
22. Shrum B, Anantha RV, Xu SX, et al. A robust scoring system to evaluate sepsis severity in an animal model. *BMC Res Notes.* 2014;7:233.
23. Tee SS, Kim N, Cullen Q, et al. Ketohexokinase-mediated fructose metabolism is lost in hepatocellular carcinoma and can be leveraged for metabolic imaging. *Sci Adv.* 2022;8:eabm7985.
24. Suchý M, Charlton TA, Ben RN, Shuhendler AJ. Synthesis of natural/$^{13}$C-enriched D-tagatose from natural/$^{13}$C-enriched d-fructose. *Carbohydr Res.* 2021;507: 108377.
25. Luurtsema G, Pichler V, Bongarzone S, et al. EANM guideline for harmonisation on molar activity or specific activity of radiopharmaceuticals: impact on safety and imaging quality. *EJNMMI Radiopharm Chem.* 2021;6:34.
26. Yang D, Dai X, Xing Y, et al. Intrinsic cardiac adrenergic cells contribute to LPS-induced myocardial dysfunction. *Commun Biol.* 2022;5:96.
27. Batista CRA, Gomes GF, Candelario-Jalil E, Fiebich BL, de Oliveira ACP. Lipopolysaccharide-induced neuroinflammation as a bridge to understand neurodegeneration. *Int J Mol Sci.* 2019;20:2293.
28. Pauly TA, Ekstrom JL, Beebe DA, et al. X-ray crystallographic and kinetic studies of human sorbitol dehydrogenase. *Structure.* 2003;11:1071–1085.
29. Rechlin C, Scheer F, Terwesten F, et al. Price for opening the transient specificity pocket in human aldose reductase upon ligand binding: structural, thermodynamic, kinetic, and computational analysis. *ACS Chem Biol.* 2017;12:1397–1415.
30. Sandner A, Ngo K, Sager CP, et al. Which properties allow ligands to open and bind to the transient binding pocket of human aldose reductase? *Biomolecules.* 2021;11:1837.
31. Pérez-Tomás R, Pérez-Guillén I. Lactate in the tumor microenvironment: an essential molecule in cancer progression and treatment. *Cancers (Basel).* 2020;12:3244.
32. Wang Z-H, Peng W-B, Zhang P, Yang X-P, Zhou Q. Lactate in the tumour microenvironment: from immune modulation to therapy. *EBioMedicine.* 2021;73:103627.
33. Sasa K, Yoshimura K, Yamada A, et al. Monocarboxylate transporter-1 promotes osteoblast differentiation via suppression of p53, a negative regulator of osteoblast differentiation. *Sci Rep.* 2018;8:10579.
34. Luo Y, Gou H, Chen X, Li L, Wang X, Xu Y. Lactate inhibits osteogenic differentiation of human periodontal ligament stem cells via autophagy through the MCT1-mTOR signaling pathway. *Bone.* 2022;162:116444.
35. Zhu Z, Chen Y, Zou J, et al. Lactate mediates the bone anabolic effect of high-intensity interval training by inducing osteoblast differentiation. *J Bone Joint Surg Am.* 2023;105:369–379.
36. Rabinowitz JD, Enerbäck S. Lactate: the ugly duckling of energy metabolism. *Nat Metab.* 2020;2:566–571.
37. Jassam YN, Izzy S, Whalen M, Mcgavern DB, El Khoury J. Neuroimmunology of traumatic brain injury: time for a paradigm shift. *Neuron.* 2017;95:1246–1265.
38. Kato T, Inui Y, Nakamura A, Ito K. Brain fluorodeoxyglucose (FDG) PET in dementia. *Ageing Res Rev.* 2016;30:73–84.
39. Marcus C, Mena E, Subramaniam RM. Brain PET in the diagnosis of Alzheimer's disease. *Clin Nucl Med.* 2014;39:e413–e422.
40. Backes H, Walberer M, Ladwig A, et al. Glucose consumption of inflammatory cells masks metabolic deficits in the brain. *Neuroimage.* 2016;128:54–62.
41. Szöllősi D, Hegedűs N, Veres DS, et al. Evaluation of brain nuclear medicine imaging tracers in a murine model of sepsis-associated encephalopathy. *Mol Imaging Biol.* 2018;20:952–962.
42. Bertagna F, Bisleri G, Motta F, et al. Possible role of F18-FDG-PET/CT in the diagnosis of endocarditis: preliminary evidence from a review of the literature. *Int J Cardiovasc Imaging.* 2012;28:1417–1425.
43. Eibschutz LS, Rabiee B, Asadollahi S, et al. FDG-PET/CT of COVID-19 and other lung infections. *Semin Nucl Med.* 2022;52:61–70.
44. Cussó L, Vaquero JJ, Bacharach S, Desco M. Comparison of methods to reduce myocardial $^{18}$F-FDG uptake in mice: calcium channel blockers versus high-fat diets. *PLoS One.* 2014;9:e107999.
45. Wykrzykowska J, Lehman S, Williams G, et al. Imaging of inflamed and vulnerable plaque in coronary arteries with $^{18}$F-FDG PET/CT in patients with suppression of myocardial uptake using a low-carbohydrate, high-fat preparation. *J Nucl Med.* 2009;50:563–568.

# Preclinical Evaluation of Gastrin-Releasing Peptide Receptor Antagonists Labeled with $^{161}$Tb and $^{177}$Lu: A Comparative Study

Nadine Holzleitner[1], Tatjana Cwojdzinski[1], Roswitha Beck[1], Nicole Urtz-Urban[1], Colin C. Hillhouse[2], Pascal V. Grundler[2], Nicholas P. van der Meulen[2], Zeynep Talip[2], Stijn Ramaekers[3], Michiel Van de Voorde[3], Bernard Ponsard[3], Angela Casini[1], and Thomas Günther[1]

[1]*Department of Chemistry, School of Natural Sciences, Technical University of Munich, Garching, Germany;* [2]*Center for Radiopharmaceutical Sciences ETH-PSI, Paul Scherrer Institute, Villigen, Switzerland; and* [3]*Nuclear Medical Applications, Belgian Nuclear Research Centre, Mol, Belgium*

To elucidate potential benefits of the Auger-electron–emitting radionuclide $^{161}$Tb, we compared the preclinical performance of the gastrin-releasing peptide receptor antagonists RM2 (DOTA-Pip$^5$-D-Phe$^6$-Gln$^7$-Trp$^8$-Ala$^9$-Val$^{10}$-Gly$^{11}$-His$^{12}$-Sta$^{13}$-Leu$^{14}$-$NH_2$) and AMTG (α-Me-Trp$^8$-RM2), each labeled with both $^{177}$Lu and $^{161}$Tb. **Methods:** $^{161}$Tb/$^{177}$Lu labeling (90°C, 5 min) and cell-based experiments (PC-3 cells) were performed. In vivo stability (30 min after injection) and biodistribution studies (1–72 h after injection) were performed on PC-3 tumor–bearing CB17-SCID mice. **Results:** Gastrin-releasing peptide receptor affinity was high for all compounds (half-maximal inhibitory concentration [nM]: [$^{161}$Tb]Tb-RM2, 2.46 ± 0.16; [$^{161}$Tb]Tb-AMTG, 2.16 ± 0.09; [$^{177}$Lu]Lu-RM2, 3.45 ± 0.18; [$^{177}$Lu]Lu-AMTG, 3.04 ± 0.08), and 75%–84% of cell-associated activity was receptor-bound. In vivo, both AMTG analogs displayed distinctly higher stability (30 min after injection) and noticeably higher tumor retention than their RM2 counterparts. **Conclusion:** On the basis of preclinical results, [$^{161}$Tb]Tb-/[$^{177}$Lu]Lu-AMTG might reveal a higher therapeutic efficacy than [$^{161}$Tb]Tb-/[$^{177}$Lu]Lu-RM2, particularly [$^{161}$Tb]Tb-AMTG because of additional Auger-electron emissions at the cell membrane level.

**Key Words:** GRPR antagonists; $^{161}$Tb; $^{177}$Lu; AMTG; RM2

**J Nucl Med 2024; 65:481–484**
DOI: 10.2967/jnumed.123.266233

In nuclear medicine, $^{161}$Tb is a promising radionuclide because it has physical properties similar to those of the clinically established $^{177}$Lu (half-life, 6.9 vs. 6.7 d; average electron energy, ~0.15 vs. ~0.14 MeV) and it additionally emits Auger electrons, which provide a higher linear energy transfer than $\beta^-$ particles (*1*). In general, the short-ranged Auger electrons must be close to the cell nucleus to inflict damage, limiting their usability to agonists. However, a recently reported study showed that a noninternalizing $^{161}$Tb-labeled somatostatin-2 receptor antagonist demonstrated therapeutic efficacy superior to a $^{161}$Tb-labeled somatostatin-2 receptor agonist, suggesting that Auger emissions at the cell membrane ("membrane effect") may be therapeutic even if they do not reach the nucleus (*2*). This membrane effect could thus pave the way for an extended use of antagonists.

Gastrin-releasing peptide receptor (GRPR) antagonists represent an alternative for detection and treatment of prostate-specific membrane antigen–negative prostate cancer lesions (*3,4*), as shown using [$^{177}$Lu]Lu-RM2 (DOTA-Pip$^5$-D-Phe$^6$-Gln$^7$-Trp$^8$-Ala$^9$-Val$^{10}$-Gly$^{11}$-His$^{12}$-Sta$^{13}$-Leu$^{14}$-$NH_2$) (*5*). To further improve the therapeutic efficacy of radiolabeled GRPR ligands, we recently developed [$^{177}$Lu]Lu-AMTG (α-Me-Trp$^8$-RM2), a RM2 derivative (Fig. 1) demonstrating favorable biodistribution and noticeably increased in vivo stability, which resulted in higher tumor retention and, thus, increased tumor-to-background ratios in all organs (*6*). Because most of the cell-associated activity of these GRPR antagonists was membrane-bound (<20% internalized) (*6*), a combination with $^{161}$Tb might result in improved therapeutic efficacy.

To elucidate whether $^{161}$Tb would be a suitable or better alternative to $^{177}$Lu in these GRPR ligands, we completed a comparative preclinical evaluation on [$^{161}$Tb]Tb-/[$^{177}$Lu]Lu-AMTG and [$^{161}$Tb]Tb-/[$^{177}$Lu]Lu-RM2 with regard to GRPR affinity (half-maximal inhibitory concentration), membrane-bound activity, lipophilicity (distribution coefficient at pH 7.4), in vivo stability, and biodistribution studies in PC-3 tumor–bearing mice.

## MATERIALS AND METHODS

### Synthesis and Labeling

Precursor synthesis and $^{161}$Tb/$^{177}$Lu labeling were performed according to a published procedure (*6*). [$^{161}$Tb]$TbCl_3$ was provided by Paul Scherrer Institute and Belgian Nuclear Research Centre. [$^{177}$Lu]$LuCl_3$ was acquired from ITM Isotope Technologies Munich SE. 3-[$^{125}$I]I-tyr$^6$-MJ9 (Supplemental Fig. 1; supplemental materials are available at http://jnm.snmjournals.org) was prepared according to reported procedures (*6,7*). Characterization of all GRPR ligands is provided in Supplemental Figure 2.

### In Vitro Experiments

All in vitro experiments (half-maximal inhibitory concentration and internalization studies, n-octanol/phosphate-buffered saline solution distribution coefficient at pH 7.4) were performed in analogy to a previously published procedure (supplemental materials) (*6*).

### In Vivo Experiments

All animal experiments were approved by the General Administration of Upper Bavaria (ROB-55.2-1-2532.Vet_02-18-109), were

Received Jun. 24, 2023; revision accepted Nov. 9, 2023.
For correspondence or reprints, contact Thomas Günther (thomas.guenther@tum.de) or Angela Casini (angela.casini@tum.de).
Published online Dec. 14, 2023.

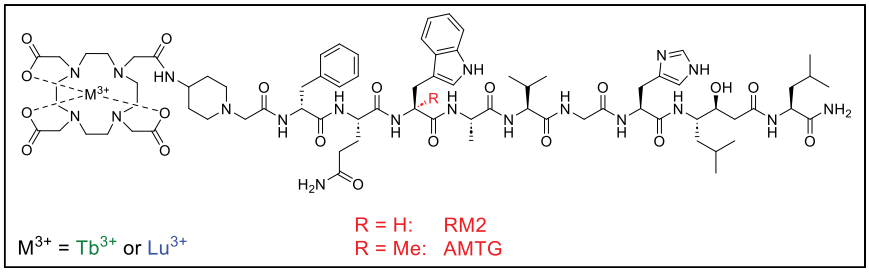


**FIGURE 1.** Chemical structures of RM2- and AMTG-based radiopharmaceuticals used in this study.

completed according to a previously published protocol (*6*), and complied with the ARRIVE (Animal Research: Reporting of In Vivo Experiments) guidelines (supplemental materials).

### Statistics

Acquired data were statistically analyzed by a Student *t*-test via Excel (Microsoft Corp.) and OriginPro software (version 9.7; OriginLab Corp.). Acquired *P* values of less than 0.05 were considered statistically significant.

## RESULTS

### Synthesis and Radiolabeling

Complexation with a 2.5-fold excess of $TbCl_3$ and $LuCl_3$ resulted in quantitative yields. $^{161}$Tb and $^{177}$Lu labeling resulted in radiochemical yields and purities of more than 98% and molar activities of 65 ± 5 GBq/μmol. Labeling with another batch of [$^{161}$Tb]$TbCl_3$ resulted in radiochemical purities of more than 95%, and 2 minor impurities were observed (Supplemental Figs. 3A and 3B). Although one impurity could be attributed to free $^{161}Tb^{3+}$ (Supplemental Fig. 3C), the other was not identified. All $^{161}$Tb- and $^{177}$Lu-labeled compounds were used without further purification.

### In Vitro Characterization

$^{nat/161}$Tb- and $^{nat/177}$Lu-labeled AMTG and RM2 revealed comparably high GRPR affinity (half-maximal inhibitory concentration, 2.2–3.5 nM; Supplemental Fig. 4), low internalization (74%–84% of cell-associated activity membrane-bound), and favorable lipophilicity (distribution coefficient at pH 7.4, −2.6 to −2.3) (Figs. 2A–2C; Supplemental Table 1). Significant differences are depicted in Figure 2.

### In Vivo Characterization

A significantly higher stability was determined for the AMTG than for the RM2 derivatives (Fig. 2D; Supplemental Fig. 5). Biodistribution studies demonstrated high activity levels in the tumor for all ligands at all time points, with [$^{161}$Tb]Tb-AMTG exhibiting the highest levels (Fig. 3A). Estimates of area under the curve (AUC) 1–72 h after injection revealed 14% higher tumor levels for [$^{161}$Tb]Tb-AMTG than for [$^{177}$Lu]Lu-AMTG and 30%–45% higher tumor levels than for either RM2 analog (Supplemental Table 2).

Activity accumulation in the pancreas was high for all GRPR ligands. However, more than 95% of the activity was cleared from the pancreas within the first 24 h for all compounds (Fig. 3B). [$^{161}$Tb]Tb-AMTG displayed a 63%, 172%, and 423% higher AUC (1–72 h after injection) for the pancreas than did [$^{161}$Tb]Tb-RM2, [$^{177}$Lu]Lu-AMTG, and [$^{177}$Lu]Lu-RM2, respectively. Apart from that, low off-target accumulation was observed for all organs (Supplemental Fig. 6; Supplemental Tables 3–6). Activity levels in the kidneys and the blood were less than 4% injected dose/g at all time points for all analogs (Figs. 3C and 3D). Activity levels in the liver and the spleen were slightly elevated for both $^{161}$Tb-labeled GRPR ligands at all time points, except at 4 h after injection.

Further imaging studies at 1, 4, 24, 72, and 168 h after injection in PC-3 tumor–bearing mice ($n$ = 1), applying [$^{161}$Tb]Tb-AMTG and [$^{161}$Tb]Tb-RM2, confirmed the favorable tumor uptake and biodistribution profiles (Fig. 4).

## DISCUSSION

The recent observation that antagonists do not internalize but are bound to the cell membrane revealed an even improved

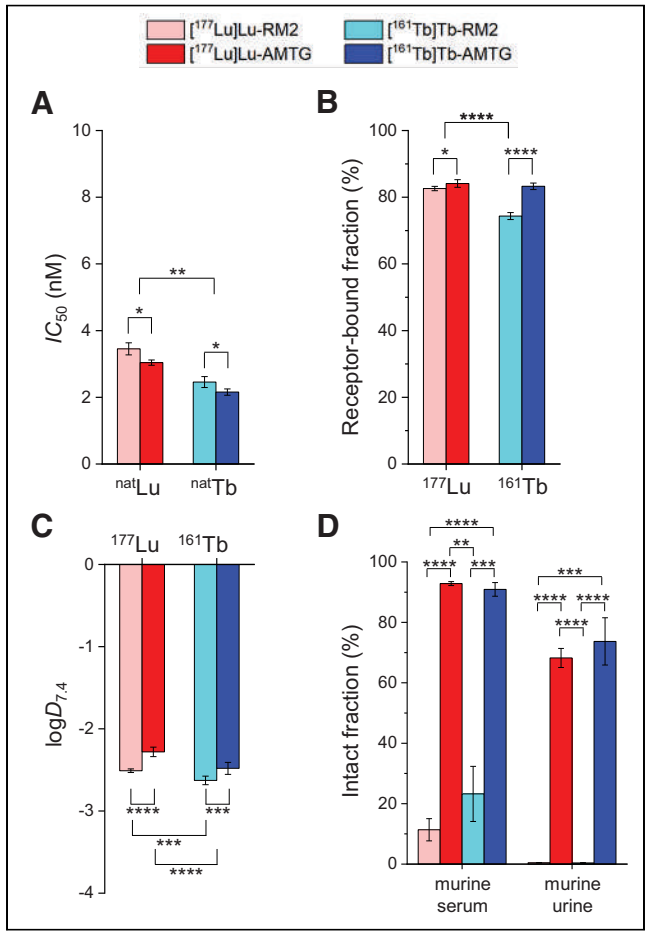


**FIGURE 2.** In vitro data of $^{161}$Tb- and $^{177}$Lu-labeled GRPR ligands. Data are expressed as mean ± SD. (A) Affinity data ($n$ = 3) on PC-3 cells ($1.5 \times 10^5$ cells/mL/well) using 3-[$^{125}$I]I-tyr$^6$-MJ9 (0.2 nM/well) as radiolabeled reference (2 h, room temperature). (B) Receptor-bound fraction ($n$ = 6) on PC-3 (1.0 nM/well) cells as percentage of cell-associated activity (37°C, 1 h, $1.5 \times 10^5$ cells/mL/well). Data are corrected for nonspecific binding ($10^{-3}$ M Lu-RM2). (C) Lipophilicity depicted as distribution coefficients at pH 7.4 ($logD_{7.4}$). (D) In vivo stability in murine serum and urine at 30 min after injection ($n$ = 3). $IC_{50}$ = half-maximal inhibitory concentration. *$P$ < 0.05. **$P$ < 0.01. ***$P$ < 0.001. ****$P$ < 0.0001.

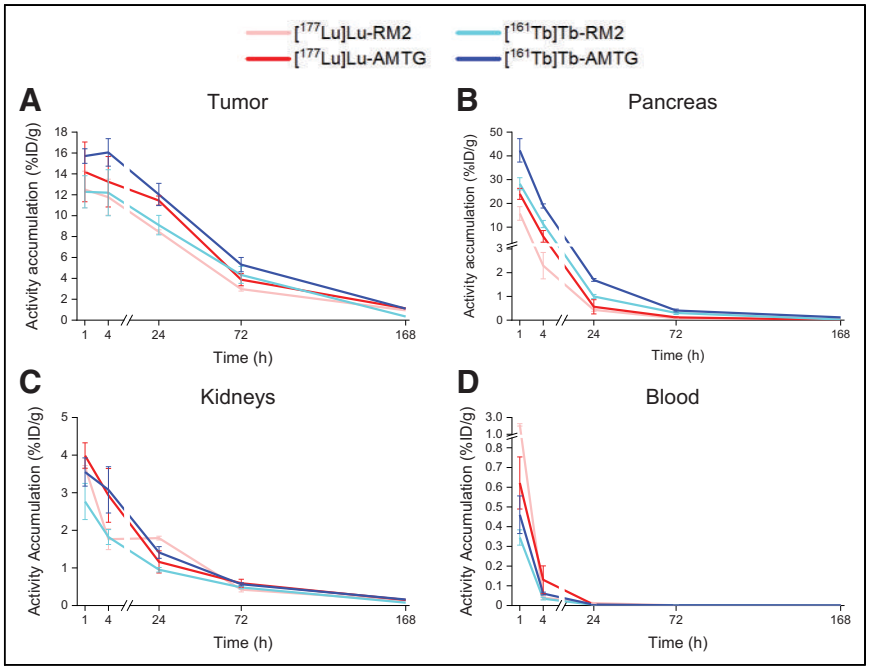


**FIGURE 3.** Activity accumulation of $^{161}$Tb- and $^{177}$Lu-labeled GRPR ligands in tumor (A), pancreas (B), kidneys (C), and blood (D) at 1, 4, 24, and 72 h after injection ($n$ = 4 each), as well as 168 h after injection ($n$ = 1 each) in PC-3 tumor–bearing CB17-SCID mice (100 pmol each). Data are expressed as mean ± SD. %ID = percentage injected dose.

therapeutic efficacy when labeled with Auger-electron–emitting radionuclides. This type of result will ensure that Auger-emitting radionuclides continue to gain attention in the field of nuclear medicine. In view of our promising data on $^{177}$Lu-labeled GRPR ligands (*6*) and the similar physical properties of $^{177}$Lu and $^{161}$Tb (similar half-lives and $\beta^-$ energies, whereas the latter additionally emits more Auger electrons per decay (*1*)), we completed a comparative preclinical study on AMTG and RM2 labeled with both radionuclides.

Although most $^{177}$Lu/$^{161}$Tb labelings resulted in radiochemical purities of more than 98%, labeling with 1 batch of [$^{161}$Tb]$TbCl_3$ resulted in approximately only 95% radiochemical purity, and 2 minor impurities were observed (used for biodistribution studies at 1, 24, and 72 h after injection). Because we consider radiochemical purity of more than 95% sufficient for preclinical experiments, no further investigation was conducted. The $^{161}$Tb- and $^{177}$Lu-labeled GRPR ligands revealed comparable in vitro properties (GRPR affinity, lipophilicity, and membrane-bound activity; Fig. 2). In vivo, although biodistribution profiles similar to those of the $^{177}$Lu-labeled analogs were observed (Supplemental Fig. 6), higher uptake and retention were observed for RM2 and AMTG labeled with this [$^{161}$Tb]$TbCl_3$ batch (at 1, 24, and 72 h after injection), particularly in the liver and the spleen, likely because of the aforementioned impurities. Notably, the compounds used for the studies at 4 h after injection (labeled with a different [$^{161}$Tb]$TbCl_3$ batch, free of impurities) did not show any enhanced uptake in these organs, which is why this elevated uptake was likely not caused by the compound itself.

High initial tumor and pancreas uptake was observed for all derivatives. However, whereas activity was retained in the tumor for several days, more than 95% of the initial activity (1 h after injection) was cleared from the pancreas within the first 24 h after injection, as was also shown for the human situation (*5*). Elevated pancreas uptake observed for the $^{161}$Tb-labeled ligands could be due to their slightly enhanced GRPR affinity. In general, higher activity levels were found for the AMTG derivatives in the tumor (except at 72 h after injection), which can be attributed to their increased in vivo stability. This led to noticeably increased AUCs (1–72 h after injection) for the tumor for the AMTG than for the RM2 analogs. On the basis of the high therapeutic efficacy observed for a noninternalizing, $^{161}$Tb-labeled somatostatin-2 receptor antagonist due to yet unknown damage by Auger electrons at the cell membrane (*2*), and the high percentage of membrane-bound

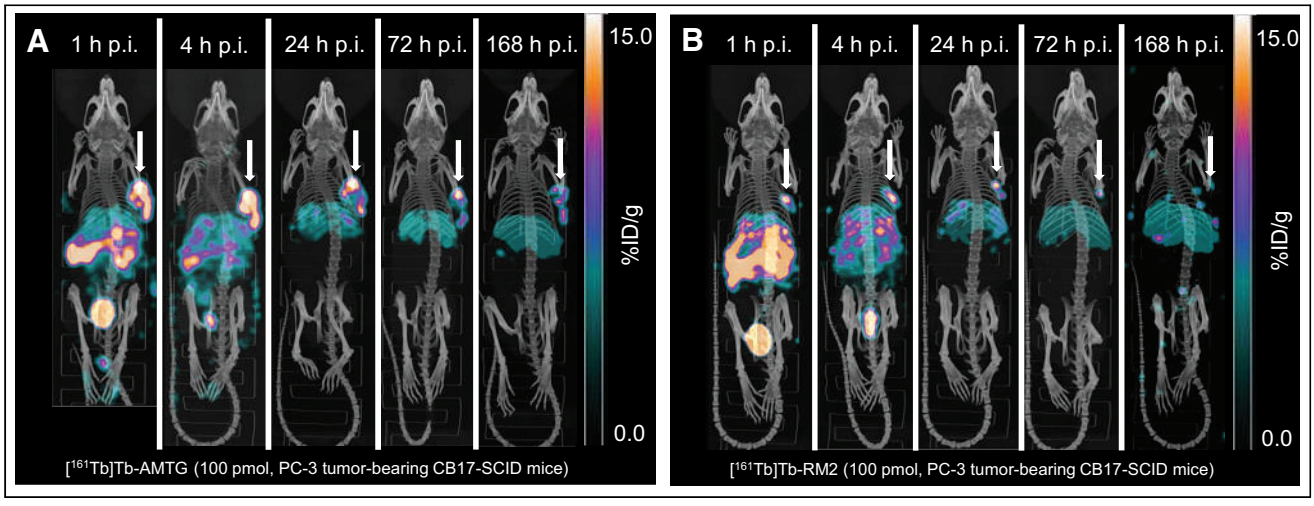


**FIGURE 4.** Maximum-intensity projection of 1 CB17-SCID mouse bearing PC-3 tumor (arrows) and injected with [$^{161}$Tb]Tb-AMTG (A) and [$^{161}$Tb]Tb-RM2 (B) (100 pmol each). Images were acquired at 1, 4, 24, 72, and 168 h after injection. %ID = percentage injected dose; p.i. = after injection.

[$^{161}$Tb]Tb-AMTG (Fig. 2B), an improved therapeutic efficacy might be predicted for this compound. Favorable biodistribution profiles for [$^{161}$Tb]Tb-AMTG over time were confirmed by imaging studies (Fig. 4) and were in agreement with previously reported profiles for [$^{177}$Lu]Lu-AMTG (*6*).

Nevertheless, AUCs (1–72 h after injection) for the pancreas were also elevated for the AMTG analogs compared with their RM2 correlates, which is why a higher dose to the pancreas is expected. However, AUCs (1–72 h after injection) for the tumor were 2- to 8-fold higher than those for the pancreas for all these compounds. Moreover, other than estimates of the dose limit for the pancreas based on external-beam radiation therapy, only limited evidence is currently available that the pancreas is a radiation-sensitive organ (*8,9*). Further studies on animals and humans must be conducted to elucidate tumor and pancreas dose, as well as the potential damage caused.

Overall, this study delivered further evidence of the potential therapeutic usability of [$^{161}$Tb]Tb- or [$^{177}$Lu]Lu-AMTG. Moreover, because of the similar physical properties of $^{177}$Lu and $^{161}$Tb but additional emission of Auger and conversion electrons by the latter, $^{161}$Tb could become a valuable addition to the armamentarium of nuclear medicine, once its clinical availability improves. Provided the membrane effect is accessible for noninternalizing GRPR antagonists, a combination with short-range Auger- and α-emitters might be applicable. A limitation of this study was the use of $^{161}$Tb-labeled RM2 and AMTG batches that contained 2 minor impurities, which likely caused increased activity retention in the liver and spleen and affected the overall tumor-to-background ratios.

## CONCLUSION

The data from this study indicate that both [$^{161}$Tb]Tb-AMTG and [$^{177}$Lu]Lu-AMTG might improve radioligand therapy because of their high tumor retention. Ongoing treatment studies in our laboratory will enable conclusions to be drawn on the potentially increased therapeutic efficacy of AMTG over RM2 (due to in vivo stability) and of $^{161}$Tb over $^{177}$Lu (due to Auger-electron emission) and whether there are detrimental effects on the pancreas.

## DISCLOSURE

This work was supported by the European Union's Horizon 2020 research and innovation program as a user project of PRISMAP—the European medical radionuclides program (GA 101008571). Thomas Günther acknowledges the 2023 Sanjiv Sam Gambhir–Philips and the 2023 Translational Research and Applied Medicine fellowships for support at Stanford University. A patent application on modified GRPR-targeted ligands, including AMTG, with Thomas Günther as the inventor has been filed (WO2021121734A1). No other potential conflict of interest relevant to this article was reported.

## ACKNOWLEDGMENTS

We thank the members of the PRISMAP consortium and the PRISMAP user selection panel, coordination and management team, for their advice and support.

## KEY POINTS

**QUESTION:** Is it possible to improve GRPR-based radioligand therapy (currently performed with [$^{177}$Lu]Lu-RM2) using the metabolically more stable AMTG peptide and alternative radionuclides such as $^{161}$Tb?

**PERTINENT FINDINGS:** Compared with [$^{161}$Tb]Tb-/[$^{177}$Lu]Lu-RM2, [$^{161}$Tb]Tb-/[$^{177}$Lu]Lu-AMTG revealed noticeably increased tumor AUCs, which might be beneficial for future clinical use.

**IMPLICATIONS FOR PATIENT CARE:** Although the clinical value of [$^{161}$Tb]Tb-/[$^{177}$Lu]Lu-AMTG and a potential dose-limiting toxicity to the pancreas have to be elucidated, improved therapeutic efficacy on the tumor and, thus, improved patient care are anticipated.

## REFERENCES

1. Lehenberger S, Barkhausen C, Cohrs S, et al. The low-energy β− and electron emitter $^{161}$Tb as an alternative to $^{177}$Lu for targeted radionuclide therapy. *Nucl Med Biol.* 2011;38:917–924.
2. Borgna F, Haller S, Rodriguez JMM, et al. Combination of terbium-161 with somatostatin receptor antagonists: a potential paradigm shift for the treatment of neuroendocrine neoplasms. *Eur J Nucl Med Mol Imaging.* 2022;49:1113–1126.
3. Afshar-Oromieh A, Holland-Letz T, Giesel FL, et al. Diagnostic performance of $^{68}$Ga-PSMA-11 (HBED-CC) PET/CT in patients with recurrent prostate cancer: evaluation in 1007 patients. *Eur J Nucl Med Mol Imaging.* 2017;44:1258–1268.
4. Eiber M, Maurer T, Souvatzoglou M, et al. Evaluation of hybrid $^{68}$Ga-PSMA ligand PET/CT in 248 patients with biochemical recurrence after radical prostatectomy. *J Nucl Med.* 2015;56:668–674.
5. Kurth J, Krause BJ, Schwarzenböck SM, Bergner C, Hakenberg OW, Heuschkel M. First-in-human dosimetry of gastrin-releasing peptide receptor antagonist [$^{177}$Lu]Lu-RM2: a radiopharmaceutical for the treatment of metastatic castration-resistant prostate cancer. *Eur J Nucl Med Mol Imaging.* 2020;47:123–135.
6. Günther T, Deiser S, Felber V, Beck R, Wester HJ. Substitution of L-tryptophan by a-methyl-L-tryptophan in $^{177}$Lu-RM2 results in $^{177}$Lu-AMTG, a high-affinity gastrin-releasing peptide receptor ligand with improved in vivo stability. *J Nucl Med.* 2022;63:1364–1370.
7. Nakagawa T, Hocart SJ, Schumann M, et al. Identification of key amino acids in the gastrin-releasing peptide receptor (GRPR) responsible for high affinity binding of gastrin-releasing peptide (GRP). *Biochem Pharmacol.* 2005;69:579–593.
8. Bresciani S, Garibaldi E, Cattari G, et al. Dose to organs at risk in the upper abdomen in patients treated with extended fields by helical tomotherapy: a dosimetric and clinical preliminary study. *Radiat Oncol.* 2013;8:247.
9. Gemici C, Yaprak G, Ozdemir S, Baysal T, Seseogullari OO, Ozyurt H. Volumetric decrease of pancreas after abdominal irradiation, it is time to consider pancreas as an organ at risk for radiotherapy planning. *Radiat Oncol.* 2018;13:238.

# Need for Objective Task-Based Evaluation of Image Segmentation Algorithms for Quantitative PET: A Study with ACRIN 6668/RTOG 0235 Multicenter Clinical Trial Data

Ziping Liu[1], Joyce C. Mhlanga[2], Huitian Xia[1], Barry A. Siegel[2,3], and Abhinav K. Jha[1–3]

[1]*Department of Biomedical Engineering, Washington University, St. Louis, Missouri;* [2]*Mallinckrodt Institute of Radiology, Washington University School of Medicine, St. Louis, Missouri; and* [3]*Alvin J. Siteman Cancer Center, Washington University School of Medicine, St. Louis, Missouri*

Reliable performance of PET segmentation algorithms on clinically relevant tasks is required for their clinical translation. However, these algorithms are typically evaluated using figures of merit (FoMs) that are not explicitly designed to correlate with clinical task performance. Such FoMs include the Dice similarity coefficient (DSC), the Jaccard similarity coefficient (JSC), and the Hausdorff distance (HD). The objective of this study was to investigate whether evaluating PET segmentation algorithms using these task-agnostic FoMs yields interpretations consistent with evaluation on clinically relevant quantitative tasks. **Methods:** We conducted a retrospective study to assess the concordance in the evaluation of segmentation algorithms using the DSC, JSC, and HD and on the tasks of estimating the metabolic tumor volume (MTV) and total lesion glycolysis (TLG) of primary tumors from PET images of patients with non–small cell lung cancer. The PET images were collected from the American College of Radiology Imaging Network 6668/Radiation Therapy Oncology Group 0235 multicenter clinical trial data. The study was conducted in 2 contexts: (1) evaluating conventional segmentation algorithms, namely those based on thresholding ($SUV_{max}$40% and $SUV_{max}$50%), boundary detection (Snakes), and stochastic modeling (Markov random field–Gaussian mixture model); (2) evaluating the impact of network depth and loss function on the performance of a state-of-the-art U-net–based segmentation algorithm. **Results:** Evaluation of conventional segmentation algorithms based on the DSC, JSC, and HD showed that $SUV_{max}$40% significantly outperformed $SUV_{max}$50%. However, $SUV_{max}$40% yielded lower accuracy on the tasks of estimating MTV and TLG, with a 51% and 54% increase, respectively, in the ensemble normalized bias. Similarly, the Markov random field–Gaussian mixture model significantly outperformed Snakes on the basis of the task-agnostic FoMs but yielded a 24% increased bias in estimated MTV. For the U-net–based algorithm, our evaluation showed that although the network depth did not significantly alter the DSC, JSC, and HD values, a deeper network yielded substantially higher accuracy in the estimated MTV and TLG, with a decreased bias of 91% and 87%, respectively. Additionally, whereas there was no significant difference in the DSC, JSC, and HD values for different loss functions, up to a 73% and 58% difference in the bias of the estimated MTV and TLG, respectively, existed. **Conclusion:** Evaluation of PET segmentation algorithms using task-agnostic FoMs could yield findings discordant with evaluation on clinically relevant quantitative tasks. This study emphasizes the need for objective task-based evaluation of image segmentation algorithms for quantitative PET.

**Key Words:** task-based evaluation; multicenter clinical trial; segmentation; quantitative imaging; deep learning; artificial intelligence

**J Nucl Med 2024; 65:485–492**
DOI: 10.2967/jnumed.123.266018

PET-derived quantitative metrics, such as tumor volumetric and radiomic features, are showing strong promise in multiple oncologic applications (*1–3*). Reliable quantification of these features requires accurate segmentation of tumors on the PET images. To address this need, multiple computer-aided image segmentation algorithms have been developed (*4*), including those based on deep learning (DL) (*5–8*). Clinical translation of these image segmentation algorithms requires objectively evaluating them with patient data.

Medical images are acquired for specified clinical tasks; thus, it is important that the performance of imaging and image-analysis algorithms be objectively assessed on those tasks. In this context, strategies have been proposed for task-based assessment of image quality (*9–12*). However, imaging algorithms, including those based on DL, are often evaluated using figures of merit (FoMs) that are not explicitly designed to measure clinical task performance (*11*). Recent studies conducted specifically in the context of evaluating image-denoising algorithms showed that task-agnostic FoMs may yield interpretations that are inconsistent with evaluation on clinical tasks (*13–17*). For example, in Yu et al. (*17*) a DL-based denoising algorithm for myocardial perfusion SPECT indicated significantly superior performance based on a structural similarity index measure and mean squared error but did not yield any improved performance on the clinical task of detecting myocardial perfusion defects.

Similar to image denoising, algorithms for image segmentation are almost always evaluated using FoMs that are not explicitly designed to quantify clinical task performance (*5*,*18–21*). These FoMs, including the Dice similarity coefficient (DSC), the Jaccard similarity coefficient (JSC), and the Hausdorff distance (HD) (*4*), quantify some measure of similarity between the predicted segmentation and a reference standard such as manual delineation. For example, the DSC measures spatial overlap between the predicted segmentation and reference standard. A higher value of

Received May 12, 2023; revision accepted Dec. 19, 2023.
For correspondence or reprints, contact Abhinav K. Jha (a.jha@wustl.edu).
Published online Feb. 15, 2024.

DSC is typically used to infer more accurate performance. However, it is unclear how these task-agnostic FoMs correlate with performance on clinically relevant tasks.

Our objective was to investigate whether evaluating PET segmentation algorithms using task-agnostic FoMs leads to interpretations that are consistent with evaluation based on clinical task performance. Performing this investigation with patient data in a multicenter setting is highly desirable because such a study offers the ability to model variabilities in both patient population and clinical scanner configurations. Toward this goal, we conducted a retrospective study using data from the American College of Radiology Imaging Network (ACRIN) 6668/Radiation Therapy Oncology Group (RTOG) 0235 multicenter clinical trial (*22*,*23*). In this trial, patients with stage IIB/III non–small cell lung cancer were imaged with $^{18}$F-FDG PET/CT studies. In the study of non–small cell lung cancer, there is a strong interest in investigating whether early changes in tumor metabolism can help predict therapy response (*24*). Although most studies have focused on SUV-based metrics, the findings have been inconsistent (*24*,*25*), motivating the need for new and improved metrics. In this context, metabolic tumor volume (MTV) and total lesion glycolysis (TLG) are showing strong promise as prognostic biomarkers in multiple studies (*3*,*26*,*27*). As introduced above, computing these features requires tumor segmentation. Thus, our study was designed to assess the concordance in evaluating various image segmentation algorithms using task-agnostic metrics (DSC, JSC, and HD) versus on the clinically relevant tasks of estimating the MTV and TLG. Initial results of this study were presented in brief previously (*28*); here, we provide a detailed description of the methods and study design, provide new findings, and conduct comprehensive analyses of the results.

## MATERIALS AND METHODS

### Study Population

This retrospective study of existing data was approved by the institutional review board, which waived the requirement to obtain informed consent. Deidentified $^{18}$F-FDG PET/CT images of 225 patients with inoperable stage IIB/III locally advanced non–small cell lung cancer were collected from the ACRIN 6668/RTOG 0235 multicenter clinical trial (*22*,*23*). The images were collected from The Cancer Imaging Archive database (*29*). Baseline PET/CT scans were acquired before curative-intent chemoradiotherapy for each patient. Demographics and clinical characteristics of the patient population are summarized in Supplemental Table 1 (supplemental materials are available at http://jnm.snmjournals.org). A standardized imaging protocol was detailed by Machtay et al. (*23*). Briefly, an $^{18}$F-FDG dose ranging from 370 to 740 MBq was administered, with image acquisition beginning 50–70 min later and including the body from the upper–mid neck to proximal femurs. The PET images were acquired from 12 ACRIN-qualified clinical scanners (*30*), including GE Healthcare Discovery LS/ST/STE/RX, GE Healthcare Advance, Philips Allegro/Guardian, and CTI PET Systems (marketed as Siemens scanners): models 1023/1024/1062/1080/1094. The image reconstruction procedure compensated for attenuation, scatter, randoms, normalization, decay, and dead time. Details of the reconstruction protocol for each PET scanner are provided in Supplemental Table 2.

### Data Curation

Evaluation of PET segmentation algorithms required knowledge of true tumor boundaries or a surrogate for ground truth, such as tumor delineations performed by an expert human reader. For this purpose, a board-certified nuclear medicine physician with more than 10 y of experience reading PET scans was tasked with defining the boundary of the primary tumor for each patient (Fig. 1). The physician was instructed to locate the primary tumor by carefully reviewing the co-registered PET/CT images along coronal, sagittal, and transverse planes and then using an edge-detection tool (MIM Encore 6.9.3; MIM Software Inc.) to obtain an initial boundary of the primary tumor. The physician was informed explicitly about potential errors in this initial boundary and was thus advised to review this boundary carefully and make any modifications as needed. The task of segmenting the tumors in the whole dataset was split into multiple sessions to avoid reader fatigue. At the end of this process, we had expert-defined segmentations for the primary tumors in the 225 PET scans in our dataset.

### Consideration of Conventional Computer-Aided Image Segmentation Algorithms

Conventional computer-aided PET segmentation algorithms are typically categorized into those based on thresholding, boundary detection, and stochastic modeling (*4*). We selected the algorithms of $SUV_{max}$ thresholding ($SUV_{max}$40% and $SUV_{max}$50%) (*31*), Snakes (*32*), and Markov random field-Gaussian mixture model (MRF-GMM) (*33*) from each of those categories, respectively. A detailed description of these algorithms is provided in the supplemental materials (*31*–*33*).

### Consideration of DL-Based Image Segmentation Algorithm

We next considered the evaluation of a state-of-the-art U-net–based algorithm (*5*,*8*,*34*,*35*). A detailed description of the network architecture is provided in Supplemental Figure 1. When DL-based algorithms are developed and evaluated, common factors known to impact the performance include the choice of network depth (*36*), network width (*37*), loss function (*38*), and data preprocessing and augmentation strategies. In this study, we focused on investigating whether evaluating the impact of network depth and loss function using the task-agnostic FoMs yields inferences that are consistent with evaluation on the tasks of estimating MTV and TLG.

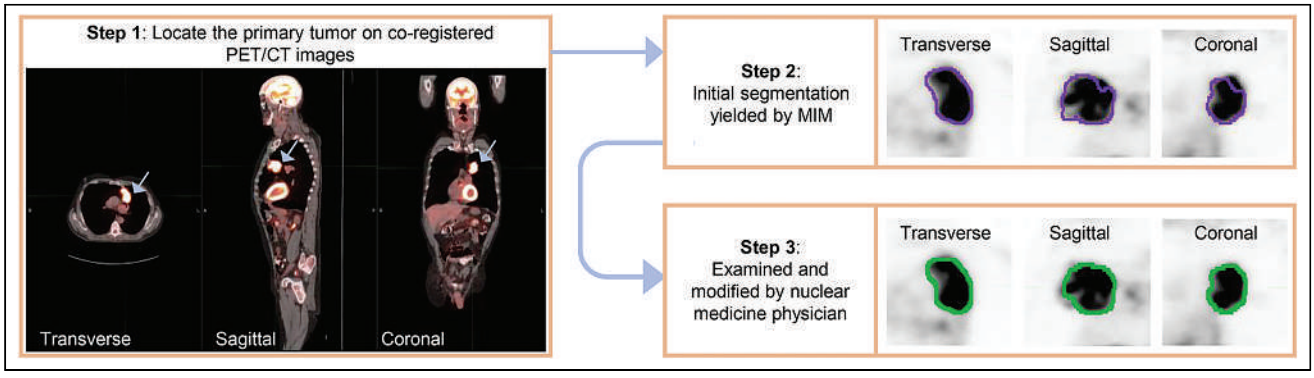


**FIGURE 1.** Workflow to obtain manual segmentation of primary tumor (arrow) for each patient. MIM = MIM Encore 6.9.3.

*Network Training.* The U-net–based algorithm was implemented to segment the primary tumor on 3-dimensional PET images on a per-slice basis. During training, 2-dimensional PET images of 180 patients with the corresponding surrogate ground truth (tumor delineations performed by the physician) were input into the U-net–based algorithm. The network was trained to minimize a loss function between the true and predicted segmentations using the Adam optimization method (*39*). The loss function will be specified in each experiment described below. Network hyperparameters, including parameters of activation function and dropout probability, were optimized via 5-fold cross-validation on the training dataset. The final optimized U-net–based algorithm was then evaluated on the remaining independent 45 patients from the same cohort. There was no overlap between the training and test sets.

*Configuring the U-Net–Based Algorithm with Different Network Depths.* We varied the network depth by setting the number of paired blocks of convolutional layers (supplemental materials) in the encoder and decoder to 2, 3, 4, and 5. The detailed network architecture that consisted of 2 paired blocks is provided in Supplemental Table 3. For each choice of depth, the network was trained to minimize a binary cross-entropy (BCE) loss between the true and predicted segmentations, denoted by $\boldsymbol{s}^t$ and $\boldsymbol{s}^p$, respectively. The number of voxels in the PET image is denoted by $N$. The BCE loss is given by

$$L_{\mathrm{BCE}}(\boldsymbol{s}^t,\ \boldsymbol{s}^p) = -\frac{1}{N}\sum_{n=1}^{N}[s_n^t \log s_n^p + (1-s_n^t)\log(1-s_n^p)]. \qquad \text{Eq. 1}$$

The network with each depth choice was independently trained and cross-validated on the training dataset. After training, each network was evaluated on the 45 test patients.

*Configuring the U-Net–Based Algorithm with Different Loss Functions.* A commonly used loss function in DL-based segmentation algorithms is the combined Dice and BCE loss, which leverages the flexibility of Dice loss for handling class-imbalance problems and the use of BCE loss for curve smoothing (*36*). In this loss function, the weight of BCE loss is controlled by a hyperparameter, denoted by λ. We investigated whether evaluating the impact of different values of λ on the performance of the U-net–based algorithm using the task-agnostic and task-based FoMs yields consistent interpretations.

The Dice loss is denoted by $L_{\mathrm{Dice}}$, such that

$$L_{\mathrm{Dice}}(\boldsymbol{s}^t,\ \boldsymbol{s}^p) = 1 - \frac{2\times\sum_{n=1}^{N} s_n^t s_n^p}{\sum_{n=1}^{N} s_n^t + \sum_{n=1}^{N} s_n^p}. \qquad \text{Eq. 2}$$

The combined Dice and BCE losses are defined as

$$L_{\mathrm{comb}}(\boldsymbol{s}^t,\ \boldsymbol{s}^p) = \lambda L_{\mathrm{BCE}} + (1-\lambda)L_{\mathrm{Dice}}, \qquad \text{Eq. 3}$$

where the term $L_{\mathrm{BCE}}$ is defined in Equation 1. In this experiment, we considered 6 different values of λ ranging from 0 to 1. We fixed the depth of the network by considering 3 paired blocks of convolutional layers in the encoder and decoder. For each value of λ, the network was independently trained and cross-validated on the same training dataset. Each trained network was then evaluated on the 45 test patients.

### Evaluation FoMs

*Task-Agnostic FoMs.* The widely used task-agnostic FoMs of DSC, JSC, and HD were used in this study. The DSC and JSC, as defined in Taha and Hanbury (*40*), measure the spatial overlap between the true and predicted segmentations. The values of both DSC and JSC lie between 0 and 1, and a higher value implies a more accurate performance. The HD quantifies the shape similarity between the true and predicted segmentations, and a lower value implies a more accurate performance. The values of DSC, JSC, and HD are reported as mean and 95% CI. Paired sample *t*-tests were performed to assess whether significant differences exist.

*Task-Based FoMs.* An essential criterion in validating algorithms to extract quantitative imaging metrics such as MTV and TLG is that the measurements obtained with the algorithm are accurate (*41*,*42*), because an algorithm that yields biased measurements would not correctly reflect the underlying pathophysiology. In a population, the bias can often vary on the basis of the true value and thus should be quantified over the entire measurable range of values to provide a more complete measure of accuracy (*43*). Ensemble normalized bias, defined as the bias averaged over the distribution of true values, helps address this issue and provides a summarized FoM for accuracy (*44*,*45*). This FoM was thus used in this study. Detailed definitions of the ensemble normalized bias are provided in the supplemental materials (*41*,*42*,*44*,*45*).

## RESULTS

### Evaluation of Conventional Computer-Aided Algorithms

Figures 2A and 2B present the quantitative assessment of conventional computer-aided segmentation algorithms over the 225

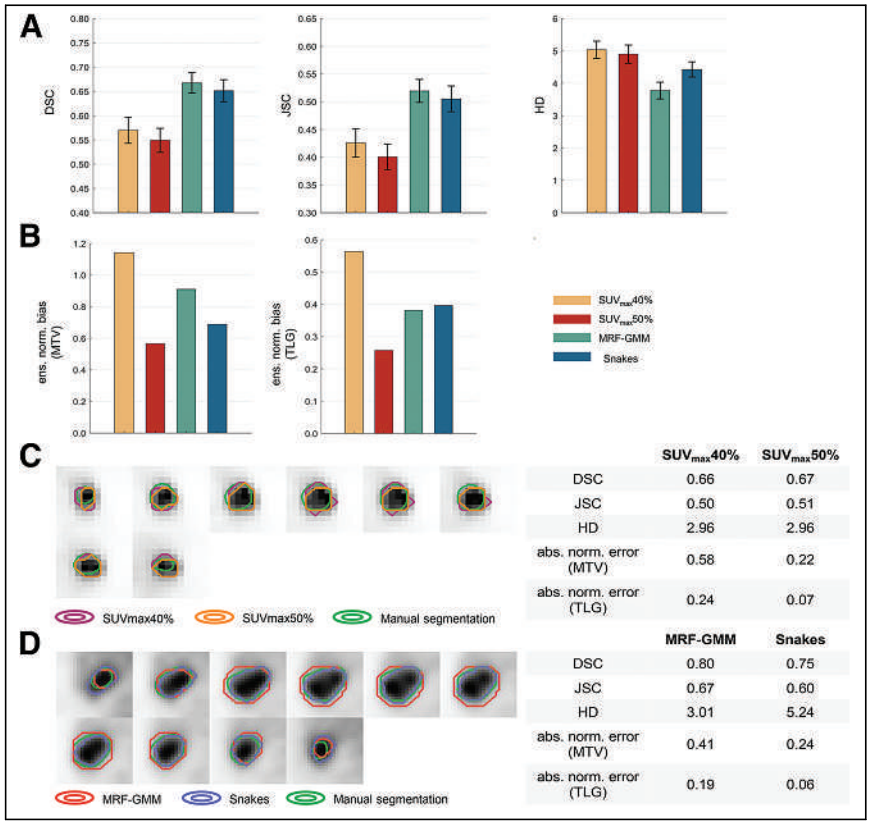


| | $SUV_{max}$40% | $SUV_{max}$50% |
|---|---|---|
| DSC | 0.66 | 0.67 |
| JSC | 0.50 | 0.51 |
| HD | 2.96 | 2.96 |
| abs. norm. error (MTV) | 0.58 | 0.22 |
| abs. norm. error (TLG) | 0.24 | 0.07 |

| | MRF-GMM | Snakes |
|---|---|---|
| DSC | 0.80 | 0.75 |
| JSC | 0.67 | 0.60 |
| HD | 3.01 | 5.24 |
| abs. norm. error (MTV) | 0.41 | 0.24 |
| abs. norm. error (TLG) | 0.19 | 0.06 |

**FIGURE 2.** Quantitative assessment of concordance in evaluation of considered conventional PET segmentation algorithms using task-agnostic FoMs of DSC, JSC, and HD (A) and on tasks of estimating MTV and TLG of primary tumor (B). Comparisons of segmentations yielded by $SUV_{max}$40% vs. $SUV_{max}$50% (C) and MRF-GMM vs. Snakes (D) were provided for 2 representative patients. ens. norm. = ensemble normalized; abs. norm. = absolute normalized.

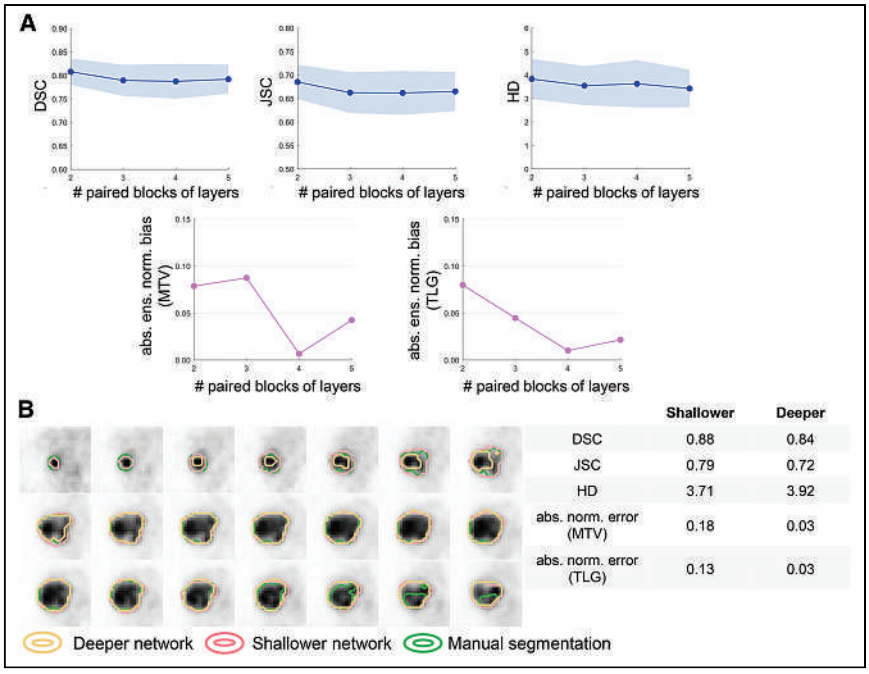


**FIGURE 3.** (A) Quantitative assessment of concordance between task-agnostic and task-based FoMs in evaluating impact of varying network depth on performance of U-net–based algorithm. (B) Comparison of segmentations yielded by deeper and shallower network for 1 representative test patient. abs. ens. norm. = absolute ensemble normalized; abs. norm. = absolute normalized.

patients using the task-agnostic and task-based FoMs. On the basis of DSC and JSC, $SUV_{max}40\%$ significantly outperformed $SUV_{max}50\%$ ($P < 0.05$). However, we observed that $SUV_{max}40\%$ yielded increased ensemble normalized bias in the estimated MTV and TLG of 51% and 54%, respectively, indicating a much less accurate performance on the clinically relevant quantitative tasks. Similarly, the MRF-GMM significantly outperformed Snakes on the basis of the DSC, JSC, and HD ($P < 0.05$) but revealed a 24% increased ensemble normalized bias in the estimated MTV.

Figure 2C shows the visual comparison of segmentations yielded by $SUV_{max}40\%$ versus $SUV_{max}50\%$ for a representative patient. We observed that both algorithms yielded very similar DSC, JSC, and HD values. However, $SUV_{max}40\%$ yielded substantially higher absolute normalized error (aNE) in the estimated MTV and TLG. For another representative patient shown in Figure 2D, the MRF-GMM yielded higher DSC and JSC and lower HD values. However, this algorithm yielded less accurate estimates of MTV and TLG, as indicated by the higher aNEs.

### Evaluating the U-Net–Based Algorithm

*Impact of Network Depth Choice.* Figure 3A shows the impact of varying network depth on the performance of the U-net–based algorithm, as evaluated using both the task-agnostic and the task-based FoMs on the 45 test patients. No significant difference was detected among any of the considered network depths on the basis of the DSC, JSC, and HD ($P < 0.05$). However, deeper networks yielded more accurate performance on the tasks of estimating MTV and TLG. Particularly, compared with the shallower network with 2 paired blocks of convolutional layers, the deeper network with 4 paired blocks yielded substantially lower absolute ensemble normalized bias in the estimated MTV and TLG, with a decrease of 91% and 87%, respectively. Segmentations of the shallower and deeper networks are shown for 1 representative test patient in Figure 3B. We observed that the deeper network yielded lower DSC and JSC and higher HD values but actually outperformed the shallower network on the tasks of estimating the MTV and TLG.

*Impact of Loss Function Choice.* Figure 4A shows the assessment of concordance between task-agnostic versus task-based FoMs in evaluating the impact of varying loss functions on the performance of the U-net–based algorithm. On the basis of the DSC, JSC, and HD, there was no significant difference among any values of the hyperparameter, λ. However, we observed substantial variations in the tasks of estimating MTV and TLG, with up to a 73% and 58% difference between the highest and lowest ensemble normalized bias in the estimated MTV and TLG, respectively. Figure 4B

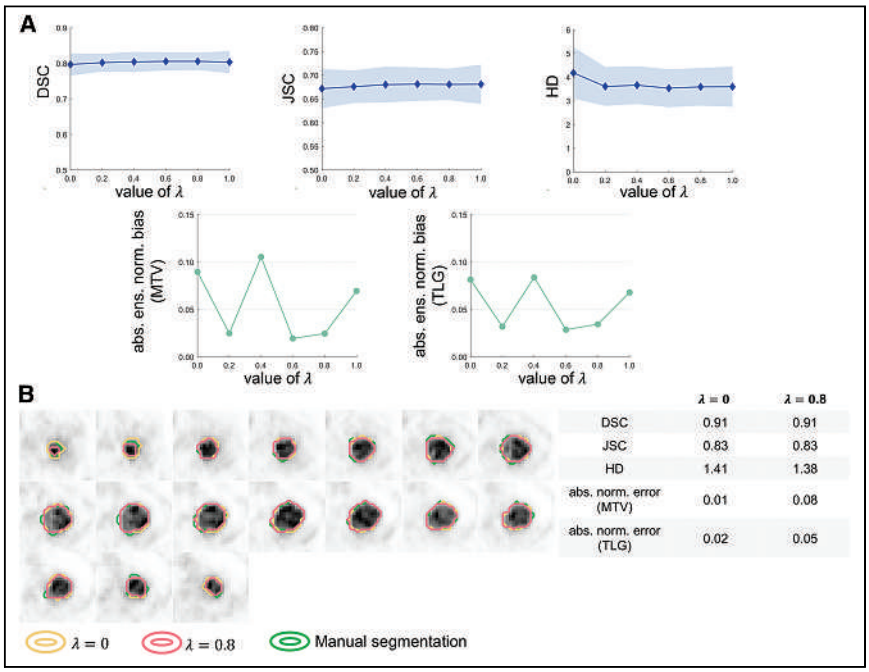


**FIGURE 4.** (A) Quantitative assessment of concordance between task-agnostic and task-based FoMs in evaluating impact of loss function on performance of U-net–based algorithm. (B) Comparison of segmentations yielded by U-net–based algorithm configured with 2 loss functions for 1 representative test patient. abs. ens. norm. = absolute ensemble normalized; abs. norm. = absolute normalized.

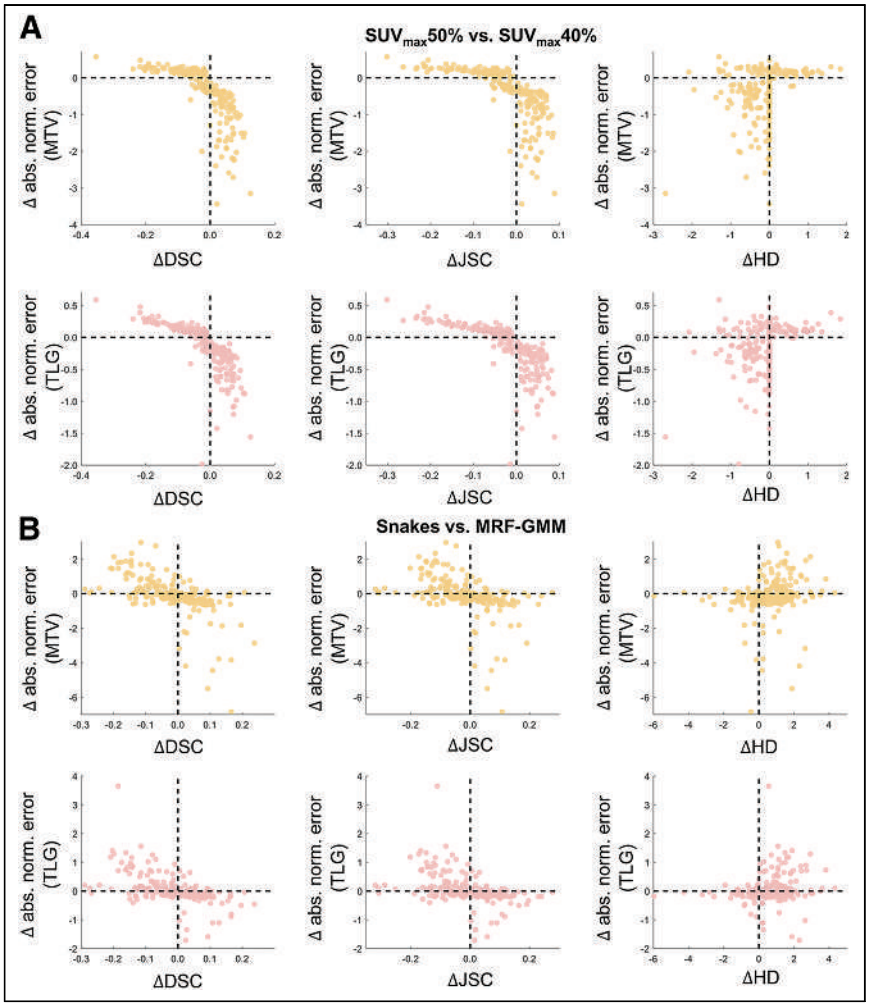


**FIGURE 5.** Quantitative assessment of concordance between interpretations obtained with task-agnostic vs. task-based FoMs on per-patient basis for considered computer-aided PET segmentation algorithms. Each point in scatter diagram represents individual patient. Horizontal position of each point indicates difference in DSC, JSC, and HD between $SUV_{max}50\%$ vs. $SUV_{max}40\%$ (A) and MRF-GMM vs. Snakes (B). Similarly, vertical position indicates difference in aNEs in estimated MTV and TLG. abs. norm. = absolute normalized.

compares the segmentations obtained with a λ of 0 versus a λ of 0.8 for a representative test patient. For this patient, whereas the values of DSC, JSC, and HD were similar, a λ of 0 yielded lower aNEs in the estimated MTV and TLG.

## DISCUSSION

Reliable performance on clinically relevant tasks is crucial for clinical translation of image segmentation algorithms. A key task for which image segmentation is often conducted in oncologic PET is quantifying features such as MTV and TLG. However, these segmentation algorithms are almost always evaluated using FoMs that are not explicitly designed to measure clinical task performance. In this study, we investigated whether evaluating PET segmentation algorithms with the widely used task-agnostic FoMs leads to interpretations that are consistent with evaluation on clinically relevant quantitative tasks.

Results from Figure 2 indicate that evaluation of conventional computer-aided PET segmentation algorithms based on task-agnostic FoMs of DSC, JSC, and HD could yield discordant interpretations compared with evaluation on the tasks of estimating MTV and TLG of the primary tumor. When evaluating the $SUV_{max}$ thresholding algorithm, initial inspection based on the task-agnostic FoMs implied that the intensity threshold of 40% $SUV_{max}$ yielded a significantly superior performance. However, further investigation showed that $SUV_{max}50\%$ provided substantially more accurate performance on estimating MTV and TLG. This discordance was also observed when comparing the MRF-GMM and Snake algorithms. Thus, these results demonstrate the limited ability of the DSC, JSC, and HD to evaluate image segmentation algorithms on clinically relevant tasks.

The limitation in task-agnostic FoMs was again observed in evaluating the impact of network depth and loss function on the performance of a state-of-the-art U-net–based image segmentation algorithm. In Figure 3, we observed initially that the deeper networks yielded DSC, JSC, and HD values statistically similar to those in the shallower networks. Considering the requirement for computational resources when training DL-based algorithms, this may motivate the deployment of shallower networks in clinical studies. However, our task-based evaluation showed that a deeper network yielded substantially higher accuracy in the estimated MTV and TLG. Similarly, we observed from Figure 4 that based on the task-agnostic FoMs, the performance of the U-net–based algorithm was insensitive to the choice of λ (the hyperparameter controlling the weight of BCE loss in the cost function). However, differences up to 73% and 58% could exist between the highest and lowest ensemble normalized bias in the estimated MTV and TLG, respectively.

To gain further insights into the observed discordance between task-agnostic and task-based FoMs, we performed secondary analyses on a per-patient basis. In Figure 5A, for each of the 225 patients, we first calculated the difference (Δ) in DSC, JSC, and HD between $SUV_{max}50\%$ and $SUV_{max}40\%$ (e.g., $\Delta DSC = DSC[SUV_{max}50\%] - [DSC[SUV_{max}40\%])$. Next, we obtained the difference in the aNE (supplemental materials; Eq. 2) in the estimated MTV and TLG (e.g., MTV $\Delta aNE$ = MTV $aNE[SUV_{max}50\%] - MTV\ aNE[SUV_{max}40\%]$). We then studied the relationship between ΔDSC (and ΔJSC and ΔHD) versus ΔMTV aNE (and ΔTLG aNE) via scatter diagrams. For 36 patients, a negative value of $\Delta DSC/\Delta JSC$ was observed, implying that $SUV_{max}50\%$ was inferior to $SUV_{max}40\%$. However, for these patients, $SUV_{max}50\%$ actually yielded better estimates of MTV, as indicated by the lower aNEs. Similarly, it was observed that interpretations obtained with ΔHD could be discordant with those based on ΔMTV aNE/ΔTLG aNE. Additionally, even for minor changes in DSC, JSC, and HD (i.e., $\Delta DSC/\Delta JSC/\Delta HD \approx 0$; close to the vertical dashed line in the scatter diagram), we observed substantial variations in the ΔMTV aNE/ΔTLG aNE values. This indicates

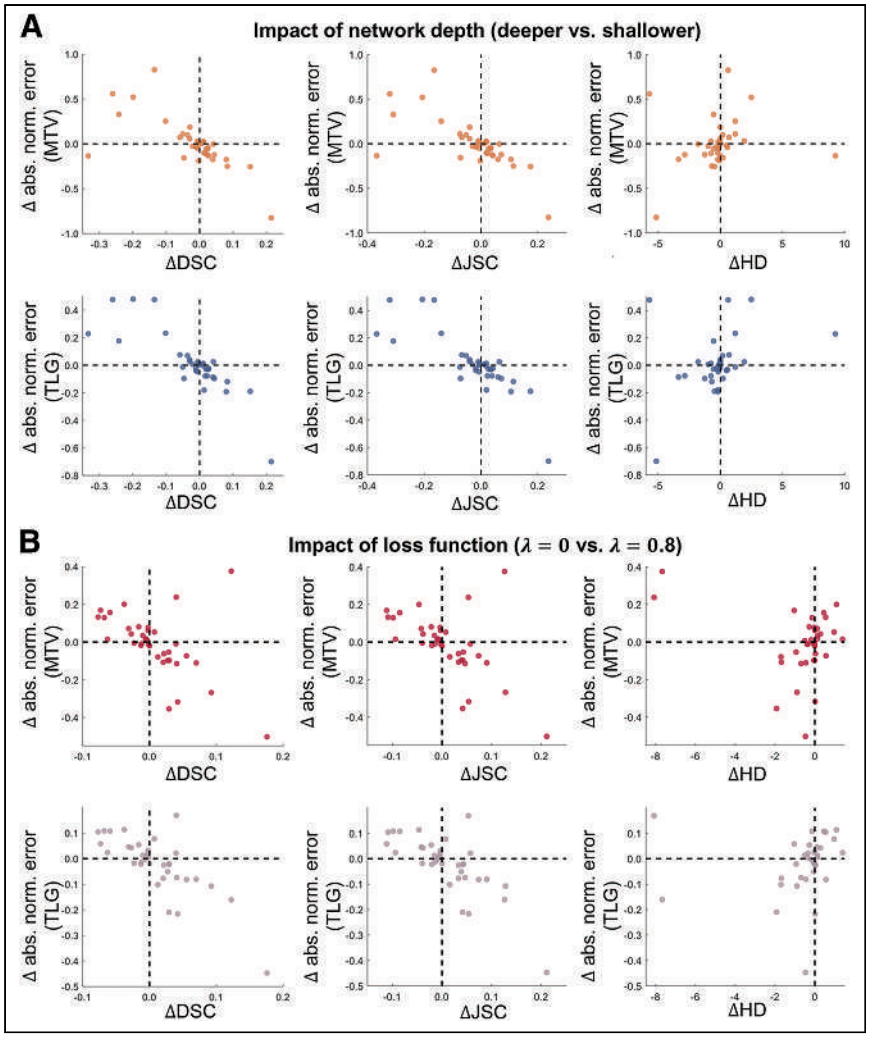


**FIGURE 6.** Quantitative assessment of concordance between interpretations obtained with task-agnostic vs. task-based FoMs on per-patient basis when evaluating impact of network depth (A) and loss function (B) on performance of U-net–based algorithm. abs. norm. = absolute normalized.

that these task-agnostic FoMs could be insensitive to even dramatic changes in quantitative task performance. This trend was again observed when comparing MRF-GMM versus Snakes (Fig. 5B) and evaluating the impact of network depth and loss function on the performance of the U-net–based algorithm (Fig. 6).

The findings of this study are not meant to suggest that the task-agnostic metrics, including the DSC, JSC, and HD, are not helpful. In fact, initial development of segmentation algorithms may not be associated with a specific task, and thus, task-agnostic FoMs are valuable for assessing the promise of these algorithms. However, for clinical application, it is important to further assess the performance of these algorithms on clinical tasks for which imaging is performed, as also emphasized in the best practices for evaluation of artificial intelligence algorithms for nuclear medicine (RELAINCE guidelines) (*44*). Results from our study further confirm the need for this task-based evaluation.

Our task-based evaluation focused on assessing the accuracy of image segmentation algorithms in quantifying features from PET images. In clinical studies, other criteria to evaluate the quantification performance could include precision, when repeatability or reproducibility are required for clinical decision-making. When the segmentation is required for radiotherapy planning, the relevant criterion is therapeutic efficacy—for example, the task of improving the probability of tumor control while minimizing the chances of normal-tissue complications. For this task, Barrett et al. proposed the use of an area under the therapy operating characteristic curve (*46*) for evaluating the segmentation algorithms. In all of these evaluation studies, clinicians (radiologists, nuclear medicine physicians, and disease specialists) have a crucial role in defining the clinically most relevant task and corresponding FoMs for the evaluation of image segmentation algorithms (*11*).

Evaluating PET segmentation algorithms on quantification tasks required knowledge of true quantitative values of interest. However, such ground truth is often unavailable in clinical studies. To circumvent this challenge, we considered quantitative values obtained using expert human-reader–defined manual delineations as surrogate ground truth. However, we recognize that this surrogate may be erroneous. To address the issue of a lack of ground truth in task-based evaluation of quantitative imaging algorithms, no-gold-standard evaluation techniques have been developed (*47–50*). These techniques have demonstrated promise in evaluating PET segmentation algorithms on clinically relevant quantitative tasks (*51–53*). As these techniques are validated further, they could provide a mechanism to perform objective task-based evaluation of segmentation algorithms with patient data. The findings from this study motivate further development and validation of these no-gold-standard evaluation techniques.

Other limitations of this study include the fact that the PET scanners used in the ACRIN 6668/RTOG 0235 multicenter clinical trial were relatively old and did not have time-of-flight capability. Thus, these scanners could yield substantially lower effective sensitivity compared with modern PET scanners. Conducting the proposed study with newer-generation scanners could provide further insights into the potential discordance between task-agnostic and task-based FoMs with more modern technologies. Additionally, the U-net–based algorithm was trained to segment tumors on a per-slice basis. As shown by Leung et al. (*5*), this strategy helped alleviate the requirement for large amounts of training data and the demand for computational resources. Results from this study motivate expanding the evaluation of 3-dimensional fully automated DL-based algorithms.

As a final remark, the purpose of this study was not to compare DL-based algorithms with conventional computer-aided algorithms. Although we observed that the considered U-net–based algorithm yielded substantially improved performance compared with conventional algorithms based on the task-agnostic and task-based metrics, this study does not intend to suggest that DL-based algorithms are preferable over conventional algorithms.

## CONCLUSION

Our retrospective analysis with the ACRIN 6668/RTOG 0235 multicenter clinical trial data shows that evaluation of PET segmentation algorithms based on widely used task-agnostic FoMs could lead to findings that are discordant with evaluation on clinically relevant quantitative tasks. The results emphasize the important need for objective task-based evaluation of image segmentation algorithms for quantitative PET.

## DISCLOSURE

This work was supported by the National Institute of Biomedical Imaging and Bioengineering through R01-EB031051, R01-EB031962, R56-EB028287, and R21-EB024647 (Trailblazer Award). No other potential conflict of interest relevant to this article was reported.

**KEY POINTS**

**QUESTION:** Are widely used metrics such as DSC, JSC, and HD sufficient to evaluate image segmentation algorithms for their clinical applications?

**PERTINENT FINDINGS:** Our retrospective analysis with the ACRIN 6668/RTOG 0235 multicenter clinical trial data shows that evaluating PET segmentation algorithms on the basis of the DSC, JSC, and HD FoMs could lead to interpretations that are discordant with evaluation on the clinically relevant quantitative tasks of estimating the MTV and TLG of primary tumors in patients with non–small cell lung cancer.

**IMPLICATIONS FOR PATIENT CARE:** Objective task-based evaluation of new and improved image segmentation algorithms is important for their clinical application.

## REFERENCES

1. Chen HH, Chiu N-T, Su W-C, Guo H-R, Lee B-F. Prognostic value of whole-body total lesion glycolysis at pretreatment FDG PET/CT in non–small cell lung cancer. *Radiology.* 2012;264:559–566.
2. Mena E, Sheikhbahaei S, Taghipour M, et al. $^{18}$F-FDG PET/CT metabolic tumor volume and intratumoral heterogeneity in pancreatic adenocarcinomas: impact of dual-time point and segmentation methods. *Clin Nucl Med.* 2017;42:e16.
3. Ohri N, Duan F, Machtay M, et al. Pretreatment FDG-PET metrics in stage III non–small cell lung cancer: ACRIN 6668/RTOG 0235. *J Natl Cancer Inst.* 2015; 107:djv004.
4. Foster B, Bagci U, Mansoor A, Xu Z, Mollura DJ. A review on segmentation of positron emission tomography images. *Comput Biol Med.* 2014;50:76–96.
5. Leung KH, Marashdeh W, Wray R, et al. A physics-guided modular deep-learning based automated framework for tumor segmentation in PET. *Phys Med Biol.* 2020; 65:245032.
6. Liu Z, Mhlanga JC, Laforest R, Derenoncourt P-R, Siegel BA, Jha AK. A Bayesian approach to tissue-fraction estimation for oncological PET segmentation. *Phys Med Biol.* 2021;66:124002.
7. Yousefirizi F, Jha AK, Brosch-Lenz J, Saboury B, Rahmim A. Toward high-throughput artificial intelligence-based segmentation in oncological PET imaging. *PET Clin.* 2021;16:577–596.
8. Zhao X, Li L, Lu W, Tan S. Tumor co-segmentation in PET/CT using multi-modality fully convolutional neural network. *Phys Med Biol.* 2018;64:015011.
9. Barrett HH, Abbey CK, Clarkson E. Objective assessment of image quality: III—ROC metrics, ideal observers, and likelihood-generating functions. *J Opt Soc Am A Opt Image Sci Vis.* 1998;15:1520–1535.
10. Barrett HH, Denny J, Wagner RF, Myers KJ. Objective assessment of image quality: II—Fisher information, Fourier crosstalk, and figures of merit for task performance. *J Opt Soc Am A Opt Image Sci Vis.* 1995;12:834–852.
11. Jha AK, Myers KJ, Obuchowski NA, et al. Objective task-based evaluation of artificial intelligence-based medical imaging methods: framework, strategies, and role of the physician. *PET Clin.* 2021;16:493–511.
12. Barrett HH, Myers KJ, Hoeschen C, Kupinski MA, Little MP. Task-based measures of image quality and their relation to radiation dose and patient risk. *Phys Med Biol.* 2015;60:R1.
13. Badal A, Cha KH, Divel SE, Graff CG, Zeng R, Badano A. Virtual clinical trial for task-based evaluation of a deep learning synthetic mammography algorithm. SPIE Digital Library website. https://doi.org/10.1117/12.2513062. Published March 7, 2019. Accessed January 12, 2024.
14. Pretorius PH, Liu J, Kalluri KS, et al. Observer studies of image quality of denoising reduced-count cardiac single photon emission computed tomography myocardial perfusion imaging by three-dimensional Gaussian post-reconstruction filtering and deep learning. *J Nucl Cardiol.* 2023;30:2427–2437.
15. Li K, Zhou W, Li H, Anastasio MA. Assessing the impact of deep neural network-based image denoising on binary signal detection tasks. *IEEE Trans Med Imaging.* 2021;40:2295–2305.
16. Prabhat K, Zeng R, Farhangi MM, Myers KJ. Deep neural networks-based denoising models for CT imaging and their efficacy. SPIE Digital Library website. https://doi.org/10.1117/12.2581418. Published February 15, 2021. Accessed January 12, 2024.
17. Yu Z, Rahman MA, Laforest R, et al. Need for objective task-based evaluation of deep learning-based denoising methods: a study in the context of myocardial perfusion SPECT. *Med Phys.* 2023;50:4122–4137.
18. Jha AK, Rodríguez JJ, Stephen RM, Stopeck AT. A clustering algorithm for liver lesion segmentation of diffusion-weighted MR images. *Proc IEEE.* 2010;2010:93–96.
19. Oreiller V, Andrearczyk V, Jreige M, et al. Head and neck tumor segmentation in PET/CT: the HECKTOR challenge. *Med Image Anal.* 2022;77:102336.
20. Song Q, Bai J, Han D, et al. Optimal co-segmentation of tumor in PET-CT images with context information. *IEEE Trans Med Imaging.* 2013;32:1685–1697.
21. Kofler F, Ezhov I, Isensee F, et al. Are we using appropriate segmentation metrics? Identifying correlates of human expert perception for CNN training beyond rolling the DICE coefficient. arXiv website. https://arxiv.org/abs/2103.06205. Published March 10, 2021. Accessed January 12, 2024.
22. Kinahan P, Muzi M, Bialecki B, Herman B, Coombs L. ACRIN 6668 (ACRIN-NSCLC-FDG-PET). Cancer Imaging Archive website. https://wiki.cancerimagingarchive.net/pages/viewpage.action?pageId=39879162. Modified November 27, 2023. Accessed January 12, 2024.
23. Machtay M, Duan F, Siegel BA, et al. Prediction of survival by [$^{18}$F]fluorodeoxyglucose positron emission tomography in patients with locally advanced non–small-cell lung cancer undergoing definitive chemoradiation therapy: results of the ACRIN 6668/RTOG 0235 trial. *J Clin Oncol.* 2013;31:3823.
24. Cremonesi M, Gilardi L, Ferrari ME, et al. Role of interim $^{18}$F-FDG-PET/CT for the early prediction of clinical outcomes of non–small cell lung cancer (NSCLC) during radiotherapy or chemo-radiotherapy: a systematic review. *Eur J Nucl Med Mol Imaging.* 2017;44:1915–1927.
25. Sheikhbahaei S, Mena E, Yanamadala A, et al. The value of FDG PET/CT in treatment response assessment, follow-up, and surveillance of lung cancer. *AJR.* 2017; 208:420–433.
26. Hyun SH, Ahn HK, Kim H, et al. Volume-based assessment by $^{18}$F-FDG PET/CT predicts survival in patients with stage III non-small-cell lung cancer. *Eur J Nucl Med Mol Imaging.* 2014;41:50–58.
27. Im H-J, Pak K, Cheon GJ, et al. Prognostic value of volumetric parameters of $^{18}$F-FDG PET in non-small-cell lung cancer: a meta-analysis. *Eur J Nucl Med Mol Imaging.* 2015;42:241–251.
28. Liu Z, Mhlanga JC, Siegel BA, Jha AK. Need for objective task-based evaluation of AI-based segmentation methods for quantitative PET. *Medical Imaging 2023: Image Perception, Observer Performance, and Technology Assessment.* SPIE;12467: 194–201.
29. Clark K, Vendt B, Smith K, et al. The Cancer Imaging Archive (TCIA): maintaining and operating a public information repository. *J Digit Imaging.* 2013; 26:1045–1057.
30. Scheuermann JS, Saffer JR, Karp JS, Levering AM, Siegel BA. Qualification of PET scanners for use in multicenter cancer clinical trials: the American College of Radiology Imaging Network experience. *J Nucl Med.* 2009;50:1187–1193.
31. Sridhar P, Mercier G, Tan J, Truong MT, Daly B, Subramaniam RM. FDG PET metabolic tumor volume segmentation and pathologic volume of primary human solid tumors. *AJR.* 2014;202:1114–1119.
32. Kass M, Witkin A, Terzopoulos D. Snakes: active contour models. *Int J Comput Vis.* 1988;1:321–331.
33. Layer T, Blaickner M, Knäusl B, et al. PET image segmentation using a Gaussian mixture model and Markov random fields. *EJNMMI Phys.* 2015;2:9.
34. Blanc-Durand P, Van Der Gucht A, Schaefer N, Itti E, Prior JO. Automatic lesion detection and segmentation of $^{18}$F-FET PET in gliomas: a full 3D U-Net convolutional neural network study. *PLoS One.* 2018;13:e0195798.

35. Ronneberger O, Fischer P, Brox T. U-net: convolutional networks for biomedical image segmentation. *Medical Image Computing and Computer-Assisted Intervention–MICCAI 2015: 18th International Conference*; Munich, Germany, October 5–9, 2015. Springer International Publishing: 234–241.
36. Jadon S. A survey of loss functions for semantic segmentation. IEEE Xplore website. https://ieeexplore.ieee.org/document/9277638. Published December 7, 2020. Accessed January 12, 2024.
37. Isensee F, Jaeger PF, Kohl SA, Petersen J, Maier-Hein KH. nnU-Net: a self-configuring method for deep learning-based biomedical image segmentation. *Nat Methods.* 2021;18:203–211.
38. Sun S, Chen W, Wang L, Liu X, Liu T-Y. On the depth of deep neural networks: a theoretical view. arXiv website. https://arxiv.org/abs/1506.05232. Published June 17, 2015. Accessed January 17, 2024.
39. Kingma DP, Ba J. Adam: a method for stochastic optimization. arXiv website. https://arxiv.org/abs/1412.6980. Published December 22, 2014. Accessed January 10, 2024.
40. Taha AA, Hanbury A. Metrics for evaluating 3D medical image segmentation: analysis, selection, and tool. *BMC Med Imaging.* 2015;15:29.
41. Prescott JW. Quantitative imaging biomarkers: the application of advanced image processing and analysis to clinical and preclinical decision making. *J Digit Imaging.* 2013;26:97–108.
42. Rosenkrantz AB, Mendiratta-Lala M, Bartholmai BJ, et al. Clinical utility of quantitative imaging. *Acad Radiol.* 2015;22:33–49.
43. Raunig DL, McShane LM, Pennello G, et al. Quantitative imaging biomarkers: a review of statistical methods for technical performance assessment. *Stat Methods Med Res.* 2015;24:27–67.
44. Jha AK, Bradshaw TJ, Buvat I, et al. Nuclear medicine and artificial intelligence: best practices for evaluation (the RELAINCE guidelines). *J Nucl Med.* 2022;63:1288–1299.
45. Barrett HH, Myers KJ., eds. *Foundations of Image Science.* John Wiley & Sons; 2013:875–877.
46. Barrett HH, Wilson DW, Kupinski MA, et al. Therapy operating characteristic (TOC) curves and their application to the evaluation of segmentation algorithms. *Proc SPIE Int Soc Opt Eng.* 2010:76270z.
47. Hoppin JW, Kupinski MA, Kastis GA, Clarkson E, Barrett HH. Objective comparison of quantitative imaging modalities without the use of a gold standard. *IEEE Trans Med Imaging.* 2002;21:441–449.
48. Jha AK, Caffo B, Frey EC. A no-gold-standard technique for objective assessment of quantitative nuclear-medicine imaging methods. *Phys Med Biol.* 2016;61:2780.
49. Kupinski MA, Hoppin JW, Clarkson E, Barrett HH, Kastis GA. Estimation in medical imaging without a gold standard. *Acad Radiol.* 2002;9:290–297.
50. Liu Z, Li Z, Mhlanga JC, Siegel BA, Jha AK. No-gold-standard evaluation of quantitative imaging methods in the presence of correlated noise. *Proc SPIE Int Soc Opt Eng.* 2022:120350M.
51. Jha AK, Mena E, Caffo BS, et al. Practical no-gold-standard evaluation framework for quantitative imaging methods: application to lesion segmentation in positron emission tomography. *J Med Imaging (Bellingham).* 2017;4:011011.
52. Liu J, Liu Z, Moon HS, Mhlanga J, Jha A. A no-gold-standard technique for objective evaluation of quantitative nuclear-medicine imaging methods in the presence of correlated noise [abstract]. *J Nucl Med.* 2020;61(suppl 1):523.
53. Zhu Y, Yousefirizi F, Liu Z, Klyuzhin I, Rahmim A, Jha A. Comparing clinical evaluation of PET segmentation methods with reference-based metrics and no-gold-standard evaluation technique [abstract]. *J Nucl Med.* 2021;62(suppl 1):1430.

# $CCK_2$ Receptor–Targeted PET/CT in Medullary Thyroid Cancer Using [$^{68}$Ga]Ga-DOTA-CCK-66

Oliver Viering[1], Thomas Günther[2], Nadine Holzleitner[2], Alexander Dierks[1], Georgine Wienand[1], Christian H. Pfob[1], Ralph A. Bundschuh[1], Hans-Jürgen Wester[2], Johanna S. Enke[1], Malte Kircher[1], and Constantin Lapa[1]

[1]*Nuclear Medicine, Faculty of Medicine, University of Augsburg, Augsburg, Germany; and* [2]*Department of Chemistry, Chair of Pharmaceutical Radiochemistry, TUM School of Natural Sciences, Technical University of Munich, Garching, Germany*

Medullary thyroid cancer (MTC), a neuroendocrine tumor arising from the parafollicular cells of the thyroid gland, accounts for approximately 1%–2% of all thyroid cancers (*1*). Only recently was cholecystokinin-2 receptor ($CCK_2R$) identified as a suitable target for PET/CT imaging of MTC (*2,3*).

We report on a 74-y-old man with a history of locally advanced MTC who had undergone tumor debulking including a hemithyroidectomy and lymph node dissection on the right side. Informed consent was obtained from the patient, and the project was approved by the institutional ethics committee of Ludwig-Maximilians-Universität München, Munich, Germany (permit 23-0627).

Postoperative [$^{18}$F]F-3,4-dihydroxyphenylalanine (DOPA) PET/CT detected residual local tumor as well as cervical and upper mediastinal lymph node metastases, prompting additional external-beam radiotherapy. After treatment, serum calcitonin levels decreased (from 5,300 to 720 pg/mL) but remained significantly elevated. Thus, another restaging with [$^{18}$F]F-DOPA PET/CT (201 MBq) was performed.

To assess the possibility of $CCK_2R$-directed radioligand therapy, the patient additionally underwent PET/CT with [$^{68}$Ga]Ga-DOTA-CCK-66 (150 MBq; time interval between scans, 16 d), a novel $CCK_2R$-directed tracer. It was well tolerated and demonstrated a favorable biodistribution with only physiologic uptake in the stomach and renal tracer excretion. In concordance with [$^{18}$F]F-DOPA, [$^{68}$Ga]Ga-DOTA-CCK-66 detected an identical number of MTC lesions composing the still viable local tumor ($SUV_{max}$ of 7.4, vs. 7.0 for [$^{18}$F]F-DOPA), as well as multiple

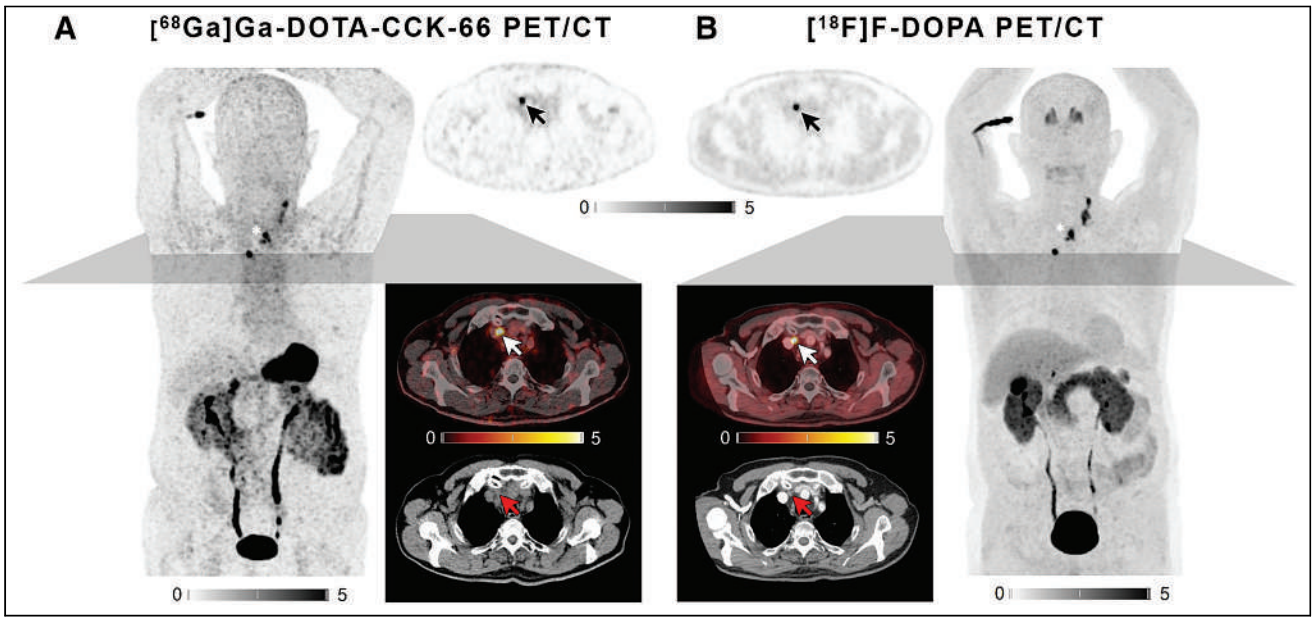


**FIGURE 1.** Maximum-intensity projections and axial sections of [$^{68}$Ga]Ga-DOTA-CCK-66 (A) and [$^{18}$F]F-DOPA (B) PET/CT. White stars indicate local tumor in left thyroid bed. Arrows indicate lymph node metastasis in right upper mediastinum. Intensity scale bars are SUV.

Received Jul. 17, 2023; revision accepted Oct. 10, 2023.
For correspondence or reprints, contact Constantin Lapa (constantin.lapa@uk-augsburg.de).
Published online Nov. 2, 2023.

DOI: 10.2967/jnumed.123.266380

cervical and mediastinal lymph node metastases ($SUV_{max}$ of 9.5, vs. 8.7 for [$^{18}$F]F-DOPA) (Fig. 1).

$CCK_2R$-directed PET imaging with [$^{68}$Ga]Ga-DOTA-CCK-66 is feasible. Given the possibility of receptor-directed radioligand therapy using its $^{177}$Lu- or $^{225}$Ac-labeled analog, this new compound might prove a valuable addition to the theranostic armamentarium in MTC. Further research with a special focus on kidney doses, which have been a relevant issue for therapeutic $CCK_2R$ ligands regarding the amount of administered activity, is warranted.

## DISCLOSURE

A patent application on $CCK_2R$-targeted compounds was filed by Thomas Günther, Nadine Holzleitner, Hans-Jürgen Wester, and Constantin Lapa. No other potential conflict of interest relevant to this article was reported.

## REFERENCES


1. Wells SA Jr, Asa SL, Dralle H, et al. Revised American Thyroid Association guidelines for the management of medullary thyroid carcinoma. *Thyroid.* 2015; 25:567–610.
2. Reubi JC, Waser B. Unexpected high incidence of cholecystokinin-B/gastrin receptors in human medullary thyroid carcinomas. *Int J Cancer.* 1996;67:644–647.
3. von Guggenberg E, Kolenc P, Rottenburger C, Mikolajczak R, Hubalewska-Dydejczyk A. Update on preclinical development and clinical translation of cholecystokinin-2 receptor targeting radiopharmaceuticals. *Cancers (Basel).* 2021; 13:5776.

## Commentary on "Radioactive Iodine: A Living History"

**TO THE EDITOR:** An article was recently published in *Thyroid* to commemorate the discovery and use of radioiodine for the management of patients with thyroid disease (*1*). Although "Radioactive Iodine: A Living History" is overall an excellent review, there are some errors of fact in the historical record that we would like to correct. The reason for these errors is unclear, as is the reason the editors of the journal did not feel the need to correct them or provide an erratum. When selling great art, it is important to know the provenance of that art. Ideally, you want a paper trail from the artist to the present owner. In medicine, that provenance is normally provided by a series of published papers available on search engines such as PubMed. However, the attestation of a particular idea may not be fully provided in scientific papers alone. Thus, to identify the provenance of radioiodine and ensure the correct attestation of ideas, it may be necessary to look at sources other than just published papers. We now have access to primary-source verification. In the case of the discovery and development of radioiodine in thyroid disease by Saul Hertz, one must look at Hertz's correspondence with other important players, such as Karl Compton, James Means, and the Markle Foundation. Fortunately, Hertz's daughter has already done much of this work, which was published in an article in the *World Journal of Nuclear Medicine* (*2*). However, when the primary-source data are consulted, it is evident that the article contains several factual errors, particularly in the attestation of the genesis and implementation of the use of radioiodine. In this letter, we aim to identify and correct these errors.

The first use of $^{131}$I to treat hyperthyroidism (Graves disease) was on March 31, 1941, not in January 1941. In honor of this first radioiodine therapy, we now celebrate Saul Hertz World Theranostics Day on March 31 (*2*).

On Nov. 12, 1936, Karl Compton, president of the Massachusetts Institute of Technology, presented a guest lecture entitled, "What Physics Can Do for Biology and Medicine," as part of a weekly luncheon lecture series at the Massachusetts General Hospital. At the end of the lecture, Saul Hertz solely conceived and spontaneously asked the seminal question "Could iodine be made radioactive artificially?" Compton was uncertain and said he would look into it. He wrote to Hertz on December 15, 1936, apologizing for the delayed response and replying that "Iodine can be made artificially radioactive." In fact, Enrico Fermi had produced $^{128}$I in 1934. Letters between Hertz and Compton make it clear that the idea of using radioactive isotopes to study metabolism came from Hertz (*2–5*). The fact that it was solely Hertz who conceived and asked the question was confirmed by James Means, chief of medicine at the Massachusetts General Hospital, in a letter to the Markle Foundation (Fig. 3 in (*3*)) in which he stated " … when it became apparent that there might be radioactive isotopes of iodine, it at once occurred to Hertz that we might make use of them to solve a problem we were already working on."

The summary at the beginning of the article in *Thyroid* states, "In 1936, Karl Compton … in a lecture attended by Massachusetts General Hospital physicians, suggested that artificially radioactive isotopes might be useful for studying metabolism." (*1*). On page 2, it is stated that Robley Evans suggested discussing "artificially radioactive isotopes" and their potential for studying metabolism. We think it highly unlikely that either Evans or Compton, who were physicists, made that suggestion. This idea actually was conceived by Hertz.

The *Thyroid* article erroneously states, "Hertz and Evans demonstrated uptake of iodine in rabbit thyroids … " (*1*). However, the evidence supports that it was Hertz and Roberts who demonstrated uptake of iodine in rabbit thyroids (*4*,*5*). Actually, Evans, who was chief of medical physics at the Massachusetts Institute of Technology, never participated in any of the studies, according to a letter by Arthur Roberts to John Stanbury in 1991 (*6*). However, Evans demanded credit (i.e., as a coauthor) because of his supervisory position.

### REFERENCES


1. Daniels GH, Ross DS. Radioactive iodine: a living history. *Thyroid.* 2023;33: 666–673.
2. Hertz B. A tribute to Dr. Saul Hertz: the discovery of the medical uses of radioiodine. *World J Nucl Med.* 2019;18:8–12.
3. Hertz B. Dr. Saul Hertz (1905–1950) discovers the medical uses of radioactive iodine: the first targeted cancer therapy. In: Ahmadzadehfar H, ed. *Thyroid Cancer: Advances in Diagnosis and Therapy.* IntechOpen; 2016:1–14.
4. Fahey FH, Grant FD, Thrall JH. Saul Hertz, MD, and the birth of radionuclide therapy. *EJNMMI Phys.* 2017;4:15.
5. Fahey FH, Grant FD. Celebrating eighty years of radionuclide therapy and the work of Saul Hertz. *J Appl Clin Med Phys.* 2021;22:4–10.
6. Obaldo JM, Hertz BE. The early years of nuclear medicine: a retelling. *Asia Ocean J Nucl Med Biol.* 2021;9:207–219.



**Bennett S. Greenspan***
**Michael S. Hofman**
**John Buscombe**
**Augusta VA Medical Center*
*Augusta, Georgia*
*E-mail: bengreenspan0708@gmail.com*



Published online Jan. 4, 2024.
DOI: 10.2967/jnumed.123.267016


## [$^{18}$F]FDG and Lymphomas: Still a Winning Golden Couple in the Era of FAPI-Based Radiotracers

**TO THE EDITOR:** We were greatly intrigued by the article titled "Fibroblast Activation Protein and Glycolysis in Lymphoma Diagnosis: Comparison of $^{68}$Ga-FAPI PET/CT and $^{18}$F-FDG PET/CT" by Chen et al. in *The Journal of Nuclear Medicine* (*1*). This article highlights the distinctive and well-established role of [$^{18}$F]FDG PET/CT in the management of lymphoma patients for determining disease extent, prognosis, and treatment response as exemplified by the Deauville score. In lymphoma patients, the superiority of [$^{18}$F]FDG over fibroblast activation protein inhibitor (FAPI)–based tracers, a new class of radiopharmaceuticals that have otherwise shown higher diagnostic performance than [$^{18}$F]FDG in various oncologic settings (*2*), raises important questions.

The paper's results are thought-provoking, particularly considering the crucial role of the tumor microenvironment in lymphoma survival and growth (*3*). Notably, there has already been significant uptake of FAPI-based agents targeting the tumor microenvironment in lymphoma (*4*). In the study by Chen et al. (*1*), immunohistochemistry analysis revealed significantly lower fibroblast activation protein expression cell densities than hexokinase 2 and glucose transporter 1 in most lymphoma subtypes ($P < 0.001$).

Although [$^{18}$F]FDG PET/CT plays a pivotal role in lymphoma management, a gray zone exists in which its diagnostic performance declines, notably in cases of indolent lymphomas or those with low [$^{18}$F]FDG avidity. It is intriguing to explore whether a FAPI-based radiotracer could complement or serve as an alternative to [$^{18}$F]FDG for these specific lymphoma subtypes. However, Chen et al. (*1*) did not thoroughly address this aspect, mainly because of the limited number of patients with indolent or low-avidity lymphomas. Additionally, their patient population is highly heterogeneous, encompassing various histopathologic patterns and clinical settings for the examinations. To address this limitation, a prospective study with a homogeneous group of patients and a well-defined study design would be desirable.

Another crucial consideration is the evolving landscape of lymphoma treatment. The current standard of care is chemoimmunotherapy, with salvage high-dose chemotherapy and autologous stem cell transplantation serving as the second-line treatments for patients with relapsed or refractory lymphomas (*5*). However, only a few patients achieve a cure with this intensive approach, and its applicability is restricted by comorbidities and advanced age (*6*). Recent advancements in immunotherapy involve CD19 chimeric antigen receptor T cells, which are autologous T cells genetically reengineered and approved for the treatment of relapsed or refractory aggressive B-cell lymphomas (*7*). Nonetheless, despite the high efficacy of chimeric antigen receptor T-cell therapy, a significant number of patients do not respond or experience relapses (*8*). In this context, FAPI-based radiotracers could be explored in a theranostic context, addressing the molecular target with appropriately radiolabeled agents, similar to current practices in the treatment of neuroendocrine tumors and prostate cancer. However, the role of the FAPI agent in refractory lymphoma patients still remains unexplored.

In conclusion, there is still much to discover regarding the role of FAPI-based radiotracers in hematology. We eagerly await the availability of commercially accessible radiopharmaceuticals to explore the advantages and potential limitations of this class of agents in various clinical settings, laying the foundation for innovative cancer monitoring strategies.

## REFERENCES


1. Chen X, Wang S, Lai Y, et al. Fibroblast activation protein and glycolysis in lymphoma diagnosis: comparison of $^{68}$Ga-FAPI PET/CT and $^{18}$F-FDG PET/CT. *J Nucl Med.* 2023;64:1399–1405.
2. Guglielmo P, Alongi P, Baratto L, et al. Head-to-head comparison of FDG and radiolabeled FAPI PET: a systematic review of the literature. *Life (Basel).* 2023;13:1821.
3. Opinto G, Vegliante MC, Negri A, et al. The tumor microenvironment of DLBCL in the computational era. *Front Oncol.* 2020;10:351.
4. Jin X, Wei M, Wang S, et al. Detecting fibroblast activation proteins in lymphoma using $^{68}$Ga-FAPI PET/CT. *J Nucl Med.* 2022;63:212–217.
5. Gisselbrecht C, Glass B, Mounier N, et al. Salvage regimens with autologous transplantation for relapsed large B-cell lymphoma in the rituximab era. *J Clin Oncol.* 2010;28:4184–4190.
6. Crump M, Neelapu SS, Farooq U, et al. Outcomes in refractory diffuse large B-cell lymphoma: results from the international SCHOLAR-1 study. *Blood.* 2017;130:1800–1808.
7. Neelapu SS, Locke FL, Bartlett NL, et al. Axicabtagene ciloleucel CAR T-cell therapy in refractory large B-cell lymphoma. *N Engl J Med.* 2017;377:2531–2544.
8. Chow VA, Gopal AK, Maloney DG, et al. Outcomes of patients with large B-cell lymphomas and progressive disease following CD19-specific CAR T-cell therapy. *Am J Hematol.* 2019;94:E209–E213.



**Priscilla Guglielmo***
**Laura Evangelista**
**Veneto Institute of Oncology*
*Padua, Italy*
*E-mail: priscilla.guglielmo@iov.veneto.it*



Published online Feb. 1, 2024.
DOI: 10.2967/jnumed.123.266939


**REPLY:** We thank Dr. Guglielmo and Dr. Evangelista for the great summary and thoughtful comments regarding our paper (*1*). We agree that there is still much to discover regarding the role of fibroblast activation protein (FAP) inhibitor (FAPI)–based radiotracers in hematology—for example, the relationship between FAPI avidity and prognosis and the correlation of heterogeneous and relapsed or refractory lymphomas.

Several recent studies have revealed the distribution of fibrosis in nodular sclerosis Hodgkin lymphoma, follicular lymphoma, and diffuse large B-cell lymphoma (*2–4*). We accidentally found that primary gastric lymphoma could accumulate $^{68}$Ga-labeled FAPI, which highlighted that $^{68}$Ga-FAPI is not cancer-specific (*5*). Most aggressive lymphomas were FAPI-avid, whereas indolent non-Hodgkin lymphoma lesions showed weak FAP staining and mild to moderate $^{68}$Ga-FAPI uptake (*6*). These results are partially consistent with the result of Tataroglu et al., which provided quantitative information about the amount of fibrosis in lymphoma lesions (*2*). The focus is now to determine which is the superior method, $^{68}$Ga-FAPI PET/CT or $^{18}$F-labeled FDG PET/CT in indolent lymphoma. Compared with FAP expression in stromal cells, glycolytic markers with high cell density were overexpressed in tumors and the tumor microenvironment, resulting in higher rates of detecting lymphoma lesions. However, our result was not very convincing because of the limited number and heterogeneity of patient population, especially the indolent type.

The ability to detect fibrosis before and after treatment with $^{68}$Ga-FAPI PET/CT could be the basis for planning prospective studies compared with treatment with $^{18}$F-FDG PET/CT. A prospective study showed that the presence of tumor sclerosis was significantly associated with poor overall survival of patients with advanced-stage nodal follicular lymphoma (*7*). As Dr. Guglielmo and Dr. Evangelista suggested, a large-scale, well-defined, prospective study should be designed in a homogeneous group to explore the potential role of $^{68}$Ga-FAPI PET/CT and the relationship between PET performance, heterogeneity, and prognostic value before and after treatment.

Malignancy theranostics is a novel approach that combines diagnostic imaging and radionuclide therapy. Only a few proof-of-concept studies have been published for FAP-targeted radioligand therapies, radiolabeled with $^{131}$I, $^{90}$Y, and $^{177}$Lu, which showed mixed responses (*8–10*). It is valuable to explore the role of FAP-targeted radionuclide therapy in refractory lymphoma patients, especially in aggressive lymphomas. Also, combination therapies of FAP-targeted radionuclide therapy and immunotherapy could be explored in relapsed or refractory aggressive non-Hodgkin lymphoma.

Overall, FAPI-based imaging and theranostics have been a highly vibrant research field over the past few years and have been the vanguard of personalized medicine. Beforehand, future larger-scale studies should be conducted to explore the diagnostic and therapeutic value of FAPI-targeted imaging and theranostics in hematology. We hope that our study arouses some interest in this research field.

## REFERENCES


1. Chen X, Wang S, Lai Y, et al. Fibroblast activation protein and glycolysis in lymphoma diagnosis: comparison of $^{68}$Ga-FAPI PET/CT and $^{18}$F-FDG PET/CT. *J Nucl Med.* 2023;64:1399–1405.
2. Tataroglu C, Sarioglu S, Kargi A, Ozkal S, Aydin O. Fibrosis in Hodgkin and non-Hodgkin lymphomas. *Pathol Res Pract.* 2007;203:725–730.
3. Lohneis P, Wienert S, Klauschen F, Anagnostopoulos I, Jöhrens K. Fibrosis in low-grade follicular lymphoma: a link to the TH2 immune reaction. *Leuk Lymphoma.* 2017;58:1190–1196.
4. Fukushima H, Ohsawa M, Ikura Y, et al. Mast cells in diffuse large B-cell lymphoma: their role in fibrosis. *Histopathology.* 2006;49:498–505.
5. Wang G, Jin X, Zhu H, et al. $^{68}$Ga-NOTA-FAPI-04 PET/CT in a patient with primary gastric diffuse large B cell lymphoma: comparisons with $^{18}$F-FDG PET/CT. *Eur J Nucl Med Mol Imaging.* 2021;48:647–648.
6. Jin X, Wei M, Wang S, et al. Detecting fibroblast activation proteins in lymphoma using $^{68}$Ga-FAPI PET/CT. *J Nucl Med.* 2022;63:212–217.
7. Klapper W, Hoster E, Rölver L, et al. Tumor sclerosis but not cell proliferation or malignancy grade is a prognostic marker in advanced-stage follicular lymphoma: the German Low Grade Lymphoma Study Group. *J Clin Oncol.* 2007;25:3330–3336.
8. Ma H, Li F, Shen G, et al. Synthesis and preliminary evaluation of $^{131}$I-labeled FAPI tracers for cancer theranostics. *Mol Pharm.* 2021;18:4179–4187.
9. Rathke H, Fuxius S, Giesel FL, et al. Two tumors, one target: preliminary experience with $^{90}$Y-FAPI therapy in a patient with metastasized breast and colorectal cancer. *Clin Nucl Med.* 2021;46:842–844.
10. Ballal S, Yadav MP, Moon ES, et al. First-in-human results on the biodistribution, pharmacokinetics, and dosimetry of $^{177}$Lu-DOTA.SA.FAPi and $^{177}$Lu-DOTA-GA.(SA.FAPi)$_2$. *Pharmaceuticals (Basel).* 2021;14:1212.



**Xuetao Chen**
**Xuejuan Wang***
*Peking University Cancer Hospital and Institute*
*Beijing, China*
**E-mail: xuejuan_wang@hotmail.com*



Published online Feb. 1, 2024.
DOI: 10.2967/jnumed.123.266989

## Aruna Bodapati Gambhir, 1962–2023

Aruna Bodapati Gambhir passed away at the age of 61 on Wednesday, November 29, 2023, after a long battle with breast cancer. Preceded in death by her husband, Sam, and their son, Milan, she was the last remaining member of the very special Gambhir family. Aruna is survived by her nieces and her nephew: Deepika, Sandhya, and Sunil Bodapati.

Aruna was born on February 4, 1962, in Bangalore and moved with her family to the United States in 1975 after spending 10 years in England. She received a bachelor's degree in biochemistry at the University of California, Berkeley, a master's degree in computer science at Santa Clara University, and an MBA from UCLA. She had a successful career in software development and executive leadership, including her role as chief executive officer of CellSight, a company focused on commercializing PET imaging tracers to visualize the immune status of patients.

There were many facets of the Aruna we knew.

There was the brilliant, witty, and immensely compassionate woman who perfectly matched her husband's intellect and passion for life, people, and purpose. In Sam's most memorable moments, Aruna was there not only as an inspiration for him but as a force of nature in her own right. It was always Sam and Aruna, Aruna and Sam. They were brilliant together, and we loved her as much as we loved and admired him. She was a tower of strength, a change agent, a sharp thinker, and an incredibly genuine person with a sassy sense of humor. She had a bold way of living—a characteristic that inspired and energized those around her. If you went to Aruna with a problem, whether it was about science, business, or life, she would get straight to the heart of the matter without wasting a moment. She wouldn't hold back, especially if the issue was one most people would be afraid to call out or tackle. She operated from a place of urgency to find solutions for the people she cared about and to make progress in medicine.

Then there was the Aruna after Milan passed away. The unimaginable loss of a child, an extraordinary child, transformed Aruna's wicked sense of humor and joie de vivre into a sadder, wry, and darker reflection of life. Her purpose was redirected to understanding "why" and how to make sure no other parent ever lost a child to cancer again. It was a testimony to her strength and intelligence that she had great success, of her own volition, in understanding this question, though at times it seemed that it may have come at the expense of her light and love for life.

And finally, there was the Aruna after Sam. She was still purposeful but was dealing with so much loss and heartache. As her health deteriorated, it was almost as though the longing to be with the great loves of her life—Sam and Milan—slowly took her away from us. Incredibly, even in this stage of her life, she put her own unfathomable grief aside to support Sam's former lab members (his "kids"), trainees, and colleagues. During what one could only imagine as the darkest of days, Aruna would tirelessly call each lab member individually to check on them, listen, and see how she could help. She provided honest advice and practical help on the next steps in their careers and supported them through their sadness while, in some cases, cooking them a dosa in her Portola Valley home.

Not only was Aruna a woman of action when it came to helping Sam's lab members find jobs and make tough decisions to improve the quality of their lives, but she also did everything she could to ensure that her late husband's vision and wishes were fulfilled. She built a house that Sam designed while he was ill. Importantly to our Stanford community, Aruna also did everything in her power to ensure that the second cyclotron and the expansion of the radiochemistry program went ahead. She met with countless people, learned about every detail of what was planned and what needed to be done, and didn't take no for an answer. Without Aruna's determination, Sam's vision for this second facility, and all the research and discoveries that will emerge as a result of its completion, would not have seen the light of day.

We are forever indebted to Aruna for her courageous, bold, and selfless acts. We thank her for always reminding us to get busy living and, without delay, to do the things that matter the most to us.

Although we miss her dearly, we will forever be inspired by her strength, her love for her family, her resilience, her ability to care and fight for others and help so many around her no matter what she was going through. She was truly a unique human being who has left an indelible mark on all who knew her.

We all love the Gambhir family. We all love Aruna. Aruna, Milan, and Sam are together now. We hope she has regained that smile that could light up a room, that throaty chuckle that infected us with laughter.

Aruna, we hope you have found peace.

**Christian Behrenbruch**
**Andrei Iagaru***
**Michelle L. James**
*Stanford University*
*Stanford, California*
**E-mail: aiagaru@stanford.edu*


Images courtesy of Sandip Biswal.

Published online Feb. 8, 2024.
DOI: 10.2967/jnumed.124.267375

# WHAT IS AN SNMMI RPT **CENTER OF EXCELLENCE?**

To learn more and apply, visit
**www.snmmi.org/RPTCOE**

SNMMI created the Radiopharmaceutical Therapy (RPT) Center of Excellence (COE) Program to allow centers with expertise in RPT to showcase their capabilities and services, including research. A designation means that your site has the personnel, expertise, and equipment to manage the care of patients requiring RPT. The designations levels are Comprehensive, Clinical, or Basic Therapy Center.

Targeted RPTs are changing the way patients with cancer are treated. These advances have allowed providers to treat and manage a multitude of other cancers and diseases. Not all sites have the expertise to use these agents clinically or in clinical trials.

If your site has experience with one or more radiopharmaceutical therapies, we encourage you to apply for the SNMMI RPTCOE designation.


## COMPREHENSIVE RPT CENTER

An application fee of $1,500 for members and $2,500 for non-members is required for a 2-year designation.

SCAN QR CODE TO APPLY


## CLINICAL RPT CENTER

An application fee of $900 for members and $1,500 for non-members is required for a 2-year designation.

SCAN QR CODE TO APPLY


## BASIC RPT CENTER

The designation does not require any application fee and is valid for a 2-year designation.

SCAN QR CODE TO APPLY

012024-9

SCAN QR CODE FOR
MORE INFORMATION

Innovate. Illuminate.

June 8-11
2024

# SNMMI ANNUAL MEETING

CANADA
TORONTO

The premier educational, scientific, research, and networking event in nuclear medicine and molecular imaging, the SNMMI Annual Meeting provides physicians, technologists, pharmacists, laboratory professionals, and scientists with an indepth view of the latest research and development in the field as well as providing insights into practical applications for the clinic.

Mark your calendars to join us in **Toronto, June 8-11, 2024**, for a front-row seat to explore the most important nuclear medicine and molecular imaging science and research happening throughout the world.

**www.snmmi.org/am**

**Registration is Now Open**

SNMMI SOCIETY OF NUCLEAR MEDICINE & MOLECULAR IMAGING
ANNUAL MEETING

022024-19

3/24

The Journal of Nuclear Medicine

March 2024 ▪ Vol. 65 ▪ Pages 337–498